

Mechanisms and Machine Science 46

Burkhard Corves
Erwin-Christian Lovasz
Mathias Hüsing
Inocentiu Maniu
Corina Gruescu *Editors*

New Advances in Mechanisms, Mechanical Transmissions and Robotics

Proceedings of
The Joint International Conference of the
XII International Conference on Mechanisms
and Mechanical Transmissions (MTM) and the
XXIII International Conference on Robotics
(Robotics '16)

Mechanisms and Machine Science

Volume 46

Series editor

Marco Ceccarelli

LARM: Laboratory of Robotics and Mechatronics

DICeM: University of Cassino and South Latium

Via Di Biasio 43, 03043 Cassino (Fr), Italy

e-mail: ceccarelli@unicas.it

More information about this series at <http://www.springer.com/series/8779>

Burkhard Corves · Erwin-Christian Lovasz
Mathias Hüsing · Inocentiu Maniu
Corina Gruescu
Editors

New Advances in Mechanisms, Mechanical Transmissions and Robotics

Proceedings of The Joint International
Conference of the XII International
Conference on Mechanisms and Mechanical
Transmissions (MTM) and the XXIII
International Conference on Robotics
(Robotics '16)

 Springer

المنارة للاستشارات

Editors

Burkhard Corves
RWTH Aachen University
Aachen
Germany

Inocentiu Maniu
University Politehnica of Timisoara
Timișoara
Romania

Erwin-Christian Lovasz
University Politehnica of Timisoara
Timișoara
Romania

Corina Gruescu
University Politehnica of Timisoara
Timișoara
Romania

Mathias Hüsing
RWTH Aachen University
Aachen
Germany

ISSN 2211-0984
Mechanisms and Machine Science
ISBN 978-3-319-45449-8
DOI 10.1007/978-3-319-45450-4

ISSN 2211-0992 (electronic)
ISBN 978-3-319-45450-4 (eBook)

Library of Congress Control Number: 2016950582

© Springer International Publishing AG 2017

This work is subject to copyright. All rights are reserved by the Publisher, whether the whole or part of the material is concerned, specifically the rights of translation, reprinting, reuse of illustrations, recitation, broadcasting, reproduction on microfilms or in any other physical way, and transmission or information storage and retrieval, electronic adaptation, computer software, or by similar or dissimilar methodology now known or hereafter developed.

The use of general descriptive names, registered names, trademarks, service marks, etc. in this publication does not imply, even in the absence of a specific statement, that such names are exempt from the relevant protective laws and regulations and therefore free for general use.

The publisher, the authors and the editors are safe to assume that the advice and information in this book are believed to be true and accurate at the date of publication. Neither the publisher nor the authors or the editors give a warranty, express or implied, with respect to the material contained herein or for any errors or omissions that may have been made.

Printed on acid-free paper

This Springer imprint is published by Springer Nature
The registered company is Springer International Publishing AG
The registered company address is: Gewerbestrasse 11, 6330 Cham, Switzerland

Preface

The present book gathers up-to-date contributions in the field of mechanisms, mechanical transmissions, robotics and mechatronics. The topics developed within this volume are as follows: analysis and synthesis of mechanisms, dynamics of mechanisms and machines, mechanical transmissions, biomechanics, precision mechanics, mechatronics, micromechanisms and microactuators, computational and experimental methods, CAD in mechanism and machine design, mechanical design of robot architecture, parallel robots, mobile robots, micro- and nanorobots, sensors and actuators in robotics, intelligent control systems, biomedical engineering, teleoperation, haptics and virtual reality.

The results reported in the papers were discussed at MTM & Robotics 2016—The Joint International Conference of the XII International Conference on Mechanisms and Mechanical Transmissions (MTM) and the XXIII International Conference on Robotics (Robotics), held in Aachen, Germany, on 26 October–27 October 2016. All 58 submitted contributions were carefully reviewed and selected for the presentation and publication by independent reviewers and the members of the International Scientific Committee. As a result of the two-stage review process, 49 contributions were selected for the presentation at the conference and publication in this book.

The previous editions of the two conferences were held in Romania, beginning in 1972, every four years until 2012, when the joint international conference was organized outside Romania for the first time at Institute Pascal, Clermont-Ferrand, France.

MTM & Robotics 2016 was organized by the Department of Mechanism Theory and Dynamics of Machines at RWTH Aachen University and the Department of Mechatronics at University Politehnica Timisoara, with the support of IFToMM Germany, the Romanian Association for Theory of Machines and Mechanisms (ARoTMM) and the Robotics Society of Romania (RSR).

We are grateful to the authors for their contributions and to the reviewers for their recommendations as improvement guidance for the selected papers. Special thanks go to our Keynote speakers, Prof. Gosselin (University Laval), Prof. Schmitt (RWTH Aachen University), Dr. Nefzi (Carl Zeiss AG) and Dr. Harmeling

(Karl Mayer GmbH), for their valuable and inspiring contributions to the scientific programme. We would like to express thanks to the International Federation for the Promotion of Mechanism and Machine Science (IFToMM) and to the Robotics Society of Romania (RSR). We also thank to the members of the Organizing Committee of MTM & Robotics 2016 and to Springer Publishers for their excellent technical and editorial support.

Aachen, Germany
Timișoara, Romania
Aachen, Germany
Timișoara, Romania
Timișoara, Romania
June 2016

Burkhard Corves
Erwin-Christian Lovasz
Mathias Hüsing
Inocentiu Maniu
Corina Gruescu

Organization

Conference Chairman

Burkhard Corves, RWTH Aachen University, Germany

Conference Co-chairmen

Erwin-Christian Lovasz, University Politehnica of Timisoara, Romania

Inocentiu Maniu, University Politehnica of Timisoara, Romania

Mathias Hüsing, RWTH Aachen University, Germany

International Scientific Committee

Oscar Altuzarra, University of the Basque Country, Spain

Jorge Angeles, McGill University, Canada

Virgil Atanasiu, Technical University of Iași, Romania

Radu Balan, Technical University of Cluj-Napoca, Romania

Stelian Brad, Technical University of Cluj-Napoca, Romania

Cornel Brișan, Technical University of Cluj-Napoca, Romania

Tobias Bruckmann, University Duisburg-Essen, Germany

Giuseppe Carbone, University of Cassino and South Latium, Italy

Marco Ceccarelli, University of Cassino and South Latium, Italy

Dorian Cojocaru, University of Craiova, Romania

Valer Dolga, Politehnica University Timisoara

Ioan Doroftei, Technical University of Iași, Romania

Mehmet Ismet Can Dede, Izmir Institute of Technology, Turkey

Jean-Christophe Fauroux, SIGMA Clermont

Grigore Gogu, SIGMA Clermont

Antoni Gronowicz, Wroclaw University of Technology, Poland

Mircea Ivănescu, Robotics Society of Romania

Nicolae Joni, Robcon TM SRL, Romania

Andres Kecskemethy, University Duisburg-Essen, Germany
 Chin-Hsing Kuo, National Taiwan University of Science and Technology, Taiwan
 Silviu Dan Mandru, Technical University of Cluj-Napoca, Romania
 Gheorghe Mogan, Transilvania University of Brasov, Romania
 Andreas Mueller, Johannes Kepler University, Austria
 Vistrian Mătieș, Technical University of Cluj-Napoca, Romania
 Mircea Neagoe, Transilvania University of Brasov, Romania
 Mircea Nitulescu, University of Craiova, Romania
 Nenad D. Pavlovic, University of Nis, Serbia
 Dan Perju, Technical University of Timisoara, Romania
 Victor Petuya, University of the Basque Country, Spain
 Doina Pisla, Technical University of Cluj-Napoca, Romania
 Iulian Tăbăra, Technical University of Bucharest, Romania
 Yukio Takeda, Tokyo Institute of Technology, Japan
 Radu Tarca, University of Oradea, Romania
 Hidetsugu Terada, University of Yamanashi, Japan
 Ioan Vela, University "Eftimie Murgu" of Reșița, Romania
 Ion Visa, Transilvania University of Brasov, Romania
 Yao Yan-An, Beijing Jiaotong University, China
 Song Lin, Tongji University, China

Organizing Committee

Claudia Cornely, RWTH Aachen University, Germany
 Stefan Kurtenbach, RWTH Aachen University, Germany
 Iosif Cărăbaș, University Politehnica of Timisoara, Romania
 Valentin Ciupe, University Politehnica of Timisoara, Romania
 Corina Gruescu, University Politehnica of Timisoara, Romania
 Dan Teodor, Margineanu University Politehnica of Timisoara, Romania
 Cristian Moldovan, University Politehnica of Timisoara, Romania

Under the Patronage of IFToMM

Teresa Zielinska, Secretary-General of IFToMM
 Erwin-Christian Lovasz, Chair of the Technical Committee for Linkages and Mechanical Controls

With the Support of

Andres Kecskemethy, Chair of IFToMM Germany
 Ioan Doroftei, Chair of the Romanian Association for Theory of Machines and Mechanisms (ARoTMM)
 Mircea Ivănescu, Chair of the Robotics Society of Romania (SRR)
 DFG Germany, German Research Foundation

Contents

Part I MTM—Mechanisms—Analysis and Synthesis

Optimal Design of a Grasping Device Through Simplified Pose Synthesis of a Four-Bar Linkage	3
V. Mesaros-Anghel, E.-C. Lovasz, C.M. Gruescu and C.E. Moldovan	
Modified Method of the Kinematic Analysis of Planar Linkage Mechanism for Non-stationary Motion Modes	15
J. Drewniak, P. Garlicka, J. Kopeć and S. Zawisłak	
A Type Synthesis Method for Parallel Mechanisms Based on SAKCs	25
Huiping Shen, Chi-Yu Sun, Dan Zhang and Ting-li Yang	
Matlab GUI for SVAJ Cam Analysis Diagrams	37
C. Pop, E.-C. Lovasz, F. Pop, A. Davidescu and S.M. Grigorescu	
On the Kinematic Analysis of a Sixth Class Mechanism	47
C.E. Moldovan, D. Perju, E.-C. Lovasz, K.-H. Modler and I. Maniu	
Zero-Free-Length Elastic Systems for Static Balancing	59
L. Ciupitu and I. Simionescu	
Analytic and FEM Study of Load Distribution on the Length of Spline Joints Under Pure Torque	69
D. Mărgineanu, C. Sticlaru, A. Davidescu and E. Mărgineanu	
Dimensional Synthesis of Planar Parallel Manipulator Using Geared Linkages with Linear Actuation as Kinematic Chains	77
S.M. Grigorescu, E.-C. Lovasz, D.T. Mărgineanu, C. Pop and F. Pop	

Part II MTM—Dynamics of Mechanisms and Machines

The Concept of Natural Motion for Pick and Place Operations 89
J.P. Barreto, F. J.-F. Schöler and B. Corves

**Structural Synthesis of Planar Geared Linkage Mechanisms
as Multibody Systems** 99
I. Visa, M. Neagoe and M.D. Moldovan

**Dynamics of a Vertical Unbalanced Gyroscopic Rotor
with Nonlinear Characteristics** 107
Zh. Iskakov

Part III MTM—Mechanical Transmissions

Edge Tooth Addendum Thickness of Hindley Worm 117
Yaping Zhao

A Single Speed (CVT) Transmission 125
K. Ivanov, B. Tultayev and G. Balbayev

**An Approach for Modelling Harvester Head Mechanism
in the Harvesting Process of Hardwood Stands** 133
B. Hatton, B.C. Bouzgarrou, J.-C. Fauroux, V. Gagnol and G. Gogu

Novel Speed Increaser Used in Counter-Rotating Wind Turbines 143
M. Neagoe, R. Saulescu, C. Jaliu and N. Cretescu

Part IV MTM—Micromechanisms and Microactuators

**On Application Melnikov Method to Detecting the Edge
of Chaos for a Micro-Cantilever** 155
J. Xie, S.-H. He, Z.-H. Liu and Y. Chen

Part V MTM—Computational and Experimental Methods

**Use of the *Structomatic* Method to Perform the Forward Kinematic
and Kinetostatic Analyses of a Hydraulic Excavator** 167
M. Mailloux, M. Éné, I. Simionescu and I. Tabara

**Application of a Cam Workbench for Education in Mechanical
Engineering** 177
H. Chen, T.T.N. Nguyen, M. Müller, S. Kurtenbach, C. Pan, M. Hüsing
and B. Corves

**Kinematic Characterization of the Origami Spring Based
on a Spherical 6R Linkage** 187
Hiroshi Matsuo, Daisuke Matsuura, Yusuke Sugahara and Yukio Takeda

Scaled Test Stand Simulation for Studying the Behavior of Anti-lock Brake Systems on Bumpy Roads	197
V. Ciupe, D. Mărgineanu and E.-C. Lovasz	
Part VI MTM—Terminology	
Activities of Russian—Speaking Scientists in Development of MMS Terminology	209
V.E. Starzhinsky, E.V. Shalobaev, M.M. Kane and V.I. Goldfarb	
State of Art in Separate Sections of MMS Terminology and Some Proposals	217
E.V. Shalobaev, S.V. Shil'ko, R.T. Tolocka, V.E. Starzhinsky, G.N. Iurkova and D.G. Surikov	
Part VII Robotics—Mechanical Design of Robot Architecture	
Design Solutions to Simplify the Calibration of a Robotic Flexible Manufacturing System	229
A.-M. Stoian, I. Maniu, E.-C. Lovasz and C.M. Gruescu	
Part VIII Robotics—Mobile Robots	
Reconbot: A Reconfigurable Rescue Robot Composed of Serial-Parallel Hybrid Upper Humanoid Body and Track Mobile Platform	241
W. Ding, T. Detert, B. Corves and Y.A. Yao	
Kinematics Modelling of Mobile Robot with Articulated Limbs Without Wheel Slip	251
P. Sperzyński and A. Gronowicz	
Experimental Platform for Hexapod Locomotion	259
M. Nițulescu, M. Ivănescu, S. Mănoiu-Olaru and V.D.H. Nguyen	
Quadcopter Propeller Design and Performance Analysis	269
Endrowednes Kuantama, Dan Craciun, Ioan Tarca and Radu Tarca	
A Method for Structural Synthesis of Cooperative Mobile Manipulators	279
Z.-E. Chebab, J.-C. Fauroux, G. Gogu, N. Bouton, L. Sabourin and Y. Mezouar	
Mobile Robot Used to Collect Data from a Difficult Access Area	287
R. Zemouri and P.C. Patie	

Part IX Robotics—Parallel Robots

Extended Procedure for Stiffness Modeling Based on the Matrix Structure Analysis	299
T. Detert and B. Corves	

Translational Parallel Manipulator with Pa² Kinematic Joints	311
A. Hernandez, Z. Zhang, V. Petuya, E. Macho and E. Amezua	

Synthesis and Modeling of Redundantly Actuated Parallel Kinematic Manipulators—An Approach to Efficient Motion Design . . .	321
T. Haschke, M. Lorenz, J. Brinker, M. Hüsing and B. Corves	

6-PSS Based Parallel Manipulators	331
T.A. Dwarakanath, K.D. Lagoo and D.N. Badodkar	

Part X Robotics—Sensors and Actuators in Robotics

Compliant Rotary Actuator Driven by Shape Memory Alloy	343
H. Yuan, X. Balandraud, J.C. Fauroux and F. Chapelle	

Modelling and Simulation of Linear Actuators in Mechatronic Systems	351
V. Dolga, L. Dolga and C. Moldovan	

Part XI Robotics—Robotic Control Systems

Dynamic Control for a Class of Continuum Robotic Arms	361
M. Ivanescu, M. Nitulescu, V.D.H. Nguyen and M. Florescu	

Actuator Design for Stabilizing Single Tendon Platforms	371
D. Haarhoff, M. Kolditz, D. Abel and S. Brell-Cokcan	

Model-Based Stability Prediction of a Machining Robot	379
S. Mousavi, V. Gagnol, B.C. Bouzgarrou and P. Ray	

Part XII Robotics—Biomedical Engineering

Augmented PID Control of a 2PPR-2PRP Planar Parallel Manipulator for Lower Limb Rehabilitation Applications	391
J.K. Mohanta, M. Santhakumar, S. Kurtenbach, B. Corves and M. Hüsing	

Human Motion Characterization Using Wireless Inertial Sensors	401
M. Olinski, A. Gronowicz, M. Ceccarelli and D. Cafolla	

Trajectory Analysis for Modified Jansen Leg Mechanism Configuration	409
F. Pop, E.-C. Lovasz, C. Pop, V. Dolga and S.M. Grigorescu	

Development of an Assisting Instrument of Standing-Up Motion Using Driving Springs for Elderly Persons	417
H. Terada, K. Makino, K. Ishida and M. Ichikawa	
An Evolutionary Computational Algorithm for Trajectory Planning of an Innovative Parallel Robot for Brachytherapy	427
F. Gîrbacia, D. Pîslă, S. Butnariu, B. Gherman, T. Gîrbacia and N. Plitea	
Inverse Kinematics and Dynamics of an Overconstrained Manipulator for Upper Extremity Rehabilitation	437
Ö. Selvi and K. Yilmaz	
Part XIII Robotics—Teleoperation, Haptics, Virtual Reality	
Image Processing Based Stiffness Mapping of a Haptic Device	447
B. Taner and M.İ.C. Dede	
Part XIV Robotics—Compliant Structures	
Kinematic Analysis of a Flexible Tensegrity Robot	457
O. Altuzarra, M. Diez, J. Corral and F.J. Campa	
Adaptive Compliant Gripper Finger with Embedded Contracting and Extending Actuators	465
A. Milojević, N.D. Pavlović and H. Handroos	
Kinematic and Dynamic Analysis of a 4DOF Parallel Robot with Flexible Links	473
N. Cretescu, M. Neagoe and R. Saulescu	
Part XV Robotics—Robotic Applications	
Automated Handling and Draping of Reinforcing Textiles—Challenges and Developments	485
J. Brinker, I. Prause, P. Kosse, H.-C. Früh, S. Printz, C. Henke, M. Hüsing, B. Corves, R. Schmitt, T. Gries and S. Jeschke	
Author Index	495

Abstracts of Keynote Speeches

Mechanism Synthesis and Design for Low-Impedance Human–Robot Interaction Based on Under-Actuated Redundancy

Clément Gosselin

Département de Génie Mécanique, Université Laval, Canada

Clement.Gosselin@gmc.ulaval.ca

This presentation addresses the synthesis of passive mechanisms that are used as a mechanical interface between a human operator and an active robotic system for physical human–robot interaction. This approach results in under-actuated redundant robots which provide a very intuitive physical interface to human operators by allowing them to display their own mechanical impedance and by decoupling the human and the robot dynamics. A serial architecture is first presented that makes use of modified straight-line Chebyshev mechanisms and of the Sarrus mechanism. Gravity is used to produce the self-centring of the Chebyshev mechanisms, while the Sarrus mechanism, used for the vertical motion, is balanced using a spring system. An alternative approach based on a three-degree-of-freedom decoupled translational parallel mechanism (the Tripteron) is then presented. It is shown that the use of the Tripteron leads to a compact and effective design. Experimental demonstrations of the mechanisms are presented.

The Demanding Implications of Nanolithography for High-Precision Opto-Mechanical Systems

Marwène Nefzi

ZEISS SMT GmbH, Oberkochen, Germany
marwene.nefzi@zeiss.com

The fabrication of complex integrated circuits needed for modern electronic devices involves different processes that aim at building billions of transistors on a semiconductor substrate (e.g. silicon wafer). Photolithography is the core process of the semiconductor manufacturing technology, since it is the key enabler for closer packing of transistors and smaller feature size. It mainly consists in projecting an image of the mask through high-performance optics onto a wafer before stepping it to a new position. This assumes not only optical systems with minimum aberrations, but also the adequate mounting and manipulation of optical elements. On the one hand, 6 DoF adjustments are required without deformations of the optical elements. On the other hand, the mounting and manipulation of the optical elements should be insensitive to different dynamic and thermal disturbances. In this presentation, we will present some generic design tasks that arise from the design and development of kinematic and dynamic architectures that make up opto-mechanical systems for nanolithography.

Metrology-Enabled Adaptive Robotic Control in Industrial Assembly

Robert Schmitt

Chair of Metrology and Quality Management
RWTH Aachen University, Germany
R.Schmitt@wzl.rwth-aachen.de

Recent developments in large-scale metrology systems and automation towards increased connectivity and interoperability facilitate their use within process control of robotic assembly systems. The metrology systems are used to obtain information on part geometry or robotic pose as input for model-based process control. Using two examples, the benefits of increased flexibility, productivity, and quality are illustrated. One example focusses on fixtureless aircraft primary structure assembly by incorporating a component deformation model into the robot controller to determine robot movements to compensate deviations and achieve nominal geometry. A second example presents a model predictive control approach to enable a robotic assembly process of a windscreen onto a moving truck cabin using iGPS. Furthermore, a vision for a fix-point free assembly system for large products based on mobile robots and metrology-assisted model-based control and the associated technical requirements is presented.

Dimensioning and Optimization of High-Precision and High-Dynamic Mechanisms

Frank Harmeling

Karl Mayer Textilmaschinenfabrik, Obertshausen, Germany

Frank.Harmeling@karlmayer.com

This keynote speech delivers insight into the model-based development of mechanisms that fulfil a highly precise motion at high production speed. One essential aspect is the interdisciplinary modelling of a system consisting of a mechanism with elasticities, the electric drive and the closed loop control. The total system model consists of finite element subsystems and multibody subsystems as well as analytic equations. Although all machines are similar, each machine development aiming at the increase of customer value has got its individual challenges. Therefore, another essential aspect is the individual adaption of the dimensioning and optimization process to fulfil the complex requirements regarding speed, durability, manufacturing costs and functional aspects. The process has to focus on the individual question that has to be answered, respectively, on the decision that has to be taken. This affords a flexible configuration of the partial models, an adequate detailing of the models and an adaption of the proceeding.

Part I
MTM—Mechanisms—Analysis
and Synthesis

Optimal Design of a Grasping Device Through Simplified Pose Synthesis of a Four-Bar Linkage

V. Mesaros-Anghel, E.-C. Lovasz, C.M. Gruescu and C.E. Moldovan

Abstract The paper shows the optimal synthesis of grasping device design based on the Chebyshev spacing method. The original grasping device uses two symmetrical four-bar linkages with opposite motion of the jaws fixed on the coupler. The goal of the study is the development of a grasping device with minimal error of the axial centering, which reduces the synthesis to a four-pose one for the four-bar linkage. In order to minimize the centering error of the grasping device an equivalent Chebyshev spacing method for establishing the synthesis poses is used. A simplified pose synthesis method for the grasping four-bar linkage is developed. The both deviations of the axial centering errors (without spacing and with spacing) for the obtained linkage are indicated and analyzed.

Keywords Grasping device · Four-bar linkage · Four-pose synthesis · Centering error

1 Introduction

The grasping devices are end-effectors of the manipulating robots, described and analyzed by several authors (ex. [1, 2]), on different criteria such as kinematic scheme, construction, technical characteristics and cost-effectiveness. A very

V. Mesaros-Anghel · E.-C. Lovasz (✉) · C.M. Gruescu · C.E. Moldovan
Universitatea Politehnica, Timișoara, Romania
e-mail: erwin.lovasz@upt.ro

V. Mesaros-Anghel
e-mail: voicu.mesaros-anghel@upt.ro

C.M. Gruescu
e-mail: corina.gruescu@upt.ro

C.E. Moldovan
e-mail: cristian.moldovan@upt.ro

up-to-date and complete description and classification of the concepts, principles and design of the grasping devices are given in [3, 4].

In comparison with a human hand (100 % dexterity), a two-finger grasping device still retains 40 % dexterity and, furthermore, satisfies many criteria (simple, cheap, functionally intelligent). This is the reason why most of the grasping devices feature two fingers, in a structure including a “carrying mechanism” and an “actuating mechanism”. An intelligent trait in grasping devices functioning is centering (along with the axis of the manipulated cylindrical parts). This type of functioning is analyzed in [5–10]. Still, for special applications, which require fine motion, complex structures containing more human-like fingers are already developed and controlled [11, 12]. Recent researches also pursue the achievement of specific grasping devices to work with soft robots, which must perform gentle tasks [13], or for handling heavy elastic objects [14]. The underactuated grasp is also a subject in regard with design, kinematic analysis and control for simple or complex anthropomorphic structures [15–18].

The authors of the paper consider that the synthesis of the grasping devices should satisfy several conditions regarding structure, design and centering precision: to eliminate higher pair, to avoid, as much as possible, the prismatic joints and to minimize the centering errors of the carrying mechanisms included in the grasping mechanisms. But, also other design aspects as grasping stability, friction, compliance and dynamics can be taken into account as optimization criteria [19].

The paper aims the synthesis of a mechanism, associated to a two-fingers grasping device, optimized in regard with minimizing the centering errors by using Chebyshev spacing of the jaws poses, using only rotational joints (without the actuator motion) and simplifying the synthesis method of the four-bar linkage.

2 Structure and Actuation Design

Pursuing the goal of centering, the idea of carrying two prismatic jaws between two limit diameters was taken into account, as represented in Fig. 1.

The assurance of centering should be achieved for a finite number of poses of the manipulated parts, as shown in Fig. 2.

Carrying of the prismatic jaws (symmetrically to the x – axis) can be achieved like in Fig. 3, by two four-bar mechanisms (A_0ABB_0 and $A'_0A'B'B'_0$), actuated by the actuating mechanism (D_0DC and its symmetrical $D_0D'C'$). Similar schemes are described in [7] for tweezers-jaws without centering, in [4] for roller-jaws with centering only for two positions, in [8, 9] where the carrying mechanisms are complicated and, therefore, expensive, including the use of higher pairs.

The synthesis of the four-bar linkage for two and three precision points is presented in [1]. The first optimization of the grasping device would result from a “particular four-position synthesis” approach. It will be further shown that the five-pose synthesis, which is the highest applicable to four-bar linkages, does not

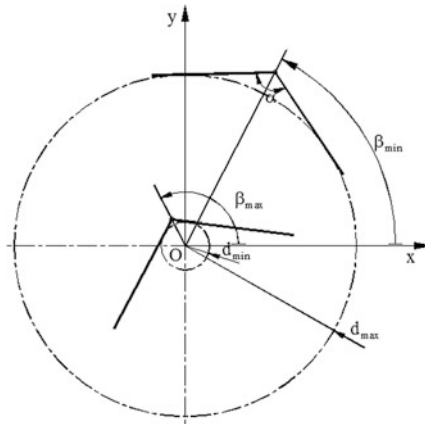


Fig. 1 The limit diameters of the prismatic jaws

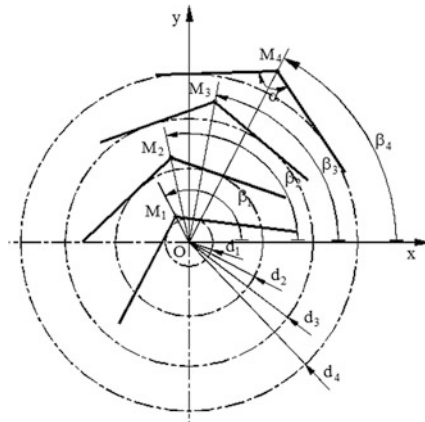


Fig. 2 The finite poses of the prismatic jaws

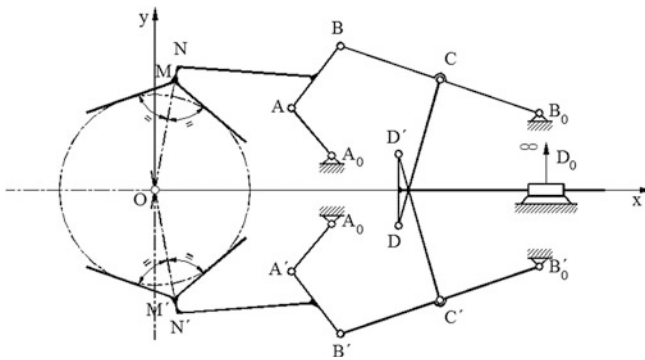


Fig. 3 Kinematic schema of the grasping device [1]

apply in this case. The four-pose synthesis ensures centering without errors in the four imposed positions and, in-between, the manipulated cylindrical parts will maintain their centers along the Ox-axis, on both sides of the origin at minimized distances (centering errors). This minimization is a second-step optimization achieved by the authors through an adequate choice of the four diameters of the manipulated part (as in Fig. 2), spanning between the limit diameters shown in Fig. 1.

3 Limitations in Applying the Five-Pose Synthesis

In order to show the limitations of the five pose synthesis, a numerical example is computed. Table 1 shows the imposed values for the diameters of the manipulated part D_i , the coordinates of the prism jaws point (x_{Mi} , y_{Mi}) with the corresponding positional angles β_i of the prismatic jaws (with $\hat{\alpha} = 120^\circ$).

Using the imposed geometrical parameters for the five poses and computing the center-point curves f_{1234} and f_{2345} in the form of “7 coefficient curve” for the positions $i = 1, 2, 3, 4$ and $i = 2, 3, 4, 5$:

$$(x^2 + y^2) \cdot (Ax + By) + Ex^2 + Fxy + Gy^2 + Hx + Iy + 1 = 0 \quad (1)$$

lead to the coefficients A, B, E, F, G, H, I of Eq. (1), printed in Table 2.

This means that the center-point curves are shaped particular. Coefficients A and B suggest a slowly ascending asymptote in curve f_{1234} and a slowly descending one in curve f_{2345} . Coefficients E, G and F suggest the existence of an approximately circular branch. Coefficients H and I in accordance with the interpretation of coefficients A and B suggest the existence of an approximately straight line branch, slowly ascending for curve f_{1234} and slowly descending for curve f_{2345} .

The two center-point curves are shown in Fig. 4, which confirms the previous interpretation of the coefficients' size. Furthermore, one can notice that the

Table 1 Geometrical parameters for the five-pose synthesis

Sizes/ i	1	2	3	4	5
Diameter D_i (mm)	5	21.25	37.5	53.75	70
Angle β_i (deg)	120	105	90	75	60
x_{Mi} (mm)	-1.443	-3.175	0	8.031	20.207
y_{Mi} (mm)	2.500	11.850	21.650	29.975	35.0

Table 2 Center-point curves coefficients

Coefficients	A	B	E	F	G	H	I
f_{1234}	-163.099	1238.862	2956.126	-22064.523	-2956.064	107155.380	-813931.800
f_{2345}	8.421	63.969	-152.643	-1139.318	152.637	-5532.957	-42027.245

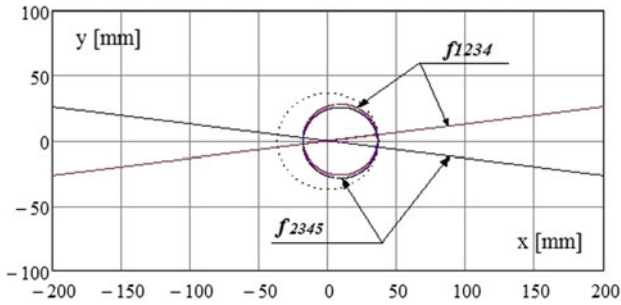


Fig. 4 Center-point curves f_{1234} and f_{2345} of the five pose synthesis

approximately straight-line branch is approximately a diametric straight line for the approximately circular branch.

Figure 4 also shows that the “un-monotone” zones of the curves superpose, which means that “here are” the solutions of the five-point synthesis and the Burmester center points (of which, one is surely very close to the origin of the axes). Thus results that the origin of the axes is not a pole.

Also in Fig. 4, in dotted line, at the same scale as curves f_{1234} and f_{2345} , the centered circle representing the part with the maximum diameter given in Table 1 was drawn. Inside this “part-circle” or right close to it (at approx. 2 mm with the current scale), it is possible to find Burmester center points, suitable to choose for the joints between the cranks/couplers and the frame element. Inside the space where the part lies, the joints are impossible to place and the trajectory of the mobile elements is forbidden, therefore, with mechanisms such as the one in Fig. 3, with prismatic jaws carried through precision points as in Fig. 2, the five-pose synthesis (maximum pose number for the four bar linkage) is not possible to apply.

4 Chebyshev Spacing Method Applied in Pose Synthesis

As demonstrated in [20] in order to increase the precision of path/function generating mechanisms, a certain arrangement of the precision points is practical and possible. Considering the same ranges of diameters and angles as in the previous chapter, and dividing the ranges into three equidistant intervals, the characteristic sizes resulted from computation as given in Table 3.

Table 3 Geometrical parameters for the equidistant chosen four pose synthesis

Sizes/i	1	2	3	4
Diameter D_i (mm)	5.0	26.667	48.333	70.0
Angle β_i (deg)	120	100	80	60
x_{Mi} (mm)	-1.443	-2.673	4.845	20.207
y_{Mi} (mm)	2.5	15.162	27.481	35.0

Table 4 Geometrical parameters for the Chebyshev spaced four pose synthesis

Sizes/i	1	2	3	4
Diameter D_i (mm)	7.474	25.062	49.937	67.526
Angle β_i (deg)	117.716	101.480	78.519	62.283
x_{Mi} (mm)	-2.007	-2.880	5.738	18.132
y_{Mi} (mm)	3.819	14.180	28.254	34.513

Table 5 Center-point curves coefficients with and without spacing

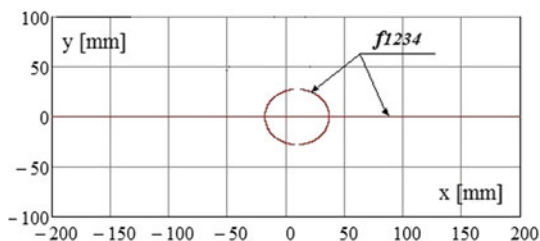
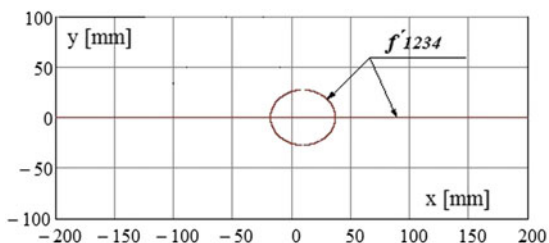
Coefficients	A	B	E	F	G	H	I
Without spacing	-0.0000433	131.21176	0.003899	-2436.525	0.001918	-0.112064	-87761.179
With spacing	0.0000411	-101.47229	-0.002251	1877.5587	-0.00518	0.000063	67591.431

The authors consider necessary to apply the Chebyshev spacing to both sizes, D_i and β_i chosen arbitrarily in Table 3. The results are shown in Table 4.

Table 5 presents the computed coefficients of the center-point curve f_{1234} and f'_{1234} , corresponding to curves with and without spacing.

Among the coefficients in Table 5 there are large differences regarding the size order. Similarly to the conclusions in Chap. 2 the center-point curves are particularly shaped and the coefficients have the same interpretation. The center-point curves without spacing f_{1234} and with spacing f'_{1234} are shown in Figs. 5 and 6.

Comparing the computed center-point curves it can be noticed that the shapes are almost identical with slight differences in quadrants I and III, each of them having an approximately circular and straight line branches.

Fig. 5 The center-point curves without spacing**Fig. 6** The center-point curves with spacing

As inside the space of the part, the joints are impossible to place and the elements of the mechanism can not pass through and considering (according to Figs. 2 and 3) that the part arrives between the jaws from the left side, the following conclusion results: for mechanisms as in Fig. 3, to which the connecting rod carries the prism jaw through precision points as in Fig. 2, in applying the four-position synthesis, only the quasi-linear branch from the right side of the quasi-circular branch of the centre-point curve is usable for placing the joints between the rocker/crank and the frame element.

5 Simplified Four-Pose Synthesis Method

One should take into account the conclusions in Chaps. 2 and 3 (tested on approx. 100 numerical syntheses) and the observation that the slope of the straight-line branch passing through the origin is usable for the synthesis, having values of 3...4 up to 1.000.000 (according to coefficients A , B in Table 5). In this context, the centers on the center-point curve, which are placed at a reasonable distance from the origin (less than 500 mm), lie very close to the abscissa (less than one micron). A point on the abscissa, adopted as center and placed at such a distance from the center-point curve, satisfies the equation of the center-point curve at least as well as a pole P_{ij}/Q_{ij} , the focus F , the principal point P , the points Newton N and Gauss G (if existing), the tangent $T1...T8$, the inflection points $I1$, $I2$, $I3$ or as other significant points [1]. This statement is true because the properties of the synthesis curves do not “fade” at such (relatively) small distances.

In the above context, the essence of the proposal to simplify the four-pose synthesis (in case of adopting the precision positions described in Chap. 3, with or without spacing) resides (paradoxically) in giving up its performing and adoption of abscissa (in its positive direction and at larger distances than the maximum radius of the manipulated part) as geometrical locus of centers (as joints with the frame element) [1].

The simplified method will be applied to the synthesis of a mechanism as in Fig. 3, with the precision points as in Fig. 2, performing the following steps:

- choosing four rational values for the angle of the prism-jaw α , the range of the manipulated part diameters D_i and of the bisecting line angles β_i ;
- dividing the ranges into equidistant or spaced intervals of the precision poses;
- choosing rationally the involute joints $A_0 \equiv A'_0$ and $B_0 \equiv B'_0$ on the abscissas (from kinetostatic point of view is more favorable for larger distance between these centers, in correlation with the axial size of the actuation cylinder);
- computing the coordinates of the corresponding mobile joints A , A' , B and B' by using the Burmester method [21];
- computing and comparing the lengths of the rockers and connecting rods for each chosen four poses;

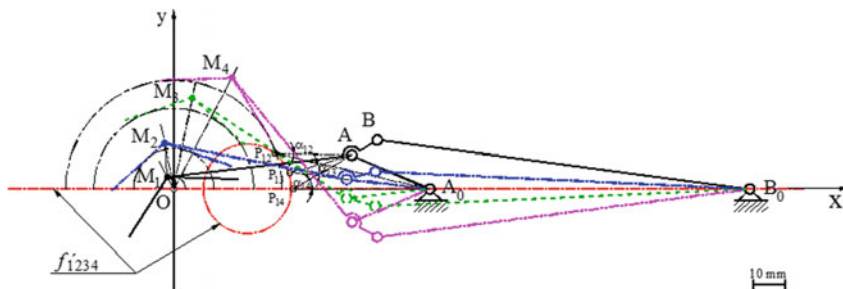


Fig. 7 The simplified synthesis method for the four bar linkage of the grasping device

- setting the final values by considering that the linkage passes through the alignment position of the revolute joints;
- performing the calculus regarding the theoretical precision of the synthesized mechanism (not mandatory);
- establishing the position of the connecting joint C on the rocker.

By using the proposed simplified synthesis method [1] for the both cases without spacing and with spacing and choosing the connecting revolute joints with the frame element at the abscissas $x_{A0} = 80\text{ mm}$ and $x_{B0} = 180\text{ mm}$ result different link lengths of the four bar linkages in different poses, but the differences are in hundredth of micron order [1] (Fig. 7). Obviously, in all cases, the frame element has the same length of $A_0B_0 = 100\text{ mm}$. The average link lengths of the four bar linkage, denoted as in Fig. 3, will be adopted as given in Table 6.

These results confirm that the simplified synthesis proposed is legitimate. It is to be emphasized that the frame element $A_0B_0 = 100\text{ mm}$, the sums $B_0B + AB$ and $A_0B_0 + A_0B$ are approximately equal (the differences are in hundredth of millimeter). As the sums above should be strictly achieved by the link lengths of the linkage, (otherwise it will not pass over the alignment position), the final link lengths were adopted as written in Table 7.

Table 6 Average link lengths of the four bar linkage

Link lengths	AoA (mm)	AB (mm)	BoB (mm)
Without spacing	26.534	9.148	117.435
With spacing	26.296	9.125	117.228

Table 7 Final link lengths of the four bar linkage

Link lengths	AoA (mm)	AB (mm)	BoB (mm)	AoBo (mm)
Without spacing	26.55	9.15	117.4	100
With spacing	26.3	9.1	117.2	100

The values in Table 7 were used in computing of centering precision and the link lengths with spacing served to practical manufacturing of the patented grasping device [22].

6 Theoretical Precision of the Grasping Device

Considering the mechanism in Fig. 3 with the link lengths given in Table 7, the theoretical centering precision was computed starting from the position relation for the four-bar linkage. The theoretical computation starts with the calculus of the positions of the point M in the top of the prism-jaw and the positions of an auxiliary point N , placed at a constant distance to M on the bisecting line of the prism.

The absolute centering error is the distance from the intersection of the bisecting line with the Ox -axis.

The average absolute centering error is 0.1971 mm for the mechanism without spacing and 0.1923 mm for the linkage with spacing (Fig. 8). The physical significance of these average absolute centering errors is a correction, which must be applied to the linkage in the practical achieving of the device or in the command of the robot, i.e. the joints A_0 and B_0 must be closer to the origin (centering position) with these values. This is necessary because the dimensions of the linkages in Table 7 do not correspond exactly to the precision points. The average values in Table 6 had to be adjusted in order to ensure the passing of the linkage through the alignment position.

Examining the absolute centering errors results that, indeed, for the linkage with spacing (Fig. 8b), the extreme errors are about one third smaller and symmetrically distributed, compared with the extreme errors for the linkage without spacing (Fig. 8a). This observation pleads for using of Chebyshev spacing method in positioning mechanisms synthesis.

The calculus of the centering errors, as described in this chapters, may be missed, considering that the relative errors (regarding the diameter of the part) are less than 1 % (in the above example the maximum relative error is 0.8 %).

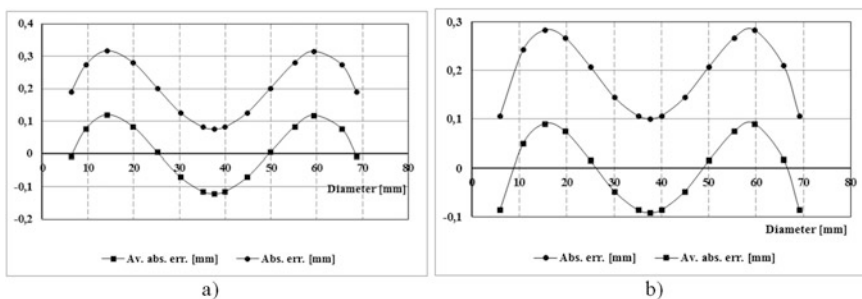


Fig. 8 The centering errors of the grasping device without spacing (a) and with spacing (b)

7 Conclusions

The paper presents a study on applying of the linkage synthesis theories for developing of a new grasping device, which use two symmetrical four-bar linkages with opposite motion of the jaws fixed on the coupler.

This study allowed the demonstration of the limitations (impossibility) in applying the five-pose synthesis and the particularities of the four-pose synthesis in the case of grasping devices. A simplified four-pose synthesis method was developed based on the analysis of the particular shape of the center-point curve in its useful zone.

By using the Chebyshev based spacing method for both sizes, namely the grasping diameter D_i and the positional angle of the prismatic jaws β_i , the theoretical centering axial precision increases in comparison with the errors obtained with equidistant chosen four-pose synthesis.

The computed centering errors of the grasping device show that between the precision poses considering the Chebyshev spacing, the errors are less than 1 %, which can be easily corrected by redesigning the grasping device through translating the whole linkage closer to the Ox-axis origin with the absolute average error.

References

1. Mesaros-Anghel, V.: Contribution to the synthesis of four-bar linkages used for designing of the grasping devices of the industrial robots (Contribuții la sinteza mecanismelor articulate aplicate în construcția dispozitivelor de prehensiune ale roboților industriali). PhD Thesis, Politehnica University of Timișoara, Romania, 1991. <http://www.dmg-lib.org/>
2. Ceccarelli, M.: Fundamentals of Mechanics of Robotic Manipulation. Kluwer Academic Publishers, Dordrecht (2004)
3. Fantoni, G., Santochi, M., Tracht, K., Scholz-Reiter, B., Fleischer, J., Kristoffer, L., Seliger, G., Reinhart, G., Franke, J., Hansen, H.N., Verl, A.: Grasping devices and methods in automated production processes. CIRP Ann.—Manuf. Technol. **63**(2), 679–701 (2014)
4. Carbone, G. (ed.): Grasping in Robotics, vol. 10. Springer Publisher, Series (2013)
5. Brukher, E.: Maschinell betatigte Zange zum Greifen von Rundkorpen, Bundesrepublik Deutschland, Patent 3717091, 21 May 1987
6. Chelpanov, I.B., Kolpashnikov, S.N.: Mecanical features of gripper in industrial robots. In: 13th International Symposium on Industrial Robots and Robots, 17–21 April 1983, Chicago Illinois. 2, 18.77–18.90 (1983)
7. Kristen, M.: Greifkonstruction mit Hilfe der Computergestutzen Lagensynthese. Maschinen-bautechnik **7**, 303–308 (1990)
8. Qingsen, H.: A linkage mechanism for concentric gripping cylindrical components. In: Proceedings of the 12 National Symposium on Industrial Robots and the 6th International Symposium on Robotised Technologies, Paris, 09–11 June 1982
9. Qingsen, H.: Concentric Gripper, UK Patent, nr. 8127255, 1981
10. Volmer, J.: Industrieroboter, Karl-Marx-Stadt. VEB Verlag Technic, Berlin (1980)
11. Butterfass, J., Grebenstein, M., Liu, H., Hirzinger, G.: DLR-H and II: Next generation of a dextrous robot hand. In: Proceedings of 2001 IEEE, International Conference on Robotics and Automation, Seoul, Korea (2001)

12. Azlan, N.Z., Yamaura, H.: Anthropomorphic finger with optimized geometric parameters for pinching and grasping tasks. *Mech. Mach. Theory* **49**, 52–66 (2012)
13. Zhou, X., Majidi, C., O'Reilly, O.M.: Soft hands: an analysis of some gripping mechanisms in soft robot design. *Int. J. Solids Struct.* **64–65**, 155–165 (2015)
14. Tilli, J., Brando, A., Fantoni, G.: Gripping device for heavy and deformable materials handling: concept, design, selection and test. *Procedia CIRP* **21**, 373–378 (2014)
15. Chen, W., Xiong, C.: On Adaptive grasp with underactuated anthropomorphic hands. *J. Bionic Eng.* **13**, 59–72 (2016)
16. Wu, L., Carbone, G., Ceccarelli, M.: Design an underactuated mechanism for a 1 active DOF finger operation. *Mech. Mach. Theory* **44(2)**, 336–348 (2009)
17. Wu, L., Kong, Y., Li, X.: Review and research Issues on underactuated finger mechanism. In: *Proceedings of the 2015 Chinese Intelligent Automatic Conference*, p. 171. Springer (2015)
18. Ceccarelli, M., Tavolieri, C., Lu, Z.: Design considerations for underactuated grasp with one DOF anthropomorphic finger mechanism. In: *Proceedings of IEEE/RSI International Conference on Intelligent Robots and Systems (IROS 2006)*, Beijing, China, (2006), pp. 1611–1616
19. Carbone, G., Ottaviano, E., Ceccarelli, M.: An optimum design procedure for both serial and parallel manipulators. *Proc. Inst. Mech. Eng., Part C: J. Mech. Eng. Sci.* **221(7)**, 829–843 (2007)
20. Perju, D.: *Mechanisms in Precision Mechanics (Mecanisme de mecanică fină)*, Litografia I.P. T.V., Timisoara, 1986. <http://www.dmg-lib.org/>
21. Modler, K.-H., Luck, K.: *Getriebetechnik—Analyse, Synthese, Optimierung*, vol. 2. Springer, Auflage (1995)
22. Mesaroş-Anghel, V., Mesaroş-Anghel, T., Groza, I.-R., Cioabă, V., Mareş, A., Czika, Z.: Centering Grasping Device (Dispozitiv de prehensiune cu centrare). Brevet nr.102291/26.06.1989, Romania

Modified Method of the Kinematic Analysis of Planar Linkage Mechanism for Non-stationary Motion Modes

J. Drewniak, P. Garlicka, J. Kopec and S. Zawislak

Abstract The aim of the paper is presentation of the modified method of utilization of the contour graphs for an analysis of kinematics of the closed crane mechanisms. An introductory phase of calculations is necessary for performance of further dynamical analysis of the mechanisms because—in the considered duty cycle—the linkages of the mechanisms are subjected to a non-stationary motion. The non-stationary motion mode is characteristic for a startup and a braking as well as during an unstable motion of the system. The results of calculations: velocities and accelerations for particular linkages of the mechanism are shown in various figures mainly as a function of the rotational angle of the drive linkage.

Keywords Linkage mechanism · Contour graph method · Analysis of kinematics

1 Introduction

The basic, classical method of kinematical analysis of mechanisms consists in differentiation (with respect to time) of the radius-vectors of positions of the mechanism nodes [1]. However, the method of an analysis of kinematics of the mechanisms based upon utilization of contour graphs allows for generation of algebraic equations. The idea of usage of graphs, block-schemes, dyads and other

J. Drewniak · P. Garlicka · J. Kopec · S. Zawislak (✉)
University of Bielsko-Biala, Bielsko-Biala, Poland
e-mail: szawislak@ath.bielsko.pl; naszdom44@gmail.com

J. Drewniak
e-mail: jdrewniak@bielsko.edu.pl

P. Garlicka
e-mail: pgarlicka@gmx.pl

J. Kopec
e-mail: jkopec@ath.bielsko.pl

algebraic tools or structures for solution of some problems of mechanisms' modeling, analysis and simulation is presented in papers [1–6]. The graph-based approach allows e.g. for systematic creation of atlases or families of mechanisms layouts or for their algorithmic synthesis [2]. The basic ideas of contour graphs are described in the Marghitu's monograph [7]. Usage of contour graphs for planetary gears modeling is presented in [1, 7]. The method could be utilized for plane as well as for spatial mechanisms, for which we consider closed kinematical chains as their calculation model. It has been assumed that the closed kinematical chain can model a crane mechanism. The mechanism consists of n moving linkages. The linkages are numbered in a consecutive way: from 0 to n . The 0 linkage is fixed to the ground (or reference system) and it is considered as the base. The absolute coordinate system OXY is attached to it. The i -th linkage is connected with the linkage $i - 1$ in point A_i , whereas with linkage $i + 1$ in point A_{i+1} . Therefore every considered point belongs to two neighbor linkages i and $i + 1$. Aiming for distinguishing of belongings of point A_i e.g. to the linkage $i - 1$ ($A_i \in i - 1$)—we can write the description of this point as one having two indexes $A_{i,i-1}$. Similarly, point $A_i \in i$ linkage is described as $A_{i,i}$.

The analysis of velocities of consecutive linkages of a mechanism (treated as a kinematic chain) is based on two fundamental kinematic relationships describing the complex motion [7]:

$$\sum_i \boldsymbol{\omega}_{i,i-1} = \mathbf{0}. \quad (1)$$

$$\sum_i \mathbf{r}_{A_i} \times \boldsymbol{\omega}_{i,i-1} + \sum_i \mathbf{v}_{A_{i,i-1}}^r = \mathbf{0}, \quad (2)$$

where $\boldsymbol{\omega}_{i,i-1}$ is a relative velocity of i linkage in relations to $i-1$ linkage, $\mathbf{r}_{A_i} = \mathbf{r}_{OA_i}$, $\mathbf{r}_{A_{i-1}} = \mathbf{r}_{OA_{i-1}}$, $\boldsymbol{\omega}_{i,i-1}$ and $\mathbf{v}_{A_{i,i-1}}^r$ is relative velocity in relation to $A_{i,i-1}$ point.

Similarly, the analysis of accelerations figures on two basic equations of the contour graphs method which initially consists in determination of relative angular accelerations $\boldsymbol{\varepsilon}_{i,i-1}$ of i linkage in relation to $i - 1$ linkage, relative linear accelerations $\mathbf{a}_{A_{i,i-1}}^r$ and Coriolis's accelerations $\mathbf{a}_{A_{i,i-1}}^c$ [7]:

$$\sum_i \boldsymbol{\varepsilon}_{i,i-1} + \sum_i \boldsymbol{\omega}_i \times \boldsymbol{\omega}_{i,i-1} = \mathbf{0}, \quad (3)$$

and

$$\begin{aligned} & \sum_i \mathbf{a}_{A_{i,i-1}}^r + \sum_i \mathbf{a}_{A_{i,i-1}}^c + \sum_i \mathbf{r}_{A_i} \times (\boldsymbol{\varepsilon}_{i,i-1} \times \boldsymbol{\omega}_i - \boldsymbol{\omega}_{i,i-1}) \\ & + \sum_i \boldsymbol{\omega}_i \times (\boldsymbol{\omega}_i \times \mathbf{r}_{A_{i,i+1}}) = \mathbf{0}. \end{aligned} \quad (4)$$

where $\mathbf{r}_{A_{i,i+1}} = \mathbf{r}_{A_i} - \mathbf{r}_{A_{i+1}}$, $\mathbf{a}_{A_{i,i-1}}^r = \mathbf{a}_{A_i,iA_{i,i-1}}^r$, $\mathbf{a}_{A_{i,i}} = \mathbf{a}_{A_{i,i-1}} + \mathbf{a}_{A_{i,i-1}}^r + \mathbf{a}_{A_{i,i-1}}^c$ and $\mathbf{a}_{A_{i,i-1}}^c = 2 \cdot \boldsymbol{\omega}_{i-1} \times \mathbf{v}_{A_{i,i-1}}^r$.

An algorithm of generation of the algebraic equations for velocities and angular accelerations describing the behavior of linear linkages of a particular mechanism based on the contour graph method can be formulated in the following steps:

- (i) drawing the scheme of the analyzed mechanism, assuming of the coordinate system X0Y and determination of geometrical layout of particular nodes of the mechanism and determination of the radius-vectors of mechanism nodes,
- (ii) calculation of the mobility of the mechanism $W = 3 \cdot n - 2 \cdot p_5 - p_4$, where n —number of movable linkages, p_5 —number of kinematics pairs of 5-th class, p_4 —number of kinematic pairs of 4-th class and checking the condition of problem solvability—i.e. the number of known velocities has to be equal to W ,
- (iii) drawing the contour graph (representing kinematics) of the mechanism having N independent contours:

$$N = c - n = c - p + 1, \tag{5}$$

where: $c = p_5 + p_4$ —number of nodes (joints) of the mechanism, n —number of movable linkages, $p = n + 1$ —total number of linkages,

- (iv) decomposition of the mechanism and generating of the system of vector equations for velocities or/and accelerations for every contour (closed loop),
- (v) finding a solution of the system of equations after transformation of the vector-type equations into the scalar ones (via projection of the vectors onto the axes x and y of the assumed coordinate system in case of planar case) and final solving of the system of algebraic equations.

2 Analysis of Velocities of the Mechanism Linkages

The analyzed mechanism is presented in Fig. 1a. The linkages 1, 3 and 5 are arms (swing-arms), whereas arm 1 is the driving linkage and arm 5—the driven one. The geometric and layout data for mechanism linkages are as follows: $|AB| = 80$, $|BC| = 80$, $|BD| = 90$, $|CD| = 80$, $|ED| = 100$, $|CG| = 150$, $A(0;0)$, $E(60;0)$,

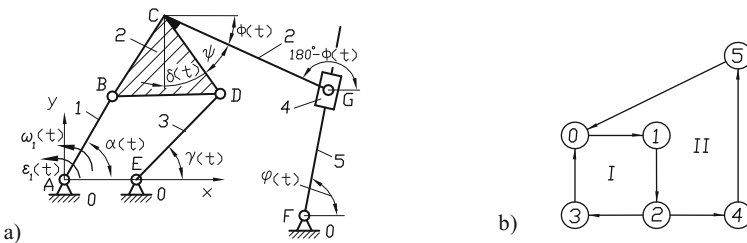


Fig. 1 Analyzed crane mechanism (a) and two-contour graph of the mechanism (b)

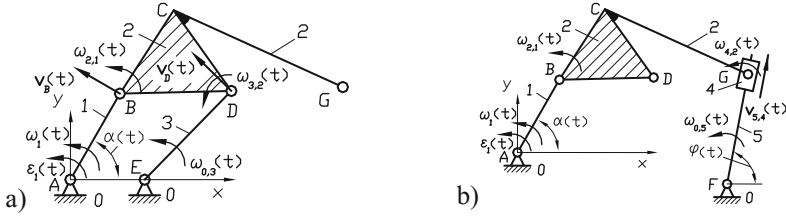


Fig. 2 First and second component of mechanism (after decomposition)

$F(200; -30)$, $\psi = 60^\circ$, $30^\circ \leq \alpha \leq 210^\circ$, where $30^\circ \leq \alpha \leq 45^\circ$ —startup, $45^\circ \leq \alpha \leq 195^\circ$ —stable motion, $195^\circ \leq \alpha \leq 210^\circ$ —braking.

In Fig. 1b, N independent contour graphs of the mechanism are presented, whereas: $N = c - n = 7 - 5 = 2$ based on Eq. 5. The nodes—shown as circles—represent the particular linkages of the mechanism corresponding to the same descriptions, whereas the edges connecting the graph nodes represent the mechanism joints. The schemas are utilized to drawing the so called expanded contour graphs (Fig. 3) corresponding to particular subsystem obtained upon the decomposition of the mechanism (Fig. 2). The considered mechanism (Fig. 1a) is a complex mechanical system which can be decomposed into two simple subsystems (Fig. 2). It allows for essential simplification of generation and solution of the system of equations corresponding to linkages velocities. Further simplification consists in creation of the extended contour graphs for particular decomposed subsystems (Fig. 2).

The system of vector equations of velocities for the first contour (Figs. 1b and 3) can be written in the following form:

$$\omega_{1,0} + \omega_{2,1} + \omega_{3,2} + \omega_{0,3} = \mathbf{0}, \tag{6a}$$

$$\mathbf{r}_{AB} \times \omega_{2,1} + \mathbf{r}_{AD} \times \omega_{3,2} + \mathbf{r}_{AE} \times \omega_{0,3} = \mathbf{0}, \tag{6b}$$

The angular velocity $\omega_{1,0}(\alpha) = \omega_1(\alpha)$ of arm 1 is presented in Fig. 2. We are looking for the relative angular velocities $\omega_{2,1} = \omega_{2,1} \cdot \mathbf{k}$, $\omega_{3,2} = \omega_{3,2} \cdot \mathbf{k}$ and $\omega_{0,3} = \omega_{0,3} \cdot \mathbf{k}$. After adequate rewriting, the system of algebraic equations is obtained, via projections on z , x , y axes respectively (Fig. 4):

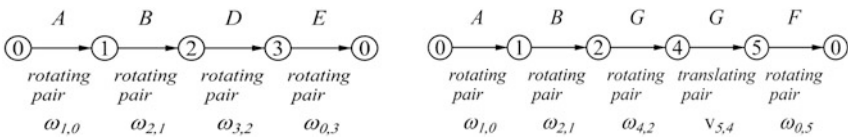


Fig. 3 Extended contour graphs corresponding to first and second component of mechanism



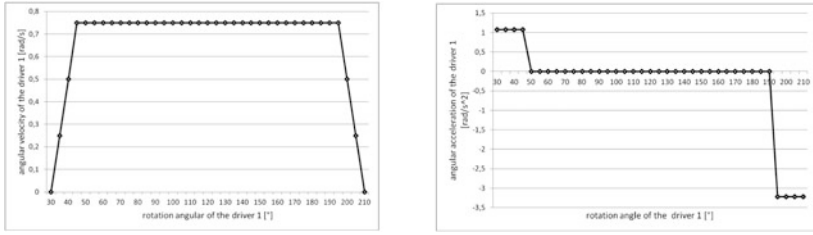


Fig. 4 Set angular velocities $\omega_1(\alpha)$ and accelerations $\varepsilon_1(\alpha)$ of driving arm 1

$$\omega_{2,1}(\alpha) + \omega_{3,2}(\alpha) + \omega_{0,3}(\alpha) = -\omega_{1,0}(\alpha) \tag{7a}$$

$$y_B(\alpha) \cdot \omega_{2,1}(\alpha) + y_D(\alpha) \cdot \omega_{3,2}(\alpha) + y_E(\alpha) \cdot \omega_{0,3}(\alpha) = 0 \tag{7b}$$

$$-x_B(\alpha) \cdot \omega_{2,1}(\alpha) - x_D(\alpha) \cdot \omega_{3,2}(\alpha) - x_E(\alpha) \cdot \omega_{0,3}(\alpha) = 0 \tag{7c}$$

Unknown velocities $\omega_{2,1}(\alpha)$, $\omega_{3,2}(\alpha)$ and $\omega_{0,3}(\alpha)$ are shown in Fig. 5, where $30^\circ \leq \alpha \leq 210^\circ$.

The system of vector equations for the second contour (Figs. 1b and 3):

$$\omega_{1,0} + \omega_{2,1} + \omega_{4,2} + \omega_{0,5} = \mathbf{0}, \tag{8a}$$

$$\mathbf{r}_{AB} \times \omega_{2,1} + \mathbf{r}_{AG} \times \omega_{4,2} + \mathbf{v}_{G,5}^r + \mathbf{r}_{AF} \times \omega_{0,5} = \mathbf{0}, \tag{8b}$$

After adequate rewriting, the system of vector equations (8a, 8b) can be presented in an algebraic form:

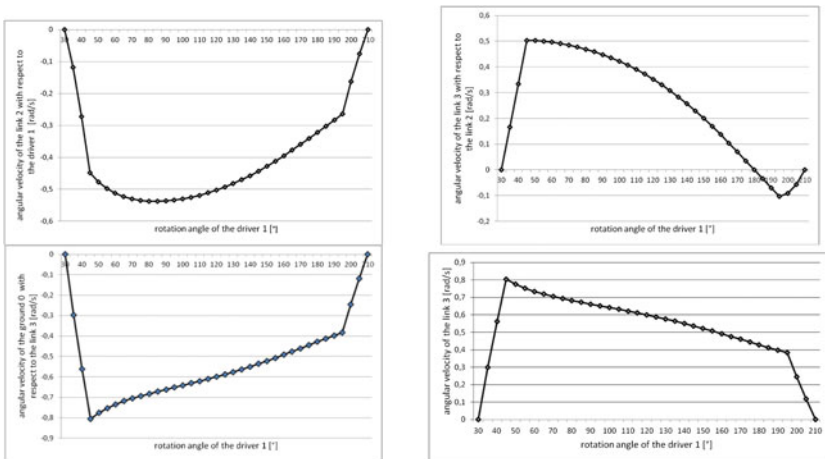


Fig. 5 Angular velocities as function of angular angle α of arm 1 (I contour)

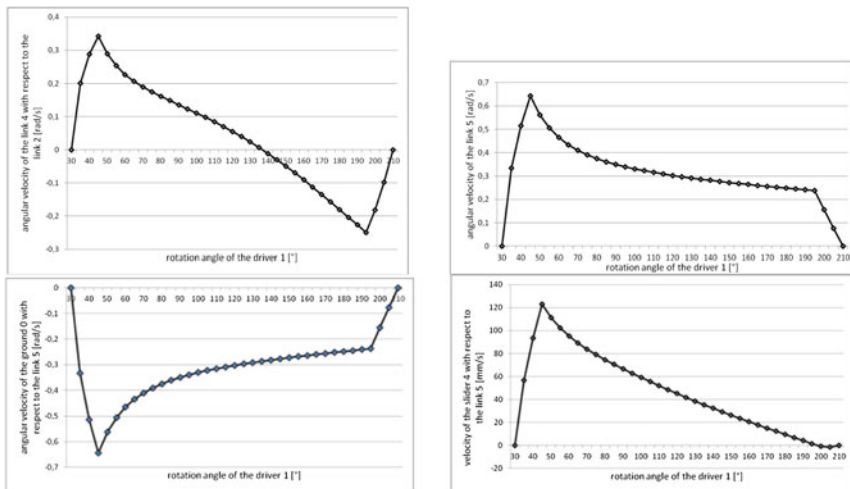


Fig. 6 Angular and linear velocities as functions of rotational angle of α arm 1 (II contour)

$$\omega_{4,2}(\alpha) + \omega_{0,5}(\alpha) = -\omega_{1,0}(\alpha) - \omega_{2,1}(\alpha), \quad (9a)$$

$$\begin{aligned} y_G(\alpha) \cdot \omega_{4,2}(\alpha) + y_F(\alpha) \cdot \omega_{0,5}(\alpha) + v_{G5,4}^r(\alpha) \cdot \cos(\alpha) \\ = -y_B(\alpha) \cdot \omega_{2,1}(\alpha), \end{aligned} \quad (9b)$$

$$\begin{aligned} -x_G(\alpha) \cdot \omega_{4,2}(\alpha) - x_F(\alpha) \cdot \omega_{0,5}(\alpha) + v_{G5,4}^r(\alpha) \cdot \sin(\alpha) \\ = x_B(\alpha) \cdot \omega_{2,1}(\alpha). \end{aligned} \quad (9c)$$

The solutions of the system of Eqs. (9a–9c) are shown in Fig. 6 in case of angles $30^\circ \leq \alpha \leq 210^\circ$.

3 Analysis of Accelerations of Mechanism Linkages

Calculations of accelerations by means of the contour graph method is performed according to the algorithm described in Chap. 1. Angular acceleration $\varepsilon_1 = \varepsilon_{1,0}$ of the driving arm 1 for a startup state is presented in Fig. 7.

Based on Figs. 7a and 8a, the following system of vector equations of accelerations can be derived:

$$\varepsilon_{1,0} + \varepsilon_{2,1} + \varepsilon_{3,2} + \varepsilon_{0,3} = \mathbf{0}, \quad (10a)$$

$$\mathbf{r}_{AB} \times \varepsilon_{2,1} + \mathbf{r}_{AD} \times \varepsilon_{3,2} + \mathbf{r}_{AE} \times \varepsilon_{0,3} - \omega_{1,0}^2 \cdot \mathbf{r}_{AB} - \omega_{0,3}^2 \cdot \mathbf{r}_{DE} = \mathbf{0}, \quad (10b)$$

where: $\varepsilon_{1,0}(\alpha) = \dot{\omega}_{1,0}(\alpha) \cdot \mathbf{k}$ —set angular acceleration (Fig. 8).

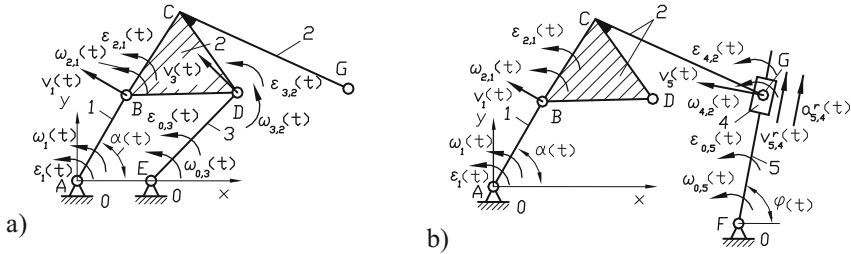


Fig. 7 First and second component of the mechanism (after decomposition)

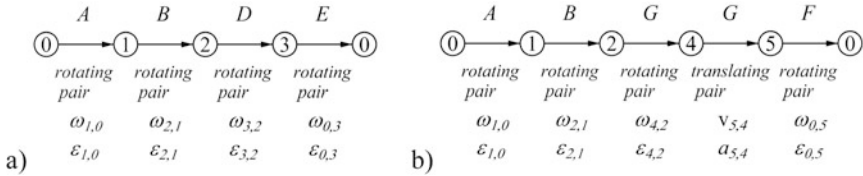


Fig. 8 Expanded contour graphs corresponding to first and second component of the mechanism

Rewritten of Eqs. (10a, 10b) give the algebraic form of the considered equation system:

$$\epsilon_{2,1}(\alpha) + \epsilon_{3,2}(\alpha) + \epsilon_{0,3}(\alpha) = -\epsilon_{1,0}(\alpha), \tag{11a}$$

$$y_B \cdot \epsilon_{2,1}(\alpha) + y_D \cdot \epsilon_{3,2}(\alpha) + y_E \cdot \epsilon_{0,3}(\alpha) = \omega_{1,0}^2(\alpha) \cdot x_B + \omega_{0,3}^2(\alpha) \cdot (x_E - x_D), \tag{11b}$$

$$-x_B \cdot \epsilon_{2,1}(\alpha) - x_D \cdot \epsilon_{3,2}(\alpha) - x_E \cdot \epsilon_{0,3}(\alpha) = \omega_{1,0}^2(\alpha) \cdot y_B - \omega_{0,3}^2(\alpha) \cdot y_D. \tag{11c}$$

The solutions of the system Eqs. (11a–11c) are presented in Fig. 9.

Based on Fig. 7b—where the second component of the mechanism is shown—and based on Fig. 8b—where the expanded contour graph of this component, it is possible to generate the following system of vector equations for accelerations:

$$\epsilon_{1,0} + \epsilon_{2,1} + \epsilon_{4,2} + \epsilon_{0,5} = \mathbf{0}, \tag{12a}$$

$$\mathbf{r}_{AB} \times \epsilon_{2,1} + \mathbf{r}_{AG} \times \epsilon_{4,2} + \mathbf{r}_{AF} \times \epsilon_{0,5} + \mathbf{a}_{G5,4}^r + \mathbf{a}_{G5,4}^c - \omega_{1,0}^2 \cdot \mathbf{r}_{AB} - \omega_{0,5}^2 \cdot \mathbf{r}_{GF} = \mathbf{0}, \tag{12b}$$

After rewriting, Eqs. (12a, 12b) can be presented in an algebraic form:

$$\epsilon_{2,1}(\alpha) + \epsilon_{4,2}(\alpha) + \epsilon_{0,5}(\alpha) = -\epsilon_{1,0}(\alpha), \tag{13a}$$



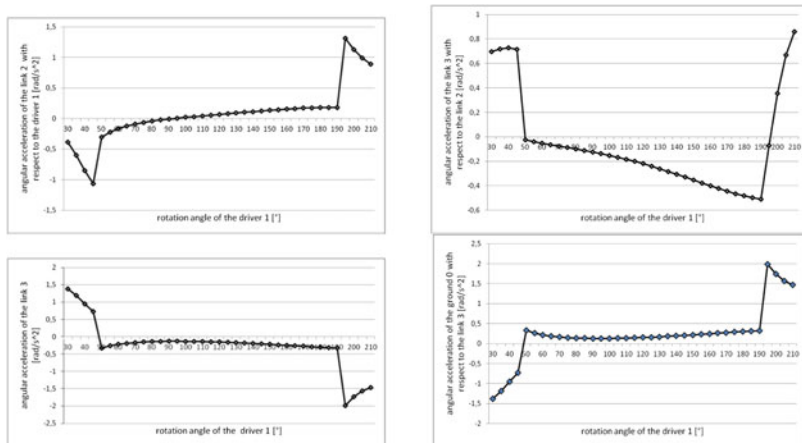


Fig. 9 Angular accelerations as functions of rotational angle α of arm 1 (I contour)

$$y_B \cdot \varepsilon_{2.1}(\alpha) + y_G \cdot \varepsilon_{4.2}(\alpha) + y_F \cdot \varepsilon_{0.5}(\alpha) + a_{G5.4}^r(\alpha) \cdot \cos \varphi = 2 \cdot \omega_{0.5}(\alpha) \cdot v_{G5.4}^r(\alpha) \cdot \sin \varphi + \omega_{1.0}^2(\alpha) \cdot x_B + \omega_{0.5}^2(\alpha) \cdot (x_F - x_G), \tag{13b}$$

$$-x_B \cdot \varepsilon_{2.1}(\alpha) - x_G \cdot \varepsilon_{4.2}(\alpha) - x_F \cdot \varepsilon_{0.5}(\alpha) + a_{G5.4}^r(\alpha) \cdot \sin \varphi = -2 \cdot \omega_{0.5}(\alpha) \cdot v_{G5.4}^r(\alpha) \cdot \cos \varphi + \omega_{1.0}^2(\alpha) \cdot y_B + \omega_{0.5}^2(\alpha) \cdot (y_F - y_G). \tag{13c}$$

The solutions of the system of Eqs. (13a–13c) are presented in Fig. 10.

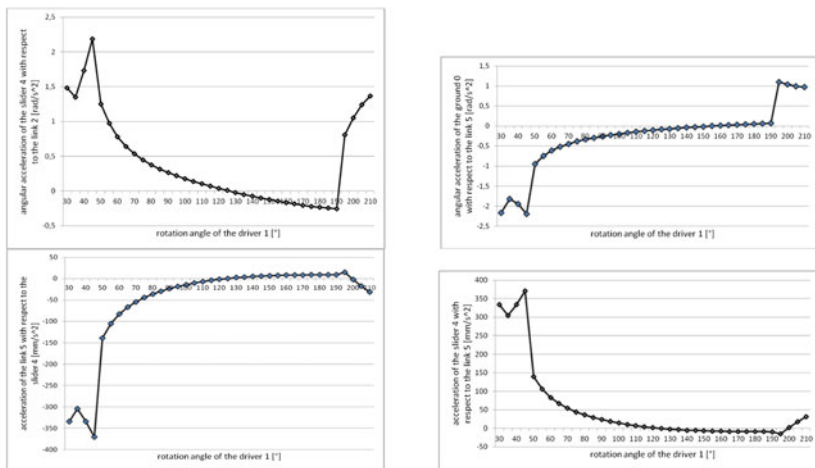


Fig. 10 Angular and linear acceleration as functions of rotational angle α of arm 1 (II contour)

4 Conclusions

It was shown, in the paper, that an application of the contour graphs method for an analysis of closed kinematical crane mechanisms essentially helps in generation and solving of the systems of equations describing the behavior of the mechanism. The main cause of this advantage is description of the motion by means of algebraic equations instead of differential ones like it is considered in classical approaches to solving similar problems. The benefits of the utilized methodology were especially evident in case of kinematical analysis of mechanisms which linkages are subjected to the non-stationary or unstable motions. It could be expected that these advantages would be also beneficiary in analysis of kinematics and dynamics of spatial mechanisms. The simulation results shown in figures confirm the design assumptions for the analyzed mechanism.

References

1. Drewniak, J., Zawislak, S.: Linear-graph and contour-graph-based models of planetary gears. *J. Theoret. Appl. Mech.* **48**(2), 415–433 (2010)
2. Ding, H., Huang, P., Zi, B., Kecskemethy, A.: Automatic synthesis of kinematic structures of mechanisms and robots especially for those with complex structures. *Appl. Math. Model.* **36**(12), 6122–6131 (2012)
3. Kecskemethy, A., Krupp, T., Hiller, M.: Symbolic processing of multi-loop mechanism dynamics using closed-form kinematics solutions. *Multibody Sys. Dyn.* **1**(1), 23–45 (1997)
4. Popescu, I., Marghitu, D.B.: Structural design of planar mechanisms with dyads. *Multibody Sys. Dyn.* **19**(4), 407–425 (2008)
5. Staretu, I., Ionescu, M., Runcan, V.: Family of mechanical anthropomorphic poly-mobile grippers for robots—synthesis, analysis, design and functional simulation. In: *Proceedings of the 15th International Workshop on Robotics in Alpen-Adria-Danube Region—RAAD*, pp. 273–277 (2008)
6. Talpasanu, I., Yih, T.C., Simionescu, P.A.: Application of matroid method in kinematical analysis of parallel axes epicyclic gear trains. *ASME J. Mech. Design* **128**, 1307–1314 (2005)
7. Marghitu, D.B.: *Kinematic Chains and Machine Components Design*. Elsevier (2005)

A Type Synthesis Method for Parallel Mechanisms Based on SAKCs

Huiping Shen, Chi-Yu Sun, Dan Zhang and Ting-li Yang

Abstract Extending Assur's kinematic chain (AKC) principle of the planar mechanisms to space parallel mechanisms, this paper studies the composition principle based on the space Assur's kinematic chain (SAKC) as well as the type synthesis method based on SAKCs for the parallel mechanisms (PM). First of all, a new expression for the PM composition based on SAKC is proposed, which has clearer physical meaning; Secondly, according to the principle of composition and the formula for calculating the value of the coupling degree k , 53 types of SAKCs with coupling degree $k = 0-3$ and the basic loop $\nu = 1-5$, as well as their analytical expressions, are presented. Also it is found that these SAKCs can express 40 types of SAKC structures which are the basic unit of PMs. Finally, a general and practical method for type design of PM is presented regarding SAKCs as the composition units and meeting the position and orientation characteristics (POC) set as the design goal. One example is illustrated.

Keywords Parallel mechanism • SAKCs • Type synthesis • Position and orientation characteristics • Coupling degree • Ordered single-open-chain unit

H. Shen (✉) · C.-Y. Sun · T. Yang
Changzhou University, Changzhou, China
e-mail: shp65@126.com

C.-Y. Sun
e-mail: 476885351@qq.com

T. Yang
e-mail: yangtl@126.com

D. Zhang
York University, Toronto, Canada
e-mail: dzhang99@yorku.ca

1 Introduction

Type synthesis (or topology design) of parallel mechanisms (PM) has always been one of the hot and difficult points in mechanism community. Theoretical basis of type synthesis includes two aspects, i.e., the mechanism composition principle and its type synthesis method.

On the mechanism composition principle, there are currently 4 types of theories and their corresponding mechanism theories [1], i.e., theory based on link and joint unit, theory based on Assur's group unit, theory based on loop unit and theory based on ordered Single-Open-Chain (SOC) unit. The first three mechanism composition theories are good for planar mechanisms but can not be used for design and analysis of spatial parallel mechanisms effectively. While mechanism composition principle based on SOC units can be used to design and analyze both any planar mechanisms and space parallel mechanisms effectively, which is illustrated in the next of the paper.

Regarding type design, there are some methods for PMs currently, for examples, screw theory based method [2], displacement subgroups based method [3], linear transformation and evolution of morphological based method [4] and Position and Orientation Characteristics (POC) and SOC units based method [1, 5]. All of these systematic theories regard legs (or limbs) between the base and moving platform as the composition units of PM, which is a precise, systematic and complex design process. Especially the first three methods require good mathematical background. Therefore, it is somewhat difficult for engineers to understand and use them.

Using the type synthesis theory based on POC (as a mathematical tool) and SOC (as a component unit), this paper extends the AKC mechanism composition principle to spatial PMs, and presents a practical method based on space AKC (denoted as SAKC) structure to meet the output requirements of position and orientation characteristics (POC) of the moving platform. This method is easy to be understood and can be used for the type design of 2–6 dof PMs. Compared with the 4 types of existing type synthesis theory [1–5], this method is simple and practical.

2 Mechanism Composition Principles and New Expression Based on SAKCs

2.1 Coupling Degree of a SAKC

Any mechanism with *DOFs* and independent loops ν can be decomposed into an ordered set of SOC [1, 5], the number of the SOC is ν . The SOC with the minimum value of constraint degree Δ will be selected as the first SOC, i.e., SOC₁, then the

rest will be SOC_2 with the minimum value of its constraint degree Δ_2, \dots In general, choose the remaining SOC as SOC_j with the smallest constraint degree Δ_j . Further more, these SOCs with Δ_j can be divided into several parts and each part need to satisfy the requirement of $\sum \Delta_j = 0$, and their coupling degree is calculated by

$$\kappa = \frac{1}{2} \sum_{j=1}^v |\Delta_j| \quad (1)$$

And the maximum value of the SAKCs k is that of the mechanism.

2.2 A New Composition Expression of the PM Based on SAKC

A new composition expression for the PM based on SAKC is presented as follows:

$$PKM^k[F, V] = F - J_{in} + \sum_{j=1}^v p_k \cdot SAKC^k(\Delta_1, \Delta_2, \dots, \Delta_j) \quad (2)$$

That is, a PKM with $DOF = F$, number of independent loops v , degree of coupling k , i.e., $PKM^k[F, v]$, can be regarded as a number of joint of inputs and several SAKCs.

Among them:

$F - J_{in}$	the number of input joints is F (=DOF)
p_k	the number of SAKC with coupling degree k (when $p_k = 1$, omission)
$AKC^k(\Delta_1, \Delta_2, \dots, \Delta_j)$	SAKC with coupling degree k , which is composed by $SOC_1, SOC_2, \dots, SOC_j$, and constraint degree of these SOCs are $\Delta_1, \Delta_2, \dots, \Delta_j$, respectively.

Formula (2) indicates three aspects of information at least: ① the number of SAKCs and their coupling degree; ② structure and composition of each SAKC (such as number of SOC and their constraint degree value); ③ the number of independent loops. Obviously, the formula (2) has clear physical meaning, which is suitable for both multi-loop planar and space mechanisms.

Example 1 Composition expression of a 6-DOF 6-SPS parallel mechanism.

Shen et al. [6] analyzed a 2-2-2-type 6-SPS parallel mechanism, as shown in Fig. 1a. The mechanism is composed of six input joints (P joints), three UUS

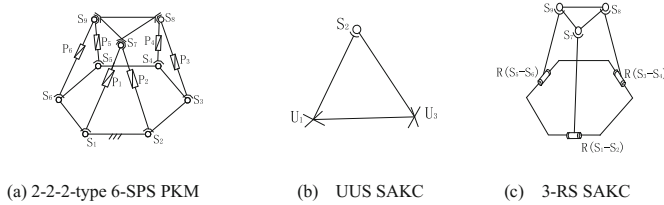


Fig. 1 2-2-2-type 6-SPS PM and its SAKC

SAKCs with $k = 0$ (Fig. 1b) and a 3-RS SAKC with $k = 1$ (Fig. 1c), which can be expressed as:

$$PKM^1[6, 5] = 6 - J_{in} + 3 AKC^0(0) + AKC^1(+1, -1)$$

3 Basic Types of SAKCs

3.1 All Possible SAKC Basic Types

A SAKC with the same coupling degree k may have different number of independent loops (ν) and different number of constraint degree. Therefore, there will be a variety of composition forms. According to Eq. (1) of k calculation and the possible composition forms of the SOC, the authors have summarized 53 types of basic SAKC with $k = 0-3$ and the basic loop $\nu = 1-5$, as shown in Table 1.

We can observe the following points from Table 1.

- (1) With the increase of the number of basic loop ν , the coupling degree k will increase, and the type and number of SAKC increase too. For example, SAKC with $k = 1$ and $\nu = 5$ has only one types. i.e., No. 26 in Table 1, while SAKC with $k = 3$ and $\nu = 5$ has 18 types, i.e., from No. 36 to No. 53, in Table 1.
- (2) Among SAKCs, there is only 1 type of SAKC with basic loop $\nu = 1$ and $k = 0$, i.e., No. 1 in Table 1, which is exactly Assur’s Kinematic Chain Group II. That is to say, SAKC is just a special case of SAKC. However there are 3, 7, 14, 28 types of SAKC with basic loop $\nu = 2, 3, 4$ and 5, respectively.
- (3) Theoretically there are 53 kinds of SAKC basic types. However, to authors’ work so far, only six kinds of SAKC basic type are used commonly in design of the typical parallel mechanisms, which are denoted with underline in Table 1. Perhaps, with the deep understanding of these SAKC, more and more parallel mechanisms based on these SSAKC basic types will be synthesized.



Table 1 Basic types and classification of SAKCs based on k and v

v	k		
	0	1	2
1	No. 1 SAKC ⁰ (0)		
2	No. 2 SAKC ¹ (1,-1)	No. 3 SAKC ² (2,-2)	No. 4 SAKC ³ (3,-3)
3	No. 5 SAKC ¹ (1,0,-1)	No. 6 SAKC ² (2,0,-2)	No. 9 SAKC ³ (3,0,-3), No. 10 SAKC ³ (3,-1,-2)
		No. 7 SAKC ² (2,-1,-1)	No. 11 SAKC ³ (2,1,-3)
		No. 8 SAKC ² (1,1,-2)	
4	No. 12 SAKC ¹ (1,0,0,-1)	No. 13 SAKC ² (2,0,0,-2)	No. 19 SAKC ³ (3,0,0,-3), No. 20 SAKC ³ (2,1,0,-3)
		No. 14 SAKC ² (2,0,-1,-1)	No. 21 SAKC ³ (1,1,1,-3), No. 22 SAKC ³ (3,0,-1,-2)
		No. 15 SAKC ² (2,-1,0,-1)	No. 23 SAKC ³ (3,-1,0,-2), No. 24 SAKC ³ (3,-1,-1,-1)
		No. 16 SAKC ² (1,0,1,-2)	No. 25 SAKC ³ (2,1,-1,-2)
		No. 17 SAKC ² (1,1,0,-2)	
		No. 18 SAKC ² (1,1,-1,-1)	
5	No. 26 SAKC ¹ (1,0,0,0,-1)	No. 27 SAKC ² (2,0,0,0,-2)	No. 36 SAKC ³ (3,0,0,0,-3), No. 37 SAKC ³ (2,1,0,0,-3)
		No. 28 SAKC ² (2,0,0,-1,-1)	No. 38 SAKC ³ (2,0,1,0,-3), No. 39 SAKC ³ (2,0,0,1,-3)
		No. 29 SAKC ² (2,-1,0,0,-1)	No. 40 SAKC ³ (1,0,1,1,-3), No. 41 SAKC ³ (1,1,0,1,-3)
		No. 30 SAKC ² (2,0,-1,0,-1)	No. 42 SAKC ³ (1,1,1,0,-3), No. 43 SAKC ³ (3,0,0,-1,-2)
		No. 31 SAKC ² (1,0,0,1,-2)	No. 44 SAKC ³ (3,0,-1,0,-2), No. 45 SAKC ³ (3,-1,0,0,-2)
		No. 32 SAKC ² (1,1,0,0,-2)	No. 46 SAKC ³ (3,0,-1,-1,-1), No. 47 SAKC ³ (3,-1,0,-1,-1)
		No. 33 SAKC ² (1,0,1,0,-2)	No. 48 SAKC ³ (3,-1,-1,0,-1), No. 49 SAKC ³ (2,0,1,-1,-2)
		No. 34 SAKC ² (1,1,0,-1,-1)	No. 50 SAKC ³ (2,1,0,-1,-2), No. 51 SAKC ³ (2,1,-1,0,-2)
		No. 35 SAKC ² (1,1,-1,0,-1)	No. 52 SAKC ³ (2,1,-1,-1,-1), No. 53 SAKC ³ (1,1,1,-1,-2)

3.2 Common SAKC Structures

Yin et al. [7] summarized 40 types of SAKC structures based on the topological analysis for the existing 2–6 *dof* PMs., their schematic diagrams of which can be checked in the Appendix of this paper and we find that

- (1) Each of the SAKC basic types will correspond to a number of SAKC structures; and each SAKC structure will correspond to several actual PMs, which means that different PMs may have the same SAKC structure. For example,



Table 2 Relations between SAKC basic types and SAKC structures commonly used

k	SAKC basic types (in Table 1)	40 kinds of SAKC structure (in Appendix)	Number	Percentage (%)
0	No. 1 SAKC ⁰ (0)	No. 4, 9, 10, 11, 15, 18, 19	7	17.5
1	No. 2 SAKC ¹ (1,-1)	No. 1, 2, 3, 5, 6, 7, 8, 12, 13, 16, 20, 21, 23, 24, 27, 28, 29, 30, 31, 39	20	57.5
	No. 5 SAKC ¹ (1,0,-1)	No. 22, 32, 38	3	
2	No. 7 SAKC ² (2,-1,-1)	No. 14, 17, 25, 26, 33, 34	6	17.5
	No. 14 SAKC ² (2,0,-1,-1)	No. 35	1	
3	No. 52 SAKC ³ (2,1,-1,-1,-1)	No. 36, 37, 40	3	7.5

although the physical structure, virtual POC set (which will be defined in Sect. 4.1) of the SAKC structures of No. 22, 32, 38 in the Appendix are different, their composition expression can be represented by the same SAKC basic type, i.e., No. 5 SAKC¹(1,0,-1), as shown in Table 2.

- (2) There are only 6 most common basic types found among these 53 SAKCs basic types, as shown in Table 2. That is to say, the number of SAKC used for common PMs is limited, most of which have low coupling degree k , say 0 or 1. For example, the general PMs are composed of SAKC with $k = 0$ or SAKCs with $k = 1$, which take 75 % (17.5 % with $k = 0$ and 57.5 % with $k = 1$) of all SAKCs. But for 6-DOF PM with $\nu = 5$, there is only one PM considered as 6-SPS PKM.
- (3) The key issues of type synthesis are to design topological structures of parallel mechanisms based on SAKC structures and virtual POC set.

Forty kinds of commonly used SAKC structures are proposed and classified by their virtual POC set, which will be defined and discussed in the coming Sect. 4.1.

4 Type Synthesis Method Based on SAKCs

4.1 Virtual POC Set of a SAKC Structure

Since the basic function of a PM is to achieve the output motions of the moving platform, translation and rotation elements of the moving platform are called position and orientation characteristic (POC) set.

In fact, an SAKC does not have POC set since the DOF of a SAKC is 0 and SAKC is a truss essentially. However, when a SAKC structure is disassembled into the moving platform and several legs, the end of each leg will produce an independent POC set. Their intersection operator of these independent POC sets under the constraints among the these legs will produce a POC set, which we call it “virtual POC set”, denoted as M_{SAKC} and expressed by symbol $\{\}$.

A SAKC will become a true PM when input joints are added into the legs of the SAKC. The elements of the POC set of a PM can be denoted as M_{pa} and be expressed by symbol $[\]$. The relations between virtual POC set and POC set is as follows

$$M_{pa} \supseteq M_{BKC} \quad (3)$$

Therefore, supposing we want to synthesize a PM having its POC with $\begin{bmatrix} t^x \\ r^y \end{bmatrix}$, then the SAKCs will have three virtual POC types, i.e., $\left\{ \begin{matrix} t^x \\ r^y \end{matrix} \right\}$, $\left\{ \begin{matrix} t^{x-1} \\ r^y \end{matrix} \right\}$ and $\left\{ \begin{matrix} t^x \\ r^{y-1} \end{matrix} \right\}$.

We classify 40 kinds of SAKC structures into A, B, C, ..., M type according to the virtual POC types, in all 13 types, as shown in the Appendix. Each virtual POC set corresponds to one or several SAKC structures, which lays the foundation for synthesis of the 13 types PMs with 2–6 *dof*.

4.2 Type Synthesis Method Based on SAKCs

The design method based on SAKC which meets the requirements of POC set includes only three main steps:

- (1) According to the given POC set, several corresponding virtual POC sets could be gotten.
- (2) For each given virtual POC set, find the appropriate SAKC structure from the Appendix;
- (3) Add input joints on each legs of SAKC, including on the legs of the adding SAKC, according to the principles given below, i.e., principles for axis orientation of input joints and principles for number of input joints [8].

Finally, we can get different mechanisms which can satisfy the expected POC set of the moving platform.

(A) The principles for axis orientation of input joints

If we want to synthesize a PM with POC set like $\begin{bmatrix} t^x \\ r^y \end{bmatrix}$, we should use virtual POC type like $\left\{ \begin{matrix} t^x \\ r^y \end{matrix} \right\}$, $\left\{ \begin{matrix} t^{x-1} \\ r^y \end{matrix} \right\}$ and $\left\{ \begin{matrix} t^x \\ r^{y-1} \end{matrix} \right\}$. Table 3 will show how to add the input joints.

Table 3 The principles for axis orientation of input joints

	Virtual POC of a SAKC	Add the input joint	Principles of the axis orientation of the input joint(s)	POC of the PKM
Principle A1	$\begin{Bmatrix} r^x \\ r^y \end{Bmatrix}$	R joint	Be parallel to the axis of any rotation joint in the SAKC, and do not add new translation elements of the moving platform	$\begin{Bmatrix} r^x \\ r^y \end{Bmatrix}$
		P joint	Be parallel to the axis of any translation joint in the SAKC	
Principle A2	$\begin{Bmatrix} r^{x-1} \\ r^y \end{Bmatrix}$	R joint	Be parallel to the axis of any rotation joint in the SAKC, and add a new translation element of the moving platform	
		P joint	Be not parallel to the axis of any translation joint in the SAKC	
Principle A3	$\begin{Bmatrix} r^x \\ r^{y-1} \end{Bmatrix}$	R joint	Be not parallel to the axis of any rotation joints in the SAKC, and do not add new translation element of the moving platform	
		P joint	Be parallel to the axis of translation joints in the SAKC	

(B) The principles for number of input joints

After selecting an SAKC structure, according to the relationship between the number of branches (n_b) and DOF of the SAKC, there are two principles to address the number of input joint.

- (1) Principle B₁: If $n_b = \text{DOF}$, add one input joint on each leg of the SAKC structure directly.
- (2) Principle B₂: If $n_b < \text{DOF}$, superimpose a new SAKC with $k = 0$ on original the SAKC structure to make $n_b = \text{DOF}$, and then add one input joint on each leg.

Example 2 Design a PM with three rotation outputs

This example will be illustrated to show how to synthesize a parallel mechanism.

Step1. Two virtual POCs like $\begin{Bmatrix} t^0 \\ r^3 \end{Bmatrix}$, $\begin{Bmatrix} t^0 \\ r^2 \end{Bmatrix}$ from the Appendix are selected to synthesis PM with POC set like $\begin{Bmatrix} t^0 \\ r^3 \end{Bmatrix}$.

Step2. To find the appropriate SAKC structure for each virtual POC set, we can find them in row of *No.G*, *No.B* of the Appendix.

Step3. To add input joints in each legs of the SAKC structure as follows, and the mechanism is obtained we want.

(1) Synthesize the PM using the SAKC which has virtual POC set $\left\{ \begin{matrix} t^0 \\ r^3 \end{matrix} \right\}$

- ① Choose No. 22 SAKC structure in the row of No.G of the Appendix, as shown in Fig. 2a;
- ② The POC set of the mechanism to be synthesized is the same as the virtual POC set of the SAKC we choose. But the number of the legs of the SAKC, 4, is larger than the DOF of the mechanism, 3, So, according to the Principles A1 and B3, we make leg {-S-} as a constraint branch, and add a P joint (P_1, P_2, P_3) into other 3 {-S-S-} legs as 3 input joints, and then we get a 3-DOF mechanism shown in Fig. 2b.

(2) Synthesize the parallel mechanism using the SAKC which has virtual POC set

$$\left\{ \begin{matrix} t^0 \\ r^2 \end{matrix} \right\}$$

- ① Choose No. 5 SAKC optionally in the row of No.B of the Appendix, as shown in Fig. 3a;

Fig. 2 Synthesis for S+3-SPS PKM

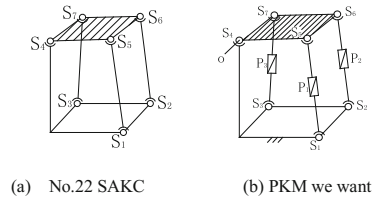
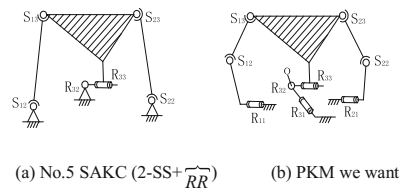


Fig. 3 Synthesis for 2-RSS+RRR PKM



- ② Because the POC set of the mechanism to be synthesized has one more rotation elements in comparison to the virtual POC set of the SAKC we choose, and the DOF of the mechanism is equal to the number of the legs of the SAKC, i.e., 3., Following the Principles A3 and B1, we add a R input joint in each legs of the SAKC (Fig. 3a). For example, we add R_{11} , R_{21} , R_{31} as three input joints, where, R_{31} shares a different direction with R_{32} and R_{33} which are on other two original legs and both of them cross at one point. Finally, a 3-DOF mechanism shown in Fig. 3b is obtained.

The details of type design process of this PM and other two PMs that have 2 translations and 1 rotation, and 3 translations and 1 rotation, respectively, could be found in [8].

5 Conclusions

In this paper, we propose and derivate the concept of SAKC into two levels, that is, the first one is the SAKC basic type and the second one is SAKC structure. The relationship between the former two and the parallel mechanism is clarified.

- (1) 53 kinds of SAKC basic types with coupling degree $k = 0 - 3$ and independent loop $\nu = 1 - 5$, as well as their analytical expressions are given. Among them, there are 6 most common SAKC basic types and they can represent analytical composition for the 40 kinds SAKC structures, which are classified according to 13 kinds of virtual POC sets with the different coupling degree k . Moreover, these SAKC structures are the basic unit of numerous parallel mechanisms.
- (2) A general and practical method for the type design of PM based on SAKC units which meet the requirements of POC set is proposed and illustrated by one example. The design unit is SAKC instead of leg (or limbs) that are units of existing other four type synthesis methods. This method has only three simple steps and has better usability and universality.

Appendix: Classification of SAKC Structures Based on Virtual POC Set

Dimen-sion	SAKC Structures			
2	A	$\left\{ \begin{matrix} t^2 \\ \mu^0 \end{matrix} \right\}$	B	$\left\{ \begin{matrix} t^0 \\ r^2 \end{matrix} \right\}$
		$\left\{ \begin{matrix} t^1 \\ r^1 \end{matrix} \right\}$		$\left\{ \begin{matrix} t^2 \\ r^1 \end{matrix} \right\}$
3	D	$\left\{ \begin{matrix} t^3 \\ \mu^0 \end{matrix} \right\}$	E	$\left\{ \begin{matrix} t^2 \\ r^1 \end{matrix} \right\}$
		$\left\{ \begin{matrix} t^1 \\ r^2 \end{matrix} \right\}$		$\left\{ \begin{matrix} t^0 \\ r^3 \end{matrix} \right\}$
4	H	$\left\{ \begin{matrix} t^3 \\ \mu^1 \end{matrix} \right\}$	I	$\left\{ \begin{matrix} t^2 \\ r^2 \end{matrix} \right\}$
		$\left\{ \begin{matrix} t^1 \\ r^3 \end{matrix} \right\}$		$\left\{ \begin{matrix} t^3 \\ \mu^2 \end{matrix} \right\}$
5	K	$\left\{ \begin{matrix} t^3 \\ \mu^2 \end{matrix} \right\}$	L	$\left\{ \begin{matrix} t^2 \\ r^3 \end{matrix} \right\}$
		$\left\{ \begin{matrix} t^3 \\ \mu^3 \end{matrix} \right\}$		
6	M	$\left\{ \begin{matrix} t^3 \\ \mu^3 \end{matrix} \right\}$		

References

1. Yang, T.-L., Liu, A.-X., Luo, Y.-F. et al.: Theory and Application of Robot Mechanism Topology. Science Press, Beijing (2012)
2. Frisoli, A., Checcacci, F., et al.: Synthesis by Screw Algebra of Translating in-Parallel Actuated Mechanisms. *Advance in Robot Kinematics*, pp. 433–440 (2000)
3. Herve, J.M.: Analyse structurelle des mécanismes par groupe des déplacements. *Mech. Mach. Theory* **13**, 437–450 (1978)
4. Gogu, G.: Structural synthesis of fully-isotropic translational parallel robots via theory of linear transformations. *Eur. J. Mech. A. Solids* **23**, 1021–1039 (2004)
5. Jin, Q., Yang, T.-L.: Theory for topology synthesis of parallel manipulators and its application to three-dimension-translation parallel manipulators. *ASME J. Mech. Des.* **126**, 625–639 (2004)
6. Shen, H.-P., Yin, H.-B., Wang, Z., et al.: Research on forward position solutions for 6-SPS parallel mechanisms based on topology structure analysis. *Chin. J. Mech. Eng.* **49**(21), 70–80 (2013)
7. Yin, H.-B., Shen, H.-P., Ma, X.-M., Li, J., Deng, J.-M.: Topology structure analysis and synthesis method of parallel mechanism based on SAKCs. *J. Mach. Design* **32**(6), 11–17 (2015)
8. Shen, H.-P., Sun, C.-Y., Zhu, X.-R., et al.: A practical method for topological design of PMs based on the basic kinematic chains as well as position and orientation characteristic. *Trans. Chin. Soc. Agric. Mach.* **46**, 337–345 (2015)

Matlab GUI for SVAJ Cam Analysis Diagrams

C. Pop, E.-C. Lovasz, F. Pop, A. Davidescu and S.M. Grigorescu

Abstract An alternative faster method for cam mechanism displacement parameters analysis based on image processing and Artificial Neural Network (ANN) is proposed. The method is developed in Matlab and consists of a Graphical User Interface that displays the cam-follower position, velocity, acceleration and jerk diagrams (svaj) versus the angle of rotation of the cam. These diagrams are generated for four types of cams based on a preliminary elevation curves of the cam-follower obtained with help of GL 112 cam analysis apparatus. The method reduces the time for calculating the parameters and the results can be compared with the ones from analytical method. The image processing algorithm considered is based on a set of images taken with a HD camera of the investigated cams. These images are further processed in order to train an ANN which it finally conducts to automatically identifying the cams.

Keywords Cam mechanism · Cam profile · Motion curves · Image processing · Artificial neural network

C. Pop (✉) · E.-C. Lovasz · F. Pop · A. Davidescu · S.M. Grigorescu
Politechnica University of Timisoara, Timisoara, Romania
e-mail: cristian.pop@upt.ro

E.-C. Lovasz
e-mail: erwin.lovasz@upt.ro

F. Pop
e-mail: florina.pop@upt.ro

A. Davidescu
e-mail: arjana.davidescu@upt.ro

S.M. Grigorescu
e-mail: sanda.grigorescu@upt.ro

1 Introduction

Cam mechanisms are widely used in industrial applications because of their particular design of various shapes that generate a specific law of motion to the follower which transmits it further to the final element. The follower can be jointed with the cam through a roller, a flat-face or a knife-edge termination [1, 2].

For designing and/or analysing a cam it is necessary to know its specifications and its motion characteristics regarding displacements, velocity, acceleration and jerk variations of the cam follower, respectively it's so called svaj diagram related to the rotation angle of the cam [3, 4]. From this diagram, an operator should understand the motion behaviour of the cam mechanism and decide if that type of cam fulfil the requirements for the application. Also, based on the same svaj diagram a cam designer will be able to choose the best mathematical functions that define the motion of the cam follower [5, 6].

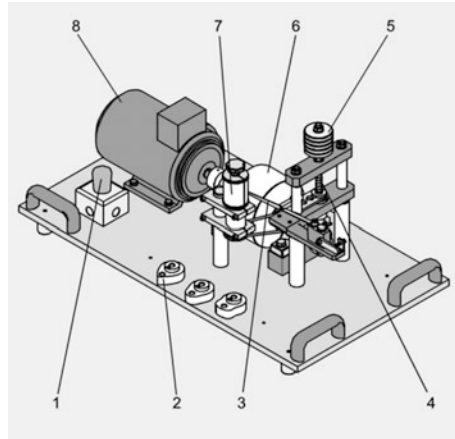
Based on different experimental methods carried on specific designed test beds utilized in laboratories, the position of a cam mechanism can be graphically determined. Also, the movements of the elements can be observed [7, 8]. By analysing the graphical results of the position parameter and using first, second and third order derivatives the other motion characteristics can be obtained such as velocity, acceleration and jerk which will be useful for further analysis. The calculations can be made with help of computer programs that will reduce the time and will increase the accuracy of the results. Matlab software, like many other similar programs is suitable in various engineering application due to its well performing mathematical and programming tools.

This paper presents a Graphical User Interface (GUI) developed in Matlab for identifying four types of cams and display the svaj diagrams based on the displacement parameter diagram of the cams preliminary obtained with a GL112 cam analysis apparatus [8]. The identification process is based on a previous research method presented in [9], which utilizes an image processing algorithm and a trained Artificial Neural Network (ANN). Two circular arc cams, one tangent cam and a hollow type of cam are analysed. The application intends to improve the cams analysis process in order to obtain the svaj diagrams based on the outputs offered by GL112 apparatus in a rapid and accurate manner. It also tries to automate the identification process of different types of cams.

2 General Description of the GL 112 Cam Analysis Apparatus

The GL 112 apparatus presented in Fig. 1 is used for investigating the dynamic behaviour of cams mechanisms in a similar manner as in real applications when are mounted on motor's shafts and actuate the valves. In this application the valves are considered to be the moving mass attached to follower and the springs. Additional 5

Fig. 1 View of the GL 112 cam analysis apparatus and its components [8]: 1 emergency stop button; 2 the investigated cams; 3 plotting spring; 4 interchangeable restoring springs; 5 mass plates; 6 centrifugal mass; 7 plotting drum; 8 electric motor with variable speed



weights mass can be lifted. The purpose of the device is to record on a wax-coated paper wrapped on the drummer the elevation curve using a fine recording stylus which is directly driven by the follower via a crossbar.

GL 112 apparatus control unit is composed by a three-phase asynchronous motor with frequency converter, the control elements and speed display.

On this experimental unit are investigated four interchangeable cams such as two circular cams, one tangent cam and a hollow cam. The dimensions of these cams are presented in Table 1. Two types of cam-followers are included, one is fitted with a flat-face termination and the other with a roller.

In practice, tangent type of cam is able to produce smooth motion in relation with a cylindrical tappet. Circular-arc cams are commonly used in various

Table 1 Cams characteristics

	Circular cam 1	Circular cam 2	Tangent cam	Hollow cam
Figure				
Base radius (mm)	25	25	25	25
Tip radius (mm)	5	10	17.2	40
Cam stroke (mm)	15	15	15	15
Action angle (°)	140	140	140	140

applications due to their economical production. Also, the flat follower can be used in conjunction with these cams. The combination of two curved flanks, one convex and the other concave of the hollow type of cam determine an ample elevation curve and a constant stroke towards a large angular range. Cylindrical type of follower is used in conjunction with this cam [8].

Based on the experiments made on this apparatus a series of observations can be done regarding comparison of different cam forms, lift curves for non-matching tracer, determination of limit speed and comparison with theory. Also, appreciations of the influence of moving mass and the influence of re-storing spring rigidity can be stated.

With the mechanical drum plotter, the graphical variation of the displacement of the cam-follower is plotted on a coated paper.

3 The Svaj Diagrams Application

In this paper an application for analysing cams in an automated manner is described. The main purpose underlying the mention application is to determine the mathematical functions used by designers to define cams. This involves determining the motion curves, which is imposed on the followers. The study considers only the planar cams, which allows a rotation motion along a fixed axis.

A fast approach, in order to obtain the “unwrapped” shape of the cams needed to determine the displacement function s , its first, second and third derivative (velocity v , acceleration a and jerk j), is to acquire images of the cams and process them. An object detection, recognition and analysis application based on image processing and artificial neural network (ANN) is presented. This application is developed and implemented in MATLAB working environment. A graphical user interface (GUI), presented in Fig. 2, is attached to this application. This interface contains different controllers grouped that represents the steps required to be covered, for accomplishing the purpose of this application.

The first step is the acquisition of the necessary images for the analysis process. This is performed by using a HD web camera (A4Tech Pk910H), whose video sensor is parallel to the cam surface, and captures images at a resolution of 1920×1080 pixels. The images are saved in PNG (Portable Network Graphics) format on a PC desktop to which the camera is attached.

The next step consists in training the artificial neural network necessary for the cam identification process. This process is accomplished by using a number of images with the four mentioned cams, having different positions and orientations regarding the reference system of the image.

The graphical user interface introduces two buttons that allow uploading the acquired images and process them. At the base of this operation an image processing algorithm is found. This algorithm uploads an image in an axes graphic object and allows the user to select a number of pixels from the surface of the cam, required for the image processing phase. The threshold level used for image

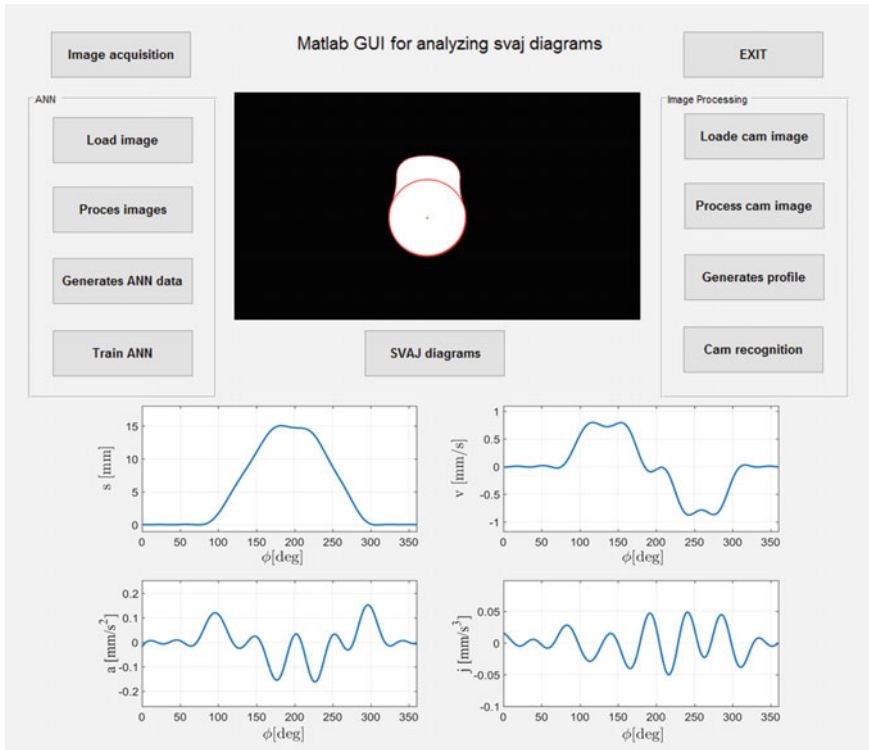


Fig. 2 Matlab GUI for cam analysis

binarization is computed based on the values of the selected pixels. Picking a set of pixels to compute a threshold value, is the easiest way to use the binarization process on an image because this classifies all pixels with values above this threshold as white, and all other pixels as black. This action is performed to simplify the cams extraction process from the one hundred images acquired, precisely twenty-five per cam. To complete processing of hundred images and retrieve the desired objects, this algorithm removes existing artefacts by applying morphological operations such as erosion and dilatation, detects edges of the object using Sobel operator, closes and fills the contour of the object. Also the algorithm enables the determination of some cam features like the centre coordinates of the base circle of the cams relative to the image coordinate system, the base circle radius, the maximum radius, the edge coordinates and the corresponding rays vectors. A more detailed presentation of obtaining these features can be seen in [7]. The result of this stage, are illustrated in Fig. 3.

After extracting the shape of the cams from the images, a sub function of the program performs some image measurements based on the mentioned regions. This step is carried out in order to determine three distinct image properties of the cams, like area, perimeter and a so called equivalent diameter. The third feature returns a

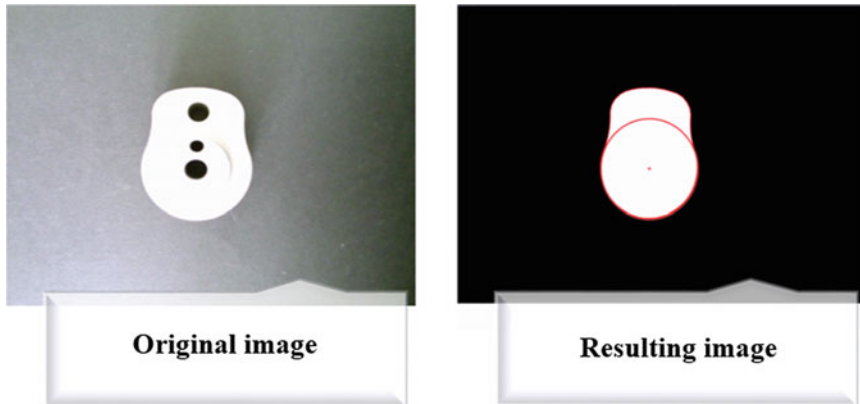


Fig. 3 Image processing results

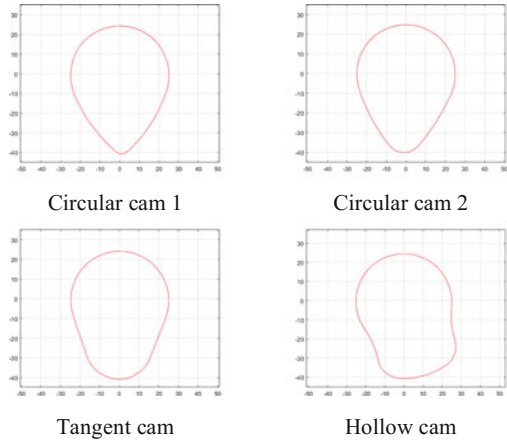
scalar that specifies the diameter of a circle with the same area as the region measured. The numerical values of the three measurements are computed for the one hundred images acquired (twenty-five per cam), and represents the input matrix (3×100) of the artificial neural network. In addition, an output matrix (3×100), that represents the type of came corresponding to every image used, is computed.

In general, an artificial neural network offers great solutions for automatic or semiautomatic applications that imply identification of different objects. This result is due to the fact that an ANN can be trained similar to a human brain neural network. The ANN used in the cam identification application was train by using the Neural Network Toolbox provided by MATLAB and a dataset for the three features mentioned. After the process of training the neural network is completed, the operator has the possibility to save the artificial neural network as a standalone function. This function is integrated in the cam recognition application as a sub function that takes as arguments an input matrix (three features values of the cam to be identified) and returns an output matrix (representing the cam).

The next step of the application consists in loading a new image in the GUI with the cam that needs to be analysed. This cam has previously been mounted on the cam analysis apparatus (GL-112), and a displacement curve has been obtained for the used cam-follower. The human operator has the possibility to process the image loaded in the interface, based on an algorithm similar to that used to train the neural network. After processing the image, the results obtained are the base circle radius and the edge coordinates of the cam. Using this features the profile of the cams can be computed (see Fig. 4).

Base on the cam analysed processed image, the numerical values of the three measurements, necessary for the identifying operation, are computed. These values allow to automatically determine the type of cam placed in the visual field of the webcam using the trained neural network that is integrated in the application. In this way the human user finds out which cam is analysing.

Fig. 4 Cams profile



After determining the type of the cam, the last step of the application consists in obtaining the svaj diagrams of the follower. This steps involves loading the displacement curve determined by the cam analysis apparatus and plotted on a coated paper. The curve is digitized using another image processing algorithm that is integrated into the application. Figure 5 presents the results of this operation.

The motion curve represents the zero order transmission function $s(\varphi)$ of the cam mechanism in the different motion section. The first, second and third derivative of

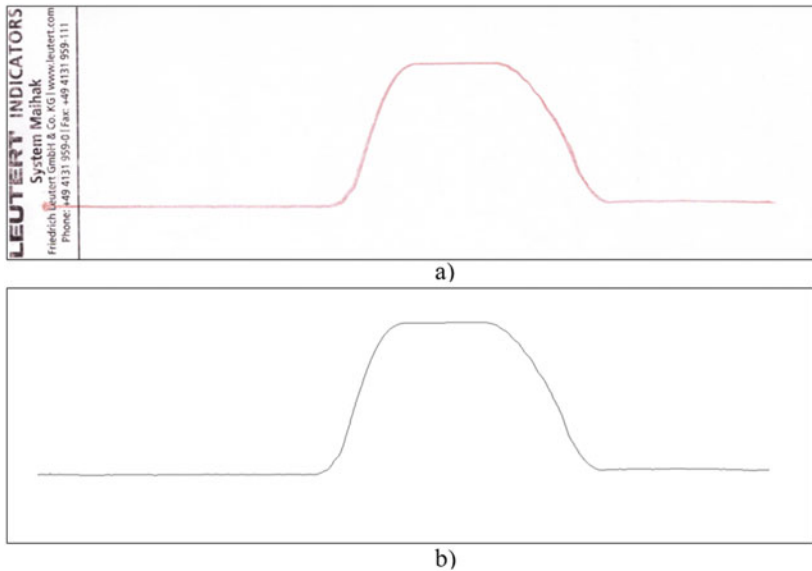


Fig. 5 Displacement curve: a) recorded on wax-coated paper; b) binary image

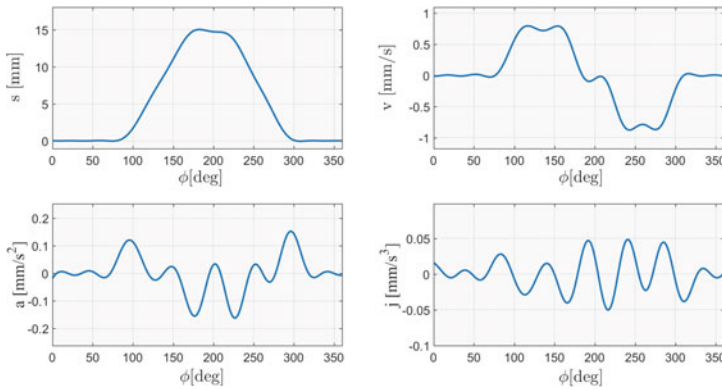


Fig. 6 The svaj diagrams

the motion curve in between of the cam angle φ give the first, second and third order transmission function.

$$\begin{aligned}
 s'(\varphi) &= ds(\varphi) / d\varphi \\
 s''(\varphi) &= d^2s(\varphi) / d\varphi^2 \\
 s'''(\varphi) &= d^3s(\varphi) / d\varphi^3
 \end{aligned}
 \tag{1}$$

The velocity v , acceleration a , and jerk j of the follower, can be computed, considering a constant angular velocity of the cam and using relationship (1). Figure 6 shows the svaj curves for the whole came over 360° of camshaft rotation.

4 Conclusions

The graphical user interface, of the proposed application, offers the possibility to analyse in a more precise and faster manner the svaj diagrams of the follower, by using a cam analysis apparatus designed for dynamic investigation of cam drives used to actuate engine valves. The obtained results are satisfactory for all four cams used. As future perspectives the application can be improved to recognize more cams by the motion laws and their specific characteristics.

References

1. Norton, R.: Cam Design and Manufacturing Handbook, 2nd edn. Industrial Press, New York (2009)
2. Lovasz, E.-C., Cărăbaș, I.: Synthesis principle of gear and cam mechanism (in Romanian). Politehnica, Timisoara (2009)

3. Doane J.: Machine Analysis with Computer Applications for Mechanical Engineers. Wiley, New York (2016)
4. Angeles, J., Lopez-Cajun, C.S.: Optimization of Cam Mechanisms. Kluwer Academics Publisher, Dordrecht (1991)
5. Sahu, L.K., Kedia, V.K., Sahu, M.: Design of cam and follower system using basic and synthetic curves: a review. IJSET **3**(2) (2016)
6. Chen, F.Y.: A survey of the state of the art of cam system dynamics. Mech. Mach. Theory **12**, 201–224 (1997)
7. Ceccarelli, M., Carbone, G., Lanni, C., Ottaviano, E.: A fairly simple method to identify the curvature of a cam profile. In: Proceedings of DECT'04, ASME 2004 Design Engineering Technical Conferences and Computer and Information in Engineering Conference, Utah (2004)
8. GL 112 Cam Analysis Apparatus, Technical Description, <http://www.gunt.de>
9. Pop, C., Lovasz, E.-C., Grigorescu, S., Pop, F., Davidescu, A., Cărbăș I.: Image processing and artificial neural network for cam identification. In: 14th World Congress in Mechanism and Machine Science, Taipei, Taiwan (2015)

On the Kinematic Analysis of a Sixth Class Mechanism

C.E. Moldovan, D. Perju, E.-C. Lovasz, K.-H. Modler and I. Maniu

Abstract The paper deals with the kinematic analysis of a particular case of a “multiple-bar mechanism” from Artobolevsky’s mechanisms collection. The structural analysis of this eight-link mechanism shows that it is a six class third order mechanism according to Assur-Artobolevsky classification. The kinematic analysis of such a mechanism is very difficult through the direct method. Usually, the kinematic analysis is performed by means of reducing the mechanism’s class through the swapping of the input and output links. The paper proposes another method to reduce the class of a mechanism, namely by choosing a certain moving link as referential and studying the relative movements of the remaining links/elements. Thus, the transmission function can be found, as a function of the original input and output links. Such a mechanism is useful for manufacturing of compound light structures.

Keywords Structural analysis · Kinematic analysis · Assur group · Relative movement · Transmission function

C.E. Moldovan (✉) · D. Perju · E.-C. Lovasz · I. Maniu
Politechnica University of Timisoara, Timisoara, Romania
e-mail: cristian.moldovan@upt.ro

D. Perju
e-mail: dan.perju@upt.ro

E.-C. Lovasz
e-mail: erwin.lovasz@upt.ro

I. Maniu
e-mail: inocentiu.maniu@upt.ro

K.-H. Modler
Technische Universität Dresden, Dresden, Germany
e-mail: karl-heinz.modler@tu-dresden.de

1 Introduction

The term “class” is based on the classification method of mechanisms proposed by Artobolevsky in [1, 2]. By definition, the Assur kinematic group represents the most simple kinematic chain, having only fifth class kinematic pairs (revolute and/or prismatic), with $DoF = 0$, which added to or extracted from a mechanism does not change its mobility (total DoF). The kinematic pairs can be reals or equivalents resulted from kinematic and structural transformation. The mechanism is now virtually split up in groups with $DoF = 0$, remaining only the driving link and its connection to the fixed element. Also, there are two additional concepts related to the Assur kinematic groups, which have to be presented. The class of an Assur kinematic group is given by the number of sides of the most complex polygonal loop (contour) existing in the group and its order is equal to the number of peripheral (potential) kinematic pairs (which connect the Assur kinematic group with the remaining mechanism). In the synthesis process of a mechanism, this method comes handy because one can simply add an Assur kinematic group (with $DoF = 0$) to an existing linkage and obtain a completely new linkage.

We consider the sixth class, third order mechanism presented in Fig. 1a. The mechanism consists of a frame, an input ternary link (1) and a sixth class—third order Assur kinematic group, which contains $n = 6$ links/elements and $c_5 = 9$ kinematic pairs of 5th class. The connection joints of the Assur kinematic group to the rest of the mechanism are the joints A, B and J. The proof that the mechanism is of sixth class, states by definition that through the removal of “any second class Assur group” there should remain no mechanism.

As objective for any mechanism classification is to find some common rules to study a certain mechanism. Different criteria are proposed and described in [3–5]. In [6] a counting method is presented for generated mechanisms subject to design constraints from candidate kinematic chains. The presented method is based on

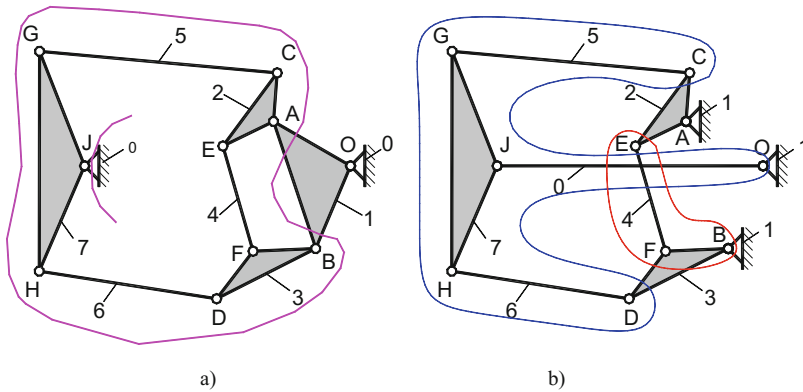


Fig. 1 The original structural scheme of the sixth class third order mechanism (a) and the structural scheme by considering the inverse motion (b)

graph theory and combinatorial mathematics. Pelecudi in [7] presents a collection of structural schemas of different classes of the Assur kinematic groups, the maximum addressed class of the groups being seven. Kinematic analysis, in principle, was performed for a fourth class mechanism in [7, 8] as well as in [9].

The state-of art shows that mechanisms of higher order than four were not studied from the kinematic analysis point of view, because of the complexity of the mathematical model. So, the paper develops a method for the kinematic analysis of a sixth class third order mechanism and refers to a particular case from Artobolevsky’s mechanisms collection [2]. This mechanism ensures a parallel displacement of the two symmetrical higher order couplers with the frame in a large motion range.

2 Kinematic Analysis of a Sixth Class Mechanism

Kinematic analysis studies the position and the motion parameters: velocities and accelerations of the elements and points belonging to the considered mechanism. The known methods for the kinematic analysis are analytical, graphic-analytical and graphical [1, 5, 8, 10, 11].

2.1 Transmission Function of 0-Order

By considering the inverse motion, the input link (1) becomes reference and the ternary output element (7) describes a complex planar motion. Admitting an inner parameter φ of the closed loop AEFBA as independent parameter, all angular parameters of the loop can be found from the vector equation, written in complex numbers as follows (see Fig. 2):

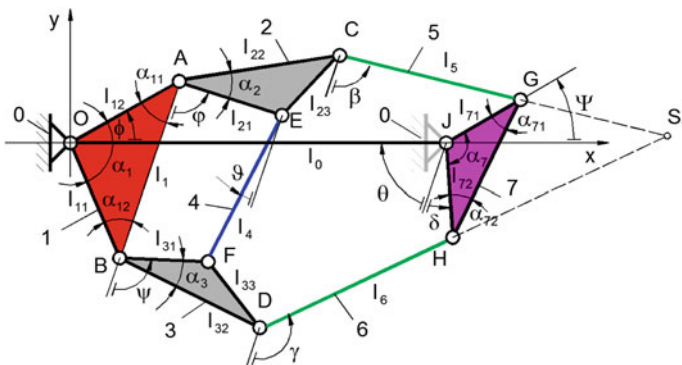


Fig. 2 Kinematic scheme of a sixth class third order mechanism

$$l_{21}e^{i \cdot \varphi} + l_4e^{-i \cdot \vartheta(\varphi)} = -l_1 + l_{31}e^{i \cdot \psi(\varphi)}. \quad (1)$$

By isolation on the left side of the Eq. (1) of the unknown parameter $\vartheta(\varphi)$ and multiplying the equation by its complex conjugate equation, results the angular parameters of the element (3) [10]:

$$\psi(\varphi) = 2 \arctan \frac{B(\varphi) \mp \sqrt{A(\varphi)^2 + B(\varphi)^2 - C(\varphi)^2}}{A(\varphi) - C(\varphi)}, \quad (2)$$

where:

$$\begin{aligned} A(\varphi) &= -2l_{31}(l_1 + l_{13} \cos \varphi), \\ B(\varphi) &= -2l_{21}l_{31} \sin \varphi, \\ C(\varphi) &= l_1^2 + l_{21}^2 - l_{31}^2 - l_4^2 + 2l_1l_{21} \cos \varphi, \end{aligned} \quad (3)$$

The angular parameters of the connecting elements (5), (0) and (6) in the inverse motion follows from the vector equations in complex numbers of the closed loops AOJGCA, BOJHDB and ACGHDBA:

$$l_{12}e^{-i \cdot \alpha_{11}} + l_0e^{i \cdot (\pi - \theta(\varphi))} + l_{71}e^{i \cdot (\delta(\varphi) + \alpha_7)} = l_{22}e^{i \cdot (\varphi + \alpha_2)} + l_5e^{i \cdot \beta(\varphi)}, \quad (4)$$

$$l_{32}e^{i \cdot (\psi(\varphi) - \alpha_3)} + l_6e^{i \cdot \gamma(\varphi)} = l_{11}e^{i \cdot (\pi + \alpha_{11})} + l_0e^{i \cdot (\pi - \theta(\varphi))} + l_{72}e^{i \cdot \delta(\varphi)}, \quad (5)$$

$$l_{22}e^{i \cdot (\varphi + \alpha_2)} + l_5e^{i \cdot \beta(\varphi)} = -l_1 + l_{32}e^{i \cdot (\psi(\varphi) - \alpha_3)} + l_6e^{i \cdot \gamma(\varphi)} + l_7e^{i \cdot (\pi + \delta(\varphi) - \alpha_{72})}. \quad (6)$$

Each of the Eqs. (4), (5) and (6) in complex numbers allows the elimination of the term containing the angular parameter $\delta(\varphi)$ of the ternary element (7) and gives a trigonometric equation system with 3 unknown angular parameters of the connection elements:

$$\begin{aligned} 0 &= l_0^2 + l_{12}^2 + l_{22}^2 + l_5^2 - l_{71}^2 - 2l_{12}l_{22} \cos(\varphi + \alpha_{11} + \alpha_2) + 2l_{22}l_5 \cos(\varphi + \beta(\varphi) + \alpha_2) \\ &\quad + 2l_0l_{22} \cos(\varphi + \theta(\varphi) + \alpha_2) - 2l_{12}l_5 \cos(\beta(\varphi) + \alpha_{11}) - 2l_0l_{12} \cos(\theta(\varphi) - \alpha_{11}) \\ &\quad + 2l_0l_5 \cos(\beta(\varphi) + \theta(\varphi)), \end{aligned} \quad (7)$$

$$\begin{aligned} 0 &= l_0^2 + l_{11}^2 + l_{32}^2 + l_6^2 - l_{72}^2 + 2l_{11}l_{32} \cos(\psi(\varphi) - \alpha_{11} - \alpha_3) + 2l_{32}l_6 \cos(\psi(\varphi) - \gamma(\varphi) - \alpha_3) \\ &\quad + 2l_0l_{32} \cos(\psi(\varphi) + \theta(\varphi) - \alpha_3) + 2l_{11}l_6 \cos(\gamma(\varphi) - \alpha_{11}) + 2l_0l_{11} \cos(\theta(\varphi) + \alpha_{11}) \\ &\quad + 2l_0l_6 \cos(\gamma(\varphi) + \theta(\varphi)), \end{aligned} \quad (8)$$

$$\begin{aligned}
0 = & l_1^2 + l_{22}^2 + l_{32}^2 + l_5^2 + l_6^2 - l_7^2 + 2l_1l_{22} \cos(\varphi + \alpha_2) - 2l_{22}l_{32} \cos(\varphi - \psi(\varphi) + \alpha_2 - \alpha_3) \\
& - 2l_1l_{32} \cos(\psi(\varphi) - \alpha_3) + 2l_1l_5 \cos \beta(\varphi) - 2l_1l_6 \cos \gamma(\varphi) + 2l_{22}l_5 \cos(\varphi - \beta(\varphi) + \alpha_2) \\
& - 2l_{22}l_{32} \cos(\varphi - \gamma(\varphi) + \alpha_2) - 2l_{32}l_5 \cos(\psi(\varphi) - \beta(\varphi) - \alpha_3) \\
& + 2l_{32}l_6 \cos(\psi(\varphi) - \gamma(\varphi) - \alpha_3) + 2l_5l_6 \cos(\beta(\varphi) - \gamma(\varphi)).
\end{aligned} \tag{9}$$

By numerical computation of the equation system results the unknown angular parameters $\beta(\varphi)$, $\gamma(\varphi)$ and $\theta(\varphi)$, and by substituting them in one of the Eqs. (4)–(6) results the angular parameter $\delta(\varphi)$ of the ternary element. Even though the equation system is complex solving it is compulsory in order to find out the correlation of the input and output angles. By means of graphical procedure, which is not treated in this study, the correlated position can only be obtained by using an iterative process.

The transmission function of the considered sixth class mechanism follows in a parametric form in correlation with the inner parameter φ , used in the inverse kinematic positional analysis:

$$\phi(\varphi) = \theta(\varphi) - \alpha_{11}, \quad \Psi(\varphi) = \theta(\varphi) + \delta(\varphi) + \alpha_7 - \pi. \tag{10}$$

The kinematic positional analysis of the sixth class mechanism is an iterative procedure in order to compute the transmission function of 0-order $\Psi(\phi)$.

2.2 Transmission Function of 1st-Order. Velocities' Distribution

The angular velocity ω_{70} of the output element follows by deriving the transmission function of 0-order, given in the parametric form (10) in respect to the time:

$$\omega_{70} = \frac{d\Psi/d\varphi \, d\phi}{d\phi/d\varphi \, dt} = Tr_{71} \cdot \omega_{10}, \tag{11}$$

where: Tr_{71} is the first order transmission function between the output (7) and input link (1).

Because the complexity of the analytical method for the computation of the derivative angular parameters $\theta(\varphi)$ and $\beta(\varphi)$, an alternative kinematical approach by using of the graphic-analytical method was taken into account.

The velocities distribution can be computed accepting the inverse motion as was mentioned above. In this case the mechanism is decomposed into a 2nd class and a 3rd class Assur group (see Fig. 1b). For the following kinematic analysis an

arbitrary value of the angular velocity is accepted, as example $\omega_{21} = 1 \text{ rad/s}$ (see Fig. 2). The velocities of the peripheral joints belonging to the new considered input element (2) can be calculated i.e.:

$$\vec{v}_E = \overline{\omega_{21}} \times \overline{l_{AE}}, \quad \vec{v}_C = \overline{\omega_{21}} \times \overline{l_{AC}}. \tag{12}$$

Knowing, that $\vec{v}_B = 0$ the velocity of point F of the link (3) can be found from the vector equations system, written for the 2nd class Assur chain:

$$\begin{cases} \vec{v}_F = \vec{v}_B + (\overline{\omega_{31}} \times \overline{l_{BF}})_{\perp BF}, \\ \vec{v}_F = \vec{v}_E + (\overline{\omega_{21}} \times \overline{l_{EF}})_{\perp EF}. \end{cases} \tag{13}$$

By using the similitude Burmester-Mehmke theorem the velocity of the point D can be obtained, i.e.:

$$\Delta bfd \approx \Delta BFD, \tag{14}$$

The velocity of the Assur point S_1 belonging to the ternary link (7), resulted as intersections of the two instantaneous center lines of the binary connecting elements (5) and (6), follows as:

$$\begin{cases} \vec{v}_{S_1} = \vec{v}_C + (\overline{\omega_{51}} \times \overline{l_{CG}} + \overline{\omega_{71}} \times \overline{l_{GS_1}})_{\perp CS_1} \\ \vec{v}_{S_1} = \vec{v}_D + (\overline{\omega_{61}} \times \overline{l_{DH}} + \overline{\omega_{71}} \times \overline{l_{HS_1}})_{\perp DS_1} \end{cases} \tag{15}$$

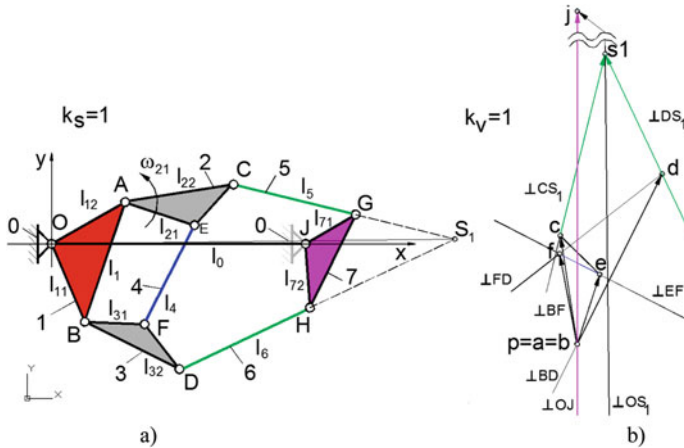


Fig. 3 Sixth class third order mechanism (a) and its velocities polygon (b) at corresponding scales by considering the $\omega_{21} = 1 \text{ rad/s}$

Because the vector products sums have same direction, the solution of the vector equations system (15) is unique (see Fig. 3b). So, by knowing $\overline{v_{S_1}}$, the velocity of point J of the ternary link (7) is computed from the vector equations:

$$\begin{cases} \overline{v_J} = \overline{v_{S_1}} + (\overline{\omega_{71}} \times \overline{l_{S_1J}})_{\perp S_1J} \\ \overline{v_J} = (\overline{\omega_{01}} \times \overline{l_{OJ}})_{\perp OJ} \end{cases} \quad (16)$$

By knowing from the velocity polygon the velocity of the joint J, $\overline{v_J}$ in the inverse motion, is possible to compute the angular velocities ω_{01} and ω_{71} as:

$$\omega_{01} = v_J / l_{OJ}, \quad \omega_{71} = (v_J - v_{S_1}) / l_{S_1J}. \quad (17)$$

The angular velocity of the sixth class third order mechanism in direct motion follows from the angular velocity correspondence:

$$\omega_{10} = -\omega_{01}, \quad \omega_{70} = \omega_{71} - \omega_{01} \quad (18)$$

The first order transmission function Tr_{71} of the mechanism according with the relationships (11) and (18) can be computed:

$$Tr_{71} = \frac{\omega_{70}}{\omega_{10}} = \frac{\omega_{71} - \omega_{01}}{-\omega_{01}}. \quad (19)$$

3 Numerical Example and Proposed Application

The numerical example considers a sixth class third order mechanism mentioned as “multiple-bar mechanism” in the Artobolevsky’s mechanisms collection ([2]—No. 609, LW.ML).

The revealed dimensions of the links (see Fig. 2) and the correlation of them given in [2] are shown in the Table 1.

The first step in designing the linkage is the computation of the angular dependence between the input and output links, by means the trigonometric equation system (7–9). As example, for the input angle $\phi = 30^\circ$ corresponds the output angle $\Psi = 76.14^\circ$, as shown in Fig. 4.

Table 1 Link length of the Artobolevsky’s sixth class third order mechanism

Link lengths (mm)	l_0	$l_{11} = l_{12}$	$l_{21} = l_{31}$	$l_{22} = l_{32}$	$l_{23} = l_{33}$	l_4	$l_5 = l_6$	$l_{71} = l_{72}$
	27.00	5.00	6.50	14.00	8.00	18.00	27.00	34.00

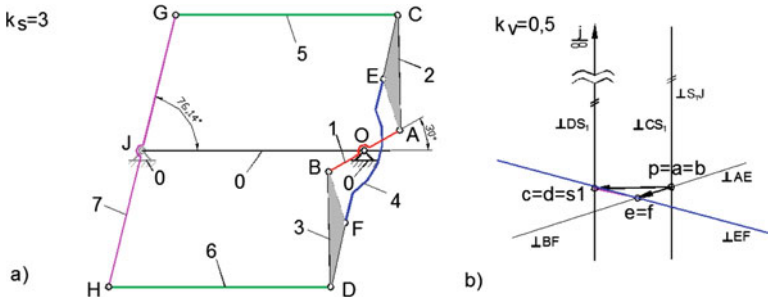
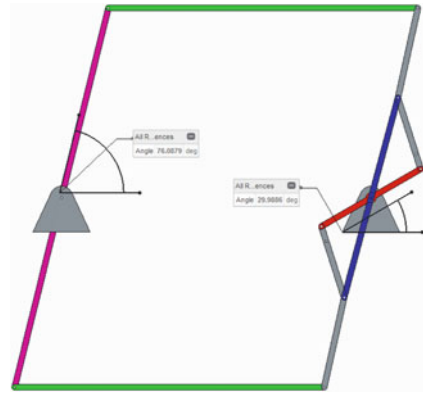


Fig. 4 Artobolevsky's sixth class mechanism in the positions $\phi = 30^\circ$ and $\Psi = 76.14^\circ$ (a) and its corresponding velocities polygons (b)

Fig. 5 Simulated CAD sixth class mechanism in the positions $\phi = 30^\circ$ and $\Psi = 76.14^\circ$



This angular correspondence is validated by simulation of the mechanism motion with a CAD program (CREO), for the previous considered position of crank (Fig. 5).

By means the graphic-analytical velocities analysis presented in Chap. 2.2 follows in Table 2 the values of the main linear and angular velocities and the corresponding first order transmission function. The graphic-analytical velocity analysis shows that the velocity of the point J $v_J \rightarrow \infty$, which means the motion of the input element (2) with respect to the element (1) in inverse motion is canceled (see Fig. 4b). This particular case corresponds with the parallel translation of the superior order couplers (5) and (6) in the original motion.

Table 2 Velocities of the sixth class mechanism for $\phi = 30^\circ$ and $\Psi = 76.14^\circ$

Parameters/position ϕ°	v_J (mm/s)	v_{S1} (mm/s)	ω_{01} (rad/s)	ω_{71} (rad/s)	ω_{10} (rad/s)	ω_{70} (rad/s)	Tr_{71} (-)
30°	$+\infty$	14.00	$-\infty$	$-\infty$	$+\infty$	$+\infty$	≈ 1



The analysis of this mechanism shows that it can perform an equivalent motion like the double parallelogram four bar linkage. In respect to this linkage the considered sixth class mechanism does preserve the parallelism of the higher order couplers to each other and to the frame in the whole rotation range of the crank. This condition is fulfilled only in counterclockwise range of the crank rotation $\phi \in [0^\circ, 134.6^\circ]$ or in clockwise range $\phi \in [0^\circ, -45.9^\circ]$ starting from the initial position. The mechanism shows a properly folded position of the links in the nearness of the input angle $\phi \cong 134.6^\circ$ (Fig. 6c), where a singularity position of the mechanism appears.

As shown in Fig. 6a the couplers remain parallel to each other, but no more to the frame before the singularity position and they are no more parallel to each other after crossing the mentioned position.

Figure 7 shows the kinematic analysis regarding the positions and the velocities of the Artobolevsky's mechanism for a position before and after the singularity.

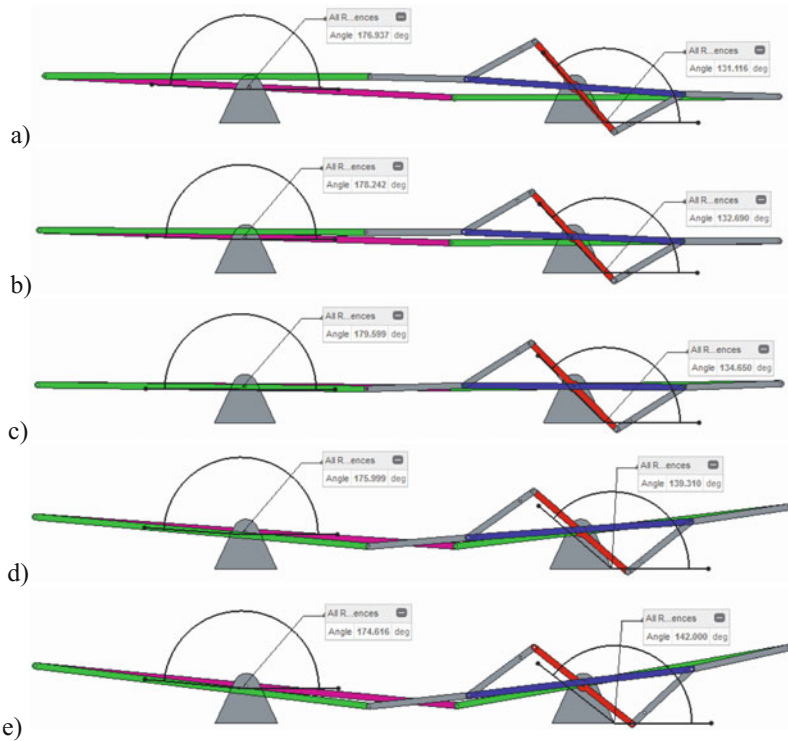


Fig. 6 Sixth class mechanism in the positions near to the singularity position for $\phi = 134.68^\circ$

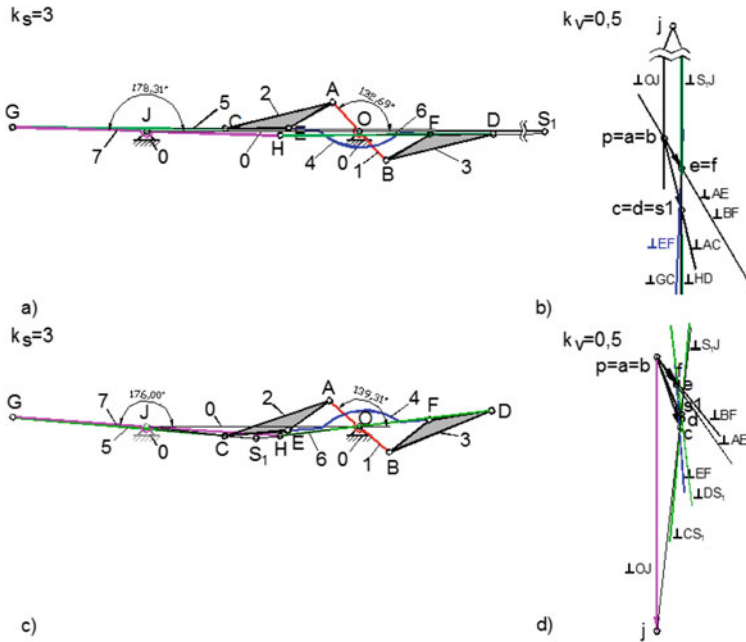


Fig. 7 Artobolevsky's sixth class mechanism in different positions (a, c, e) and its corresponding velocities polygons (b, d, f)

Table 3 Velocities of the sixth class mechanism near the singularity position

Parameters/position φ°	v_J (mm/s)	v_{S1} (mm/s)	ω_{01} (rad/s)	ω_{71} (rad/s)	ω_{10} (rad/s)	ω_{70} (rad/s)	Tr_{71} (-)
132.69°	3075.95	14.00	-113.92	-34.93	113.92	78.99	0.69
139.31°	51.98	11.82	-1.93	-2.87	1.93	-0.95	-0.49

In the nearness of the singularity position as shown in the Fig. 7a, c, the velocity v_J becomes high and finite values, but changes the direction of the oscillating motion of the element (7) (see Table 3).

This kind of sixth class mechanism can be used as mechanism for tensioning composite textile-reinforced preform spacers taking advantage of the self-locking property in the rectangular position, as the higher order couplers are parallel to each other and to the frame [12]. The tensioned preform structure in the manufacturing process is consolidated in an autoclave and then the linkage can be easily extracted by rotating the crank. As shown in the previous example the linkage has a very compact size near the singularity position, which is convenient for inserting and extracting the linkage in and out of narrow spaces.



4 Conclusions

The combined analytic and graphic-analytical kinematic analysis method of the sixth class third order mechanism can be performed by accepting the inverse motion, considering the input element of the original mechanism as frame and one of the adjacent ternary element as drive element. The analysis of the mechanism is reduced to the study of third and second class Assur kinematic groups. The positional kinematic analysis shows that the most difficult problem is the solving of a trigonometric equations system by means of numerical methods.

The kinematic analysis of a particular case indicated by Artobolevsky highlights the difficulties in computing the velocities in particular positions.

However, some properties of the mechanism recommend it to be used in applications which need the preservation of parallel positions of the higher order couplers in self-locked extreme position and its compact size in folded position.

References

1. Artobolevsky, I.I.: Theory of Mechanisms. Izdatelstvo Nauca, Moskow (1955). (in Russian)
2. Artobolevsky, I.I.: Mechanisms on Modern Engineering Design, vol. 1. Mir Publisher, Moskow (1975)
3. Hain, K.: Systematik der zwanglaufigen achtgliedriger Getriebe, Maschinenmarkt, vol. 37 (1964)
4. Corves, B., Kurtensbach, S., Hüsing, M., Schneider, C.: A general classification for mechanisms regarding the motion task. Mechanisms, Transmissions and Applications, Series Mechanisms and Machine Design, vol. 3, pp. 59–66. Springer (2012)
5. Hartenberg, R.S., Denavit, J.: Kinematic Synthesis of Mechanisms. McGraw-Hill B.C, NY (1964)
6. Hung, C.-C., Yan, H.-S., Pennock, G.R.: A procedure to count the number of planar mechanisms subject to design constraints from kinematic chains. Mech. Mach. Theory **43**, 676–694 (2008)
7. Pelecudi, C. (ed.): Basics of Mechanisms Analysis. Academiei Romane, Bucharest (1967)
8. Pelecudi, C., Maroş, D. (eds.): Mechanisms. Didactică și Pedagogică, Bucharest (1985)
9. Moldovan, C.E., Lovasz, E.-C., Perju, D., Modler, K.-H., Maniu, I.: On the kinematic analysis of the fourth class mechanisms. In: Proceedings of the 14th IFToMM World Congress, Taipei, Taiwan, 25–30 Oct 2015, OS8-023 (2015) www.iftomm2015.tw
10. Luck, K., Modler, K.-H.: Getriebetechnik—Analyse, Synthese. Springer, Optimierung (1995)
11. Perju, D.: Mechanisms in Precision Mechanics (Mecanisme de mecanică fină), Litografia I.P. T.V., Timisoara, 1990. <http://www.dmg-lib.org/>
12. Lin, S., Modler, K.H., Hanke, U.: The application of mechanisms in producing textile-reinforced thermoplastic composite. Mach. Design Res. **24**, 380–384 (2008)

Zero-Free-Length Elastic Systems for Static Balancing

L. Ciupitu and I. Simionescu

Abstract The static balancing of the weight forces is necessary to any mechanical system which is not working in horizontal plane. The effect is the decreasing of the acting power. From practical point of view two main passive ways of static balancing could be taken into consideration: by mass redistribution of components or/and by adding counterweights, and by elastic forces of the springs or of the gases. The first solution is not always possible due to the dimensions of mechanical systems and due to increasing of the dynamic stresses of components. Second solution is more and more used to various mechanical systems. The complexity of balancing systems with springs comes from the need of using *zero-free-length* springs. Instead of using complex balancing systems with real springs, some *zero-free-length* elastic systems are proposed. Present paper is continuing former papers of authors and is presenting some new constructive solutions of *zero-free-length* elastic systems. Finally an example is solved.

Keywords Static balancing · Cylindrical helical extension spring · Zero-free-length

1 Introduction

The static balancing of the weight forces is necessary to any mechanical system which is not working in horizontal plane [1, 4–6, 9, 13, 17, 19, 21–24, 26, 31–33]. The effect is the decreasing (until to vanishing) of the acting power [5]. For the case of passive balancing two main ways of static balancing could be considered in practice: mass redistribution of components [28, 33] or adding counterweights [18, 32], and by elastic forces of the springs [1–10, 12–14, 16, 17, 19–27, 29–32] or

L. Ciupitu (✉) · I. Simionescu
Politechnica University of Bucharest, Bucharest, Romania
e-mail: liviu.ciupitu@upb.com; liviu.ciupitu@upb.ro

I. Simionescu
e-mail: simionescu2@gmail.com

of the gases [33]. The first solution is unsuitable and not always possible due to the increasing of the dimensions of mechanical systems and due to the increasing of the dynamic stresses of components [15]. Second solution is more and more used to various mechanical systems and many constructive solutions were proposed in last time [10, 18, 21, 30].

The complexity of the balancing systems with springs resides in the necessity of using the so-called *zero-free-length* springs. This could be shown by studying the simplest solution of balancing a rocking arm by using a single cylindrical helical extension spring [8] attached like in Fig. 1a.

The spring is joined between a point *A* belonging to the rocking arm and a fixed *B* one. The gravity load moment acting upon the rocking arm ① is balanced by the moment of the elastic force of the helical spring ②.

Using the virtual power principle, the next equilibrium equation is obtained:

$$[m_1 OG_1 \cos \varphi_1 + m_{2A} OA \cos(\varphi_1 + \alpha)] g + F_s OA \sin(\varphi_1 - \theta + \alpha) = 0 \quad (1)$$

where G_1 represents the gravity center of the link ①, m_1 is the mass of the arm ①, m_{2A} is a fraction of the mass of the spring ② concentrated in the point *A*, and:

$$\begin{pmatrix} X_A \\ Y_A \end{pmatrix} = \begin{pmatrix} \cos \varphi_1 & -\sin \varphi_1 \\ \sin \varphi_1 & \cos \varphi_1 \end{pmatrix} \begin{pmatrix} x_{1A} \\ y_{1A} \end{pmatrix}, \theta = \text{atan} \frac{Y_A - Y_B}{X_A - X_B}, a = \text{atan} \frac{y_{1A}}{x_{1A}}, \quad (2)$$

$$OA = \sqrt{x_{1A}^2 + y_{1A}^2}, AB(\varphi_1) = \sqrt{(X_A - X_B)^2 + (Y_A - Y_B)^2} = l_s. \quad (3)$$

The mobile axis system $x_1 O y_1$ was chosen so that point G_1 is upon the Ox_1 axis (Fig. 1a).

The elastic force of the helical spring ② is supposing to have a linear evolution (see Fig. 2) in first approximation [10]:

$$F_s = F_{s0} + k(l_s - l_{s0}). \quad (4)$$

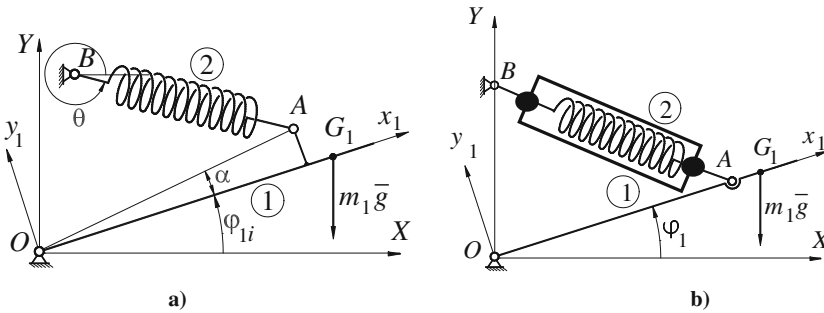
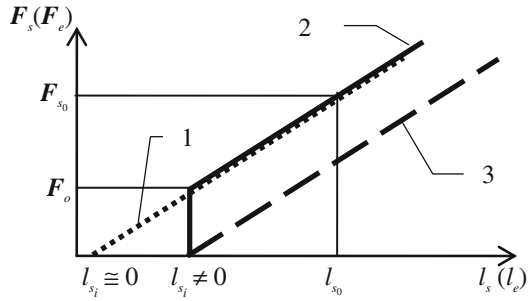


Fig. 1 Rocking body statically balanced by a cylindrical helical extension spring (version 1)

Fig. 2 Helical spring and elastic system stiffness characteristics



In order to obtain full balancing of the arm ①, for any value of the positioning angle $\varphi_1 \in [0, 2\pi]$, is necessary to have: $X_B = y_{1A} = l_{s_0} = F_{s_0} = 0$. In this particular case (see Fig. 1b), the spring should have the initial length in relaxed state (when $F_s = F_{s_0} = 0$ [N]): $l_{s^*} = l_{s_i} = l_{s_0} = 0$ [m] i.e. *zero-free-length*. By replacing these values in relationships (4), (3), (2) and (1) the stiffness constant of this “spring” results:

$$k = \frac{(m_1 OG_1 + m_{2A} x_{1A})g}{Y_B x_{1A}} \tag{5}$$

But, some complications may occur in the balancing system implementation [6], since it is not possible to use a real helical spring for extension [7].

Even in the case when $X_B \neq 0$ and $y_{1A} \neq 0$, a small value for the length l_{s_0} of the needed helical spring results [9], corresponding to the force F_{s_0} (see linear characteristic represented by dotted line 1 from Fig. 2).

Same results are obtained when the joint from A is on the opposite side than the mass center G_1 [11] with respect to pin joint O (Fig. 3).

Many authors who studied static balancing problem proposed solutions that need *zero-free-length* springs, without concerning how these springs are to be realized. Maybe Carwardine was the first author that introduced the concept of *zero-free-*

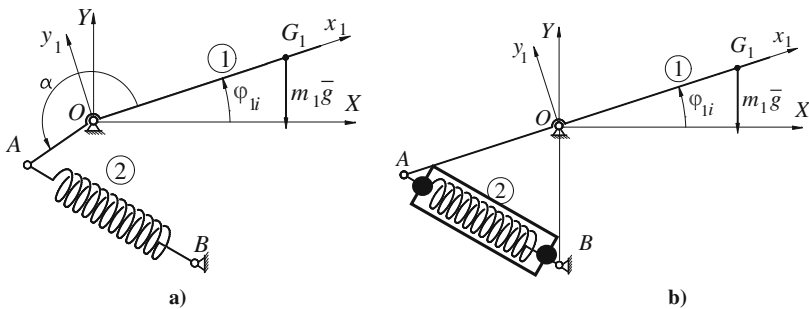


Fig. 3 Rocking body statically balanced by a cylindrical helical extension spring (version 2)

length as he described in one of his patents from 1934 [4] how to manufacture these springs by increasing the preload (poly-line 2 from Fig. 2). The opening force F_o of a preloaded spring is limited by material of spring and can not always satisfy the results from design.

The modification of the straight characteristic position to the necessary spring for balancing, i.e. to obtain an acceptable free length l_{si} from the constructional point of view (straight discontinuous line 3 - Fig. 2), may be achieved by replacing the fixed point B (Figs. 1 and 3) of spring articulation [12], or the point A of spring articulation to the arm ①, by a movable one [6], or by using *zero-free-length* elastic systems.

2 Zero-Free-Length Elastic Systems

The *zero-free-length* elastic systems are elastic systems stressed at tension, with stiffness characteristics passing through the origin of the axes system (F_e, l_e)— Fig. 2, where l_e is the length of elastic system and F_e is the elastic force developed by the system.

These elastic systems have various design solutions; one of these consists of a compression spring ① joined between links ② and ③ which have relative translational movement (Fig. 4a). The joining points of elastic system are the revolute pairs A and C , with parallel axes.

The advantages of this elastic system are:

- a long stroke of relative movement $l_{e\max}$ between links ② and ③;
- if the friction forces from prismatic pairs B are neglected, then the proportionality between elastic force of system and the deformation l_e is theoretically exact.

The main disadvantage is the possible buckling of compression spring. If the buckling occurs, supplementary friction forces between spring ① and case ② appears, and also in prismatic pairs B , so that the elastic system characteristic is

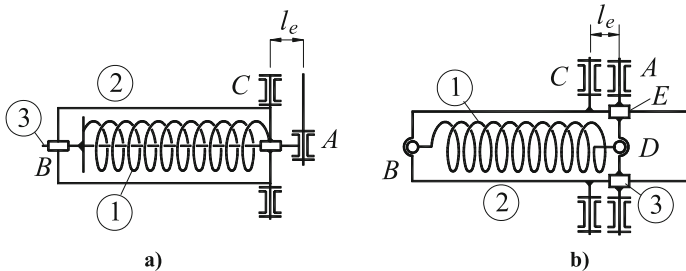


Fig. 4 Zero-free-length elastic systems

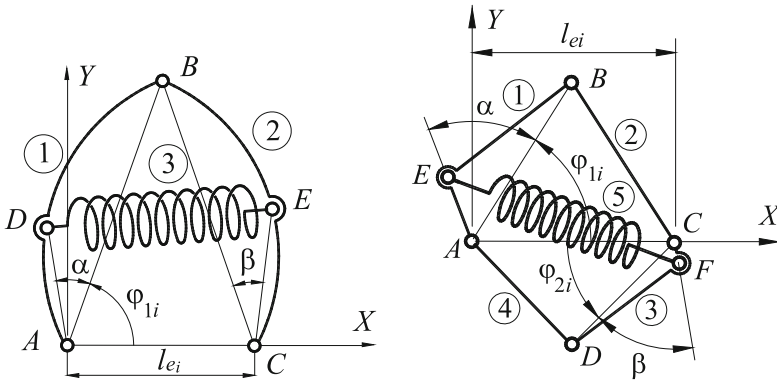


Fig. 5 Zero-free-length elastic systems with revolute pairs

changed. This disadvantage is overcome by elastic system from Fig. 4b, where the helical spring ① is of extension type.

Elastic systems of zero-free-length type, with links and extension helical springs (Fig. 5), can be designed with linear stiffness characteristics (Fig. 2).

The number n of design parameters of elastic system is finite and small so that the number of positions (denoted by index $i = \overline{1, n}$) where the equilibrium is perfect, is also small and equal with n . For continuity reason, in all the other positions from work-field the errors between the theoretically necessary elastic characteristic and the real one are very small.

A possible solution is presented in Fig. 5a. The extension helical spring is joined between two links, ① and ②. The unknown parameters of this elastic system:

- lengths: $AB = BC$, AD and CE ,
- angles: α and β ,
- helical spring stiffness constant k_s ,

are computed as solutions of the following equations:

$$b_i k_s (DE_i - DE_0) - 0.5 k_e l_{e_i}^2 \tan \varphi_{1i} = 0, \quad i = \overline{1, 6}, \quad (6)$$

where:

$$b_i = \frac{(Y_{D_i} - Y_{E_i})(0.5l_{e_i} - X_{D_i}) - (0.5l_{e_i} \tan \varphi_{1i} - Y_{D_i})(X_{D_i} - X_{E_i})}{DE_i} \quad (7)$$

$$DE_i = \sqrt{(X_{D_i} - X_{E_i})^2 + (Y_{D_i} - Y_{E_i})^2}; DE_0 = \sqrt{AD^2 + CE^2 - 2ADCE \cos(\alpha + \beta)}; \quad (8)$$

$$X_{D_i} = AD \cos(\varphi_{1i} + \alpha); Y_{D_i} = AD \sin(\varphi_{1i} + \alpha); \quad (9)$$

$$X_{E_i} = l_{e_i} - CE \cos(\varphi_{1i} + \beta); Y_{E_i} = CE \sin(\varphi_{1i} + \beta); \varphi_{1i} = \arccos \frac{l_{e_i}}{2AB}, i = \overline{1, 6}, \quad (10)$$

and where k_e is the imposed stiffness constant of the elastic system.

The gravity forces of the links and of the helical spring are neglected, because this elastic system is working in any position with respect to gravitational line.

The *zero-free-length* elastic system with links shown in Fig. 5b consist of four links with equal lengths two by two; between any two opposite links is joined the helical extension spring ⑤.

The unknown dimensions of elastic system:

- lengths of links: $AB = BC, AD = CD, AE, CF,$
- angles: α and $\beta,$
- stiffness constant k_s of helical spring,

are computed as solutions of following equations:

$$k_e l_{e_i} - (EF_i - EF_0) k_s \frac{dEF_i}{dl_e} = 0, i = \overline{1, 7}, \quad (11)$$

$$Y_{E_i} = AE \sin(\varphi_{1i} + \alpha); X_{E_i} = AE \cos(\varphi_{1i} + \alpha); \varphi_{1i} = \arccos \frac{l_{e_i}}{2AB} \quad (12)$$

$$X_{F_i} = l_{e_i} - CF \cos(\varphi_{2i} + \beta); Y_{F_i} = -CF \sin(\varphi_{2i} + \beta); \varphi_{2i} = \arccos \frac{l_{e_i}}{2AD} \quad (13)$$

$$EF_i = \sqrt{(X_{E_i} - X_{F_i})^2 + (Y_{E_i} - Y_{F_i})^2}; EF_0 = \sqrt{AE^2 + CF^2 + 2AE CF \cos(\alpha - \beta)}; \quad (14)$$

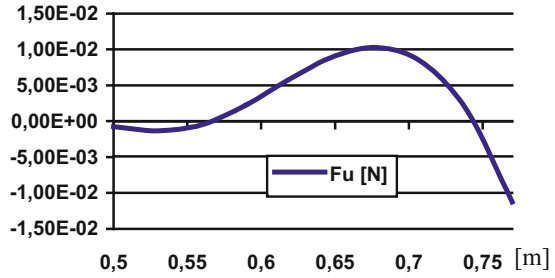
$$\frac{dEF_i}{dl_e} = \frac{(X_{E_i} - X_{F_i}) \left(\frac{dX_{E_i}}{dl_e} - \frac{dX_{F_i}}{dl_e} \right) + (Y_{E_i} - Y_{F_i}) \left(\frac{dY_{E_i}}{dl_e} - \frac{dY_{F_i}}{dl_e} \right)}{EF_i}; \frac{d\varphi_{2i}}{dl_e} = \frac{-1}{2CD \sin \varphi_{2i}} \quad (15)$$

$$\frac{dX_{E_i}}{dl_e} = -AE \sin(\varphi_{1i} + \alpha) \frac{d\varphi_{1i}}{dl_e}; \frac{dY_{E_i}}{dl_e} = AE \cos(\varphi_{1i} + \alpha) \frac{d\varphi_{1i}}{dl_e}; \frac{d\varphi_{1i}}{dl_e} = \frac{-1}{2AB \sin \varphi_{1i}}; \quad (16)$$

$$\frac{dX_{F_i}}{dl_e} = 1 + CF \sin(\varphi_{2i} + \beta) \frac{d\varphi_{2i}}{dl_e}; \frac{dY_{F_i}}{dl_e} = -CF \cos(\varphi_{2i} + \beta) \frac{d\varphi_{2i}}{dl_e}; \quad (17)$$

The advantage of this *zero-free-length* elastic system is the quasi-symmetric distribution of link masses with respect to line AC , which represents the support of elastic force of the elastic system.

Fig. 6 Variation of unbalancing force with respect to length of elastic system l_e



3 Example

The balancing mechanism from Fig. 5b with following dimensions: $AB = 0.763393$ [m], $BC = 1.068337$ [m], $CD = 0.795088$ [m], $AD = 1.111559$ [m], $DF = 0.541328$ [m], $AE = 0.483578$ [m], $\alpha = 0.178723$ [rad], $\beta = 0.369568$ [rad], is used for balancing a load attached in point C with weight $G_6 = 10$ [N]. The characteristics of helical spring ⑤ are: $F_{s_0} = 7.60683$ [N], $l_{s_0} = 0.5$ [m] and $k_s = 123.731$ [N/m]. Masses $m_j = 0$ [kg], $j = \overline{1, 5}$.

In these conditions the variation of unbalancing force is presented in Fig. 6 where the maximum unbalancing force $F_u = 0.011232$ [N] is corresponding to maximum length of the elastic system $l_e = 0.77$ [m].

4 Conclusions

The *zero-free-length* elastic systems are built in order to obtain approximate discrete static balancing. Elements that are storing and returning energy from/to the mechanical system, in the form of potential energy, are normal cylindrical helical springs for extension. By proper designing of the elastic systems many interesting solutions could be found. Static balancing is also very good and by optimization [8] better solution could be obtained.

References

1. Agrawal, A., Agrawal, S.K.: Design of gravity balancing leg orthosis using non-zero free length springs. *Mech. Mach. Theory* **40**, 693–709 (2005)
2. Bätge, J., Goetze, R., Leistner, F., Kunad, G., Soldatkin, J., Gutschtschin, W., Novikov, W.: Mechanischer Ausgleichmechanismus für Gelenkgetriebe, insbesondere Industrieroboter, Patent DD 252148 (1987)
3. Bechek, R.I.: Dispositif d'équilibrage d'un pendule, notamment d'un bras de manipulateur, et bras de manipulateur équipé d'un tel dispositif, Patent FR 2 532 578 - A1 (1982)
4. Carwardine, G.: Improvements in equiposing mechanism, UK Patent 404.615 (1934)

5. Ciupitu, L.: The Weight Forces Balancing of Industrial Robots Arms—Ph.D Thesis Extended Abstract, (Ph.D Thesis defended on October 1997) “Politehnica” University of Bucharest, Romania, 56 pages, (2002)
6. Ciupitu, L., Toyama, S., Purwanto, E.: Robotic arm with 9 DOF driven by 3 spherical ultrasonic motors. In: IFAC volume with the Proceedings of the Workshop Intelligent Assembly and Disassembly IAD’2003, Elsevier, Oxford, ISBN 0 08 044065, 7, 85–90 (2003)
7. Ciupitu, L.: Optimum design of balancing systems with real springs, In: Appl. Mech, Mater. J, **555**, 593–598 (2014). ISSN 1660-9336, ISBN 978-3-03835-502-1, Trans Tech Publications, Switzerland, doi:[10.4028/www.scientific.net/AMM.555.593](https://doi.org/10.4028/www.scientific.net/AMM.555.593)
8. Ciupitu, L., Simionescu, I.: Optimum design of balancing systems with cylindrical helical extension springs, In: Appl. Mech. Mater. **656**, 232–241 (2014). ISSN 1660-9336, ISBN 978-3-03785-274-7, Trans Tech Publications, Switzerland, doi:[10.4028/www.scientific.net/AMM.656.232](https://doi.org/10.4028/www.scientific.net/AMM.656.232)
9. Dranga, M.: Dispozitiv de echilibrare statică a unui corp în mișcare de rotație în plan vertical (Static balancing device of a rotating body in vertical plane), Patent RO 90828 (1987)
10. Duval, E.F.: Counter balance system and method with one or more mechanical arms, US Patent 7,428,855 B2 (2003)
11. Gerlach, R., Reichel, J.: Die bahngeführte Gasdruckfeder-ein vollkommenes Ausgleichssystem für quasistatisch bewegte Massen. VDI Berichte, nr. **1281**, 425–447 (1996)
12. Hain, K.: Spring mechanisms—point balancing and spring mechanisms—continuous balancing. In: Chironis, N.D. (ed.) Spring Design and Application, pp. 268–275. McGraw-Hill, New York (1961)
13. Hervé, J.M.: Device for counter-balancing the forces due to gravity in a robot arm, US Patent 4,620,829 (1986)
14. Hervé, J.M.: Design of Spring Mechanisms for Balancing the Weight of Robot. In: Morecki, A., Bianchi, G., Kędziór, K. (eds.) Sixth CISM-IFTOMM Symposium on Theory and Practice of Robots and Manipulators, pp. 564–567 Hermes, Paris (1987)
15. Kolarski, M., Vukobratovic, M., Borovac, B.: Dynamic analysis of balanced robot mechanisms, Mech. Mach. Theory, **29**(3), 427–454 (1994)
16. Korendiasev, A.I., Salamandra, B.L., Tyves, L.I., Vladov, I.L., Danilevskii, V.N., Zhavner, V. L., Koliskor, A.Sh., Petrov, L.N., Serkov, N.A., Modestov, M.B., Ushakov, V.I., Tichomirov, V.G., Kovalev, V.E.: Manipulation Systems of Robots (In Russian), Popov, E.R. (ed.) Mashinostrojenie, ISBN 5-217-00461-4, Moscow (1989)
17. Kromer, G. and Pagel, J.: Vorrichtung zum Schwerkraftmomentausgleich der Drehgelenke von Robotern, Patent DD 219427 A1 (1985)
18. Lacasse, M.-A., Lachance, G., Boisclair, J., Ouellet, J., Gosselin, C.: On the design of statically balanced serial robot using remote counterweights, In: Proceedings of 2013 IEEE International Conference on Robotics and Automation (ICRA 2013), pp. 4189–4194. Karlsruhe, Germany (2013). ISBN 978-1-4673-5643-5/13, 6–10 May 2013
19. Leistner, F., Bätge, J., Soldatkin, E.P., Novikov, W.: Massenausgleich-mechanismus für Industrieroboter. Maschinenbautechnik, Berlin, Germany **37**(5), 196–198 (1988)
20. Lowen, G.G., Tepper, F.R., Berkof, R.S.: Balancing of linkages—an update. Mech. Mach. Theory **18**(3), 213–220 (1983)
21. Lundström, C., Nissfolk, R.: Industrial robot with balancing device, US Patent 6,848,333 B2 (2005)
22. Petrov, L.N., Maksimov, V.P., Lacota, N.A., Ivkin, A.M.: An executing manipulator organ (In Russian), Patent SU 476971 (1976)
23. Popov, M.V., Tyurin, V.N.: A balanced manipulator (In Russian), Patent SU 1000271 (1983)
24. Richter, H.: Apparatus for Weight Balancing an Industrial Robot, US Patent 4,455,120 (1984)
25. Riele F.L.S., Herder, J.L.: Perfect static balance with normal springs. In: Proceedings ASME Design Engineering Technical Conference, p. 8. Pittsburgh, Pennsylvania, DETC2001/DAC21096 (2001). 9–12 Sept 2001
26. Sensenschmidt, H., Keler, F., Weidhaas, W.: Vorrichtung zum Massenausgleich bei Schwenkarmen an Gelenkrobotern. DDR Patent **228484**, A1 (1985)

27. Simionescu, I., Ciupitu, L.: The static balancing of industrial robot arms, part I: discrete balancing. *Mech. Mach. Theory J.* **35**(9), 1287–1298 (2000)
28. Tepper, F.R., Lowen, G.G.: General theorems concerning full force balancing of planar linkages by internal mass redistribution, *J. Eng. Ind.* **94B**(3), 789–796 (1972)
29. Tuda, G., Kada, H., Sekino, T., Nagahama, Y.: Gravity balancing device for rocking arm, US Patent 4,592,697 (1986)
30. Yamamoto, R., Hirakawa, A., Horikawa, O., Load balancer with automatic lifting force compensation. In: *ABCM Symposium Series in Mechatronics*, vol. 4, pp. 580–589 (2010)
31. Yasuoka, H.: Dispositif manipulateur automatique d'un type perfectionné, pour le soudage à l'arc, Patent FR 2 539 663 - A1 (1984)
32. ABB: Industrial robots IRB 6499 RF, Västerås, Sweden
33. KUKA GmbH: Industrial robots IR 160/60 and IR 601/60, Augsburg, Germany

Analytic and FEM Study of Load Distribution on the Length of Spline Joints Under Pure Torque

D. Mărgineanu, C. Sticlaru, A. Davidescu and E. Mărgineanu

Abstract Because spline joints transmit torque from shafts to rotors by multiple contact surfaces, the joint's mechanical system is undetermined, thus, the actual load distribution is greatly influenced by the joint's elements elastic properties. In previous works, an analytical method using differential equations of 2nd order to determine load distribution on joints' length was proposed. In this paper, a comparison between analytical and experimental study results for the load distribution on the length of joints under pure torque is presented.

Keywords Spline joints · Load distribution · Differential equation · FEM

1 Introduction

Spline joints transmit torque from shafts to rotors by multiple contact surfaces. The joint's mechanical system is over constrained, i.e. the number of contact points is much larger than the number of restricted degrees of freedom. The contact results in elastic deformations of elements, and the load distribution on the joint's length and between the bearing surfaces depends on combined factors as loads on the joint (other than torque), manufacturing errors, etc.

Analytical studies on the effect of individual causes have the purpose to develop engineering tools for optimal design. Adey et al. developed [1] analysis tools for

D. Mărgineanu (✉) · C. Sticlaru · A. Davidescu · E. Mărgineanu
Politechnica University of Timisoara, Timișoara, Romania
e-mail: dan.margineanu@upt.ro

C. Sticlaru
e-mail: carmen.sticlaru@upt.ro

A. Davidescu
e-mail: arjana.davidescu@upt.ro

E. Mărgineanu
e-mail: eugenia.margineanu@upt.ro

spline couplings. A Barrot et al. studied, in [2], the torsional stiffness as result of rotations due to various phenomena involving distortions such as bending, shear, compression, rotation of the teeth base, and the teeth sliding, and, in [3], they investigated the distortions of involute spline teeth.

Finite element method (FEM) analysis is also used for engineering studies. Adey [4], Cuffaro et al. [5] modeled and simulated the behavior of spline couplings by FEM. Leen et al. [6] used FEM analyses to study the frictional contact conditions in a helical spline joint coupling under torsional and axial loads. Pardhi and Khambekar [7] studied the stress in the spline shaft under various loading conditions of given torque with FEM along with photo elasticity. An analysis of load distribution on spline joints [8] is done by Hong et al. using a finite elements-based contact model to predict load distribution along the spline joint interfaces.

The joint's bearing capacity is limited by the maximal pressure on the contact surfaces. The average pressure p_m is calculated [9] with a formula:

$$p_m = \frac{k_a \cdot 2T}{d_m \cdot z \cdot S_1 \cdot L} [\text{MPa}] \quad (1)$$

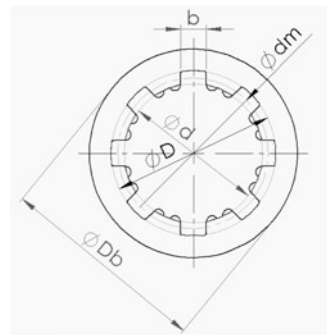
where k_a [-] is the correction coefficient, T [mNm], the torque loading the joint, d_m [mm], joint's mean diameter, $d_m = 0.5(D + d)$ (Fig. 1); z [-], the number of bearing surfaces; S_1 [mm²/mm], the contact surface area/length unit, L [mm], the joint length.

The mean pressure p_m is then compared with the allowable pressure p_a , given in design manuals or norms, different for various spline joints types and much lower than the compression limit, depending on the parts' materials, but also on the joint type, precision and running conditions, etc., thus including correction coefficients to assume the maximal pressure p_{\max} .

In previous works, the authors proposed an analytic method to describe the load distribution on joint's length [10] by the use of a differential equation of 2nd order, a method to calculate the rigidity of the spline joint [11] and compared the results with an experimental study [12], using strain gauges to measure the torque on the outer cylindrical surface of the hub.

In this paper, the analytic results are compared with those of a FEM study.

Fig. 1 The spline joint



2 Analytic Model

The analytic model considers a cylindrical splined hub with the torque applied at the distance x_T (Fig. 2) from the joint's end. The torque on the shaft is applied at a distance from the joint, so it does not influence the load distribution in the joint.

The joint is composed of two zones: zone 1, from the free end of the hub to the section in which the torque is applied, outside the torque applying sections; and zone 2, inside the torque applying sections.

The torque transfer differential equations (3) and (5) are:

$$\frac{d^2 T_x}{dx^2} - \mu^2 \cdot T_x = 0 \quad (2)$$

for zone 1 and,

$$\frac{d^2 T_x}{dx^2} - \mu^2 \cdot T_x = -\mu^2 \lambda T \quad (3)$$

for zone 2, with:

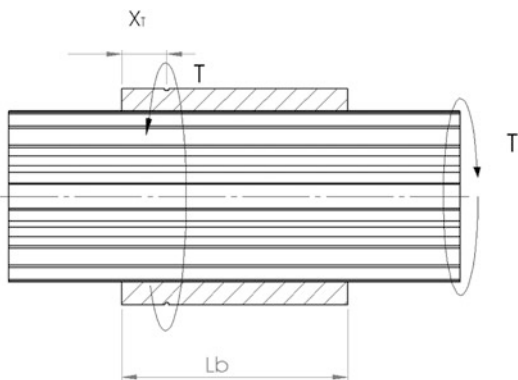
$$\mu^2 = c_T \left(\frac{I}{G_1 \cdot I_{p1}} + \frac{I}{G_2 \cdot I_{p2}} \right), [\text{mm}^{-2}] \quad (4)$$

and

$$\lambda = \frac{G_1 \cdot I_{p1}}{G_1 \cdot I_{p1} + G_2 \cdot I_{p2}} [-] \quad (5)$$

where $G_{1,2}$ [MPa] is the transversal elasticity module for the shaft and hub material, respectively, $I_{p1,2}$ [mm⁴], the polar inertial moment for the shaft and hub cross-section, respectively, and c_T , the spline joint rigidity, $c_T = 0.5 \cdot z \cdot c_F \cdot d_m$, with c_F , combined rigidity of the spline relative to the core of the shaft and hub [11].

Fig. 2 Spline joint with the torque applied on the hub in a given position



The linear differential equations (2) and (3) are solved with limit conditions:

$$T_x = 0 \quad \text{for } x = 0; \quad T_x = T \quad \text{for } x = L \quad (6)$$

and continuity conditions:

$$T_{x1} = T_{x2} \quad \text{and} \quad \frac{dT_{x1}}{dx} = \frac{dT_{x2}}{dx} \quad \text{for } x = x_T \quad (7)$$

The pressure p_x on the bearing surface on zones 1 and 2 is obtained by differentiating the solutions of the differential equations (2), (3), respectively:

$$p_x = p_m \cdot \frac{\mu \cdot L \cdot [1 - \lambda + \lambda \cdot \text{ch}(\mu \cdot L - \mu \cdot x_T)] \cdot \text{ch}(\mu \cdot x)}{\text{sh}(\mu \cdot L)} \quad (8)$$

$$p_x = p_m \cdot \frac{\mu \cdot L \cdot [(1 - \lambda) \cdot \text{ch}(\mu \cdot x) + \lambda \cdot \text{ch}(\mu \cdot x_T) \cdot \text{ch}(\mu \cdot L - \mu \cdot x)]}{\text{sh}(\mu \cdot L)} \quad (9)$$

The maximum pressure p_{\max} is in the cross-section $x = L$.

3 FEM Model

The FEM model, as the analytic calculus example, is done for a standardized joint with the dimensions given in Table 1. The shaft and hub are made of steel.

In Fig. 3, the 3D model used for the FEM analysis is presented. The torque loading the joint is $T = 100 \text{ Nm} = 10^5 \text{ N mm}$, i.e. the active torque is applied on the hub in section A, at a distance x_T to its outer end. In section B, the resisting torque is applied at the shaft's end.

The analysis is done using the Ansys Workbench software. The software allows several types of contacts to be defined (bonded, no separation, frictionless, rough, frictional). A bonded contact is imposed between the active bearing surfaces of the hub and shaft, in order to obtain a linear analysis, which assures a rapid and convergent solution.

In Fig. 4, the equivalent von Mises stresses in the hub splines are displayed. The concentration on the joint's ends, especially on the inner end, is obvious, as predicted by the analytic model.

Table 1 Joint's dimensional parameters

Inner diameter d (mm)	Outer diameter D (mm)	Spline width b (mm)	Number of splines z	Hub outer diameter D _e (mm)	Hub length L (mm)
32	38	6	8	48	50

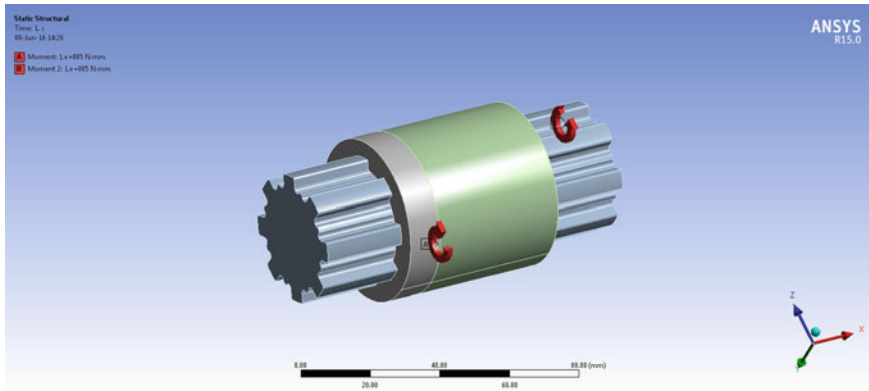


Fig. 3 FEM model with applied loads on hub and on shaft

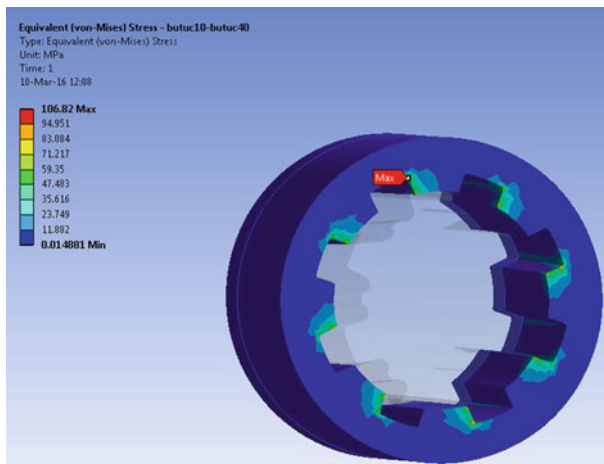


Fig. 4 FEM analysis results: equivalent stress on the hub

Figure 5 details the radial stress distribution on splines' 3 mm height on the most loaded area on the hub: near the inner end edge. For an average value of roughly 70 MPa, the peak value of more than 120 MPa represents an increase of 75 %, i.e. an additional concentration coefficient of 1.75.

The obtained results demonstrates a good fitting between the simulation in Ansys and the analytical approach.

Along the joint's length, the load concentration is also obvious as may be seen in Fig. 6. For an average pressure of 6 MPa, as given by Eq. 1 for the model dimensions, a concentration coefficient 22.5 results for the maximal pressure of 135 MPa. However, it is both the result of load concentration on the length and on the height of the spline.

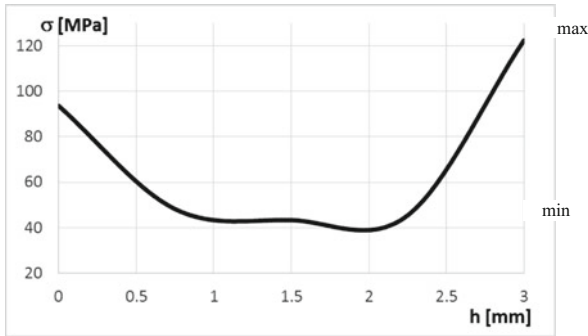


Fig. 5 FEM analysis results: details equivalent stress on the maximal loaded edge of the hub

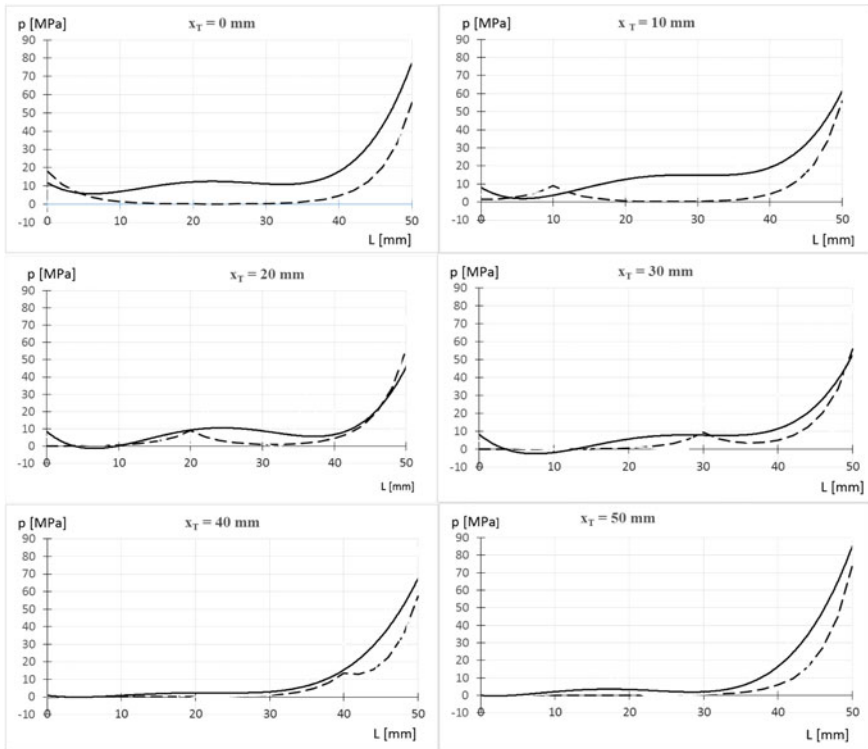


Fig. 6 Comparison between analytic (---) and FEM (—) analysis results for applying torque on different sections on the hub

4 Results Comparison

The analytic and FEM model analysis results are compared in Fig. 6 for applying torque on different sections on the hub. The pressure values are given in MPa, along the joint's length in mm. Both show a severe load concentration at the inner end of the joint, as the outer end and the middle sections are practically unloaded for applying the torque at the inner end or the outer end, respectively.

A pressure peak occurs by analytical results in the section where the torque is applied on the hub, due to the simplified calculus procedure that considers the hub as a cylindrical tube and the splines attached as cantilevers.

By FEM results, similar pressure increase is present, but smoother and slightly shifted because of the continuous load transfer between hub and splines. Regarding the FEM's trend, it presents a concavity slightly less than the analytical model, maintaining overall a good overlap with the analytical one.

It can be seen, Fig. 6, that the difference between analytical and FEM results decreases as x_T variable (distance from the joint's end to applied torque) increases. Starting from half of the x_T distance, the differences are almost negligible. The results are in close agreement with each other with a small percentage of error.

It may be observed also that the pressure distribution presents two characteristic zones: one zone showing a pressure peak (at the ends of the contact's zone of the spline coupling) and the other one having a relatively low pressure (low pressure zone). It may be also emphasized that the overlap between trends (analytical and FEM) is generally good.

The results are comparable, thus validating the analytic model for the use in initial stages of the design.

5 Conclusions

In this article, the pressure distribution along the teeth of spline couplings has been analyzed. Using FEM analyses allow investigating a proper model, with fewer simplifying hypothesis. The results obtained by this analysis are useful to better understand the stress state, the contact stress map for spline joints etc.

By updating the geometry model in Ansys, the FEM analysis updates immediately and the results for different torque's application sections can be picked out.

Some final conclusions can be pointed out:

- FEM analyses facilitates modelling and simulation of spline joints;
- stress maps and contact stress regions for different load conditions may be visualised;
- the post processing data for contact regions between the shaft and hub can be emphasises.

Using the parameterized capabilities of the Creo 2.0 and the link between Creo 2.0 and ANSYS, many models can be developed easily starting from this one.

The FEM analysis results confirm the severe load concentration on the joint's ends, as predicted by the analytic model. Furthermore, the peak's values are reasonably close. The finer FEM analysis adds the description of the load distribution on the spline's height that was considered constant in the analytic model.

Good agreement has been showed between analytical and FEM analyze results in both low and high contact pressure zones. However, the pressure peaks are greater than the experimental analysis [10] show. The contact rigidity and deformations, especially the plastic deformation of the surface roughness on the most loaded areas during running-in of the joint are to be taken into account for more accurate results.

References

1. Adey, R.A., Baynham, J., Taylor, J.W.: Development of analysis tools for spline couplings. Proc. Inst. Mech. Eng. Part G J. Aerosp. Eng. **214**(6), 347–357 (2000)
2. Barrot, A., Sartor, M., Paredes, M.: Investigation of torsion teeth stiffness and second moment of area calculations for an analytical model of spline coupling behavior. Proc. Inst. Mech. Eng. Part C, J. Mech. Eng. Sci. **222**(6), 891–902 (2008)
3. Barrot, A., Paredes, M., Sartor, M.: Determining both radial pressure distribution and torsional stiffness of involute spline couplings. Proc. Inst. Mech. Eng. Part C J. Mech. Eng. Sci. **220** (12), 1727–1738 (2006)
4. Adey, R.A.: Modeling and simulation of spline couplings. In: IMechE Transmission seminar (1999)
5. Cuffaro, V., Curà, F., Mura A.: Analysis of the pressure distribution in spline couplings, 2. Proc. Inst. Mech. Eng. Part C J. Mech. Eng. Sci. (2012)
6. Leen, S.B., et al.: Development of a representative test specimen for frictional contact in spline joint couplings. J. Strain Anal. Eng. Design **35**, 521–544 (2000)
7. Pardhi, D.G., Kamankar, S.D.: Stress analysis of spline shaft using finite element method and its experimental verification by photo elasticity. Int. J. Mech. Eng. Robot. Res. **4**, 451–458 (2014)
8. Hong, J., Talbot, D., Kahraman A.: Load distribution analysis of spline joints, Gear Technology, pp. 44–48 (May 2014)
9. Kollmann, F.G.: Welle-Nabe-Verbindungen. Auswahl. Springer-Verlag, Berlin, Gestaltung, Auslegung (1984)
10. Mărgineanu, D.: Repartiția sarcinii pe lungimea îmbinărilor arbore-butuc prin caneluri datorită rigidității finite elementelor îmbinării, (Load distribution on the joint's length due to the finite rigidity of the joint's elements) In: 7th Symposium Mechanisms and Mechanical Transmissions, Timișoara (1996)
11. Mărgineanu, D.: Spline joints rigidity. In: 8th Symposium on Mechanisms and Mechanical Transmissions, Timișoara (1996)
12. Mărgineanu, D.: Analytic and experimental study of the load distribution on spline joints length considering the contact rigidity of the bearing surfaces. MTM-Robotics, Clermont-Ferrand (2012)

Dimensional Synthesis of Planar Parallel Manipulator Using Geared Linkages with Linear Actuation as Kinematic Chains

S.M. Grigorescu, E.-C. Lovasz, D.T. Mărgineanu, C. Pop and F. Pop

Abstract The behaviour of the kinematic chain R(RPRGR)RR using geared linkages with linear actuation recommends to be used as connection kinematic chain (RPRGR) for the parallel manipulators. The paper proposes a dimensional synthesis method for the planar parallel manipulator using geared linkages with linear actuation. It computes the minimum link lengths of the connection chain by considering the condition to avoid the desired trajectory intersection with the singularities loci in the achieved workspace. The synthesis results were analysed by means of inverse kinematic analysis.

Keywords Parallel planar manipulator · Geared linkage with linear actuator · Synthesis · Singularity

1 Introduction

Parallel manipulators with their advantages are used in several technical applications and opened a new research field in the development of new structures suitable to dedicated tasks. The large number of possible architectures inspired approaches in generalization or classification by Gogu [1], Hernandez et al. [2]. Many

S.M. Grigorescu (✉) · E.-C. Lovasz · D.T. Mărgineanu · C. Pop · F. Pop
Politechnica University of Timisoara, Timișoara, Romania
e-mail: sanda.grigorescu@upt.ro

E.-C. Lovasz
e-mail: erwin.lovasz@upt.ro

D.T. Mărgineanu
e-mail: dan.margineanu@upt.ro

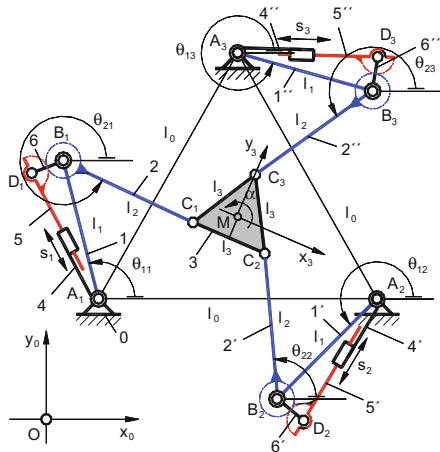
C. Pop
e-mail: cristian.pop@upt.ro

F. Pop
e-mail: florina.pop@upt.ro

researchers [1–11] investigated several mechanism configurations with non-redundant or redundant mechanisms, with arbitrary kinematic chains, regarding the kinematic geometry, singularity loci efficiency, workspace, backlash-free workspace and design. Merlet [3] in his book shows the problems of parallel robots regarding the structural synthesis, the direct and inverse kinematic analysis, singularities, workspace, static and dynamic analysis, calibration and design. Karimia et al. in [5] deals with the avoidance of singularities of 3-RPR parallel manipulator for a given workspace, using the approaches of dimensional synthesis for a prescribed singularity-free workspace, and their reconfiguration via actuation redundancy. By using a genetic algorithm, Gallant et al. in [6] developed the synthesis of the three-degree-of-freedom planar parallel manipulators, optimizing in the first step the prescribed workspace without the singularity loci and in the second step avoiding the singularity loci. An optimum synthesis method of planar parallel manipulators with the constraints of the minimization of the overall deviation number of the manipulator Jacobian matrix is developed by Alici et al. in [7]. This deviation number was minimized from the ideal condition number and from bearing forces throughout the manipulator workspace, for force balancing. Jiang et al. in [8] proposed a geometric synthesis of planar 3-RPR parallel mechanisms in order to guarantee a singularity-free workspace for a desired orientation range and analyzed the results. Based on different design criteria as symmetry, existence of a nonvanishing workspace for every orientation of the gripper, maximization of the global workspace and the isotropy of the Jacobian, Gosselin and Angeles in [9] developed a designing method for the planar three-degree-of-freedom parallel manipulator having optimum characteristics. Arsenault and Boudreau presented in [10] a synthesis method using genetic algorithm with design criteria of workspace optimization, mechanism dexterity maximization and avoiding singularities. Ur-Rehman et al. in [11] proposed a multiobjective optimization method for computing the optimum structural and geometric parameters of parallel manipulators in order to minimize the mechanism mass in motion and to maximize the shaped workspace.

The authors performed the kinematic-positional analysis and the singularities study for a planar parallel manipulator, using a novel connection kinematic chain with geared linkages with linear actuation in [12, 13]. This connection chains (RPRGR) allow mainly a large rotation angle of the driven element (links 2, 2' and 2'' in Fig. 1) with a favorable transmission angle of the chains base mechanism (RPRR) and an approximately constant transmission ratio in a large range. The aim of the present study is to develop a dimensional synthesis for the planar parallel manipulator using geared linkages with linear actuation, in order to compute the link lengths of the connection chain. This allows the avoiding the intersection of a desired trajectory with the singularities loci in the resulted workspace, for the minimum elements lengths.

Fig. 1 Kinematic schema of 3-R(RPRGR)RR manipulator [12]



2 Synthesis of the 3-R(RPRGR)RR Manipulator

The dimensional synthesis process of the planar parallel manipulator is divided in two steps, firstly it will be computed the connection chain minimum lengths for given mobile/fixed platforms dimensions and desired end-effector trajectory; secondly, the previously obtained solution values will be applied, as input data into the RPRPG kinematic chain design analysis process.

To determine the input data values for the first step is necessary to define these in relation with the parallel robots application goal. For instance, if the robot is component of complex automated equipment, the overall dimension constrains are important, such as the fixed and mobile platform dimensions. The mobile platform dimensions depend on the end-effector size.

Input data in the first synthesis step are given values of fixed and mobile platforms dimensions (l_0 and l_3), trajectory curves of the M point and orientation angle variation α , as noted in Fig. 1.

The crank and rod dimensions (l_1 and l_2 , in Fig. 1) are the output data of the synthesis process. The target is finding out the minimum values of these elements lengths, for a given trajectory.

Considering a given trajectory of the M point (characteristic point of the manipulator), obtained as a function, $y_{Mj} = f_1(x_{Mj})$, $j = 1 \div n$ and a given function for the mobile platform orientation angle, $\alpha_j = f_2(\varphi)$, $j = 1 \div n$, $\varphi = 0^\circ \div 360^\circ$, it can be computed the Cartesian coordinates of the C_i points ($i = 1 \div 3$) with respect to the Mx_3y_3 coordinate system:

$$x_{C_i}^{(3)} = l_3 \cos\left(\frac{\pi}{2} + i\frac{\pi}{3}\right), \quad y_{C_i}^{(3)} = l_3 \sin\left(\frac{\pi}{2} + i\frac{\pi}{3}\right), \quad i = 1 \div 3. \quad (1)$$



The position vectors $\overline{OC_{ij}}$ and coordinates of the points C_{ij} ($i = 1 \div 3, j = 1 \div n$) are:

$$\overline{OC_{ij}} = \overline{OM_j} - \overline{M_jC_{ij}} \quad (2)$$

$$\begin{bmatrix} x_{C_{ij}}^{(0)} \\ y_{C_{ij}}^{(0)} \end{bmatrix} = \begin{bmatrix} x_{M_j}^{(0)} \\ f_{1j}(x_{M_j})^{(0)} \end{bmatrix} - \begin{bmatrix} \cos(f_2(\alpha_j)) & -\sin(f_2(\alpha_j)) \\ \sin(f_2(\alpha_j)) & \cos(f_2(\alpha_j)) \end{bmatrix} \cdot \begin{bmatrix} x_{C_i}^{(3)} \\ y_{C_i}^{(3)} \end{bmatrix}, \quad i = 1 \div 3, j = 1 \div n. \quad (3)$$

The array of values $x_{C_{ij}}^{(0)}, y_{C_{ij}}^{(0)}$ in Eq. (3) is used for the calculus of the vector modules A_iC_{ij} , as shown in Eq. (4).

$$\overline{A_iC_{ij}} = \overline{OC_{ij}} - \overline{OA_i}; \quad |\overline{A_iC_{ij}}| = \sqrt{(x_{A_i} - x_{C_{ij}})^2 + (y_{A_i} - y_{C_{ij}})^2}, \quad i = 1 \div 3, j = 1 \div n \quad (4)$$

Considering the three kinematic chains vectors, l_1 and l_2 fulfill the condition in Eq. (5), the preliminary calculus is according to inequalities (6).

$$((\overline{l_1} + \overline{l_2})_i)_j = \overline{OC_{ij}} - \overline{OA_i}; \quad j = 1 \div n, i = 1 \div 3 \quad (5)$$

$$\begin{aligned} l_1 + l_2 &> \max(\max(|\overline{A_1C_{1j}}|), \max(|\overline{A_2C_{2j}}|), \max(|\overline{A_3C_{3j}}|)); \\ l_2 - l_1 &< \min(\min(|\overline{A_1C_{1j}}|), \min(|\overline{A_2C_{2j}}|), \min(|\overline{A_3C_{3j}}|)); \end{aligned} \quad (6)$$

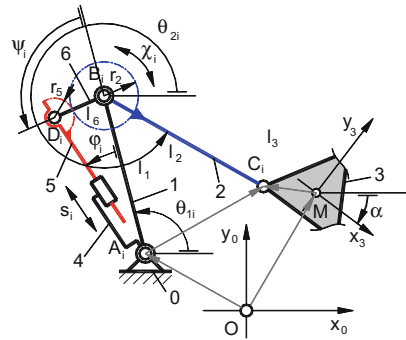
These preliminary values are used in a further determination of workspace and second type singularities loci. These can be obtained when the Jacobian matrix determinant is zero, as presented in detail in [12], (Eq. 7).

$$\begin{aligned} F_i(X, Q) = 0; \quad i = 1 \div 3; \quad X = [x_M, y_M, \alpha]; \quad Q = [\theta_{21}, \theta_{22}, \theta_{23}]; \\ \det(J_q) = \det \begin{bmatrix} \frac{\partial F_1(X, Q)}{\partial x_M} & \frac{\partial F_1(X, Q)}{\partial y_M} & \frac{\partial F_1(X, Q)}{\partial \alpha} \\ \frac{\partial F_2(X, Q)}{\partial x_M} & \frac{\partial F_2(X, Q)}{\partial y_M} & \frac{\partial F_2(X, Q)}{\partial \alpha} \\ \frac{\partial F_3(X, Q)}{\partial x_M} & \frac{\partial F_3(X, Q)}{\partial y_M} & \frac{\partial F_3(X, Q)}{\partial \alpha} \end{bmatrix} = 0; \end{aligned} \quad (7)$$

Next calculus applied inverse kinematic analysis of M point movements on the given trajectory and orientation, for checking out smooth variation of driven angles θ_{2i} , $i = 1 \div 3$ and avoiding the intersection with singularities loci.

The second condition verifies if the needed stroke of the linear actuators belong to the computed stroke range for the geared linkage chains. The link lengths of the RPRPG are imposed excepting the link length of element (1), previously resulted.

Fig. 2 Simplified computing model for the synthesis of the geared linkage with linear actuation



By considering $\Delta\chi_i$ the constant designing values of the geared linkage chain, results the generalized coordinates for the forward positional kinematic:

$$\theta_{2i}(s_i) = \chi_i(s_i) + \Delta\chi_i. \tag{8}$$

The actuation of the planar parallel manipulator follows through a parallel connected geared linkage with linear actuation chain (see Fig. 2). The transmission function of this chain $\chi_i(s_i)$ can be computed as:

$$\chi_i(s_i) = (1 - \rho) \cdot \psi_i(s_i) + \rho \cdot \phi_i(s_i), \tag{9}$$

where the angular functions and the transmission ration are:

$$\phi_i(s_i) = \arccos \frac{l_6^2 - l_1^2 - (s_0 + s_i)^2}{2 \cdot l_1 \cdot (s_0 + s_i)}, \psi_i(s_i) = \arccos \frac{(s_0 + s_i)^2 - l_1^2 - l_6^2}{2 \cdot l_1 \cdot l_6}, \rho = -r_5/r_2. \tag{10}$$

For the inverse positional kinematic, the input parameter $\chi_i(t)$ of the geared linkage chain depend on the desired path parameter t can be computed as:

$$\chi_i(t) = \theta_{2i}(t) - \Delta\chi_i, \quad i = \overline{1 \div 3}, t \in [0, 1]. \tag{11}$$

The corresponding stroke of the actuator follows from the interpolation function of the inverse transmission function [13]:

$$s_i(\chi_i) = \sum_{k=1}^4 \left((s_i)_k \cdot \prod_{\substack{j=1 \\ j \neq k}}^4 \frac{(\chi_i) - (\chi_i)_j}{(\chi_i)_k - (\chi_i)_j} \right). \tag{12}$$

3 Numerical Examples

The synthesis process of the base kinematic chain firstly achieves the minimum lengths values of l_1 and l_2 , values obtained from inequalities (6), transformed in equalities. In Table 1 there are given the input values and the output parameters of this phase, the same circular trajectory center pose corresponds to case 1 and 2, as represented in Fig. 3a, b. The crank and rod lengths values are then imported in second type singularities check program and the outcomes are shown in Fig. 4 a-case 1 and Fig. 4b-case 2. If the singularity loci intersect the desired trajectory, the program increases the l_1 and l_2 by an increment, until there is no intersection between the two curves. Finally, these values are introduced into another program module for inverse kinematic analysis. This module program checks the values of driven elements angles in correlation with determined crank and rod dimensions and the results are represented in Fig. 5, for the first synthesis case.

Table 1 Input and output values of the first synthesis process

Input parameters		Output parameters	
Parameter and abbreviation	Values	Parameter and abbreviation	Values (mm)
Fixed and mobile platform triangle side l_0, l_3	500 mm, 50 mm	A_1B_1 element length l_1 in case 1	93.22
Circles center point coordinates in case 1	(250, 144.33) mm	B_1C_1 element length l_2 in case 1	260.04
Circles center point coordinates in case 2	(400, 166.66) mm	A_1B_1 element length l_1 in case 2	209.04
Circle radius and orientation angle function	93 mm, $\varphi = 0^\circ \div 360^\circ$ $\alpha_j = f_2(\varphi) = 10 \cdot \sin(\varphi)$	B_1C_1 element length l_2 in case 2	288.20

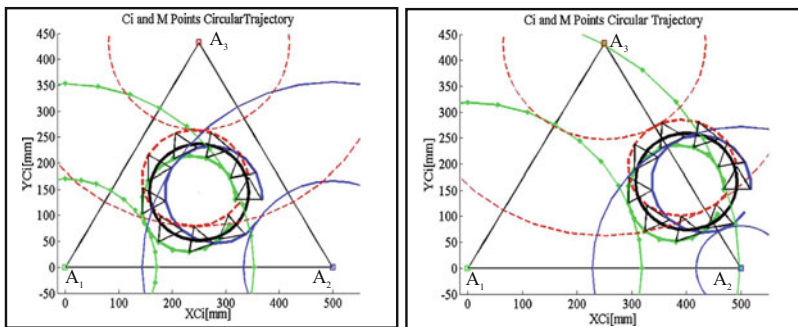


Fig. 3 a Case 1 of manipulator synthesis b Case 2 of manipulator synthesis

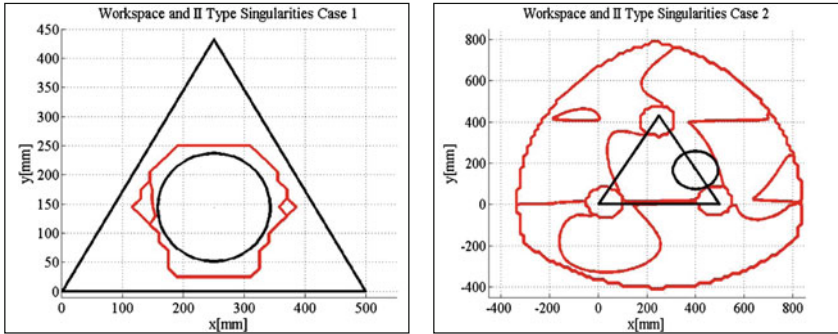
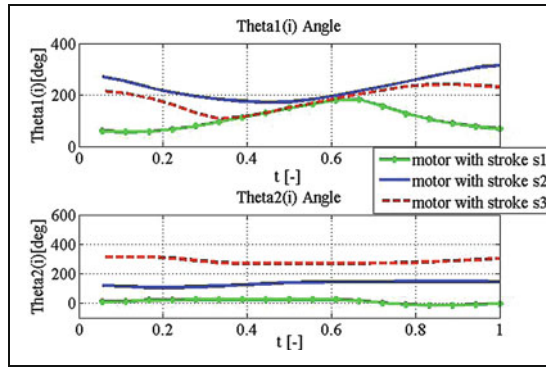


Fig. 4 a Case 1 Manipulator singularities b Case 2 Manipulator singularities

Fig. 5 Angles θ_{1i} and θ_{2i} variation for the first case synthesis



The variation of angles θ_{1i} θ_{2i} (as represented in Fig. 1) in the first case of the synthesis process is shown in Fig. 5.

The synthesized geometrical parameters with the correlated link length l_l of the geared linkage with linear actuation are given in the Table 2 and its corresponding transmission function is shown in Fig. 6a. The stroke was limited in the range $s_i \in [5, 35]$ mm in order to allow an approximately linear transmission function and the oscillating angle to $\chi_i(s_i) \cong 145^\circ$. Figure 6b shows the inverse transmission function of the geared linkage.

Table 2 Geometric parameters of the geared linkages with linear actuation

Parameter	Abbreviation	Values
Chain link length (l, l', l'')	l_l	103.00 mm
Carrier length (6)	l_6	20.00 mm
Gear ratio	ρ	0.5 [-]
Initial stroke	s_0	105.00 mm
Stroke	h	30.00 mm



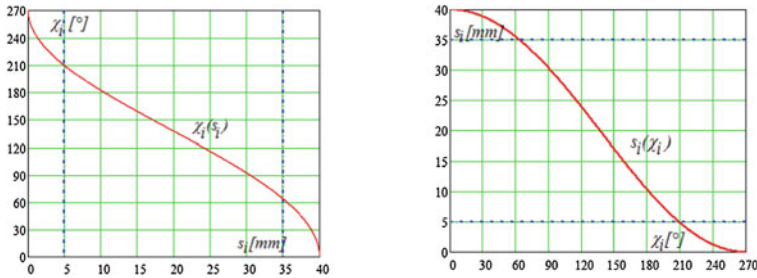


Fig. 6 a Transmission function b Interpolated inverse transmission function

4 Conclusions

The paper presents the synthesis process of a planar parallel 3-R(RPRGR)RR manipulator, resulting minimum link lengths values of connection chains, for a given circular trajectory and sinusoidal variation of orientation angle. Singularity free manipulator movements are analyzed in two cases, the same circular curve is posed in fixed platforms center or eccentric. In the second case, a singularity free manipulator trajectory determines increased values of connection chains elements. Further validation of an optimal synthesis process should include also manipulator dynamic analyses and smooth mobile platform motions.

References

1. Gogu, G.: Structural Synthesis of Parallel Robots. Part 3: Topologies with Planar Motion of the Moving Platform. Springer (2010)
2. Hernandez, A., Ibarreche, J.I., Petuya, V., Altuzarra, O.: Structural synthesis of 3-DoF spatial fully parallel manipulators. Int. J. Adv. Robot. Syst. **11**(101), 1–8 (2014)
3. Merlet, J.-P.: Parallel Robots, Series: Solid Mechanics and Its Applications. Springer
4. Buium, F., Duca, C., Leonchi, D.: Problems regarding singularities analysis of a 0/3/3 parallel mechanism. Appl. Mech. Mater. **658**, 569–574 (2014)
5. Karimia, A., Masouleha, M.T., Cardou, P.: Avoiding the singularities of 3-RPR parallel mechanisms via dimensional synthesis and self-reconfigurability. Mech. Mach. Theory **99**, 189–206 (2016)
6. Gallant, M., Boudreau, R.: The synthesis of planar parallel manipulators with prismatic joints for an optimal, singularity-free workspace. J. Robot. Syst. **19**(1), 13–24 (2002)
7. Alici, G., Shirinzadeh, B.: Optimum synthesis of planar parallel manipulators based on kinematic isotropy and force balancing. Robotica **22**(1), 97–108 (2004)
8. Jiang, Q., Gosselin, C.M.: Geometric Synthesis of Planar 3-RPR Parallel Mechanisms for Singularity-Free Workspace. Trans. Can. Soc. Mech. Eng. **33**(4), 667–678 (2009)
9. Gosselin, C., Angeles, J.: The optimum kinematic design of a planar three-degree-of-freedom parallel manipulator. J. Mech. Transm. Autom. Design **110**, 35–41 (1988)
10. Arsenault, M., Bourdeau, R.: The synthesis of three-degree-of-freedom planar parallel mechanisms with revolute joints (3-RRR) for an optimal Singularity-free workspace. J. Robot. Syst. **21**(5), 259–274 (2004)

11. Ur-Rehman, R., Caro, S., Chablat, D., Wenger, P.: Multiobjective design optimization of 3-PRR planar parallel manipulators. In: 20th CIRP Design conference, pp. 1–10. Nantes, France. (2010)
12. Lovasz, E.-C., Grigorescu, S., Margineanu, D., Gruescu, C.M., Pop, C., Ciupe, V., Maniu, I.: Geared linkages with linear actuation used as kinematic chains of a planar parallel manipulator. In: Proceedings of 3rd MeTrApp Conference, Mechanisms, Transmissions and Applications, Series Mechanism and Machine Science, vol. 31, pp. 21–31 (2015)
13. Lovasz, E.-C., Grigorescu, S., Margineanu, D., Gruescu, C.M., Pop, C., Maniu, I.: Kinematics of the planar parallel manipulator using geared linkages with linear actuation as kinematic chains 3-R(RPRGR)RR. In: Proceedings of 14th IFToMM World Congress Conference, 25–30 October 2015. doi Nr: [10.6567/IFToMM.14TH.WC.OS8.026](https://doi.org/10.6567/IFToMM.14TH.WC.OS8.026)

Part II
MTM—Dynamics of Mechanisms
and Machines

The Concept of Natural Motion for Pick and Place Operations

J.P. Barreto, F. J.-F. Schöler and B. Corves

Abstract In pick and place operations a mechanism moves an object from an initial to a final pose and repeats, with frequencies of operation that can achieve 150 picks per minute. The paper presents the concept of natural motion for this kind of operations, where the basic idea is to add elastic elements to the mechanism and try to match the desired motion with the natural motion of the system. This concept was implemented in a multibody simulation of a five-bar linkage by using numerical optimization to find the required spring constants as well as the trajectory that minimize the torque on the motors. The required energy of the system using the concept of natural motion was compared with that of a typical trajectory, finding that the use of springs and natural motion reduces the energy consumption by 68 % per cycle.

Keywords Pick and place · Five-bar linkage · Natural motion

1 Introduction

One of the most common tasks of industrial robots are pick and place operations. According to [1], in pick and place operations, a robotic manipulator is meant to take a workpiece from a given initial pose to a final pose. This type of operation is exploited in tasks like loading and unloading of conveyor belts, changing tools in machine tools or putting roller bearings on a shaft [1]. The most common robots performing this task are the SCARA and Delta. The SCARA (Selective Compliance Assembly Robot Arm) has three revolute joints and one prismatic joint, with the axes of the four joints being parallel [7]. The SCARA is of the serial robot type, because

J.P. Barreto (✉) · F.J.-F. Schöler · B. Corves
RWTH Aachen University, Aachen, Germany
e-mail: barreto@igm.rwth-aachen.de

F.J.-F. Schöler
e-mail: schoeler@igm.rwth-aachen.de

B. Corves
e-mail: corves@igm.rwth-aachen.de

its structure takes the form of an open-loop kinematic chain. On the other hand, the Delta robot is a parallel robot, because it is made up of a closed-loop kinematic chain [8]. These robots are very common, because they perform pick and place operations in a really short time. The SCARA robot can achieve a frequency of 120 picks per minute [1], while according to [7], the Delta can achieve frequencies of 150 picks per minute. This means, in just one hour, around 9000 cycles can be completed. Because of this large number of operations, and taking into account the expected service life of 12–15 years [7], energy expenditure of these robots has to be studied.

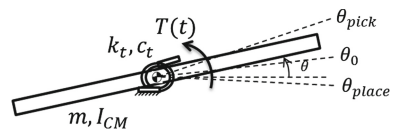
Traditional strategies for the operation of robots are based on the actuators only: they have to introduce all the necessary energy to generate the motion. However, if elastic elements are attached to the robot, then most part of the required energy to carry out the task could be supplied by the elastic elements instead of the actuators. This happens, because the elastic elements store energy during part of the cycle as potential elastic energy and then release it to the rigid bodies, increasing their kinetic energy [4]. Then they return the energy to the springs, and so on. In the absence of dissipative forces, the robot would continue oscillating indefinitely, but in real systems energy is dissipated via friction forces in the joints and the structure. However, if the actuator only has to counteract the effect of dissipative forces and guide the mechanism through the desired trajectory, instead of introducing all the necessary energy for every cycle, then the energy expenditure will be reduced. This concept is called natural motion.

This paper presents the use of natural motion on a five-bar linkage. The paper is divided in four sections, in the first one the concept of natural motion is explained using a single-degree of freedom rotational system. Then, the methodology for the implementation on the five-bar linkage is explained and finally the results of this implementation for a given mechanism are presented.

2 The Concept of Natural Motion

The concept of natural motion is based on the free response of a dynamic system. In pick and place operations there is an oscillatory motion of the manipulator. A simplified pick and place operation requires the manipulator to achieve a specific pose, perform a short stop and return to the initial pose (Fig. 1). In the simplest case of a rotating bar, it should have to sweep a defined angle $\Delta\theta = \theta_{place} - \theta_{pick}$ in a specific time (Δt), then return and repeat.

Fig. 1 Model of a 1-DOF rotating system with spring



The manipulator would normally follow a trajectory between the stops that satisfies some boundary conditions and some level of smoothness. Some examples of trajectory are cycloid, polynomial, modified sine and modified trapezoid. However, when a spring is added to the system, the free response of the system can be used to join the two stops and significantly reduce the torque applied by the motor (and therefore the energy). The equation of motion of the system in Fig. 1 is:

$$I_{CM}\ddot{\phi} + c_t\dot{\phi} + k_t\phi = T(t) \quad (1)$$

where ϕ is the angle measured from the equilibrium position θ_0 , c_t is the damping constant and k_t is the spring stiffness. If damping is neglected, and we want the bar to oscillate between θ_{pick} and θ_{place} with an angular frequency $\omega = \pi/\Delta t$ starting from θ_{pick} , we need to define $\theta_0 = (\theta_{pick} + \theta_{place})/2$. The desired motion would be described by (2).

$$\theta(t) = \theta_0 + (\theta_{pick} - \theta_0)\cos(\omega t) \quad (2)$$

If the duration of the stop is zero, the torque that the motor had to exert on the system to keep it oscillating is:

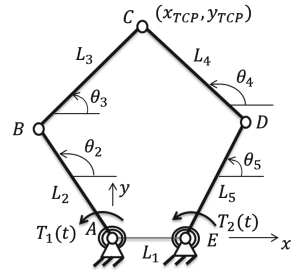
$$T(t) = (\theta_{pick} - \theta_0)(k_t - I_{CM}\omega^2)\cos(\omega t) \quad (3)$$

This torque is reduced to zero when the torsional constant of the spring is equal to $I_{CM}\omega^2$, because the free response of the system matches the desired motion. The initial drawback of including a spring is that the torque is increased during the stops. While the motor in the system without spring does not have to exert any torque during the stops, the system with spring requires a torque during the stops to hold the bar at the required angle. However, if a mechanical brake is included, the motors would not have to apply any torque during the stops nor during the motion. For this undamped system, external energy would only be required to give the bar an initial displacement and to operate the mechanical brake. Now the question arises of how to implement the same concept on a more complex system. Only a few works have analyzed the impact of natural motion on the performance of an industrial robot. In particular, Goya et al. [3] proposed the use of elastic elements and resonance to reduce the energy consumption of a SCARA robot for pick and place operations. They found an energy saving of 72 % in a pick and place operation with two different sinusoidal trajectories. This is clearly a good indicator for the positive impact that exploiting the concept of natural motion in industrial robots could have.

3 Natural Motion of a Five Bar Linkage

The implementation of the natural motion on the five-bar linkage follows the same logic as for the bar in Sect. 2. The idea is to have a model that allows us to predict how the free response of the system to an initial condition is, and based on this model find

Fig. 2 Model of a five-bar linkage



the values of stiffness and natural angle of the springs that result in a motion which takes the tool center point (TCP) from the pick position to the place position and vice versa.

3.1 Kinematic and Dynamic Model

A multibody model of the system in Fig. 2 was implemented in Simmechanics. The motors are located in A and E and they apply a Torque T_1 and T_2 on bars 2 and 5 respectively. There are two rotational springs located in A and E, which are connected in parallel to the bars. In this model the springs have a linear behavior $T_{sj} = k_{ij}(\theta_{sj} - \theta_{0j})$. Where T_{sj} is the torque exerted by the spring, k_{ij} is the stiffness constant, θ_{sj} is the angle and θ_{0j} is the natural angle of the spring j . In addition, all the bars are rigid, the aerodynamic forces are neglected, and there are no dissipative forces.

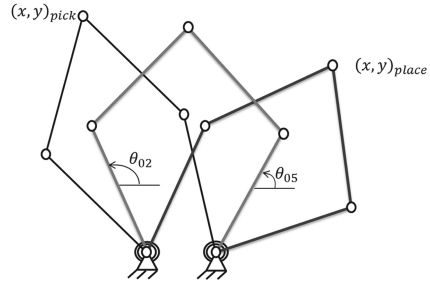
This multibody model calculates the motion of the mechanism for a given initial orientation of the bars and a given torque on the motors as a function of time. It can also be used to do the opposite, that is, to calculate the required torque for a given angular motion of the input bars (bar 2 and bar 5). In addition, an analytical model was developed to find the torque on the motors for a desired trajectory of the TCP. Using this trajectory as an input, the required angles, angular velocities and angular accelerations of the bars are calculated using inverse kinematics, then the acceleration of the center of gravity of each bar is calculated using relative motion between points for a rigid bar, and finally the torques are calculated using a 12×12 system of equations. This model was verified by comparing to the result of the Simmechanics model.

3.2 Determination of the Appropriate Springs and Trajectory

The first question to be answered is if there is a trajectory between stops, and a combination of stiffness constants (k_{t1}, k_{t2}) and natural angle of the springs (θ_{02}, θ_{05}) that reduce the torque during the motion to zero. Contrary to the 1-DOF system presented



Fig. 3 Five-bar linkage in the home, pick and place positions



in Sect. 2, it is not easy to answer this question by finding the exact solution of the differential equation of motion of the five-bar mechanism with springs, because it is a non-linear system. As a result, we use the multibody model to find the motion of the mechanism for a given initial rotation of the input bars. When an initial angle is given to these bars relative to the natural angle of the spring and they are released, they start moving, trying to return to the natural angle. They will find a maximum angle, stop and return. The oscillation can later be very irregular; however, the first stop should always occur. The idea is to match the first stop of both bars with the desired place position (see Fig. 3).

In other words, after releasing the mechanism from the initial condition $(x, y)_{pick}$, the TCP will follow a trajectory towards the place position $(x, y)_{place}$. The x component will start, for instance, increasing until at some point the speed component in x is zero and the value of x starts decreasing. The same happens to the y component of the TCP. The idea is to find the value of $k_{t1}, k_{t2}, \theta_{02}, \theta_{05}$ that makes the motion of the x – y components of the TCP stop for the first time at $(x, y)_{place}$ and the desired time t_{place} . In order to do so, an objective function is defined as:

$$I_{dif} = \left(\frac{t_{place} - t_1}{t_{place}} \right)^2 + \left(\frac{t_{place} - t_2}{t_{place}} \right)^2 + \left(\frac{x_{place} - x_{stop}}{x_{place}} \right)^2 + \left(\frac{y_{place} - y_{stop}}{y_{place}} \right)^2 \quad (4)$$

where, t_1 and t_2 are the times at which the stop (maximum or minimum of x and y) occurs, t_{place} is the desired time for the place operation, $(x, y)_{place}$ are the coordinates of the place position, and $(x, y)_{stop}$ are the coordinates at which the stop actually occurs. The ranges for the design variables are $0 < \theta_{0i} < 2\pi$ and $k_{ti} > 0$. The results of this process are the values of these variables that minimize the objective function, and the trajectory that the TCP follows. After finding this trajectory, the entire pick and place trajectory is completed by adding the stops and creating the returning trajectory as a mirror of the first trajectory. If the initial guess for this optimization is selected randomly, it does not converge. Consequently, this initial value is obtained by means of a preliminary minimization of the torque on the motors for a given cosine trajectory connecting the pick and place points. These two optimization problems were solved using Matlab and the Nelder-Mead direct search algorithm [5].



3.3 Estimation of the Energy Consumption

A good index to compare the proposed motion between stops with typical trajectories is the electric energy consumed by the motors. To calculate this index we use a simplified model of the motor assuming that the effect of the inductance, the damping on the motor and the inertia of the motor are negligible [6]. Moreover we assume electric energy recuperation every time it is possible, and no further inefficiencies beyond the energy lost in the armature resistance. Taking this into account, the required input power to generate the desired motion on each input bar has two parts, as shown in (5). The first term is the mechanical power and the second term is the electrical power dissipated in the resistance. When P_i is positive, the motor is taking energy from the source and when P_i is negative, the motor returns energy to the source through regenerative braking.

$$P_i = T_i \dot{\theta}_i + \frac{R_i T_i^2}{(k_{ii}^* G_i)^2} \quad (5)$$

$$E = \int (P_1 + P_2) dt \quad (6)$$

In (5), R_i is the armature resistance of the motor i , T_i is the torque that the motor exerts on the mechanism, k_{ii}^* is the torque constant of the motor, $\dot{\theta}_i$ is the angular speed of the motor and G_i the gear ratio of the motor. The total energy E is then calculated as the integral of the power P_i over time (6).

4 Results

The methodology explained in Sect. 3 was simulated on a five-bar linkage, whose properties are presented in Table 1. The optimization was conducted on this mechanism for pick and place positions that were selected randomly within its workspace. The characteristics of the pick and place operation as well as the results of the optimization are presented in Table 2.

The motion that the TCP follows when the springs have the values of k_{ij} and θ_{0j} presented in Table 2 and the mechanism is released from the pick position, is shown

Table 1 Properties of the mechanism and motors being simulated

L_1	[m]	0.25	R_j	[Ω]	0.0189
L_i	[m]	0.5	G_j	[-]	16
m_i	[kg]	1.9	k_{ij}^*	[$\frac{Nm}{A}$]	1.08
I_i	[kgm ²]	0.08	$i = 2 - 5;$		$j = 1, 2$

Table 2 Pick and place characteristics and results of the optimization

$(x, y)_{pick}$	[m]	(-0.233, 0.737)	Δt	[s]	0.4	k_{r1}	$[\frac{Nm}{rad}]$	47.82	k_{r2}	$[\frac{Nm}{rad}]$	46.25
$(x, y)_{place}$	[m]	(0.568, 0.500)	Δt_{stop}	[s]	0.1	θ_{02}	[rad]	2.15	θ_{05}	[rad]	0.75

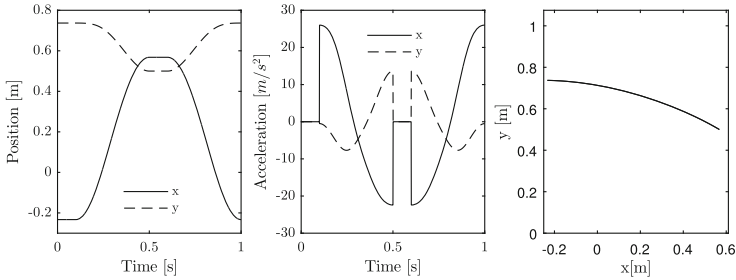


Fig. 4 Trajectory for the natural motion

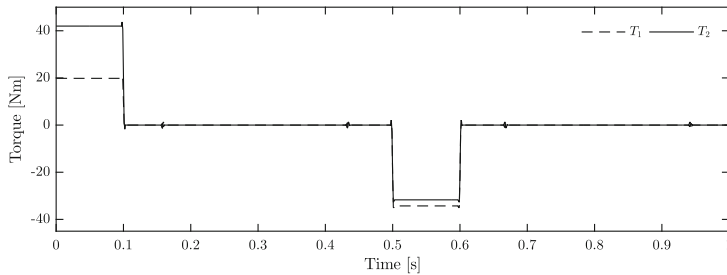


Fig. 5 Torque on the motors for pick and place with natural motion without mechanical brake

Table 3 Estimation of the energy expenditure for the natural motion (without mechanical brake)

			Motor 1	Motor 2
Maximum torque	T_{max}	[Nm]	35.98	43.66
RMS of the torque	T_{RMS}	[Nm]	12.47	16.60
Energy	E	[J]	1.60	

in the right plot of Fig. 4. According to the simulation, the difference between the achieved and the desired place position in both coordinates has an order of magnitude of 10^{-8} m. The torque that the motors have to perform to achieve this motion is presented in Fig. 5. This torque is zero during the motion and is constant during the stops. During the stops the torque can actually also be zero if a mechanical brake is used to keep the orientation of the bar, instead of using the motor. The values of the maximum and the RMS torque, as well as the energy consumption of the system without mechanical brake is presented in Table 3.



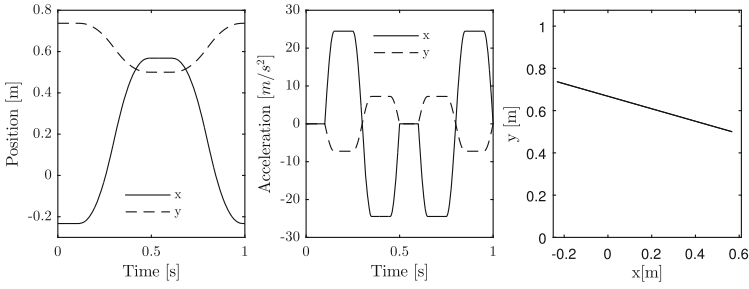


Fig. 6 Pick and place using the modified trapezoidal acceleration

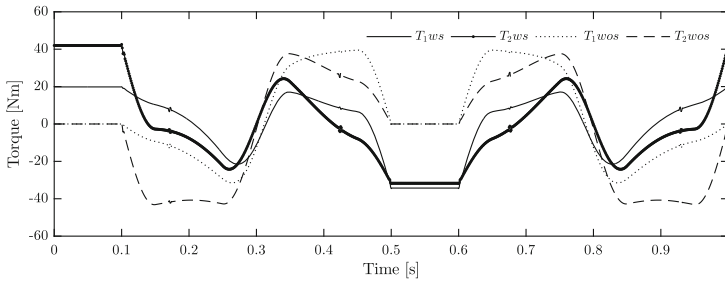


Fig. 7 Torque for the modified trapezoidal acceleration

Table 4 Estimation of the energy expenditure for the modified trapezoidal acceleration (with and without mechanical springs)

			Without spring		With springs	
			Motor 1	Motor 2	Motor 1	Motor 2
Maximum torque	T_{max}	[Nm]	39.51	43.18	34.59	51.71
RMS of the torque	T_{RMS}	[Nm]	23.07	28.70	17.01	21.62
Energy	E	[J]	5.05		2.82	

In order to compare these results with a commonly used trajectory, the modified trapezoidal acceleration trajectory [2] was used to joint the pick and place positions. This trajectory is one of the most common types of motion used in robotics to take a motor to a final position in a certain time. It has good characteristics in terms of maximum acceleration, maximum jerk and maximum speed. Figure 6 shows the position and acceleration as well as the motion of the TCP in the $x - y$ plane.

The torque and energy were calculated for this trajectory with and without springs in the mechanism. The results are presented in Fig. 7 and Table 4.

Figure 5 shows the torque that the motors need to apply to the mechanism to accomplish the required task when the optimal springs are attached to the same joint as the motors. The trajectory that the tool center point follows in this case is shown in Fig. 4. This trajectory results from applying the concept of natural motion. On



the other hand, Fig. 7 shows the torque that the motors have to apply when a typical trajectory (modified trapezoidal acceleration) is followed by the TCP. For each motor there are two different lines: the continuous line called w_s correspond to the system including springs on the joint of the motors, and the dashed line called w_{os} correspond to the system without springs (a normal five-bar linkage). This system without springs following a modified trapezoidal acceleration is the base for comparison. When springs are added to this system, the energy expenditure per cycle is reduced by 44 %. When instead of following the modified trapezoidal acceleration, the system with springs follow the natural motion trajectory (Fig. 4), the energy is reduced by 68 % per cycle. The reason for this reduction is that during the motion from pick to place, the torque that the motors have to exert on the mechanism is reduced, because it naturally tends to go to the desired place position in the required time. The reduction in the energy consumption could be even larger if a mechanical brake is used to hold the mechanism during the stops in the pick and place positions instead of using the motors.

5 Conclusion and Outlook

Simulations of a five-bar linkage without friction conducting a pick and place operation indicated that adding torsional springs to the fixed joints with appropriate parameters may reduce the energy expenditure per cycle. When springs are added to a mechanism following a typical trajectory, the reduction could be of 44 % per cycle. However the use of springs and a different motion strategy called natural motion reduce the energy expenditure by 68 %. The main reason is that the natural motion of the system starting from the pick position can match the desired place position in the required time, saving energy by taking advantage of the energy that was initially stored on the springs. One of the key points is to find the parameters of the springs that achieve this. The proposed methodology uses a multibody model of the system to solve the direct kinematics and an optimization function to minimize the difference between the desired and the actual position and time at the end of the motion. Future research could include the use of a more refined model with friction, a study on the structural effects of the proposed trajectory and experimental validation of the methodology.

References

1. Angeles, J.: Fundamentals of robotic mechanical systems, 3 edn. Springer (2007)
2. Biagiotti, L., Melchiorri, C.: Trajectory planning for automatic machines and robots. Springer (2008)
3. Goya, H., Matsusaka, K., Uemura, M., Nishioka, Y., Kawamura, S.: Realization of high-energy efficient pick-and-place tasks of scara robots by resonance. In: 2012 IEEE/RSJ International Conference on Intelligent Robots and Systems (IROS) (2012)

4. Jafari, A., Tsagarakis, N., Caldwell, D.G.: Exploiting natural dynamics for energy minimization using an actuator with adjustable stiffness (awas). In: 2011 IEEE International Conference on Robotics and Automation (ICRA) (2011)
5. Lagarias, J., Reeds, J., Wright, M., Wright, P.: Convergence properties of the nelder-mead simplex method in low dimensions. *SIAM J. Optim.* **9**(1), 112–147 (1998)
6. Pellicciari, M., Berselli, G., Leali, F., Vergnano, A.: A method for reducing the energy consumption of pick-and-place industrial robots. *Mechatronics* **23**(3), 326–334 (2013)
7. Siciliano, B.: *Robotics*. Springer (2009)
8. Tsai, L.W.: *Robot analysis*. Wiley (1999)

Structural Synthesis of Planar Geared Linkage Mechanisms as Multibody Systems

I. Visa, M. Neagoie and M.D. Moldovan

Abstract Geared linkage structure is defined in literature considering the type of linkage, usually four-bar or five-bar, and different versions are obtained by changing the input/output, the fixed link and the gears connections with linkage links. The paper proposes the structural synthesis of the planar geared linkage mechanisms with one pair of gears, as multibody systems with four bodies. The algorithm derived from the structural synthesis of the linkages as multibody systems with four bodies lead to eight distinct general kinematic chains, from which two contain a rigid sub-chain and, from the other six, only four contain the sub-chain formed by three bodies with five kinematic constraints. Replacing these sub-chains by the gearing sub-chain, seven variants of distinct kinematic chains with 1 DOF for geared linkages are identified (four general and three particular). Based on these, 27 distinct geared linkage mechanisms were obtained. This approach allowed to identify already known mechanisms but also new ones.

Keywords Geared linkage · Structural synthesis · Planar mechanism · Multibody systems method

1 Introduction

A geared linkage mechanism is defined as a planar linkage with one or more pairs of gears parallel coupled to it, [4, 5, 8]. For one pair of gears, the geared linkage mechanisms are formed based on one loop with 1 DOF (mobility $M = 1$) of four-bar type, and respectively five-bar linkage.

I. Visa (✉) · M. Neagoie (✉) · M.D. Moldovan
RESREC Research Center, Transilvania University of Brasov, Braşov, Romania
e-mail: visaion@unitbv.ro

M. Neagoie
e-mail: mneagoie@unitbv.ro

M.D. Moldovan
e-mail: macedon.moldovan@unitbv.ro

A four-bar geared linkage with one pair of gears has five links, one of the gear being rigidly connected to a link of the four-bar linkage (a loop with 1 DOF). By changing the input/output link, the fixed link and the pair of gears positioning, different types of four-bar geared linkages are obtained [10].

An analysis of five-link geared linkages based on crank-and-rocker mechanisms, double-crank mechanisms, inverted slider-crank mechanisms, slider crank mechanisms and scotch-yoke mechanisms is presented in [8]. A five-bar geared linkage with one pair of gears also has five links; in this case the gears are rigidly connected each to another link. The linkage initially has 2 DOF, but by the pair of gears the mechanism turns into 1 DOF.

By changing the input/output fixed link and the pair of gears connections, different versions of this type of geared linkage mechanisms can be obtained, [5].

Related to the pair of gears, most usually external gears are used, however, internal gears are reported, [4].

Geared four-bar mechanisms with collinear input and output shafts are usually employed for function generation (with approximatively constant transmission ratio, [10]); geared five-bar mechanisms having the gears positioned on the basis are also used for path generation (following a pre-set trajectory). The synthesis of a 1-DOF geared five-bar linkage using the evolutionary algorithm is described in [13]. An atlas with 732 coupler curves and linkage optimisation for a required path are presented in [1].

Optimized geared linkages are obtained by replacing circular gears with non-circular gears, [8, 9].

Geared linkage mechanisms are part of a broad variety of technical applications, as tracking systems for photovoltaic modules/platforms, [2], to reach large angular motions with optimum transmission angle; these types of mechanisms are also reported for mobile platforms of planar parallel manipulators [7], or for knee prosthesis [6]. These geared linkage mechanisms are actuated by rotational or linear displacement motions.

Literature reports on geared mechanisms based on graphs and structural decomposition in linkage and gear or in units as links and dyad link groups [5].

Thus, literature mentioned different approaches for the analysis and synthesis of the geared planar linkage mechanisms according to the mechanism structure.

This paper proposes a unitary method for the structural analysis and synthesis of the geared linkage mechanisms, by considering them as multibody systems.

2 Structural Synthesis of Mechanisms as Multibody Systems

A multibody system consists of bodies connected by kinematic (geometric) constraints and driving constraints. Two bodies can be connected by a joint (R-revolute pair, T-translational pair, C-curve pair) or by an intermediary binary link (RR, RT, TT) [3, 12].

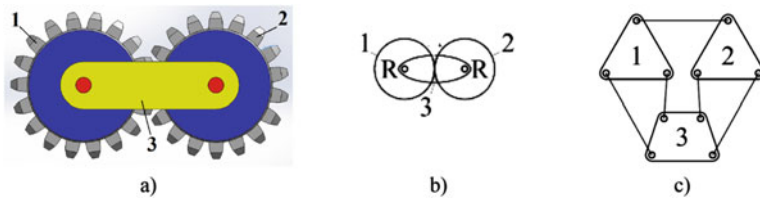


Fig. 1 Gearing sub-chain models: **a** CAD representation; **b** associated particular kinematic chain; **c** associated general kinematic chain

In the case of the R or T connection, the number of kinematic constraints equals 2, similarly with the 2RR, 2RT or 2TT connections.

A geared linkage planar mechanism with one pair of gears contains the sub-chain from Fig. 1, where between the gears 1–2 there is a curve-curve connection, and rotations between 1–3 and 2–3, thus a total of five kinematic constraints (1 + 2 + 2).

A multibody system with three bodies is considered for a pair of gears (Fig. 1b), with the general linkage form described in Fig. 1c. Based on, a geared planar linkage must have at least four bodies. By using the general form (Fig. 1c) the algorithm developed in [11] can be applied to identify all possible kinematic chains based on four bodies. From these, the kinematic chains that contain the sub-chain in Fig. 1c can become geared mechanisms.

In the space S , for a given number of bodies n_b (in this case $n_b = 4$), the number of kinematic constraints N_{kc} imposed between bodies by kinematic pairs to fulfil the requirement of $M = 1$ is given by:

$$N_{kc} = S \cdot (n_b - 1) - M = 3 \cdot (4 - 1) - 1 = 8 \tag{1}$$

The total number of pairs of bodies N_{pb} is obtained according to:

$$N_{pb} = C_{n_b}^2 = C_4^2 = 6 \tag{2}$$

where C_m^k counts the combinations of m taken k .

Thus 6 unknowns are used in the equation of the kinematic constraints [11]

$$\sum_{i=1}^{n_b-1} \sum_{j=i+1}^{n_b} r_{ij} = N_{kc} \Rightarrow r_{12} + r_{13} + r_{14} + r_{23} + r_{24} + r_{34} = 8 \tag{3}$$

where r_{ij} represents the number of the kinematic constraints between the i and j bodies. Maximum two kinematic constraints can be introduced between two different bodies, thus $r_{ij} \in \{0, 1, 2\}$, $i < j$. As a result, the number of distinct constraint combinations is $3^{N_{pb}} = 3^6 = 729$, from which 90 combinations $[r_{ij}] = [r_{12} \ r_{13} \ r_{14} \ r_{23} \ r_{24} \ r_{34}]^T$ are solutions of Eq. (3).

According to the structural synthesis algorithm presented in [11], by numerical processing of the 90 solutions and eliminating the isomorphic structures, eight

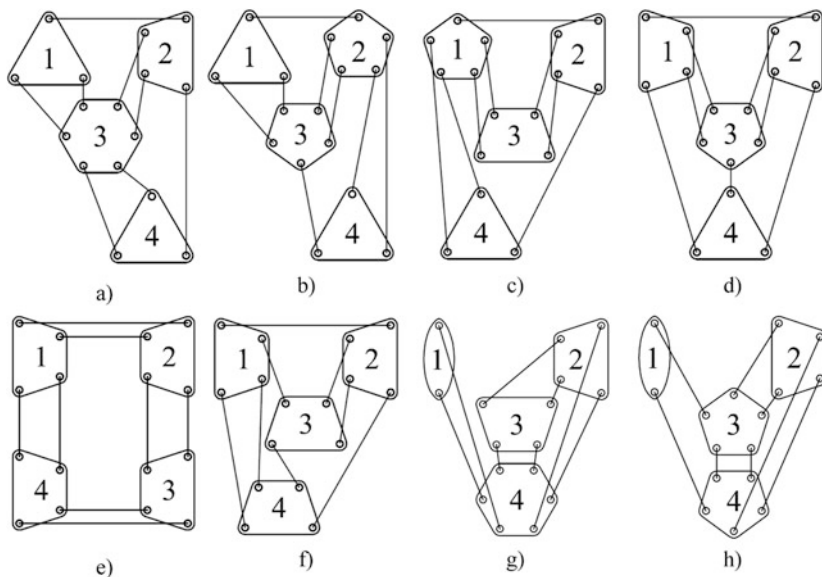


Fig. 2 Distinct general kinematic chains for $n_b = 4$ and $M = 1$ associated to the eight numerical solutions from rel. (4)

distinct solutions and the associated kinematic chains are identified, rel. (4) and Fig. 2:

$$[\mathbf{r}_{ij}]_1 = [1 \ 2 \ 0 \ 2 \ 1 \ 2]^T, \quad [\mathbf{r}_{ij}]_2 = [1 \ 2 \ 0 \ 2 \ 2 \ 1]^T \quad (4a, b)$$

$$[\mathbf{r}_{ij}]_3 = [1 \ 2 \ 2 \ 2 \ 1 \ 0]^T, \quad [\mathbf{r}_{ij}]_4 = [1 \ 2 \ 1 \ 2 \ 1 \ 1]^T \quad (4c, d)$$

$$[\mathbf{r}_{ij}]_5 = [2 \ 0 \ 2 \ 2 \ 0 \ 2]^T, \quad [\mathbf{r}_{ij}]_6 = [1 \ 1 \ 2 \ 2 \ 1 \ 1]^T \quad (4e, f)$$

$$[\mathbf{r}_{ij}]_7 = [0 \ 0 \ 2 \ 2 \ 2 \ 2]^T, \quad [\mathbf{r}_{ij}]_8 = [0 \ 1 \ 1 \ 2 \ 2 \ 2]^T \quad (4g, h)$$

From the eight distinct kinematic chains in Fig. 2, the two solutions in Fig. 2g, h contain one rigid sub-chain (the bodies 2-3-4) and thus are not feasible.

The gearing sub-chain (Fig. 1) is defined by three bodies with five kinematic constraints and, according to the graphical representations in Fig. 2, the variants in Fig. 2e, f do not fulfill this requirement and thus they are removed.

As a result, only the four solutions (4a–d) correspond to geared linkages. This four feasible solutions allow to generate seven distinct kinematic chains described in Fig. 3a₁, a₂, b₁, b₂, c₁, c₂, d₁.

A mechanism is obtained from a kinematic chain by considering one body as fixed body (reference body). As example, 27 distinct mechanisms are obtained as

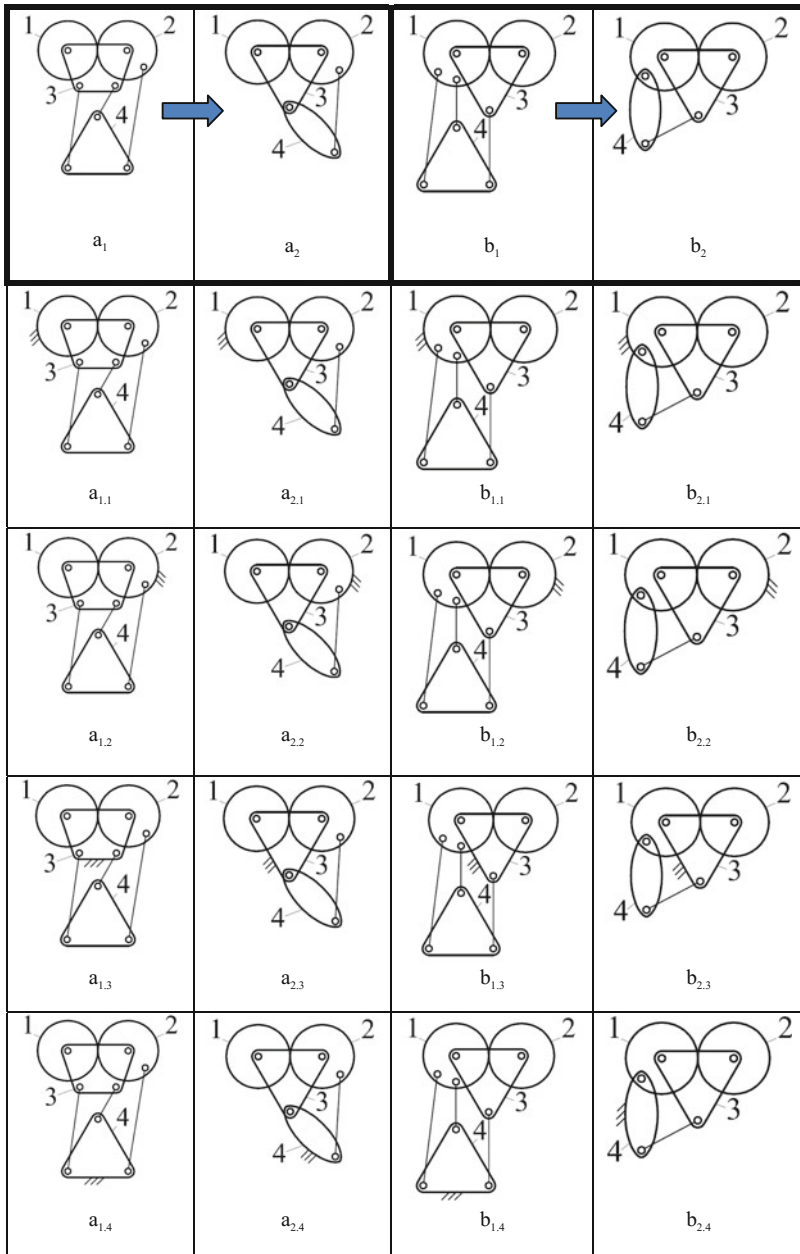


Fig. 3 a, b Gear linkage mechanisms obtained from Fig. 2: a_1, a_2 from Fig. 2a; b_1, b_2 from Fig. 2b. c, d Gear linkage mechanisms obtained from Fig. 2: c_1, c_2 from Fig. 2c; d_1 from Fig. 2d

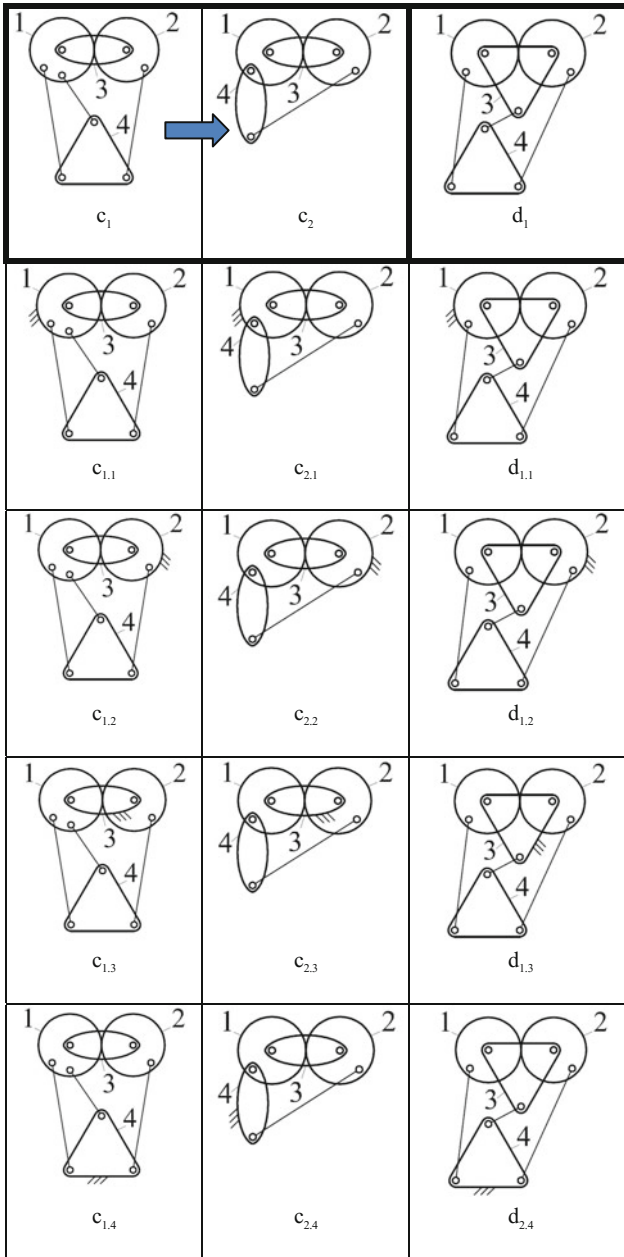


Fig. 3 (continued)

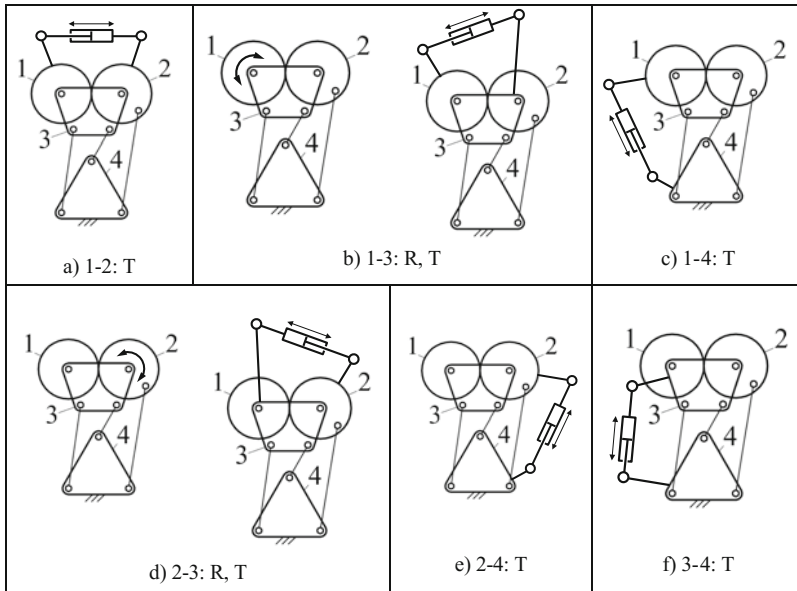


Fig. 4 Variants of driving motions for the mechanisms described in Fig. 3a_{1,4}

presented in Fig. 3 (mechanisms in Fig. 3d_{1,1} and d_{1,2} are symmetric thus are identical).

Driving motions are introduced between two bodies, Fig. 4. For a mechanism with four bodies, six pairs of bodies are identified thus, six variants of driving motions could be used (as rotation or translation motions). As example for the mechanism described in Fig. 3a_{1,4} there are the variants from Fig. 4 considering translation or rotational driving motions.

3 Conclusions

A new approach for automatic structural synthesis of planar geared linkage mechanism as multibody systems is developed in this paper.

Considering a pair of gears and their carrier as multibody sub-system with three bodies, the method is detailed for the case of four bodies planar geared mechanism. A unitary structural synthesis method could be used for both linkage and geared linkage mechanisms.

Following the algorithm previously reported, seven distinct kinematic chains were identified out of which 27 new and already existent mechanisms were obtained.



The algorithm can be extended for geared linkage mechanisms with more than one pair of gears and also for a higher number of bodies than four. This method offers the opportunity for a unitary kinematic and dynamic study of planar geared linkage mechanisms.

Acknowledgments The project EST IN URBA, PN-II-PT-PCCA-2011-3.2-051, Program Cooperation in Priority Fields - PNII, developed with the support of ANCS, CNDI-UEFISCDI, Romania is gratefully acknowledged.

References

1. Buskiewicz, J.: Use of shape invariants in optimal synthesis of geared five-bar linkage. *Mech. Mach. Theory* **45**, 273–290 (2010)
2. Creanga, N., Diaconescu, D., Hermeneanu, I.: Four-bar geared linkage used for photovoltaic azimuth orientation. *Env. Eng. Manag. J.* **10**(8), 1139–1148 (2011)
3. Haug, J.E.: Computer aided kinematics and dynamics of mechanical systems. In: *Basic Methods*. vol. I. Allyn and Bacon, USA (1989)
4. Li, T., Cao, W.: Kinematic synthesis of planar geared four-bar linkages with prescribed dwell characteristics. In: Huang, T. (ed.) *Proceedings of the 11th World Congress in Mechanism and Machine Science*, Tianjin, China, China Machinery Press (2003)
5. Li, T., Cao, W.-Q.: Kinematic analysis of geared linkage mechanisms. *Mech. Mach. Theory* **40**, 1394–1413 (2005)
6. Lovasz, E.-C., Ciupe, V., Modler, K.-H., Gruescu, C.M., Hanke, U., Maniu, I., Margineanu, D.: Experimental design and control approach of an active knee prosthesis with geared linkage. In: *New Advances in Mechanisms, Transmission and Applications*, Series: Mechanisms and Machine Science, vol. 17, pp. 149–156. Springer Publisher (2013)
7. Lovasz, E.-C., Grigorescu, S., Margineanu, D., Gruescu, C.M., Pop, C., Ciupe, V., Maniu, I.: Geared linkages with linear actuation used as kinematic chains of a planar parallel manipulator. In: *Proceedings of 3rd MeTrApp Conference, Mechanisms, Transmissions and Applications*, Series Mechanism and Machine Science, pp. 21–31 (2015)
8. Modler, K.-H., Lovasz, E.-C., Bar, G.F., Neumann, R., Perju, D., Perner, M., Margineanu, D.: General method for the synthesis of geared linkages with non-circular gears. *Mech. Mach. Theory* **44**, 726–738 (2009)
9. Mundo, D., Gatti, G., Dooner, D.B.: Optimized five-bar linkage with non-circular gears for exact path generation. *Mech. Mach. Theory* **44**, 751–760 (2009)
10. Parlaktas, V., Soylemez, E., Tanik, E.: On the synthesis of a geared four-bar mechanism. *Mech. Mach. Theory* **45**, 1142–1152 (2010)
11. Visa, I., Neagoe, M., Moldovan, M.: Algorithm for structural synthesis of planar mechanisms as multibody systems. In: *14th World Congress of Mechanisms and Machine Science*, Taipei, Taiwan (2009). doi:[10.6567/IFTtoMM.14TH.WC.OS8.029](https://doi.org/10.6567/IFTtoMM.14TH.WC.OS8.029)
12. Visa, I.: Structural synthesis of the planar-cam linkage mechanisms as multibody systems. mechanisms as multibody systems. In: *Proceedings of SYROM 2009*, Springer Science and Business, pp. 67–84 (2009)
13. Zhang, C., Norton, P.E.R.L., Hammonds, T.: Optimization of parameters for specified path generation using an atlas of coupler curves of geared five-bar linkages, *Mech. Mach. Theory*, **19**(6), 459–466 (1984)

Dynamics of a Vertical Unbalanced Gyroscopic Rotor with Nonlinear Characteristics

Zh. Iskakov

Abstract This study proposes to use the non-linear properties of the support bearing viscoelastic material for damping of resonance oscillations of a vertical unbalanced gyroscopic rotor. To this end, it analyzes in detail the impact of non-linear damping and non-linear elastic characteristics of the support bearing material on the resonance curve and vibration stability. The options of nonlinear quadratic and cubic stiffness of the material are considered. If a cubic nonlinear stiffness influences the transmissibility to much higher resonance regions, on the contrary a quadratic nonlinear stiffness influences the transmissibility to much lesser resonance regions. Under the influence of the nonlinear damping and nonlinear elastic characteristics of support bearing not only the resonance amplitude of oscillations greatly decreases, but also the boundaries of the instability region are moved down, and its width reduces significantly. The results are of significant importance in the analysis and design of nonlinear passive vibration isolators.

Keywords Gyroscopic rotor • Viscoelastic support • Non-linear characteristic • Non-linear damping • Resonance oscillations

1 Introduction

Vibration usually occurs in the rotating equipment during its start-up, in operating mode and at shutdown. Simplified model with the lumped parameters of rotor system is used as a rule for studying of the one rotor's shaft dynamics in the bearing supports. Supports are the connector of device between the rotor and supporting structure having the various forms and designs depending on the specific assumptions. Support of bearings on the viscoelastic elastomeric supports is a convenient way to introduce damping. In parallel with development of modelling of

Zh. Iskakov (✉)

Institute of Mechanics and Machine Science, Almaty University of Power Energy and Telecommunication, Almaty, Kazakhstan
e-mail: iskakov53@mail.ru

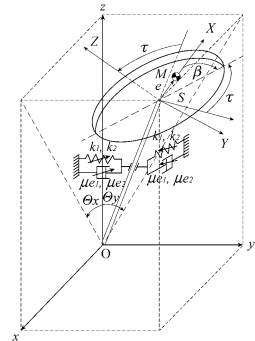
the viscoelastic material [1, 3, 9] which helps to describe a complexity of material properties, application of viscoelastic components in the rotor and vibration systems dynamics [2, 4, 5, 7, 8, 10] also has been increased generally, including with nonlinear elastic characteristics and damping. For example, Ravindra and Mallik [8] studied parametrically the effects of various types of damping on the performance of nonlinear vibration isolators under harmonic excitations. In the article [7] the efficiency of passive vibration isolators with linear damping and cubic nonlinear damping in the resonance and non-resonance ranges of vibrations has been studied. The excellent review regarding study of linear and nonlinear vibration isolation systems is given right there. In paper [4] an influence of the material cubic nonlinear stiffness on isolator capacity has been taken into consideration additionally in the studies.

In this paper, as opposed to previous studies, the impact of the bearing support material with quadratic nonlinear elastic characteristic and quadratic nonlinear damping on the resonance curve and stability of the vertical rigid gyroscopic rotor has been studied. Besides, the results are supplemented by the analysis of impact of cubic nonlinear elastic characteristic of material on the vibration parameters.

2 Rotor Motion Equations

Figure 1 shows the rotor's geometric layout. A shaft with a length L is mounted vertically, via lower hinged bearing and an upper elastic support (located at a l_0 distance). At the free shaft end a disk is fixed, with mass m (weight G), polar moment of inertia I_p and cross-section moment of inertia I_T which is the same for all directions). The shaft speed ω is so large that the rotor can be regarded as a gyroscope, a fixed point of which is the lower shaft bearing. The geometric center of disk position S is determined by the coordinates x, y , and position of shaft and rotor in the space by angles θ_x, θ_y and the angle of rotation $\varphi = \omega t$. We also assume that the linear eccentricity e lies on the axis SX and lags behind the plane of angular

Fig. 1 Rotor geometry



eccentricity τ by an angle β . We confine ourselves to small deviations of the rotor axis, and therefore, in our calculations we only consider terms that are linear relative to small values: e, τ .

The upper elastic support bearing of the gyroscopic rotor can be made of non-linear materials such as raw rubber, rubber and other polymers widely used as a damper of the occurring oscillations. Their pronounced dissipative properties are characterized by nonlinear-viscous damping, and they have soft or rigid type non-linear elastic characteristic. In the gyroscopic rotor μ_{e1} is coefficient of viscous damping and μ_{e2} is coefficient of nonlinear term of viscous damping, k_1 is the support stiffness factor and k_2 is a coefficient in the nonlinear term of the elastic force.

Motion equations of a vertical unbalanced gyroscopic rotor were obtained in the paper [5]. Having introduced the following non-dimensional parameters

$$\varepsilon = e/L; l = l_0/L; \bar{t} = t\omega_0; \Omega = \omega/\omega_0; \bar{I}_p = I_p/(mL^2); \bar{I}_T = I_T/(mL^2); K_1 = k_1/(m\omega_0^2); K_2 = k_2L/(m\omega_0^2); P = G/(mL\omega_0^2); \mu_1 = \mu_{e1}/(mL^2\omega_0); \mu_2 = \mu_{e2}/(mL^2),$$

where

$$\omega_0 = \sqrt{(k_1 l_0^2 - GL) / [mL^2 - (I_p - I_T)]}$$

is the critical speed of the linear system without damping, using the symbols of amplitude

$$M = \sqrt{[(\Omega^2 + P)\varepsilon + H\tau\Omega^2 \cos \beta]^2 + H\tau^2\Omega^4 \sin^2 \beta}$$

and the initial phase

$$\gamma = \tan^{-1} \frac{H\tau\Omega^2 \sin \beta}{(\Omega^2 + P)\varepsilon + H\tau\Omega^2 \cos \beta}$$

of the forcing torque and expressing its with some harmonic functions the motion equations in the case soft type non-linear elastic characteristic of elastic support can be rewritten in compact form:

$$\begin{aligned} (1 + \bar{I}_T)\theta_x'' + \bar{I}_p\Omega\theta_y' + \mu_1\theta_x' + \mu_2\theta_x^2 + (K_1 l^2 - P)\theta_x + K_2 l^3 \theta_x^2 &= M \cos(\Omega \bar{t} + \gamma), \\ (1 + \bar{I}_T)\theta_y'' - \bar{I}_p\Omega\theta_x' + \mu_1\theta_y' + \mu_2\theta_y^2 + (K_1 l^2 - P)\theta_y + K_2 l^3 \theta_y^2 &= M \sin(\Omega \bar{t} + \gamma), \end{aligned} \quad (1)$$

where $H = \bar{I}_p - \bar{I}_T$ is the conditional disk thickness.

3 Amplitude-Frequency and Phase-Frequency Characteristics and Stability of Oscillations

Considering the system resonance (1) on the basic frequency, it is possible to approximate its solution by the simple harmonic with vibration frequency equal to the frequency of disturbance torque

$$\begin{aligned}\theta_x &= A_0 + A \cos(\Omega \bar{t} - \alpha), \\ \theta_y &= A_0 + A \sin(\Omega \bar{t} - \alpha).\end{aligned}\quad (2)$$

After applying the harmonic balance method [5], we obtain the amplitude-frequency and phase-frequency responses

$$\begin{aligned}(K_1 l^2 - P)A_0 + K_2 l^3 A_0^2 + \frac{1}{2}(\mu_2 \Omega^2 + K_2 l^3)A^2 &= 0, \\ \left\{ [(1-H)\Omega^2 - (K_1 l^2 - P) - 2K_2 l^3 A_0]^2 + \mu_1^2 \Omega^2 \right\} A^2 &= M^2\end{aligned}\quad (3)$$

$$\tan \alpha = \frac{[(1-H)\Omega^2 - (K_1 l^2 - P) - 2K_2 l^3 A_0] \tan \gamma + \mu_1 \Omega}{(1-H)\Omega^2 - (K_1 l^2 - P) - 2K_2 l^3 A_0 - \mu_1 \Omega \tan \gamma}.\quad (4)$$

System linearization (1) leads to amplitude-frequency and phase-frequency characteristics for the rotor linear model [6].

Assuming that M expression due to an external torque is zero and damping coefficients μ_1 and μ_2 in Eq. (1), we obtain the equation of the supporting curve for oscillations at the fundamental resonance frequency

$$A = \sqrt{(K_1 l^2 - P)^2 - (1-H)^2 \Omega^4} / (\sqrt{2} K_2 l^3),\quad (5)$$

where $\Omega \leq \sqrt{(K_1 l^2 - P)/(1-H)}$.

Formula (5) shows that supporting curve is a parabola that is symmetrical about the axis Ω ; the greater the value of K_2 , the greater the inclination of the supporting curve to the left.

According to Eq. (3), we have

$$f(\Omega, A) = \left\{ [(1-H)\Omega^2 - (K_1 l^2 - P) - 2K_2 l^3 A_0]^2 + \mu_1^2 \Omega^2 \right\} A^2 - M^2 = 0,\quad (6)$$

where

$$A_0 = \left[-(K_1 l^2 - P) + \sqrt{(K_1 l^2 - P)^2 - 2K_2 l^3 (\mu_2 \Omega^2 + K_2 l^3) A^2} \right] / (2K_2 l^3).\quad (7)$$

From reasoning that geometric locus at which the amplitude curves for the main resonance oscillations have vertical tangents, we obtain the stability criterion

$$\partial f / \partial A = 0. \quad (8)$$

Equality (8), considering (6), leads to the equation

$$\left\{ \left[(1-H)\Omega^2 - \sqrt{(K_1 l^2 - P)^2 - 2K_2 l^3 (\mu_2 \Omega^2 + K_2 l^3) A^2} \right]^2 + \mu_1^2 \Omega^2 \right\} \\ \times \sqrt{(K_1 l^2 - P)^2 - 2K_2 l^3 (\mu_2 \Omega^2 + K_2 l^3) A^2} \\ + 4K_2 l^3 (\mu_2 \Omega^2 + K_2 l^3) A \left[(1-H)\Omega^2 - \sqrt{(K_1 l^2 - P)^2 - 2K_2 l^3 (\mu_2 \Omega^2 + K_2 l^3) A^2} \right] = 0. \quad (9)$$

Equation (9) describes the boundary curves of the stability range for oscillations at the fundamental resonance frequency. Consequently, the geometric locus at which the amplitude curves have vertical tangents, determines the stability boundary.

4 Numerical Results and Assessment of Parameters Impact

The solution of simultaneous Eqs. (3), (5) and (9) was obtained using numerical methods in the symbolic computation system “Maple 11” for the following rotor parameters: $H = +0, 1$; $\varepsilon = 0, 01$; $\tau = 0, 02$; $L = 0, 88$; $\bar{I}_p = 0, 2$; $\bar{I}_T = 0, 1$; $K_1 = 1, 19$; $K_2 = 2, 19; 3, 19$; $P = 0, 012$; $\mu_1 = 0$; $\mu_2 = 0; 0, 5$.

Figure 2 shows the amplitude-frequency characteristics and the instability region boundary at the fundamental resonance frequency in different values μ_2 of nonlinear damping. Amplitude curves illustrated in solid lines, and the boundaries between stable and unstable regions illustrated in dotted lines. The area between these lines is an instability region. Under the influence of nonlinear damping, the middle part of the upper boundary line is shifted down significantly more than the middle part of the lower boundary line of the instability region, in other words, the middle part of the instability region is narrowed, which shows the damping effect of the nonlinear damping. Due to the absence of angle β in the stability criterion (9), this angle does not affect the stability boundary. The calculations also show that the coefficient of nonlinear damping μ_2 has virtually no effect on the main resonance's phase-frequency characteristics. Changes in the thickness of the rotor disc affect the location of the resonance curves; the region of instability of the rotor with a thick disk is wider than for the rotor with a thin disk.

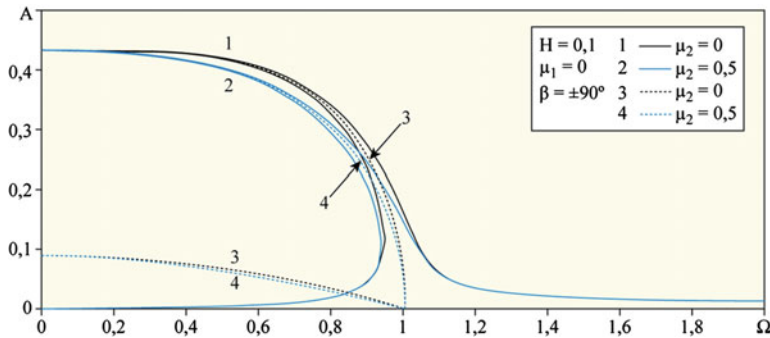


Fig. 2 Amplitude-frequency characteristics and instability region boundaries at different values of the nonlinear damping coefficient

When increasing the coefficient K_2 of the nonlinear component of the elastic force at a constant ratio μ_2 of the nonlinear damping, we observe the pattern shown in Fig. 3. When we increase the parameter K_2 , the resonance curves are drawn from the end and are bent to the left to the region of lower frequencies, with decreasing amplitude. Quadratic nonlinear stiffness affects the transmissibility significantly least resonance region. Under the influence of the coefficient K_2 , the instability region shifts downward, and the upper limit is shifted more than the lower one. As a result, the position of the instability region changes and the width decreases. It is clear that an increase in the elastic force, directed to the equilibrium position, with growth of factor K_2 , limits the amplitude of oscillation.

In the event of a rigid-type non-linear elastic characteristic nonlinear viscous damping does not affect practically on the frequency response of the system. The amplitude-frequency characteristics of the rotary machine, at various values of the

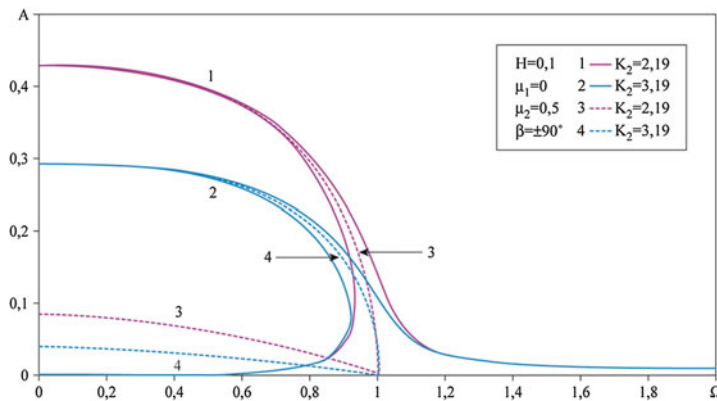


Fig. 3 Influence of the coefficient of nonlinear component elastic force to amplitude-frequency characteristics and the instability region boundaries

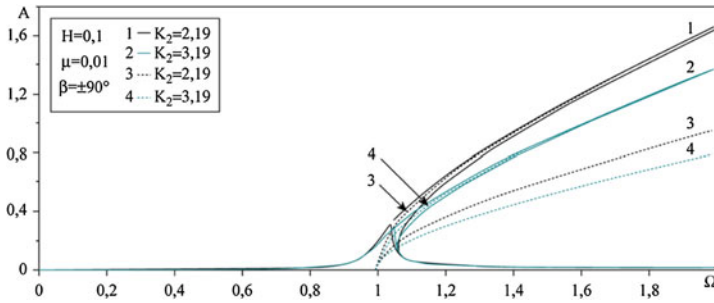


Fig. 4 Influence of the coefficient of nonlinear component elastic force to amplitude-frequency characteristics and the instability region boundaries. Case of the rigid-type non-linear elastic characteristic

coefficient of nonlinear elastic force component of support looks like as shown in Fig. 4. From that follows that the strengthening of the rigid-type non-linear elastic characteristics leads to a tightening of the resonance curves to the area of higher angular velocities with decreasing of amplitude. Cubic nonlinear stiffness influences the transmissibility significantly over resonance region. The instability region is moved downwards and its width decreases. However, at the non-resonance region the nonlinear stiffness have almost no effect on the isolators.

Therefore, the results obtained above are of prime importance for analysis and design of vibration isolators and can be used as a benchmark in development and selection of supports and isolators in the engineering applications.

5 Conclusions

The basic resonant oscillations and stability of a vertical rigid gyroscopic rotor with nonlinear damping and nonlinear elastic characteristics (skewed disk has an imbalance mass) are studied. Under the influence of nonlinear viscous damping the middle part of the upper resonant curves bends down. The instability region is displaced and its width is narrowed, though the downward displacement of the average part of the upper bound is greater than the average displacement of the lower border, which demonstrates the damping effect of the external nonlinear damping. Variants such as soft and rigid-type nonlinear elastic characteristics are studied. In the case of soft characteristics under the influence of nonlinear components of the elastic force, the resonance curves are drawn from the end and bent to the left, to the low speed region, the amplitude decreases, and the instability region shifts downward; the upper bound is greater than that of the lower bound. In the case of rigid characteristics, the resonance curves are drawn from the end and bent to the right, to the high speed region, the amplitude decreases, and the instability region shifts downward. If quadratic nonlinear stiffness affects the

transmissibility significantly least resonance region, on the contrary cubic nonlinear stiffness influences the transmissibility significantly over resonance region. These conclusions are of significant importance in the analysis and design of nonlinear passive vibration isolators in the rotary machines.

References

1. Adolffson, K., Enelund, M., Olsson, P.: On the fractional order model of viscoelasticity. *Mech. Time-Depend. Mater.* **9**(1), 15–34 (2005)
2. Bavastrri, C.A., Ferreira, E.M.D.S., Espíndola, J.J.D, Lopes, E.M.D.O.: Modeling of dynamic rotors with flexible bearings due to the use of viscoelastic materials. *J. Braz. Soc. Mech. Sci. Eng.* **30**(1), 22–29 (2008)
3. Gil-Negrete, N., Vinolas, J., Kari, L.: A nonlinear rubber material model combining fractional order viscoelasticity and amplitude dependent effects. *J. Appl. Mech.* **76**(1), 011009 (2009)
4. Ho, C., Lang, Z., Billings, S.A.: The benefits of nonlinear cubic viscous damping on the force transmissibility of a Duffing-type vibration isolator. In: *Proceedings of UKACC International Conference on Control*, Cardiff, UK (2012)
5. Iskakov, Zh.: Resonant Oscillations of a Vertical Unbalanced Gyroscopic Rotor with Nonlinear Characteristics. In: *Proceedings of 2015 IFToMM World Congress*, Taipei, Taiwan (2015)
6. Iskakov, Zh., Kalybaeva, A.: Vibrations and stability of vertical gyro rotor with warped disk and mass imbalance. In: *Proceedings of the International Symposium Fundamental and applied problems of science*, Moscow, vol. 2, pp. 50–57 (2010)
7. Peng, Z.K., Meng, G., Lang, Z.Q., Zhang, W.M., Chu F.L.: Study of the effects of cubic nonlinear damping on vibration isolations using harmonic balance method. *Int. J. Non-Linear Mech.* **47**(10), 1065–1166 (2012)
8. Ravindra, B., Mallik, A.K.: Performance of non-linear vibration isolators under harmonic excitation. *J. Sound Vib.* **170**, 325–337 (1994)
9. Richards, C.M., Singh, R.: Experimental characterization of nonlinear rubber isolators in a multi-degree-of-freedom system configuration. *J. Acoust. Soc. America* **106**, 2178 (1999)
10. Shabaneh, N.H., Zu, J.W.: Dynamic analysis of rotor–shaft systems with viscoelastically supported bearings. *Mech. Mach. Theory* **35**(9), 1313–1330 (2000)

Part III
MTM—Mechanical Transmissions

Edge Tooth Addendum Thickness of Hindley Worm

Yaping Zhao

Abstract For a Hindley worm, the addendum thickness of its edge tooth intensely affects its working performance and the manufacturability of its mating worm gear, whose computation is thus taken into consideration. The analytical solution to the addendum thickness is obtained for the edge tooth. The numerical results declare that the TA worm has a stronger resisting ability to the pointing of its edge tooth. Even though the number of worm thread is more or the velocity ratio is less, the edge tooth is also able to be kept thick enough. The further related research should focus on the influence of the modification on the pointing of the edge tooth.

Keywords Hindley worm drive • Addendum thickness • Edge tooth • Axial section • Tooth profile

1 Introduction

The Hindley worm drive is also known as the TA worm drive, or the globoidal worm drive, which is widely used in various industrial sections nowadays owing to its outstanding meshing characteristics.

Up to now, the history of the Hindley worm pair has been more than 250 years roughly. As reported by Buckingham [1] and Crosner [2], the Hindley worm drive was initially invented approximately in 1765 by Henry Hindley. About in 1909, Samuel I. Cone greatly boosted the Hindley worm drive and got his first related patent in 1932 [3, 4]. The Hindley worm drive improved by Cone is also known as Cone Drive. Afterwards the basic design and fabrication approaches of the Hindley worm drive were preliminarily summarized in Refs. [5, 6].

A main shortcoming of the toroidal worm drive is the pointing of the edge tooth of the worm. Because if the pointing is severe, the corresponding toroidal hob cannot be manufactured and thus there is no way to generate the worm gear.

Y. Zhao (✉)
Northeastern University, Shenyang, China
e-mail: zhy_p_neu@163.com

Therefore, it is necessary to check out the edge tooth top width in the course of designing an hourglass worm.

For the purpose to study the pointing of the edge tooth, the computation problem of the addendum thickness of the edge tooth has to be solved in advance. In 1980s, Shen [7] and Hu [8] proposed a method to compute the addendum thickness of the edge tooth for the plane double-enveloping toroidal worm drive (the TP worm drive). The investigating result shows that the tapering problem for the TP worm is relatively serious. After entering the 21st century, Dong [9] improved the work of Shen and Hu, and suggested a universal method to compute the top thickness of the edge tooth for the enveloping worm. A little later, Zhao [10] investigated the addendum thickness of the edge tooth for the dual tori double-enveloping toroidal worm drive (the DTT worm drive).

The investigation on computing the top thickness of the edge tooth for a TA worm is rather sparse in the literature. In the process of calculating the top thickness of the edge tooth, several systems of nonlinear equations generally have to be solved iteratively and, in general, only the numerical solution can be obtained.

In the current study, a methodology to count the addendum thickness of the edge tooth is suggested for the TA worm and, unlike the previous work, the analytical solution regarding the top thickness of the edge tooth is attained.

2 Equations of Hindley Worm Surface and Its Axial Tooth Profile

As illustrated in Fig. 1, by right of the principle to machine a Hindley worm, two fixed coordinate systems, $\sigma_{o1} \{O_1; \vec{i}_{o1}, \vec{j}_{o1}, \vec{k}_{o1}\}$ and $\sigma_{od} \{O_d; \vec{i}_{od}, \vec{j}_{od}, \vec{k}_{od}\}$, are used to indicate the initial positions of the worm blank and the tool post, respectively. Herein

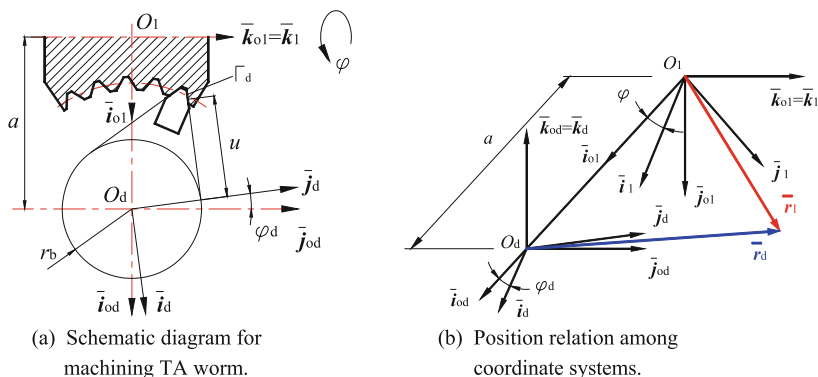


Fig. 1 Drawings to account for formation of Hindley worm pair

the two unit vectors, \vec{k}_{o1} and \vec{k}_{od} , lie along their axial lines. Such two unit vectors are mutually perpendicular and the shortest distance between them is the distance from the point O_1 to O_d , and $|O_1O_d| = a$. Therein a is the center distance of the worm pair.

Over and above that, two rotating coordinate systems, $\sigma_1 \{O_1; \vec{i}_1, \vec{j}_1, \vec{k}_1\}$ and $\sigma_d \{O_d; \vec{i}_d, \vec{j}_d, \vec{k}_d\}$, are linked to the worm roughcast and the cutter frame, respectively. When the rotation angle of the worm roughcast is φ , the interconnected rotating angle of the tool apron is φ_d and $\varphi_d = \varphi/i_{12}$, in which i_{12} is the transmitting ratio of the worm drive.

In σ_d , the vector equation of the straight cutting edge can be represented as

$$(\vec{r}_d)_d = -u\vec{i}_d + r_b\vec{j}_d, \quad (1)$$

where r_b is the main basic circle radius of the worm gear.

Via the coordinate transformation, the equation of the locus surface of the straight cutting edge in σ_{od} can be obtained from Eq. (1) as

$$(\vec{r}_d)_{od} = R[\vec{k}_{od}, \varphi_d] (\vec{r}_d)_d = x_{od}\vec{i}_{od} + y_{od}\vec{k}_{od}, \quad (2)$$

where $x_{od} = -u \cos \varphi_d - r_b \sin \varphi_d$, $y_{od} = -u \sin \varphi_d + r_b \cos \varphi_d$ and the notation $R[\vec{k}_{od}, \varphi_d]$ denotes the rotation transformation matrix around the axis [11] \vec{k}_{od} and

$$R[\vec{k}_{od}, \varphi_d] = \begin{bmatrix} \cos \varphi_d & -\sin \varphi_d & 0 \\ \sin \varphi_d & \cos \varphi_d & 0 \\ 0 & 0 & 1 \end{bmatrix}.$$

From Eq. (2), the equation of the helicoidal surface of the Hindley worm can be reaped in σ_1 as

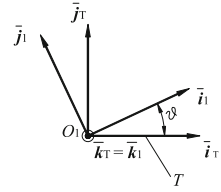
$$(\vec{r}_1)_1 = R[\vec{k}_1, -\varphi] \left(R[\vec{i}_{o1}, \frac{\pi}{2}] (\vec{r}_d)_{od} + a\vec{i}_{o1} \right) = x_1\vec{i}_1 + y_1\vec{j}_1 + y_{od}\vec{k}_1, \quad (3)$$

where $x_1(u, \varphi) = (x_{od} + a) \cos \varphi$, $y_1(u, \varphi) = -(x_{od} + a) \sin \varphi$. Therein u and φ are the parameters of the Hindley worm helicoidal surface. In Eq. (3), the symbol $R[\vec{i}_{o1}, \frac{\pi}{2}]$ denotes the rotation transformation matrix around the axis \vec{i}_{o1} and

$$R[\vec{i}_{o1}, \frac{\pi}{2}] = \begin{bmatrix} 1 & 0 & 0 \\ 0 & 0 & -1 \\ 0 & 1 & 0 \end{bmatrix}.$$

A rotatable coordinate system $\sigma_T \{O_1; \vec{i}_T, \vec{j}_T, \vec{k}_T\}$ is built in association with the worm and the unit vectors, \vec{k}_T and \vec{k}_1 , coincide with each other as shown in Fig. 2.

Fig. 2 Position of axial section T in σ_1



Thereby the plane $O_1 - \vec{i}_T \vec{k}_T$ forms an axial section T of the worm. The rotating directed angle around the axis \vec{k}_T between σ_T and σ_1 is θ . When θ takes a constant value, the axial tooth profile of the worm in T can be represented as

$$(\vec{r}_1)_T = R[\vec{k}_T, \theta](\vec{r}_1)_1 = x_{1T}\vec{i}_T + y_{1T}\vec{j}_T + y_{od}\vec{k}_T, y_{1T} = 0, \tag{4}$$

where $x_{1T} = x_1 \cos \theta - y_1 \sin \theta$, $y_{1T} = x_1 \sin \theta + y_1 \cos \theta = (x_{od} + a) \sin(\theta - \varphi)$.

From Eq. (4), it is easy to find that $\varphi = \theta$ along the axial tooth profile of the worm.

3 Top Thickness Computation of Edge Tooth

As depicted in Fig. 3a, in the axial section T , the point C is at the inlet portion of the worm and on its reference anchor ring. As a result, the system of nonlinear equations to determine such a point C with unknowns u , φ and θ can be represented as

$$(a - x_{1T})^2 + y_{od}^2 = \frac{d_2^2}{4}, y_{od} = \frac{L_w}{2}, y_{1T} = x_1 \sin \theta + y_1 \cos \theta = 0; \tag{5}$$

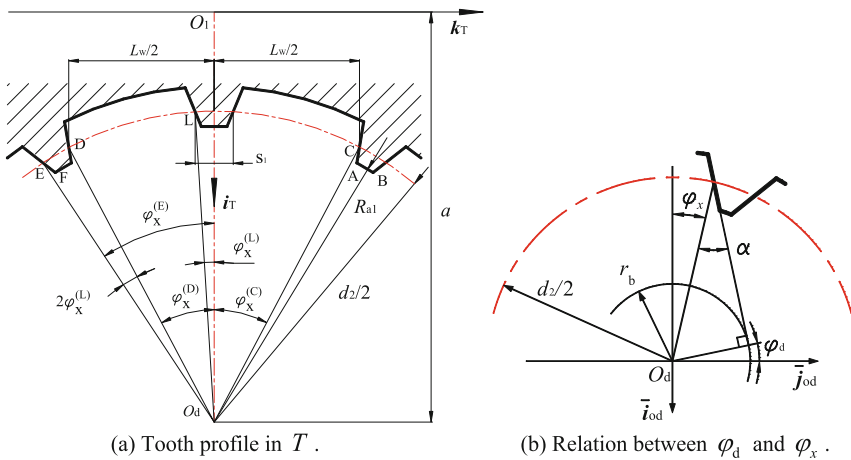


Fig. 3 Geometry of Hindley worm in its axial section T

where d_2 is the diameter of the reference circle of the worm gear and L_w is the length of the worm thread.

Solving System (5) may yields

$$u_C = \sqrt{\frac{1}{4}d_2^2 - r_b^2}, \varphi_C = \theta_C = i_{12} \left(\arctan \frac{2r_b}{\sqrt{d_2^2 - 4r_b^2}} - \varphi_w \right); \quad (6)$$

where φ_w is the half angle of the worm surrounding the mating worm gear.

The point A is also in the axial section T , together with the point C . Hence $\theta_A = \theta_C$. Besides, the point A is on the top toroidal surface of the worm. Thus the equations to ascertain the point A can be represented as

$$(a - x_{1T})^2 + y_{od}^2 = R_{a1}^2, y_{1T} = x_1 \sin \theta_C + y_1 \cos \theta_C = 0; \quad (7)$$

where R_{a1} is the radius of the top arc of the worm.

Solving System (7) may lead up to

$$u_A = \sqrt{R_{a1}^2 - r_b^2}, \varphi_A = \theta_A = \theta_C. \quad (8)$$

After computing further, it is easy to have

$$x_{1T}^{(A)} = x_{od}^{(A)} + a, y_{od}^{(A)} = \sqrt{R_{a1}^2 - [x_{od}^{(A)}]^2}; \quad (9)$$

where $x_{od}^{(A)} = -\sqrt{R_{a1}^2 - r_b^2} \cos \frac{\theta_C}{i_{12}} - r_b \sin \frac{\theta_C}{i_{12}}$.

The point L is on the reference torus and on the left tooth profile at the throat portion. In consequence, the equations for the point L can be expressed as

$$(a - x_{1T})^2 + y_{od}^2 = \frac{d_2^2}{4}, y_{od} = -\frac{s_1}{2}, y_{1T} = x_1 \sin \theta + y_1 \cos \theta = 0; \quad (10)$$

where s_1 is the chordal tooth thickness of the worm on its reference ring surface at its throat portion.

Solving System (10) may cause

$$u_L = u_C, \varphi_L = \theta_L = i_{12} \left(\arctan \frac{2r_b}{\sqrt{d_2^2 - 4r_b^2}} + \arcsin \frac{s_1}{d_2} \right). \quad (11)$$

Also as demonstrated in Fig. 3a, the point D is symmetrical with the point C regarding the axial line $\vec{\tau}_T$ so that $\varphi_x^{(D)} = -\varphi_x^{(C)}$. Here φ_x is the nominal angle of the straight cutting edge. By virtue of the geometric relationship shown in Fig. 3b, the following estimating formula for the angle φ_x is approximately true

$$\varphi_x = \alpha - \varphi_d, \quad (12)$$

in which α is the pressure angle of the worm on its reference torus.

Therewithal, based on Eq. (12), it is undemanding to achieve

$$\varphi_d^{(D)} = 2\alpha - \varphi_d^{(C)}. \quad (13)$$

Besides, Fig. 3a makes clear that $\varphi_x^{(E)} = \varphi_x^{(D)} + 2\varphi_x^{(L)}$. As a consequence, by means of Eq. (12), it is trouble-free to acquire

$$\varphi_d^{(E)} = -\varphi_d^{(C)} + 2\varphi_d^{(L)}. \quad (14)$$

According to the transmitting ratio relation, Eq. (14) can be transformed into $\varphi_E = -\varphi_C + 2\varphi_L$. Consequently, $\theta_E = -\theta_C + 2\theta_L$. The point F is also in the axial section T , together with the point E . Hence $\theta_F = \theta_E$. For this reason, the equations to ascertain the point F can be represented as

$$(a - x_{1T})^2 + y_{od}^2 = R_{a1}^2, y_{1T} = x_1 \sin\theta_E + y_1 \cos\theta_E = 0. \quad (15)$$

Solving System (15) gives out $u_F = u_A$ and $\varphi_F = \theta_E$. The further calculation gives rise to

$$x_{1T}^{(F)} = x_{od}^{(F)} + a, y_{od}^{(F)} = -\sqrt{R_{a1}^2 - [x_{od}^{(F)}]^2}; \quad (16)$$

where $x_{od}^{(F)} = -\sqrt{R_{a1}^2 - r_b^2} \cos \frac{\theta_E}{i_{12}} - r_b \sin \frac{\theta_E}{i_{12}}$.

Due to the symmetry between the points B and F , the top thickness of the edge tooth can be worked out as

$$s_{a1} = |AB| = \sqrt{[x_{od}^{(A)} - x_{od}^{(F)}]^2 + [y_{od}^{(A)} + y_{od}^{(F)}]^2}. \quad (17)$$

4 Numerical Examples and Discussion

Three numerical examples are taken into account in this section. Their geometric design is performed in accordance with the popular methodology [8, 9] and the achieved outcomes are listed in Table 1.

The main calculating consequences associated with the addendum thickness of the edge tooth are supplied in Table 2. Among these consequences, φ_d is an acute angle and $\varphi_x^{(C)} = \varphi_w$. On top of that, the absolute values of $y_{od}^{(A)}$ and $y_{od}^{(F)}$ are all close to $L_w/2$. All these imply the exactness of the computing results.

Table 1 Computing outcomes of basic parameters of numerical examples

	A	B	C
$a/(mm)$	160	180	200
i_{12}	64	8	4
Z_1	1	6	12
$r_b \approx 0.625a/2/(mm)$	50	56.5	62.5
$d_2 \approx 2a - 0.681a^{0.875}/(mm)$	262	296	330
$m_t = d_2/(i_{12}Z_1)/(mm)$	4.0938	6.1667	6.875
$\alpha = \arcsin(2r_b/d_2)/(^{\circ})$	22.4377	22.4425	22.2586
$R_{a1} = a - 0.681(a^{0.875}/2) - 0.75m_t/(mm)$	127.9297	143.375	159.8438
$Z_k = 4$, if $i_{12}Z_1 \leq 40$; $Z_k = i_{12}Z_1/10$, round-off, if $Z_2 > 40$	6	5	5
$\varphi_w = (180^{\circ}/Z_2)(Z_k - 0.45)/(^{\circ})$	15.6094	17.0625	17.0625
$L_w = d_2 \sin \varphi_w/(mm)$	70.4983	86.8508	96.8269
circumferential backlash of worm pair, $j_i/(mm)$	0.25	0.38	0.38
$s_1 = d_2 \sin \left[\frac{81^{\circ}}{i_{12}Z_1} - \arcsin \left(\frac{j_i}{d_2} \right) \right]/(mm)$	5.5370	8.3368	9.3381

Table 2 Computing outcomes of top thickness of edge tooth

		A	B	C			A	B	C
C	$\theta/(^{\circ})$	437.0158	43.0403	20.7845	A	$\theta/(^{\circ})$	/	/	/
	$\varphi_d/(^{\circ})$	6.8284	5.38	5.1961		$\varphi_d/(^{\circ})$	/	/	/
	$\varphi_x/(^{\circ})$	15.6094	17.0625	17.0625		$\varphi_x/(^{\circ})$	/	/	/
	$x_{1T}/(mm)$	/	/	/		$x_{1T}/(mm)$	37.1365	43.5099	47.8260
	$y_{od}/(mm)$	/	/	/		$y_{od}/(mm)$	35.6449	43.8959	48.9194
L	$\theta/(^{\circ})$	1513.5	192.4519	95.5206	F	$\theta/(^{\circ})$	2590	341.8635	170.2567
	$\varphi_d/(^{\circ})$	23.6487	24.0565	23.8801		$\varphi_d/(^{\circ})$	40.4690	42.7329	42.5642
	$\varphi_x/(^{\circ})$	-1.2110	-1.6139	-1.6215		$\varphi_x/(^{\circ})$	-18.0313	-20.2904	-20.3055
	$x_{1T}/(mm)$	/	/	/		$x_{1T}/(mm)$	37.9660	44.8695	49.3685
	$y_{od}/(mm)$	/	/	/		$y_{od}/(mm)$	-38.3888	-47.9182	-53.4805
$s_{a2}/(mm)$	2.8666	4.2459	4.8149						
$k_s = s_{a2}/m_t$	0.7002	0.6885	0.7004						

Usually, the pointing degree of the edge tooth is reflected by the addendum thickness coefficient, k_{s1} , which is defined as $k_{s1} = s_a/m_t$. Hereinto, m_t is the transverse module of the worm gear. In general, it is believed that the top thickness is abundant if $k_{s1} \geq 0.35$ [9].



According to the preceding criteria, the top thickness of the numerical examples is sufficient.

As indicated by the example C, as far as the Hindley worm is concerned, more number of worm thread and less drive ratio is not sure to lead to the pointing of the edge tooth.

5 Conclusions

The addendum thickness computation of the edge tooth is taken into account for the Hindley worm. The analytical solution to the addendum thickness is obtained. The numerical results declare that the Hindley worm has a stronger resisting ability to the pointing of its edge tooth. Even in the case that the number of worm thread is more and the velocity ratio is less, the edge tooth is also able to be kept thick enough. The further research should focus on the influence of the modification on the pointing of the edge tooth.

Acknowledgments The research work in this paper was fully supported by National Natural Science Foundation of China under Grant No. 51475083, New Century Excellent Talents Project by Education Ministry of China under Grant No. NCET-13-0116, National Key Basic Research Development Plan of China (the 973 Program) under Grant No. 2014CB046303, and Excellent Talents Support Program in Institutions of Higher Learning in Liaoning Province China under Grant No. LJQ2013027.

References

1. Buckingham, E.: Analytical Mechanics of Gears, 3rd edn. Dover Publications, INC, New York (1988)
2. Crosher, William P.: Design and application of the worm gear. ASME Press, New York (2002)
3. Litvin, L.F.: Development of Gear Technology and Theory of Gearing. NASA Reference Publication, Cleveland, Ohio (1997)
4. Dudas, I.: The Theory and Practice of Worm Gear Drives. Penton Press, London (2000)
5. Dudley, D.W. (ed.): Gear Handbook. McGraw-Hill Book Company, Inc (1962)
6. Editorial committee for gear handbook, Gear Handbook, vol. 1, 2nd edn. China Machine Press, Beijing (2004)
7. Shen, Y, et al.: Spatial Meshing Principle and Type SG-71 Worm Pair. Beijing (1983)
8. Hu, S., Li, S., et al.: Design of Worm Drives, vol. 2. China Machine Press, Beijing (1987)
9. Dong, X.: Design and Modification of Hourglass Worm Drives. China Machine Press, Beijing (2004)
10. Zhao, Y., et al.: Meshing analysis and technological parameters selection of dual tori double-enveloping toroidal worm drive. Mech. Mach. Theory **45**, 1269–1285 (2010)
11. Dong, X.: Foundation of Meshing Theory for Gear Drives. China Machine Press, Beijing (1989)

A Single Speed (CVT) Transmission

K. Ivanov, B. Tultayev and G. Balbayev

Abstract The subject of research is a planetary train with two planetary rows and two carriers. The plot of linear speeds of the mechanism with two carriers shows an unexpected phenomenon: each carrier has direct kinematic constraint with satellite of opposite row. The interacting point of satellite with the carrier can be presented in the form of an engagement of the additional wheels connected to the satellite and to the carrier. Additional constraint creates brand new phenomena in the theory of mechanisms and machines. Paper presents the analysis of a phenomenon of additional constraint in the planetary train.

Keywords Planetary train • Two carriers • Additional constraint • CVT

1 Introduction

The planetary wheelwork, as is known [1], contains carrier, satellite, solar wheel and ring wheel. The mechanism with two carriers is generated by join of two oppositely located planetary trains. In the combined planetary train solar wheels are combined in the block of solar wheels, ring wheels are combined in the block of the ring wheels, each satellite is located on the carrier, and carriers are external links. The planetary train with two carriers has two planetary rows and two degree of freedom.

The plot of linear speeds of the mechanism with two carriers shows an unexpected phenomenon. At construction of the plot of linear speeds of the carrier. The virtual interacting point of satellite 5 with the carrier H1 can be emulated by a gear

K. Ivanov (✉) · G. Balbayev

Almaty University of Power Engineering and Telecommunication, Almaty, Kazakhstan
e-mail: ivanovgreek@mail.ru

K. Ivanov · B. Tultayev · G. Balbayev (✉)

Institute of Mechanics and Mechanical Engineering after Academician U.A. Dzholdasbekov,
Almaty, Kazakhstan
e-mail: gani_b@mail.ru

consist of wheel 7 connected to satellite 5 and wheel 8 connected to carrier H_1 . [2]. Speeds of the carrier and the satellite in this point are equal. On the stopped carrier this point represents the instant centre of turn of the satellite concerning wheels connected to the satellite and to the carrier. The found point of interacting of links defines additional constraint.

Paper is devoted to expanded analysis of a phenomenon of additional constraint in the planetary train.

2 Kinematic Analysis of the Planetary Train with Two Carriers

The planetary train with two carriers and its plots of linear speeds are presented in Fig. 1. The planetary train (Fig. 1a) contains carrier H_1 , satellite 2, block of solar wheels 1–4, block of ring (epicyclical) wheels 3–6, satellite 5 and carrier H_2 . Mechanism has two degree of freedom and two input links—carriers H_1 and H_2 . We will perform the kinematic analysis by means of the plot of linear speeds.

At first we will construct the plot of linear speeds at motionless carrier H_2 (Fig. 1b). In Fig. 1 linear speeds are denoted by horizontal vectors, angular velocities are denoted by inclined lines. We specify angular velocity ω_5 of satellite 5 and we line the angular velocity line through point K . We construct speeds V_6 and V_4 .

We line a line of angular velocity ω_3 through point A and terminus V_6 . We construct vector V_3 .

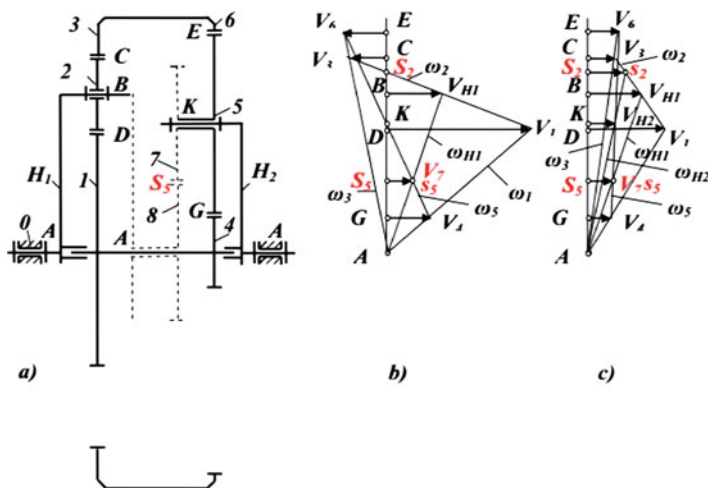


Fig. 1 Planetary train with two carriers and its plots of linear speeds

We line a line of angular velocity ω_1 through point A and terminus V_4 . We construct vector V_1 .

We line a line of angular velocity ω_2 of satellite 2 through the terminuses V_1 and V_3 . We construct vector V_{H1} and a line of carrier H_1 angular velocity ω_{H1} .

The constructed plot of speeds contains surprising result: lines of angular velocity ω_{H1} of the carrier H_1 and angular velocity ω_5 of the satellite 5 are cross in one point S_5 and define terminus V_7 of some point S_5 belonging simultaneously to the carrier H_1 and the satellite 5. Speeds of these two points of different links are coinciding. Such point S_5 can be realized practically in the form of a pitch point of two toothed wheels 7 and 8 (it is shown by a dot line). The wheel 7 is rigidly connected with the satellite 5, the wheel 8 is rigidly connected with the carrier H_1 . Obviously at constant angular velocity of carrier H_1 linear speed V_7 of a point S_5 of a wheel 7 should be constant, and the point S_5 should occupy an invariable position. To be convinced of that, we will construct the plot of linear speeds of the mechanism for the general case ($\omega_{H2} \neq 0$) at former angular velocity of the carrier H_1 , and angular velocity of a wheel 2 we will change (Fig. 1c).

We specify angular velocity ω_2 of the satellite 2 and we will line a line angular velocity ω_2 through terminus V_{H1} . We construct speeds V_1 and V_3 .

Let's line a line of angular velocity ω_3 through point A and terminus V_3 . We construct vector V_6 . We will line a line of angular velocity ω_1 through point A and terminus V_1 . We construct vector V_4 .

We line a line of angular velocity ω_5 of the satellite 5 through the terminuses V_4 and V_6 . Position of intersection point S_5 of line of angular velocity ω_5 and line of angular velocity ω_{H1} remains invariable. The vector V_7 has former magnitude and defines simultaneously speed of the input carrier H_1 and the output satellite 5. The found point S_5 we name the centre of coincidence of speeds of carrier and opposite satellite.

In the turned motion at the motionless carrier H_1 the point S_5 is the instantaneous center of turn of the satellite 5 concerning the carrier H_1 .

Singularity of the found phenomenon consists in the following. The carrier and opposite satellite have no direct connection and perform independent motions. But the speeds of some contact point of these links are equal in each instant time. Practical realization of such point is possible in the form of engagement of two toothed wheels. One wheel belongs to the carrier; other wheel belongs to the satellite.

Let's prove analytically an invariance of this contact point position on the mechanism. It is possible most simply to install the point S_5 position using the plot of linear speeds of the mechanism in initial position (Fig. 1b) when the speed V_{H1} is specified and carrier H_2 is stopped $V_{H2} = 0$ (point K).

In this case the vector V_7 of the conditional wheel 7 rigidly connected with the satellite 5, lined out of point S_5 , is simultaneously a vector of speed V_8 of the conditional toothed wheel 8 rigidly connected with the input carrier. The point S_5 position is defined by radius of a conditional toothed wheel 7. We will determine the radius out of a condition

$$V_7 = V_8 \quad (1)$$

Let's express linear speeds through angular velocities $\omega_7 = \omega_5$, $\omega_8 = \omega_{H1}$ and radiuses of wheels r_7 , $r_8 = r_{H2} - r_7$. Taking into account directions of angular velocities we will get next result

$$-\omega_5 r_7 = \omega_{H1} (r_{H2} - r_7) \quad (2)$$

The formulas of angular velocities of planetary mechanism with two carriers are presented in article [3]. The carrier H_2 in the considered instant time is motionless, $\omega_{H2} = 0$. Therefore $\omega_5 = u_{56}^{(H2)} \omega_6$. Then

$$\omega_6 = \omega_3 = -\omega_{H1} \frac{1 - u_{13}^{(H1)}}{u_{13}^{(H1)} - u_{45}^{(H2)}},$$

$$u_{13}^{(H1)} = -z_3/z_1, u_{46}^{(H2)} = -z_6/z_4, u_{56}^{(H2)} = z_6/z_5.$$

After substitution of these magnitudes in the Eq. (2) there will be a cancellation of angular velocity ω_{H1} . From the Eq. (2) we will get the next

$$u_{56}^{(H2)} \frac{1 - u_{13}^{(H1)}}{u_{13}^{(H1)} - u_{46}^{(H2)}} r_7 = r_{H2} - r_7 \quad (3)$$

From the Eq. (3) we will define radius of a conditional wheel 7

$$r_7 = r_{H2} \frac{u_{13}^{(H1)} - u_{46}^{(H2)}}{u_{56}^{(H2)} (1 - u_{46}^{(H2)})} \quad (4)$$

The Eq. (4) does not contain angular velocities; hence, the radius of a wheel 7 and a point S_5 position does not depend on magnitudes of angular velocities. The point S_5 occupies a constant position on the plot of linear speeds.

Appearance of the centre of coincidence of speeds S_5 of two independently moving links represents brand new phenomenon in the mechanics.

To fathom mechanical essence of a phenomenon we will consider habitual concept of the transfer ratio. The transfer ratio (or the ratio of angular velocities) can be expressed through force parameters (the moments of forces) on the basis of law of conservation of energy. In the presence of ideal constraints between input link 1 and output link 2

$$M_1 \omega_1 = M_2 \omega_2 \quad (5)$$

From here we will get next transfer ratio for the mechanism with one degree of freedom

$$u_{12} = \omega_1 / \omega_2 = M_2 / M_1 \quad (6)$$

The Eq. (6) divides force and kinematic parameters.

It is necessary to note that the law of conservation of energy can be used only in that case when the kinematic chain has the kinematic and structural definability. For example, this law can be applied to the mechanism with two degree of freedom only in the presence of two initial (input) links. The considered planetary train with two degree of freedom and with one input has structural and kinematic definability due to additional constraint. But in this mechanism the separation of force parameters from kinematic parameters is impossible because when having constant input angular velocity $\omega_{H1} = const$ the output angular velocity ω_{H2} can be variable (Fig. 1 b, c). The line of angular velocity ω_5 of satellite 5 can rotate around the centre of coincidence of speeds S_5 (terminus V_7) and can change speed V_{H2} of output carrier. Considering the named regularity in the mechanism with two carriers we will present the law of conservation of energy matching the formula (5) in a following aspect

$$\omega_{H2} = M_{H1} \omega_{H1} / M_{H2} \quad (7)$$

Formula (7) defines brand new phenomenon in the mechanics and in the theory of machines and mechanisms: effect of force self-regulation. If constant input power takes place then the output angular velocity inversely proportional to output resistance moment.

3 Start-up of Mechanism with Two Carriers

Two alternatives of start-up of the mechanism are possible:

1. Moment of resistance less than the driving moment (or it is equal to it).
2. Moment of resistance more than the driving moment.

At the first we will consider the first alternative.

The mechanism with two carriers has major property at start of motion. At the stopped output carrier the mechanism has one degree of freedom. The transfer of force to the output carrier is impossible in the absence of a moment of resistance on the output satellite. Theoretically it is not possible to create start-up without this moment. However additional constraint in the centre of coincidence of speeds transforms the kinematic chain into a rigid structure with zero mobility. Such design cannot be set in motion. But the mechanism with two carriers has the major structural feature. All rotational kinematic pairs connecting links of a mechanism with a rack are located on one axis. This structural feature allows to rotate the absolutely rigid structure around a motionless axis and to begin mechanism motion. Thus the resistance moment on the output satellite it is not required. Equilibrium of a rigid structure at starting is defined by the equation of the moments concerning a

motionless axis. At presence only output resistance on the output carrier the driving moment on the input carrier is equal to a starting torque.

$$M_{H1} = M_{H2} \quad (8)$$

After the beginning of motion the mechanism passes in a condition with two degree of freedom with relative motion of links by increase in a moment of resistance.

The second alternative defines the motion beginning when a starting torque is bigger than the driving moment. It leads to a conditional stop of the moving mechanism which allows transferring force from the input carrier to supporting point K of the satellite 5 in the absence of resistance moment on the satellite. The increase in the input power transferred to the satellite 5 will lead to increase in force R_{5H2} transferred in point K on the motionless carrier and to the beginning of its motion.

Constraint between input and output moments is defined by formula (8) taking into account that M_{H1} is the input moment of the mechanism driving the satellite 5 with motionless supporting point and $M_{H1} = R_{5H2}r_{H2}$ —moment keeping in a motionless condition a supporting point of satellite 5.

4 Conclusion

The phenomenon of the centre of coincidence of speeds provides appearance of additional constraint in considered kinematic chain with two degree of freedom. Additional constraint reduces number of a degree of freedom of the kinematic chain per unit. The considered kinematic chain with two carriers is the mechanism at presence only one input link. Thus the mechanism gets brand new properties. The mechanism with two carriers creates effect of force self-regulation.

The found brand new effect of force self-regulation provides the possibility of mechanism to adapt independently for variable force loading. Independent adaptation is performed only at the expense of mechanical properties of the mechanism without any control system. Practical implementation of the found effect opens brand new prospects of creation of engineering industry manufactures. One of the most perspective aspects of new self-controlled engineering is the self-controlled toothed variator replacing the heavy and bulky gear box of the car.

Simplicity and ideal adequacy of a self-controlled gear variator to working conditions create incontestable advantages in front of operated step gear boxes and frictional variators.

References

1. Artobolevsky, I.I.: Theory of mechanisms. Publishing house “Science”, 720 p. Moscow, (1967)
2. Ivanov, K.S.: Paradox in Mechanism Science. In: 1st International Symposium on Education in Mechanism and Machine Science, pp. 132–138. Madrid. Spain, 1 and 14 June 2013
3. Ivanov, K.S.: Creation of adaptive-mechanical continuously variable transmission. In: 5th International Conference on Advanced Design and Manufacture (ADM 2013), pp. 63–70. Valencia. Spain (2013)

An Approach for Modelling Harvester Head Mechanism in the Harvesting Process of Hardwood Stands

B. Hatton, B.C. Bouzgarrou, J.-C. Fauroux, V. Gagnol and G. Gogu

Abstract This paper presents an approach for modelling and simulating of harvester head mechanism in the harvesting process of hardwood stands. This type of trees is characterized by flexuous trunks and big branches. Hence, the current harvester heads are not enough efficient to process such trees. In order to predict the process performances associated with several novel architectures of harvester heads, in preliminary design stage, a modelling of the process has been developed. It is based on parameterized tree models with realistic geometry by adapting an existing method. Dynamic modelling of the delimiting process proposed in this paper uses original cutting and feeding models which have been validated experimentally. The modelling and simulation of harvester head mechanisms have been implemented in a numerical multibody environment. Simulation results of the global model are in a good agreement with the observed behaviour of the real system.

Keywords Harvester head mechanism • Parameterized tree model • Dynamic modelling • Delimiting process

B. Hatton • B.C. Bouzgarrou (✉) • J.-C. Fauroux • V. Gagnol • G. Gogu
Institut Pascal, UMR 6602 CNRS, Université Clermont Auvergne—SIGMA,
Clermont-Ferrand, France
e-mail: belhassen-chedli.bouzgarrou@sigma-clermont.fr

B. Hatton
e-mail: benjamin.hatton@ifma.fr

J.-C. Fauroux
e-mail: jean-christophe.fauroux@sigma-clermont.fr

V. Gagnol
e-mail: vincent.gagnol@sigma-clermont.fr

G. Gogu
e-mail: grigore.gogu@sigma-clermont.fr

1 Introduction

This paper presents a part of researches carried-out within the ECOMEF project (Eco-design of mechanized equipment for hardwood harvesting) framework. This project aims to develop a harvester head more adapted to process and fell broad-leaved trees, in order to face the lack of motor manual workers and the low rate of mechanization in hardwood logging operations [1]. The processing operation is composed of delimiting trunks and bucking them into logs [2] (Fig. 1a). Due to crooked trunks, bigger branches with sharper angles and hardwood, broad-leaved trees are indeed harder than conifers to feed and delimit. Therefore, specific tools to improve the energy efficiency and the productivity of the operation are required [3]. In the existing harvester head mechanisms (Fig. 1b), the action of the mobile knives (2 & 2' and 5 & 5') constrains the trunk, by surrounding and tackling it against the support (0) and the fixed knife (1), to translate relatively to the support under the action of the feeding rollers (3 & 3'). Tanks to the straight shape of the trunks in conifers, this motion is rapid and continuous and knives spacing self-adapts to the variations of the trunk diameter. The delimiting is produced by the impact of the knives' sharp edges against the branches. However, the processing of crooked trunks may fail with these harvester head mechanisms. Therefore, the EOMEF project has addressed the challenging task of designing new mechanisms inside which crooked trunks can slide while ensuring power transmission and avoiding locking phenomena: biting, over-center locking. In order to predict, from the

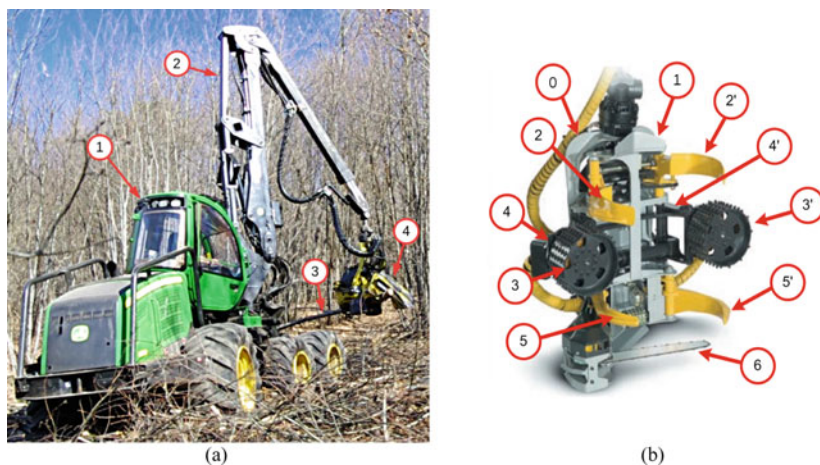


Fig. 1 **a** A harvesting machine felling trees: all-terrain vehicle (1), hydraulic arm (2), fallen trunk (3), harvesting head during logging (4). **b** Detailed view of a harvesting head: tilt support (0), upper fixed knife (1), upper mobile knives (2 & 2'), feeding rollers (3 & 3'), roller arms (4 & 4'), lower mobile knives (5 & 5'), retractable logging chainsaw (6)

preliminary design stages, the performances of these mechanisms, in terms of energy efficiency and productivity, an approach based on process modelling and simulation has been implemented. Process simulations should enable testing and comparing several designs of harvester mechanisms.

In Sect. 2, an existing method for geometric modelling of trees has been developed in order to integrate trunk flexuosity. The modelling building blocks, used to describe the interactions between the harvester head mechanism and the trunk, are presented in Sect. 3. The cutting and feeding models are integrated into the global model of the process. The multibody system model and simulation results are presented in Sect. 4.

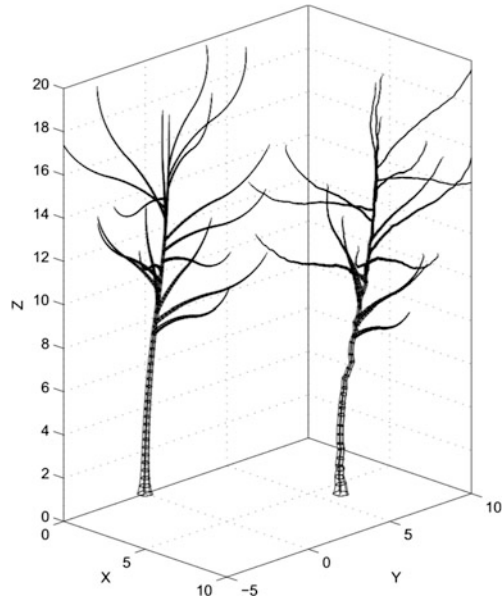
2 Geometric Modelling of Crooked Trunks

Hardwood species are characterized by the sinuosity of their trunks. In this section we focus on the geometric description of this type of trees. In order to evaluate and compare by simulation the performances of different designs, it is useful to generate realistic tree models. Therefore, a number of representative trunks will then allow the comparison of simulations while avoiding the morphological changes observed during tests in operating conditions. This work is carried out before the simulation step.

We propose to develop a model that can adapt to several cases, in which the contact can be modelled by planar or 3D kinematic constraints, or more complex dynamic studies with contact handling based on a collision detection algorithm. Generated trunks must incorporate representative breaks and discontinuities of more or less crooked trees as well as the first level of branches in order to simulate delimiting operations. The complexity of vision-based reconstruction methods as well as the difficulty of selecting representative samples of the great morphological diversity of trees led us to move towards a parameterized model, especially the model of Weber and Penn [4]. This type of model offers an important versatility regarding the considered simulation context. It offers the following possibilities:

- Recursive model: each child stem inherit its properties from its parent.
- More than 80 parameters defining the general shape, and each level of stem.
- General structure of each stem: tapered extrusion of a section curve along a profile.
- Iterative definition of the profile curve: the position of $(N + 1)$ th point is determined from the position of N th point.
- Circular section of stems: parameterized curve (sinusoidal variation of the radius with the angle of rotation) for the trunk (Fig. 2).

Fig. 2 Generated trees:
Weber–Penn method (*left*),
proposed method (*right*)



3 Modelling Building Blocks

Cutting the branches off the trunk is usually achieved by feeding the tree at $3\text{--}7\text{ m s}^{-1}$ using feed rollers, and creating an impact of the branches against delimiting knives. Cutting and feeding models are integrated in the dynamic modelling of the delimiting process.

3.1 Cutting Model

Unlike many cutting studies based on the type and the section of a chip for several machining operations, it is not possible in this case to define a chip, since the ‘chip’ is the whole branch. To identify the cutting situation process involved, the definition proposed by McKenzie [5] can be used. In this notation, two angles are used to define cutting process. The first one is formed by the cutting edge with the grain direction γ_r , the second one by the cutting speed direction with the grain direction ($\alpha + \beta + \gamma_r$) according to Fig. 3 notations. Delimiting can thus be considered as a $90^\circ\text{--}90^\circ$ orthogonal cutting process, sometimes called cross-cutting. In the same way, chipping can follow the same definition. That is why the work from [6] can be adapted to define the cutting situation, as presented in Fig. 3.

Such a definition of cutting angles conserve the usual relation $\alpha + \beta + \gamma = 90$. Based on image correlation analysis, performed in a preliminary study, the

- α clearance angle
- β the sharpness angle
- γ the rake angle
- γ_r the real rake angle
- ε the implantation angle
- e the blade thickness
- δ the oblique cutting angle
- V_c the cutting speed
- \emptyset the diameter of the branch

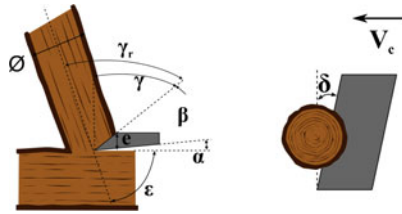


Fig. 3 Cutting angle parameters

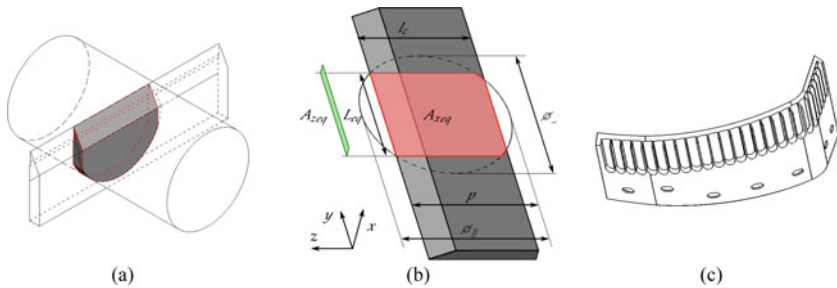


Fig. 4 Cutting angle parameters

principles for the definition of a reduced model have been defined. The calculation of cutting force (Eq. 1) is based on three components and certain geometric parameters presented in Fig. 4b.

- The component F_L (Eq. 1) is representative of fibre incision phenomenon and the behaviour at the cutting edge. It is related to equivalent length Leq (length of engaged part of the cutting edge evolving according to the depth of penetration p of the blade inside the branch, Fig. 4b);
- The component F_{Sx} (Eq. 1) takes into account the friction forces applied on the blade rake and clearance surfaces (friction and tackling of the blade against wood, etc.). It is attached to the equivalent cutting area A_{xeq} (projection on the cutting plane of the intersection between the branch and the part of the blade delimited by the equivalent length Leq).
- The component F_{S_z} (Eq. 1) takes into account the edge effect depending on the equivalent surface A_{zeq} normal to the feeding direction.

All these components depend on the penetration depth p . Constants k_{Sx} , k_{S_z} and k_L have been identified experimentally by using two types of test benches for slow and rapid delimiting [7]. They depend on the humidity ratio T_H of the wood.

$$F(p) = \underbrace{k_{Sx}(T_H)A_{xeq}(p)}_{F_{Sx}} + \underbrace{k_{S_z}(T_H)A_{zeq}(p)}_{F_{S_z}} + \underbrace{k_L(T_H)L_{eq}(p)}_{F_L} \quad (1)$$

The Eq. (1) underlines the importance of the projected surface A_{zeq} that should be reduced to decrease the cutting force along the feeding direction z . This design rule has been used to develop an innovative ribbed knife (Fig. 4c) where the A_{zeq} has been decreased by milling grooves along z , only keeping ribs for bending stiffness around y . This design was published in [8] and patented [9].

3.2 Feeding Model

Most of the harvesting heads use rollers for trunk feeding. As explained in [10], concentric gripping mechanisms are not very suitable for small stems, whereas lateral gripping mechanisms facilitates passing of crooked parts of the trunk but could lack pressing force when processing large trunks. Several hybrid solutions adapting the kinematics of the gripping motion to the diameter of the trunk, in order to be efficient on the whole range of considered diameters have been proposed [10].

The adopted approach to compute feeding forces is similar to that used by Klamecki [11] to calculate the friction coefficient due to the creation of a furrow by a conical asperity travelling through the chip (Fig. 5a). Klamecki expresses the transverse and frontal forces on the asperity using the simple relation $F = \sigma S$, F being the force and S the projected area in the considered direction. For the transverse force T , the considered surface A_t is half a disk of diameter d (maximum penetration of the cone into the chip, Fig. 5a), and the stress linking force and area is the yield strength of the chip material. For the frontal force N , the A_f area represents the projection of the cone in a radial plane, perpendicular to the force (triangle of the height of x and of the base of d). The considered stress is associated with the strength of the chip material.

The feeding model follows a similar approach. First, the maximum stress admissible by a given wood species in the gripping direction (perpendicular to fibres) needs to be experimentally determined, in order to link the measured gripping force with the projected area normal to this direction. Then, an analytical model allows the calculation of the penetration depth and the projected area normal

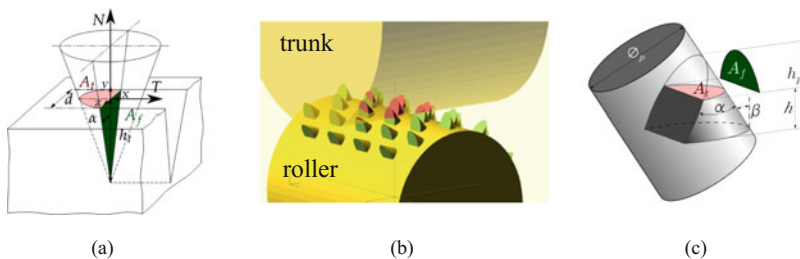


Fig. 5 **a** Klamecki model of force generated by a conical asperity. **b** Variable penetrations of several spikes of the roller into the trunk **(c)**. Projected surfaces A_f (frontal) and A_t (tangential) used for calculation of the force transmitted by the spike to the trunk

to the feeding direction (parallel to fibres). Finally, the maximum stress admissible in this direction (to be determined experimentally too) will enable calculating the maximum transmissible feeding force. Still being one of the most used types of stud on feed rollers, the elliptical stud or steel spike could be geometrically obtained by two successive oblique cuts in a rod (Fig. 4c).

Stress values required for determining normal and tangential transmissible force have been identified experimentally [12] with an average stress of 18 MPa. The proposed model allows calculating the areas when using elliptical studs. To extend the study to other shapes of studs, derived analytical formulations or a CAD-based calculation method are proposed to help engineers to optimize the feeding process: maximizing the maximum transmissible feeding force by adapting the roller geometry as well as the shape and the pattern of the studs.

4 Delimiting Process Simulation

In order to simulate the global process, feeding and cutting models, presented in the previous section, have been integrated in multi-body models of the developed harvester head mechanisms. In these simulations, cutting and feeding forces are generated as function of the trunk motion relatively to the knives and the rollers. Phenomena affecting process efficiency, such as over-centre locking and biting, can be reproduced in order to compare several design solutions for a given geometry of the tree.

The approach adopted to integrate feeding model consisted in using equivalent sticking coefficient for the contact modelling between the trunk and the rollers. This coefficient has been determined experimentally. Nevertheless, analytic calculation of surfaces offers the possibility to determine such a coefficient for different dimensions of the rollers. Indeed, this approach requires the numerical coupling and co-simulation between ADAMS[®], MATLAB[®], OpenSCAD and Blender based on Boolean intersection evaluations and the use of analytical expressions of the equivalent surfaces used for force estimations.

Process simulations have been performed on a standard trunk in a one-piece frame (constituting the reference architecture) as well as on articulated frame, in order to compare these two architectures. Since roller speeds are imposed, torque picks (5000 N m), exceeding the real values (2500 N m), are registered when the branches come in contact with knives. These power picks correspond to the speed slow-down on the upper curve in Fig. 6. In certain cases, this isn't due to branch cutting but to the sudden recovery of contact between the trunk and the fixed knife. This can be illustrated by the lower curve of the fixed knife angle relatively to the speed direction of the trunk and the corresponding biting risk indicator in Fig. 6.

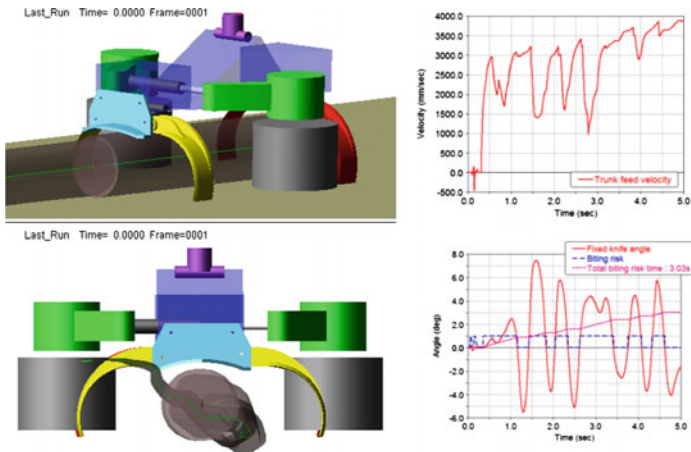


Fig. 6 Delimiting process simulation on ADAMS software with articulated harvester head mechanism

5 Conclusions

In this paper, a modelling approach for simulating the delimiting process of hardwood stands has been presented. An existing method for generating realistic tree geometric model has been developed. Parameterized trees with irregular and crooked trunks provided with branches are generated. A multibody system, integrating the developed models of cutting and feeding, has been implemented on ADAMS[®] software. It allows predicting and comparing the performances of several novel harvester head mechanisms from preliminary design stages. Future work will focus on enhancing simulation realism in order to reproduce precisely biting and over-center locking phenomena and optimize the energetic efficiency of the proposed design solutions.

Acknowledgments This research work is part of ECOMEF project founded by Conseil Regional Auvergne and by the program Regional competitiveness and employment 2007–2013 (European Regional Development Fund—Auvergne region). These organisms are acknowledged for their financial support.

References

1. Cacot, E., Bigot, M., Cuchet, E.: Developing full-mechanized harvesting systems for broadleaved trees: a challenge to face the reduction of the manual workforce and to sustain the supply of hardwood industries. In: 29th Council on Forest Engineering (COFE) Conference Proceedings: “Working globally—Sharing forest engineering challenges and technologies around the world” (2006)

2. Ćuprić, L., Bajić, V.: Cut-to-length machines. In: Bošnjak, S., Zrnić, N. (eds) Proceedings of the XIX International Conference on “Material Handling, Constructions and Logistics”, University of Belgrade, Faculty of Mechanical Engineering, Serbia, pp. 109–118 (2009)
3. Cacot, E.: Mechanization of the hardwood exploitation: evolutions and questions. *Forêt Wallonne* **102**, 34–44 (2009)
4. Weber, J., Penn, J.: Creation and rendering of realistic trees. In: Proceedings of the 22nd Annual Conference on Computer Graphics and Interactive Techniques, pp. 119–128 (1995)
5. McKenzie, W.M.: Fundamental analysis of the wood-cutting process. PhD thesis, Department of Wood Technology, School of Natural Resources, The University of Michigan (1961)
6. Abdallah, R., Auchet, S., Méausoone, P.J.: Experimental study about the effects of disc chipper settings on the distribution of wood chip size. *Biomass Bioenergy* **35**(2), 843–852, ISSN 0961-9534 (2011)
7. Hatton, B., Pot, G., Bouzgarrou, B.C., Gagnol, V., Gogu, G.: Experimental determination of delimiting forces and deformations in hardwood harvesting. *Croatian J. Forest Eng.* **36**(1), (2015)
8. Dargnat, G., Devemy, C., Fauroux, J.-C., Pellet, H.-P., Hatton, B., Perriguy, N., David Goubet, D., Chebab, Z., Bouzgarrou, B.C., Gagnol, V., Gogu, G.: Determination and optimization of delimiting forces on hardwood harvesting heads. In: 5th Forest Engineering Conference, Gerardmer, France, 23rd–26th Sept (2014)
9. Dargnat, G., Devemy, C., Pellet, H.-P., Fauroux, J.-C.: Curved delimiting blade, use of same, corresponding delimiting head and cutting kit. PCT patent WO 2015177432. Institut Français de Mécanique Avancée (IFMA)/Intégration & Solutions Industrielles (ISI), 30p (2015)
10. Goubet, D., Fauroux, J.-C., Gogu, G.: Gripping mechanisms in current wood harvesting machines. *Frontiers Mech. Eng.* **8**(1), 42–61, Springer, ISSN: 2095-0233 (2013)
11. Klamecki, B.E.: Friction mechanisms in wood cutting. *Wood Sci. Technol.* **10**, 209–214 (1976)
12. Hatton, B., Gagnol, V., Bouzgarrou, B.C., Gogu, G.: Modelling of the hardwood harvesting process: feeding model. 21ème Congrès Français de Mécanique (CFM), Bordeaux (2013)

Novel Speed Increaser Used in Counter-Rotating Wind Turbines

M. Neagoe, R. Saulescu, C. Jaliu and N. Cretescu

Abstract The speed increasers are typical components of a large diversity of renewable energy systems (RES), like wind turbines or hydropower plants, used to harmonize the low input speed of wind rotor/hydro turbine with the higher speed requirement of the electric generator. The counter-rotating turbines are able to generate more electricity in comparison with the classical systems with one input due to the summation of the two independent input speeds and implicitly of two power flows, but they have a relatively complex control for matching the generator requirements. This drawback can be mitigated by using 1 degree of freedom (DOF) speed increasers with more inputs and one output. The paper deals with the kinematic and static analysis of a novel 1DOF planetary transmission, with two inputs and one output, used as speed increaser in wind/hydro RES. Starting from its property of summing two external torques and the speed amplification ratio imposed on the main power flow, the transmitting functions of speeds and torques, considering gear friction, as well as the mechanism efficiency are established in the paper. A dimensionless parameter k , defined as ratio of the input torques, is introduced and, based on numerical simulations, the transmission behaviour is highlighted. The results allow the formulation of useful recommendations for optimal design of planetary transmissions implemented in RES.

Keywords Planetary transmission · Speed increaser · Efficiency · Counter-rotating rotor

M. Neagoe (✉) · R. Saulescu (✉) · C. Jaliu · N. Cretescu
RESREC Research Center, Transilvania University of Brasov, Brasov, Romania
e-mail: mneagoe@unitbv.ro

R. Saulescu
e-mail: rsaulescu@unitbv.ro

C. Jaliu
e-mail: cjaliu@unitbv.ro

N. Cretescu
e-mail: ncretescu@unitbv.ro

1 Introduction

A primary requirement for society sustainable development refers to increasing the share of energy produced from renewable sources by expanding renewable production capacities and better exploitation of the existing renewable potential. The increase of the performances of wind/hydro energy conversion systems is an ongoing challenge for specialists, who proposed in the literature a variety of novel solutions for efficient energy conversion into electricity. Thus, especially in the last two decades, new concepts have been developed: (a) systems with counter-rotating rotors [1], which improve the installed capacity by using a secondary rotor connected in parallel with the main one, (b) systems with multiple rotors that totalize the electricity produced by the component subsystems [2], (c) systems with 2DOF planetary speed increasers driven by a classical wind rotor and a servomotor [3] or with variable speed transmissions [4, 5] on the secondary input aiming at maintaining the optimal generator speed at variable input speeds. These solutions provide increased energy performances, but they need a complex control system.

The wind or hydro conversion systems usually require speed increasers to harmonize the rotors' relatively low speed with the generators' higher speed [1]. The use of planetary transmissions is recommended in the case of systems with high amplification ratio due to the advantages of overall dimensions and efficiency compared with the fixed axes transmissions. The 1DOF planetary transmissions with one input and one output are usually integrated in classical systems with one rotor, while the counter-rotating systems use differential planetary transmissions for summing the two rotors' speeds [1], and, thus, increasing the speed of the electric generator. The modelling of the planetary transmissions aiming at identifying their optimal performances and the optimal synthesis have been performed in literature by many authors using different methods. A kinematical analysis of planetary gear trains by using graphs is presented in [6], in the work [7] a general algorithm for analysing the transmission ratios and the efficiency of 1DOF planetary transmissions is proposed. Two general methods for the analytical modelling of the efficiency of planetary transmissions usable as speed reducers or increasers are presented in [8].

Starting from the classical running cases of a planetary gear [9] defined through its degree of freedom, the number of external connections, and the configuration of inputs-outputs, the authors highlight in the paper the possibility of using the planetary transmissions in applications with higher number of external connections. Therefore, a novel approach of a 1DOF planetary transmission with two inputs and one output, designed for transmitting the mechanical power from two counter-rotating wind rotors to an electric generator with fixed stator, is approached in the paper. Compared with the classical turbines with one rotor, the proposed solution is able to bring an additional supply of power by using a secondary rotor dependent kinematically on the main rotor. The description of the planetary transmission is firstly introduced in the paper, followed by the analytical modelling of its transmitting functions and of the efficiency. The numerical simulations of the obtained models are approached and final conclusions are drawn in the last part of the paper.

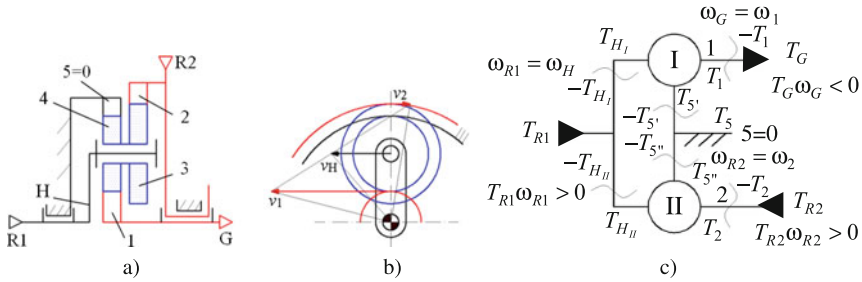


Fig. 1 1DOF planetary speed increaser with two inputs (R1, R2) and one output (G): **a** the structural scheme, **b** the speed diagram, and **c** the block diagram

2 Problem Formulation

The renewable energy systems with two counter-rotating rotors usually include 2DOF planetary speed increasers with three external connections ($L = 3$), used to sum the two input motions from the wind rotors [10–12]. This paper proposes the use of a 1DOF planetary transmission with $L = 3$ aiming at increasing the speed and summing two external torques, Fig. 1. This transmission has an extra torque from the secondary rotor R2, thus bringing additional power, which leads to an increase in performance versus the conventional systems with one rotor by: (a) the use of electric generators of the same speed, but of higher powers; (b) the size reduction of the two rotors to get the same output performances of the electric generator.

The proposed speed increaser (Fig. 1) consists of a 1DOF planetary unit PU_I ($H-4-5 = 0-1$) connected in parallel to the secondary planetary unit PU_{II} ($2-3 = 4-H-1$) whose input motion is dependent on the PU_I input motion and its input torque is less than the torque generated by the main rotor R1 (connected to the PU_I input). This transmission with two inputs and one output allows transmitting an external motion (ω_H) in a determined way, and summing the torques from the two inputs (rotors). The transmission kinematical, static and power analysis is further presented in order to highlight the system advantages versus the classical single rotor systems.

3 Transmission Modelling

According to the structural scheme of the speed increaser (Fig. 1a), the planetary transmission has three sun gears (1, 2 and 5), one double satellite gear (3–4) and a carrier H. The mechanism is obtained by parallel connection of two 1DOF planetary units—I and II (Fig. 1c). R1 is considered the main input and R2—the secondary input, with the angular speed ω_{R2} dependent on the main one, ω_{R1} . According to the



block diagram depicted in Fig. 1c, the transmitting functions of the two planetary units, considered isolated, and the relations representing the connections to the two rotors and generator can be obtained as follows:

- the kinematical and static equations by considering friction [13]:

$$PU_I: \begin{cases} i_{15'}^{H_I} = i_{0I} = \frac{\omega_{1H_I}}{\omega_{5'H_I}} = -\frac{z_5}{z_1} \\ \omega_1 - \omega_{5'} i_{0I} - \omega_{H_I}(1 - i_{0I}) = 0 \\ T_1 + T_{5'} + T_{H_I} = 0 \\ T_1 i_{0I} \eta_{0I}^x + T_{5'} = 0 \end{cases}, PU_{II}: \begin{cases} i_{25''}^{H_{II}} = i_{0II} = \frac{\omega_{2H_{II}}}{\omega_{5''H_{II}}} = \frac{z_3 z_5}{z_2 z_4} \\ \omega_2 - \omega_{5''} i_{0II} - \omega_{H_{II}}(1 - i_{0II}) = 0 \\ T_2 + T_{5''} + T_{H_{II}} = 0 \\ T_2 i_{0II} \eta_{0II}^w + T_{5''} = 0 \end{cases} \quad (1)$$

- the system interior correlations:

$$R_1 \equiv H_I \equiv H_{II} \begin{cases} \omega_{R1} = \omega_{H_I} = \omega_{H_{II}} = \omega_H \\ T_{R1} - T_{H_I} - T_{H_{II}} = 0 \end{cases}, 2 \equiv R_2 \begin{cases} \omega_2 = \omega_{R2} \\ T_{R2} - T_2 = 0 \end{cases} \\ 5 \equiv 5' \equiv 5'' \begin{cases} \omega_{5'} = \omega_{5''} = \omega_5 = 0 \\ T_5 - T_{5'} - T_{5''} = 0 \end{cases}, 1 \equiv G \begin{cases} \omega_1 = \omega_G \\ T_G - T_1 = 0 \end{cases} \quad (2)$$

- the correlations of the system external connections (the power and coaxial torques equilibrium equations by considering friction):

$$\begin{cases} (\omega_{R1} T_{R1} + \omega_{R2} T_{R2}) \eta + \omega_G T_G = 0 \\ T_{R1} + T_{R2} + T_G + T_5 = 0 \end{cases} \quad (3)$$

The relations (1)–(3) are basic equations used to derive the kinematic, static and power models of the proposed planetary transmission.

A. Kinematical modelling

The purpose of kinematical modelling is to find out the output angular speed (ω_G) and the secondary rotor speed (ω_{R2}) as functions of the main rotor angular speed (ω_{R1}). The kinematical ratios of the $PU_{I, II}$ can be obtained from rel. (1):

$$i_{1H_I}^{5'} = \frac{\omega_{15'}}{\omega_{H_I 5'}} = 1 - i_{0I}, i_{2H_{II}}^{5''} = \frac{\omega_{25''}}{\omega_{H_{II} 5''}} = 1 - i_{0II} \quad (4)$$

from which the following correlations result:

$$\omega_{15'} = \omega_{H15'}(1 - i_{0I}), \omega_G = \omega_{R1}(1 - i_{0I}) \quad (5)$$

$$\omega_{25''} = \omega_{H15''}(1 - i_{0II}), \omega_{R2} = \omega_{R1}(1 - i_{0II}) \quad (6)$$

B. Static modelling and efficiency

The efficiencies of the two planetary units $PU_{I, II}$ are obtained based on the following relations [11]:

$$\eta_{H1}^{5'} = \frac{-\omega_{15'} T_1}{\omega_{H15'} T_{H1}} = \frac{-T_1/T_{H1}}{\omega_{H15'}/\omega_{15'}} = \frac{\overline{i_{H1}^{5'}}}{i_{H1}^{5'}} = \frac{1 - i_{0I}}{1 - i_{0I}\eta_{0I}^x} \quad (7)$$

$$\eta_{2H11}^{5''} = \frac{-\omega_{H15''} T_1}{\omega_{25''} T_{H11}} = \frac{-T_{H11}/T_2}{\omega_{25''}/\omega_{H15''}} = \frac{\overline{i_{2H11}^{5''}}}{i_{2H11}^{5''}} = \frac{1 - i_{0II}\eta_{0II}^w}{1 - i_{0II}} \quad (8)$$

where

$$\eta_{15'}^{H1} = \eta_{0I} = \eta_{14}^H \eta_{45}^H, x = \text{sgn}(\omega_{1H1} T_1) = \text{sgn}\left(\frac{i_{0I}}{1 - i_{0I}}\right) = -1, \quad (19)$$

$$\eta_{25''}^{H11} = \eta_{0II} = \eta_{23}^H \eta_{45}^H, w = \text{sgn}(\omega_{2H11} T_2) = \text{sgn}\left(\frac{i_{0II}}{i_{0II} - 1}\right) = +1.$$

The relations of the torques on the main rotor shaft (T_{H1}) and on the generator shaft (T_G) can be deduced from the power equilibrium equations written for $PU_{I, II}$, rel. (9):

$$\omega_{H15'} T_{H1} \eta_{H1}^{5'} + \omega_{15'} T_1 = 0, \omega_{H15''} T_{H11} \eta_{H11}^{5''} + \omega_{25''} T_2 = 0 \quad (9)$$

$$T_{H1} = -T_1 \frac{\omega_{15'}}{\omega_{H15'} \eta_{H1}^{5'}} = -T_1 \frac{i_{H1}^{5'}}{\eta_{H1}^{5'}} = T_1 \left(\frac{i_{0I}}{\eta_{0I}} - 1 \right) \quad (10)$$

$$T_{H11} = -T_2 \frac{\omega_{25''}}{\omega_{H15''} \eta_{H11}^{5''}} = -T_2 \frac{i_{2H11}^{5''}}{\eta_{H11}^{5''}} = T_2 \left(\frac{i_{0II}}{\eta_{0II}} - 1 \right) \quad (12)$$

$$T_1 = -\frac{T_{R1}}{1 - i_{0I}/\eta_{0I}} - \frac{T_{R2}(1 - i_{0II}/\eta_{0II})}{1 - i_{0I}/\eta_{0I}} \quad (13)$$

$$T_G = -\frac{T_{R1}}{1 - i_{0I}/\eta_{0I}} - \frac{T_{R2}(1 - i_{0II}/\eta_{0II})}{1 - i_{0I}/\eta_{0I}} \quad (14)$$

The efficiency of the transmission from Fig. 1a, with three sun gears can be obtained by replacing rel. (5), (6) and (14) into rel. (3):

$$\eta = \frac{\frac{T_{R1}(1-i_{0I})}{1-i_{0I}/\eta_{0I}} + \frac{T_{R2}(1-i_{0II}/\eta_{0II})(1-i_{0I})}{1-i_{0I}/\eta_{0I}}}{T_{R1} + (1-i_{0II})T_{R2}} = \frac{1-i_{0I}}{1-\overline{i_{0I}}} \cdot \frac{1+k(1-\overline{i_{0II}})}{1+k(1-i_{0II})} \quad (15)$$

where k is the ratio of the secondary and main input torques ($k = T_{R2}/T_{R1} \in [-1, 0]$), $\overline{i_{0I}} = i_{0I}\eta_{0I}^x$, $\overline{i_{0II}} = i_{0II}\eta_{0II}^w$.

4 Numerical Simulations: Results and Discussions

Considering the efficiency of the spur gear $\eta_{14} = \eta_{45} = \eta_{23} = 95\%$, the influences of the k factor for different values of the amplification ratio $i_a = \omega_G/\omega_{R1}$ on the transmission efficiency (Fig. 2), and on the additional supply of power brought by the secondary rotor (Fig. 3 and 4) are further established.

The additional power contribution brought by the secondary rotor is described by the ratio λ_{R2} :

$$\lambda_{R2} = \frac{P_{R2}}{P_{R1}} = k(1-i_{0II}), \quad (16)$$

where

$$P_{R2} = \omega_{R1}T_{R1}k(1-i_{0II}) = P_{R1}k(1-i_{0II}). \quad (17)$$

The generator mechanical power (P_g) can be obtained as function of the main rotor power (P_{R1}) based on a dimensionless parameter λ_G . Replacing the efficiency from rel. (15) and the power on the secondary shaft from rel. (17) into relations (3), it results:

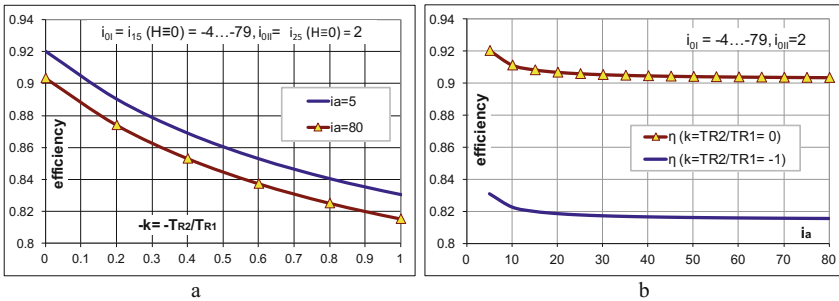


Fig. 2 The transmission efficiency as function of: **a** k parameter, for different values of the amplification ratio, **b** the amplification ratio i_a , for the extreme values of k



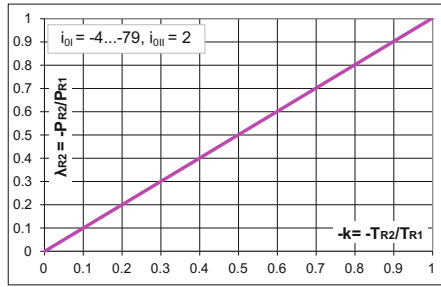


Fig. 3 The power of the secondary rotor as function of parameter k and the power of the main rotor

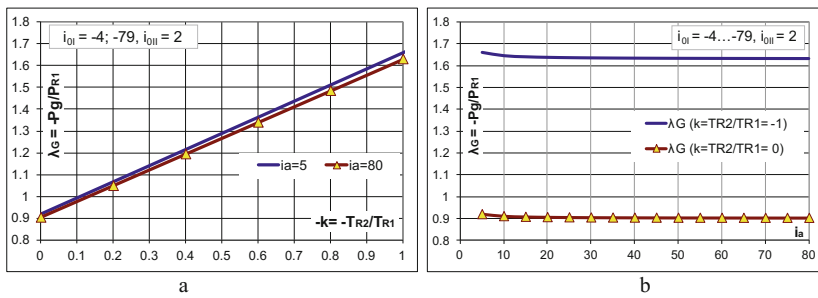


Fig. 4 The mechanical power at the generator input (P_g) as function of the main rotor's power (PR_1) and of: **a** the k parameter, **b** the amplification ratio i_a

$$\lambda_G = - \frac{P_g}{P_{R1}} = \frac{(1 - i_{0I})(1 + k(1 - \overline{i_{0II}}))}{1 - \overline{i_{0I}}}, \tag{18}$$

where $P_g = \omega_G T_G$.

The considered transmission run as a classical transmission with one input R_1 and one output G if the torque given by the secondary rotor is zero, i.e. $k = 0$, case highlighted by the ordinate point at origin in the diagrams depicted in Figs. 2a, 3 and 4, and by distinctive curves in Figs. 2b and 4b. The comparative analysis of the diagrams from Figs. 2, 3 and 4 allow to formulate the following remarks:

- the increase of the amplification ratio is accompanied by the decrease of efficiency; the decrease is relatively low (approx. 2 %) for a given value of the parameter k and for the kinematical ratio $i_a \in [5-80]$, Fig. 2a;
- with the increase of the k absolute values from 0 to 1, it results:
 - the decrease of the transmission efficiency η with ~ 10 %, Fig. 2b;
 - the increase of the power brought in the system by the secondary wind rotor (can reach the power introduced by the main rotor for $|k| = 1$), Fig. 3;

- the increase of the transmission output power P_G , Fig. 4a. The output power is linearly dependent on the torques ratio k , enabling the increase of the λ_G ratio up to 180 % for $|k| = 1$ compared with the classical case of a single wind rotor ($k = 0$).
- for a given k value, the amplification ratio i_a has a lower influence on the generator power P_g , Fig. 4b.

The diagrams from Figs. 2, 3 and 4 can be used in the selection and adjustment of the mechanical transmissions used in renewable energy systems, in which both the input speed amplification and output power increase are critical requirements.

5 Conclusions

The analysed renewable energy conversion system uses two counter-rotating rotors, a complex 1DOF speed increaser consisting of two planetary units connected in parallel and characterized by two inputs—the rotors—and one output linked to the rotor of a classical electric generator (with fixed stator). The use of this type of wind/hydro systems has the following advantages:

- due to the secondary power input, the speed increaser allows the increase of the output torque and, therefore, an additional power supply on the generator input shaft even for high transmission ratios and better efficiency than in the case of a transmission with single input are assured;
- a compact design, enabling transmission implementation into renewable energy systems with overall size restrictions, including medium and small size power systems;
- the counter-rotating system allows a higher dynamic balancing than in the case of a system with one rotor.

Depending on the power required by the electric generator, the proposed modelling algorithm can be used to find out the parameters of the mechanical power on the two input shafts, and, consequently, the system proper functioning by adjusting the k ratio.

Acknowledgments We acknowledge UEFISCDI and the PNII Partnership program, Sim-PhotoAd project no PN-II-PT-PCCA-2013-4-0726 for supporting this work.

References

1. Climescu, O., Saulescu, R., Jaliu, C.: Specific features of a counter-rotating transmission for renewable energy systems. *Environ. Eng. Manage. J.* **10**, 1105–1113 (2011). ISSN 1582 – 959
2. Shin, C.: Multi-unit rotor blade system integrated wind turbine, US Patent Nr. 5876181 (1999)

3. Zhao, X., Maißer, P.: A novel power splitting drive train for variable speed wind power generators. *Renewable Energy* **28**, 2001–2011 (2003)
4. Bottiglione, F., De Pinto, S., Mantriota, G.: Infinitely Variable Transmissions in neutral gear: Torque ratio and power re-circulation. *Mech. Mach. Theory* **74**, 285–298 (2014)
5. Pennestrì, E., Mariti, L., Valentini, P.P., Mucino, V.H.: Efficiency evaluation of gearboxes for parallel hybrid vehicles: Theory and applications. *Mech. Mach. Theory* **49**, 157–176 (2012)
6. Gomà Ayats, J.R., Diego-Ayala, U., Minguella Canela, J., Fenollosa, F., Vivancos, J.: Hypergraphs for the analysis of complex mechanisms comprising planetary gear trains and other variable or fixed transmissions. *Mech. Mach. Theory* **51**, 217–229 (2012)
7. Salgado, D.R., del Castillo, J.M.: Analysis of the transmission ratio and efficiency ranges of the four-, five-, and six-link planetary gear trains. *Mech. Mach. Theory* **73**, 218–243 (2014)
8. del Castillo, J.M.: The analytical expression of the efficiency of planetary gear trains. *Mech. Mach. Theory* **37**, 197–214 (2002)
9. Arnaudov, K., Genova, P., Dimitrov, L.: For an unified and correct IFToMM terminology in the area of gearing. *Mech. Mach. Theory* **40**, 993–1001 (2005)
10. Saulescu, R., Jaliu, C., Munteanu, O., Climescu, O.: Planetary gear for counter-rotating wind turbines. *Appl. Mech. Mater.* **658**, 135–140 (2014). doi:[10.4028/www.scientific.net/AMM.658.135](https://doi.org/10.4028/www.scientific.net/AMM.658.135)
11. Saulescu, R., Jaliu, C., Climescu, O., Diaconescu, D.: On the use of 2 DOF planetary gears as “speed increaser” in small hydros and wind turbines. In: *Proceedings of the ASME 2011 International Design Engineering Technical Conferences and Computers and Information in Engineering Conference, IDETC/CIE 2011*, 28–31.08, Washington, DC, USA (2011), ISBN: 987-0-7918-3856-3
12. Saulescu, R., Neagoe, M., Jaliu, C., Munteanu, O.: Comparative analysis of two wind turbines with planetary speed increaser in steady-state. *Appl. Mech. Mater.* **823**, 355–360 (2016). doi:[10.4028/www.scientific.net/AMM.823.355](https://doi.org/10.4028/www.scientific.net/AMM.823.355)
13. Miloiu G., Dudita Fl., Diaconescu D.V.: *Modern Mechanical Transmissions (in Romanian)*, Ed. Tehnica, Bucharest (1971)

Part IV
MTM—Micromechanisms
and Microactuators

On Application Melnikov Method to Detecting the Edge of Chaos for a Micro-Cantilever

J. Xie, S.-H. He, Z.-H. Liu and Y. Chen

Abstract In this paper, Melnikov method is employed to detecting the edge of chaos for a micro-cantilever. The difficulties arising from the integrals in Melnikov method are refrained through using MATLAB/Simulink. The edge of chaos plotted on a two parameter plane indicate that the condition of chaos occurrence derived from Melnikov method is compact for some system parameters, but is conservative for the others. Therefore, applying Melnikov method to detecting edge of chaos is far from perfect method.

Keywords Edge of chaos · Melnikov method · MEMS · Micro-cantilever · Chaos

1 Introduction

The nonlinearity of MEMS (Microelectromechanical System) has attracted much more attentions in recent years [1]. Chaos, as a characteristic phenomenon arising from nonlinear dynamic system, has great impact on the performance of MEMS [2].

The edge of chaos refers to the parameter regimes between the rigid order and chaos [3]. It is of great significance for design of MEMS devices. However, since the long term behavior of a nonlinear dynamic system cannot be predicted, the

J. Xie (✉) · S.-H. He · Z.-H. Liu · Y. Chen
School of Mechanical Engineering, Southwest Jiaotong University, Leshan,
People's Republic of China
e-mail: xj_6302@263.net

S.-H. He
e-mail: shanghong2012@qq.com

Z.-H. Liu
e-mail: zhhlui@home.swjtu.edu.cn

Y. Chen
e-mail: cykine163@163.com

usually used method to determine the edge of chaos is numerical method, which is computational cost and inefficient.

Melnikov method [4, 5] is one of rare analytical method used in the nonlinear dynamics. This method allows one to predict chaos in a nearly Hamiltonian system with homoclinic or heteroclinic orbits.

Melnikov method has been employed to establish analytical criterions for a variety of MEMS by other authors [6–8]. These investigations arrived at different conclusions. Some conclusions state that the onset value of chaos by Melnikov method is almost same as that by numerical simulation technique. But the others state that the value by Melnikov method is too conservative that modification of Melnikov method is necessary [9, 10]. In this paper, a scenario of edge of chaos is provided. It can help us to understand the difference in these conclusions.

Another issue concerning with the application of Melnikov method is that it is needed to integral the Melnikov function, which is based on the residue theorem and likewise mathematics. To overcome such difficulty, some numerical algorithms were proposed in [11–13]. In this paper, Simulink of MATLAB[®] is utilized for the sake of refraining from such recondite mathematics.

The organization of this paper is as follows. The dynamics model of a micro-cantilever is developed in Sect. 2. Melnikov method is employed to analyze the heteroclinic orbits analytically and numerically in Sect. 3, and to detect the edge of chaos in Sect. 4. The conclusions are provided in Sect. 5.

2 The Dynamics Modeling of Micro-Cantilever

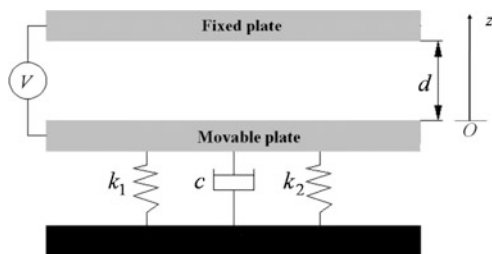
The schematic diagram of a micro-cantilever under the actuation of voltage V is shown in Fig. 1.

The equation of motion of the movable plate can be expressed as [14–16]

$$m \ddot{z} + c \dot{z} + k_1 z - k_2 z^3 = F_e(t) \quad (1)$$

where z is the vertical displacement of the movable plate relative to the fixed plate, and the symbols $\ddot{\bullet}$ and $\dot{\bullet}$ over z respectively denote the second and first derivative of z with respect to time t , m is the mass of movable plate, c is the effective damping

Fig. 1 Schematic diagram of a micro-cantilever



coefficient, k_1 and k_2 respectively denote the effective linear and cubic spring stiffness. With ignoring the fringe effects at the edges of the plate, the electrostatic force $F_e(t)$ generated by the applying voltage $V(t)$ between the fixed plate and movable plate is

$$F_e(t) = \frac{\varepsilon_0 A V^2(t)}{2(d_0 - z)} \quad (2)$$

where ε_0 is the absolute dielectric constant of vacuum, A is the overlapping area of the two plates, and d_0 is the initial distance between the two plates.

With the dimensionless variables

$$y = \frac{z}{d_0}, \quad \gamma = \frac{c}{\sqrt{k_1 m}}, \quad \omega_0 = \sqrt{\frac{k_1}{m}}, \quad \tau = \omega_0 t, \quad \alpha_0 = \frac{k_0 d_0^2}{m \omega_0}, \quad \beta = \frac{\varepsilon_0 A}{2m d_0^3 \omega_0^2}$$

and since $y \ll 1$,

$$\frac{1}{(1-y)^2} \approx 1 + 2y + 3y^2 + O(y^3) \quad (3)$$

Equation (1) can be rewritten as

$$\ddot{y} + \gamma \dot{y} + y - \alpha y^3 = f(1 + 2y + 3y^2) \cos^2(\Omega t) \quad (4)$$

where $\Omega = \omega/\omega_0$, $f = \beta V^2$.

Further letting $x = \sqrt{\alpha}y$, $x_1 = x$, $x_2 = \dot{x}$, $\gamma = \varepsilon\gamma_1$, $f = \varepsilon f_1$, the state space representation of Eq. (4) is given below

$$\begin{cases} \dot{x}_1 = x_2 \\ \dot{x}_2 = -x_1 + x_1^3 - \varepsilon[\gamma_1 x_2 + f_1 \left(\sqrt{\alpha} + 2x_1 + \frac{3x_1^2}{\sqrt{\alpha}} \right) \cos^2(\Omega t)] \end{cases} \quad (5)$$

3 Melnikov Function and Its Solutions

3.1 Melnikov Function

For $\varepsilon = 0$ in Eq. (5), a Hamiltonian unperturbed system is obtained in the form of

$$\begin{cases} \dot{x}_1 = x_2 \\ \dot{x}_2 = -x_1 + x_1^3 \end{cases} \quad (6)$$

The potential function of Eq. (6) can be defined as follows

$$H(x_1, x_2) = \frac{1}{2}x_2^2 + \frac{1}{2}x_1^2 - \frac{1}{4}x_1^4 \tag{7}$$

From Eq. (7), three fixed points [17] can be found, they are (0, 0), (±1, 0).

It is obvious that both $x_p^+ = (+1, 0)$ and $x_p^- = (-1, 0)$ are saddle points, and fixed point (0, 0) is a center point. As $H(x_1, x_2) = H(\pm 1, 0) = \frac{1}{4}$, the trajectories connecting the two saddle points form a heteroclinic orbits, as shown in Fig. 2, in which $W^{(S)}$ and $W^{(U)}$ respectively represent the stable and unstable manifolds.

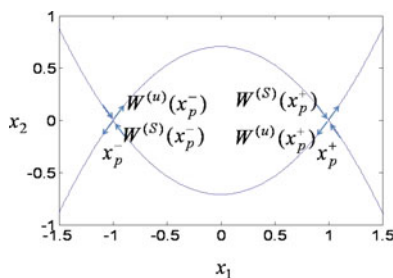
Assuming $q_i^0(t) = \{x_{1i}(t), x_{2i}(t)\}$ is the parametric equation of heteroclinic orbits, the approximate distance between the stable and unstable manifolds with small perturbation to the system can be projected onto a plane normal to the heteroclinic orbits, which is proportional to $M_i(t_0)$ defined as Melnikov function. For the heteroclinic orbits shown in Fig. 2, the Melnikov function is

$$\begin{aligned} M_i(t_0) &= \int_{-\infty}^{+\infty} \left\{ x_{2i}(t) \left[-\gamma_1 x_{2i}(t) + f_1 \left(\sqrt{\alpha} + 2x_{1i}(t) + \frac{3x_{1i}^2(t)}{\sqrt{\alpha}} \right) \cos(\Omega(t + t_0)) \right] \right\} dt \\ &= -\gamma_1 I_1 + \frac{1}{2} f_1 \sqrt{\alpha} I_3 + \frac{3f_1 I_6}{2\sqrt{\alpha}} + f_1 S \cos(2\Omega t_0 + \varphi) \end{aligned} \tag{8}$$

where

$$\begin{aligned} I_1 &= \int_{-\infty}^{+\infty} x_{2i}^2(t) dt, \quad I_2 = \int_{-\infty}^{+\infty} x_{2i}(t) \cos(2\Omega t) dt, \quad I_3 = \int_{-\infty}^{+\infty} x_{2i}(t) dt \\ I_4 &= \int_{-\infty}^{+\infty} x_{1i}(t)x_{2i}(t) \cos(2\Omega t) dt, \quad I_5 = \int_{-\infty}^{+\infty} x_{1i}^2(t)x_{2i}(t) \cos(2\Omega t) dt \\ I_6 &= \int_{-\infty}^{+\infty} x_{1i}^2(t)x_{2i}(t) dt, \quad S = \sqrt{\left[\frac{1}{2} f_1 \sqrt{\alpha} I_2 + \frac{3f_1 I_5}{2\sqrt{\alpha}} \right]^2 + I_4^2}, \end{aligned} \tag{9}$$

Fig. 2 Phase portrait of heteroclinic orbits for the system of Eq. (6)



$$\varphi = \arctan\left(\frac{I_4}{\frac{1}{2}f_1\sqrt{\alpha}I_2 + \frac{3}{2}\frac{f_1f_5}{\sqrt{\alpha}}}\right)$$

3.2 Analytical Solution of Melnikov Function

The function of heteroclinic orbits should satisfy the following functions

$$\begin{cases} \dot{x}_1 = \frac{dx_1}{dt} = x_2 \\ H(\pm 1, 0) = \frac{1}{2}x_2^2 + \frac{1}{2}x_1^2 - \frac{1}{4}x_1^4 = \frac{1}{4} \end{cases} \quad (10)$$

Denoting solution of Eq. (10) as $q_i^0(t) = \{x_{1i}(t), x_{2i}(t)\}$, $x_{1i}(t)$ should be an odd function and $x_{2i}(t)$ should be an even function [18, 19]. The concrete expressions of $x_{1i}(t)$ and $x_{2i}(t)$ are

$$\begin{cases} x_{1i}(t) = \pm \tanh\left(\frac{\sqrt{2}}{2}t\right) \\ x_{2i}(t) = \pm \frac{\sqrt{2}}{2} \operatorname{sech}^2\left(\frac{\sqrt{2}}{2}t\right) \end{cases} \quad (11)$$

Substituting Eq. (11) into Eq. (9), $I_1 \sim I_6$ in Eq. (9) can be calculated. For example, I_2 in Eq. (9) is

$$I_2 = \int_{-\infty}^{+\infty} x_{2i}(t) \cos(2\Omega t) dt = \int_{-\infty}^{+\infty} \frac{\sqrt{2}}{2} \operatorname{sech}^2\left(\frac{\sqrt{2}}{2}t\right) \cos(2\Omega t) dt = 2\sqrt{2}\pi\Omega \operatorname{csch}(\sqrt{2}\pi\Omega) \quad (12)$$

Moreover, The Melnikov function can be obtained by Eq. (8).

3.3 Numerical Solution of Melnikov Function

For $t > 0$, and from Eq. (10), one can get

$$x_2 = \frac{dx_1}{dt} = \mp \sqrt{2H(\pm 1, 0) - x_1^2 + \frac{x_1^4}{2}} = \mp \sqrt{\frac{1}{2} - x_1^2 + \frac{x_1^4}{2}} \quad (13)$$

Alone the same thought presented in [12], the time variable t can be transformed into a function of the state variable x_1 on the heteroclinic orbits. It is

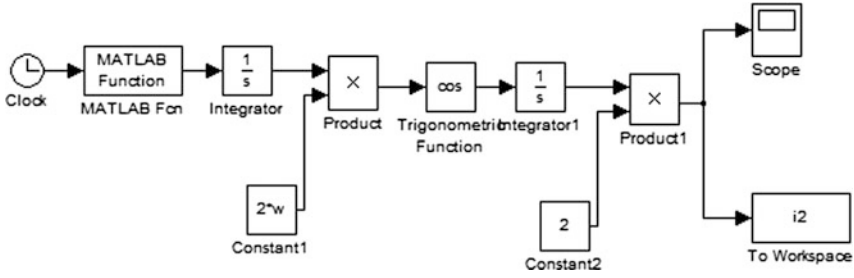


Fig. 3 Simulink block diagram for calculation of I_2

$$t = \mp \int_{x_p^-}^{x_p^+} \frac{d\xi}{\sqrt{\frac{1}{2} - \xi^2 + \frac{\xi^4}{2}}} \tag{13}$$

With Eq. (13), I_2 in Eq. (9), for example, can be rewritten as

$$I_2 = \int_{-\infty}^{+\infty} x_{2i}(t) \cos(2\Omega t) dt = \mp \int_{x_p^-}^{x_p^+} \cos(2\Omega \int_{x_p^-}^{x_p^+} \frac{d\xi}{\sqrt{\frac{1}{2} - \xi^2 + \frac{\xi^4}{2}}}) dx_1 \tag{14}$$

Here the integral of Eq. (14) is carried out using MATLAB/Simulink. The block diagram is shown in Fig. 3.

In the same manner, all the integrals in Eq. (9), $I_1 \sim I_6$ will be implemented. And Melnikov function can be obtained by Eq. (8).

4 The Conditions of Chaos Occurrence and Results

As the fact that the distance of stable and unstable manifolds can be measured by Melnikov function, $M_i(t_0)$, then

$$M_i(t_0) = 0, \quad \frac{dM_i(t_0)}{dt_0} \neq 0 \tag{15}$$

implies that the stable and unstable manifolds intersect transversely, meanwhile, there are many transverse heteroclinic orbits. In this situation, Smale horseshoe map exists, and chaos may occur [20].

Equation (15) can be regarded as the conditions of chaos occurrence. From Eq. (8), it is yielded that



$$\begin{aligned}
 -\gamma I_1 + \frac{1}{2}f_1\sqrt{\alpha}I_3 + \frac{3f_1I_6}{2\sqrt{\alpha}} + f_1S \cos(2\Omega t_0 + \varphi) &= 0 \\
 2\Omega f_1S \sin(2\Omega t_0 + \varphi) &\neq 0
 \end{aligned}
 \tag{16}$$

Equation (16) leads to following inequality

$$R_{\min} < \frac{\gamma}{\beta} < R_{\max}
 \tag{17}$$

where

$$R_{\min} = \max\left(\frac{\frac{1}{2}\sqrt{\alpha}I_3 + \frac{3I_6}{2\sqrt{\alpha}} - S}{I_1}, 0\right), \quad R_{\max} = \frac{\frac{1}{2}\sqrt{\alpha}I_3 + \frac{3I_6}{2\sqrt{\alpha}} + S}{I_1}.$$

By the definition, the edge of chaos is the domains between the curves of R_{\max} and R_{\min} as depicted in Fig. 4.

Figure 4a shows a good match between the analytical and numerical solutions for Melnikov function. In Fig. 4b, the plane of parameters (Ω, γ) is uniformly sampled in rectangle parallelepiped by 100×100 nodal point, which are utilized to carry out numerical simulation, and will be assigned with blue if the parameters lead to chaos in the system, otherwise will be assigned with white. It is seen that the condition of chaos occurrence derived from Melnikov function is necessary but not sufficient ones. Only in small part of domain is the condition compact, and the remained is much conservative.

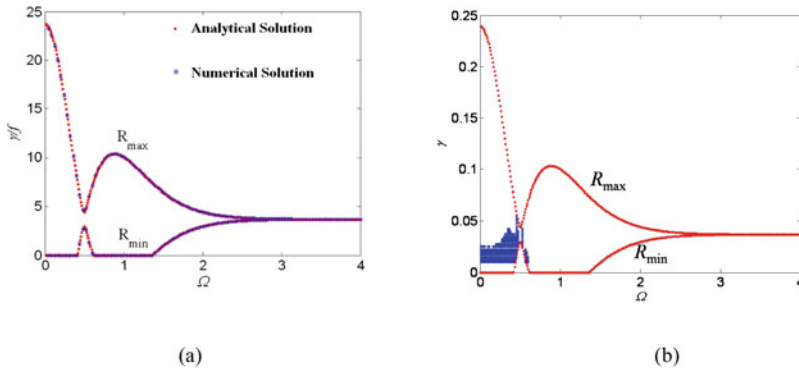


Fig. 4 Edge of chaos of micro-cantilever



5 Conclusions

Micro-cantilever, as a physical modeling of many MEMS devices and components, is identified the occurrence of chaos in recent years. Melnikov method is employed to detect the edge of chaos for a micro-cantilever. Although the results show that Melnikov method is far from perfect method to detecting edge of chaos, it might provide the clue for further investigation on the detecting the edge of chaos.

Acknowledgments The authors would like to acknowledge the financial support of NSFC (National Natural Science Foundation of China) under the grant No. 51175437 and No. 51575457.

References

1. Rhoads, J.F., Shaw, S.W., Turner, K.L.: Nonlinear dynamics and its applications in micro- and nanoresonators. *J. Dyn. Syst. Meas. Control* **132**(3), 034001–34002 (2010)
2. Seleim, A., Towfighian, S., Delande, E., Abdel-Rahman, E., Heppler, G.: Dynamics of a close-loop controlled MEMS resonator **69**(1), 615–633 (2012)
3. Langton, C.G.: Computation at the edge of chaos: phase transition and emergent computation. *Phys. D* **42**, 12–37 (1990)
4. Melnikov, V.K.: On the stability of the centre for time periodic perturbations. *Trans. Moscow Math.* **12**, 1–57 (1963)
5. Awrejcewicz, J., Holicke, M.: *M: Smooth and Nonsmooth High Dimensional Chaos and the Melnikov-Type Methods*. World Scientific Publishing Co. Pre Ltd, Singapore (2007)
6. Haghghi, H.S., Markazi, A.H.D.: Chaos prediction and control in MEMS resonators. *Commun. Nonlinear Sci. Numer. Simul.* **15**(10), 3091–3099 (2010)
7. Siewe, M.S., Hegazy, U.H.: Homoclinic bifurcation and chaos control in MEMS resonators. *Appl. Math. Model.* **35**(12), 5533–5552 (2011)
8. Han, J.-X., Zhang, Q.-C., Wang, W.: Design considerations on large amplitude vibration of a doubly clamped microresonator with two symmetrically located electrodes. *Commun. Nonlinear Sci. Numer. Simul.* **22**(1–3), 492–510 (2015)
9. Maani Miandoab, E., Pishkenari, H.N., Yousefi-Koma, A., Tajaddodianfar, F.: Chaos prediction in MEMS-NEMS resonators. *Int. J. Eng. Sci.* **82**, 74–83 (2014)
10. Tajaddodianfar, F., Nejat Pishkenari, H., Hairi Yazdi, M.R.: Prediction of chaos in electrostatically actuated arch micro-nano resonators: Analytical approach. *Commun. Nonlinear Sci. Numer. Simul.* **30**(1–3), 182–195 (2016)
11. Ling, F.H., Bao, G.W.: A numerical implementation of Melnikov's method. *Phys. Lett. A* **122**(8), 413–417 (1987)
12. Bruhn, B., Koch, B.P.: Homoclinic and heteroclinic bifurcations in rf SQUIDS. *Zeitschrift fur Naturforschung* **43**, 930–938 (1988)
13. Yagasaki, K.: Chaos in a pendulum with feedback control. *Nonlinear Dyn.* **6**, 125–142 (1994)
14. Zhang, W.-M., Meng, G.: Nonlinear dynamical system of micro-cantilever under combined parametric and forcing excitation in MEMS. *Sens. Actuators A* **199**(2), 291–299 (2005)
15. Jimenez-Triana, A., Zhu, G.-C., Saydy, L.: Chaos synchronization of an electrostatic MEMS resonator in the presence of parametric uncertainties. In: *Proceedings of 2011 American Control Conference*, San Francisco, CA, USA, pp. 5115–5120 (2011)
16. Mestrom, R.M.C., Fey, R.H.B., van Beek, J.T.M., Phan, K.L., Nijmeijer, H.: Modelling the dynamics of a MEMS resonator: simulations and experiments. *Sens. Actuators A* **142**, 306–315 (2008)

17. Robinson, R.C.: An Introduction to Dynamical Systems: Continuous and Discrete. Pearson Education Inc. (2004)
18. Xu, P.-C., Jing, Z.-J.: Heteroclinic orbits and chaotic regions for Josephson system. *J. Math. Anal. Appl.* **376**(1), 103–122 (2011)
19. Doroshin, A.V.: Heteroclinic dynamics and attitude motion chaotization of coaxial bodies and dual-spin spacecraft. *Commun. Nonlinear Sci. Numer. Simul.* **17**(3), 1460–1474 (2012)
20. Wiggins, S.: Introduction to Applied Nonlinear dynamical Systems and Chaos. Springer (2003)

Part V
MTM—Computational
and Experimental Methods

Use of the *Structomatic* Method to Perform the Forward Kinematic and Kinetostatic Analyses of a Hydraulic Excavator

M. Mailloux, M. Éné, I. Simionescu and I. Tabara

Abstract As part of this paper, a hydraulic excavator analyzed by Hall et al. [7] is studied on both kinematic and kinetostatic points of view by means of a modern approach: the *structomatic* method. The main steps of this method are explained and highlight its potential for the study of complex mechanisms by decomposing the hydraulic excavator into unique groupings called *structomats*. These ones allow to solve the closed-loop vectorial equations separately and can be found in any mechanisms, which facilitate the computer-aided implementation of this method due to the fact that the subroutines related to the *structomats* can be employed to study other mechanisms. The *structomatic* method is used to compute the kinematic parameters of the bucket's centroid along with the active force of each of the three actuators depending on their predetermined sequence of motion. The *structomatic* method is straightforward and systematic for the study of a large amount of mechanisms and acts as an alternative to existing methods.

Keywords *Structomatics* · *Structomats* · Forward kinematics · Kinetostatics · Linkage mechanisms

M. Mailloux (✉) · M. Éné
Université du Québec en Abitibi-Témiscamingue, Rouyn-Noranda, Canada
e-mail: maxime.mailloux@uqat.ca

M. Éné
e-mail: marin.ene@uqat.ca

I. Simionescu · I. Tabara
Politehnica Bucharest University, Bucharest, Romania
e-mail: simionescu2@gmail.com

I. Tabara
e-mail: iuliantabara2511@yahoo.com

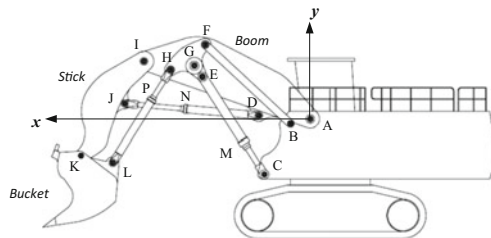
1 Introduction

The hydraulic excavator of Fig. 1 is a heavy plant machinery widely used for public works, mining exploitations, building construction, material handling, demolitions, etc. and has three primary links: the boom $ADGI$, the stick IJK and the bucket KL . These links are set in motion due to the movement of three actuators CME , DNJ and HPL . This mechanism was frequently studied and, in this paper, the forward kinematic as well as the kinetostatic analysis will be broached with a fresh eye.

The mechanism shown at Fig. 1 was formerly studied by Hall et al. [7]. In fact, the authors were interested by the trajectory taken by the bucket according to the extension and the retraction of each of the three actuators composing the hydraulic excavator. In order to do this, a nonlinear system of equations was generated by writing four closed-loop vectorial equations considering the entire mechanism. These nonlinear equations were solved by using an adaptation of the Newton-Raphson numerical method. The fact that the mechanism is not decomposed in unique groupings require more mathematical work due to the need to solve all the nonlinear equations simultaneously which necessitate all the initial conditions (angles and lengths describing the motion of the hydraulic excavator) to be accurate to ensure the convergence of the method.

In this paper, a modern approach is presented. This method allows the characterization of the mechanism using unique groupings termed *structomats* which are used to perform in a systematic way the kinematic and kinetostatic analyses. Over the sections, the required steps to obtain the position, the velocity and the acceleration of all the joints of the hydraulic excavator along with the reactions of both passive and active joints will be made explicit. In this way, the kinematic parameters of the bucket according to the predetermined sequence of motion of each actuators and the distribution of the active forces of these actuators will be computed for any loading soliciting the bucket. This method is called the *structomatic* method and was explained by Éné [6]. The aim of this approach is to study complex mechanisms by decomposing them in *structomats*. It is important to mention that every mechanism is composed by these *structomats* like every living organisms stores genetic information. It is more mathematically effective to compute the kinematic parameters of the elements of each *structomats* separately and combine

Fig. 1 Representation of the hydraulic excavator



the results in order to study the entire mechanism instead of approaching the mechanism as a whole from the outset because a fewer nonlinear equations are involved at the same time.

The structure of kinematic chains has been, for a long time, a topic in constant evolution and a decisive concept for the design of mechanisms. In fact, Mruthyunjaya [9] resumed the different methods employed to sketch the relation between elements and joints of a linkage mechanism. In the mid-1960s, the Franke's condensed notation used a polygon to represent the mechanism where each vertex was related to an element and where the edges were referred to a joint. Furthermore, the graph theory [1] was also introduced to smarten up the sketch of mechanism and also to favor the implementation of the synthesis of kinematic chains on computers. Another approach makes a reference to the Assur groups [8, 10]. Actually, Assur exposed the statement that each mechanism can be composed of the same passive groups (no degree of mobility) included in a library. The main concept of the *structomatic* method is based on the Assur's theory but is extended to groups or, in our case, *structomats*, that are called active which means that they own a degree of mobility greater than zero. However, more often than not, the active *structomats* that describe a mechanism has one degree of mobility. These active *structomats* were introduced by Duca and Simionescu [2]. Figure 2 presents some of the most common *structomats*: (a) dyad RRR/motodyad RRT_aR; (b) triad RR-RR-RR/mototriad RR-RR-RT_aR and (c) tetrad R-RRRR-R/mototetrad R-RRRT_aR-R where R implies a revolute joint and where T_a corresponds to an active prismatic joint.

The *structomatic* method can be adapted to study planar mechanisms with *M* degrees of freedom that are driven by revolute joint and/or prismatic joint actuation. The omnipresence of computer software allows the implementation of efficient and accurate algorithms. In the context of this article, Matlab[®] is used for numerical calculations and presentation of the results.

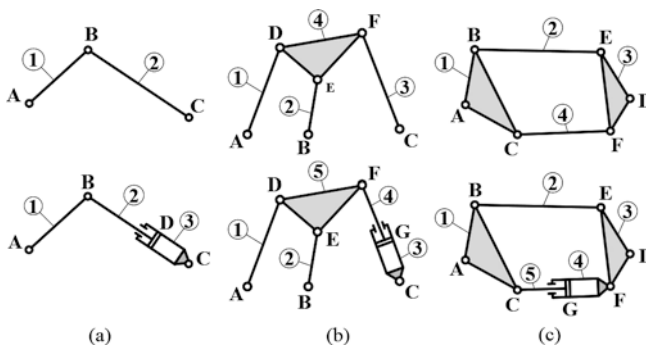


Fig. 2 Most common *structomats*

2 Structomatic Analysis

Based on the morphology of the hydraulic excavator of Fig. 1, the *structomats* characterizing this mechanism are observed. By identifying the revolute and prismatic joints associated with each element, the diagram of Fig. 3a, named the graph diagram, can be presented. This graph diagram illustrates the connections between the elements regardless of their geometry. The element labeled 0 is termed zeropole and corresponds to the fixed joints linked to the basis of the hydraulic excavator (A, B and C). Thus, each of the vertices of Fig. 3a is related to a joint while each one of the edges is associated to an element. It is with this diagram that the unique *structomats* of a mechanism can be detected. Because the excavator has three degrees of mobility and due to the fact that the most common *structomats* describing a planar mechanism are whether passive or own only one degree of freedom, it is expected that at least three *structomats* will describe this mechanism. The joint labeled M in the graph diagram are active joints (motor). The *structomats* of the excavator are identified through the graph diagram illustrated in Fig. 3a and are transposed into the block diagram Fig. 3b. This diagram shows the transmission of the motion starting from the zeropole to the bucket. In this way, all the joints at the left of a block or *structomat* (called input joints) are always known.

This condition is mandatory to be able to solve the nonlinear position equations related to each *structomat*. Thus, with the help of Figs. 2 and 3a, it is possible to conclude that the hydraulic excavator is composed of three *structomats*: a mototriad formed with the elements (1, 2, 3, 4, 5) and two successive motodyads which correspond to the elements (6, 7, 8) and (9, 10, 11).

3 Kinematic Analysis

The objective of the kinematic analysis is to compute the position, the velocity and the acceleration of each joint along with the angle, the angular velocity and the angular acceleration of each of the elements and that, for all the configurations

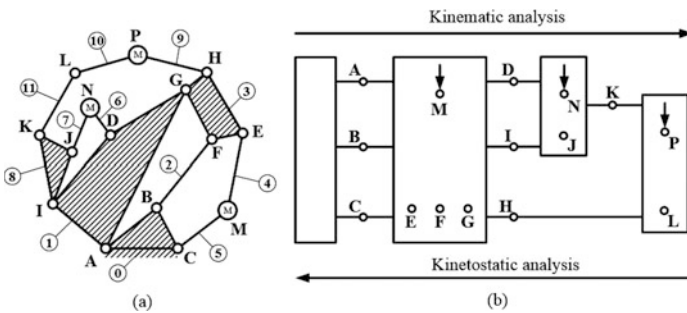


Fig. 3 Graph and block diagrams of the hydraulic excavator

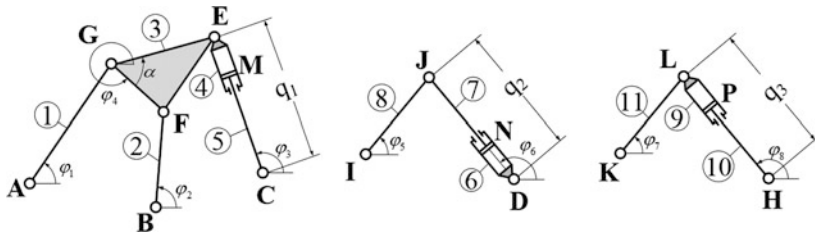


Fig. 4 Kinematic drawings for each *structomats* describing the hydraulic excavator

taken by the excavator. To do so, the closed-loop vectorial position equations of each *structomats* must be solved in the order provided by the block diagram.

For a specific *structomats*, it is always the same position equations associated with it, regardless of the studied mechanism [4, 5]. Figure 4 shows the kinematic drawing of the three *structomats* of the excavator. In order to write down the position equations for each *structomats*, an angle φ is related to each revolute joint whereas a length q is associated to a prismatic joint. Thus, to perform the kinematic analysis of the excavator composed of eleven elements which three are called active, a total of eight position equations is needed (four for the mototriad and two for each successive motodyads).

These nonlinear equations are solved one *structomats* at a time using the Newton-Raphson numerical algorithm.

$$\mathbf{x}_{k+1} = \mathbf{x}_k - \mathbf{W}_k^{-1} \mathbf{f}_k \tag{1}$$

where k is the actual iteration, \mathbf{x} is the unknown vector, \mathbf{W} is the jacobian matrix and \mathbf{f} is the vector where the position equations are stocked.

Once the position equations are solved, the systems of equations of velocity and acceleration become linear and can be solved with the Eqs. (2) and (3).

$$\dot{\mathbf{x}} = \mathbf{W}^{-1} \mathbf{V} \tag{2}$$

$$\ddot{\mathbf{x}} = \mathbf{W}^{-1} (\dot{\mathbf{V}} - \dot{\mathbf{W}}\dot{\mathbf{x}}) \tag{3}$$

where the vector \mathbf{V} in Eq. (2) is the vector of free terms, that is to say, it contains terms that are not a function of any unknowns.

4 Kinetostatic Analysis

The kinetostatic analysis is used to compute the reactions in the passive joints of the excavator as well as the active forces of each cylinders when the kinematic parameters of the centroid of each element in addition to the angular velocity and

angular acceleration of each element are known. The aim of this analysis is to proceed to the design of actuators along with calculations belonging to the mechanics of material, fatigue and vibrations fields. In this paper, the friction inside the joint will not be considered. However, it is possible to introduce an algorithm to approximate the force-moment related to friction in each *structomat* [3]. This analysis requires that the study of *structomats* occurs in the opposite direction that the one explained for the kinematic analysis (see Fig. 3b): from the bucket to the zeropole. Kinetostatic calculations are based mainly on the principle of d'Alembert. This one states that the sum of the applied forces, the forces of inertia and the reactions forces along with the sum of the moments of these forces are zero which results in a linear system of equations. Knowing the arrangement of each *structomats*, a unique algorithm for each of them can be implemented to compute the reactions and the active forces by decomposing those ones into elements and applying the three equations of statics on each of them. For this study, a loading \mathbf{Q} will be considered and will act at the centroid of the bucket. The kinetostatic drawing of the motodyad composed by the elements 9, 10 and 11 (bucket) can be seen in Fig. 5 with all the inertia forces \mathbf{F}_i and moment \mathbf{M}_i applied at the center of mass G_i of each elements, the passive reactions \mathbf{R}_i and moment \mathbf{CR}_3 , the active forces \mathbf{P}_3 and the loading \mathbf{Q} . The distance between the rotary joints L and H is labeled q_3 where the length of the cylinder rod is noted D_3 . We use the subscript 3 because this motodyad is the third *structomat* of the block diagram of Fig. 3 (considering the kinematic way). The same approach can be done with the other *structomats* of the excavator.

Another approach can also be used to perform the kinetostatic analysis of a mechanism with M degree of mobility: the principle of virtual power. This principle, derived from analytical mechanics, indicates that the instantaneous power balance generated by the active elements, the applied forces and those related to the inertia of each elements is zero for at any instant. The advantage of this approach is that the reactions of each joint do not need to be calculated. It can be employed to validate the results obtained with the kinetostatic analysis.

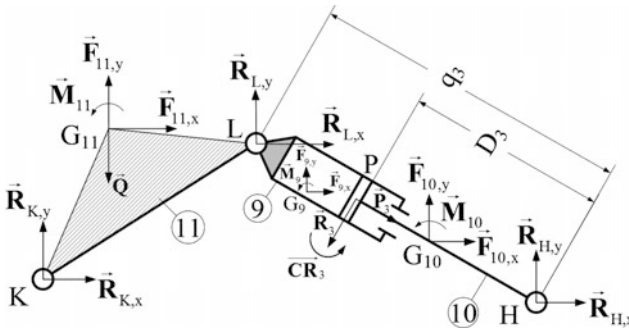


Fig. 5 Kinetostatic drawing for the *structomat* where the bucket is included



$$\sum_{i=1}^n P = \sum_{i=1}^n \vec{F}_i \cdot \vec{v}_i + \sum_{i=1}^n \vec{M}_i \cdot \vec{\omega}_i \tag{4}$$

$$\sum_{i=1}^n P = \sum_{i=1}^n m_i [(\ddot{G}_{i,x} \dot{G}_{i,x}) + (\ddot{G}_{i,y} + g) \dot{G}_{i,y}] + \sum_{i=1}^M P_i \dot{q}_i + \sum_{i=1}^n I_{G_i} \dot{\varphi}_i = 0$$

where G_i is the position of the center of mass of the element i with respect to the ground frame, P_i and \dot{q}_i are respectively the active force and the velocity of the actuator i , m_i and I_{G_i} are the mass and the mass moment of inertia of the element i whereas $\dot{\varphi}$ and $\ddot{\varphi}$ are the angular velocity and angular velocity of the element i .

5 Implementation and Results

Figure 6 illustrates the main steps to follow to accomplish the complete study of the hydraulic excavator by means of the *structomatic* method.

The sequence of motion of the actuators were decomposed into six intervals (one extraction and one retraction for each actuator). By applying the method of Fig. 6, it is possible to compute the kinematic parameters of the bucket and the profile of the active force of each actuator. To obtain the results presented in Fig. 7, the length of AG was fixed to 1 m and the other dimensions required are proportional to this length. The results are therefore for general purposes.

The discontinuities that are observable in the graphs of Fig. 7 correspond to the instant where one actuator stops its motion before another one takes the lead.

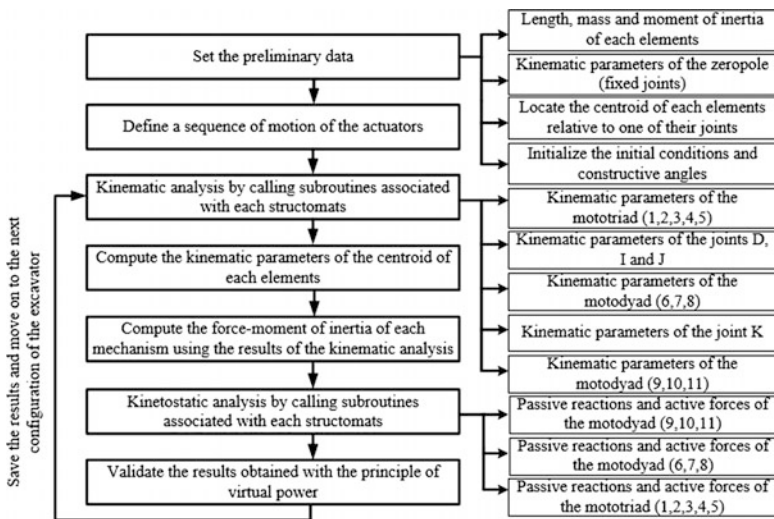


Fig. 6 Schematic summary of the steps to follow



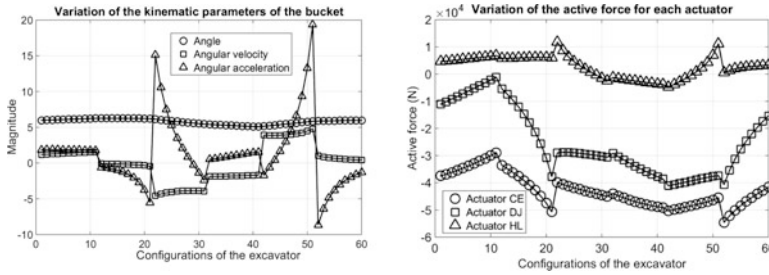


Fig. 7 Kinematic parameters of the bucket and the variation of the active force for each actuators

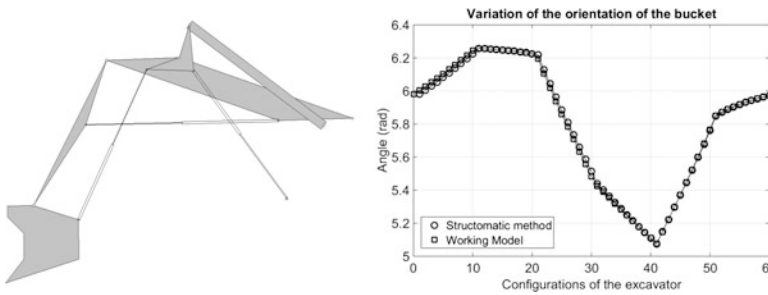


Fig. 8 Comparison between the *structomatic* method and working model

Moreover, to prove the veracity of the results shown in Fig. 7, the kinematic analysis has also been done using Working Model which is well known motion simulation software. Thus, the variation of the orientation of the bucket using the *structomatic* method and Working Model can be observed in Fig. 8. The comparison could have also been done successfully considering the other kinematic parameters of the bucket and for the computation of the active force related to each actuator.

6 Conclusion

In this paper, it was shown that each *structomat* is equivalent to a specific arrangement of elements of a mechanism which, once identified as a part of the composition of a mechanism, is related to a unique mathematical model to directly compute the kinematic and kinetostatic parameters. Thus, if several mechanisms are formed by the same *structomats*, these predefined models can directly be used reducing significantly the mathematical effort due to the fact that the closed-loop vectorial equations are already included in these models. It just depends on the

transmission of motion of the block diagram. Thus, the *structomatic* method is adapted for computer-aided design of mechanisms and can be applied in a systematic way to perform the kinematic and kinetostatic analyses.

References

1. Dobrjanskyj, L., Freudenstein, F.: Some applications of graph theory to the structural analysis of mechanisms. *J. Eng. Ind.* **89**, 153–158 (1967)
2. Duca, C., Simionescu, I.: Un principe général de formation des mécanismes. *Studii si Cercetari de Mecanica Apicata* 32 (1973)
3. Durango, S., Calle, G., Ruiz, O.: Analytical method for the kinetostatic analysis of the second-class RRR Assur group allowing for friction in the kinematic pairs. *J. Braz. Soc. Mech. Sci. Eng.* **32**, 200–207 (2010)
4. Éné, M.: Analyse structomatique, cinématique, cinétostatique et dynamique du mécanisme du concasseur à mâchoires. In: *Proceedings of the Canadian Engineering Education Association* (2004)
5. Éné, M., Moise, V.: *Mécanisme à membrures: une approche structomatique d'analyse avec Matlab*. Éditions Printech (2010)
6. Éné, M.: *Introduction à la théorie des mécanismes: modèles et méthodes*. Fégalma (2013)
7. Hall, A.S., McAree, P.R.: Robust bucket position tracking for a large hydraulic excavator. *Mech. Mach. Theory* **40**, 1–16 (2005)
8. Hansen, M.R.: A general method for analysis of planar mechanisms using a modular approach. *Mech. Mach. Theory* **31**, 1155–1166 (1996)
9. Mruthyunjaya, T.S.: Kinematic structure of mechanisms revisited. *Mech. Mach. Theory* **38**, 279–320 (2003)
10. Pelecudi, C.: Kinematic multipoles with rigid links. *Revue roumaine de science et technique-mécanique appliquée* 13 (1968)

Application of a Cam Workbench for Education in Mechanical Engineering

H. Chen, T.T.N. Nguyen, M. Müller, S. Kurtenbach, C. Pan,
M. Hüsing and B. Corves

Abstract The paper shows the conception of a cam workbench for educational purposes. The cam workbench aims at sustaining the learned design process and visualizing learned effects. Therefore different cams with typical transfer functions are selectable for both follower types, translating and oscillating. The properties of these cams can be analyzed by students. Besides, kinematical length of the mechanism like eccentricity and the central distance can be varied. So the students can experience the influence of the pressure angle on the complete mechanisms. In addition, the students can calculate and design their own cam. Therefore, they can practice the learned theory in exercises. The designed cams can be manufactured by 3D-printing and plugged on to the different cam shafts.

Keywords Cam workbench · Education · Transfer function · Design process

H. Chen · C. Pan
National University of Defense Technology, Changsha, China
e-mail: chenhu19861124@163.com

C. Pan
e-mail: pancunyun@sina.com

T.T.N. Nguyen · M. Müller (✉) · S. Kurtenbach (✉) · M. Hüsing · B. Corves
RWTH Aachen University, Aachen, Germany
e-mail: mueller@igm.rwth-aachen.de

S. Kurtenbach
e-mail: kurtenbach@igm.rwth-aachen.de

T.T.N. Nguyen
e-mail: Nguyen-Thi@igm.rwth-aachen.de

M. Hüsing
e-mail: huesing@igm.rwth-aachen.de

B. Corves
e-mail: corves@igm.rwth-aachen.de

1 Introduction

Even though the use of servo motors becomes more and more economical, cam–follower systems are still frequently used in all kinds of machines [1]. Reasons for that are the remaining advantages of cam mechanism in general like high load-carrying ability, low shock and acceleration, very long life and a high reliability [2]. Because of the importance of this kind of mechanisms in motion technology, it is necessary to include the basic design theory of cam mechanisms in the educational content of engineers.

The basic design process of cam mechanisms can be divided into three stages. The first stage is the motion design in which the transfer function of the mechanism is defined. The second stage is the determination of the dimensions of the cam mechanism such as the base circle radius. This step is followed by the determination of the cam-shape [3].

At present, many educational physical and virtual assistance machines are in use to achieve a highly sustainable knowledge. The brake test bench from Graz University of Technology in Austria is an example of such a workbench [4]. Because of the successful application of workbenches in education, an educational cam workbench is a good way to sustain the students' knowledge of the cam–design process.

Nowadays there are already different cam test benches in use. The Laboratory of Robotics and Mechatronics (LARM) in Cassino for example designed a cam workbench for non-educational purposes [5].

Due to the different requirements of workbenches for industrial and for educational purpose, it is necessary to design a new educational cam workbench. The design process of such a workbench is described within this paper.

2 Requirements of a Cam Workbench for Education

Because of the application of the workbench in education, the requirements are different to other cam workbenches such as the workbench from LARM [5]. In contrast to the industrial workbench the educational workbench aims at answering the following questions:

1. How do different cam mechanisms structures work?
2. What is the difference between the properties of common transfer functions?
3. Which affection do key parameters such as eccentricity and central distance have?
4. What is the phenomenon of hill up of the follower?

The course ends with the design of a self-made cam to sustain the learned cam design process.

Based on these requirements the workbench should have

- several cams with different, but commonly used transfer functions for the same motion task;
- a selection of the most common types of followers;
- a possibility to change the kinematic parameters of the cam mechanism;
- ample space to install additional cams designed by students.

For the input motion, cams are usually driven by motors. Beside this, it should be possible to actuate the workbench by a handle at the end of the cam shaft. So the students also can manipulate the test workbench by themselves. Thus, they can feel haptic experience variances between the different transfer functions. This experience can help them to understand the influence of parameters like eccentricity and center distance and their influence on the pressure angle.

Besides this haptic feedback the workbench offers a sensory output as well. Therefore, sensors that measure the displacements, velocity and acceleration of the output motion are necessary. The measured data can be analyzed and interpreted by the students.

3 Conceptual Design of the Cam Workbench

The requirements mentioned in the chapter before lead to different properties of the actual workbench. Within this chapter it is described which effect the requirements have on the properties of the designed workbench.

3.1 *Realized Transfer Function*

The first step within the design process is the motion design [3]. To allow the students to practice both type of follower motion, the workbench should have a translational and a rotational output motion.

The aim of showing the differences between several common transfer functions leads to the requirement that different cams with several transfer functions should be applied. The most common sequence of follower operation is the Dwell-Rise-Dwell also called Rise-Dwell-Fall-Dwell cam [6, 7] that leads to a transfer function similar to Fig. 1. The dashed lines show the rise part respectively the fall part of the transfer function.

These parts can be realized by different kinds of mathematical functions. In literature it is recommended to use functions that are continuous through the first and second derivatives of displacement [1, 8]. Therefore, fifth and seventh degree polynomials as well as a cycloidal transfer functions are recommended [8]. Nevertheless, for education purpose other transfer functions, that don't fulfill the

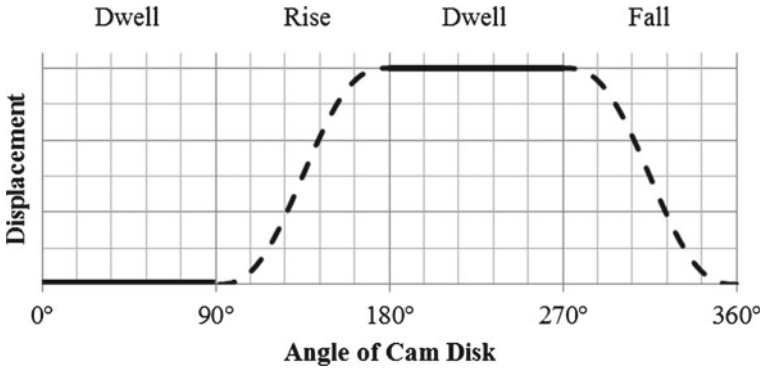


Fig. 1 Most common sequence of follower operation

recommendation, make sense as well. Students can experience the influence of infinite spikes in the jerk function caused by a discontinuous acceleration function. So the transfer functions of a quadratic parabola, a third degree polynomial and a simple harmonic motion are realized, too.

In total these six transfer functions lead to six different cams for each type of follower motion (see Chap. 4). These cams do not just differ in the infinite spikes of the jerk function, but also in different properties like the maximum velocity or acceleration for the same motion task. These properties have also a great influence on the static or dynamic forces and so hence on the required motor torque.

The equations of the transfer functions for an oscillating follower are listed in Table 1. In these equations ψ_H is the total lift of the follower and φ_{p1} is the camshaft angle of the rise part.

Table 1 Transfer functions for a dwell-dwell motion of an oscillating follower [8]

Transfer function	Equation(s)
2nd deg. polynomial	$\psi(\varphi) = 2 \cdot \psi_H \cdot \left(\frac{\varphi}{\varphi_{p1}}\right)^2 \quad 0 \leq \varphi \leq \frac{\varphi_{p1}}{2}$ $\psi(\varphi) = \psi_H \left(-1 + 4 \frac{\varphi}{\varphi_{p1}} - 2 \left(\frac{\varphi}{\varphi_{p1}}\right)^2\right) \quad \frac{\varphi_{p1}}{2} \leq \varphi \leq \varphi_{p1}$
3rd deg. polynomial	$\psi(\varphi) = \psi_H \left(3 \left(\frac{\varphi}{\varphi_{p1}}\right)^2 - 2 \left(\frac{\varphi}{\varphi_{p1}}\right)^3\right)$
5th deg. polynomial	$\psi(\varphi) = \psi_H \left(6 \left(\frac{\varphi}{\varphi_{p1}}\right)^5 - 15 \left(\frac{\varphi}{\varphi_{p1}}\right)^4 + 10 \left(\frac{\varphi}{\varphi_{p1}}\right)^3\right)$
7th deg. polynomial	$\psi(\varphi) = \psi_H \left(-20 \left(\frac{\varphi}{\varphi_{p1}}\right)^7 + 70 \left(\frac{\varphi}{\varphi_{p1}}\right)^6 - 84 \left(\frac{\varphi}{\varphi_{p1}}\right)^5 + 35 \left(\frac{\varphi}{\varphi_{p1}}\right)^4\right)$
Sinusoid function	$\psi(\varphi) = \frac{1}{2} \psi_H \left(1 - \cos\left(\pi \frac{\varphi}{\varphi_{p1}}\right)\right)$
Cycloidal function	$\psi(\varphi) = \psi_H \left(\frac{\varphi}{\varphi_{p1}} - \frac{1}{2\pi} \sin\left(2\pi \frac{\varphi}{\varphi_{p1}}\right)\right)$

3.2 Determination of the Cam Dimension

The dimension of the actual cam mechanism depends on the transfer function and the parameters shown in Fig. 2. These parameters highly involve the transmission angle of the mechanism [1]. As shown in Fig. 2, the transmission angle δ is the angle between the direction of motion of the follower and the direction of the axis of force transmission. Thus, the sum of the pressure angle δ and the transmission angle μ is equal to 90° . The definition of the minimal transmission angle μ_{min} is used in many cam-sizing-methods. One is the hodograph methods described in [9]. The other one is Flocke design procedure, which simplifies the hodograph method [10].

Based on experiences, the minimal transmission angle can be equal to the values in Table 2. This recommendation helps to define the kinematic length of the mechanisms and size the cams.

If every cam has a sufficient minimal transmission angle, there is no possibility to show students the influence of bad transmission angles. So it is necessary to change the minimal transmission angle for the manufactured cams by changing the pressure angle. Therefore, the equation for the pressure angle δ of the mechanism shown in Fig. 2a is given in Eq. (1) and for Fig. 2b in Eq. (2) [1, 7].

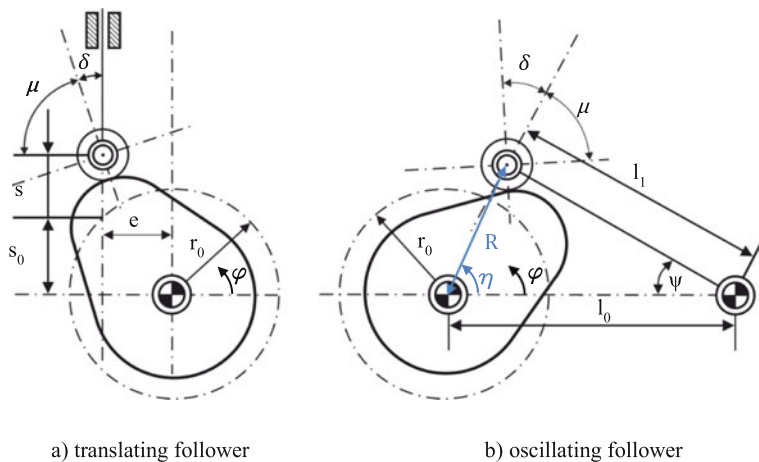


Fig. 2 Sizing parameters of the cam structures

Table 2 Recommendation of the minimal transmission angles [12]

Transmission angle	Condition of the process
$\mu_{min} \geq 45^\circ$	In case of slowly moving cam disks with oscillating follower ($n_0 \leq 30 \text{ min}^{-1}$)
$\mu_{min} \geq 60^\circ$	In case of cam mechanisms with translation follower or fast moving cam disks ($n_0 > 30 \text{ min}^{-1}$)

$$\delta = \text{atan} \left(\frac{s' \pm e}{s + \sqrt{r_0^2 - e^2}} \right) \quad (1)$$

$$\delta = \pm \frac{\pi}{2} \mp \text{asin} \left(\frac{l_0}{R} \cdot \sin(\psi) \right) + \text{atan} \left(\frac{1}{\frac{R^2}{l_1 l_0 \sin \psi \cdot \psi'} - \frac{l_0^2 - R^2 - l_1^2}{2Rl_0 \sin \eta}} \right) \quad (2)$$

The pressure angle in Eq. (1) depends on the velocity of the follower s' in units length per radian, the eccentricity of the follower e , the shift s and the base circle radius r_0 . The variation of the sign depends on whether the movement is a rise or a fall. The pressure angle in Eq. (2) depends upon the central distance l_0 , the length of the follower l_1 , the velocity of the follower ψ' and the parameters described in Eqs. (3) and (4).

$$R = \sqrt{l_1^2 + l_0^2 - 2l_1 l_0 \cos \psi} \quad (3)$$

$$\eta = \cos^{-1} \left(\frac{(l_0^2 - R^2 - l_1^2)}{2Rl_0} \right) \quad (4)$$

Since the cam is already manufactured, and the transfer function is fixed, all parameters that influence the transfer function are already designed and cannot be changed easily. The only parameter of Eq. (1) respectively Eq. (2) that is not related to the cam size is the eccentricity e respectively the central distance l_0 and the kinematic length l_1 . By shifting l_0 , the minimal pressure angle decreases. But of course not only l_0 changes, the other parameters change as well. An example for changing the transfer function by changing the central distance is given in Fig. 3. In this case the cam is designed for a central distance of $l_0 = 230$ mm and $l_1 = 170$ mm.

A similar effect occurs by varying the eccentricity e of the structure shown in Fig. 2a. By variation of these two parameters it is possible to change the occurring minimal pressure angle by unchanging cams.

3.3 Calculation of the Cam Surface

In the case that the students design cams for a specific motion task, they have to calculate the cam surface for the 3D-printing process. In general two different ways of determining the cam curvature are possible. The first way is the graphical construction of the curvature and the second one is the mathematical calculation of the curvature [3]. Both ways are based on the same approach which is described within this chapter using an oscillating roller follower. In contrast to the real

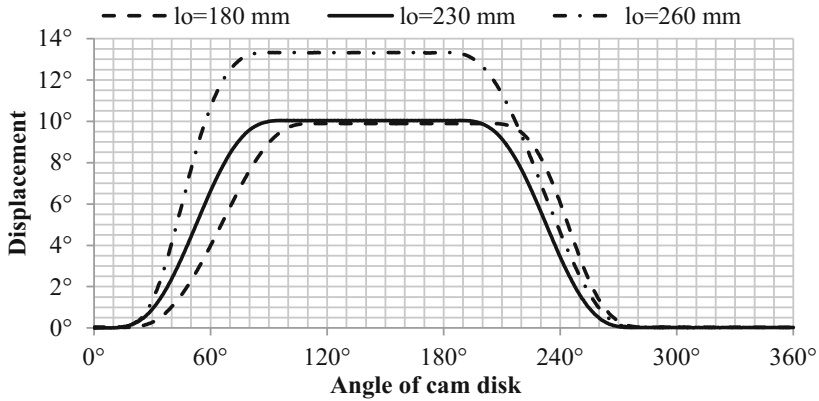


Fig. 3 Change of the transfer function for varying eccentricity and unchanged cam

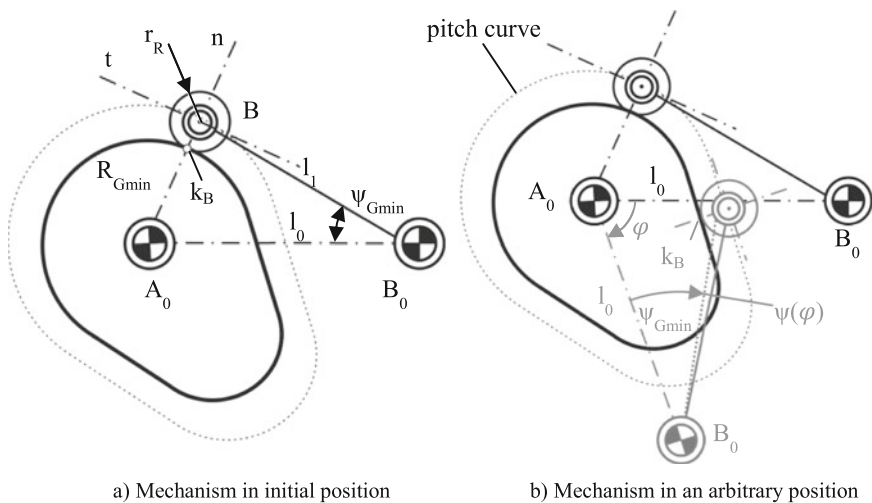


Fig. 4 Approach of calculating the cam curvature for an oscillating roller follower

movement of the mechanism, the approach is based on kinematic inversion. The base link is rotated and the cam is fixed (compare Fig. 4).

The first step is rotating the base from the initial position (Fig. 4a) into an arbitrary position (Fig. 4b) by the angle of the cam disk φ . The second step is the additional rotation of the follower by the angle $\psi(\varphi)$ around the fixed joint B_0 . By this approach the pitch curve can be determined. For the selected follower type, the cam surface is an equally spaced curvature of the pitch curve. Thus, the contact point k_B is shifted by the roller-radius r_R perpendicular to the pitch curve.



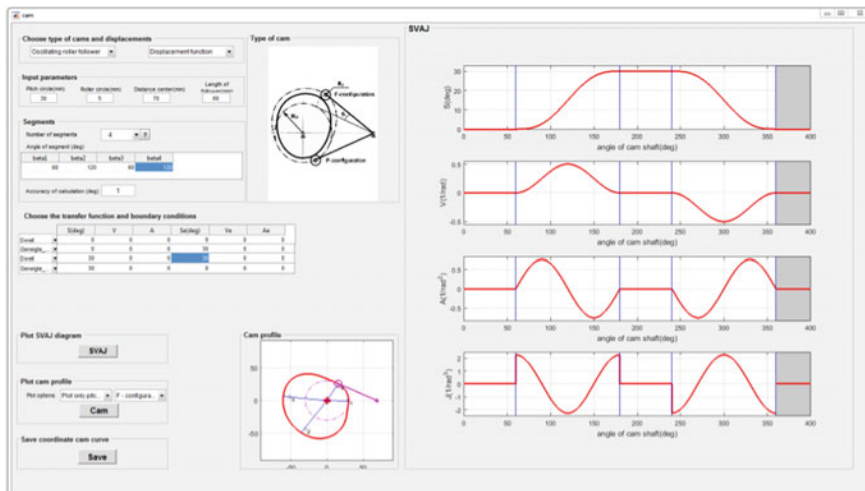


Fig. 5 Cam design program for cam design

This approach has to be done for different cam angles φ to get as many points of the cam surface as needed for the manufacturing process. Since this approach is difficult for the students to do by hand, a cam design program has been developed, which offers an automated calculation of the cam surface. The graphic user interface is shown in Fig. 5. The points of the calculated cam surface can be exported to an Excel sheet which can be imported to a CAD-software to complete the cam design.

Within this program, the most common cam mechanism structures can be selected which are the translating and oscillating followers with roller or flat-face follower. Afterwards, the favored motion task can be specified. Therefore, different segments with different transfer functions and different boundary conditions can be defined. On this basis and the necessary input values like the kinematic parameters of the specific mechanism, the cam surface is calculated. Therefore, the equations for the calculation of the underlying cam surface are implemented in that tool and can be taken from [3, 11]. Hence, the design process is completed.

4 Embodiment Design of the Workbench

Within this chapter the resulting cam workbench is presented. The detailed structure of the workbench is shown in Fig. 6. The main parts of the cam workbench are the two camshafts with their two followers.

Each camshaft has six different cams according to the six realized transfer functions mentioned in Table 1. The joint closure is realized by springs integrated in each follower. To keep balance and reduce occurring vibrations, two adjacent cams are arranged conversely. Both cam shafts have a connection to plug in cams



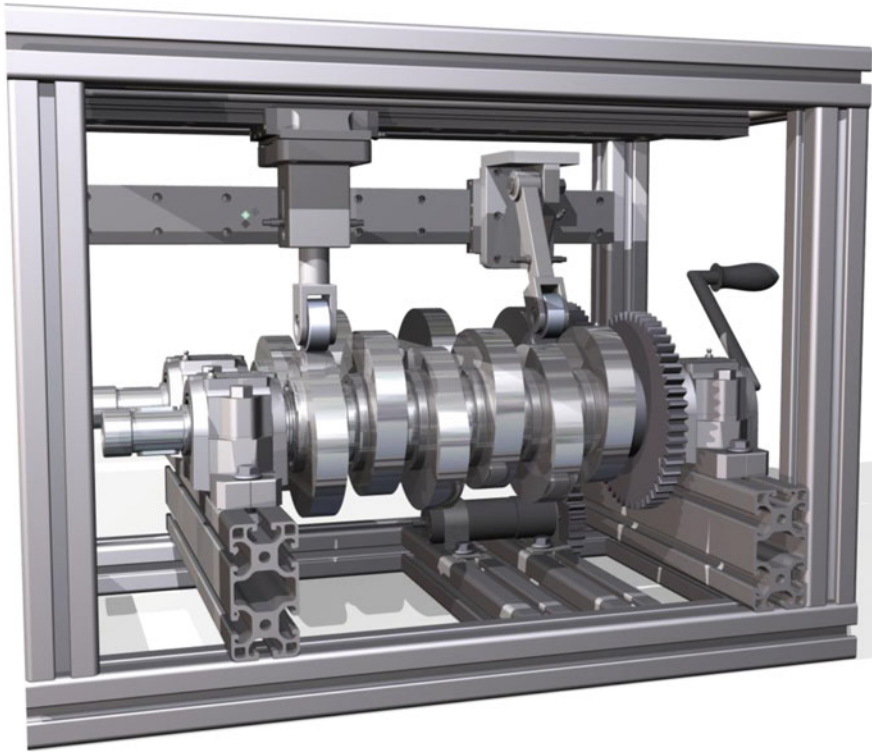


Fig. 6 Design of the cam work bench

designed by students. These can be easily manufactured by 3D-printing. The two cam shafts are equipped on bearing housings and connected with each other by gears. So the integrated electromotor drives both shafts at the same time. To change between the different cams, both followers are mounted on linear bearings. These are connected with the frame flexibly for adjusting the kinematic parameters of the mechanism for changing the pressure angle analog to the description in Sect. 3.2. Relative to the frame, the linear bearing of the translating follower moves horizontally to change the eccentricity of the tappet. In contrast, the linear bearing of the oscillating follower moves vertically to vary the center distance between cam axis and rocker pivot.

5 Conclusions

In this paper, a cam workbench for education use is presented. The cam workbench helps students to sustain their knowledge about cam mechanisms. They can learn the differences between the properties of diverse transfer functions. For both types

of follower, each transfer function is realized by a cam mounted on a camshaft. The transfer functions involve quadratic parabola, 2-3 polynomial, 3-4-5 polynomial, 4-5-6-7 polynomial, sinusoid and cycloidal. The eccentricity of translating follower and the central distance of oscillating follower are both changeable. This can help students to learn the effect of the kinematical length. The entire mechanism is driven by a motor but it can also be actuated manually by a handle.

This cam workbench can not only stimulate students' enthusiasm for learning but impress them with the cam knowledge greatly. It combines education and entertainment effectively.

References

1. Norton, R.L.: Design of Machinery—An Introduction to the Synthesis and Analysis of Mechanisms and Machines, 5th edn. (2011)
2. Bickford, J.H.: Mechanisms for Intermittent Motion, p. 113. Industrial Press Inc., U.S. (1972)
3. Kerle, H., et al.: Getriebetechnik – Grundlagen, Entwicklung und Anwendung ungleichmäßig übersetzender Getriebe, 5. Springer Verlag, Auflage (2015)
4. Horn, M. et al.: A brake-testbench for research and education. In: 16th IEEE International Conference on Control Applications Part of IEEE Multi-conference on Systems and Control (2007)
5. Ottaviano, E., et al.: Numerical and experimental analysis of non-circular gears and cam-follower systems as function generators. Mech. Mach. Theory **43**, 996–1008 (2008)
6. Moon, C.: Cam Design: a Manual for Engineers Designers and Draftsmen. Published by Commercial Cam Division, Emerson Electric Company (1961)
7. Norton, R.L.: Cam Design and Manufacturing Handbook. Industrial Press (2009)
8. VDI: Bewegungsgesetze für Kurvengetriebe – Theoretische Grundlagen VDI 2143 Blatt 1 (2002)
9. Huhn, E.: Die Beziehung zwischen Übertragungswinkel und Abmessungen bei Kurvengetrieben. Maschinenbautechnik 14 (1965)
10. Flocke, K.A.: Zur Konstruktion von Kurvengetrieben bei Verarbeitungsmaschinen. VDI-Forschungsheft 345 (1931)
11. Rothbart, H.A.: Cam Design Handbook. McGraw-Hill Companies (2004)
12. Volmer, J.: Getriebetechnik – Leitfaden, p. 216. Springer Auflage (1987)

Kinematic Characterization of the Origami Spring Based on a Spherical 6R Linkage

Hiroshi Matsuo, Daisuke Matsuura, Yusuke Sugahara and Yukio Takeda

Abstract This paper presents a kinematic characterization of the Origami Spring, which can change its shape from a flat, contracted state to a solid, extended state. Through observation using a real model, the Origami Spring was modelled as a spherical 6R linkage with 3 degrees of freedom (DOF). To obtain a kinematic model, which enables kinematic design of the Origami Spring for real applications, mobility analysis and displacement analysis have been performed. To reveal the actual behavior of the Origami Spring: it behaves like a single DOF, displacement analysis has been formulated as an optimization problem with a single input using objective functions taking into consideration collision between links. Numerical examples were presented to discuss the kinematic characteristics of the Origami Spring.

Keywords Origami spring · Kinematic modeling · Mobility analysis · Displacement analysis

1 Introduction

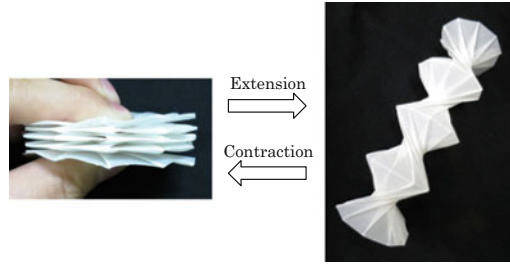
There are various types of Origami that can transform, extend, and contract. The so-called “Origami Spring” [1], invented by Jeff Beynon and Tomoko Fuse, which is shown in Fig. 1, can change its shape from a flat, contracted state to a solid,

H. Matsuo (✉) · D. Matsuura · Y. Sugahara · Y. Takeda
Tokyo Institute of Technology, Tokyo, Japan
e-mail: matsuo.h.ae@m.titech.ac.jp

D. Matsuura
e-mail: matsuura.d.aa@m.titech.ac.jp

Y. Sugahara
e-mail: sugahara.y.aa@m.titech.ac.jp

Y. Takeda
e-mail: takeda.y.aa@m.titech.ac.jp

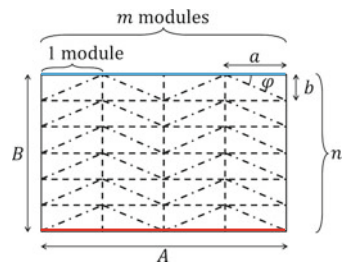
Fig. 1 Origami spring

extended state. By applying the Origami Spring to machines, we can develop new devices that have a high range of extension and contraction, and use them for applications such as object manipulation and human-assisting. For the purpose of applying this unique structure, its mobility and input-output relationship should be clarified. A simple analysis of the Origami Spring structure [2] and an origami-inspired approach to robots [3] have already been done in separate works, but the kinematic characteristics of the Origami Spring remain unclear.

In this research, in order to enable the application of this structure to new devices, the features of the Origami Spring were investigated to obtain a kinematic model. Then, a kinematic characterization was performed by displacement analysis of a spherical 6R linkage as a kinematic model of the Origami Spring, and taking into consideration collision between links.

2 Features of the Origami Spring

The Origami Spring can be fabricated according to the folding diagram shown in Fig. 2. In the diagram, the parameters are the number of modules, m , the number of sides of the regular polygon, n , that are determined by the diagram, and the length of the long and short side of the paper, A and B , respectively. Therefore, the parameters of the right angled triangle are a , b and φ , as illustrated in Fig. 2. The relationships between the parameters are indicated in Eq. (1). The original Origami Spring was made with $n = 12$, which is the version to be analyzed in this paper.

Fig. 2 Folding diagram

$$\varphi = \pi / n, b = B / n, a = b \cot \varphi, A = ma \tag{1}$$

The Origami Spring transforms between the contracted state, which is flat and thin, and the extended state, which has an elongated cylindrical profile. The folds of the Origami Spring function as revolute joints and the motion of the Origami Spring can be seen as a single degree-of-freedom (DOF) linkage. As shown in Fig. 3, when the Origami Spring extends, one of the edges of the paper coils into the inside of the opposite edge. Therefore, there is a limit to the extension caused by edge collisions.

In order to confirm that the Origami Spring can be built with links that have a notable thickness, a simple physical model was constructed from sticks as shown in Fig. 4. The motion of this model was confirmed as comparable to the motion of the Origami Spring made from paper. It additionally has the same limit of extension, as well as a limit on contraction caused by stick collisions.

Fig. 3 Coiling motion with extension

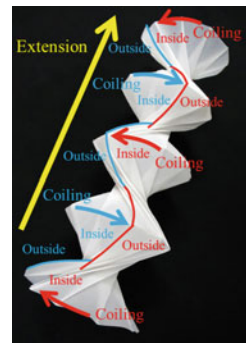
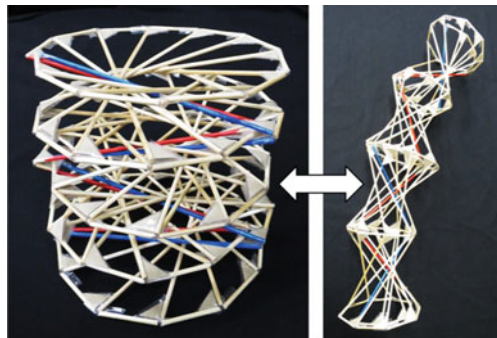


Fig. 4 Simple physical model



3 Theoretical Kinematic Characterization

In order to analyze the mobility of the Origami Spring, a fundamental composition of the Origami Spring was derived, as shown in Fig. 5. Since the axes of rotation of the sixfolds as 6-revolute joints intersect at a single point, and a spherical 6R linkage with 3 DOF is obtained as a kinematic model. In addition to this, a boundary condition should also be considered that in the theoretical motion of the Origami Spring, the planes of each module which are made by the short sides of the right angled triangles, should be spatially parallel as shown in Fig. 6. When this boundary condition is taken into account, the revolute joints 2 and 6 become unable to move, and a spherical 4R linkage is obtained as a simplified kinematic model as illustrated in Fig. 6. According to this result, the DOF of the Origami Spring then becomes 1 as anticipated. This is a simplest theoretical kinematic characterization of the Origami Spring, although the thickness of links and collision between them are not considered.

The theoretical kinematic configuration of the Origami Spring is calculated based on following analysis. There are three essential variables, θ_1 , θ_2 and θ_3 , as shown in Fig. 7. The angle between the right angled triangle and the lower plane is θ_1 (Fig. 7a), the angle between neighbored right angled triangles 1 and 2 is θ_2 (Fig. 7b) and the angle between the short sides of the right angled triangles is θ_3 (Fig. 7c), respectively. Among them, θ_1 is given as an independent parameter, and θ_2 and θ_3 are considered as dependent parameters. The results of the calculations are shown in Fig. 8, which represent the consequent theoretical motion.

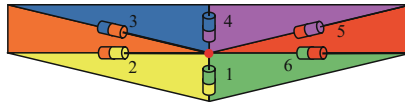


Fig. 5 Spherical 6R linkage model

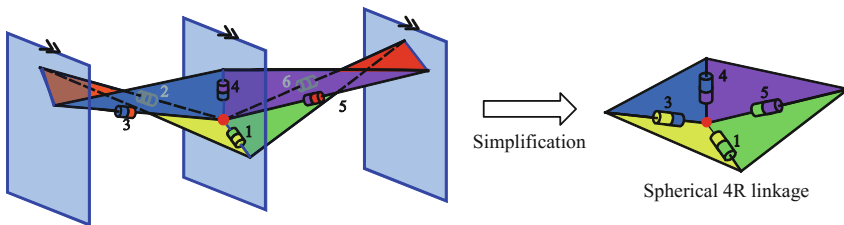


Fig. 6 Simplification arising from the boundary conditions

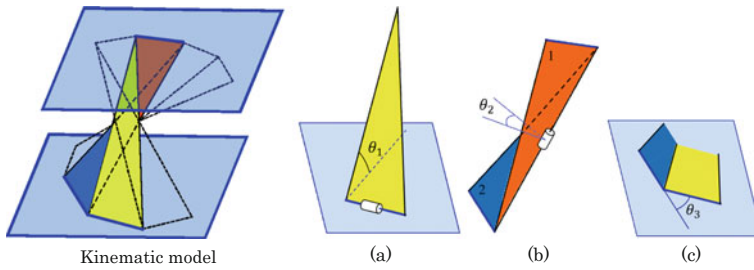


Fig. 7 Definition of variables

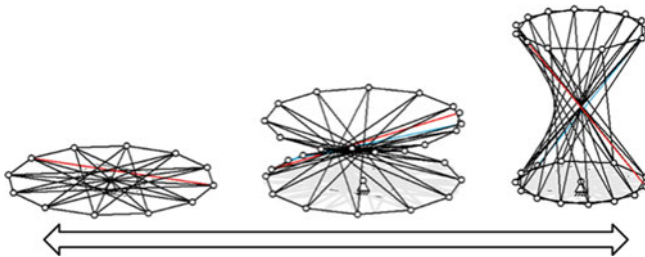


Fig. 8 Theoretical motion of the Origami Spring

4 Practical Kinematic Characterization

There are several in-negligible key differences between the above theoretical motion and the real motion of the Origami Spring. In the theoretical case, the locus of the coiling motion is a perfectly round shape. However, that of the real coiling motion is a spiral in a plane as shown in Fig. 9. The real Origami Spring thus poses bending along the coiling motion’s spiral locus during extension as shown in Fig. 10, while the theoretical Origami Spring extends vertically. These differences occur due to the thickness of the links and collision between them, and are inevitable during the extension and contraction of the Origami Spring. Namely, these two are resultant motion from the extension-contraction motion. According to this relation, the spiral locus and the bending can be considered as a parasitic motion of the Origami Spring. In order to precisely describe the real motion of the

Fig. 9 Locus of the coiling motion

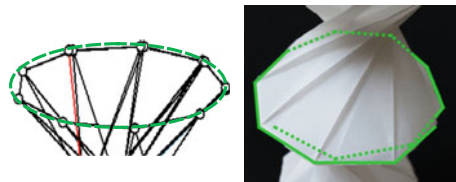


Fig. 10 Bending during extension of the real mechanism

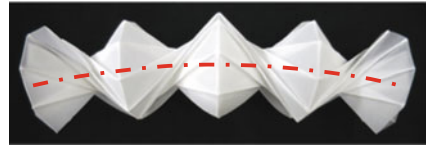
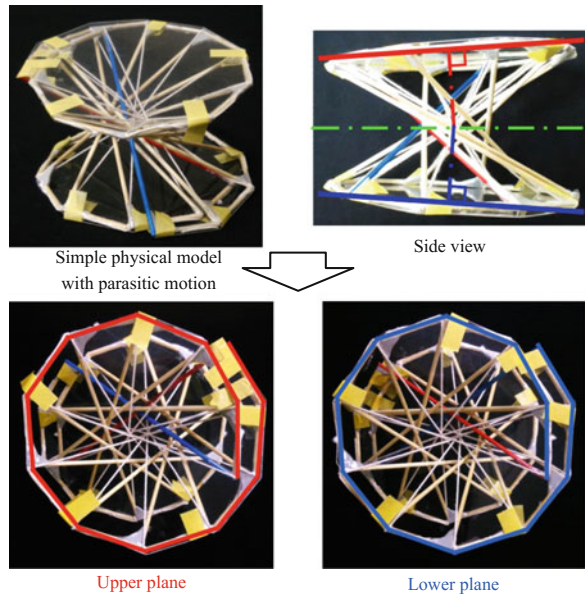


Fig. 11 Spiral loci in the simple physical model



Origami Spring and to enable application of it for new devices, this parasitic motion should be analyzed.

When the links have a notable thickness, the short sides of the right angled triangles (the top and bottom edges in the side and isometric views of Fig. 11) keep creating two planes as seen in the above kinematic model, however these planes are no longer parallel to each other when the bending motion is taken into account. For the purpose of investigating the case of the parasitic motion, the bottom and top edges of the simple physical model (which consists of only one module) were fixed to a pair of plates made of a typical plastic for better representation of the lower and upper planes. From this model, displayed in Fig. 11, the two planes are indeed shown to be non-parallel, and the lower and upper spiral locus are line-symmetric to each other. Based on this simple observation, it is hypothesized that the spiral loci are line-symmetric for the real case of the mechanism.

Taking the parasitic motion into consideration, the mobility of the Origami Spring was then re-analyzed. According to the simplified spherical 4R linkage, the overall DOF of the theoretical Origami Spring was 1. On closer observation, the simple physical model showed that the revolute joints 2 and 6 did not move in the

Fig. 12 The practical model a spherical 6R linkage

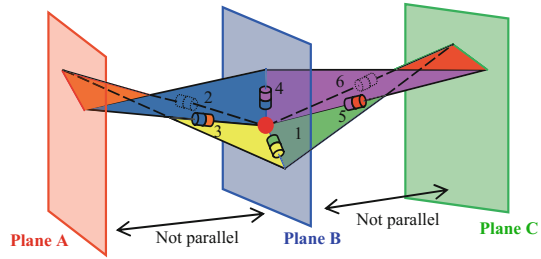
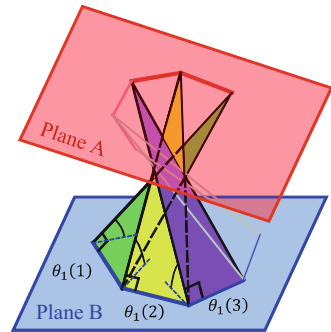


Fig. 13 Inputs of the practical model



previous model but did move in the physical model actually. Knowing this, its kinematic model then returns to the spherical 6R linkage as shown in Fig. 12. When the boundary condition that the edges of the physical model are in two separate planes are considered, the mobility of an entire Origami Spring as the practical model becomes 3, as illustrated in Fig. 13. The inputs are then $\theta_1(1)$, $\theta_1(2)$ and $\theta_1(3)$; the angles between the plane B and the right angled triangles whose short side exists in the plane B.

Based on the analysis results, the mobility of the practical kinematic model is 3. On the other hand, the real Origami Spring behaves like a single DOF mechanism, which demonstrates an unanticipated difference in mobility. In order to eliminate this difference and correctly represent the kinematics of the real Origami Spring with only one input, new boundary conditions are introduced. The additional boundary condition which has not been considered yet is collision between the individual links. There are 13 cylindrical links which correspond to the long sides of the right angled triangles, which may satisfy the remaining boundary conditions, as the 1st link contacts the 13th link and the $i + 1$ th link is always above the i th link ($i = 1$ to 13 and when $i = 13$, $i + 1 = 1$), as illustrated in Fig. 14. Using these boundary conditions, $\theta_1(2)$ and $\theta_1(3)$ would then be determined with respect to $\theta_1(1)$ and the link thickness d . This was formulated as an optimization problem with the objective functions G_1 , G_2 and G based on the boundary conditions defined in the following equations.

Fig. 14 Relation between two links

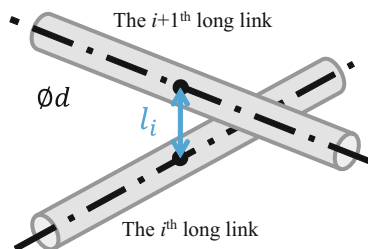


Table 1 Example of the optimization result

$\theta_1(1)$ (°)	30	35	40	45	50	55
G_1	0	0	0	0	0	+
G_2	+	0	0	0	0	
$\theta_1(2)$ (°)	(27.0)	31.4	35.9	40.7	45.4	
$\theta_1(3)$ (°)	(24.9)	28.9	32.5	36.2	40.0	
Angle of the upper plane (°)	(10.0)	11.4	12.3	13.5	15.0	

$$G_1 = (l_{13} - d)^2 \quad (2)$$

$$G_2 = \sum_{i=1}^{13} g_i \left(\begin{array}{ll} \text{when } l_i - d \geq 0; & g_i = 0 \\ \text{otherwise;} & g_i = (l_i - d)^2 \end{array} \right) \quad (3)$$

$$G = G_1 + G_2 \quad (4)$$

In the optimization, the sought area satisfies the condition where the objective function G_2 becomes 0 with $\theta_1(2)$ and $\theta_1(3)$ changing by 0.1° . From this, the pair of $\theta_1(2)$ and $\theta_1(3)$ where the objective function G_1 is smaller than the threshold is determined as the most likely solution obtained from the optimization problem. After $\theta_1(2)$ and $\theta_1(3)$ are successfully determined by optimization, the objective function becomes $G = 0$. It can be said that a determination of practical kinematic model having 1-DOF is possible when optimum solution of a couple of $\theta_1(2)$ and $\theta_1(3)$ is uniquely obtained as dependent on a given input $\theta_1(1)$, and this is actually possible. For example, if the link thickness is fixed as $d = 1.0$ mm, and range for $\theta_1(1)$ is given from $30 < \theta_1(1) < 55^\circ$, then the resulting optimization outputs the results shown in Table 1 and Fig. 15.

In the results, $\theta_1(2)$ and $\theta_1(3)$ are determined to have unique solutions depending on given input $\theta_1(1)$ in the range of $35 < \theta_1(1) < 50^\circ$. Additionally, the resulting contraction limit is $30 < \theta_1(1) < 35^\circ$ and the extension limit is $55 < \theta_1(1) < 50^\circ$. However, the real limit to contraction as observed from the physical model is approximately $\theta_1(1) = 12^\circ$ and the real limit to extension is about $\theta_1(1) = 53^\circ$. Therefore, the extension limit from the results closely matches that of

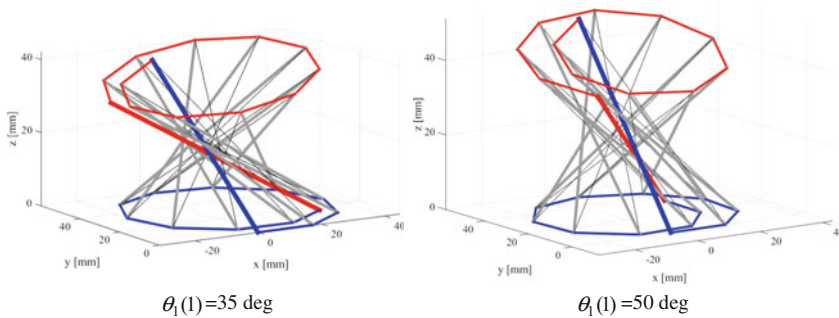


Fig. 15 Optimization result

the real Origami Spring, while on the other hand the contraction limit is inconsistent with the real one.

The angle of the upper plane also increases with $\theta_1(1)$. This result correctly indicates the bending during extension of the real Origami Spring. As for the spiral loci, the lower and upper spiral loci are line-symmetric when $\theta_1(1) = 35^\circ$. However, the difference becomes larger with increasing $\theta_1(1)$, which does not match with the prior hypothesis.

In the results, the contraction limit and the line-symmetry of the spiral loci differ from those of the real Origami Spring. The authors hypothesize that these differences might be caused by the boundary conditions. At the contraction limit, all of the long links should be in contact with each other. However, it is difficult to determine that exact point using the currently considered boundary conditions. Furthermore, in the real Origami Spring, the links might become bent by collisions, so the real contraction limit may be smaller than the contraction limit derived from the optimization. For the spiral locus, the optimization with the current boundary conditions regards only in the case where the 1st cylindrical link contacts with the 13th link as the solution, but other cases where the other links make contact could provide other solutions. In addition, there is a possibility that further solutions could be obtained by increasing the optimization resolution. In accordance with this, the evaluation functions should be reconsidered and more detailed optimization would be carried out.

5 Conclusions

In this paper, the Origami Spring was modeled as a spherical 6R linkage, and its kinematic characterization was performed by considering collision between links. To construct a practical kinematic model, displacement analysis was formulated as an optimization problem with objective functions taking into consideration the thickness of the links. The obtained results were compared with the observations

using a real model, and discussed. Future work includes the determination of the objective function and more detailed investigation which can model the real behavior of the Origami Spring.

References

1. Fuse, T.: SPIRAL Origami Design Art. Vieweg Verlag (2012). ISBN 978-3-941327-06-1
2. Min, C.C., Suzuki, H.: Geometrical properties of paper spring. In: Manufacturing Systems and Technologies for the New Frontier. Springer, London (2008)
3. Onal, C.D., Wood, R.J., Rus, D.: An origami-inspired approach to worm robots. IEEE/ASME Trans. Mechatron. **18**(2), 430–438 (2013)

Scaled Test Stand Simulation for Studying the Behavior of Anti-lock Brake Systems on Bumpy Roads

V. Ciupe, D. Mărgineanu and E.-C. Lovasz

Abstract The paper presents a design concept for a scaled-down test stand that allows studying of various possible anti-lock brake system algorithms, by considering a quarter car model traveling over an uneven road surface (a bumpy road, or a road with continuous variable friction coefficient), represented by a rolling inertial tambour track, in contact with an articulated braking wheel. The concept is transposed in a CAD model simulation where motion analysis can be conducted. Also a software application is designed for generating a road surface profile (for the CAD model) and verifying it against the real motion of a smart servo motor. The combined simulation results prove the viability of the concept and encourage the authors to further develop this scaled test stand.

Keywords Anti-lock brakes · Scaled test stand · Bumpy roads · Smart servo · Simulation

1 Introduction

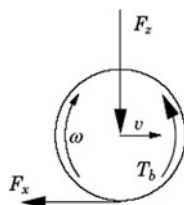
A top priority for automotive engineers and researchers alike is to make vehicles and roads safer for everyone. One way is enhancing the ability to brake and steer safely in difficult road conditions, by having the anti-lock braking system installed.

The ABS is now available as standard equipment on all passenger vehicles with the main goal of improving vehicle steering ability during hard braking, by preventing wheel locking. This phenomenon can occur if the applied braking torque surpasses the value of the rolling friction force so that the tire stops rotating and

V. Ciupe (✉) · D. Mărgineanu · E.-C. Lovasz
Politehnica University of Timisoara, Timisoara, Romania
e-mail: valentin.ciupe@upt.ro

D. Mărgineanu
e-mail: dan.margineanu@upt.ro

E.-C. Lovasz
e-mail: erwin.lovasz@upt.ro

Fig. 1 Quarter car model

starts sliding onto the road surface. Consequently the steering of the vehicle is almost impossible and also the stopping distance increases. The ABS system mitigates this aspect by alternating the stopping pressure in the wheel's brake caliper with a certain frequency and duty cycle by freeing-up the brake and allowing the wheel to roll and then re-applying maximum pressure and locking the wheel. This fast cycling of the pressure (5–10 times a second) tries to emulate a mean tire slip percentage of about 10–20 %, which is the interval where, for almost all types of road surface, the friction coefficient is at its highest values [1].

As an option to study and enhance the ABS algorithms the quarter car model of a car can be employed (Fig. 1) [2].

The present paper proposes the design of a scaled test stand based on this model that can be able to simulate braking of a wheel that travels over a bumpy road surface, so that different anti-lock algorithms can be employed to increase the braking-steering efficiency over an uneven road surface. Scaled test stands have been used in automotive industry for a long time and, for antilock brake systems, similar stands were approached before [3, 4] for testing braking algorithms on even road surfaces.

2 The Scaled Stand Design Concept

Figure 2 depicts a simplified CAD model of the scaled test stand, developed using SolidWorks. All elements are geometrically constrained in such a way that motion analysis can be applied upon the mechanism. Also the balancing weights are applied on the model (Figs. 2, 3) and a Dynamixel smart servo motor [5] was selected for road surface profile replication.

In order to observe both the vertical swing of the track-wheel assembly, an oscillating motion was imposed to the servo model's output shaft with an angular range in the interval $[\frac{\pi}{2} \dots \frac{3 \cdot \pi}{2}]$, and another continuous rotational motion was applied to the track tambour.

For a better understanding of this application, a schematic equivalent of the stand in depicted in Fig. 3, where some of the dimensional constraints have been preset in order to facilitate the CAD model generation and further calculation of required values: $a = b/2 = 20$ mm, $c_1 = c_2 = e_2 = d = 120$ mm, $r_1 = 70$ mm, $r_2 = 100$ mm, $e_3 = 40$ mm. The decision of selecting certain dimensions from the start is due to some pieces of equipment being already available for building the physical scaled stand.

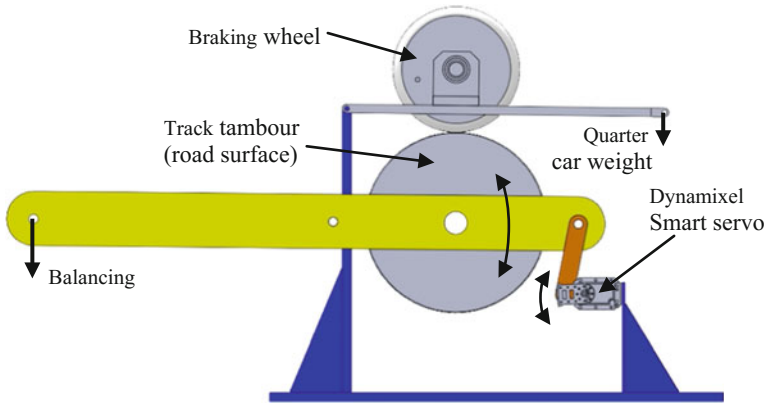


Fig. 2 Scaled stand CAD model

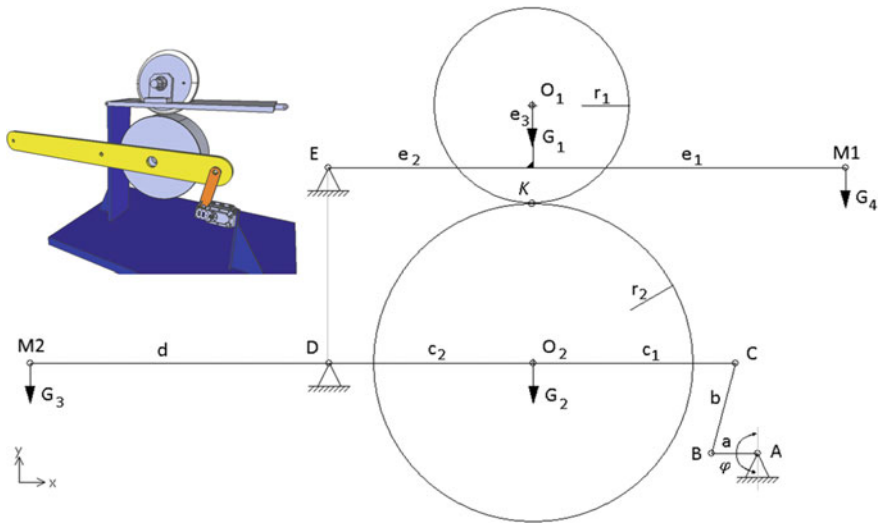


Fig. 3 Scaled stand equivalent schematic (inset perspective CAD model)

To be able to analyze the motion of the track tambour when imposing various angular values to the smart servo, two four bar linkage mechanisms are presented in Fig. 4 and the vertical stroke of point K is extracted.

By considering the first four bar linkage ABCD (Fig. 4a) and its closed loop vector equation written in complex number form, the following results:

$$l_1 \cdot e^{i \cdot \varphi} + l_2 \cdot e^{i \cdot \beta} = (x_D + i \cdot y_D) + l_3 \cdot e^{i \cdot \psi} \tag{1}$$

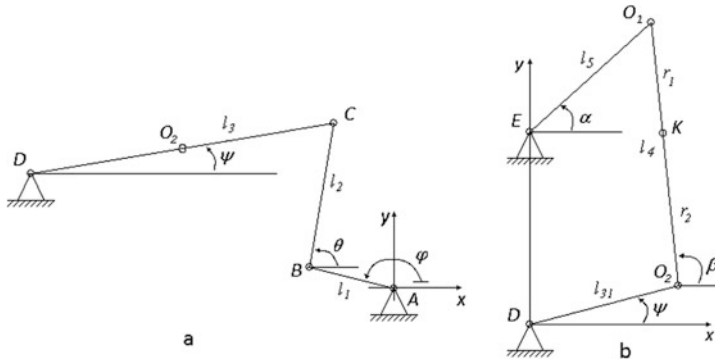


Fig. 4 **a** Tambour oscillation equiv. mechanism; **b** contact point K oscillation equiv. mechanism

The computation of the angle $\psi(\varphi)$ from the Eq. (1) follows by isolating of the term which contains the angle ϑ and by multiplication with its conjugate complex vector equation:

$$\begin{aligned} l_2 \cdot e^{i \cdot \vartheta} &= (x_D + i \cdot y_D) - l_1 \cdot e^{i \cdot \varphi} + l_3 \cdot e^{i \cdot \psi} \\ l_2 \cdot e^{-i \cdot \vartheta} &= (x_D - i \cdot y_D) - l_1 \cdot e^{-i \cdot \varphi} + l_3 \cdot e^{-i \cdot \psi} \end{aligned} \quad (2)$$

The result of the multiplication is the transmission function of the first order of the considered four bar linkage:

$$\begin{aligned} 0 &= x_D^2 + y_D^2 + l_1^2 - l_2^2 + l_3^2 - 2 \cdot l_1 \cdot x_D \cdot \cos \varphi + 2 \cdot l_1 y_D \cdot \sin \varphi \\ &+ 2 \cdot l_3 \cdot x_D \cdot \cos \psi - 2 \cdot l_3 \cdot y_D \cdot \sin \psi - 2 \cdot l_1 \cdot l_3 \cdot \cos(\varphi - \psi) \end{aligned} \quad (3)$$

The computing of the transmission function $\psi(\varphi)$, having angle φ placed in the selected quadrants, is accomplished by:

$$\psi(\varphi) = 2 \cdot \operatorname{atan} \left(\frac{B1(\varphi) - \sqrt{A1(\varphi)^2 + B1(\varphi)^2 - C1(\varphi)^2}}{A1(\varphi) - C1(\varphi)} \right) \quad (4)$$

where: $A1(\varphi) = 2 \cdot l_3 \cdot (x_D - l_1 \cdot \cos \varphi)$; $B1(\varphi) = 2 \cdot l_3 \cdot (y_D - l_1 \cdot \sin \varphi)$;
 $C1(\varphi) = (x_D^2 + y_D^2) + l_1^2 - l_2^2 + l_3^2 - 2 \cdot l_1 \cdot (x_D \cdot \cos \varphi + y_D \cdot \sin \varphi)$.

By considering another equivalent four bar linkage DO_2O_1E (Fig. 4b) and writing the closed loop vector equation referencing in point D :

$$l_{31} \cdot e^{i \cdot \psi} + l_4 \cdot e^{i \cdot \beta} = l_5 \cdot e^{i \cdot \alpha} + i \cdot (y_E - y_D) \quad (5)$$

a similar procedure can be employed for computing the equiv. coupler angle $\beta(\psi(\varphi))$:

$$\beta(\psi(\varphi)) = 2 \cdot \operatorname{atan} \left(\frac{B2(\psi(\varphi)) + \sqrt{A2(\psi(\varphi))^2 + B2(\psi(\varphi))^2 - C2(\psi(\varphi))^2}}{A2(\psi(\varphi)) - C2(\psi(\varphi))} \right) \quad (6)$$

where: $A2(\psi(\varphi)) = 2 \cdot l_{31} \cdot l_4 \cdot \cos \psi(\varphi)$; $B2(\psi(\varphi)) = 2 \cdot l_4 \cdot (l_{31} \cdot \sin \psi(\varphi) - y_E + y_D)$; $C2(\psi(\varphi)) = (y_E - y_D)^2 + l_{31}^2 + l_4^2 - l_5^2 - 2 \cdot l_{31} \cdot (y_E - y_D) \sin \psi(\varphi)$

Knowing the oscillating angles ψ and β and accepting that the point K belongs to the equivalent coupler, the coordinates of the contact point K can be determined:

$$\begin{aligned} x_K(\varphi) &= l_{31} \cdot \cos \psi(\varphi) + r_2 \cdot \cos \beta(\psi(\varphi)) \\ y_K(\varphi) &= l_{31} \cdot \sin \psi(\varphi) + r_2 \cdot \sin \beta(\psi(\varphi)) \end{aligned} \quad (7)$$

By numerically solving the above expressions a total value $y_K(\varphi) = 20$ mm is obtained (approx. ± 10 mm) which is appropriate for the scope of the scaled test stand.

3 Solution Implementation

The scaling of the system is achieved by conserving the volumetric density of an average vehicle traveling at a maximum constant speed of $v_I = 15$ m/s. For this purpose a vehicle was selected, having an inertial mass of $m_I = 1400$ kg (considered with 2 passengers and luggage), and overall outside dimensions of $4.2 \times 1.8 \times 1.5$ m.

3.1 System Scaling

The scaling factor is dependent of the already existing equipment (the braking wheel, with an outer diameter of 140 mm) having a dimensional reducing proportionality K_S value of 4.6. The volumetric density of the full size vehicle, considering the values given above, is $\rho = 123.5$ kg/m³.

The virtual scaled vehicle should then have a mass of 14.38 kg resulting a virtual quarter car model inertial mass of $m_Q = 3.59$ kg, traveling at $v_Q = 3.26$ m/s, as per Eq. (8).

$$m_Q = \frac{m_I}{4 \cdot K_S^3}; v_Q = \frac{v_I}{K_S}. \quad (8)$$

Since the scaled stand concept consists of a rotating track tambour (the road surface) it means that the mass that needs to be stopped by the braking wheel is

transferred as the inertial mass of the track tambour, m_D , rotating with the angular velocity ω . In order to obtain this mass a kinetic energy equilibrium must be enforced between the two components, $E_K = E_R$:

$$E_K = \frac{m_Q \cdot v_Q^2}{2}; E_R = \frac{J \cdot \omega^2}{2} \quad (9)$$

Considering a simplified approach where the track tambour is a disc with uniformly distributed mass and the rotating braking wheel (not braking it yet!) has non-slip contact with the track tambour (same peripheral velocity), the following assumptions can be made: the angular velocity of the track is $\omega = v_Q/r_D$ and the inertial moment of the disc is $J = m_D \cdot r_D^2/2$, where r_D is the tambour/disc radius (imposed at 100 mm). Then the energy equilibrium gives Eq. (10):

$$\frac{m_Q \cdot v_Q^2}{2} = \frac{m_D \cdot r_D^2 \cdot v_Q^2}{4 \cdot r_D^2}; m_D = 2 \cdot m_Q, \quad (10)$$

resulting that the track tambour mass must be $m_D = 7.18$ kg. For an aluminum disc of $r_D = 100$ mm this gives a tambour width of approx. 85 mm.

Further considering that a balancing mass of 12 kg applied at point $M2$ (Fig. 3) keeps the system in static equilibrium and that $c_1 = c_2 = d = 120$ mm, the necessary torque for accelerating the system with $\alpha = 4\pi$ rad/s² must be determined as per Eq. (11):

$$\tau_Q = J_S \cdot \alpha; \tau_Q = \sum m_S \cdot r_S^2 \cdot \alpha \quad (11)$$

where: m_S are the total inertial stand masses rotating about point D , in total approx. 24 kg; r_S is the inertial masses' gyration radius, $r_S = c_2$ (Fig. 3) and τ_Q is the required inertial torque, $\tau_Q = 4.34$ Nm.

Then the necessary input torque T_S from the servo-motor can be expressed as:

$$T_S = \tau_Q \cdot \frac{\omega_{c2}}{\omega_a} \quad (12)$$

where: ω_{c2} is the angular velocity of the oscillating arm (c_2 in Fig. 3); ω_a is the angular velocity of the servo shaft and T_S is the required servo torque, $T_S = 0.22$ Nm.

Since the maximum torque developed by the selected servo motor is 2.5 Nm [5], it can be considered as perfectly suitable for this task.

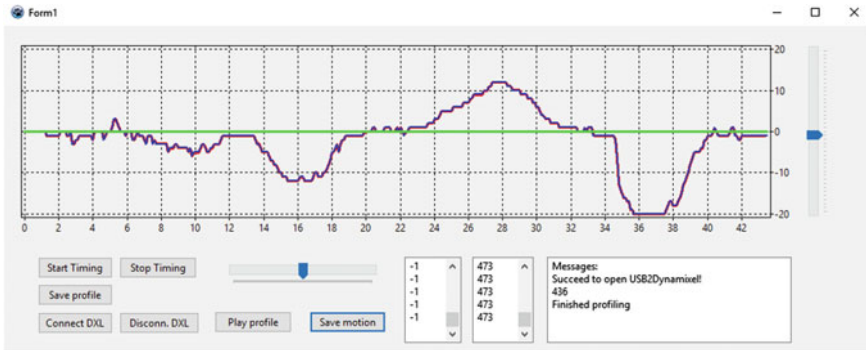


Fig. 5 Road profile generation application

3.2 Profile Generation

In order to be able for the motion analysis package of SolidWorks to reproduce a certain road surface profile, the servo shaft angular position values must be taken from a formatted data file [6].

This file is produced using a custom built software application where the user can graphically impose a longitudinal road profile with the desired dips and bumps (Fig. 5) in real time, by moving the slider on the right. Once the profile is considered complete it can be saved in a csv data file with a time base of 0.1 s.

At this point the generated profile can be tested on the scaled test stand by connecting via a USB port the smart servo motor [7]. The servo will attempt to follow the profile and will return its actual position for the current time, which will be plotted over the user imposed graph.

The values returned from the servo can also be saved and used further, and it can be inspected if the motor lags behind the originally imposed values. The program also allows the user to manually move the servo and record its actual positions for further analysis or reference.

Upon saving the desired data file which contains the timestamp and angular position for each record, it can be transferred to the motion analysis package.

4 Simulation Results

Once the profile data file has been imported as position values and the motion analysis has completed the vertical stroke of a point (K) from the model, this can be plotted and exported as another csv data file. Also the model is now animated following the virtual motion of the servo shaft angular positioning. The resulting values are graphically represented in Fig. 6. It can be noted that the resulting motion follows the imposed road profile, but having some deviations towards the



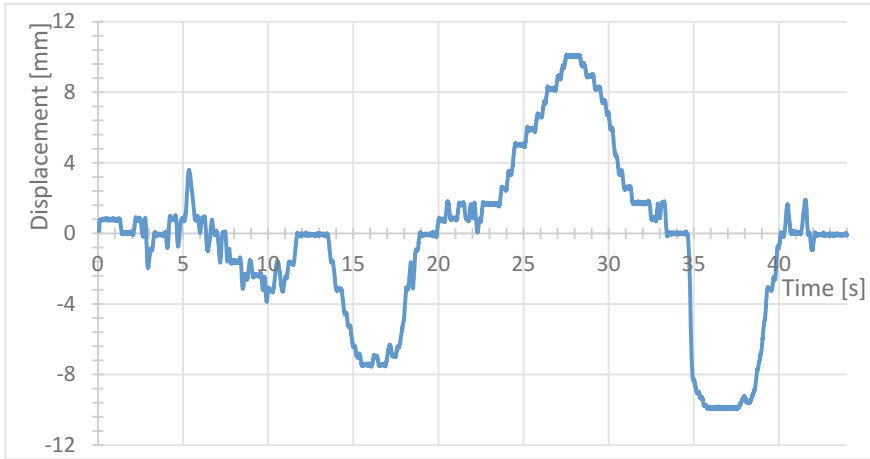


Fig. 6 Simulation result of track tambour vertical movement

angular limits, due to the non-linearity resulting from the angle dependencies $\psi(\varphi)$ and $\beta(\psi)$.

It can also be observed that the vertical stroke of the tambour is near ± 10 mm, which is consistent with the numeric modelling and, considering the dimensional scaling factor of the stand, equates to an equivalent vertical motion of the full size vehicle of ± 46 mm. This limit is acceptable since bumps or dips in the road surface having such an abrupt maximum height/depth are at the limit of driving, taking into account the imposed initial speed of 15 m/s.

5 Conclusions

Previous tests done on a similar scaled test stand demonstrate that this approach is a viable solution.

By adding the controlled vertical motion of the track tambour new ways of studying the behavior of anti-lock algorithms can be developed. Two distinct aspects are presented through this vertical motion: the simulation of a bumpy road or with a sudden dip or bump, and the simulation of a road surface with continuous variable friction coefficient (if the vertical travel of the braking wheel is restricted).

The results of the CAD model motion analysis enforces the viability of the concept and gives momentum for further developing the test stand, into a practical experimentation platform (for both research and didactical activities). Future work will concentrate on completing the building of the stand, following the presented concept and developing an integrated hardware-software design which should be able to combine and analyze wheel braking with the track vertical motion. Also a suspension component should be present to better simulate real conditions.

References

1. Canudas de Wit, C., Tsiotras, P.: Dynamic tire friction models for vehicle traction control. In: Proceedings of the 38th IEEE Conference on Decision and Control, vol. 4, Phoenix AZ, USA, pp. 3746–3751 (1999). doi:[10.1109/CDC.1999.827937](https://doi.org/10.1109/CDC.1999.827937)
2. Ciupe, V., Maniu, I.: Small scale stand for testing different control algorithms on assisted brake systems. In: Proceedings of the 12th World Congress in Mechanism and Machine Science, IFToMM, Besancon, France (2007)
3. Ciupe, V. et al.: Scaled experimental stand for testing control algorithms on brake systems with anti-lock capability. *Robot. Autom. Syst.* **166–167**, 121–126 (2010). doi:[10.4028/www.scientific.net/SSP.166-167.121](https://doi.org/10.4028/www.scientific.net/SSP.166-167.121)
4. Longoria, L.G., Al-Sharif, A., Patil, C.: Scaled vehicle system dynamics and control: a case study on anti-lock braking. *Int. J. Veh. Auton. Syst.* **2**(1/2), 18–39 (2004)
5. Robotis Inc: Dynamixel RX-24F Smart Servo e-Manual. http://support.robotis.com/en/product/dynamixel/rx_series/rx-24f.htm. Accessed 03 16
6. Dassault Systemes: SolidWorks online help—defining profiles by importing or manually entering data points. http://help.solidworks.com/2012/English/SolidWorks/motionstudies/t_functions_from_Imported_Data.htm. Accessed 03 16
7. Ciupe, V. et al.: Testing the haptic exoskeleton actuators in a virtual environment. In: The 14th IFToMM World Congress, Taipei (2015). doi:[10.6567/IFToMM.14TH.WC.PS13.015](https://doi.org/10.6567/IFToMM.14TH.WC.PS13.015)

Part VI
MTM—Terminology

Activities of Russian—Speaking Scientists in Development of MMS Terminology

V.E. Starzhinsky, E.V. Shalobaev, M.M. Kane and V.I. Goldfarb

Abstract Participation of scientists from CIS and former USSR countries in development of terminology for Mechanism and Machine Science (MMS) is considered. Identification of notions in the field of MMS as well as in the frame of IFToMM Permanent Commission “Standardization of Terminology for MMS” activity at execution of other programs is analyzed. Analysis is provided for IFToMM Terminology in general, and specifically for the following sections: Gearing, Quality Factors of Machines and their Components. Problems of gear drive types classification and gear failure modes are discussed too.

Keywords Theory of mechanisms and machines (TMM) • Mechanism and machine science • IFToMM terminology • Classification of gear drives • Gear failure modes

V.E. Starzhinsky (✉)

Metal Polymer Research Institute of National Academy of Sciences of Belarus,
Gomel, Belarus

e-mail: star_mpri@mail.ru

E.V. Shalobaev

Saint-Petersburg National University of Informative Technologies,
Mechanics and Optics, Saint-Petersburg, Russia

e-mail: shalobaev47@mail.ru

M.M. Kane

Belarus National Technical University, Minsk, Belarus

e-mail: metech@bntu.by

V.I. Goldfarb

Izhevsk State Technical University, Izhevsk, Russia

e-mail: veniamingoldfarb@yahoo.com

© Springer International Publishing AG 2017

B. Corves et al. (eds.), *New Advances in Mechanisms,*

Mechanical Transmissions and Robotics, Mechanisms and Machine Science 46,

DOI 10.1007/978-3-319-45450-4_21

1 Introduction

It is notoriously known that terminology plays an essential role in effective functioning and developing of the respective scientific discipline. It should follow specific principles of elaboration: every notion and definition should be multiply rechecked in any terminological system. In the former USSR common principles of architecture and ordering system of terms in the field of Theory of Mechanisms and Machines (TMM) have been elaborated by Committee of Scientific-Technical Terminology of the USSR Academy of Sciences [1–3]. On the basis of the above [1–3] numerous collections of recommended terms on different branches of knowledge have been composed and edited. Significant role in the art of unification of terminology and propagation of perfect notions in mechanics and allied disciplines have been performed by publishing dictionaries [4–6].¹

Here it is pertinent to note that Prof. N.I. Levitskij, the author of publications [4, 6], is a famous Soviet Scientist in TMM; his scientific carrier started in Moscow Aeronautical Institute (1944–1948), then his activity was associated with Institute of Machine Science of Academy of Sciences of the USSR (from 1946).

2 Activities at Preparation of “IFToMM Terminology”

Similar work in TMM Terminology has been started in IFToMM Permanent Commission “Standardization of Terminology for MMS” (PCA) established by the IFToMM Executive Council in 1969 at IFToMM formation. Prof. D.S. Muster (USA) and Prof. N.I. Levitskij (USSR) were from the ground up of PCA activity as its Chairman and Vice-Chairman accordingly [8]. It is reasonable to present IFToMM Terminology according to the following schedule: paper 1991 [9], paper 2003 [10] and electronic [11] versions.

“IFToMM Terminology-1991” (hereinafter “Term-91”) [9] was created on the base of “IFToMM Terminology-83” (hereinafter “Term-83”) [12] which includes 5 Chaps. (0–4) + Appendix; 742 terms in English only; Chapters are arranged as natural divisions of TMM; terms—in order of importance [13]. During the Working Meetings (from 1984 till 1990) the German, French and Russian versions have been refined. Based on “Term-83”, other dictionaries for TMM, including others languages—Bulgarian (1965), Romanian (1989), Georgian (2008), Armenian (2009), have been edited (see references in [8]).

Russian version of Terminology has been prepared by Prof. Y.L. Sarkissyan and presented at the 9th Working Meeting (1987, Seville, Spain).

¹All terms in [4–7] have been adduced in Russian, English, German, French. Quantity of terms: [4]—69, [7]—187, [5]—139.

Prof. Y.L. Sarkissyan (Yerevan Polytechnic Institute, since 1971—Armenian State Technical University) was nominated for a member of the PCA in 1983 as a USSR delegate and Russian editor. For the first time ever he took part in PCA 6th Working Meeting (1983, Delhi, India) and then—in 13th one (1991, Prague, Czechoslovakia) (more detailed scientific biographies of USSR and CIS-countries scientists see in [14]). It is pertinent to note that the first works on the four-link mechanisms were published by Prof. Y.L. Sarkissyan as a co-author of Prof. N.I. Levitskij (see, for example [15]).

Final version of four-language IFToMM Terminology “Term-91” [9] contains 5 Chaps. + Appendix; 746 terms in English, French, German and Russian; Chapters and terms were arranged the same as in [12].

In 2000, as is known [16, 17], the notion MMS was adopted by the IFToMM Community instead of the TMM notion. New IFToMM concept has been developed starting from the 18th Working Meeting (1998, Brno, Czech Republic) by restructuring sub-commissions “Compliant Mechanisms”, “Mechatronics” and “Biomechanics”, setting up sub-commission “New Ordering System”, and continued at the follow-up meetings by updating new sections of Terminology: Rotor Dynamics and Measuring, Vibrations and Oscillations, Stability, Biomechanics, Gearing, Mechatronics.

Russian part of IFToMM Terminology 2003 (hereinafter “Term-2003”) (New Chaps. 7–13) has been provided by Prof. V.D. Plakhtin (Moscow State Open University)—a member of the IFToMM PC A since 1995 till 2008. At a certain time, V.D. Plakhtin collaborated with Prof. N.I. Levitskij in All-Union Correspondents Polytechnic Institute (from 1993 Moscow State Open University) by joint publications, for example [18].

Since 2000 to 2011 Prof. V.D. Plakhtin and Prof. V.E. Starzhinsky (Metal Polymer Research Institute of NASB, Belarus) as the Russian editors with the participation of Prof. A.J. Klein Breteler (University of Technology, Delft, The Netherlands) and Prof. Dr. S. Segl’a (Technical University of Kosice, Slovakia) were engaged in preparation and modification of Index-Russian taking into account new terms from the new Chaps. 7–13, permanent running terminology modification in whole of Chapters, incorporation of new terms from the Chap. 14 (2011) (adding new terms, removing deleted terms, renumbering terms, etc.).

Discussion on new forms of publishing was began during the 18th Working Meeting (1998, Brno, Czech Republic) [19]. The activity on preparation of Terminology digital version has been initiated by Prof. A.J. Klein Breteler at the 20th Working Meeting (2002, Mezötúr, Hungary) and followed by him on the next Meetings (2005–2012) [8]. Detailed information about rules and procedure on preparation and operation of electronic dictionary software has been described in [19, 20].

Here we turn attention only to the problem of the so-called “missing links” which is related to the necessity of identification of different grammatical forms of the term in its nominative case. It seems to us that the problem is most specific for Russian where six cases, singular and plural forms of nouns exist. In given situation the problem has been solved by Prof. S. Segl’a and Prof. V.E. Starzhinsky who,

exchanged by “out links” terms with software host Prof. A.J. Klein Breteler successively reconstructed these “missing links”. The first person was fulfilled the work in Chaps. 0–6, second one—in Chaps. 7–13.

In this context, special mention should be given to “Term-91” and “Term-s2003” analysis of 0, 1, 2, 3 and 6 TMM sections carried out by Prof. E.E. Peisach (Saint–Petersburg University of Technology and Design) where he proposed certain Terminology improvements [21, 22]. Our comments on the subject can be found in [14]. Note that Prof. E.E. Peisach took part in 19th (2000, Kaunas, Lithuania) and 21st (2005, Bardejov Spa, Slovakia) IFToMM PC A Working Meetings.

3 Individual Sections of the IFToMM Terminology

Some authors made a decision to set aside certain sections of IFToMM Terminology in order to expedite preparation of its Russian part.

3.1 *Gearing Terminology*

It should be noted that before TMM (“Term-1991”) [9] was extended to MMS, the Gearing section included 22 terms.

At the 19th IFToMM PC A Working Meeting (2000, Kaunas, Lithuania) the sub-commission “Gearing” was organized and Prof. V.E. Starzhinsky was nominated as a sub-commission Chair.

In accordance with the taken decision, the draft version of Chap. 12 Gearing containing Russian, English, French and German equivalents, have been recommended for further discussion.

After the presentation and discussion at a regular meeting of the IFToMM TC “Gearing and Transmissions” (2002, Bratislava, Slovakia) it was accepted as a version for discussion at the 20-th Working Meeting of PC A (2002, Mezotur, Hungary). As a result, some remarks were formulated, according to which, and due to general rules of presentation of information in IFToMM editions, the next steps are to be made.

So, English terms in Chap. 12, as well as the terms in other new Chaps. (7–11, 13) were included in the new edition of “Term-2003” [10] in the view of separate chapters with general English Index only.

At the 21-st IFToMM PC A Working Meeting (2005, Bardejov Spa, Slovakia) the activity was addressed to editing the text by the English, French, German and Russian editors.

At the 22-nd Working Meeting (2008, Lyon, France) the decision on altering Chap. 12 structure was accepted: to change the alphabetical order to topical one and divide the term massive into subdivisions. It was offered to consider the following

new structure: 12.1. Gear and tooth geometry (94); 12.2. Gear pair basics (40); 12.3. Gear pair with parallel axes (19); 12.4. Gear pair with intersecting axes (35); 12.5. Cross axes gear pair (28); 12.6. Geared mechanisms (10).

New structure of Chap. 12 was discussed at the 23-rd Working Meeting (2010, Minsk/Gomel, Belarus); a few terms were excluded; a few new ones were added. To summarize the discussion, Prof. A.J. Klein Breteler, IFToMM PC A Chair (2006–2013), has submitted his proposals for final approval. The given Chap. 12 Gearing form was integrated in electronic dictionary placed at the IFToMM site [13].

In addition to the above it is appropriate to address the Gearing Classification. In our opinion the most generalized review for classifying gear meshing, gears and gear pairs according to different criteria (the spatial arrangement of shaft axes to transmit the rotation; relative position of the pinion and gear wheel bodies, tooth shape; different types of hyperboloid worm gear pairs in accordance with axoid surfaces; location of meshing zone; shape of the worm bodies; shape of the component initial surfaces, etc.) was given in [23]. Identified English—Russian Gearing Classification prepared by Prof. V.E. Starzhinsky is reproduced in [24].

3.2 *Quality Factors of Machines and Their Components*

The work on the terminology in the field of machine quality has been started since 2005 with the advent of Prof. M.M. Kane (Belarussian National Technical University) in the staff of the PC A members at the 21st Working Meeting (2005, Bardejov Spa, Slovakia) [14]. Initial structure of Chap. 15 consisting of 9 sections with 704 terms has been presented [25]. After discussion on the 24th Working Meeting (2012, Ilmenay, Germany) the following structure of Chap. 15 has been accepted: 15.1 General notions of quality (33 factors); 15.2 Quality factors concerning human safety and health (16); 15.3 Factors on dependability and reliability (37); 15.4 Constructive and technological factors (23). Therefore, in its final version Chap. 15 contains 109 notions on machine quality.

The final version of Chap. 15 has been presented at 25th Working Meeting of PC A (2014, Saint-Petersburg, Russia) [26].

4 **Separate Projects for Gearing Terminology**

In parallel to the activity in IFToMM Terminology, CIS country scientists were also working on development of separate projects in the Gearing Terminology.

1. Identification of the terms in the section “Gear failure modes” was provided with exhaustive normative sources ISO 10825:1995, ANSI/AGMA 110-E95, DIN 3979:1979, Gear Failure Atlas of R. Errichello [27] and ZFN 201:1990 [28].

Above 200 gear failure modes have been analyzed. Staff and staple of the Standard was published in “Journal of Friction and Wear” [29] and officially was issued in 2009 [30]. The standard contains a list of terms for durability, interchangeability, metal corrosion, friction, wear and lubrication, calculation methods of gear drives on strength and scuffing, classification of fracture modes including table of gear failure mode classification with different levels—classes, general failure modes, sub-modes, degree of failure. The description of 76 gear failure modes is given and 104 standard photo-examples are shown, as well as possible reasons of their appearance and recommendations for failure prevention.

2. Section “Spiroid gear pairs” based on the Standard GOST 22850-70 regulating terminology in spiroid gear drives. USSR Standard was developed by the team under the guidance of Prof. V.I. Goldfarb and then was extended with terms and definitions in English and terms in French and German. The section in [24] contains the following subsections: (1) Types of Spiroid Gears (9); (2) Types of cylindrical Spiroid Worms (15); (3) Types of bevel and reserve bevel Spiroid Worms (11); (4) Types of Spiroid Wheels (3); (5) Elements and parameters of Spiroid Worms and Spiroid Wheels (41).
3. The terminology in the section “Facial gearing” has been elaborated by a team under the guidance of Prof. G.N. Raikhman (The Immigrant Scientists Association of Israel) et al. [31] and contains terms and definitions of facial toothed joints and gearing, distributed for the sections [24]: (1) Classes of the facial gears and toothed joints (4); (2) Basic concepts (4); (3) Facial toothed joints and gear pairs. Basic concepts (9); (4) Types of facial meshing (8); (5) Types of facial gear pairs (9); (6) Types of facial gear wheels and worms (3); (7) Methods and ways of machining facial tooth. Basic terms and definitions (22).
4. The parameters concerning gear strength and scuffing calculations have been compiled from the GOST, ISO, DIN and VSM standards. All together the 249 parameters were identified in four languages—Russian, English, French, German [24]. Compilation was fulfilled by a team under the guidance of Dr. Yu.L. Soliterman (Joint Institute of Mechanical Engineering of National Academy of Science of Belarus).
5. Other sections of Gearing Terminology compiled in [24] are as follows: terms and symbols for gear accuracy and inspected parameters; illustrated list of forms and location of tooth contact parameters; illustrated dictionary of terms for gear cutting tools.

5 Conclusions

Within the framework of IFToMM activities the scientists from the Russian-speaking CIS (former USSR) countries are successfully working on the problems of terminology of the theory of mechanisms and machines (the science of

mechanisms and machines in the current treatment MMS), including identification and definition of the terms and concepts, translation from English into Russian, draw up alphabetic indices. In the recent years the electronic dictionary for MMS has been prepared and terminology for new MMS sections has been discussed and broadened in line with IFToMM PC A regularities. The following scientists from the CIS countries participated and continue to work as a part of IFToMM PC A: Prof. N.I. Levitskij (1969–1975), Prof. Yu.L. Sarkissyan (1983—to the present day), Prof. D.N. Levitskij (1995–2010), Prof. V.D. Plakhtin (1998–2012), Prof. R. T. Tolocka (1998—to the present day), Prof. V.E. Starzhinsky (2000—to the present day), Prof. E.E. Peisach (2000–2005), Prof. M.M. Kane (2005—to the present day), Prof. E.V. Shalobaev (2010—to the present day), Dr. S.V. Shil'ko (2014—to the present day).

The main result of the activities of IFToMM PC A is the creation of the electronic MMS dictionary [11]. IFToMM Terminology presents today a strictly verified information databases that facilitates communication and understanding of the experts of the Global Scientific Community.

Acknowledgments Authors express grateful acknowledgment to post PC A Chairmen Dr. Ing. Teodor Ionescu and Prof. Antonius J. Klein Breteler for the creative help during on-line communication and at the Working Meeting sessions.

References

1. How to Work under Terminology. Basic and Techniques. Nauka, Moscow (1968)
2. Lotte, D.S.: Basics of Architecture of Scientific and Technical Terminology. Moscow, Academy of Sciences of USSR (1961). (in Russian)
3. Short Text-Book of Methods on the Development and Ordering Scientific and Technical Terminology. Nauka, Moscow (1979) (in Russian)
4. Mechanical Oscillations. Basic Notions. Terminology Alphabetical Symbols of Sizes. Collected Volume of Recommended Terms, Issue 106. Executive editor Prof. N.I. Levitskij. Academy of Sciences of USSR, Nauka, Moscow (1987) (in Russian)
5. Levitskij, N.I. (ed.): Theory of mechanisms and machines. Basic Notions. Terminology. Lettering. Collected Volume of Recommended Terms, Issue 99. Academy of Sciences of USSR, Nauka, Moscow (1984) (in Russian)
6. Theory of Mechanisms and Machines. Basic Notions, Structure of Mechanisms, Kinematics of Mechanisms. Terminology. Compiler: E.E. Peisach. Saint-Petersburg: University of Technology and Design (1996) (in Russian)
7. Ishlinskij, A.Y. (ed.): Theoretical Mechanics. Terminology. Collected Volume of Recommended Terms, Issue 90. Academy of Sciences of USSR, Nauka, Moscow (1977)
8. Boegelsack, G., Breteler K.A.J.: Concise chronicle of the IFToMM commission for standardization of terminology (1969–2009). In: Proceedings of the Scientific Seminar “Terminology for the Mechanism and Machine Science, Minsk-Gomel, Belarus, Minsk: BelGISS, pp. 7–15 (2010)
9. IFToMM Commission. A terminology for the theory of machines and mechanisms. Mech. Mach. Theory, **26**(5), 435–539 (1991)
10. Ionescu, T.: IFToMM Commission. A terminology for the mechanism and machine science. Mech. Mach. Theory, **38**(7–10), 597–1111 (2003)

11. Electronic Recourse. www.iftomm.org, www.iftomm.3me.tudelft.nl, www.thinkmotion.eu
12. Boegelsack, G., Gierse, F.J., Oravský, et al.: Terminology for the theory of machines and mechanisms, IFToMM. *Mech Mach Theory* **18**(6), 379–408 (1983)
13. Ionescu, T.: IFToMM Terminology: 1998–2005. In: Proceedings of the Scientific Seminar “Terminology for the Mechanism and Machine Science. Stefan Segl’a. Bardejov Spa, Slovakia, pp. 17–22 (2005)
14. Starzhinsky, V.E., Goldfarb, V.I., Algin, V.B. et al.: Participation of scientists from the USSR and currently CIS countries in IFToMM activities. In: Proceedings of the Scientific Seminar “Terminology for the Mechanism and Machine Science”, 2nd edn, pp. 13–42. MPRI NASB, Gomel–Saint-Petersburg (2016). <http://en.mpri.org.by/publications/iftomm-terminology>
15. Levitskij, N.I., Sarkissyan, Y.L., Gekchyan, G.S.: Optimum synthesis of four bar function generating mechanism. *Mech. Mach. Theor* **7**, 387–398 (1972)
16. Ceccarelli, M.: From TMM to MMS: a vision of IFToMM. *Bull. IFToMM Newslett.* **10**(1) (2001). <http://www.iftomm.org>
17. Ceccarelli, M.: On the meaning of TMM over time. *Bull IFToMM Newslett.* **8**(1) (1999). <http://www.iftomm.org>
18. Levitskij, N.I., Hurevich, Y.Y., Plakhtin, V.D., et al.: Theory of Mechanisms and Machines. Editor K.V. Frolov. N.E. Bauman MSTU, Moscow (2004)
19. Breteler, K.A.J.: On the development of terminology and electronic dictionary for mechanism and machine science. technology developments: the role of mechanism and machine science and IFToMM. In: Ceccarelli, M. (ed.) *Mechanism and Machine Science*, pp. 95–105. Springer (2011)
20. Breteler, K.A.J.: On the development of an electronic dictionary for IFToMM. In: Segla, S. (ed.) Proceedings of Scientific Seminar “Terminology for the Mechanism and Machine Science”, Bardjev Spa, Slovakia, pp. 83–90 (2005)
21. Peisach, E.E.: About the terminology on the theory of mechanisms and machines. *Theory of Mech Mach* **2**(2), 80–94 (2004). (<http://tmm.spbstu.ru/02.2004.html>) (in Russian)
22. Peisach, E.E.: On terminology for the theory of mechanisms. In: Proceedings of the Scientific Seminar “Terminology of the Theory of Machines and Mechanisms”. Lithuania, Technologija, Kaunas, pp. 13–19 (2000)
23. Goldfarb, V.I., Lunin, S.V., Trubachyov, E.S.: *Direct Digital Simulation for Gears*, vol. 1. IzhSTU, Izhevsk (2004)
24. Starzhinsky, V.E.: Reference-Dictionary Book on Gearing. Russian-English-German-French. MPRI NASB, Gomel (2011)
25. Kane, M., Starzhinsky, V.: Quality factors of machines and their components. role of quality factors in provision on machine service properties. In: Proceedings of the 22th working meeting of the IFToMM Permanent Commission for Standardization of Terminology, Villeurbanne, France. Lyon, INSA de Lyon, pp. 77–80 (2008)
26. Kane, M.M., Starzhinsky, V.E.: State of art and perspectives of terminology development on Chapter 15 “Quality factors of machines and their components”. In: Proceedings of the Scientific Seminar “Terminology for the Mechanism and Machine Science”, 2nd edn. MPRI NASB, Gomel–Saint-Petersburg, pp. 43–46 (2016). <http://en.mpri.org.by/publications/iftomm-terminology>
27. Errichello, R (ed.): *Gear Failure Analysis*. Townsend. Montana (2000)
28. ZFN 201. *Zahnradshaeden Begriffs bestimmung. Berechnungen und Ursachen* (1990)
29. Starzhinsky, V.E., Soliterman, Y.L., Goman, A.M., Ossipenko, S.A.: Forms of damage to gear wheels: typology and recommendation on prevention. *J Frict Wear* **29**(5), 340–353 (2008)
30. GOST 31381-2009. *Gear Wheels. Modes of Damages. Classification and Description* (in Russia)
31. Raikhman, G.N., Bartov, M., Starzhinsky, V.E.: Terminology and classification of geometrical parameters of facial gears, their processing methods and regimes. In: Proceedings of the 12th IFToMM World Congress, Besancon, France, GT-P1 A153 (2007)

State of Art in Separate Sections of MMS Terminology and Some Proposals

E.V. Shalobaev, S.V. Shil'ko, R.T. Tolocka, V.E. Starzhinsky,
G.N. Iurkova and D.G. Surikov

Abstract Separate sections of MMS Terminology are considered. Separate sections from Special Issue “Terminology for the Mechanism and Machine Science” and Electronic Dictionary elaborated on the base of abovementioned Issue analyzed. Some proposals for the next step forward of MMS Terminology made.

Keywords MMS terminology · Biomechanics · Gearing · Mechatronics · Transportation machinery and logistics · Quality factors of machines · Compliant mechanisms

E.V. Shalobaev (✉) · G.N. Iurkova · D.G. Surikov
Saint-Petersburg National Research University of Informative Technology,
Mechanics and Optics, Saint-Petersburg, Russia
e-mail: shalobaev47@mail.ru

G.N. Iurkova
e-mail: iurkova12@mail.ru

D.G. Surikov
e-mail: surikov77@mail.ru

S.V. Shil'ko · V.E. Starzhinsky
Metal Polymer Research Institute of National Academy of Sciences of Belarus,
Gomel, Belarus
e-mail: shilko_mpri@mail.ru

V.E. Starzhinsky
e-mail: star_mpri@mail.ru

R.T. Tolocka
Kaunas University of Technology, Kaunas, Lithuania
e-mail: tadas.tolocka@ktu.lt

1 Introductions

Without any prejudice towards canonical sections of TMM Terminology (Structure of Machines and Mechanisms, Kinematic, Dynamic etc.) or intending to give a comprehensive long-term prognosis for further development of MMS Terminology, the authors have estimated the current state of Terminology in the separate MMS sections that are closer to them in the topic and included some additional notions and terms for discussion. The question concerns MMS sections “Biomechanics”, “Gearing”, “Mechatronics” with well-established in the four-language terminology, one can find in Electronic Dictionary [1] (Chap. 11 “Biomechanics”; Chap. 12 “Gearing”; Chap. 13 “Mechatronics”). New Sects. 14–16 there are in uncompleted state, namely: Chap. 14 “Transportation Machinery and Logistics” (English and Russian in Electronic Dictionary [1]); Chapter 15 “Quality Factors of Machines and Their Components” (only Edit.log.table paper English-Russian version, but no electronic one); Chapter 16 “Compliant Mechanisms” (in Electronic Dictionary [1] only English terms are presented, Russian equivalents are in Edit.log.table; French and German terms are in the stage of elaboration). Likewise, in different stay of readiness of MMS Terminology sections, the proposals are offered in different forms—some of proposals concern directly the offered terms, some represent common recommendations.

2 Proposals for “Biomechanics” Terminology

Sub-commission on Biomechanics has been established at 18th Working Meeting of IFToMM Permanent Commission “Standardization of Terminology for MMS” (IFToMM PC A) (1998, Brno, Czech Republic) under the chairmanship of Prof. G. Boegelsack (Ilmenau Technical University, Germany) when the first draft version of the Chap. 11 Biomechanics has been presented. At the following Working and Informal Meetings (1999, Oulu; 2000, Kaunas; 2002, Mezötur) usual steps for modifications, corrections etc. were undertaken and the final English version of Chap. 11 was placed in [2]. Translation into Russian has been fulfilled by Prof. V. D. Plakhtin (Moscow State Regional University). Now Chap. 11 contains in total 238 terms divided into the following groups: 11.1 General (49); 11.2 Generation of notion and force (63); 11.3 Transmission of motion and force (39); 11.4 Movement of body and body parts (60); 11.5 Situation and orientation of body (27).

The improvement of terminology in this field is expressed in addition of definitions characterizing the mechanical properties of biological tissues and organs, as well as their adequate reproduction in prosthetic devices. For example, new terms are proposed to be introduced in Sect. 11.1 related to the attributes of living systems which are actively studied in order to create “smart” mechanisms (“adaptability” and “implant”) as well as terms “elasticity”, “plasticity” and “viscoplasticity”. It is useful to introduce the terms “endoprosthesis”; “actomyosin interaction” in

Sect. 11.2 describing force generation at the elementary level of muscle contraction; “myometry”—the procedure for determining of elastic and viscous parameters as well as tonus of muscle. Section 11.3 is proposed to be complemented with definitions of “vertebra” and “vertebral column” which are very important components of the musculoskeletal system of humans and other organisms.

3 The Current State and Proposals for Development of Gearing Terminology

At that time paper version of IFToMM Terminology Chap. 12 Gearing contains 223 terms, located in alphabetical order [2].

In results of discussion on the 22nd Working Meeting of PC A (2008, Lyon, France) and on the 23rd one (2010, Minsk/Gomel, Belarus) all terms were discussed; most terms were accepted without modification; renumbering of the terms in accordance with the accepted new structure was made; improvement of some English definitions was provided; a few terms were excluded, a few new ones were added.

In the same place the new structure of Chap. 12 was accepted: location of terms in topical order with dividing section into subsections: 12.1. Gear and tooth geometry (94); 12.2. Gear pair basics (40); 12.3. Gear pair with parallel axes (19); 12.4. Gear pair with intersecting axes (35); 12.5. Cross axes gear pair (28); 12.6. Geared mechanisms (10).

In above mentioned structure in the paper version Chap. 12 was reproduced in the source [3] and contains some new added terms: 12.1.30 Datum line; 12.1.31 Datum plane; 12.1.56 Opposite flanks; 12.1.82 Overlap length; 12.2.9 Pressure angle of a gear pair Chap. 15 structure was presented in Electronic Dictionary [4] in the same view.

Concerning the proposals on further development of Gearing Terminology let us to refer common remark mentioned in the (Draft) Minutes of the 25th Working Meeting of IFToMM PC A (2014, Saint Petersburg, Russia): “Taking into account the appearance of new types of toothed meshing’s and new types of gear drives, which are already used in industry and because of this situation there is a strong necessity to complete the terminology with new terms. We believe it may become a solution for deciding newly appeared”.

4 The State of Terminology in the Field of Mechatronics

Work on the preparation of terminology in Mechatronics started in 1998 at the 18th international seminar (1998, Brno, Czech Republic) with the organization of the sub-Commission “Mechatronics” under the chairmanship of Prof. R. T. Toločka

(Kaunas University of Technology, Lithuania). The list of terms, remarks, suggestions for improvement and modifications, alphabetical order, numbering etc., was discussed at the following international workshops: 19th (2000, Kaunas, Lithuania) and 20th (2002, Mezötur, Hungary). The commentaries and suggestions on the list of terms were introduced by members of the sub-Commission: Prof. G. Boegelsack (Ilmenau Technical University, Germany), Prof. C.W. Stammers (University of Bath, United Kingdom), Prof. J. Novotny (Charles University in Prague, Czech Republic) and Prof. E.V. Shalobaev (Saint-Petersburg National Research University of Information Technologies, Mechanics and Optics, Russia) [5–10] who joined the Commission online. The edited Chap. 13 of “Mechatronics” paper version [2] contains 63 terms with definitions, in the Electronic Dictionary it is divided on the sub-sections: 13.1 Specific fields of work (8); 13.2 Systems and devices (23); 13.3 Properties and behavior.

Active discussion of problems in Mechatronics, including terminology issues, is continuing (the list of information sources [11] and publications [12–20] illustrate the activities). They are devoted to the problems of Mechatronics terminology and contain a number of proposals for consideration by the IFToMM PC A, including the initiated scientific circulation of the concept of “Level Approach” to Mechatronics for linking it with microsystems engineering and nanoindustry on macro-, micro- and nano-levels [7].

Suggestions on introducing the term “Mechatronic Module” are under discussion, thus developing the proposal presented in [10] that the modular principle is a certain alternative for the systematic (mechatronical) principle, as it proposes decomposition of sophisticated technical systems. The term “Quasi-Mechatronic Systems” [21] is introduced for the systems which may not correspond to the canonical definition of Mechatronics in some aspect, but allow to apply all the methods and means of mechatronical design to them.

Basic schemes of different level Mechatronics objects [7] that are used for solving problems of design practice [12] have been proposed.

It should be noted that the term “Adaptive Mechanics”, defining the area of Mechanics and Mechatronics which refers to smart devices and adaptive structures capable to change their behavior in accordance with changes in the environment and their internal state [22], has been coined and now is used for naming study courses (e.g., at Kaunas University of Technology) as well as in scientific research. To date classification of mentioned structures is suggested [23, 24]. Currently, the authors of monographs and textbooks in Russia, Ukraine, Estonia began to introduce in their publications special sections on Terminology [6, 25, 26]. This demonstrates the understanding of the role of terminology and what the basic terminology is already formed.

It is necessary to state that Mechanics, both traditional and with its applications in Mechatronics, is developing as well. Mechatronics is not replacing it, only complementing and developing it, not excluding the study of traditional issues in Mechanics [4, 9].

Based on the above it is proposed to fix in the Mechatronic Terminology the following notions:

- mechatronic objects, mechatronic systems and mechatronic devices are equivalent notions;
- the basis of mechatronic systems is the “triad” consisting of a sensor—controller—actuator;
- mechatronic modules are the mechatronic objects which designed as a metabolic construction in accordance with principle of life-limit durability and non-entitled to repair;
- mechatronic complexes are distributed mechatronic systems.

In conclusion, it should be note that the parallel (joint) design of heterogeneous components of mechatronic systems is the methodological basis of mechatronic approach.

5 Transportation Machinery and Logistics

The work under the new Chap. 14 Transportation Machinery and Logistics has been started in 2008 on the initiative of Prof. A.J. Klein Breteler. In accordance with Edit.log.table agreed at December 2011 Chap. 14 contains 5 groups, 165 terms: 14.1 General terms and transport motion (28); 14.2 Hoisting and lifting equipment (57); 14.3 Belts and conveyors (16); 14.4 Vehicle science (23); 14.5 Transportational logistics (41).

In the 2008–2011 period the following activities were carried out: clarification of Chapter title, refining structure, discussion on remarks, permanent renumbering, excluding incorrect terms and including new terms, correction of definitions. Prof. V.D. Plakhtin and Prof. V.E. Starzhinsky took part in the procedure of correcting English and Russian versions and adding to common Russian Index terms from the Chapter under consideration. Some terms were presented by Dr. O. Antonescu at the 24th Working Meeting of PC A (2012, Ilmenau, Germany). They are continued in discussion English-Russian dictionary is available in electronic form [1] with amplification by terms: “Short sea shipping”; “Modal center [Modal point]”.

6 The Proposals for Section of Quality Factors of Machines

Initial the first version of given section (Chap. 15 of MMS Terminology) has been presented at the 21st Working Meeting of the PC A (2005, Bardejov Spa, Slovakia). After discussion on the 24th Working Meeting (2012, Ilmenau, Germany) the following structure of Chap. 15 has been accepted: 15.1 General notions of quality

(33 factors); 15.2 Quality factors concerning human safety and health (16); 15.3 Factors on dependability and reliability (37); 15.4 Constructive and technological factors (23).

The final version of Chap. 15 consisting of 109 terms has been presented at 25th Working Meeting of PC A (Saint-Petersburg, Russia, 2014) [27]. At this date Chap. 15 Terminology is under development and its list of terms is only in the view of Edit.log.table.

We suppose that in future it is necessary to expand and refine this section by making more precise and extended volumes of the current parts and introducing new ones. For example, “Selection of requirements to the quality of machines and their components”, “Technique of checking and diagnostics of quality of machines and their components”, “Testing of machines and their components”.

7 Compliant Mechanisms

As far as we know the Compliant Mechanisms were first mentioned at the 18th PC A Working Meeting (1998, Brno, Czechoslovakia) when the corresponding sub-commission was established. The first person who proposed to include the corresponding data in IFToMM Terminology was Prof. Boegelsack (TU Ilmenau, Germany). Originally, in 2010, he set forward 12 terms with definitions in German and English. Then, in 2011, Prof. Klein Breteler (TU Delft, the Netherlands) proposed to prepare the initial text for the 24th Working Meeting in Ilmenau.

Presentation of Compliant Mechanisms Terminology was started by Dr.-Ing. Nenad T. Pavlovic (University of Nis, Serbia), a new invited member of the Commission. Co-reporter Dr. L. Centner (TU Ilmenau, Germany) also presented a report. In the period between the 24th and 25th Working Meetings the following persons contributed to the process: Dr. N.T. Pavlovic and Prof. V.E. Starzhinsky; the last has translated English terms and definitions into Russian, Dr. N.A. Barmina (Izhevsk State Technical University, Institute of Mechanics, IFToMM Webpage Administrator) has proposed some clarification in English and Russian. Before the 25th Working Meeting (2014, Saint-Petersburg, Russia) the Edit.log.table of Chap. 16 containing 34 terms with refinement, elimination or addition of the terms has been circulated among the PC A members. At the 25th Working Meeting the updated Chap. “Compliant Mechanisms” with definitions has been presented [28] with additional terms, offered for discussion: “Multilayered compliant mechanisms”, “Compliance—adjustable, active, passive”.

In conclusion, it is pertinent to note that a number of diagrams and drawings (about 40 units of compliant mechanisms taken from the information source [29]) have been reproduced as an appendix to the paper [28] with the picture caption in English and Russian; identified by Prof. V.E. Starzhinsky.

8 Conclusions

Certain efforts were directed to estimate the current state of Terminology in separate MMS sections including Biomechanics, Gearing, Mechatronics, Transportation Machinery and Logistics, Quality Factors of Machines, as well as Compliant Mechanisms. Summarized the whole array of terms in the hard version of MMS Terminology has been revised [2] numbering 1596. The Electronic Dictionary [1], involves some excluded terms and some included ones in Chap. 12 (plus three terms); 167 terms in the new Chap. 14; 30 terms in the new Chap. 16; additional terms in Chaps. 0 and 1 (0.5 Mechanism analysis; 1.2.27 Input kinematic pair [Input joint]) contains in total 1796 terms.

Actually, in future MMS Terminology will propagate extend together with elaboration of new industrial technologies and corresponding new sections of MMS. In conformation of our words IFToMM President, Prof. M. Ceccarelli has mentioned in one of his latest papers [30]: “Thus, the main challenges for future success in MMS may be recognized in the community capability of being able to keep updating the field and therefore in being ready to solve new and updated problems with new ideas or by refreshing past solutions, as has been done successfully in the past”.

Acknowledgments Authors extend gratefulness to colleagues for support of idea of given publication and have reliance in understanding Chairmen of IFToMM PC A sub-commissions, which Terminological content has been used in given paper.

References

1. Electronic Resource <http://iftomm-terminology.antonkb.nl/>, www.iftomm.3me.tudelft.nl, <http://www.dmg-lib.org/dmglib/thesaurus>
2. Ionescu, T. (ed.): IFToMM Commission A terminology for the mechanism and machine science. Mech. Mach. Theory **38**(7–10), 597–1111 (2003)
3. Starzhinsky, V.E. (ed.): Reference-Dictionary Book on Gearing. Russian-English-German-French. MPRI NASB, Gomel (2011)
4. Ceccarelli, M.: IFToMM and MMS: history, structure, trend and challenges. In: Proceedings of the Scientific Seminar “Terminology for the Mechanism and Machine Science”, 2nd edn., pp. 9–19. MPRI NASB, Gomel–Saint-Petersburg (2016). <http://mpri.org.by>
5. Arshansky, M.M., Shalobaev, E.V.: Mechatronics: the basis of the glossary. Mechatronics **4**, 47–48 (2001). (in Russian)
6. Poduraev, YuV: Mechatronics: Fundamentals, Methods, Applications. Mashinostroenie, Moscow (2006). (in Russian)
7. Shalobaev, E.V.: Mechatronics and Microsystems engineering: the ratio of macro and micro levels. Microsyst Engi. **4**, 8–10 (2000). (in Russian)
8. Shalobaev, E.V.: Theoretical and practical aspects of mechatronics. The collection of articles “Modern technologies” edited by Prof. S.A. Kozlov, pp. 44–64. St.-Petersburg state University ITMO, St.-Petersburg (2001). (in Russian)

9. Shalobaev, E.V.: To the question about the definition of mechatronics and mechatronic hierarchy of objects. *Sensors Syst* **7**, 64–67 (2001). (in Russian)
10. Shalobaev, E.V.: To the question of international translator in mechatronics. *Mechatronics* **2**, 13–14 (2002). (in Russian)
11. Starzhinsky, V.E., Goldfarb, V.I., Algin, V.B., et al.: Participation of scientists from the USSR and currently CIS countries in IFToMM activities. In: *Proceedings of the Scientific Seminar “Terminology for the Mechanism and Machine Science”, 2nd edn.*, pp. 21–50. MPRI NASB, Gomel–Saint-Petersburg (2016). <http://mpri.org.by>
12. Gorbатов, P.A., Lysenko, N.M., Podobedov, N.I.: Mathematical and structural model for optimal design of subsystems of hunger and traversing actuating element of tunneling machines of mechatronic Class. *Mining Equip. Electromech* **7**, 9–15 (2010). (in Russian)
13. Korikov, A.M.: One more time about mechatronics as a science. *Mechatron. Autom. Control* **1**, 2–8 (2011). (in Russian)
14. Poduraev, Y.V., Shalobaev, E.V.: Mechatronics and Robotics—Interrelations of notions: point of view of Russian encyclopedia. In: *Proceedings of the Scientific Seminar “Terminology for the Mechanism and Machine Science”, 2nd edn.*, pp. 61–63. MPRI NASB, Gomel–Saint-Petersburg (2016). <http://mpri.org.by>
15. Shalobaev, E.V.: Mechatronics: today problems and development trends of terminology. In: *Proceedings 23th Working Meeting of the IFToMM Permanent Commission for Standardization of Terminology on MMS. Minsk-Gomel, Belarus*, pp. 111–118 (2010)
16. Shalobaev, E.V.: Problems in terminology and miniaturization of aerospace systems. *Mechatron. Autom. Control* **10**, 60–66 (2013). (in Russian)
17. Smirnov, Y.S., Yurasov, V.E., Katz, D.A., Nikitin I.S.: With. educational, scientific and applied components of mechatronics. *Bulletin of the South Ural state University. Series: Computer technology, control, Radioelectronics*, **1**, 81–88 (2014)
18. Teryaev, E.D., Filimonov, N.B., Petrin, K.V.: Mechatronics as a computer paradigm for the development of technical Cybernetics. *Mechatron. Autom. Control* **6**, 2–10 (2009). (in Russian)
19. Teryaev, E.D., Filimonov, N.B.: Nanoelectronics: state, problems, prospects. *Mechatron. Autom. Control* **1**, 2–14 (2010). (in Russian)
20. Yurevich, E.I., Ignatova, E.I.: Basic principles of mechatronics. *Mechatron. Autom. Control* **3**, 10–12 (2006). (in Russian)
21. Shalobaev, E.V., Shil’ko, S.V.: Modern mechanics as a basic of Mechatronics. In: *Proceedings of the Scientific Seminar “Terminology for the Mechanism and Machine Science”, 2nd edn.*, pp. 65–70. MPRI NASB, Gomel–Saint-Petersburg (2016). <http://mpri.org.by>
22. Shalobaev, E.V., Tolocka, R.T.: Terminological aspects of modern mechatronics. *Fundam. Appl. Prob. Eng. Technol.* **5**, 122–133 (2013). (in Russian)
23. Goldade, V., Shil’ko, S., Neverov A.: *Smart Materials Taxonomy*. CRC Press, Taylor & Francis Group (2015)
24. Pleskachevsky, YuM, Shilko, S.V., Stelmakh, S.V.: evolution and structural levels of materials: adaptive composites. *J. Wave-Material Interact.* **14**(1–2), 49–58 (1999)
25. Brindtfeld, E., Grin’ko, A.: *Mechatronic devices [Electronic Course]*. Tallinn University of Technology, Tallinn (2013). (in Russian)
26. Grabchenko, A.I., Klepikov, V.B., Dobroskok V.L., et al.: *Introduction to Mechatronics*. NTU “Kharkov Polytechnic Institute”, Kharkov (2014). (in Russian)
27. Kane, M.M., Starzhinsky, V.E.: State of art and perspectives of terminology development on Chapter 15 “Quality Factors of Machines and Their Components”. In: *Proceedings of the Scientific Seminar “Terminology for the Mechanism and Machine Science”, 2nd edn.* MPRI NASB, Gomel–Saint-Petersburg, pp. 51–54 (2016). <http://mpri.org.by>

28. Pavlovic, N.T., Breteler, K.A.J., Centner L., et al.: About preparation of new section of terminology IFToMM on MMS: Chapter 16 “Compliant mechanisms”. In: Proceedings of the Scientific Seminar “Terminology for the Mechanism and Machine Science”, 2nd edn., pp. 55–59. MPRI NASB, Gomel–Saint-Petersburg (2016). <http://mpri.org.by>
29. Larry, L.H., Magleby, S.P., Olsen, B.M. (eds.): Handbook of Compliant Mechanisms. John Wiley & Sons Ltd (2013)
30. Ceccarelli, M.: History and trends of mechanism science with an IFToMM pole. In: Proceedings of the International symposium “Theory and Practice of Gearing”. IzhsUT, Izhevsk, Russia (2013)

Part VII
Robotics—Mechanical Design
of Robot Architecture

Design Solutions to Simplify the Calibration of a Robotic Flexible Manufacturing System

A.-M. Stoian, I. Maniu, E.-C. Lovasz and C.M. Gruescu

Abstract For increasing the performances and for a proper working of a robotized flexible manufacturing system (FMS), it is necessary to calibrate the components' parameters of the relative positions. Also the robotized FMS must be implemented into a complex control system program related to a specific application. The calibration method can be simplified by using design solutions with a common base plate. The uncoupling of the robots' movements is proposed as simplified method for the calibration of FMS.

Keywords Flexible manufacturing system · Uncoupling of movements · Kinematic joints · Calibration

1 Introduction

The calibration of a robotic *FMS* aims to correlate the parameters of relative positions of its components and it is necessary for the implementation into the complex control system program related to an application, when, subsequent to the installation on a foundation, position errors between the robot and the peripheral components result.

A.-M. Stoian (✉) · I. Maniu · E.-C. Lovasz · C.M. Gruescu
Politechnica University of Timisoara, Timisoara, Romania
e-mail: anamaria.stoian@upt.ro

I. Maniu
e-mail: inocentiu.maniu@upt.ro

E.-C. Lovasz
e-mail: erwin.lovasz@upt.ro

C.M. Gruescu
e-mail: corina.gruescu@upt.ro

Several researches show non-contact methods for measurement and calibration of robot's end-effectors position using digital automatic theodolites [1, 2], laser interferometers [3], 3D cameras [4], markers or grids [5] or light stripes on targets [6].

A calibration method for a robotic system, presented in [7], uses a laser sensor attached to the robot's end-effector for measuring the distance between the robot tool, the measurement surface and a grid on the floor. The real robot's kinematic parameters are computed by measuring the relative position between two consecutive pulses [8]. A self-calibration method by using an automatic registration algorithm for a medical robotic system with automatic registration and storing of the different positions of a body attached to the robot TCP is described in [9].

The author of [10] started from the existing calibration methods [11, 12] and improved them by implementing precise optical vision systems. A method based on the full pose measurement of robot's end-effector for calibration is also shown in [13]. This method analyses the features of a set of target points on a circular trajectory.

In order to reduce the installation errors, constructive solutions are developed, allowing the simplifying of the calibration operation in relation with the complexity of the robotic *FMS*. Some of these solutions aim to reduce pose errors by setting up all components on a common base plate [14–16], rigid enough not to cause other errors by its own deformation. Another part of the solutions aim the uncoupling of some of the robots' movements in order to simplify the geometric patterns of the guiding device, for a simpler system calibration algorithm.

2 Calibration Solutions Using a Common Base Plate

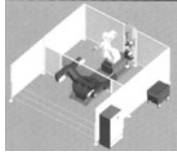
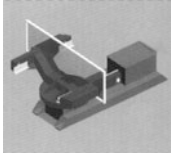
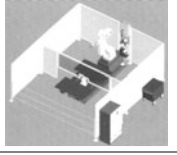
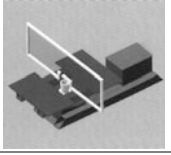
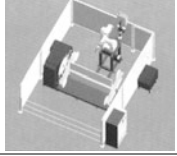


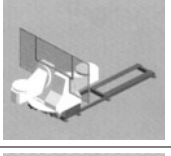
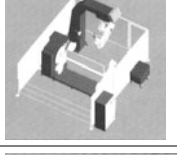
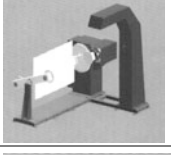
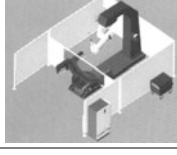
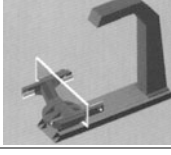

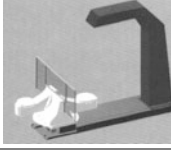
The setup of the robotic system on a single rigid base plate, which is properly machined on all faces on which components are mounted, allows the precise relative layout of these components. The single common base plate also prevents uneven distribution of foundation errors on system's components.

In order to exemplify the solutions based on the use of a common base plate, Table 1 shows variants of robotic welding *FMS* proposed by CLOOS Company [14]. In all cases, the base plate supports one positioning and orientation table with two workstations (peripheral system components) and either a rectangular support or a column to install the robot.

Since the common base plate ensures the precise relative positioning of the components, the online application programs instructed from one station can also be implemented without calibration in the other workstations.

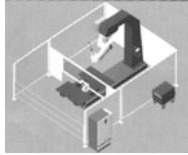
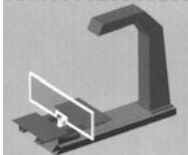

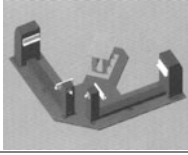
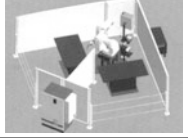
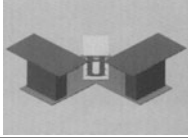
Implementing an offline application program in the system with the components placed on the same base plate, requires the calibration of the application for a single workstation. For this purpose, it is sufficient to provide a single quartet of calibration points in the working station, which ensures an unequivocal numerical transforming matrix from the workstation to the robot. Switching application in the second workstation can be done without further calibration.

Table 1 Calibration solutions using a common base plate

No	Robotic welding	Peripheral device
1		
2		
3		
4		
5		
6		
7		

(continued)

Table 1 (continued)

No	Robotic welding	Peripheral device
8		
9		
10		

Installation of the components on a common base plate is only suitable to applications with all precision points located within the robot’s workspace. Otherwise, it is necessary to implement solutions that uncouple some movements.

To illustrate the calibration solutions using a common base plate shown in Table 1, an example is detailed in Fig. 1. The compact system contains a welding robot *R*, placed on a support *SR* and two workstations with rotary table *RT* separated with a dividing panel *P*. The whole system is controlled by a main board *TC*.

Both robot support and the two rotary tables are placed on a common base plate *BP*. This situation allows a quick calibration, short commissioning time due pre-assembly, high productivity thanks to parallel workstations, low space requirement due to compact design and easy integration into any production line.

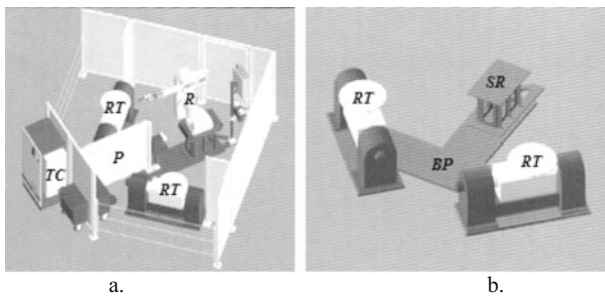


Fig. 1 Compact welding robot system (a) Peripheral devices (b)

3 Design Solutions for Uncoupling the Position Movements

The rotations of the robots' guiding devices elements produce a location of the end-effector that is influenced by the coupling of the movements. By serial structures, the coupling degree of the movements increases with the number of the driving rotational joints, existing in the trajectory generating mechanism.

The maximum degree of couplings occurs in polar coordinates architectures. To these, all 3 degrees of freedom (α, β, γ) of the trajectory generating mechanism influence the orientations (ψ, φ, θ) of the the end element of the guiding device.

For calibration of the robotic *FMS* by transferring the driving software from the reference system of a peripheral component to the robot's reference system, coupling the movements represents a disadvantage because it complicates the analytical relations necessary for the calibration algorithm.

For a simple exposure, let us consider the case of a guiding device that through joint parameters (α, β, γ) allows 3D positioning, but provides orientation only around a single flexion-extension axis (φ). The scheme of the device which corresponds to the variant with coupled movements is shown in Fig. 2. One can see that if the axis Dy' is defined in extension of the forearm, then the orientation of the element DP within the reference system $OXYZ$, connected to the fixed base of the robot, requires the specification of all four angles ($\alpha, \beta, \gamma, \varphi$).

To reduce the coupling degree, it is necessary to impose the orientation of some axes belonging to the $Dx'y'z$ system on fixed directions. So, if the axis Dz' keeps the vertical orientation during the modification of the position, as shown in Fig. 3, then the orientation of the line DP would result independent from the angles (α, β), and depending only on (γ, φ).

Maintaining the orientation of the axis Dz' always vertically involves releasing the reference system $Dx'y'z$ from the forearm and binding it to another element, always oriented vertically. The problem can be solved using decoupling kinematic chains, achieved either by parallelogram mechanisms (Fig. 4) or with cycloid

Fig. 2 Case when the orientation of the line DP must be imposed through 4 parameters ($\alpha, \beta, \gamma, \varphi$)

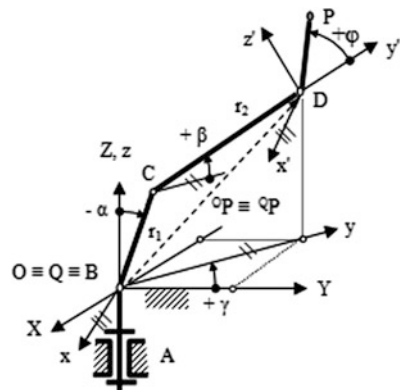


Fig. 3 Case when the orientation of the line DP can be imposed through 2 parameters (γ, φ)

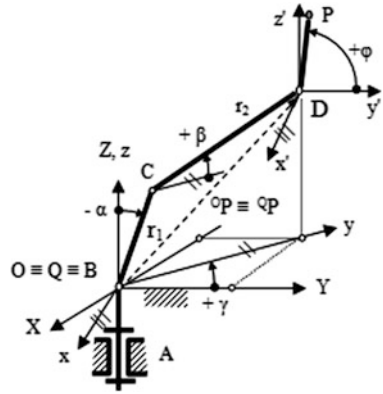


Fig. 4 Uncoupling the rotations (α, β) by means of the parallelogram mechanism

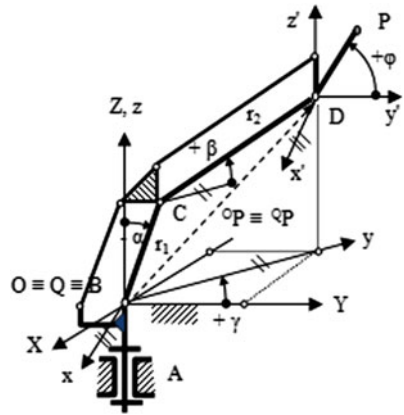
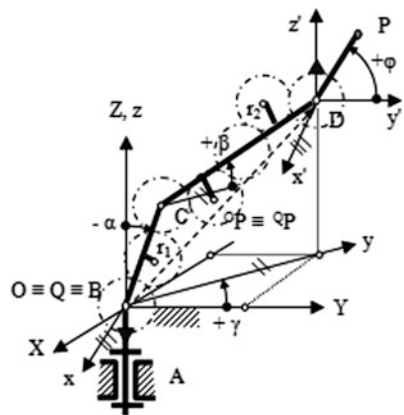


Fig. 5 Decoupling the rotations (α, β) by means of the Ferguson gearing



Ferguson mechanisms, with rigid intermediate satellites (Fig. 5), or with a flexible intermediate element such as the cog belt (Fig. 6).

The decoupling of kinematic chain of movements complicates the guiding device structure, but it simplifies the relations in the direct and inverse geometric models, and thus the calculations made when applying the calibration algorithm of the robots “driving program”.

These decoupling solutions remove the coplanar rotations of the trajectory generating mechanism from the orientation parameters of the end-effector. If a full decoupling of orientation in respect with the positioning movements is desired, the influence of the pivoting angle γ , must be also removed. This goal requires the changing of the robot’s architecture. For example, for the architecture in Cartesian coordinates, the problem of movements’ coupling disappears.

Unfortunately, constructive achieving of prismatic joints decreases the flexibility of the robot, which prevents the access to hidden application targets. Therefore, the architectural modifications of the robot must be minimal.

To eliminate the influence of γ on the orientation of the element DP , it is sufficient that, at the architecture in polar coordinates, provided with mechanisms of decoupling the rotation (α, β) , the driving rotation joint A be replaced with a prismatic one, resulting the structure $TRRR$ shown in Fig. 7.

Fig. 6 Decoupling the rotations (α, β) by means of the cycloid transmission cog belt

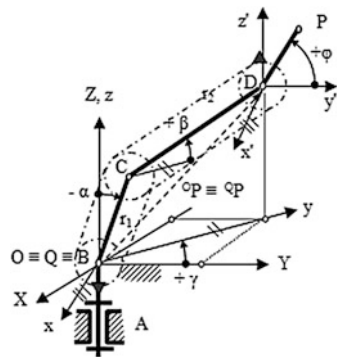


Fig. 7 TRRR structure for achieving an orientation φ independently from the positioning parameters (s, α, β)

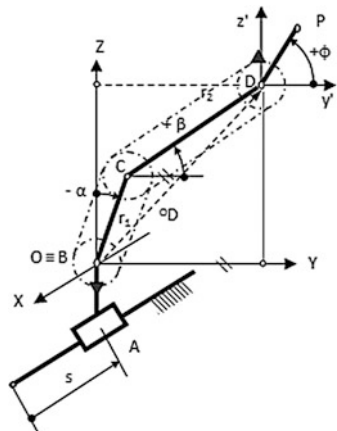
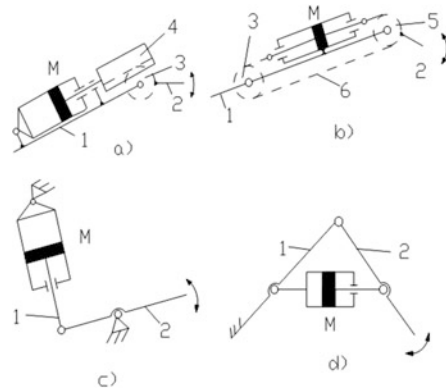


Fig. 8 Translation units attached to movement converting mechanisms



Surely, changing the structure of the guiding device only in order to simplifying a calibration algorithm implies major consequences on other aspects (construction of the robot, driving program, workspace shape, attaching peripheral components to the robot, organizing the entire system). Such an issue must be decided before purchasing the robotic *FMS*, taking into account the particularities required by the types of programs that will be implemented through calibration, to achieve various applications. In order to achieve the rotation movements in the driving joints of the guiding device, rotational engines can be used as well as translational units with hydraulic or pneumatic actuation, attached to movement converting mechanisms (Fig. 8). Their role is to materialize a degree of mobility and to ensure all forces and moments needed for the whole working stroke and for certain kinematic sizes (speed and acceleration).

Translation units contain a linear motor (generally a hydraulic or pneumatic double-action cylinder) and the associated control and adjusting elements for stopping the piston in a number of predetermined positions. The problem of achieving the necessary forces and speeds is relatively easy to solve through the appropriate choice of the supply pressure, the cylinders diameter and the supply section.

Because of their simplicity in construction, reliability, and security in service, hydraulic/pneumatic linear engines (cylinders) are used not only to achieve the translation in the driving kinematic joints but also the rotation movements. Figure 7 presents four such situations. The linear movement of the motor *M* is transformed into a rotary motion of the element 2 in relation with the element 1 through: the pinion 3 and the rack 4 (Fig. 8a); chain or cog belt transmission 6 and the wheels 5 (Fig. 8b); a simple lever (Fig. 8 c); or a deformable triangle (Fig. 8d).

4 Conclusions

There are different variants in organizing robotized FMS. If the system contains only a single robot servicing two theoretically identical peripheral components, with real different places in regard with the robot (as in Fig. 1), it is recommended to assemble all components on a common base plate. Previous to general calibration of the FMS, must be checked the correctness in placing of the robot on the foundation. This checking can be achieved through checking the place in space of the guiding device axes, using adequate instruments (square, level, lead line, theodolite).

A more complex guiding device or a peripheral component with specific own mobility leads to altering of the geometric models of the system, so that the number of parameters to be taken into account becomes larger. In addition to relative errors of the robotic FMS components, the calibration algorithm depends on the structure of the robot and its coupling of movements.

The solutions presented above serve to reduce relative errors of the FMS components for decoupling movements and for choosing convenient guiding devices.

References

1. Morris, R., Uday, S.: Robot calibration using an automatic theodolite. *Int J Adv Manuf Technol* **9**, 114 (2005)
2. Vacarescu, V., Lovasz, E.-C., Buciuman, C.F.: Research on multi-directional pose accuracy variation to a welding robot. In: *Advances in Mechanisms Design. Mechanisms and Machine Science*, vol. 8, pp. 323–328. Springer (2012)
3. Slamani, M., Nubiola, A., Bonev, I.: Assessment of the positioning performance of an industrial robot. *Ind Robot Int J* **39**(1), 57 (2012)
4. Zhang, Z., Luong, Q.-T., Faugeras, O.: Motion of an un-calibrated stereo rig: Self-calibration and metric reconstruction. *IEEE Trans. Robot. Autom.* **12**, 103–113 (1996)
5. Dudek, G., Jenkin, M., Milius, E., Wilkes, D.: Using multiple markers in graph exploration. *Proc. SPIE* **1989**(1195), 77–87 (1989)
6. Khadraoui, D., Motyl, G., Martinet, P., Gallice, J., Chaumette, F.: Visual servoing in robotics scheme using a camera/laser-stripe sensor. *IEEE Trans. Robot. Autom.* **12**, 743–750 (1996)
7. Conrad, K.L., Shiakolas, P.S., Yih, T.C.: Robotic calibration issues: accuracy, repeatability and calibration. In: *Proceedings of the 8th Mediterranean Conference on Control & Automation (MED 2000)*, Rio, Patras, GREECE, 17–19 July 2000
8. In-Chul, H.: Kinematic parameter calibration method for industrial robot manipulator using the relative position. *J. Mech. Sci. Technol.* **22**, 1084–1090 (2008)
9. Mönnich, H., Stein, D., Raczkowski, J., Wörn, H.: An automatic and complete self-calibration method for robotic guided laser ablation. In: *2010 IEEE International Conference on Robotics and Automation Anchorage Convention District*, 3–8 May, 2010, Anchorage, Alaska, USA, pp. 1086–1087 (2010)
10. Shu, F.: High-precision calibration approaches to robot vision systems. PhD thesis, University of Hamburg (2009)
11. Tsai, R.Y.: An Efficient and Accurate Camera Calibration Technique for 3D Machine Vision *Proceedings CVPR'86*, pp. 364–374. Florida, June, Miami Beach (1986)

12. Tsai, R.Y.: A versatile camera calibration technique for high-accuracy 3D machine vision metrology using off-the-shelf TV cameras and lenses. *IEEE J Robot Autom* **RA-3**, 4 1987
13. Nguyen, H.-N., Zhou, J., Kang, H.-J.: A new full pose measurement method for robot calibration. *Sensors* **13**, 9132–9147 (2013)
14. Product catalogue 2013. www.cloos.hu/index Accessed 14 Mar 2016
15. Maniu, I., Varga, Ș., Rădulescu, C., Dolga, V., Ciupe, V., Bogdanov, I.: *Robotică. Aplicații robotizate*. Politehnica, Timișoara (2009)
16. Maniu, I., Dolga, V., Ciupe, V., Bogdanov, I., Rădulescu, C., Varga, S.: *Robotică. Sistemul de acționare*. Politehnica, Timișoara. (2009)

Part VIII
Robotics—Mobile Robots

Reconbot: A Reconfigurable Rescue Robot Composed of Serial-Parallel Hybrid Upper Humanoid Body and Track Mobile Platform

W. Ding, T. Detert, B. Corves and Y.A. Yao

Abstract The mobility analysis of a 2-URU parallel mechanism (PM) using the screw theory and its novel application for constructing reconfigurable mobile robot are the main focus of this paper. By taking advantage of the singularity positions, the PM can reconfigure into different mobility configurations, which enable the robot to multi-mode collaborative locomotion and cooperative serial-parallel hybrid manipulation. Integrating these properties, a novel reconfigurable rescue robot called Reconbot composed of a track platform, a reconfigurable 2-URU PM with an equal offset in its two universal joints and two 7-DoF serial arms is proposed. The PM consisted of two offset URU branch chains and two platforms serves as dexterous upper body with base platform mounted on the track platform and two arms attached to the moving platform. The Reconbot can deform into folding compact state, serial two-leg state, parallelogram five-bar linkage state, etc.

Keywords Mobile robot • Reconfigurable parallel mechanism • Dual-arm • Collaborative locomotion • Cooperative manipulation

W. Ding (✉) • T. Detert • B. Corves
RWTH Aachen University, Aachen, Germany
e-mail: ding@igm.rwth-aachen.de

T. Detert
e-mail: detert@igm.rwth-aachen.de

B. Corves
e-mail: corves@igm.rwth-aachen.de

Y.A. Yao
Beijing Jiaotong University, Beijing, China
e-mail: yayao@bjtu.edu.cn

1 Introduction

In the serious natural and man-made disasters, robots assisting or replacing humans to carry out efficient search and rescue in high risk regions will be the inevitable choice in future [1]. The DARPA Robotics Challenge (DRC) viewed as a world-wide highest level rescue robot competition designed the extremely difficult disaster scene for participating teams to address the challenges of modern rescue scenarios. Many of the developed robots for the challenge can be classified by their sub-structures: A high mobility platform and flexible 7-DoF redundant dual-arms. Even though the tasks are designed with a focus to humanoid robots, teams with hybrid designs of the mobile platform, such as wheeled, track, or quadruped hybrid mobile platform obtained higher score [2]. Therefore, besides the essential environment operation by dual-arm cooperation, the high mobility and stable locomotion platform are critical for survivability and efficiency in rescue environments [3]. This motivation led to the design of the proposed robot.

2 Robot Structures for Complex Environments

For general scenes of disaster in complex environments, rescue robots need capabilities of high mobility for efficiency; large payload, workspace, and high stiffness for manipulation; compact configuration for transportation and narrow passage rescue [4]. Packbot viewed as a typical representative of hybrid track platform systems exerts a high mobility and stability performance in urban cities [5]. Its single arm and long link structure obtains a large workspace, while it restricts the abilities in heavy load and complex operational tasks.

Dual-arm mounted on wheeled, tracked or hybrid platforms are an effective way to preserve mobility and improve operability. Such as hybrid humanoid robots, Golem Krang equips with two robotic arms connected to a two-wheeled base by a fold revolute joint [6]; Momaro consists of an anthropomorphic upper body connected to a legged-wheeled mobile base by a twist revolute joint [7].

For enhancing the high stiffness and strength, hydraulic actuation and parallel mechanism can be considered as potential solutions. Vecna BEAR, as a human-like battlefield rescue robot, is a hybrid robot with two connected tracks serving as legs and a humanoid body with two hydraulic arms [8]. A six-legged walking robot with identical parallel kinematic 3-DoF IUP-2UPS legs can be used for drilling holes on the fuselage [9].

To enlarge the workspace and allow compact configurations, a foldable function between main body and mobile platform is beneficial for the rescue performance. Surrogate, from NASA's JPL team for DRC, possesses a track platform and a dexterous spine that holds an upper body with two limbs attached to it [10]. What's more, the bending revolute joint of Vecna BEAR and Golem Krang can fold into a compact state for quick and stable locomotion.

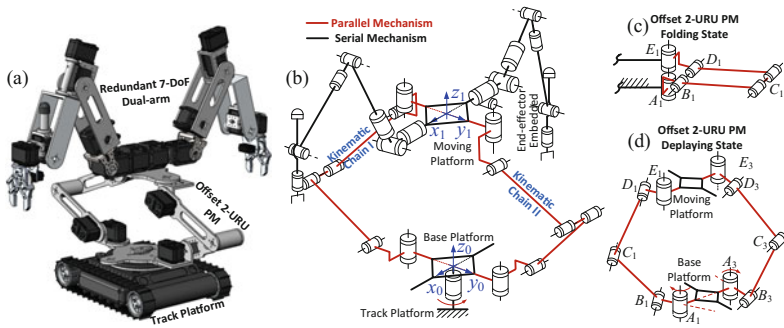


Fig. 1 Reconbot concept and mechanism design

3 Reconbot Concept and Mechanism Design

By considering the aforementioned aspects, the Reconbot composed of a track platform, a reconfigurable offset 2-URU PM [11], and two 7-DoF dual-arms is proposed. The PM provides large flexibility, foldability, and stiffness for the hybrid upper body [12], and it can cooperate with the track platform for locomotion.

Figure 1a shows the design concept of the Reconbot. Figure 1b is the sketch diagram of the upper body connected track platform with a revolute joint. A support link is embedded into wrist end-effector for locomotion collaboration. Figure 1c, d depict the sketch diagram of offset URU branch chain and a random configuration of the offset 2-URU PM, respectively.

4 Mobility Analysis

The DoF F of the offset 2-URU PM can be calculated by the modified Grübler-Kutzbach criterion [13]:

$$F = d(n - g - 1) + \sum_{i=1}^g f_i + v - \zeta \tag{1}$$

where, λ is the number of independent common constraints in the mechanism, $d = 6 - \lambda$ is called order of the mechanism, n is the total number of links, g is the number of kinematic pairs, f_i is the DoF of the i th kinematic pair, v represents the number of redundant constrains, and ζ is the passive DoF.



4.1 Screw System of Single Offset URU Branch Chain

Five conditions of single chain are shown in Fig. 2. The z_i axis of the local frame A_i passes through the revolute joint located at A_i , the x_i axis is parallel to revolute joint B_i , C_i , and D_i , and the y_i axis is perpendicular to $x_i z_i$ plane. The unit screw of a revolute joint is given by $\$ = (\mathbf{s}; \mathbf{r} \times \mathbf{s}) = (L_i M_i N_i; P_i Q_i R_i)$, where, $\mathbf{s} = (L_i M_i N_i)$ denotes the three direction cosines of the revolute axis, \mathbf{r} is the position vector of any point on the screw axis [14].

The constraint screw analysis of a single branch chain shown in Table 1 in the local frame A_i is calculated for each condition illustrated in Fig. 2. The twist system, reciprocal screw, and its generated constraints on the moving platform are listed. Note that, for Fig. 2d, two joints (B_i and D_i) are overlapped and links $B_i C_i$ and $C_i D_i$ form a single serial link, which exerts three constraint forces. For Fig. 2e,

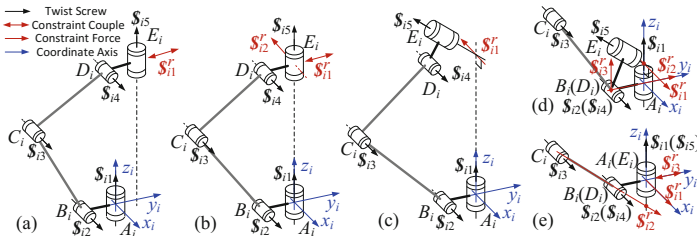


Fig. 2 Twist system in five conditions

Table 1 Constraint analysis of single branch chain

Figure 2	Twist system		Reciprocal screw	Constraint
(a)	$\$_{i1} = (0 \ 0 \ 1; 0 \ 0 \ 0)$	$\$_{i5} = (0 \ 0 \ 1; y_E \ 0 \ 0)$	$\$_{i1}^r = (0 \ 0 \ 0; 0 \ 1 \ 0)$	Couple($\$_{i1}^r$)
(b)	$\$_{i2} = (1 \ 0 \ 0; 0 \ 0 \ -y_B)$	$\$_{i5} = \$_{i1} = (0 \ 0 \ 1; 0 \ 0 \ 0)$	$\$_{i1}^r = (1 \ 0 \ 0; 0 \ 0 \ 0)$	Force($\$_{i1}^r$)
	$\$_{i3} = (1 \ 0 \ 0; 0 \ z_C \ -y_C)$		$\$_{i2}^r = (0 \ 0 \ 0; 0 \ 1 \ 0)$	Couple($\$_{i2}^r$)
(c)	$\$_{i4} = (1 \ 0 \ 0; 0 \ z_D \ -y_D)$	$\$_{i5} = (0 \ M_5 \ N_5; O_5 \ 0 \ 0)$	$\$_{i1}^r = (M_5 \ 0 \ 0; 0 \ Q_5 \ 0)$	Force($\$_{i1}^r$)
(d)	$\$_{i1} = (0 \ 0 \ 1; 0 \ 0 \ 0)$	$\$_{i4} = \$_{i2}$	$\$_{i1}^r = (-M_5 \ 0 \ 0; 0 \ Q_5 \ 0)$	Force($\$_{i1}^r$)
	$\$_{i2} = (1 \ 0 \ 0; 0 \ 0 \ -y_B)$	$\$_{i5} = (0 \ M_5 \ N_5; O_5 \ 0 \ 0)$	$\$_{i2}^r = (0 \ 1 \ 0; 0 \ 0 \ 0)$	Force($\$_{i2}^r$)
	$\$_{i3} = (1 \ 0 \ 0; 0 \ z_C \ -y_C)$		$\$_{i3}^r = (0 \ 0 \ 1; y_B \ 0 \ 0)$	Force($\$_{i3}^r$)
(e)		$\$_{i4} = \$_{i2}$	$\$_{i1}^r = (1 \ 0 \ 0; 0 \ 0 \ 0)$	Force($\$_{i1}^r$)
		$\$_{i5} = \$_{i1}$	$\$_{i2}^r = (0 \ 0 \ 0; 0 \ 1 \ 0)$	Couple($\$_{i2}^r$)
			$\$_{i3}^r = (L \ M \ N; P \ 0 \ 0)$	Force($\$_{i3}^r$)

Notes $O_5 = N_5 y_E - M_5 z_E$, $(L \ M \ N; P \ 0 \ 0) = (0 \ y_C - y_B, z_C - z_B; z_B(y_C - y_B) - y_B(z_C - z_B) \ 0 \ 0)$



two groups of joints (A_i and E_i , B_i and D_i) are coincided, and the branch chain forms a two link serial chain with two revolute joints, which generates one constraint couple and two constraint forces [15].

4.2 Mobility Analysis of the Offset 2-URU PM

Due to the parallel arrangement of the two terminal revolute joints attached to the moving platform, the two offset universal joints are always co-plane. Therefore, four different cases need to be considered (see Table 2 for details).

Case I: two platforms are parallel including four conditions classified by the conditions in Fig. 2a, b. Condition in Fig. 2a: Condition I: $\$_{11}^r \parallel \$_{21}^r$, Condition II: $\$_{11}^r$ intersects with $\$_{21}^r$. Condition in Fig. 2b: Condition III: $\$_{11}^r \parallel \$_{21}^r$ and $\$_{12}^r \parallel \$_{22}^r$, Condition IV: $\$_{11}^r$ and $\$_{21}^r$ intersects with $\$_{12}^r$ and $\$_{22}^r$ correspondingly.

Case II: two platform planes intersect, which exert two constraint forces (condition in Fig. 2c), including two cases: Condition I: $\$_{11}^r \parallel \$_{21}^r$; Condition II: $\$_{11}^r$ is co-axis with $\$_{21}^r$;

Case III: one branch chain reaches condition in Fig. 2d in which forms a local serial link and the other satisfies condition in Fig. 2c. The final configuration is a planar four-bar linkage mechanism.

Case IV: both of branch chain reaches the singularity condition in Fig. 2e, and then, the robot forms a serial mechanism.

Taking Cases I Condition I ($\$_{11}^r \parallel \$_{21}^r$) and Cases II Condition I as example, the descriptions are described as (the offset universal joint is viewed as one link):

- (1) Cases I, Condition I: the two constraint couples are parallel, co-plane, and dependent. In this instantaneous configuration, two rotation freedoms are perpendicular to the direction of the constraint couple. Then, $\lambda = 1$, $\nu = \zeta = 0$, thus, the DoF is calculated as $F = 5 \times (10 - 10 - 1) + 10 = 5$. Note that, for Cases I, condition II ($\$_{11}^r$ intersects with $\$_{21}^r$) and III ($\$_{11}^r \parallel \$_{21}^r$ and $\$_{12}^r \parallel \$_{22}^r$), the DoF are 4 and 3 (except 2 passive DoFs), respectively.
- (2) Cases II, Condition I ($\$_{11}^r \parallel \$_{21}^r$): Two constraint forces are parallel but independent. Setting two intersection points of $\$_{i1}$ and $\$_{i5}$ of two branch chains are $(0, y_1, z_1)$ and $(0, y_2, z_2)$, and $L_1M_2 - L_2M_1 = 0$. This instantaneous configuration possesses four freedoms including two translation freedom that are two mutually perpendicular direction (perpendicular to $\$_{m1}^r$) and two rotation freedom of which two axes are parallel to $\$_{m1}^r$ and cross two intersection points of $\$_{11}^r$ and $\$_{21}^r$. Thus, $F = 6 \times (10 - 10 - 1) + 10 = 4$.

The potential actuation strategies for each configuration cases are shown in Table 2. However, reconfigurable deformation among them needs the offset 2-URU PM to overcome different singularity positions. Therefore, the number of actuators should be six with three mounted in each branch chain for redundant actuation and symmetric layout.

Table 2 Reconfiguration cases

Cases	Case I		Case II
	Condition I	Condition IV	Condition I
BC	Figure 2a	Figure 2b	Figure 2c
Constraint system	$S_{m1}^r = (0\ 0\ 0; L_1\ M_1\ 0)$	$S_{m1}^r = (1\ 0\ 0; 0\ 0\ R_1)$ $S_{m2}^r = (0\ 1\ 0; 0\ 0\ 0)$ $S_{m3}^r = (1\ 0\ 0; 0\ 0\ R_2)$ $S_{m4}^r = (0\ 0\ 0; 0\ 1\ 0)$	$S_{m1}^r = (L_1\ M_1\ 0;$ $-M_1z_1\ L_1z_1 - L_1y_1)$ $S_{m1}^r = (L_2\ M_2\ 0;$ $-M_2z_2\ L_2z_2 - L_2y_2)$
DoFs	5	2 (+2 passive DoFs)	4
MP mobility	3T2R	1T1R	2T2R
Configuration and actuation			
Cases	Case II	Case III	Case V
	Condition II		
BC	Figure 2c	Figure 2c + Fig. 2d	Figure 2e
Constraint system	$S_{m1}^r = (0\ 1\ 0; -z_1\ 0\ 0)$	$S_{m1}^r = (1\ 0\ 0; 0\ Q_1\ R_1)$ $S_{m2}^r = (0\ 1\ 0; 0\ 0\ 0)$ $S_{m3}^r = (0\ 0\ 1; P_3\ 0\ 0)$ $S_{m4}^r = (1\ 0\ 0; 0\ Q_4\ R_4)$	$S_{m1}^r = (1\ 0\ 0; 0\ 0\ 0)$ $S_{m2}^r = (0\ 0\ 0; 0\ 1\ 0)$ $S_{m3}^r = (L_3\ M_3\ N_3; P_3\ 0\ 0)$ (Single serial chain)
DoFs	5	2 (+1 passive DoF)	0 (+4 passive DoFs)
MP mobility	2T3R	2R	Fixed
Configuration & Actuation			

Notes: BC, Branch Chain; MP, Moving Platform

4.3 Reconfigurable Functions Description

As discussed above, the reconfigurable deformation of the Reconbot is mainly based on the offset 2-URU PM. In Fig. 3, a reconfiguration processes of offset 2-URU PM is shown for better understanding of the reconfigurable process. The PM takes advantage of the singularity position rather than avoids it, which forms a parallelogram and generates a passive DoF to rotate the obverse of the



moving platform to the reverse. The Figs. 3c–f show the critical steps. The passive DoF is controlled and rotated redundantly by two actuators displayed in Fig. 3d, e. After that, the PM forms a new planar six-bar linkage depicted in Fig. 3g. Figure 3h illustrates a singularity position where two end joints are co-axis to form a serial chain and the rest links forms a four-bar linkage.

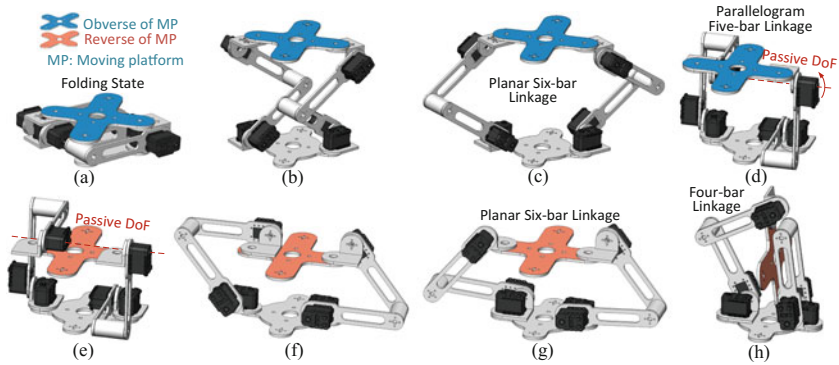


Fig. 3 Reconfiguration process (reverse motion) of the moving platform

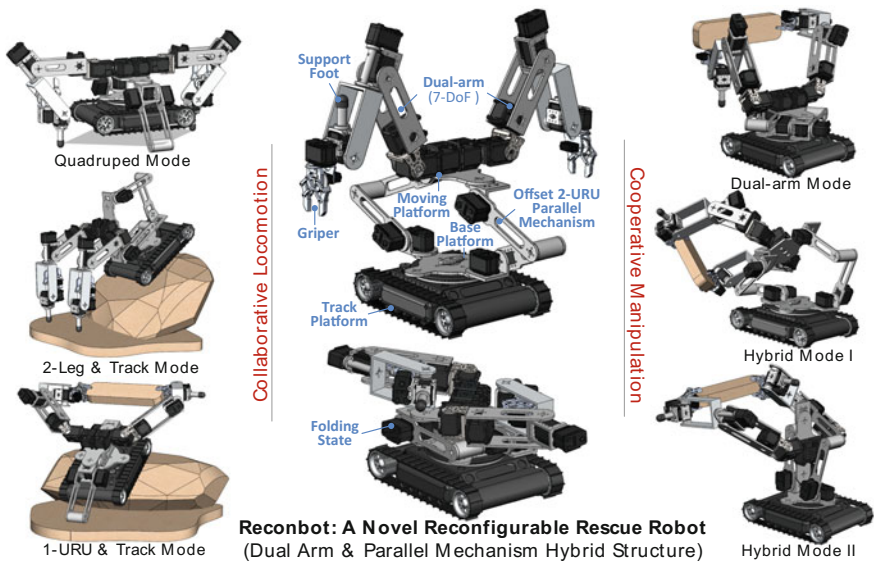


Fig. 4 Locomotion and manipulation functions



5 Locomotion and Manipulation Functions

As illustrated in Fig. 4, the hybrid design and deformation capabilities enable the robot to generate multi-mode collaborative locomotion and large reachability and flexibility cooperative manipulation. What's more, the reconfigurable PM makes it easy to fold into a compact state for transportation or pass through narrow passage. For collaborative locomotion, three potential modes are displayed, which are quadruped mode, track with 2-leg (dual-arm) collaboration, and track with 1-URU folding serial chain collaboration. For cooperative manipulation, three situations generated by three conditions of the PM are depicted, which are pure dual-arm operation, serial-parallel hybrid mode I with random PM configuration, and serial-parallel hybrid mode II with planar four-bar linkage configuration.

6 Conclusions

A reconfigurable rescue robot called Reconbot was proposed by integrating a track platform for high mobility, a serial-parallel hybrid configuration for large payload, workspace, and high stiffness and a reconfigurable parallel mechanism for large deformation capabilities and collaborative locomotion. Each offset URU chain of the PM was analyzed to possess five different constraints on the moving platform. The PM can be divided into four cases including eight different conditions decided by the combination of constraints. The mobility and DoF properties for each condition were analyzed. By properly choosing the configuration, the Reconbot provides three collaborative locomotion modes and three cooperative manipulation modes.

For the next step, the kinematics, dynamics, reconfiguration recognition and control, dynamic simulation, motion and trajectory planning, hardware and control system construction, experiments will be carried out accordingly.

Acknowledgments This work was supported by Sino-German (CSC-DAAD) Postdoc Scholarship Program, 2015 (57165010).

References

1. Tadokoro, S.: Rescue Robotics: DDT Project on Robots and Systems for Urban Search and Rescue. Springer Science & Business Media (2009)
2. DARPA Robotics Challenge Final 2015. <http://www.theroboticschallenge.org/>
3. Matsuno, F., Tadokoro, S.: Rescue robots and systems in Japan. In: IEEE International Conference on Robotics and Biomimetics, pp. 12–20 (2004)
4. Murphy, R.R., et al.: Search and Rescue Robotics. In: Springer Handbook of Robotics, pp. 1151–1173. Springer, Berlin, Heidelberg (2008)

5. Rudakevych, P., Ciholas, M.: PackBot EOD firing system. Defense and security. Int. Soc. Optic. Photon. pp. 758–771 (2005)
6. Stilman, M., Olson, J., Gloss, W.: Golem krang: dynamically stable humanoid robot for mobile manipulation. In: IEEE International Conference on Robotics and Automation (ICRA), pp. 3304–3309 (2010)
7. Rodehutsors, T., Schwarz, M., Behnke, S.: Intuitive bimanual telemanipulation under communication restrictions by immersive 3D visualization and motion tracking. In: IEEE-RAS 15th International Conference on Humanoid Robots, pp. 276–283 (2015)
8. Theobald, D.: Mobile extraction-assist robot. U.S. Patent 7,719,222 (2010)
9. Pan, Y., Gao, F.: A new 6-parallel-legged walking robot for drilling holes on the fuselage. In: Proceedings of the Institution of Mechanical Engineers, Part C: Journal of Mechanical Engineering Science, 0954406213489068 (2013)
10. JPL's Surrogate Robot. <http://www.jpl.nasa.gov/spaceimages/details.php?id=PIA18792>
11. Varedi, S.M., Daniali, H.M., Ganji, D.D.: Kinematics of an offset 3-UPU translational parallel manipulator by the homotopy continuation method. Nonlinear Anal. Real World Appl. **10**(3), 1767–1774 (2009)
12. Kong, X.W.: Reconfiguration analysis of a 3-DOF parallel mechanism using Euler parameter quaternions and algebraic geometry method. Mech. Mach. Theory **74**, 188–201 (2014)
13. Huang, Z.: The kinematics and type synthesis of lower-mobility parallel manipulators. In: Proceedings of the 11th World Congress in Mechanism and Machine Science, Tianjin, China, pp. 65–76 (2004)
14. Huang, Z., Liu, J.F., Zeng, D.X.: A general methodology for mobility analysis of mechanisms based on constraint screw theory. Sci. China Ser. E: Technol. Sci. **52**(5), 1337–1347 (2009)
15. Huang, Z., Li, Q.C.: Construction and kinematic properties of 3-UPU parallel mechanisms. In: ASME International Design Engineering Technical Conferences and Computers and Information in Engineering Conference, pp. 1027–1033 (2002)

Kinematics Modelling of Mobile Robot with Articulated Limbs Without Wheel Slip

P. Sperzyński and A. Gronowicz

Abstract This paper presents a formulation of the kinematics model of wheeled mobile robot with articulated limbs. In order to describe the contact motion between robot wheels and ground, a differential kinematics model is used. Following the already mentioned, nonholonomic constraints of the wheel no-slip movement are introduced in a form of Pfaffian constraints. Further section of this article describes the kinematics control system preventing wheel slip. To ensure the no-slip motion conditions, null space of a Pfaffian constraints matrix is taken into consideration. Finally, numerical simulation is presented as proof of validity for the previously developed and proposed control system.

Keywords Mobile robot · Kinematics modelling · Nonholonomic constraints

1 Introduction

Wheeled-legged robots are the subject of research and development amongst many research centres all over the world. Robots Hylos [1] or WorkPartner [2] are the representants of such multibody systems. The wheeled-legged mobile robot LegVan [3, 4] presented in this paper, features similar kinematics structure to the above-mentioned Hylos robot. Legvan is a four limbs structure, with four actuators in each limb, which gives us sixteen actuators in total.

Kinematics model of such robot is highly complex due to the existence of either holonomic and nonholonomic constraints. Wheeled-legged robots are capable of negotiating obstacles mostly in two ways. It can walk over obstacles without using its wheel drives, or simply bypass them only by rolling the wheels. When movement is based on robot's wheel drives, it is highly desirable to execute it without the wheel slip. Simply due to the fact that it causes huge energy losses and robot odometer system gets much more complicated. Paper [5] introduces a robot model where wheels

P. Sperzyński (✉) · A. Gronowicz
Wrocław University of Science and Technology, Wrocław, Poland
e-mail: przemyslaw.sperzynski@pwr.edu.pl

are modelled as a torus moving over uneven terrain, but especially designed passive joints are used to prevent wheel slip. The general kinetostatic formulation of quasi-static motion regarding articulated wheeled rovers with non-ideal contact conditions is presented in [1].

This paper deals with wheel slippage phenomenon using Pfaffian constraints matrix and its null space matrix mentioned above. Based on those constraints, control system providing the movement of a robot platform without slipping is proposed.

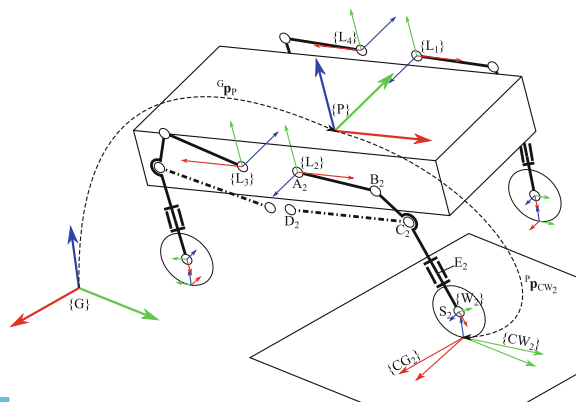
2 Kinematics Modelling of Holonomic Constraints

This section presents a kinematic constraints. The description of relations between coordinate frames is enclosed, which aims at introducing the configuration (locations and orientations) of robot platform and limbs over a terrain surface.

Configuration of Mobile Robot platform considered in the article has been presented as follows (Fig. 1):

- $\mathcal{F}_i = ({}^i\mathbf{p}_i, {}^j\mathbf{R}_i)$ —coordinate frame defined by location vector ${}^j\mathbf{p}_i$ and rotation matrix ${}^j\mathbf{R}_i = [{}^j\mathbf{e}_{x,i}, {}^j\mathbf{e}_{y,i}, {}^j\mathbf{e}_{z,i}]$, specifying axes of i^{th} frame expressed in j^{th} frame,
- \mathcal{F}_G —global, inertial coordinate frame, frame of ground surface,
- $\mathcal{F}_P = ({}^G\mathbf{p}_P, {}^G\mathbf{R}_P) = \mathbf{T}([x_P, y_P, z_P])\mathbf{R}_Z(\zeta)\mathbf{R}_Y(\gamma)\mathbf{R}_X(\rho)$ mobile robot platform frame describing its configuration relative to global frame. Orientation of the frame has been parametrized as Roll, Pitch, Yaw angles (RPY),
- $\mathbf{x} = (\mathbf{x}_P, \mathbf{x}_R)^T = (x_P, y_P, z_P, \rho, \gamma, \zeta)^T$ —platform configuration vector,
- n_L —number of robot limbs,
- $\mathcal{F}_{Li} = ({}^P\mathbf{p}_{Li}, {}^P\mathbf{R}_{Li}) = \mathbf{T}([\pm x_L, \pm y_L, z_L])\mathbf{R}_Z(k\pi)\mathbf{R}_X(\pi/2)$ —frame of i th limb fixed to the platform (expressed relative to \mathcal{F}_P frame), where $i = 1, \dots, n_L, k = 0$ in case of front limbs and $k = 1$ in case of rear. Frames are orientated thus, axis $\mathbf{e}_{y, Li} \parallel \mathbf{e}_{z, P}$ and $\mathbf{e}_{x, Li} \parallel \mathbf{e}_{x, P}$, which makes transformation between limbs frames \mathcal{F}_{Li} , and wheel frame are identical for each limb.

Fig. 1 Mobile robot configuration relative to terrain



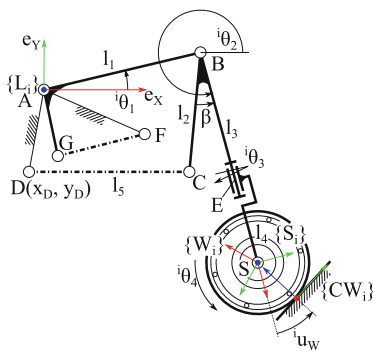
Kinematics model describing transformation between base frame of a limb \mathcal{F}_{Li} and wheel (end-effector) frame has been presented as follows:

- ${}^i\theta_j$ —denotes j^{th} actuator in i^{th} limb, $i = 1, \dots, n_L, j = 1, \dots, 4$,
- ${}^i\theta$ —vector of all actuators in i^{th} limb,
- $\mathcal{F}_{Si} = ({}^Li\mathbf{p}_{Si}, {}^Li\mathbf{R}_{Si}) = \mathbf{R}_Z({}^i\theta_1)\mathbf{T}_X(l_1)\mathbf{R}_Z({}^i\theta_2 - {}^i\theta_1)\mathbf{T}_X(l_3)\mathbf{R}_X({}^i\theta_3)\mathbf{T}_X(l_4)$ —frame attached to last link in limb kinematics chain, located in centre of a i^{th} wheel,
- $\mathcal{F}_{Wi} = (\emptyset, {}^Si\mathbf{R}_{Wi}) = \mathbf{R}_X({}^i\theta_4)$ —frame attached to wheel.

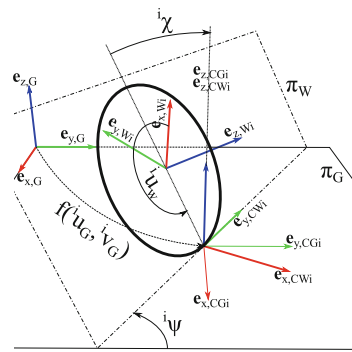
For a purpose of analysis conducted in this paper, kinematics of a limb has been simplified. Angles ${}^i\theta_1$ and ${}^i\theta_2$ representing the position of the wheel with respect to the robot platform, are determined by stroke of linear actuators labelled in Fig. 2, as *DC* and *FG*.

The wheel has been described as flat disc rolling on a ground surface which subsequently has been modelled as parametric surface. The corresponding equation with two describing parameters $f_i(u, v) : \mathbb{R}^2 \rightarrow \mathbb{R}^3$, has been used so that each of the wheels could move over a different surface. The following parameters are proposed:

- $\mathcal{F}_{CWi} = \mathcal{F}({}^Wi\mathbf{p}_{CWi}, {}^Wi\mathbf{R}_{CWi}) = \mathbf{R}_Z({}^iu_w - {}^i\theta_4)\mathbf{T}_X(r_w)\mathbf{R}_Y({}^i\chi - \frac{\pi}{2})$ —contact frame connected to i^{th} wheel, placed in the point of contact between wheel and a ground,
- iu_w —rotates axis $\mathbf{e}_{x,Wi}$ to make it aim a point of contact,
- ${}^i\chi$ align axis $\mathbf{e}_{z,Wi}$ to coincide with $\mathbf{e}_{z,CGi}$ (camber angle),
- $\mathcal{F}_{CGi} = ({}^G\mathbf{p}_{CGi}, {}^G\mathbf{R}_{CGi})$ —frame defined by parametric equation $f_i(u, v)$ of a ground surface, located in a point of contact,
- ${}^G\mathbf{p}_{CGi} = f_i({}^iu_G, {}^iv_G)$,
- ${}^G\mathbf{R}_{CGi}$ — $\mathbf{e}_{x,CGi} = \partial f_i / \partial u|_{u={}^iu_G, v={}^iv_G}$, $\mathbf{e}_{y,CGi} = \partial f_i / \partial v|_{u={}^iu_G, v={}^iv_G}$, and axis $\mathbf{e}_{z,CGi} = \mathbf{e}_{x,CGi} \times \mathbf{e}_{y,CGi}$,
- ${}^i\psi$ rotation angle between frames \mathcal{F}_{CWi} and \mathcal{F}_{CGi} along axis \mathbf{e}_z ,



(a) Limb parameters of the robot.



(b) Contact parameters.

Fig. 2 Kinematics parameters of a limb and parameters related to the contact between wheel and the ground



- ${}^i\boldsymbol{\eta} = ({}^i u_G, {}^i v_G, {}^i u_W, {}^i \chi, {}^i \psi)^T$ —vector of a variables containing all parameters describing contact frames,
- π_G —plane tangent to a surface of a ground in point of contact, described by point ${}^G \mathbf{p}_{CGi}$ and normal vector $\mathbf{e}_{z,CGi}$,
- π_W —plane of a wheel, given by centre point of a wheel ${}^G \mathbf{p}_{Wi}$ and normal vector $\mathbf{e}_{z,Wi}$.

Robot state variables vector denoting its configuration (platform pose, limbs configurations, points of contact, etc.) is:

$$\mathbf{q} = (\mathbf{x}, {}^i\boldsymbol{\theta}, {}^i\boldsymbol{\eta})^T, \quad i = 1, \dots, n_L \tag{1}$$

For each limb, loop-closure equations of holonomic constraints are provided. All that with respect to the fact that contact frames have to meet at one point ($\mathcal{F}_G \rightarrow \mathcal{F}_P \rightarrow \mathcal{F}_{Wi} \rightarrow \mathcal{F}_{CWi} = \mathcal{F}_G \rightarrow \mathcal{F}_{CGi}$):

$$\underbrace{{}^G \mathbf{p}_P + {}^G \mathbf{R}_P}_{\mathbf{x}} \underbrace{({}^P \mathbf{p}_{Li} + {}^P \mathbf{R}_{Li})}_{const} \underbrace{({}^{Li} \mathbf{p}_{Wi} + {}^{Li} \mathbf{R}_{Wi})}_{{}^i\boldsymbol{\theta}} \underbrace{{}^{Wi} \mathbf{p}_{CWi}}_{{}^i u_W} = \underbrace{{}^G \mathbf{p}_{CGi}}_{{}^i u_G, {}^i v_G} \tag{2}$$

Wheel (modelled as a circle) has to be tangent to plane π_G . As presented in Fig. 2b, axis $\mathbf{e}_{y,CWi}$ tangent to the wheel is aligned collinear to straight line obtained as intersection of planes π_G and π_W . This results in the formulation of the next constraint equation:

$$\det([\underbrace{\mathbf{e}_{x,CGi}, \mathbf{e}_{y,CGi}}_{{}^i u_G, {}^i v_G}, \underbrace{\mathbf{e}_{y,CWi}}_{{}^i \theta, {}^i u_W}]^T) = 0. \tag{3}$$

The already mentioned equation checks if two axes \mathbf{e}_x and \mathbf{e}_y within a ground contact frame \mathcal{F}_{CGi} stay coplanar with axis $\mathbf{e}_{y,CWi}$, which represents the trace of a wheel movement.

Finally, the system of four holonomic constraints for each limb has been derived in a form of Eqs. (2) and (3). This has led to the system of $4 \cdot n_L$ equations in total. The above-mentioned variables are the platform configuration \mathbf{x} , limb actuators ${}^i\boldsymbol{\theta}_{j=1,\dots,3}$ neglecting wheel drive (θ_4 does not affect displacement of point of contact ${}^G \mathbf{p}_{CGi}$) and contact variables ${}^i\boldsymbol{\eta}_{j=1,\dots,3}$ without angles χ, ψ . In conclusion, from the analysis conducted arises $6 + 3n_L + 3n_L$ variables. When taken only three of four limbs into consideration (minimal number of contact points to achieve a static pose of a robot), 12 equations with 24 variables has been defined. Taken into account all robot actuators (neglecting wheel drive actuators), the following three variables have to be assumed. Authors propose to adopt 3 out of 6 contact parameters (${}^i u_G, {}^i v_G$) to satisfy the constraint for ensuring contact between wheel and the ground.

Configuration of robot platform \mathbf{x} would be obtained as a solution of system (2, 3). Afterwards, wheels \mathcal{F}_{Wi} and contact \mathcal{F}_{CGi} frames would be calculated respectively. Therefore last parameters ${}^i \chi, {}^i \psi$ can be achieved from relation between frames:



$${}^G \mathbf{R}_{W_i} \cdot \mathbf{R}_Z({}^i u_W) \cdot \mathbf{R}_Y({}^i \chi - \frac{\pi}{2}) \mathbf{R}_Z({}^i \psi) = {}^G \mathbf{R}_{CG_i}. \quad (4)$$

Throughout modification of this expression, angles can be extracted from rotation matrix, described as follows:

$$\mathbf{R}_Y({}^i \chi - \frac{\pi}{2}) \mathbf{R}_Z({}^i \psi) = \mathbf{R}_Z({}^i u_W) {}^G \mathbf{R}_{W_i}^T {}^G \mathbf{R}_{CG_i} \quad (5)$$

Assuming 12 parameters, the complete configuration of a robot \mathbf{q} may be obtained using numerical methods.

3 Differential Kinematics Model of the Robot

Differential kinematics of motion between the two bodies in contact sets the example of nonholonomic constraints. Motion of two bodies characterized by parametric surfaces, lasting in contact conditions, has been defined in [6]. Transforming it into the previously presented flat disc model, system of velocities equation has been obtained:

$$\begin{cases} \mathbf{v}_{CW_i/W_i}^b + \mathbf{v}_{in} = {}^{CG_i} \mathbf{R}_{CW_i}^T \mathbf{v}_{CG_i/G}^b \\ \boldsymbol{\Omega}_{CW_i/W_i}^b + \boldsymbol{\Omega}_{in} = \boldsymbol{\Omega}_{CW_i/CG_i}^b + {}^{CG_i} \mathbf{R}_{CW_i}^T \boldsymbol{\Omega}_{CG_i/G}^b \end{cases} \left| \begin{array}{l} \mathbf{v}_{j/i}^b = {}^i \mathbf{R}_j^T \dot{\mathbf{p}}_j \\ \boldsymbol{\Omega}_{j/i}^b = {}^i \mathbf{R}_j^T \dot{\mathbf{R}}_j^T \end{array} \right. \quad (6)$$

where described velocity $\mathbf{v}_{j/i}^b$, $\boldsymbol{\Omega}_{j/i}^b$ is so-called *body velocity*, which denotes velocity of j th frame relative to i th frame, expressed in body j th frame. Introduced system of equations depends on five contact variables ${}^i \dot{\boldsymbol{\eta}}$ and input motion velocities \mathbf{v}_{in} , $\boldsymbol{\Omega}_{in}$, denoting velocity of a wheel with respect to the terrain, expressed in \mathcal{F}_{CW_i} . Velocity $\mathbf{v}_{in} = [v_x, v_y, v_z]^T$ determines wheel slip velocities, and its particular components describe: v_x —side (lateral) slip, v_y —longitudinal slip and v_z —possible lost of contact or deformation of a wheel. Angular velocity is a skew-symmetric matrix which may be defined by vector $\boldsymbol{\Omega}_{j/i}^b = S(\boldsymbol{\omega}_{j/i})$. As a result, input angular velocity can be represented by three parameters $\boldsymbol{\Omega}_{in} = S([\omega_x, \omega_y, \omega_z]^T)$, where specific components of velocity are ω_x —wheel roll rate, ω_y —camber angle rate, ω_z —steering angle rate. Due to the fact that velocity $v_z = 0$, it is not taken into account in further analysis, noting that holonomic constraints, studied in previous section, have to be sustained. As a consequence, Eq. (6) provides the system of 5 equations comprising 5 contact variables ${}^i \dot{\boldsymbol{\eta}} = f(v_x, v_y, \omega_x, \omega_y, \omega_z)$.

As presented in [6], \mathbf{v}_{in} and $\boldsymbol{\Omega}_{in}$ are relative velocities between two bodies remaining in contact conditions, expressed in a contact frame of one of those two. Following formulation presented in [6], the input velocities are connected with velocities between local coordinate frames of the bodies. Taken the frame \mathcal{F}_G as a terrain's and \mathcal{F}_{W_i} as a wheel's local body frame, input velocities has been formulated as follows:

$$\begin{aligned} \mathbf{v}_{in} &= {}^{CW_i}\mathbf{R}_{W_i} \cdot \mathbf{v}_{W_i/G}^b + {}^{CW_i}\mathbf{R}_{W_i} \cdot \boldsymbol{\Omega}_{W_i/G}^b \cdot {}^{Wi}\mathbf{P}_{CW_i} \\ \boldsymbol{\Omega}_{in} &= {}^{CW_i}\mathbf{R}_{W_i} \cdot \boldsymbol{\Omega}_{W_i/G}^b \cdot {}^{Wi}\mathbf{R}_{CW_i} \end{aligned} \quad (7)$$

Slip velocity \mathbf{v}_{in} of a wheel, provided by Eq. (7), may be expanded based on the following frame relations: $\mathcal{F}_G \rightarrow \mathcal{F}_P \rightarrow \mathcal{F}_{Li} \rightarrow \mathcal{F}_{Wi}$. This enables the expression of wheel slip relative to the ground surface:

$$\mathbf{v}_{in} = \underbrace{{}^{CW_i}\mathbf{R}_P \mathbf{J}_{P_i} \dot{\mathbf{x}}_P}_{\mathbf{J}_{P_i} \dot{\mathbf{x}}_P} + \underbrace{{}^{CW_i}\mathbf{R}_P \mathbf{J}_{R_i} \dot{\mathbf{x}}_R}_{\mathbf{J}_{R_i} \dot{\mathbf{x}}_R} + \underbrace{{}^{CW_i}\mathbf{R}_{W_i} \mathbf{J}_{L_i}^i \dot{\boldsymbol{\theta}}}_{\mathbf{J}_{L_i}^i \dot{\boldsymbol{\theta}}} + {}^{CW_i}\mathbf{R}_P \boldsymbol{\Omega}_{P/G}^b \cdot \mathbf{P}_{CW_i} + {}^{CW_i}\mathbf{R}_{W_i} \mathbf{v}_{W_i/Li}^b + {}^{CW_i}\mathbf{R}_{W_i} \boldsymbol{\Omega}_{W_i/Li}^b \cdot \mathbf{P}_{CW_i} \quad (8)$$

Assuming the no-slip wheel movement, velocities of a wheel measured at a point of contact, in reference to ground frame, have to be equal to zero $\mathbf{v}_{in} = 0$. This, in a straightforward manner, leads to a system of nonholonomic constraints. Further analysis will only regard three out of four robot limbs. Such a case represents the conditions when robot overcomes obstacles taking one step forward, thus has to rise one of its limbs. In such a system, the fourth limb can be controlled to keep point of contact with a ground in order to extend the field of stability of the robot’s platform, but the aforementioned circumstance is not presented in this article. Constraints in a form of Pfaffian matrix are defined in the following manner:

$$\mathbf{A}(\mathbf{q})(\dot{\mathbf{x}}, \dot{\boldsymbol{\theta}})^T = \mathbf{0}_{9 \times 1} = \begin{bmatrix} \mathbf{J}_{P1} & \mathbf{J}_{R1} & \mathbf{J}_{\theta1} & 0 & 0 & \mathbf{j}_{\theta1} & 0 & 0 \\ \mathbf{J}_{P2} & \mathbf{J}_{R2} & 0 & \mathbf{J}_{\theta2} & 0 & 0 & \mathbf{j}_{\theta2} & 0 \\ \mathbf{J}_{P3} & \mathbf{J}_{R3} & 0 & 0 & \mathbf{J}_{\theta3} & 0 & 0 & \mathbf{j}_{\theta3} \end{bmatrix}_{9 \times 18} (\dot{\mathbf{x}}, \dot{\boldsymbol{\theta}})^T \quad (9)$$

Jacobian matrix $\mathbf{J}_{Li} \in \mathbb{R}^{3 \times 4}$, corresponding to actuators velocities in a robot limb was divided into two parts, square matrix $\mathbf{J}_{\theta i} \in \mathbb{R}^{3 \times 3}$ and column vector $\mathbf{j}_{\theta i} \in \mathbb{R}^{3 \times 1}$ separating one of the actuators as described: $\mathbf{J}_{Li} = [\mathbf{J}_{\theta i}, \mathbf{j}_{\theta i}]$.

If null space matrix $\mathbf{G}(\mathbf{q})$, of constraint matrix $\mathbf{A}(\mathbf{q})$, such as $\mathbf{A}(\mathbf{q})\mathbf{G}(\mathbf{q}) = 0$ is defined, then using any input vector $\mathbf{u} \in \mathbb{R}^{9 \times 1}$, velocities vector $(\dot{\mathbf{x}}, \dot{\boldsymbol{\theta}})^T$ is obtained in a span of this kernel matrix:

$$(\dot{\mathbf{x}}, \dot{\boldsymbol{\theta}})^T = \mathbf{G} \cdot \mathbf{u} \quad (10)$$

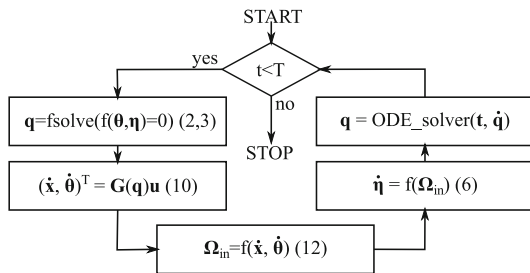
Kernel matrix is defined as:

$$\begin{aligned} \mathbf{G} &= \begin{bmatrix} \mathbf{G}_1 & \mathbf{0} \\ \mathbf{G}_2 \mathbf{G}_3 \mathbf{G}_1 & \mathbf{G}_2 \mathbf{G}_4 \\ \mathbf{0} & \mathbf{I}_3 \end{bmatrix}, \mathbf{G}_1 = \begin{bmatrix} \mathbf{J}_{P2} & \mathbf{J}_{R3} \\ -\mathbf{J}_{R2} & -\mathbf{J}_{P3} \end{bmatrix}, \mathbf{G}_3 = \begin{bmatrix} \mathbf{J}_{P1} & \mathbf{J}_{R1} \\ \mathbf{J}_{P2} & \mathbf{J}_{R2} \\ \mathbf{J}_{P3} & \mathbf{J}_{R3} \end{bmatrix}, \\ \mathbf{G}_2 &= \text{diag}(\mathbf{J}_{\theta1}^{-1}, \mathbf{J}_{\theta2}^{-1}, \mathbf{J}_{\theta3}^{-1}), \mathbf{G}_4 = \text{diag}(\mathbf{j}_{\theta1}, \mathbf{j}_{\theta2}, \mathbf{j}_{\theta3}) \end{aligned} \quad (11)$$

Matrix $\mathbf{G}_2 \in \mathbb{R}^{9 \times 9}$ is a block matrix, divided into equal blocks of square matrices 3×3 , same as $\mathbf{G}_2 \in \mathbb{R}^{9 \times 3}$ is divided into a blocks of column vectors 3×1 .



Fig. 3 Robot movement simulation scheme



Based upon (10) and adoption of some control input $\mathbf{u} \in \mathbb{R}^9$, velocities of robot platform and actuators has been obtained, so that they satisfy constraints released in (11). As a straight consequence of the above and in order to complete calculation of velocities, angular velocity $\boldsymbol{\Omega}_{in}$ has to be determined. Taken into consideration Eq. (7) which introduces the relation between angular velocity of a wheel with respect to the ground (similarly to case of \mathbf{v}_{in} in Eq. (7) expanded to Eq. (8)), the following connection has been acquired:

$$\boldsymbol{\Omega}_{in} = {}^{CWi}\mathbf{R}_P \cdot \boldsymbol{\Omega}_{P/G}^b + {}^{CWi}\mathbf{R}_{Wi} \cdot \boldsymbol{\Omega}_{Wi/Li}^b \quad (12)$$

Throughout the substitution of $\boldsymbol{\Omega}_{in}$ values in already introduced (12) into the expression of wheel velocities in a point of contact (6), $\dot{\boldsymbol{\eta}}$ are solved.

System of Eqs. (10), (12), and (6), which presents full system for velocities of state variables $\dot{\mathbf{q}}$, can be solved using numerical methods, likewise in the case of holonomic constraints where MATLAB software was used. Simulation scheme of a robot movement due to input \mathbf{u} has been presented in Fig. 3.

4 Results of Simulation

In order to present the effects of simulation conducted, an exemplary simulation has been performed. For simplification purposes a ground surface has been modelled as a flat inclined plane (rotated 10° about $\mathbf{e}_{x,G}$ axis), but some other parametric surfaces (ex. bezier surfaces) can be used without changing the system formulation. The last three rows of a kernel matrix \mathbf{G} are equal to $[\mathbf{0}, \mathbf{I}]$. As a result, the last three control inputs $\mathbf{u}_{7\dots 9}$ are equal to three actuator velocities separated from \mathbf{J}_{Li} matrices. Limbs no. 2, 3 and 4 (Fig. 1) have been taken into consideration. In case of a limb 2 wheel steering ${}^2\dot{\theta}_3$ has been chosen as equivalent input u_7 , in case of limbs no. 3 and 4 wheel drives ${}^{3,4}\dot{\theta}_4$ has been selected as inputs u_8 and u_9 . First six inputs has been calculated to obtain velocities of the ${}^{2,3,4}\dot{\theta}_{1,2}$ actuators (six actuators, further named as \mathbf{a}) equal to 0. All that to prevent movement of the wheels relative to the robot platform. Once the input vector $\mathbf{u}_1 = (\mathbf{0}, u_7, u_8, u_9)^T$ is introduced to the control system (10), velocities of the described actuators \mathbf{a} , has been calculated and

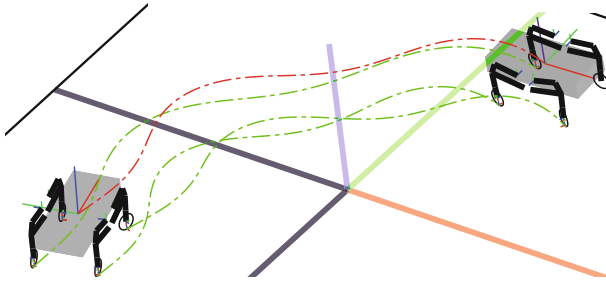


Fig. 4 Exemplary simulation results

denoted as vector \mathbf{b} . Following, the 6 rows of matrix \mathbf{G} , corresponding to the actuators \mathbf{a} and first six columns corresponding to six inputs $\mathbf{u}_{1...6}$ has been extracted as matrix $\mathbf{G}' \in \mathbb{R}^{6 \times 6}$. Finally, inputs $\mathbf{u}_{1...6}$ has been calculated as $\mathbf{u}_{1...6} = -(\mathbf{G}')^{-1} \cdot \mathbf{b}$. The $u_{7...9} = 2\pi \cdot (-\frac{35}{360} \sin(\frac{2\pi}{5}t), 1, 1.2)^T$ has been assumed. Centre point of the robot platform (red line) and contact points trajectories (green lines), calculated by MATLAB, has been presented in Fig. 4.

5 Conclusions

In the paper, kinematics controller of the constrained mechanical system has been introduced. Holonomic and nonholonomic constraints have been described. Based on those constraints, control system has been developed, to meet conditions of movement of the robot wheels without slip. To solve holonomic constraints position of wheels contact points has been assumed. In the future there is a need to check experimentally if the contact points obtained from simulation of ODE system, corresponds to real position of the wheel relative to the ground.

References

1. Grand, C., Benamar, F., Plumet, F.: Motion kinematics analysis of wheeled-legged rover over 3D surface with posture adaptation. *Mech. Mach. Theory* **45**(3), 477–495 (2010)
2. Ylnen, S., Halme, A.: Centaur like service robot. In: *Proceedings of IEEE/RSJ International Conference on Intelligent Robots and Systems*, Lausanne Switzerland, 30 Sept–4 Oct 2002
3. Sperzyński, P., Szrek, J.: Control of constrained dynamic system of leg of wheel-legged mobile robot. In: *Proceedings of the Second Conference MeTrApp 2013*, Bilbao, Spain (2013)
4. Bałchanowski, J.: Modelling and simulation studies on the mobile robot with self-levelling chassis. *J. Theor. Appl Mech.* **54**(1), 149–161 (2016)
5. Chakraborty, N., Ghosal, A.: Kinematics of wheeled mobile robots on uneven terrain. *Mech. Mach. Theory* **39**, 87–1273 (2004)
6. Montana, D.J.: The kinematics of contact and grasp. *Int. J. Robot. Res.* **7**(3), 17–32 (1988)

Experimental Platform for Hexapod Locomotion

M. Nițulescu, M. Ivănescu, S. Mănoiu-Olaru
and V.D.H. Nguyen

Abstract This paper presents an experimental platform developed for hexapod locomotion analysis and experiments over common types of obstacles. The platform contains two elements: a model of a six legged mobile robot used for real tests on different obstacle categories and a software simulator interface which allows study of the robot stability in gravitational field, assuring in the same time the control of the mobile robot during real experiments. For the hexapod robot this paper presents our design for the leg, its kinematical model and workspace analysis. The control part is a combination between Matlab, a micro-controller based development board and dedicated servomotor controller board. The trajectory generator for the leg tip was implemented using piecewise cubic spline interpolation method. Finally, this paper presents some experiments on spiral stairs for which the locomotion sequences strategies were designed in order to overcome them using the following constrains: maintain the robot's body parallel with respect to the ground and maintain the maximum height of the robot during locomotion.

Keywords Hexapod robot platform • Locomotion • Control • Spiral stairs experiments

M. Nițulescu (✉) · M. Ivănescu · V.D.H. Nguyen
University of Craiova, Craiova, Romania
e-mail: nitulescu@robotics.ucv.ro

M. Ivănescu
e-mail: ivanescu@robotics.ucv.ro

V.D.H. Nguyen
e-mail: donghai.spkt@gmail.com

S. Mănoiu-Olaru
Hella Craiova, Craiova, Romania
e-mail: manoiusorin2006@yahoo.com

1 Introduction

One of the most important features for a mobile robot is to walk in its environment in a stable, efficient and naturalistic manner. If we examine the current state of art we can see that a robot can have either stability and versatility or efficiency and naturalism but never all four of them [1, 2].

Most arthropods have six legs to easily maintain static stability, and it has been observed that a larger number of legs do not necessarily increase walking speed [3]. The large diversity of existing walking animals offers innumerable examples of locomotion possibilities. There are two main types of legs configurations that are biological inspired. The main difference is in the way the leg swing relative to body. The first type is similar to human’s hip where the leg swings around a horizontal axis. The second type is similar to insects where the legs swing around a vertical axis providing better stability.

2 The Hexapod Mobile Robot

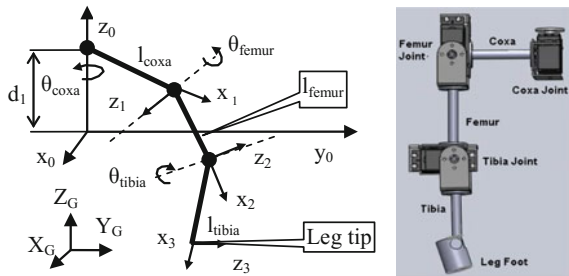
The successful design of a legged robot depends mostly on the mechanical characteristics of the chosen leg [4]. Since all aspects of locomotion are ultimately governed by the physical limitations of the leg, it is important to select a mechanical design that will maximize motion and impose fewer constraints during walking.

2.1 Leg Design and Kinematics

A kinematical chain with three rotational joints (RRR) has been chosen for each leg mechanism in order to mimic the leg structure (Fig. 1).

A direct geometrical model for each leg is formulated between the moving frame $O_i(x_i, y_i, z_i)$, $i = 0 \dots 3$ attached to the leg base and the fixed frame $O_G(x_G, y_G, z_G)$

Fig. 1 Robot leg, CAD and kinematic models



attached to the world, as reference. The assignment of link frames follows the Denavit-Hartenberg direct geometrical modeling algorithm and the coordinates of the leg tip are depicted in Eq. (1), where: d_1 —the height from O_G to coxa joint frame along Z axis; l_i —length of the coxa (1), femur (2) and tibia (3) segments; θ_i —coxa (1), femur (2) and tibia (3) joint variables:

$$\begin{aligned}x &= [l_1 + l_2 \cos \theta_2 + l_3 \cos(\theta_2 - \theta_3)] \cos \theta_1 \\y &= [l_1 + l_2 \cos \theta_2 + l_3 \cos(\theta_2 - \theta_3)] \sin \theta_1 \\z &= d_1 + l_2 \sin \theta_2 + l_3 \sin(\theta_2 - \theta_3)\end{aligned}\quad (1)$$

The direct geometrical model described by Eq. (1) establishes a connection between the joint variables and the position of the leg tip in the leg frame (Fig. 3a).

In order to transform the motion assigned by the trajectory generator to the leg tip into the corresponding joint angle motions we need to calculate the joint variables coxa, femur and tibia, θ_1 , θ_2 and θ_3 , functions of leg tip coordinates as in Eq. (2), the inverse geometrical model, where x , y are the coordinates of the leg tip in the leg frame and x' , y' are the coordinates of the leg tip in the coxa frame.

$$\begin{aligned}\theta_1 &= \begin{cases} \arctg\left(\frac{y}{x}\right) + \pi, & x < 0 \\ \arctg\left(\frac{y}{x}\right), & \text{otherwise} \end{cases} \\ \theta_2 &= \arccos \frac{l_2^2 + x'^2 + y'^2 - l_3^2}{2l_2 \sqrt{(x'^2 + y'^2)}} + \arctg \frac{y_3}{x_3} \\ \theta_3 &= \pi - \arccos \frac{l_3^2 + l_2^2 - (x'^2 + y'^2)}{2l_2 l_3}\end{aligned}\quad (2)$$

2.2 Workspace Analysis of the Leg

The actuators used in joints are capable of rotating π rad. In order to minimize leg collisions the coxa joint was limited between $-\pi/4$ and $\pi/4$. This restriction was introduced due to mechanical construction of the leg (Fig. 1). To get the most out of motion the operation space of variable θ_2 was set from $-\pi/2$ to $\pi/4$ and θ_3 from 0 to $3\pi/4$. In our case there is a singularity when the x and y coordinates of the leg tip are zero. In this configuration the value for θ_1 is arbitrary. To avoid this scenario we can define the x coordinate greater than zero. The leg workspace with the important points is presented in Fig. 2 and is valid for $l_1 = 10$ cm, $l_2 = 15$ cm, $l_3 = 20.2$ cm and for coxa joint coordinates (0, 15 and 20 cm).

Fig. 2 Leg workspace, extreme interest points

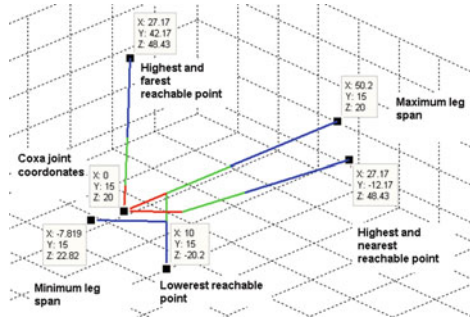
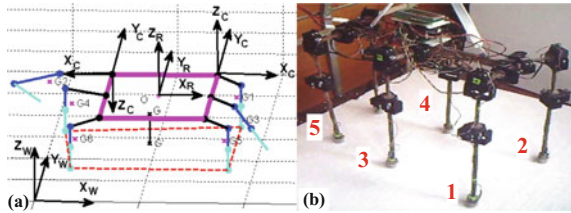


Fig. 3 Matlab model (a) and physical model of the hexapod robot (b)



2.3 Hexapod Robot Model

The robot structure (Fig. 3) has 6 identical legs (Fig. 1). In [2] are explained all the relevant points that have been put on the model. The overall transformation from global frame to each leg tip is obtained in Eq. (3), where T_R^W —transformation matrix between the global frame and the robot frame and defines the rotation about y, x, z and $T_{coxa_i}^R$ —transformation matrix from the robot centre to each leg:

$$T_{tip_i}^W = T_R^W T_{coxa_i}^R T_{tip}^{coxa_i} \tag{3}$$

3 Software Platform for Hexapod Robot Simulations

One of the main purpose of this developed software platform is the stability analyze during different motions. It shows how the support polygon (defined by the contact points of the feet to the ground) modifies when legs lose contact with ground and if the projection of the center of mass rest within the support polygon during locomotion over various types of obstacles (assuring so the static stability of the robot). This Matlab software can be used to analyze static stability of the hexapod robot in gravitational field, locomotion analysis and also allows communication with the physical model of the robot. Figure 4 presents the graphical user interface (GUI) of this platform which depicted the initial stage of locomotion over a straight stair having 5 steps, each having 5 cm in width and height.



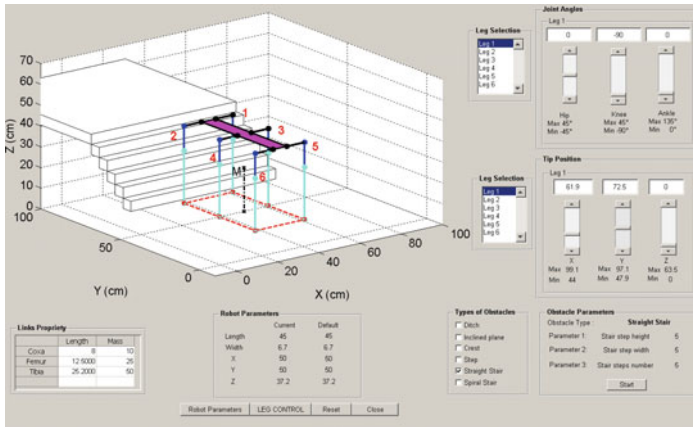


Fig. 4 GUI of software platform for locomotion analysis

The free fall analysis represents what happens with the robot left to fall on the ground from a height greater than the extension of the legs. Keeping in mind that the joints are locked by the values prescribed by the user, no extra movements are allowed (no active stability).

In the example of Fig. 5, the only force that acts upon the robot is the gravitational force. For a given set of joint values the robot passes through many transitory stages until it becomes statically stable (Fig. 5a–c). Legs that have contact with the ground determine the shape of the support polygon (triangle, quadrilateral, pentagon or hexagon). In order to know if the robot achieves static stability, the projection G' of G must be inside the support polygon. To solve this problem some designed algorithms are applied.

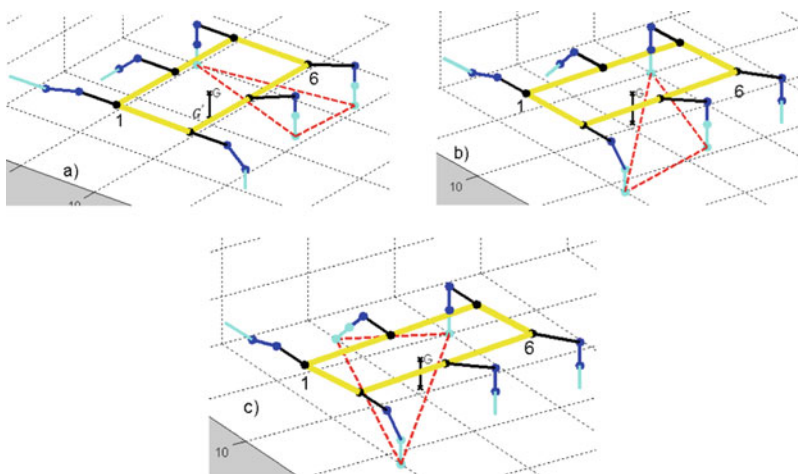


Fig. 5 Example of free fall analysis: **a** faze one of falling, **b** faze two of falling, **c** faze three statically stable

4 Experiments in Locomotion

All the tests presented next were made using the physical model of the hexapod robot. Initially, experiments in locomotion were made on all typically fundamental classes of obstacles. Earth provides an extremely large variety of terrains, but the obstacles encountered can be classified in 4 groups [2, 5]: crest, ditch, step and inclined plane.

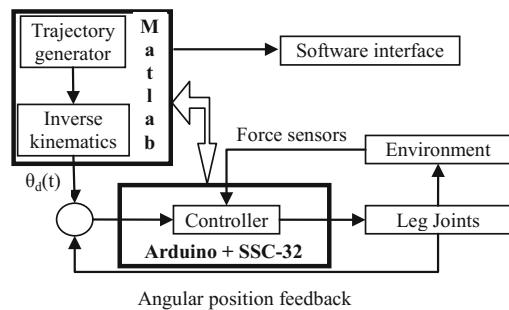
Figure 6 presents the block diagram for controlling the robot along the trajectory. The Arduino micro-controller board is the part that connects the real robot with software Matlab platform, and SSC32 is a servo controller board used to control all the joints of the hexapod mobile robot. Each leg tip is equipped with a force sensor to detect when the leg touches the ground or obstacle.

4.1 Locomotion Strategy on a Spiral Stair

The main difference between the locomotion on a spiral stair and a straight stair [6] is that the robot has to rotate around its vertical axis to be able to continue its motion. The minimum angle of rotation for the robot to maintain the trajectory is $\alpha = \arccos\{1 - [l^2/(2L^2)]\}$, where l is the width of the stair step and L is the length of the stair step. To simplify the locomotion algorithm the rotation of the robot is made in certain moments of time identified by the position of the robot on the spiral stair. Rotation of the robot on spiral stair is a 3 step algorithm. First, the legs 2, 3 and 6 are lifted then the robot is rotated around its vertical axis using coxa joints of legs 1, 4 and 5. After the rotation of the robot it's done the legs 2, 3 and 6 are lowered and the locomotion is resumed.

For validating the algorithm from Fig. 7 the height of the step is 5 cm, the width is 15 cm and number of steps are 3. Some images from experimental tests using the model of the hexapod robot in locomotion over a spiral stairs are depicted in Fig. 8. In Fig. 8a the robot places the front legs on the first step. In Fig. 8b is presented the position prior the process of rotating the robot. In Fig. 8c the legs 2, 3 and 6 are

Fig. 6 Block diagram for controlling the model of the hexapod robot



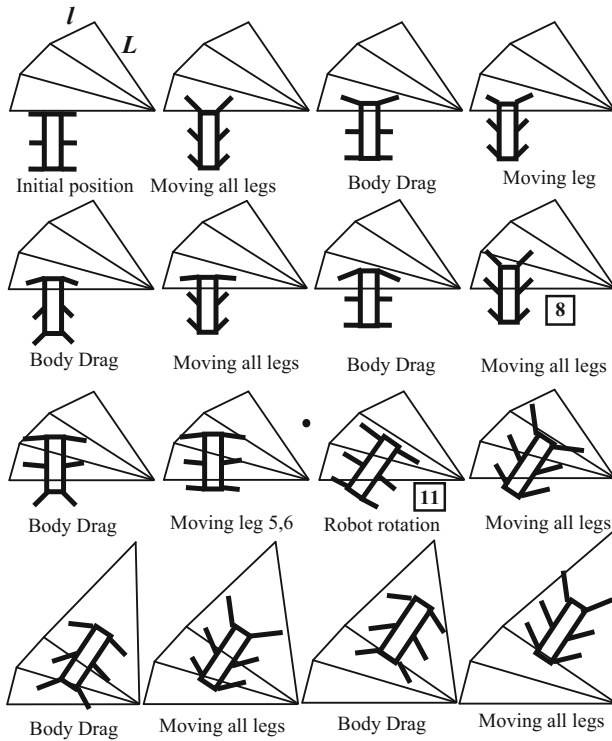
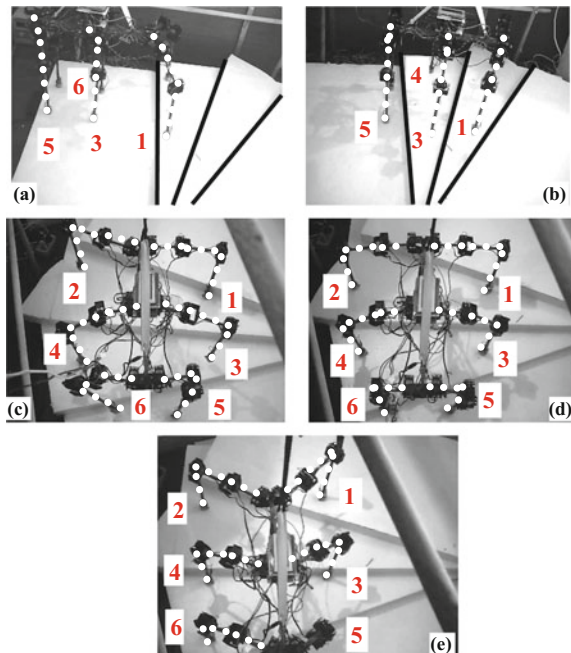


Fig. 7 Hexapod robot locomotion strategy on a complex obstacle like spiral stairs

Fig. 8 Experiments with the hexapod model on spiral stairs



lifted and using the coxa joints of leg 1, 4 and 5 the robot rotate around its vertical axis. In Fig. 8d is the position of the robot after the rotation process is over. After the rotation process is over the robot resumes the locomotion algorithm (Fig. 8e).

5 Conclusions

This paper presents an experimental platform developed for hexapod locomotion analysis and experiments over common types of obstacles. The platform contains two elements: a model of a six legged mobile robot used for real tests on different obstacle categories and a software simulator interface which allows study of the robot stability in gravitational field, assuring in the same time the control of the mobile robot during real experiments.

For the hexapod robot this paper presents the leg design, its kinematical model and workspace analysis. The control part is a combination between Matlab, a micro controller based development board and dedicated servomotor controller board. The trajectory generator for the leg tip was implemented using piecewise cubic spline interpolation method.

Finally, this paper presents some experiments on spiral stairs, one of the most complex obstacles. In this case the locomotion sequences strategies were designed in order to overcome them using the following constrains: maintain the robot's body parallel with respect to the ground and maintain the maximum height of the robot during locomotion. Regarding the experimental results obtained we can conclude the following aspects. It was necessary to implement intermediary sequence to correct the positions of leg tips after some body drag. In some cases the position of the leg tips was made closer to the edge of the obstacle than in the simulation. During body drag the leg tips tends to slip. During the process of body lifting the robot oscillated because are actuated all the femur joints and then all the tibia joints. Further work includes perfecting all locomotion sequences and implementing algorithms so that the robot can autonomously navigate in outside environment.

References

1. Lewinger, W.A., Quinn, R.D.: Neurobiologically-based control system for an adaptively walking hexapod. *Ind. Robot Int. J.* **38**(3) (2011)
2. Manoiu-Olaru, S., Nițulescu, M.: Hexapod robot. mathematical support for modeling and control. In: *Proceedings of 15th International Conference on System Theory, Control and Computing*, pp. 385–390, Romania (2011)
3. Manchester, I., et al.: Stable dynamic walking over uneven terrain. *Int. J. Robot. Res.* 265–279 (2011)
4. Ding, X., et al.: Locomotion analysis of hexapod robot. *Climbing Walking Robots* 291–310 (2010)

5. Figliolini, G.P., Rea, P.: Mechanics and simulation of six-legged walking robots. Climbing and Walking Robots, Towards New Applications. Itech Education and Publishing, Vienna (2007)
6. Manoiu-Olaru, S., Nitulescu, M.: Locomotion analysis of a hexapod robot using a dedicated Matlab interface. In: Proceedings of 18th International Conference on System Theory, Control and Computing, pp. 568–573, Romania (2014)
7. Bensalem, S., Gallien, M., Ingrand, F., Kahloul, I., Thanh-Hung, N.: Designing autonomous robots. IEEE Robot. Autom. Mag. **16** (2009)
8. Manoiu-Olaru, S., Nitulescu, M.: Matlab simulator for gravitational stability of a hexapod robot. Rom. Rev. Precis. Mech. Opt. Mechatron. **39**, 157–162 (2011)
9. Manoiu-Olaru, S., Nitulescu, M.: Stability analysis software platform dedicated for a hexapod robot. In: Proceedings of 18th International Conference on Control Systems and Computer Science, vol 1, pp. 385–390, Romania (2011)
10. Tarokh, M., Lee, M.: Systematic method for kinematics modeling of legged robots on uneven terrain. Int. J. Control Autom. **2**(2), 9–18 (2009)
11. Tomoya, N., Shinkichi, I., Tatsuya, S.: Locomotion control of multi-legged robot based on follow-the-contact-point gait. ICROS-SICE Int. Joint Conf. Jpn. 2247–2253 (2009)

Quadcopter Propeller Design and Performance Analysis

Endrowednes Kuantama, Dan Craciun, Ioan Tarca and Radu Tarca

Abstract In quadcopter design process, usually the selection of rotor and propeller are treated carefully because they will determine the maneuver abilities as well as the speed and maximum carry load. Among various methods used to choose the best combination of rotor and propeller, this research used Solidworks software computational method. The final result was compared with data-sheets of three commercial rotor specification for quadcopters in order to ascertain its validity. The designed propeller's size is 16×5 inch with two blades, and connected to a rotor having angular velocity between 1000 and 9000 rpm. In order to analyze the air pressure around propeller, Solidworks flow simulation was conducted. Information achieved from analyzed data show that the maximum thrust was 4144 g-force (gf), with propeller's coefficient thrust of 0.04. These data can be used to analyze the power efficiency in rotor propeller which is then useful in choosing the right size of propeller, according to the desired thrust.

Keywords Propeller · Quadcopter · Propeller design · Thrust · Solidworks

1 Introduction

The development of quadcopter as Unmanned Aerial Vehicle (UAV) has been continuously evolved over the past few years. Some of quadcopter researches focused on modeling [1], control [2], application [3], mathematics formula [4] and

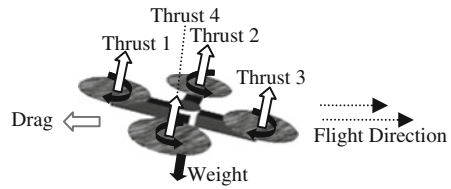
E. Kuantama (✉) · D. Craciun · I. Tarca · R. Tarca
University of Oradea, Oradea, Romania
e-mail: endrowednes@gmail.com

D. Craciun
e-mail: danraciun28@yahoo.com

I. Tarca
e-mail: nelut@uoradea.ro

R. Tarca
e-mail: rtarca@uoradea.ro

Fig. 1 Aerodynamic forces on quadcopter



many others. Quadcopter has four rotors; each pair of opposite rotors are spinning in the same direction; for instance, both the front and back rotors are spinning clockwise, while the right and left rotors are spinning counterclockwise (or vice versa). If the rotors spin at particular velocity, the quadcopter will gain lifting force, yaw/roll/pitch movement in corresponding direction, or simply hover in the air. The theory can be seen in quadcopter control and stability [5].

The aerodynamic forces (consisting of thrust, drag, lift and weight) and torques were calculated using a combination of torque and blade propeller theory. These forces can be seen in Fig. 1. Aerodynamic forces are generated by propeller's movement, which lift up the quadcopter. Thrust is generated by propeller rotation, which is opposed to the weight and the gravity acceleration which runs vertically downward through its mass center. Dragging is deceleration force generated by propeller. The resultant forces of lift and drag in each rotor determine the quadcopter's direction of movement.

Solidworks flow simulation software has been used to simulate and analyze the magnitude of thrust generated by propeller rotation. Propeller rotation produce airflow, so that, based on angular speed and the size of propeller, one can analyze air pressure and also calculate the thrust in each rotor. In this research, propellers having 16×5 inch in size and various angular velocities have been used.

2 Propeller Performance Parameters

The aerodynamics of the propellers and the motion of the rigid frame can produce a coupled dynamic assuming that the propeller's rotation is such that the local angle of attack is constant along the blades in stationary flight and the local induced velocity is also constant along the blades [6]. The propellers create a thrust force out of the supplied power. The magnitude of this force is not constant for a given propeller, but depends both on the velocity of the incoming air and also on the rotating speed of the propeller itself. The performance of propeller can be described by dimensionless (normalized) coefficients. An airfoil can be characterized by relations between angle of attack, lift and drag coefficient as it can be seen in Fig. 2.

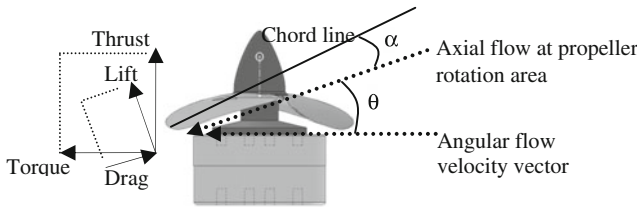


Fig. 2 Illustration of lift and drag thrust

The resultant forces of lift and drag in each rotor determine the quadcopter’s direction of movement. The angle between the flow direction and the rotation plane, known as the inflow angle, is represented by (θ) and the angle between the propeller chord line and axial flow, or resultant relative wind, is represented by (α) and also known as the angle of attack. To calculate the efficiency of propeller, all three coefficients, i.e. advance ratio, thrust and power coefficient must be properly calculated. The thrust can be calculated and explained using momentum theory. Simple momentum theory can be combined with blade element theory to achieve better and more adequate results [7, 8]. Relationship between angular velocity and thrust coefficient is shown in Eq. (1).

$$C_T = \frac{T}{\rho D^4 \omega^2} \tag{1}$$

Propeller computation can be done using thrust coefficient based on airscrew diameter (D) and rotation per second in propeller angular velocity which driven by the rotor torque (ω). Air is defined only by its density ($\rho = 1.225 \text{ kg/m}^3$). The thrust coefficient (C_T) is a propeller parameter defined as a function of pitch, diameter, angular velocity and propeller shape. The performance of a propeller is indicated by thrust coefficient (C_T), power coefficient (C_p) and efficiency (η).

The thrust coefficient basically relies on advance ratio (J) as a parameter that controls the propeller loading. The advance ratio is affected by propeller velocity (V), its diameter and rotor torque, as explained in Eq. (2). As the propeller rotates, it generate the forward velocity of the propeller (V). A given J defines the inflow angle at any point of the blade and, for a propeller blade at a static pitch angle, the angle of attack distribution. When plotting propeller coefficients, the advance ratio is the natural choice for independent variable, as it maps to the general angle of attack state of the propeller blade over the operating range [9].

$$J = \frac{V}{\omega D} \tag{2}$$

The power efficiency is defined as the ratio of thrust power to rotor power (P). By using Eqs. (1) and (2), the power efficiency coefficient can be defined similar to Eq. (3). Mathematic formula for propeller is given using the thrust and power coefficient as function of the advance ratio, thus the propeller efficiency can also be served as function of the advance ratio [10].

$$\eta = \frac{(J C_T \rho n^3 D^5)}{P} \quad (3)$$

Based on all these equations, it is safe to conclude that propeller design cannot be separated from aerodynamic effect occurred around the propeller. The forward velocity produced by aerodynamic movement is affected by the angle of attack and wind inflow angle in propeller.

3 Propeller Design Profile

As quadcopter has static rotors, the propeller was designed in an unstressed state regardless of the gravitational effects. However to simulate a rotating propeller, it must be exposed to pre-stressed inertial load state which yield from a constant rotational velocity [11]. In this simulation design, the propeller size is 16 (length) \times 5 (pitch) inch. Pitch is the space in which the propeller will travel onward through a solid medium with one complete revolution. CAD design for propeller can be seen in Fig. 3.

The angle of attack was designed 3 degrees for every point of pitch distribution. There are 10 points of pitch distribution in this design, in which the propeller radius (R) is 203.2 mm. The propeller used was asymmetric so it had different curvature surface on every point of pitch distribution. This design was based on the size of a commercial propeller that is 16 \times 5 inch, whose surface affects the way in which the axial flow occurs on the rotating propeller. The coefficient thrust of the designed propeller was determined using Solidworks flow simulation.

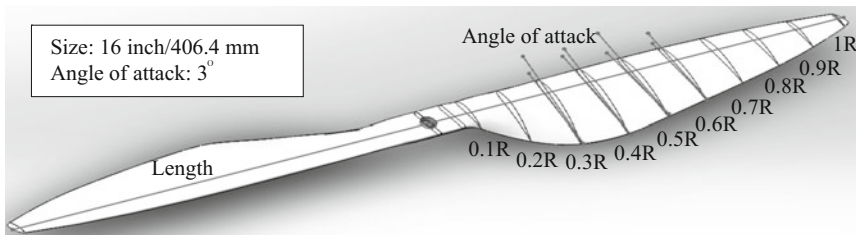


Fig. 3 Propeller design using Solidworks

4 Simulation Results and Discussions

By using Solidworks to design the propeller, one can make simulation to calculate the air pressure around propeller. Mathematically, one can use Eq. (1) to calculate coefficient thrust on rotor based on the thrust data given by simulation. The propeller’s surface area in this simulation is 0.3181 m². Pressure as a function of surface area can be used to calculate thrust as seen in Eq. (4).

$$T = P \cdot A \tag{4}$$

From the equation above, P is the average value of pressure on propeller and A is the propeller’s surface area. Thrust is a reaction force described quantitatively by Newton’s second and third laws which in this case force exerted by a rotation propeller perpendicular to the surface. Thrust movement, which generated by each rotor propeller through the torque, creating two kinds of force i.e. force of gravity which acts earthward and the total force in the vehicle frame. The pressure exerted by propeller airflow is identical in magnitude in all directions, hence it is scalar, and can be defined as force per unit area.

Quadcopter has four rotors and four propellers with identical size and specifications. The distance between each rotor propeller is also identical, therefore only a part of quadcopter frame was used in this modeling to get the illustration of airflow trajectory, as seen on Fig. 4. As one pair of opposite rotors spin clockwise and the other pair spin counter clockwise, each will produce thrust due to the change in

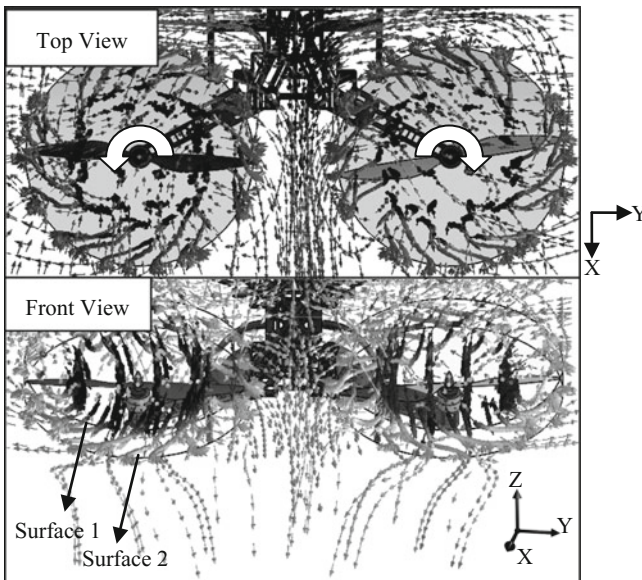


Fig. 4 Illustration of propeller’s flow trajectory

momentum of the downward moving air. This process is called the dynamic effect of the air acting by the airfoil propeller. With the same velocity, each rotor will also generate the same thrust providing the resulted airflow not affecting each other. If they affect each other, it will inflict the instability of thrust produced by each rotor, because the air velocity was affected by outlet airflow generated by surrounding rotor [12]. By knowing the rotor's maximum velocity and the size of propeller used, one can calculate the required size of quadcopter frame based on airflow movement on each propeller.

Using this illustration, one can simulate pressure on surface 1 and surface 2 according to specific angular velocity. Surface 1 is the top of propeller and surface 2 is the bottom. The magnitude of pressure occurred on propeller's surface area is equal to the difference between both average values of surface area. Propeller's angular velocity lies in the range of 1000–9000 rpm. Inside this interval, angular velocity will produce pressure across the propeller rotation area. Based on airfoil theory, the pressure on the surface 1 should be lower than the pressure on surface 2. This theory was proved true by the simulation result as seen on Fig. 5 in which the angular velocity of 5000 rpm generate average pressure of 101369 Pa on surface 2, which was bigger compared with the average pressure of 101328 Pa on surface 1. As much as 129 iterations were done during simulation process to get the amount of air pressure produced by propeller rotation.

Pressure data gathered from each rotation surface area showed that thrust generated by propeller can be calculated using Eq. (4). The results were obtained by increasing propeller's angular velocity in steps of 1000 rpm in the entire specified domain (1000–9000 rpm) and these can be seen on Table 1.

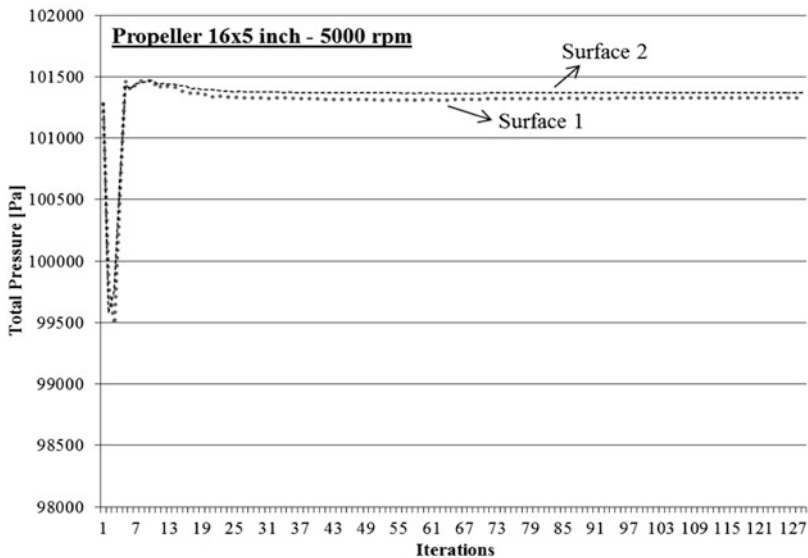


Fig. 5 Air pressure around propeller

Table 1 Simulation thrust results for propeller 16 × 5 inch

Angular velocity (rpm)	Average pressure 1 (Pa)	Average pressure 2 (Pa)	P2 – P1 (Pa)	Thrust (N)	Thrust (gf)
1000	101325.1478	101326.8054	1.65758985	0.527279331	53.76752829
2000	101325.59	101332.26	6.67	2.121727	216.3559421
3000	101326.3431	101341.3027	14.95954363	4.758630828	485.2453007
4000	101327.4095	101354.1243	26.71471157	8.497949749	866.5497136
5000	101328.89	101369.81	40.92	13.016652	1327.329108
6000	101330.427	101388.1671	57.74002751	18.36710275	1872.923246
7000	101331.3793	101409.8204	78.4410744	24.95210577	2544.40668
8000	101334.2537	101437.6685	103.4148486	32.89626334	3354.485307
9000	101335.6342	101463.3904	127.756233	40.63925772	4144.050998

The thrust generated by propeller rotation significantly increases when the angular velocity is greater than 5000 rpm. One rotor can generate maximum thrust of 4144 g-force (gf) at 9000 rpm, so that, by using all 4 rotors, quadcopter can generate 16.6 kgf of thrust. From this simulation result, one can estimate the maximum carry load and flying speed of quadcopter. To ensure the validity of this simulation results, the data was compared with commercial rotor specification having the same propeller size [13]. Figure 6. shows the comparison chart of simulation data and rotor type MT4144, 4004 and MN3508. The results show that the simulation data were not significantly different from existing commercial rotors when the angular velocity was lower than 5000 rpm. For the propeller angular velocity of 6000 rpm, the error was 16 %. This difference can be explained due to differences in propeller geometry used in measurements, such as differences in chord line, angle pitch, etc.

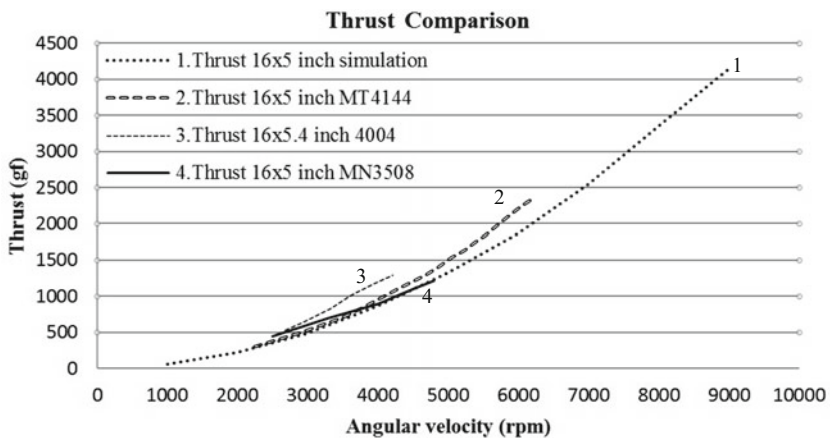


Fig. 6 Comparison between simulation and rotor specifications

Data from Table 1 can be used to analyze propeller's thrust coefficient using Eq. (1) for each angular velocity. The coefficient thrust for designed propeller 16×5 inch is 0.04. From this data, the magnitude of propeller's power efficiency can be calculated based on power needed to generate specific thrust. This obviously depends on the type of the rotor used. Equation (3) can be used to calculate the power efficiency of propeller based on power consumption in each rotor.

5 Conclusions

Designing the model for propeller helps on computing the generated thrust, thus one can decide which propeller type can be properly used. Not all commercial rotor propellers have thrust specification. Propeller with size 16×5 inch was analyzed and the result was similar to the specification of existing commercial rotor. This proved that computational modeling can be used to analyze propeller. The thrust generated was 53–4144 gf for 1000–9000 rpm. The designed propeller has a thrust coefficient of 0.04 which affect the angle of attack in chord line propeller. One can notice a little difference in thrust result between simulation and commercial thrust, due to different thrust coefficient on propeller, which in this case could not be compared since there is no geometry specification for commercial rotor.

Acknowledgments This work has been funded under the LEADERS—Erasmus Mundus Grant (agreement number 2014-0855/001-001) by European Commission, through the Education, Audiovisual and Culture Executive Agency, in the Action Plan 2 for the years 2014–2018.

References

1. Veloso, R., et al.: A platform for the design, simulation and development of quadcopter multi-agent systems. *Inf. Syst. Technol. (CISTI)* 1–6 (2014)
2. Gheorghita, V.-M.: Quadcopter control system. In: *System Theory, Control and Computing (ICSTCC)*, pp. 421–426 (2015)
3. Haque, M.-S., Muhammad, M., Swarnaker, D.: Autonomous quadcopter for product home delivery. In: *Electrical Engineering and Information and Communication Technology (ICEEICT)*, pp. 1–5 (2014)
4. Magnussen, O., Ottestad, M., Hovland, G.: Experimental validation of a quaternion-based attitude estimation with direct input to a quadcopter control system. In: *International Conference of Unmanned Aircraft Systems (ICUAS)*, pp. 480–485 (2013)
5. Bouabdallah, S., Siegwart, R.: Full control of a quadrotor. In: *International Conference on Intelligent Robots and Systems*, pp. 153–158 (2007)
6. Bristeau, P.J., et al.: The role of propeller aerodynamics in the model of a quadrotor UAV. In: *The European Control Conference, Budapest-Hungary*, pp. 683–688 (2009)
7. Czyba, R., Szafranski, G.: Control structure impact on the flying performance of the multi-rotor VTOL platform—design, analysis and experimental validation. *Int. J. Adv. Robot. Syst.* (2012)

8. Yang, Y., Veldhuis, L.L.M., Eitelberg, G.: Investigation of propeller induced ground vortices by numerical and experimental methods. In: AIAA Applied Aerodynamics Conference, pp. 1–12 (2015)
9. Heinzen, S.B., Hall Jr, C.E.: Development and testing of a passive variable-pitch propeller. *J. Aircr.* 748–763 (2015)
10. Gur, O.: Maximum propeller efficiency estimation. *J. Aircr.* 2035–2038 (2015)
11. Petrova, R., Lemu, H.G.: Design study for dynamic behavior of wind turbine blade. In: International Workshop of Advanced Manufacturing and Automation, pp. 131–138 (2010)
12. Shyam, S., et al.: Computational fluid dynamic study on a novel propulsive system and its integration with an unmanned aerial vehicle (UAV). *J. Aerosp. Eng.* 1–16 (2015)
13. Available via T-Motor website <http://www.rctigermotor.com/>. Accessed 21 Jan 2016

A Method for Structural Synthesis of Cooperative Mobile Manipulators

Z.-E. Chebab, J.-C. Fauroux, G. Gogu, N. Bouton, L. Sabourin and Y. Mezouar

Abstract This paper deals with the design of cooperative mobile manipulators, that are not simply considered as the union of an existing mobile platform with an arm, leading to a highly redundant system, but as a system redesigned from scratch with an original minimal kinematics suitable for robot-robot collaboration. In order to design cooperative mobile manipulators adequate with the environment and the considered task, functional specifications are first expressed and partially translated into constraints on the structural parameters, both for single robotic units (m-bots) and the poly-robot resulting of the cooperation (p-bot). This method allows to obtain a set of robotic architectures that also verify other functional specifications.

Keywords Mobile manipulators · Robotic cooperation · Structural synthesis · Structural parameters

Z.-E. Chebab · J.-C. Fauroux (✉) · G. Gogu · N. Bouton · L. Sabourin · Y. Mezouar
Université Clermont Auvergne, Sigma-Clermont, Institut Pascal, BP 10448, 63000
Clermont-Ferrand, France
e-mail: jean-christophe.fauroux@sigma-clermont.fr

Z.-E. Chebab
e-mail: zine-elabidine.chebab@sigma-clermont.fr

G. Gogu
e-mail: grigore.gogu@sigma-clermont.fr

N. Bouton
e-mail: nicolas.bouton@sigma-clermont.fr

L. Sabourin
e-mail: laurent.sabourin@sigma-clermont.fr

Y. Mezouar
e-mail: youcef.mezouar@sigma-clermont.fr

Z.-E. Chebab · J.-C. Fauroux · G. Gogu · N. Bouton · L. Sabourin · Y. Mezouar
CNRS, UMR 6602, Institut Pascal, 63178 Aubière, France

1 Introduction

Factories of the Future are becoming a strong concern for European industry and research [3]. Industry 4.0 is also supposed to become the fourth revolution of the industry (after steam power, electricity and automation revolutions) by making the different industrial processes more modular, with real-time reconfigurability of production systems for customizable products. Different ways to achieve this revolution are considered. For example, the technical report [4] covers the domains and tasks that can be upgraded and how to perform them. In robotics, two major issues have been identified: collaborative robots and flexibility of conventional manufacturing processes. Therefore, in our DC^2M^3 project (Design and Control of Collaborative Modular Mobile Manipulators) both aspects are mixed with the goal of providing ground Mobile Manipulators (MMs) that can perform a wide range of tasks in a collaborative way by using different mobile manipulators called mono-robots (m-bots) and associate them to form a poly-robot (p-bot). The interest of the p-bot is that it can perform tasks not possible with separate m-bots and benefits from different properties. This project is the continuity of the previous C^3Bots project that dealt with payload transport using multiple mobile robots [6]. Additionally, the current project considers different manipulative tasks. Both the C^3Bots and the DC^2M^3 projects focus mostly on robot-robot cooperation, although human-robot collaboration could also be considered in future work. The interest of cooperative and collaborative systems is to help human operators for heavy duty tasks while performing them with more efficiency brought by the reconfigurability and modularity of the robots. A previous bibliographical study [2] has shown that most of mobile collaborative systems are classical MMs, which are the association of a conventional mobile platform with a manipulator arm, without a prior study on the mechanical structure. This kind of association of MMs is not optimized for cooperative use and task performance. Different methods of structural synthesis for parallel manipulators can be found in the literature [1, 5], but this paper focuses on cooperative mobile manipulators: a general approach and preliminary implementation of the structural synthesis is presented, both for elementary mobile manipulators (m-bots) and for their combination into a poly-robot (p-bot), including also hypotheses for contact joints of the wheels on the ground, considered as ordinary kinematic joints.

2 Specific Approach of Structural Synthesis of m-Bots and p-Bots

This section proposes the method that is based on structural parameters and applied to the specific case of designing m-bots that will be connected to form a p-bot. Several simplifying hypotheses will be presented for this brief paper.

2.1 Structural Parameters

Structural parameters are commonly used for specifying robotic systems. They define the mechanical characteristics of the considered kinematic chain in the robot: for instance, the serial chain that guides the end-effector of a manipulating arm, the parallel locomotion chains that support the platform of a mobile robot. Four structural parameters are used; connectivity, mobility, redundancy and degree of overconstraint. These parameters are here presented based on the definitions of the IFTOMM online dictionary [5, 7], whose notations are used for this paper:

- **Connectivity:** The connectivity S_F of a kinematic chain F is the number of independent displacements between its base and its end-effector. It represents the dimension of the operational velocity space of the kinematic chain R_F , with: $S_F = \dim(R_F)$; $0 \leq S_F \leq 6$.
- **Mobility:** The mobility M_F , also called Degree of Freedom (DoF), of a mechanism F is the “number of independent variables that must be considered for input motion” [7] (definition 1.3.11). In the field of mechanical theory, the mobility is “the number of independent finite displacements in the joints needed to define the configuration of the mechanism” ([5], p. 79). The mobility depends on the kind and number of joints and the nature of links and is strongly related to the connectivity of the kinematic chain(s) that form(s) the mechanism, with: $M_F \geq S_F$
- **Redundancy:** A mechanism is called redundant when it exists “more than one means for accomplishing a given function” ([7], 13.3.18). The redundancy T_F of a kinematic chain F is “the difference between the dimension of the joint space and the dimension of the operational space”, which is the difference between the mobility and the connectivity of the kinematic chain [5]: $T_F = M_F - S_F$
- **Overconstraint:** The degree of overconstraint N_F of a mechanism F is the number of kinematic constraints in excess with respect to the minimal number required to close the loops of the mechanism, with [5]: $N_F = 6q - r_F$ with q the number of independent closed loops and r_F the number of joints parameters that lose their independence in mechanism F .

2.2 Specifications of the m-Bots/p-Bots and Simplifying Hypotheses

The general structure of p-bot is presented in Fig. 1 and includes m m-bots. Each m-bot includes a mobile base supported by l locomotion chains connected to the ground and supporting several manipulation and connecting chains towards the payload or other m-bots.

- **Description of the environment:** In this paper, structured environments with flat ground will be considered such as industrial halls or construction sites for civil

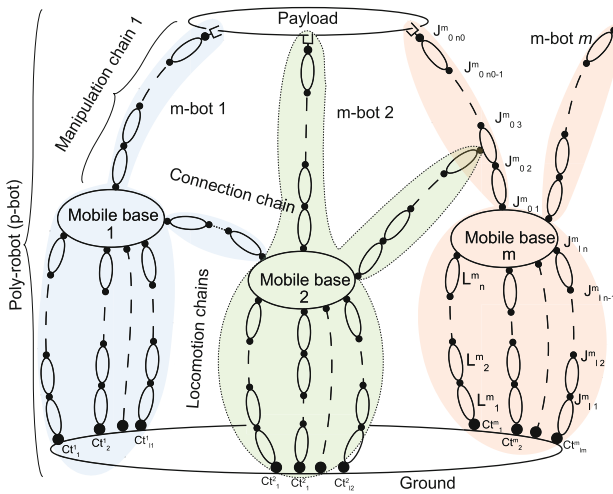


Fig. 1 General kinematic graph of a poly-robot (p-bot) based on multiple mono-robots (m-bots); *L* Links, *J* Joints

engineering applications. Future work will deal with other kinds of unstructured environments.

- *Number ‘m’ of m-bots:* In general, the number *m* of m-bots in a p-bot depends on the payload mass and the payload capacity of each m-bot, as well as the task to be performed. For this paper, the p-bot will contain no more than two identical m-bots (*m* = 2).
- *Locomotion:* In this paper, the locomotion device will be limited to wheels that are considered as the most efficient mean of locomotion in the considered environment. A previous study [8] calculated the mobility only of mobile platforms without specifying the wheel shape. In our work, mobility as well as the three other structural parameters are calculated for toric wheels specifically. In a reference frame where *x* represents the direction of advance of the wheel, *z* is opposed to the gravity and *y* is chosen as $z = x \otimes y$, the difference between cylindrical wheel and toric wheel is that the latter allows large rotations around the *x* axis (Fig. 2). Furthermore, longitudinal and lateral slipping are not allowed. Rolling without slipping hypotheses are made for $\omega_y \leftrightarrow v_x$ and $\omega_x \leftrightarrow v_y$, with ω for rotational and *v* for translational speeds. The contact joint (*Ct*) of a toric wheel with the ground has three DoF $f_{Ct} = 3$, with its operational velocity space $(R_{Ct}) = (v_x, \omega_x, \omega_z)$.
- *Manipulation:* Each m-bot includes a manipulator with a manipulation chain supporting an end-effector. Their architecture depends on the required functional specifications of the task.
- *Connection capacity between m-bots:* It is achieved with a connection chain that can connect one body of m-bot *i* to another body of m-bot *i+1*. The body can be the mobile platform for simple attachment between m-bots. It can also be a body of the manipulation chain for manipulation reinforcement, similarly to a human that

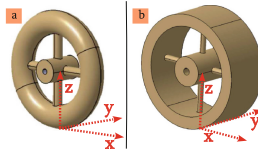


Fig. 2 Toric (a) and cylindrical (b) wheels

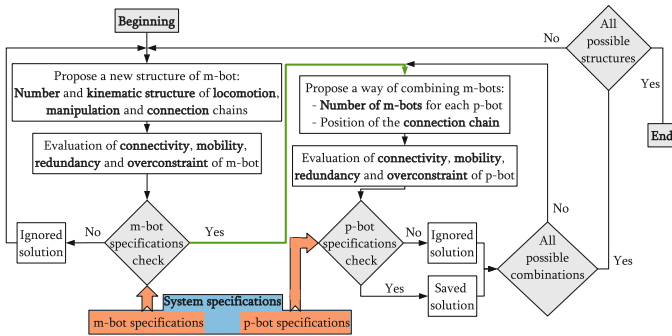


Fig. 3 The proposed structural synthesis approach

would catch its right wrist with its left hand for manipulating heavier payloads with the right hand (Fig. 1).

- *Description of the task:* In this project, the goal is to design a robotic modular system that can achieve various kinds of tasks, from machining to manipulating. For this paper, the considered task is to pick an object from the ground in a given pose *A* and transfer it to another location with pose *B*. This includes translational and rotational motions for manipulation. The industrial applications considered in this project are mechanical manufacturing and assembly. The m-bots will perform this task for small parts, whereas the bigger parts will be manipulated with a whole p-bot.

The considered approach of structural synthesis is presented in Fig. 3.

3 Application of the Approach for the Design of m-Bots/p-Bots

Some of the previous specifications may be now converted into constraints on structural parameters to be used into the structural synthesis approach. Two different sets of constraints will be defined: one for the m-bots and one for the p-bots. The index *m* will be used for the structural parameters of m-bots and the index *p* for the structural parameters of p-bots. The constraints only concern three of the four structural



parameters as mobility M_F derives from redundancy T_F and connectivity S_F with $M_F = T_F + S_F$.

- *Constraints on m-bots:*

- Connectivity: For the considered pick and place task on a plane ground, the operational velocity space needed for m-bots is $(R_m) = (v_x, v_y, v_z, \omega_z)$ ((v_x, v_y, ω_z) for the planar movement and (v_z) for picking and placing the payload) therefore $S_m \geq 4$. Choosing $S_m = 5$ or $S_m = 6$ can be useful for payload orientation and manipulation dexterity.
- Redundancy: To simplify the control of the m-bots, a low redundancy is preferred. So, a zero degree of redundancy is chosen on m-bots ($T_m = 0$). This means that $M_m = S_m$. This redundancy is different from the operational redundancy that occurs when the number of mobilities $S_{m'}$ of the robot is superior to the required mobilities S_m to perform the task, e.g. $S_{m'} = 5$.
- Overconstraint: The required degree of overconstraint is null ($N_m = 0$). Verifying this condition ensures that all the wheels maintain their contact with the ground, a necessary condition for rolling without slipping.

- *Constraints on the p-bot:*

- Connectivity: The minimum required connectivity is the same as for the m-bots due to the same specifications (planar movement and task specifications), therefore $S_p = 4$
- Redundancy: The more redundant the system, the more complex is its control. Consequently, platforms with the lowest degree of redundancy will be preferred. This condition regulates also the mobility of the system, where $T_p = M_p - S_p$ and $M_p \geq S_p$.
- Overconstraint: The lowest degree of overconstraint is required to ensure a good association of m-bots that form the p-bot. A null N_p means all the wheels are in contact with the ground, a necessary condition to avoid longitudinal and lateral slipping.

After the definition of the specifications of both m-bots and p-bots, the structural synthesis approach proposed in Fig. 3 is used to get the wanted solutions. For this paper, and for demonstration purpose, only two specific configurations of two wheeled and tricycle mobile platforms are presented. Figure 4 represents the four proposed structures of m-bots (CAD model, kinematic chain and structural parameters). It is noted that the structural parameters are evaluated using Gogu's formulae [5].

Among the four proposed solutions, only the solution a_2 verifies the specifications made on m-bots, where the operational velocity space (R_m) can be obtained by transforming ω_y into v_z . Using this configuration, and for demonstration purpose, only one configuration of possible p-bots is presented in Fig. 5. The construction of the p-bot is done by connecting the end effector $3a$ of the m-bot_a to the link $1b$ of the m-bot_b (Fig. 5-1). The associated kinematic chain is represented in Fig. 5-2 and structural parameters are presented in Fig. 5-3.

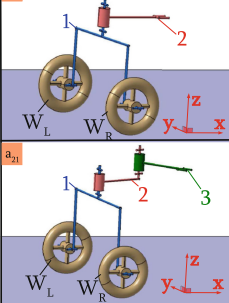
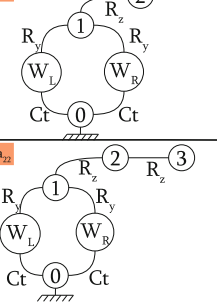
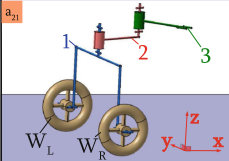
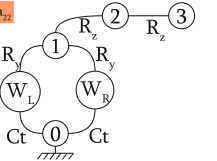
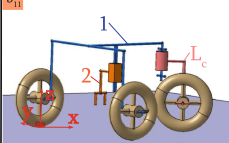
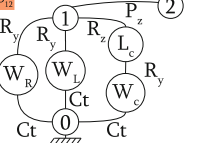
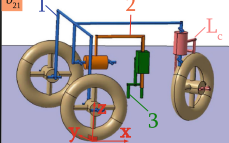
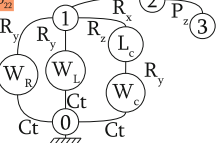
	Mono-robots	Kinematic chains	Structural parameters
2 wheels			$(R_m) = (v_x, \omega_y, \omega_z)$ $S_m = 3 ; M_m = 3$ $T_m = 0 ; N_m = 0$
			$(R_m) = (v_x, v_y, \omega_y, \omega_z)$ $S_m = 4 ; M_m = 4$ $T_m = 0 ; N_m = 0$
3 wheels			$(R_m) = (v_x, v_z)$ $S_m = 2 ; M_m = 2$ $T_m = 0 ; N_m = 0$
			$(R_m) = (v_x, v_z, \omega_z)$ $S_m = 3 ; M_m = 3$ $T_m = 0 ; N_m = 0$

Fig. 4 Resulted mono-robots (m-bots) from the structural synthesis

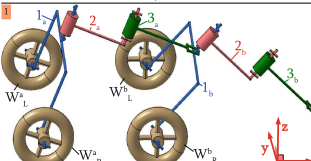
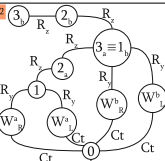
Poly-robot	Kinematic chain	Structural parameters
		$(R_p) = (v_x, v_y, \omega_z)$ $S_p = 3 ; M_p = 3$ $T_p = 0 ; N_p = 1$

Fig. 5 Resulted poly-robot (p-bot) from the association of two mono-robots (m-bots)

The presented solution of p-bot doesn't respect the condition upon connectivity ($S_p = 1$). Arriving at this point, it is said that this configuration doesn't respect the specifications of the p-bot, and other ways of combining m-bots must be explored to get an adequate solution. If none of the ways of connecting the m-bots suits the p-bot specifications, another m-bot structure is proposed and the approach proposed in Fig. 3 is applied again.



4 Conclusion

The purpose of this paper was to present a method of structural synthesis of cooperative mobile manipulators. The process of structural synthesis began with the definition of structural parameters and specifications for mono-robots (m-bots) and poly-robots (p-bot) that had to be respected. Then, an approach of structural synthesis was proposed for designing m-bots and p-bots. A set of constraints on structural parameters was issued from functional specifications for both m-bots and p-bots in their environment and during their task. The proposed structural synthesis approach used these constraints on the structural parameters to select a group of solutions and to demonstrate the design process. The originality of the synthesis approach is to use mobility/connectivity as well as less used parameters such as redundancy or overconstraint indices. Contacts of non-slipping toric wheels on the ground are also treated as ordinary kinematic joints. In future work, a set of solutions that can pass all the process will be obtained and passed through another selection process that depends on constraints related to the task, technical feasibility and singularity analysis to finally converge to an adequate solution for a given task and environment.

Acknowledgments This project acknowledges the financial support of the following entities: LabEx IMobS³ Innovative Mobility: Smart and Sustainable Solutions, the French National Centre for Scientific Research (CNRS), Auvergne Regional Council and the European funds of regional development (FEDER).

References

1. Alizade, R., Bayram, Ç.: Structural synthesis of parallel manipulators. *Mech. Mach. Theory* **39**(8), 857–870 (2004)
2. Chebab, Z.E., Fauroux, J.C., Bouton, N., Mezouar, Y., Sabourin, L.: Autonomous collaborative mobile manipulators: State of the art. In: *Symposium on Theory of Machines and Mechanisms/UMTS2015/TrISToMM*, June 14–17, 2015, Izmir, Turkey, 8p. IZTECH/IFTOMM
3. Effra: ‘Factories of the Future 2020’: Roadmap 2014–2020. <http://www.effra.eu>
4. Fédération des Industries de Mécanique: Guide pratique de l’Usine du Futur Enjeux et panorama de solutions. Technical report (2015). <http://industriedufutur.fim.net>
5. Gogu, G.: *Structural Synthesis of Parallel Robots. Part 1—Methodology*. Springer (2008)
6. Hichri, B., Fauroux, J.C., Adouane, L., Doroftei, I., Mezouar, Y.: Lifting mechanism for payload transport by collaborative mobile robots. In: *New Trends in Mechanism and Machine Science*, pp. 157–165. Springer (2015)
7. IFToMM: IFToMM online dictionary. <http://iftomm.3me.tudelft.nl/2057/frames.html>
8. Kim, W., Lee, S.E., Yi, B.J.: Mobility analysis of planar mobile robots. In: *IEEE International Conference on Robotics and Automation, ICRA’02*, vol. 3, pp. 2861–2867. IEEE (2002)

Mobile Robot Used to Collect Data from a Difficult Access Area

R. Zemouri and P.C. Patie

Abstract Building a robot requires knowledge from very different fields. In order to achieve even a very simple task, it requires complicate systems. Robots must, generally, feel to be able to get information about the environment. A robot must “understand” what happens, build plans or assess situations. Domains where robots are being used more and more are: transport and agriculture, various industries, in services, in scientific research, the knowledge of the ocean and outer space. The robots are equipped with various devices: systems for voice recognition, gyroscopes systems, wireless communication systems, global positioning systems (GPS) and various types of sensors (for detecting heat, force, ultrasound, chemicals and radiation etc.). This paper presents the opportunity for using a mobile robot for testing an inaccessible environment for humans and, eventually, the detection of a hostile area.

Keywords Microcontroller • MikroPascal • Mobile robot • Sensors • Solar cell

1 Introduction

Nowadays the use of robots has become necessary. In a world in which human operates in an environment increasingly hostile and unfavorable for him, his replacement by the robots is the best way to continue the activity.

There are environments or areas where robots are used to the detriment of the people, because they serve much better requirements (can provide better quality, better productivity, greater flexibility and better accuracy, such as in micro domains) or human does not want to perform certain tasks because it is dangerous

R. Zemouri
CNAM Paris, Paris, France
e-mail: ryad.zemouri@ensam.fr

P.C. Patie (✉)
Valahia University of Targoviste, Targoviste, Romania
e-mail: patie@valahia.ro

for him or is difficult work (e.g. in isolated places, such as ships sunken, islands or spaceships, etc.).

Because that, performing similar actions as well of human, the robot requires certain devices to collect information from the environment. All through these devices must be made robot interaction with the environment or objects in the environment and a central unit that processes sensory information in real time and transforms it into an accessible way for control system [1].

These sensors, because of their characteristics can explore: the work area, the contact area (the closest or faraway) and powerful sensors even very remote areas. The information recorded by the sensory systems is used to build a model of the environment around the robot model that underlies the decisions taken by it.

Building a robot requires knowledge from very different fields. In order to achieve even a very simple task, it requires complicated systems. A robot must “understand” what happens, build plans, assess situations etc. [2].

Perception includes virtually everything related to sensors that the robot can receive information about the environment in which it operates.

Diversity of sensors is virtually unlimited: a robot can record, measure distances, acceleration, magnetic fields, guidelines, geographical positions, velocities etc. [3, 4].

One of the key objectives of robotics is to develop autonomous robots. Progress autonomous robot has a major interest in a range of areas of applications including various processes, construction, waste processing, space exploration, the oceans and high risk areas, medical assistance disabled etc. Orientation in a totally unknown environment using sensors to detect obstacles and communicate with a remote computer is two important aspects to be taken into account when working with a mobile robot [5].

Robots ability to “feel” the environment and change their behavior based on environmental information is what makes the robots, especially mobile ones, being so interesting to build and use. Without sensors, robots could perform tasks other than fixed before repeating the operations that they have done over and over, but equipped with sensors, robots have the ability to do much more than that [3].

Mobile robot is a complex system that can perform various tasks in a variety of specific situations of the real world. It is a combination of devices equipped with actuators and sensors operating in a real space, marked by a number of physical properties and the need to plan the movements of the robot so as to carry out a task according to the initial state of the system and a priori information based on the existing related to the working environment [6, 7].

Mobile robots are actually some land, air or water vehicles, endowed with intelligence, which enables them to act autonomously. They have application in all other areas of robotics.

Building a robot requires knowledge in various fields because, even for fulfillment of a simple task, complicated systems are needed. To receive information from and about the environment, a robot must generally “feel”.

But, the information itself, not use as long as the robot does not ‘understand’ the information retrieved. Understanding them requires their use for an operation (moving, transforming intentionally environment, exploration, etc.).

The perception refers of the information received from the robot sensors. With help of a robot sensors can capture images, measure distances, acceleration, orientation, magnetic fields, geographical positions, speeds etc. [8, 9].

2 Mobile Robots

Develop autonomous robots is one of the key objectives of robotics. Their progress represent a major interest in many fields, such as construction, waste processing, medicine, space exploration, oceans, high risk areas, assistance to disabled persons etc.

Two key aspects of a mobile robot are: orientation in an unfamiliar environment with sensors used to detect obstacles and remote communication with a computer. Mobile robots, in contrast with industrial fixed robots, have capacity to operate in areas that exceed their size.

Mobile robot is equipped with a degree of autonomy and is capable of performing a range of tasks [8].

Mobile robot represents a combination of mechanisms equipped with servo motors, stepper motors or DC motors and sensors.

Sensors operating in the real space, having a range of physical properties, by means of which the robot can perform a task (depending on the initial state of the system and pre-existing information) related to the environment.

To successfully fulfill the tasks set, the robot is based on information about the initial configuration of the workspace, but also those obtained in the course of evolution.

Robots equipped with decision-function can trace their path of travel and may be included in the category of intelligent robots. There is also the robot for which the trajectory is fixed and marked on the ground. In these circumstances, must be avoided only the obstacles accidentally placed on the established path and navigation information has to be processed. Mobile robots that meet these conditions cannot be treated as intelligent robots, but are useful to provide transport in flexible production workshops [10].

To accomplish these tasks, the robot needs sensors with which information is retrieved from the work environment, conducting interaction between it and the robot, but also by a central unit that processes in real-time information taken from sensors and turns it to be accessed by the control system.

The sensory system can be called measurement system. It deals with the measurement of physical parameters and, eventually, observing the significant changes possibly of parameters.

Sensory system presents geometric and chemical characteristics of objects in the environment. The sensors can analyze the work area and the contact area (near and far) and more powerful sensors can explore even in very remote areas. With the help of information from the sensory system it builds a model of the real world in which the robot operates and according to this model, the robot will act.

To build a robot are necessary knowledge of very different areas. To receive information about the environment, a robot must be equipped with sensors. Information taken from sensors, after being processed, helps the robot to build plans, to evaluate situations and decide on a plan of action [8, 10, 11].

3 The Presentation of the Mobile Robot and Its Electronic Design

The presented application was performed using knowledge from another practical achievement, namely a mobile robot powered by solar cells that having a series of photovoltaic panels that take the solar energy, store it and then allow the robot to have sufficient autonomy to move into an enclosed space to retrieve data from that environment.

This application is designed with the idea of the possibility of using mobile robot for inspection of hard to reach areas. It was equipped with sensors to retrieve information from a tunnel that simulated different environmental conditions.

To avoid human exposure to harmful substances or different threats that may occur in a crash, for example, can use the robot, and with data received from its sensors will decide how safe that environment is for humans.

The application consists of a tunnel in which will create different environmental conditions and the mobile robot equipped with sensors from dust, moisture, temperature, pressure, light, smoke and flammable gases, will cross the tunnel and the data values will be recorded.

For that, components that make up the whole robot prototype are: 3—GP2Y0A21YK Sharp distance sensors; 2—DC motors, operating at 6 V; 1—PIC16F877 microcontroller and related installation; 1—LCD display 4×16 ; 1—6 V battery; 5—batteries of 1.2 V; 1—engine driver LM 298; 1—temperature sensor DS 1820; 1—pressure sensor BMP180; 1—smoke and gases sensor kit MQ2; 1—optical sensor for dust GP2Y1010AU0F; 1—light sensor LDR07; 1—humidity sensor SHT11D.

LCD display is used to display alphanumeric characters on four lines, each with 16 characters. The time operation may be greater than 50,000 h.

The presented robot is a mobile robot powered by batteries. It has its own algorithm and is able to make its own decisions by comparing the generated type 2 Sharp distance sensors GP2Y0A21YK.

On display located on the front of the robot it displays the battery load factor in percent and, eventually, can be shown the direction of movement of the robot.

The operating principle is based on the comparison by a PIC16F877 type microcontroller the digital signals obtained from GP2Y0A21YK Sharp distance sensors, and then by the manipulating the type 2 integrated drivers ULN 2003 all for the DC motor control that moves the robot [12, 13].

BMP180 is a high precision sensor for barometric pressure. BMP180 can be measured from 300 to 1100 hPa with an absolute accuracy of up to 0.02 hPa. This sensor supports a voltage between 1.8 and 3.6 V DC. It is designed to be connected directly to a microcontroller via I2C protocol (2-wire digital interface). It also has low power consumption and a very low noise.

BMP180 is based on the piezo resistive technology for EMC robustness, high accuracy and linearity and long term stability. It is designed to be connected directly to a microcontroller of a mobile device via I2C protocol. It delivers unmatched pressure values [14, 15].

The smoke and gases sensor kit contains a PCB specially designed to any of the above sensors, a resistor, a potentiometer for adjusting the sensitivity and a three-pin angle connector. Biometric sensors detect and measure the amount of alcohol, smoke, gas, carbon monoxide, methane. The sensor signal is analogue.

The optic sensor for dust GP2Y1010AU0F (with dimensions $46.0 \times 30.0 \times 17.6$ mm) from Sharp is an optical sensor for measuring air quality, designed to detect dust particles. An infrared emitting diode and a phototransistor are arranged diagonally into this device, to enable him to detect light reflected by dust in the air. It is particularly especially efficient to detect the fine particles like cigarette smoke, and is often used in air purification systems. The sensor has very low power consumption (maximum 20 mA, typically 11 mA) and can be powered with DC 7 V maximum. Analog sensor output voltage is proportional to the density of dust measured with a sensitivity of $0.5 \text{ V}/0.1 \text{ mg}/\text{m}^3$.

Sensors are duplex. They will transmit a signal of infrared light type through a LED emitter and by reflection the received signal by a phototransistor thereby can be determined the distance between robot and obstacles in front of it. By comparing signals from sensors was created a logical flowchart of operations of the robot program. Normally, sensors do not generate any signals, and the robot goes forward. When it detects a signal from the left sensor of the robot the microcontroller command the motors for steering right and when the sensor detects a signal from the right side of the robot, the microcontroller gives control to the motors to turning left. When comparing the signals from both sensors and they are equal, the robot goes back until when the sensors do not have the identical values.

In Fig. 1, can be seen the entire mobile robot.



Fig. 1 The entire mobile robot

Fig. 2 The bottom side of the robot after adding the microcontroller kit

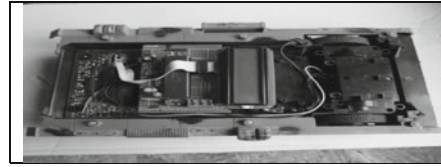
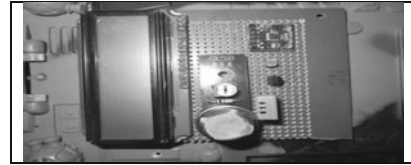


Fig. 3 The sensor Kit and the LCD display



In Fig. 2 can be seen the entire mobile robot by adding in the bottom side of the Robot. On the upper side was pulled over the LCD screen, for better reading of displayed information and added sensor kit assembly, for example, Fig. 3.

In normal condition, remote sensors do not generate any signals, and the robot goes forward. When it detects a signal from the sensor to the left of the robot, microcontroller gives control motors for steering right and when it detects a signal from the sensor to the right of the robot the microcontroller gives control motors for steering left [10].

The robot assembly has a pretty good grip, but because it is wheeled locomotion system can appear obstacles that they may not pass.

Regarding the electronic design, the software interface design of electrical diagrams used is called Proteus. This program is a utility used to create and verify the wiring diagrams, create and verify wiring, placement of electronic components on the plate. The following figure is a schematic diagram wiring performed with Proteus, for example, Fig. 4.

The software used to create the program to be implemented in the microcontroller is mikroPascal, for example Fig. 5. MikroPascal is an application development tool for PIC microcontrollers. This software has a rich set of libraries and hardware and it is an easy way to program PIC microcontrollers.

Fig. 4 Wiring diagram made with Proteus



Fig. 5 Installation wiring diagram for microcontroller

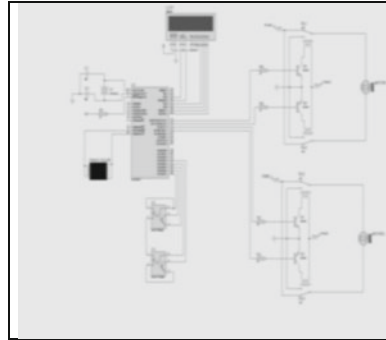


Fig. 6 MikroPascal programming developing tool



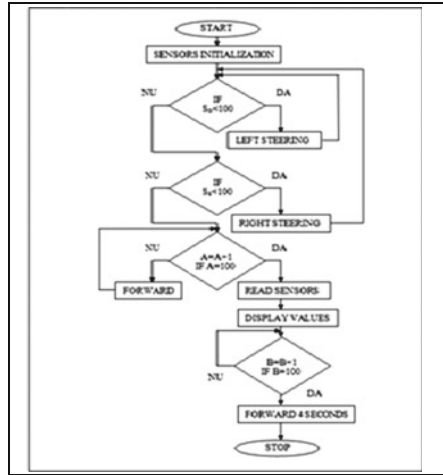
MikroPascal is a high-level language, as well as MikroC or Basic that simplifies programming by allowing writing in a row or several rows of what would require many lines of assembly language program.

Its interface is an integrated compiler and changing variables and performance of the program can easily follow. The program, once it is done, is compiled both in specific format *.ppas and in classic programming formats *.asm and *.hex.

Below, in Fig. 6, one presents mikroPascal interface programming developing tool. After a successfully compiling of the program in *.hex, one use IC-Prog software interface loading the program into the microcontroller PIC16F877.

Programming with this software developing tool is relatively easy, being necessary to choose the type of component which will be programmed, and then to open the *.hex file to be uploaded. The programmer is connected initially to the PC and the microcontroller it is in programming socket. So, for the programming is choose the command "Program All", and then to check if the data was written

Fig. 7 Logical scheme for informatics application



correctly microcontroller memory, one choose the command “Verify”. Verification can also be done automatically after writing if is fulfilled a setting program options. Also, the logical scheme of programming robot is detailed below, in Fig. 7.

4 Conclusions

Mobile robot is forced to carry out actions similar with the human operator. This makes the existence of certain devices which shall be collected from work environment to achieve robot interaction. Of course, on long-term autonomy of mobile robots, whatever of the displacement environment is constrained by available energy and movement efficiency.

In some areas, robots fulfill much better the tasks and they can ensure a better quality of products or services, or the productivity is higher than humans. But there are situations in which a person prefers not to expose themselves to the risks and uses a robot to accomplish the proposed task. To achieve this, the robot needs some devices that can offer information, can process that information and process them so that the robot can choose the best solution to perform work.

The application was made in the idea of using a mobile robot for testing an inaccessible environment for humans. With small dimensions (27 cm length × 15 cm width × 5 cm tall) robot can penetrate into impossible areas by humans. Also, in case of the human body harmful substances, it is preferable that the robot to identify the hazards to which man can be exposed before it affected once ran in that environment without having detailed information on it. To achieve this, the robot uses sensors with which can collect data about the environment in which penetrate.

The application presented above, was equipped with sensors for temperature, humidity, dust, smoke and flammable gases, pressure and light. They take



information from the environment they are in, and according to the recorded values, which are then displayed on an LCD screen, one can appreciate the degree of risk to which it is subjected to a human when he arrived in the area.

As improvements that can be made of the mobile robot, in a further approach, one stated: equipping it with a storage device for retaining a longer period of time the information recorded; equipping with a transceiver that allows transmission of information in real time to a remote person; equipping with a video camera, for a better control of the robot and image acquisition in that environment; endowment with more sensors (for detecting life forms etc.).

References

1. Iovine, J.: Robots, Androids and Animatrons. McGraw-Hill, USA (2002)
2. Cojocaru, G., Kovaci, Fr.: Robots in Action. Facla Publishing House, Timișoara (1998)
3. Handra-Luca, V., Brișan, C., Mătieș, V., Tiuca, T.: Robots - Structure, Kinematics and Characteristics. Cluj-Napoca Publishing House (1996)
4. Nițulescu, M.: Mobile Robots. Sitech Publishing House, Craiova (1998)
5. Ispas, V.: Cinematics Applications in Manipulators and Industrial Robots Constructions. Romanian Academy Publishing House, București (1990)
6. Gheorghe, Gh. I., Palade, D.D., Valentin Pau: Mechatronics - Fundaments - Applications – Trends. Cefin, București (2002)
7. Siegwart, R., Nourbakhsh, I.: Introduction to Autonomous Mobile Robots. The MIT Press, USA (2004)
8. Nițulescu, M.: Experiments for Performance Evaluation of a Mobile Robot Trajectory Tracking. Appl. Mech. Mater. Trans. Tech. Publ. **162**, 302–307 (2012)
9. Patic, P.C., Pascale, L., Mainea, M.: Designing of a mobile robot using photovoltaic cells. J. Appl. Mech. Mater.—Adv. Mechatron. Control Eng. III **678**, 373–376 (2014)
10. Dragomir, F., Patic, P.C., Dragomir, O.: Intelligent robot with microcontroller for obstacles avoiding. J. Solid State Phenom. **166–167**, ISSN: 1012-0394. Title: Robotics and Automation Systems, pp. 179–184. Trans Tech Publications, Switzerland (2010)
11. Patic, P.C., Pascale, L., Mantescu, G.: Mobile robot powered by solar cells. J. Appl. Mech. Mater. Eng. Solutions Ind. **681**, 96–99 (2014)
12. Munteanu, O.: Bazele Roboticii—Non-manufacturing Robotics. Transilvania University Publishing House, Brașov (2003)
13. Munteanu, O.: Bazele Roboților—Architectures of Manufacturing Robots. Transilvania University Publishing House, Brașov (2003)
14. Pop, E., Leba, M.: Microcontrollers and Programmable Automation. Didactic and Pedagogical Publishing House, București (2003)
15. Popa, I.F., Marin, C., Filip, V.: Modelling and Simulation of Robotics Systems. Bibliotheca Publishing House (2005)

Part IX
Robotics—Parallel Robots

Extended Procedure for Stiffness Modeling Based on the Matrix Structure Analysis

T. Detert and B. Corves

Abstract For handling tasks requiring high accuracy and high dynamics, good stiffness properties of the manipulator are crucial and need to be taken into account in the design phase. Known methods to calculate the stiffness properties of a mechanical structure are the Finite Element Analysis, the Virtual Joint Method and the Matrix Structure Analysis. These methods trade off the complexity and computational costs against the accuracy of the results. This paper presents an extended procedure to model and analyze the stiffness properties of mechanical structures based on the Matrix Structure Analysis. The stiffness matrix of the structure is assembled automatically, following the described algorithm. The deformation of the structure under external load can then be calculated directly. In this procedure, complex links and joints with force dependent (non-linear) stiffness properties can be taken into account. This extended procedure is validated by measurements on a robotic arm.

Keywords Matrix structure analysis · Stiffness modelling · PARAGRIP · Validation · Non-linear

1 Introduction

In robotic applications high stiffness of the mechanical structure and control allow for high precision even for highly dynamic applications and high payloads. The stiffness of a structure relates external forces and torques to the translational and rotational distortion of the elements, caused by these external forces and torques. It is expressed using the stiffness matrix K . The ability to calculate the stiffness of a mechanical structure, considering different mechanical elements such as links,

T. Detert (✉) · B. Corves
RWTH Aachen University, Aachen, Germany
e-mail: detert@igm.rwth-aachen.de

B. Corves
e-mail: corves@igm.rwth-aachen.de

bearings and drives, is crucial for the analysis and optimization of the stiffness properties. In the design process the analysis of the main contributors to the compliance of a structure gives useful information for the efficient improvement of a structure. Furthermore, gravity compensation can be used to increase the accuracy of an robotic system, if the stiffness properties are known. In this paper an easy to use and convenient procedure for the stiffness calculation is presented. It is based on the Matrix Structure Analysis (MSA) using a database with pre-defined flexible elements. The stiffness matrix of the structure is assembled automatically, using the element stiffness matrices and their connection and position. The final goal is to obtain the deformation of the structure under a given external load and this deformation can be calculated directly, as soon as the stiffness matrix of the structure is known. In this procedure, complex links and joints with force dependent (non-linear) stiffness properties can be taken into account. In particular, force dependent, non-linear elements like rolling contact bearings are considered by iteration of the linear model. The implementation is validated by measurements on a robotic arm of the PARAGRIP handling system [1].

2 Methods of Stiffness Analysis—State of the Art

In literature three main methods are introduced to derive the stiffness matrix K of a mechanical structure: The Finite Elements Analysis (FEA), the Virtual Joint Method (VJM) and the Matrix Structure Analysis (MSA).

In the well-known Finite Elements Analysis (FEA) the overall structure is sub-divided into a large number of finite elements that are connected to each other elastically. The solution to the resulting system of partial differential equations is approximated numerically. The FEA is the most accurate and reliable method, its accuracy is only limited by the level of discretization [2]. However, it requires a high computational effort for the calculation of the system of equations and re-meshing the model in each configuration of the manipulator. Hence, the method is mainly used for final design considerations and stiffness analysis of complex sub-systems [3]. Based on the FEA, other methods have been developed, like Floating Frame of Reference Formulation (FFRF) for high rotational distortions and the Absolute Nodal Coordinates Formulation (ANCF) for high rotational and translational distortions [4, 5].

Using the Virtual Joint Method, also known as “lumped modeling”, the compliance of every element in a structure is reduced to the compliance of the actuators by means of virtual compliant joints [6]. It is based on the work of Salisbury and Gosselin [7, 8], where the stiffness of a structure is derived considering only the actuator stiffness. The main drawback of this method is that the stiffness of an element cannot be reduced to the drives if its distortion due to external loads does not correspond to the compliance of an actuator. In comparison to the FEA, the VJM gives accurate results with much lower computational effort [2, 9]. In recent works, the VJM was extended by using 6D virtual joints to account for cross coupling effects and the stiffness properties of all links [10] as well as non-linear

properties [11]. The Conservative Congruence Transformation [12] extends the conventional formulation by considering changes in the Jacobian due to deformation of the robotic system.

The Matrix Structure Analysis (MSA) relies on the same ideas as the FEA, modeling the mechanical structure as a combination of beams connected by nodes, where the stiffness properties of every beam element are represented as a stiffness matrix [13]. The displacement of every node is calculated analytically from the overall stiffness matrix. The MSA as introduced originally is limited to relatively simple elements, but however, it can be extended to integrate more complex effects such as joint stiffness [14]. Furthermore, the representation of the elements allow for a parametric description [15, 16]. Compared to the FEA, the MSA is less computational expensive [2, 5] and results in a good balance between computational costs and accuracy [17]. In the proposed stiffness calculation method a catalog of predefined elements is introduced to allow for a fast and convenient assembly of the stiffness model. The stiffness properties are calculated analytically for beam elements and by using characteristic curves for the non-linear and force dependent rolling contact bearings. To account for the force dependency of the stiffness properties, the linear stiffness model is solved iteratively. This approach allows a computational inexpensive determination of stiffness properties for many robotic structures.

3 Extended Procedure for Stiffness Modeling

As introduced in the beginning, the Cartesian stiffness matrix ${}^0K_{struc O}$ of the structure links the displacement (translation and orientation) of all nodes ${}^0\delta\chi_O$ to the external loads 0F_O :

$${}^0F_O = {}^0K_{struc O} \cdot {}^0\delta\chi_O \quad (1)$$

The superscripts indicate the coordinate system of reference; the last subscript indicates the point of reference for the equivalent load or displacement. In this procedure, the element stiffness matrices are generalized by calculating equivalent displacements and loads at the origin O of the global coordinate system 0 as introduced by Lončarić [18]. Even though this approach is crucial for the proposed procedure, details of mathematical description cannot be given within the scope of this paper.

3.1 Elements and Element Stiffness Matrices

As described above, different element types are available in the implementation. The calculation of the element stiffness matrix is shown for some elements in this section. The focus is on the elements, used in the later example of the PARAGRIP

Fig. 1 General beam element under load



manipulator. The two most important are beam elements representing the robot links and ball bearings used as revolute joints.

Most robotic links can be approximated by beam elements. Their compliance matrix can be derived from Timoshenko’s beam theory [19] as shown in Eq. 3. Let the rigid node k be attached to beam i with a fixed reference frame i0 as shown in Fig. 1.

The compliance matrix iC_i in Eq. (2) links the displacement $\delta\chi_k$ of the attached rigid node k to the external load F_k on k . Calculating the generalized inverse of iC_i leads to the required element stiffness matrix ${}^0K_{i0}$.

$$\delta\chi_k = {}^iC_i \cdot F_k \tag{2}$$

$${}^iC_i = \frac{l}{E} \begin{pmatrix} \frac{1}{A} & 0 & 0 & 0 & 0 & 0 \\ 0 & \frac{1}{3} \frac{l^2}{I_z} + \frac{E}{G \cdot A} & 0 & 0 & 0 & \frac{1}{2} \frac{l}{I_z} \\ 0 & 0 & \frac{1}{3} \frac{l^2}{I_y} + \frac{E}{G \cdot A} & 0 & -\frac{1}{2} \frac{l}{I_y} & 0 \\ 0 & 0 & 0 & \frac{E}{G \cdot I_T} & 0 & 0 \\ 0 & 0 & -\frac{1}{2} \frac{l}{I_z} & 0 & \frac{1}{I_y} & 0 \\ 0 & \frac{1}{2} \frac{l}{I_z} & 0 & 0 & 0 & \frac{1}{I_z} \end{pmatrix} \tag{3}$$

The stiffness properties of rolling contact bearings are non-linear and load dependent with cross coupling effects between radial displacement, axial displacement and torsion. Current approaches consider these complex correlations including clearance and dynamic effects but they are very computational expensive e.g. [20–22]. The manufacturer of the ball-bearings used in the handling system offers the extensive calculation tool Bearinx® [23] to calculate the nonlinear displacement characteristics, taking into account the internal load distribution, the bearing deformations, the clearance and tolerances, pre-tensioning and a large set of further characteristics. To reduce the complexity of the overall stiffness model, characteristics curves for the axial and radial displacement δ_{ax} and δ_{rad} and the torsion φ_{rad} under different load conditions were generated for a range of ball-bearings, as shown exemplary in Fig. 2.

The characteristics curves were calculated for a uniaxial load (F_{ax} , F_{rad} and M_{rad}) and for all possible load combinations and take into account the backlash of the bearing. The combined loads are scaled with respect to the maximum load considered. For example an axial load $F_{ax} = 500$ N (20 % of the 2500 N maximum force) was combined with a moment $M_{rad} = 40$ Nm (also 20 % of the 200 Nm maximum moment).



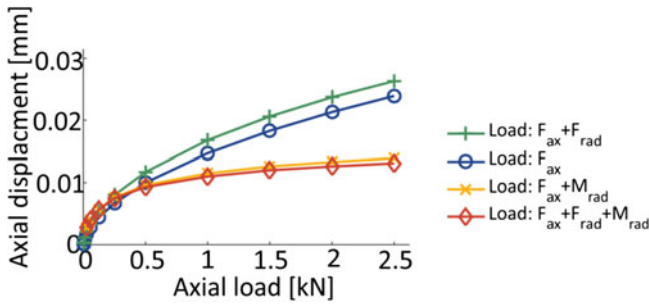


Fig. 2 Characteristics curves for axial displacement of a FAG 3807 ball-bearing under axial (uniaxial) and combined loads

It is evident that combined loads influence the stiffness properties of the ball-bearings. These combined loads can be interpreted as pre-tensioning, increasing the stiffness of the bearing. This effect can be accounted for with a linear interpolation between the uniaxial characteristic curve and the curve for the combined load. The stiffness matrix in Eq. (4) for the ball-bearings is derived by linear interpolation from the characteristic curves, neglecting cross-coupling effects.

$$K_i = \begin{pmatrix} k_{rad} & 0 & 0 & 0 & 0 & 0 \\ 0 & k_{ax} & 0 & 0 & 0 & 0 \\ 0 & 0 & k_{rad} & 0 & 0 & 0 \\ 0 & 0 & 0 & k_{tor} & 0 & 0 \\ 0 & 0 & 0 & 0 & 0 & 0 \\ 0 & 0 & 0 & 0 & 0 & k_{tor} \end{pmatrix} \tag{4}$$

$$k_{rad} = \frac{F_{rad}}{\delta_{rad}} \quad k_{ax} = \frac{F_{ax}}{\delta_{ax}} \quad k_{tor} = \frac{M_{rad}}{\varphi_{rad}}$$

Further elements (e.g. linear ball bearings, linear spindle-drive actuators and complex links using FEA results) are implemented in the proposed method, but will not be discussed in detail. For the end-effector used at the PARAGRIP prototype, characteristic curves were determined in measurements. Furthermore, any other kind of stiffness properties based on analytical relations, characteristic curves or fixed values can be implemented easily by defining new element types. The introduced element stiffness matrices are expressed with respect to the local element coordinate system. For the matrix assembly, described below, the element stiffness matrices are generalized. That means displacements and loads are expressed with respect to a global coordinate system by calculating equivalent displacements and loads as introduced by Lončarić [18].



3.2 Stiffness Modeling by Matrix Assembly

The generalized Cartesian stiffness matrix of the structure ${}^0K_{struc O}$ is assembled from the generalized element stiffness matrices ${}^0K_{iO}$ for element i . They link the equivalent relative (translational and rotational) displacement of two attached rigid nodes k and l to the equivalent cut load ${}^0F_{iO}$, both at the origin 0O of the global coordinate system 0:

$${}^0F_{iO} = {}^0K_{iO} \cdot ({}^0\delta\chi_{kO} - {}^0\delta\chi_{lO}) \quad (5)$$

The generalized Cartesian Stiffness Matrix the whole structure ${}^0K_{struc O}$ can be derived by superposition of all ${}^0K_{iO}$. Let n be the number of elements in the structure and i be the explicit index to identify each element of the structure. Each element is attached to two rigid nodes k and l with $k < l$ and we index the according element stiffness matrix ${}^0K_{iklO}$. Let j be the number of rigid nodes in the structure, including the fixed base $k=0$. ${}^0K_{struc O}$ is a $6j \times 6j$ zero matrix, filled up with the superposition of ${}^0K_{iklO}$:

$$\begin{aligned} {}^0K_{struc O}(6k-5:6k, 6k-5:6k) &= \sum_{i=1}^n ({}^0K_{iklO} | k > 0) \\ {}^0K_{struc O}(6k-5:6k, 6l-5:6l) &= \sum_{i=1}^n ({}^0K_{iklO} | k > 0) \\ {}^0K_{struc O}(6l-5:6l, 6k-5:6k) &= \sum_{i=1}^n ({}^0K_{iklO} | k > 0) \\ {}^0K_{struc O}(6l-5:6l, 6l-5:6l) &= \sum_{i=1}^n ({}^0K_{iklO} | l > 0) \end{aligned} \quad (6)$$

where ${}^0K_{struc O}(a:b, c:d)$ indicate the sub-matrix of ${}^0K_{struc O}$ in the columns a to b and the rows c to d . With exception of elements attached to the fixed base, that is $k=0$, the generalized 6×6 element stiffness matrices are super-positioned four times to the stiffness matrix of the structure. This corresponds to the well-known 12×12 stiffness matrices used for the MSA of connected beam elements [24, 25].

3.3 Implementation of the Extended Procedure

To overcome the limitations of the original MSA element representation exclusively by beam theory, a method to automatically calculate the global stiffness matrix and distortion of a given structure composed of different elements under external load is introduced. The stiffness assembly is universally valid for all stiffness matrices representing an element, as long as the local stiffness matrix is given or can be determined automatically. The proposed method and database is

implemented in MATLAB. For each type of flexible element the specific calculation procedure for the local stiffness matrix is stored. For each element the following parameters need to be predefined:

- Connecting nodes.
- Position of the flexible element represented in the global coordinate system.
- Orientation of the flexible element represented in the global coordinate system.
- Element type (e.g. Euler beam (rectangular/cylindrical, solid/hollow), rolling contact bearing, linear bearing, rotary drive, spindle drive (linear actuation), predefined local stiffness matrix (e.g. derived from FEA analysis for complex elements)).
- Element properties dependent on the element type (e.g. length, height, width, Young's modulus, shear modulus for rectangular beams or identification number for bearings).

The positions and orientations of the elements are not calculated automatically, as the method does not include the kinematic calculation. However, usually the kinematic calculations are known and the position and orientation of each element can be calculated with minor effort. With the predefined properties the generalized stiffness matrix and distortion of the given structure is assembled automatically using the following algorithm:

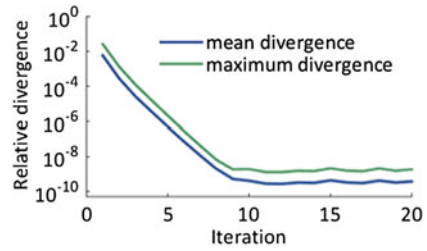
- (1) Calculation of the local stiffness matrix for each flexible element based on the element type and element properties (compare Sect. 3.1). For elements with a force dependent local stiffness matrix (e.g. ball bearings) a predefined unit force effective on the element is assumed.
- (2) Generalization of the local stiffness matrices to the global coordinate system based on the position and orientation of the element.
- (3) Stiffness assembly of the overall stiffness matrix ${}^0K_{struc O}$, based on the connecting nodes (Eq. 6).
- (4) Derivation of ${}^0\delta\chi_O$ by solving Eq. (1).

If elements with a force dependent local stiffness matrix exist, proceed with step (5), otherwise jump to step (7).

- (5) Calculation of the cut load ${}^0F_{i0}$, effective on the element i with the attached rigid nodes k and l , as shown in Eq. (5). The displacement vectors ${}^0\delta\chi_{k0}$ and ${}^0\delta\chi_{l0}$ can be extracted from ${}^0\delta\chi_O$.
- (6) Repeat step 1–4 with the calculated force, effective on the elements until a defined threshold divergence or maximum number of iterations is reached.
- (7) Reverse the generalization of the distortion ${}^0\delta\chi_O$ to the local coordinate systems if requested.
- 8) Output of the global stiffness matrix and displacement for each element.

As described above, the linear system of equations is solved in a set of iterations based on an updated overall stiffness matrix ${}^0K_{struc O}$, if elements with a force dependent local stiffness matrix (e.g. bearings) are present. Comparison with

Fig. 3 Relative divergence in the stiffness calculations from previous iterations (for 100 combinations of arbitrary load and position of the PARAGRIP arm)



kinetostatic calculations and the analysis of multiple iteration steps show that two additional iterations are sufficiently accurate for low distortions in comparison to the dimensions of the given structure. As shown in Fig. 3, the maximum divergence (for any direction of translation or rotation) to the previous iteration is about 0.1 % for the second iteration.

4 Application and Validation for the Example Structure PARAGRIP

The reconfigurable modular multi-arm robot system PARAGRIP was developed, designed and tested at the Department of Mechanism Theory and Dynamics of Machines (IGM) of the RWTH Aachen University [1]. With this multi-arm robotic system, object integrative handling operations are performed. The proposed stiffness model is implemented and validated by measurements for a single robotic arm.

The arm structure is modeled using the introduced stiffness elements (Fig. 4): Beams (k_3, k_5, k_6, k_{10}), ball-bearings ($k_2, k_4, k_7, k_9, k_{11}$) and pre-defined stiffness elements from FEA analysis (k_8). The drive stiffness (k_{drive0}, k_{drive1} and k_{drive2}),

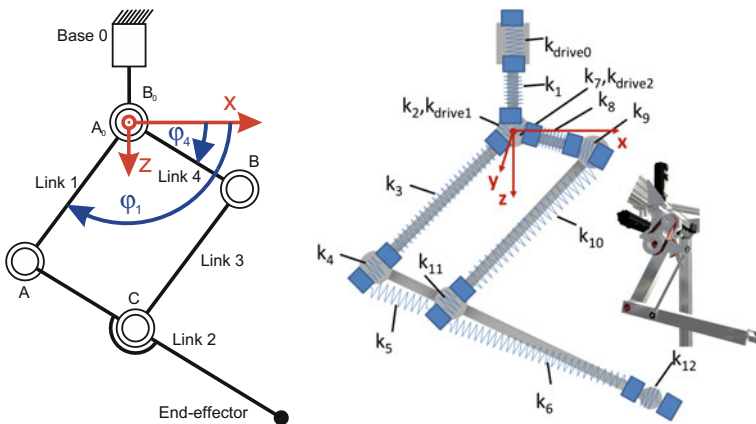


Fig. 4 Structure and stiffness representation of a single PARAGRIP arm

Table 1 Load cases

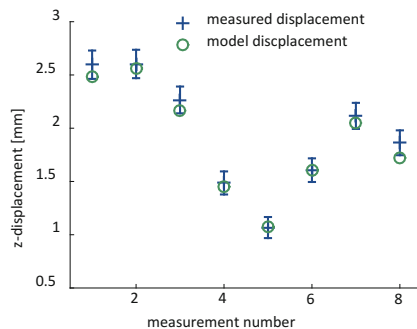
	Static load	Drive angles φ_1, φ_4 (°)	Calculated displacement (x, y, z) (mm)
1	25.34 N in z-direction	45, 3.1	-0.63, -0.41, 2.48
2	25.34 N in z-direction	47.9, 17.8	-1.23, -0.55, 2.56
3	25.34 N in z-direction	57.7, 32.5	-1.73, -0.59, 2.17
4	25.34 N in z-direction	91.3, 25	-0.88, -0.16, 1.45
5	25.34 N in z-direction	149, 46	-0.61, -0.04, 1.07
6	25.34 N in z-direction	146, 26.5	-0.51, -0.10, 1.61
7	25.34 N in z-direction	143, 7	-0.07, -0.21, 2.05
8	25.34 N in z-direction	90.5, 5	-0.38, -0.82, 1.72

including the belt gear and the stiffness properties of the central housing k_1 cannot be derived analytically or by FEA. The stiffness parameters are derived by optimization, based on 3 simple load cases for the structure using static loads on the joints k_4 and k_9 and on the end-effector.

The translational deviation of the end-effector under static load in z-direction is measured to validate the stiffness model. The load was applied using a spring balance (accuracy 2.25 % for the given load), while the displacement is measured using an optical coordinate measurement machine (accuracy 0.15 mm). The different load cases are listed in Table 1, they represent typical positions within the workspace. All measurements were performed for the same position of the actuator at the base, as a rotation of the planar structure will not alter its stiffness properties.

The calculated displacements are in very good agreement with the measurements, as shown in Figs. 5 and 6. The displacement in the direction of load, as well as cross coupling effects can be calculated within the measurement precision, using the introduced model. Furthermore, the model and measurements show a similar agreement for higher and lower loads. First Measurements for arbitrary loads in x- and y-direction show a convincing agreement with the model and will be subject to further investigation. The very good agreement for loads in z-direction enables the use for the compensation of position dependent deformations due to gravitational forces.

Fig. 5 Measured and calculated z-displacement of the end-effector under uniaxial load in z-direction



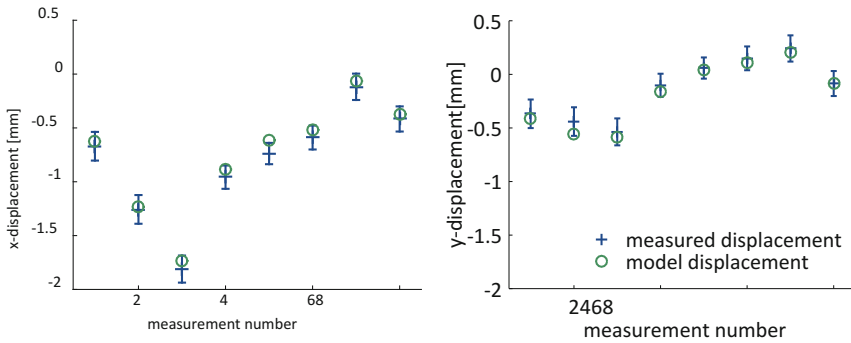


Fig. 6 Measured and calculated x- and y-displacement of the end-effector under uniaxial load in z-direction

5 Conclusions

An extended method for the stiffness calculation of mechanical structures based on the MSA has been introduced and has been proven to be effective. Complex joints and links, e.g. with force dependent stiffness properties, can be implemented with minor effort as shown for the PARAGRIP handling system. The implementation of predefined elements e.g. Euler Beams and especially rolling contact bearings (using characteristic curves to determine the stiffness properties) allows an easy set up and calculation of complex structures. Force dependent, non-linear stiffness properties can be accounted for with few iterations of the linear model. The stiffness model was validated by measurements on a robotic arm. The comparison to the measurements showed a very good agreement for the main deviations and cross coupling effects for loads in z-direction. In the future work, the derived stiffness model will be used to increase the capabilities of kinematic parameter identification by compensating the gravitational forces on the structure.

Acknowledgments The authors would like to thank the German Research Foundation DFG for the kind support within the Cluster of Excellence “Integrative Production Technology for High Wage Countries”.

References

1. Riedel, M.: Flexible Bauteilhandhabung auf Basis einer rekonfigurierbaren parallelkinematischen Struktur, Dissertation (2014). ISBN 978-3-8440-2534-7
2. Briot, S., Pashkevich, A., Chablat, D.: Reduced elastodynamic modelling of parallel robots for the computation of their natural frequencies. In: 13th World Congress in Mechanism and Machine Science, Guanajuato, Mexico, 19–25 June 2011

3. Ahmad, A., Anderson, K., Sellgren, U.: An approach to stiffness analysis methodology for haptic devices. In: ICUMT Ultra Modern Telecommunications and Control Systems and Workshops (2011)
4. Cammarata, A.: On the Stiffness Analysis and Elastodynamics of Parallel Kinematic Machines, in Serial and Parallel Robot Manipulators—Kinematics, Dynamics, Control and Optimization. In: Kucuk, S. (ed.), pp. 85–109. InTech (2012)
5. Kucuk, S. (ed.): Serial and Parallel Robot Manipulators—Kinematics, Dynamics, Control and Optimization. InTech (2012)
6. Taghvaeipour, A., Angeles, J., Lessard, L.: On the elastostatic analysis of mechanical systems. *Mech. Mach. Theory* **58**, 202–216 (2012)
7. Salisbury, J.: Active stiffness control of a manipulator in cartesian coordinates. In: 19th IEEE Conference on Decision and Control including the Symposium on Adaptive Processes, pp. 95–100 (1980)
8. Gosselin, C.: Stiffness mapping for parallel manipulators. *IEEE Trans. Robot. Autom.* **6**(3), 377–382 (1990)
9. El-Khasawneh, B.S., Ferreira, P.M.: Computation of stiffness and stiffness bounds for parallel link manipulators. *Int. J. Mach. Tools Manufact.* **39**(2), 321–342 (1999)
10. Pashkevich, A., Chablat, D., Wenger, P.: Stiffness analysis of multi-chain parallel robotic systems. In: 9th IFAC Workshop on Intelligent Manufacturing Systems, France, pp. 127–132 (2008)
11. Pashkevich, A., Klimchik, A., Chablat, D.: Enhanced stiffness modeling of manipulators with passive joints. In: *Mechanism and Machine Theory*, vol. 46 5, pp. 662–679 (2011). doi:[10.1016/j.mechmachtheory.2010.12.008](https://doi.org/10.1016/j.mechmachtheory.2010.12.008)
12. Gosselin, C., Li, S.: Stiffness analysis of 3-RRR planar parallel mechanisms based on CCT. In 12th IFToMM World Congress, Besancon (France), June 18–21 2007
13. Goncalves, R.S., Carvalho, J.C.M.: Stiffness analysis of parallel manipulator using matrix structural analysis. In: The Second European Conference on Mechanism Science, Proceedings of Eucomes 08, Great Britain. Springer (2009)
14. Deblaise, D., Hernot, X., Maurine, P.: A systematic analytical method for PKM stiffness matrix calculation. In: 2006 IEEE International Conference on Robotics and Automation, pp. 4213–4219 (2006)
15. Taghvaeipour, A., Angeles, J., Lessard, L.: Online computation of the stiffness matrix in robotic structures using finite element analysis. Master Thesis (2010)
16. Nagai, K., Liu, Z.: A systematic approach to stiffness analysis of parallel mechanisms. *IEEE J. Robot. Autom.* 1543–1548 (2008)
17. Pashkevich, A., Chablat, D., Wenger, P.: Stiffness analysis of overconstrained parallel manipulators. *Mech. Mach. Theory* **44**(5), 966–982 (2009)
18. Loncaric, J.: Normal forms of stiffness and compliance matrices. In: *IEEE J. Robot. Autom.* **3** (6), 567–572 (1987). doi:[10.1109/JRA.1987.1087148](https://doi.org/10.1109/JRA.1987.1087148)
19. Dieker, S.: *Elementare Festigkeitslehre im Leichtbau*. Donat, Bremen (2005). ISBN 978-3924444587
20. Hernot, X., Sartor, M., Guillot, J.: Calculation of the stiffness matrix of angular contact ball bearings by using the analytical approach. *J. Mech. Des.* **122**(1), 83 (2000). doi:[10.1115/1.533548](https://doi.org/10.1115/1.533548)
21. Noel, D., Ritou, M., Furet, B., Le Loch, S.: Complete analytical expression of the stiffness matrix of angular contact ball bearings. *J. Tribol.* **135**(4), 041101 (2013). doi:[10.1115/1.4024109](https://doi.org/10.1115/1.4024109)
22. Daidi, A., Chaïb, Z., Ghosn, A.: 3D Simplified finite elements analysis of load and contact angle in a slewing ball bearing. In: *J. Mech. Des.* **130**(8), 082601 (2013). doi:[10.1115/1.2918915](https://doi.org/10.1115/1.2918915)

23. Schaeffler Technologies AG and Co. KG: Bearinx[®]-online Wellenberechnung, http://www.schaeffler.com/remotemedien/media/_shared_media/08_media_library/01_publications/schaeffler_2/brochure/downloads_1/pbo_de_de.pdf. Accessed 28 July 2015
24. Cammarata, A.: On the stiffness analysis and elastodynamics of parallel kinematic machines. In: Kucuk, S. (ed.) Serial and Parallel Robot Manipulators—Kinematics, Dynamics, Control and Optimization. InTech (2012). ISBN 978-953-51-0437-7
25. Deblaise, D., Hernot, X., Maurine, P.: A systematic analytical method for PKM stiffness matrix calculation. In: ICRA IEEE International Conference on Robotics and Automation, Orlando, FL, USA, pp. 4213–4219 (2006)

Translational Parallel Manipulator with Pa² Kinematic Joints

A. Hernandez, Z. Zhang, V. Petuya, E. Macho and E. Amezua

Abstract The kinematic pair Pa² is composed of two interlinked parallelograms. It has two degrees of freedom that generate a translational plane variable with position. It has a structure different from the PaPa pair, which is composed also by two parallelograms but generates a constant translational plane. Currently, the Pa² pair is used at conceptual level but it is not used in almost any practical application. There are advantages and drawbacks in using it. The main drawback is the high number of redundant constraints that this pair possesses. However, substituting carefully the revolute joints by spherical joints can eliminate these redundant constraints. Also, this pair constitutes a more rigid structure that replaces adequately the problematic passive prismatic joints. In this paper, will be presented a preliminary study of a translational parallel manipulator (PM) based on the use of the Pa² pair: the 3-PPa² that contains redundant constraints in its global structure. To study the potentiality of the PM presented in this paper, the following analyses will be done: position and velocity (direct and inverse kinematics), workspace and singularity analysis. Also the potentiality to be optimised will be studied.

Keywords Pa² joint · Translational parallel manipulator · Kinematic analysis

A. Hernandez · Z. Zhang · V. Petuya (✉) · E. Macho · E. Amezua
Mechanical Engineering Department, University of the Basque
Country UPV/EHU, Leioa, Spain
e-mail: victor.petuya@ehu.eus

A. Hernandez
e-mail: a.hernandez@ehu.eus

Z. Zhang
e-mail: zhangzhen_tust@163.com

E. Macho
e-mail: erik.macho@ehu.eus

E. Amezua
e-mail: enrique.amezua@ehu.eus

1 Introduction

In pick-and-place operations, three translations are commonly required to move the object from one position to another. In this case, a 6-DOF fully-parallel manipulator is too expensive to be used because six actuators are required to control the posture of end-effector. Therefore, it is more economical to employ lower mobility parallel robots since less actuators are used. Additionally, lower mobility parallel robots have simpler architecture and simpler forward and inverse kinematics.

In the field of parallel manipulators generating three translations, many architectures [1, 2] have been proposed by academic researchers in past years. Between them, Delta [2] robot could be highlighted as a successful application of a lower mobility architecture, which is famous for its high acceleration capabilities. The end-effector is triangular and is connected to the legs by revolute (R) joints. Also, each leg contains a parallelogram whose coupler link generates a circumferential translation with respect to its opposite bar.

In this paper, to explore new three-translation generators, the Pa^2 pair, which contains two interlinked parallelograms, is used to build a translational PM.

2 PMs with Pa and Pa^2 Pairs

A Pa kinematic pair (also called Π pair) is composed of one parallelogram, which can generate a circumferential translation with respect to the fixed bar. An early application of Pa pairs in the structural synthesis of parallel robots can be found in the manipulator developed at Maryland University (or in its equivalent without redundant restrictions, the Delta robot). Its moving platform can perform three translations in 3D space, and its legs are RRPaR kinematic chains. In the field of academic research, the Pa pair was firstly introduced by Wohlhart [3]. After then, different architectures with Pa pairs have been proposed [4].

In comparison with the Pa pair, Pa^2 pairs have received little attention by researchers. As far as we know, there are no PMs with Pa^2 pairs in the scientific bibliography. However, it is worth noticing that some structures (called Pa^2 equivalents) with similar functions as Pa^2 have been involved in some research developments.

A more similar case is proposed by Angeles [5]. He constructed a Π^2 pair with two parallelograms sharing the same moving platform and the same fixed one, while the joints in Π^2 are replaced by universal joints. This Π^2 pair is characterized by a 2-DOF displacement generator being its displacements elements of the T^3 subgroup. In addition, the points of the moving platform have a spherical motion with respect to the base plate. These kinematic characteristics are similar to those of the Pa^2 pair.

Another architecture with a function equivalent to a Pa^2 joint is the use of two Pa pairs in the Micro Finger [6]. In this case, the two Pa pairs are connected in serial

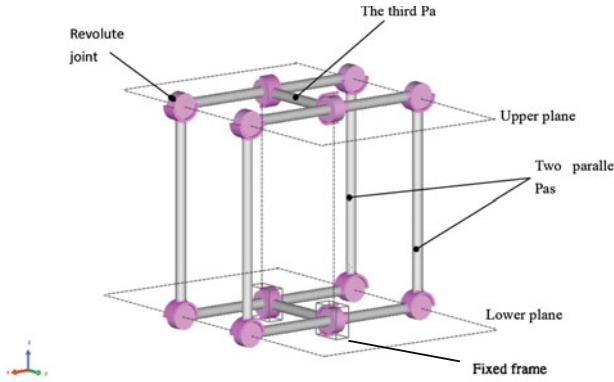


Fig. 1 Pa² joint

instead of in parallel. The two Pa pairs are interlinked with an angle, while the first Pa’s moving platform is the fixed plate of the second Pa. Similar to the Micro Finger, in [7] two Pa pairs connected in serial are also used as a Sch nflies Motion Generator.

In the design proposed in this paper, the Pa pairs are located as shown in Fig. 1. Using Malishev’s formula, the mobility analysis of the Pa² pair has been done obtaining two translational degrees of freedom (2T). Also, there are eight geometrical redundant restrictions introduced by the R joints. Most of them can be eliminated replacing carefully some R joints by S joints.

3 Pa² Kinematic Joint Study

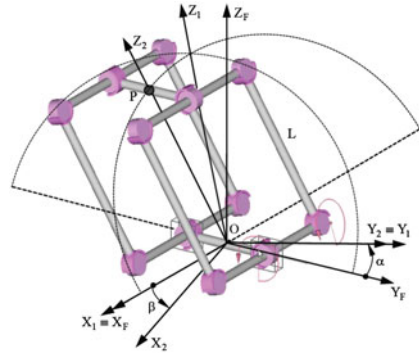
As shown in the Fig. 1, a Pa² pair has three parts: two Pa pairs parallel to each other and a third Pa pair cross-linked with the other Pa pairs. The two parallel Pa pairs form two planes: upper and lower, being the upper plane always parallel to the lower one. In this Pa² pair, only R joints are used to connect the two adjacent links. The axes of the R joints in the two parallel Pa pairs have the same direction, while the axes in the cross-linked Pa are perpendicular to them.

In order to study the potentiality of the Pa² pair, a fixed reference frame O-X_FY_FZ_F is defined as shown in the Fig. 2. The origin of the reference frame O is located at the center of the lower link, X_F axis is perpendicular to the cross-linked Pa² plane and goes through the center of the lower link, Y_F axis is defined along the lower link, while Z_F axis is obtained applying the right hand rule. In addition, point P is defined at the center of the upper link.

Without considering the third parallelogram, the two parallel parallelograms would generate 1-DOF circumferential translation along X_F axis if they move simultaneously with respect to the lower plane with an angle β. Similarly, the third



Fig. 2 Pa² joint frames



Pa could just generate a circumferential translation along Y_F axis with an angle α without the constraints of the two parallel parallelograms. Thus, α and β are rotational parameters of Pa². Once interlinking the two parallel Pa pairs with the third Pa, the new structure would generate 2-DOF translations with respect to the plane X_FY_F. Besides, any point located at the upper plane has a spherical trajectory with respect to the fixed one with a radius of OP (the common length of Pa²). As a consequence, this pair is a translational generator of dimension 2 included in {T₃}. However, this bond does not constitute a subgroup because the plane of translations is not constant.

Although, a Pa² pair is more complicated than a Pa joint in terms of motions involved, the position of any point of the upper plane onto the trajectory surface can be obtained by two sequential rotations.

In a first step, the cross-linked Pa pair rotates an angle α around the axes of its revolute joints. In a second step, the two parallel Pa pairs rotate an angle β around the axes of their revolute joints. Two local reference frames corresponding to the first step and the second one are defined as shown in the Fig. 2. When the values of α and β are 0°, the Pa² pair is in the posture shown in Fig. 1.

Thus, the position of point P expressed in the fixed frame is,

$$\begin{bmatrix} x \\ y \\ z \end{bmatrix} = \begin{bmatrix} L \sin \beta \\ -L \cos \beta \sin \alpha \\ L \cos \beta \cos \alpha \end{bmatrix} \tag{1}$$

Thus, an position equation of point P expressed the fixed frame can be obtained,

$$x^2 + y^2 + z^2 = L^2 \tag{2}$$

In general, any point onto the upper plane will draw a spherical trajectory. Compared with other kinematic joints, Pa² has greater rigidity.



4 Position Problems of the 3-PPa² PM

In this section, the loop closure equations of the 3-PPa² parallel manipulator are obtained.

As shown in Fig. 3, a fixed reference frame is defined along the three linear actuators located at points A₁, A₂ and A₃ respectively. Also, three local reference frames are defined by rotating the fixed frame around the actuator’s axes corresponding to three legs respectively, which are depicted in Fig. 3.

Vectors **i**, **j**, and **k** denote the unit vectors of X₀, Y₀ and Z₀ axes respectively. Vectors **u_i**, **v_i** and **w_i** are unit vectors corresponding to the local frame of *i*th leg. In addition, OA_{*i*} denotes the stroke of the *i*th leg, defined as s₁, s₂, and s₃ while L and l are geometrical dimensions of the manipulator.

4.1 Direct Position Problem of 3-PPa² PM

The purpose of the direct position problem is to obtain the position of the end-effector, defined by the position vector $\mathbf{x}_p = [x_p \ y_p \ z_p]^T$ of the reference point P, as a function of input parameters, i.e., the strokes of actuators s₁, s₂, and s₃.

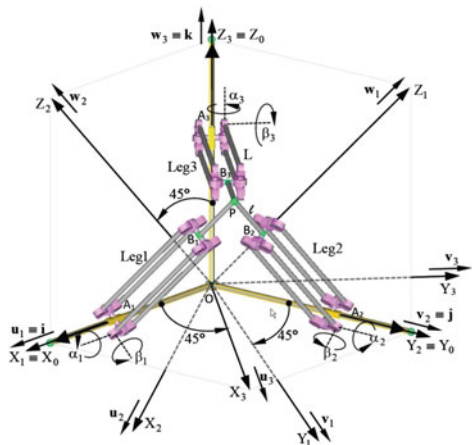
The absolute position of point P can be expressed for leg 1,

$$\mathbf{x}_P = \mathbf{x}_{A_1} + \mathbf{x}_{A_1B_1} + \mathbf{x}_{B_1P} \tag{3}$$

$$\mathbf{x}_{A_1} = s_1 \mathbf{i} \tag{4}$$

$$\mathbf{x}_{A_1B_1} = {}^0_1\mathbf{R}(L \sin \beta_1 \mathbf{u}_1 - L \cos \beta_1 \sin \alpha_1 \mathbf{v}_1 + L \cos \beta_1 \cos \alpha_1 \mathbf{w}_1) \tag{5}$$

Fig. 3 3-PPa²



$$\mathbf{x}_{B_1P} = {}^0_1\mathbf{R}(0\mathbf{u}_1 + 0\mathbf{v}_1 + \ell\mathbf{w}_1) \quad (6)$$

where \mathbf{u}_1 , \mathbf{v}_1 and \mathbf{w}_1 denote the unit vectors corresponding to the leg 1 local frame and ${}^0_1\mathbf{R}$ denotes the matrix that rotates leg 1 local frame ($O - X_1Y_1Z_1$) to the fixed frame ($O - X_0Y_0Z_0$).

Equivalently, the position vectors of legs 2 and 3 are obtained by rotating leg 1.

Imposing that the modules of vectors $\mathbf{x}_{A_iB_i}$ must be equal to L , the nonlinear equations for 3-PPa² are obtained,

$$(x_p - s_1)^2 + (y_p - n)^2 + (z_p - n)^2 = L^2 \quad (7)$$

$$(x_p - n)^2 + (y_p - s_2)^2 + (z_p - n)^2 = L^2 \quad (8)$$

$$(x_p - n)^2 + (y_p - n)^2 + (z_p - s_3)^2 = L^2 \quad (9)$$

where $n = \frac{\sqrt{2}}{2}\ell$. These equations lead to a quadratic univariate polynomial that must be solved numerically.

4.2 Inverse Position Problem of 3-PPa² PM

The aim of inverse position problem is to obtain the values of the input parameters s_1 , s_2 and s_3 for a given posture of the end-effector defined by the position vector \mathbf{x}_p .

From Eqs. (7)–(9), all inputs can be obtained in a straightforward way:

$$s_1 = x_p \pm \sqrt{L^2 - (y_p - n)^2 - (z_p - n)^2} \quad (10)$$

$$s_2 = y_p \pm \sqrt{L^2 - (x_p - n)^2 - (z_p - n)^2} \quad (11)$$

Fig. 4 3-PPa² path

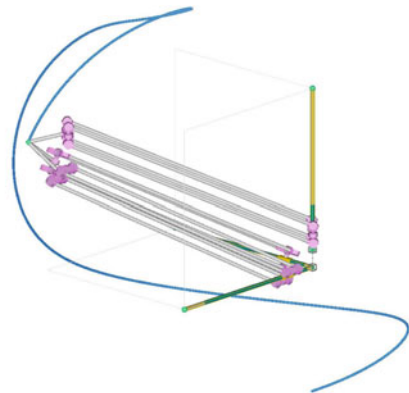
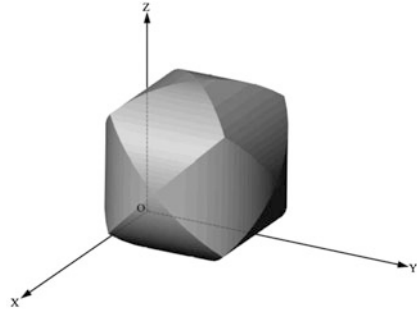


Fig. 5 Workspace

$$s_1 = z_p \pm \sqrt{L^2 - (x_p - n)^2 - (y_p - n)^2} \quad (12)$$

where $n = \frac{\sqrt{2}}{2}\ell$. In Fig. 4 is shown a path of the 3-PPA² obtained using GIM software (<http://www.ehu.eus/compmech/software/>).

4.3 Workspace

For the manipulator under study, the workspace is defined by the intersection of three cylinders,

$$(y_p - n)^2 + (z_p - n)^2 \leq L^2 \quad (13)$$

where $n = \frac{\sqrt{2}}{2}\ell$. In Fig. 5 is shown a 3D view of the workspace.

5 Singularities

In order to analyze the singularities, Jacobian matrices are obtained. Differentiating Eq. (3) for each leg and dot-multiplying both sides by $\mathbf{x}_{A_i B_i}$, the velocity equation in matrix form is obtained,

$$\begin{bmatrix} \mathbf{x}_{A_1 B_1}^T \\ \mathbf{x}_{A_2 B_2}^T \\ \mathbf{x}_{A_3 B_3}^T \end{bmatrix} \begin{bmatrix} \dot{x}_p \\ \dot{y}_p \\ \dot{z}_p \end{bmatrix} = \begin{bmatrix} L \sin \beta_1 & 0 & 0 \\ 0 & -L \sin \beta_2 & 0 \\ 0 & 0 & -L \sin \beta_3 \end{bmatrix} \begin{bmatrix} \dot{s}_1 \\ \dot{s}_2 \\ \dot{s}_3 \end{bmatrix} \quad (14)$$

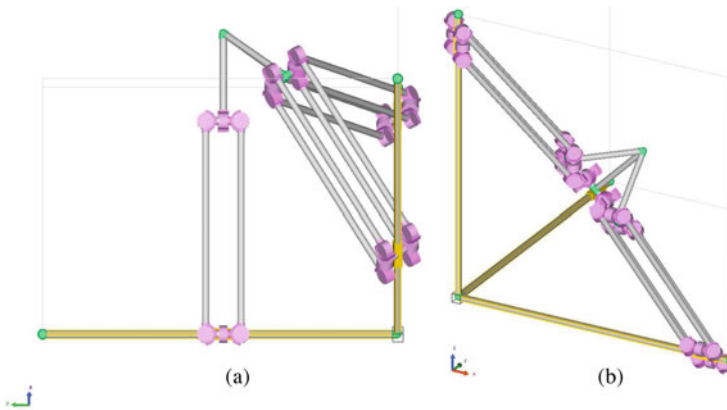


Fig. 6 Inverse (a) and Direct (b) kinematic singularity

When the manipulator is in the inverse kinematic singularity, the end-effector loses one or more degrees in one direction. For this manipulator, this singularity occurs when the value of any $\beta_i (i = 1, 2, 3)$ is 0° or 180° (Fig. 6).

A direct kinematic singularity happens when the rank of the direct Jacobian reduces. For the manipulator under study, this singularity appears when any two of legs are parallel to each other, or the three legs are on the same plane.

6 Conclusions

In this paper, the potential use of the Pa^2 pair as a part of a PM's kinematic chain is studied. From a theoretical approach, this kinematic structure has been proposed in some designs. However, the authors have not found an analyzed PM including this type of pairs. The manipulator presented in this paper, 3-PPa^2 , includes redundant restrictions and constitutes a preliminary study of the use of this type of Pa^2 pairs.

References

1. Carricato, M., Parenti-Castelli, V.: A family of 3-DOF translational parallel manipulators. *ASME J. Mech. Des.* **125**, 302–307 (2003)
2. Clavel, R.: Delta, a fast robot with parallel geometry. In: *Proceedings of the 18th International Symposium Industrial Robots*, pp. 91–100. Lausanne (1988)
3. Wohlhart, K.: Der homogene paralleltrieb-mechanismus. *Math. Pannonica* **2**(2), 59–76 (1991)

4. Salgado, O., Altuzarra, O., Petuya, V., Hernández, A.: Synthesis and design of a novel 3T1R fully-parallel manipulator. *ASME J. Mech. Des.* **130**(4), 042305 (2008)
5. Angeles, J.: The qualitative synthesis of parallel manipulators. *ASME J. Mech. Des.* **126**, 617–624 (2004)
6. Arai, T., Hervé, J.M., Tanikawa, T.: Development of 3DOF Micro Finger. In: *Proceedings of the IRO'96*, pp. 981–987. Osaka, 5–8 Nov 1996
7. Angeles, J., Morozov, A.: A device for the production of Sch nflies motions. Patent Filed to the PCT on 6 Nov 2002

Synthesis and Modeling of Redundantly Actuated Parallel Kinematic Manipulators —An Approach to Efficient Motion Design

T. Haschke, M. Lorenz, J. Brinker, M. Hüsing and B. Corves

Abstract Spatial object manipulation is subject to various parameters, which can be optimized by means of suitable motion strategies. In addition, corresponding strategies can be adapted to specified handling devices enabling efficient motion design with respect to kinematic and dynamic characteristics of particular manipulators. Further optimization is provided by the application of robot redundancy, whose resolution can be adapted to efficient motion planning. In this context, parallel kinematic systems featuring kinematic redundancy or a redundant actuator concept can be operated with an optimal set of actuator parameters allowing a resource-efficient object manipulation. This contribution is devoted to the conception and modeling of redundantly actuated parallel kinematic manipulators (RA-PKM) in order to realize optimal configuration strategies and motion design. Accordingly, the structure selection and the dimensional synthesis of a translational RA-PKM are presented based on parametric kinematic and dynamic modeling. Corresponding models provide an application-oriented transformation from intuitive CAD design software to technical computing and simulation software. The developed manipulator is suitable for the comparison of different redundant and non-redundant actuator configurations as well as optimal trajectories. Concluding analyses exemplarily refer to a non-redundant 3-arm and a redundant n -arm PRPaR system.

T. Haschke (✉) · M. Lorenz · J. Brinker · M. Hüsing · B. Corves
RWTH Aachen University, Aachen, Germany
e-mail: haschke@igm.rwth-aachen.de

M. Lorenz
e-mail: lorenz@igm.rwth-aachen.de

J. Brinker
e-mail: brinker@igm.rwth-aachen.de

M. Hüsing
e-mail: huesing@igm.rwth-aachen.de

B. Corves
e-mail: corves@igm.rwth-aachen.de

Keywords Parallel manipulators • Actuation redundancy • Dimensional synthesis • Motion design • Dynamics

1 Introduction

Due to their excellent dynamic properties and a high structural stiffness, PKM are particularly suited for high-speed and high-accuracy object handling [1]. Accordingly, parallel manipulators are able to perform with an excellent payload-to-weight ratio, whereas the most notable disadvantages are their comparatively small and limited workspace [2]. As the kinematic structure and dimensioning of corresponding manipulators have a direct and significant impact on several aspects of motion design, development and construction of PKM can be arranged for optimal path and trajectory planning. Accordingly, the optimal trajectory planning problem generally addresses the relation between a predetermined object motion to be performed in a specific time. For this purpose, a trajectory is mostly expressed by time-parametrized sequences of object positions and orientations [3]. With respect to automated object handling, the optimal trajectory is also affected by manipulator parameters, such as acceleration and inertia. In order to improve the efficiency of PKM motion design, additional optimization can be gained through robot redundancy. This contribution intends to develop a suitable simulation model for testing efficient trajectory and motion design using redundantly actuated PKM.

Robot redundancy can generally be subdivided into four different classes, namely *sensor/measurement redundancy*, *task redundancy*, *kinematic redundancy* and *actuation redundancy*, whereas the two last-mentioned are referred to as *mechanical redundancy* [4, 5]. Furthermore, two different types of actuation redundancy can be specified: On the one hand, *in-branch redundancy* occurs, when existing passive joints are replaced by additional actuators. *Branch redundancy*, on the other hand, results from adding actuated branches to the kinematic structure of a PKM [6]. This study is limited to branch redundant systems, which do not have a unique solution to the inverse kinematics problem [7]. Thus, in case of actuation redundancy the actuator space parameters can specifically be affected for given task space parameters. In prior research this characteristic of actuation redundancy has been used in order to optimize the performance of PKM [7]. In this context, actuation redundancy is used to avoid singularities and to enlarge the reachable workspace of parallel manipulators [8]. Furthermore, end-effector forces can be homogenized over the workspace due to improved force transmission capabilities, enabling the application of actuators with less inertia [9]. In addition, control methods have been developed in terms of backlash avoidance [10] and to improve the manipulator's operational stiffness [11]. Further analyses of redundant parallel manipulators show the potential of improving acceleration capabilities by means of homogenization [12].

The paper is organized as follows: Sect. 2 illustrates the selection process of suitable kinematic structures including a detailed description of existing

manipulators featuring actuation redundancy. In Sect. 3 the inverse kinematics problem of the n -PRPaR (*with* $n \geq 3$) manipulator is introduced. In order to provide an analytic model of the manipulator in motion, Sect. 4 presents the corresponding inverse dynamics problem applying motion equations in minimal coordinates and the Principle of Virtual Work. In Sect. 5 an extensive simulation model is presented enabling a user-friendly transformation between visual CAD design and technical computing software. Finally, an outlook on future research and a conclusion are given in Sect. 6.

2 Selection of the Kinematic Structure

For this paper the inclined configuration of the Delta (i.e. n -PRPaR) is investigated. As an example the 4-PRPaR and its kinematic structure is shown in Fig. 1. The main reason for that is its vertical support of the push axis against the gravitational forces. In [7] it is also shown that especially the inclined configuration provides superior behavior in case of redundantly actuated systems. During preceding evaluation, the n -PRPaR was compared to n -CRR and n -PCR manipulators. During the selection process the n -PRPaR was compared to n -CRR and n -PCR manipulators. The n -CRR is highly sensitive in respect of the size of the end-effector. Thus, the reachable workspace is relatively small compared to the workspace reached by the n -PRPaR. Moreover, a similar workspace volume is accompanied by particularly large end-effector size and thus, high moving masses. Hence, the n -CRR is excluded from any further investigation. A similar problem occurs in case of the n -PCR where the sliding length of the cylindrical joint leads to a drastic reduction of the workspace when collisions are taken into account. Finally, the n -PRPaR is chosen due to its well-known characteristics and extensive previous research. Linear Deltas or also called Linapods can be subdivided into orthogonal (e.g. the Orthoglide), horizontal (e.g. Triglide and Urane SX), vertical (as e.g. commonly used for 3D-printing) and inclined versions (e.g. Delta Keops). In addition, hybrid versions (e.g. Delta Ibis) with linear and rotary actuation exist. In [13] a version with reversed chains is presented. In this type, the linear actuators are not fixed to the base but attached to the platform. Brinker and Corves [14] gives an extensive overview on parallel robots with Delta-like architecture and rotary as well as linear actuation. The unique feature of this approach is seen in the redundant actuation of linear Deltas.

3 Inverse Kinematics Problem

The inverse kinematics leads to the relation between the given end-effector velocity and the desired velocity of the actuated joint. The position equation in the base coordinate system 0 is given as

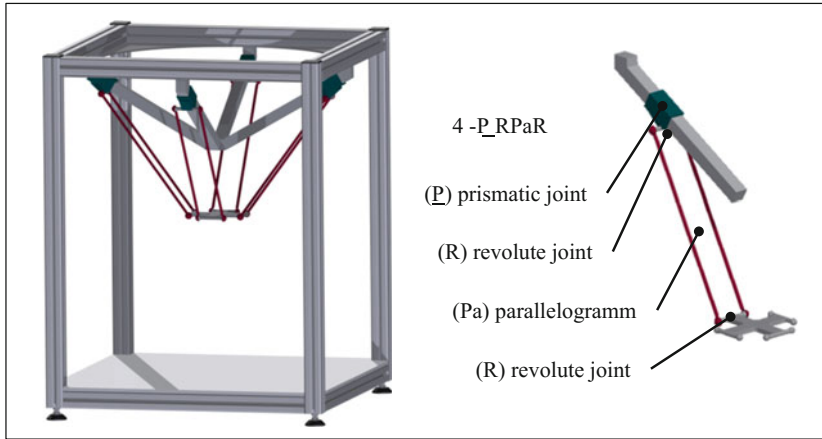


Fig. 1 Assembly of the 4-PRPaR (*left*) and one leg with the PRPaR structure (*right*)

$${}^0\mathbf{p} = {}^0\mathbf{a}_i + {}^0\mathbf{l}_{1,i} + {}^0\mathbf{l}_{H,i} + {}^0\mathbf{l}_{2,i} - {}^0\mathbf{b}_i \quad (1)$$

Differentiation of (1) results in

$${}^0\dot{\mathbf{p}} = {}^0\dot{\mathbf{l}}_{1,i} + {}^0\omega_{2,i} \times {}^0\mathbf{l}_{2,i} \quad (2)$$

Dot-multiplying (7) with ${}^0\mathbf{l}_{2,i}$ resolves the cross product and taking into account that ${}^0\dot{\mathbf{l}}_{1,i} = \dot{x}_i {}^0\mathbf{e}_{1,i}$ leads to

$${}^0\mathbf{l}_{2,i}^T {}^0\dot{\mathbf{p}} = {}^0\mathbf{l}_{2,i}^T {}^0\mathbf{e}_{1,i} \dot{x}_i \quad (3)$$

and after rearranging:

$$\dot{x}_i = \underbrace{{}^0\mathbf{l}_{2,i}^T / {}^0\mathbf{l}_{2,i}^T {}^0\mathbf{e}_{1,i}}_{J_{p,i}} {}^0\dot{\mathbf{p}} \quad (4)$$

Finally, the Jacobian matrix \mathbf{J}_p , relating the given end-effector velocity to the velocity of the actuated joint, can be obtained:

$$\dot{\mathbf{x}} = \begin{bmatrix} {}^0\mathbf{l}_{2,1}^T / {}^0\mathbf{l}_{2,1}^T {}^0\mathbf{e}_{1,1} \\ \vdots \\ {}^0\mathbf{l}_{2,n}^T / {}^0\mathbf{l}_{2,n}^T {}^0\mathbf{e}_{1,n} \end{bmatrix} {}^0\dot{\mathbf{p}} = \mathbf{J}_p {}^0\dot{\mathbf{p}} \quad (5)$$

4 Inverse Dynamics Problem

The most common analytical approaches for dynamic modeling are the Principle of Virtual Work, the Newton-Euler Formulation and the Lagrangian Formulation. In [15] a comparative study of inverse dynamics based on Clavel's Delta robot is presented concluding that, for rotationally actuated 3-dof Delta robots, the Lagrangian approach is most efficient in respect of computation times. However, for more complex kinematics, e.g. serial-parallel Delta robots with orientation capabilities, partial derivatives of the energy-based approach become very cumbersome leading to considerable computation times [16]. In addition, the virtual work approach deploys Link Jacobian Matrices which can be validated easily. Thus, in the following investigation of a similar manipulator, the inverse dynamics problem for the n-PRPaR is solved using the virtual work approach.

Taking advantage of (2), the solution for ${}^0\omega_{2,i}$ can be found.

$${}^0\omega_{2,i} = \frac{{}^0\mathbf{l}_{2,i} \times ({}^0\dot{\mathbf{p}} - {}^0\dot{\mathbf{l}}_{1,i})}{l_2^2} \quad (6)$$

The velocities of the centers of gravity for the slider and the distal link are given by the following equations:

$${}^0\mathbf{v}_{1,i,COG} = {}^0\dot{\mathbf{l}}_{1,i} = \dot{x}_i {}^0\mathbf{e}_{1,i} \quad (7)$$

$${}^0\mathbf{v}_{2,i,COG} = {}^0\mathbf{v}_{COG1,i} + {}^0\omega_{2,i} \times \frac{1}{2} {}^0\mathbf{l}_{2,i} \quad (8)$$

Differentiation of (2) gives the relations for the accelerations:

$${}^0\ddot{\mathbf{p}} = {}^0\ddot{\mathbf{l}}_{1,i} + {}^0\dot{\omega}_{2,i} \times {}^0\mathbf{l}_{2,i} + {}^0\omega_{2,i} \times ({}^0\omega_{2,i} \times {}^0\mathbf{l}_{2,i}) \quad (9)$$

with ${}^0\dot{\mathbf{l}}_{1,i} = \dot{x}_i {}^0\mathbf{e}_{1,i}$. The acceleration \ddot{x}_i can be found by dot-multiplying (9) with ${}^0\mathbf{l}_{2,i}$:

$${}^0\ddot{\mathbf{p}} \cdot {}^0\mathbf{l}_{2,i} = {}^0\dot{\mathbf{l}}_{1,i} \cdot {}^0\mathbf{l}_{2,i} + {}^0\omega_{2,i} \times ({}^0\omega_{2,i} \times {}^0\mathbf{l}_{2,i}) \cdot {}^0\mathbf{l}_{2,i} \quad (10)$$

which, after rearranging, leads to

$$\ddot{x}_i = \frac{[{}^0\ddot{\mathbf{p}} + {}^0\omega_{2,i} \times ({}^0\omega_{2,i} \times {}^0\mathbf{l}_{2,i})] \cdot {}^0\mathbf{l}_{2,i}}{{}^0\mathbf{e}_{1,i} \cdot {}^0\mathbf{l}_{2,i}} \quad (11)$$

With the knowledge about \ddot{x}_i the unknown value ${}^0\dot{\omega}_{2,i}$ can be found by resolving the cross product and further conversion, i.e.

$${}^0\dot{\omega}_{2i} = \frac{{}^0\mathbf{l}_{2i} \times [{}^0\ddot{\mathbf{p}} - {}^0\dot{\mathbf{i}}_{1,i} - {}^0\omega_{2i} \times ({}^0\omega_{2i} \times {}^0\mathbf{l}_{2i})]}{l_2^2} \quad (12)$$

With this information the accelerations of the centers of gravity are given by:

$${}^0\mathbf{a}_{1,i,COG} = {}^0\dot{\mathbf{i}}_{1,i} = \ddot{x}_i {}^0\mathbf{e}_{1,i} \quad (13)$$

$${}^0\mathbf{a}_{2,i,COG} = {}^0\dot{\mathbf{i}}_{1,i} + {}^0\dot{\omega}_{2,i} \times \frac{1}{2} {}^0\mathbf{l}_{2,i} + {}^0\omega_{2,i} \times \left({}^0\omega_{2,i} \times \frac{1}{2} {}^0\mathbf{l}_{2,i} \right) \quad (14)$$

The forces and moments out of gravitational and inertial effects for the end-effector and the links are given by:

$$\mathbf{Q}_p = \begin{bmatrix} \mathbf{f}_p \\ \mathbf{m}_p \end{bmatrix} = \begin{bmatrix} m_p ({}^0\mathbf{g} - {}^0\ddot{\mathbf{p}}) \\ 0 \end{bmatrix} \quad (15)$$

Referring to the leg-specific coordinate systems, the resultant forces and moments of links are

$${}^i\mathbf{Q}_{1,i} = \begin{bmatrix} {}^i\mathbf{f}_{1,i} \\ {}^i\mathbf{m}_{1,i} \end{bmatrix} = \begin{bmatrix} m_1 ({}^i\mathbf{g} - {}^i\mathbf{a}_{1,i,COG}) \\ 0 \end{bmatrix} \quad (16)$$

$${}^i\mathbf{Q}_{2,i} = \begin{bmatrix} {}^i\mathbf{f}_{2,i} \\ {}^i\mathbf{m}_{2,i} \end{bmatrix} = \begin{bmatrix} m_2 ({}^i\mathbf{g} - {}^i\mathbf{a}_{2,i,COG}) \\ -{}^i\mathbf{I}_{2,i} \dot{\omega}_{2,i} - {}^i\omega_{2,i} \times ({}^i\mathbf{I}_{2,i} \omega_{2,i}) \end{bmatrix} \quad (17)$$

To consider the relations between the end-effector movement and different links, it is necessary to define Link Jacobian Matrices [17]. For the proximal link this matrix is defined as:

$${}^i\mathbf{v}_{1,i,COG} = \begin{bmatrix} \dot{x}_i \\ 0 \\ 0 \end{bmatrix} = \begin{bmatrix} \mathbf{J}_{p,i} \\ 0 \\ 0 \end{bmatrix} {}^0\dot{\mathbf{p}} = \mathbf{J}_{1,i,COG} {}^0\dot{\mathbf{p}} \quad (18)$$

$$\mathbf{J}_{1,i,\omega} = 0 \quad (19)$$

with the Jacobian matrices $\mathbf{J}_{1,i,\omega}$ and the torque matrices ${}^i\mathbf{m}_{1,i}$ being zero since the first link is a pure prismatic joint and thus, no rotational movements exist. The angular velocity of the distal link within the local coordinate system can be written as:

$${}^i\omega_{2,i} = \frac{[\mathbf{T}_{20,i} {}^0\mathbf{l}_{2,i}]_x [\mathbf{T}_{20,i} - \mathbf{J}_{1,i,COG}]}{l_2^2} {}^0\dot{\mathbf{p}} = \mathbf{J}_{2,i,\omega} {}^0\dot{\mathbf{p}} \quad (20)$$

With the information about the angular velocity, the velocities of the centers of mass are given as:

$${}^i v_{2,i,COG} = \left[T_{20,i} - \frac{[T_{20,i} {}^0 l_{2,i}]_x [T_{20,i} - J_{1,i,COG}] [T_{20,i} {}^0 l_{2,i}]_x}{2l_2^2} \right] {}^0 \dot{p} = J_{2,i,COG} {}^0 \dot{p} \quad (21)$$

Finally, the Principle of Virtual Work can be stated as follows:

$$\delta x^T \tau + \delta \chi_P^T Q_P + \sum_{i=1}^z \delta^i \chi_{1,i}^T \cdot {}^i Q_{1,i} + \sum_{i=1}^z \delta^i \chi_{2,i}^T \cdot 2 \cdot {}^i Q_{2,i} = 0 \quad (22)$$

Taking advantage of the Jacobian matrices between the end-effector movement and the local coordinate systems, i.e.:

$$\delta x = J_P \cdot \delta \chi_P \quad (23)$$

$$\delta^i \chi_{1,i} = J_{1,i}^* \cdot \delta \chi_P \quad (24)$$

$$\delta^i \chi_{2,i} = J_{2,i}^* \cdot \delta \chi_P \quad (25)$$

and cancellation of $\delta \chi_P$ leads to the desired actuation forces

$$\tau = -J_P^{-T} \left[Q_P + \sum_{i=1}^z (J_{1,i}^{*T} \cdot {}^i Q_{1,i} + J_{2,i}^{*T} \cdot 2 \cdot {}^i Q_{2,i}) \right] \quad (26)$$

5 Simulation Modeling

The design process of parallel manipulators is usually characterized by multiple loops of iterations concerning the kinematic and dynamic parameters. These parameters are commonly found by optimization algorithms for certain criteria as e.g. maximal workspace or minimal static actuation forces. It is possible that the one manipulator needs to be optimized for different tasks under changing boundary conditions. The most important requirement for a corresponding optimization is an analytical model of the inverse kinematics and inverse dynamics problem as found in Sects. 3 and 4. For computation, these models are implemented in technical computing software like e.g. Matlab. At this early stage of the design process these computations are essential for gaining information about the system's behavior. Despite the strength and importance of this knowledge, the model does not provide any explanatory power about collisions and constructive feasibility of the n -PRPaR. Subsequent to analytical investigations it is often useful in order to setup a controlled simulation model for further verification. With this in mind, Fig. 2 illustrates a holistic approach for improved development of a controlled simulation model which is more flexible, faster and above all more robust. The main target of this approach is the dynamic mutual interrelation between the parameters used in Matlab and an assembly in the CAD software Autodesk Inventor.

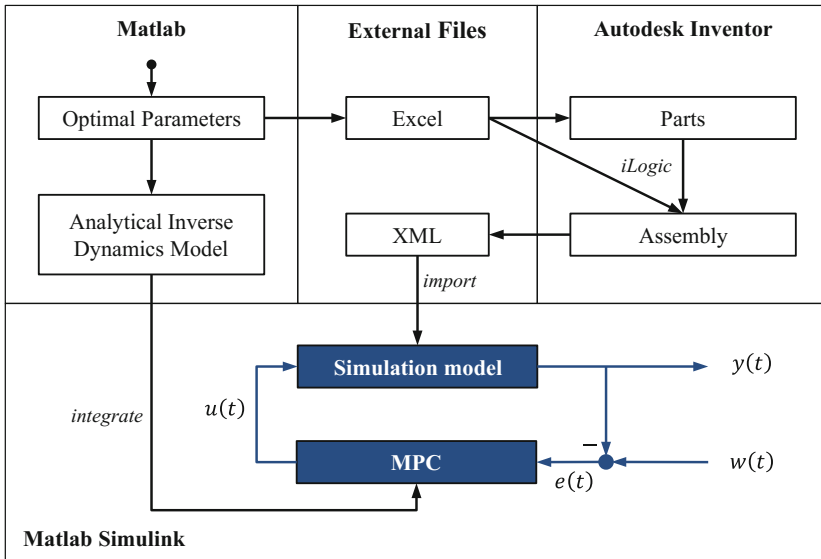


Fig. 2 Automated workflow of a controlled simulation model

The basic concept of CAD systems is similar to the idea of object oriented programming languages. In this case each part is created once and can be used as often as necessary within different configurations by adjusting its parameters. The basic characteristics are defined by the user and more detailed and complex information about the parts are calculated automatically by a numerical engine in the background. For example, the computations of inertia within Matlab often need to be simplified, while the inertia provided by CAD systems is more exact and realistic for the developed parts. For synchronizing the assembly and the analytic calculations the defining parameters are stored outside the CAD environment within an excel data sheet that is provided by Matlab. With the built-in programming language iLogic of Inventor it is possible to monitor every parameter change immediately and to refresh the assembly within the new configuration. Out of this, the Matlab computations and the assembly are never getting out of synchronization. Issues concerning collision problems or constructive feasibility can be seen immediately in the assembly. Furthermore, the rapid modeling tool of Matlab, called 'SimMechanics Link', is used to export the assembly with all mechanical properties from Inventor over XML into SimMechanics. In Fig. 2 also a model-predictive controller (MPC) is used to control the generated simulation model. As a high-level controller it is proven of controlling redundant actuated systems [10]. One of the main advantages is the consideration of constraints during the control process and an optimization of the control values with an analytical dynamic model of the system. Taking this approach of mutual interrelation between the computing and designing tools into account, a rapid modelling workflow of high-level controlled PKM is found.

6 Discussion and Outlook

In this paper, the inverse kinematics and inverse dynamics models of the n-PRPaR are shown. Based on these models a rapid modelling workflow for controlled PKM simulation models is presented. The five main advantages of this workflow are listed below.

- No differences between technical computation and CAD files
- Rapid creation of simulation models
- More realistic simulation models
- Good visualization of collision issues in CAD
- High flexibility in case of new optimization strategies

Further investigations of redundantly actuated PKM and model-based motion design algorithms can be made with higher quality and less modelling effort within this framework.

References

1. Merlet, J.-P.: *Parallel Robots (Series: Solid Mechanics and Its Applications)*. Springer (2006)
2. Gogu, G.: *Structural Synthesis of Parallel Robots—Part 1: Methodology*. Springer, Dordrecht, Heidelberg, London, New York (2008)
3. Biagiotti, L., Melchiorri, C.: *Trajectory Planning for Automatic Machines and Robots*. Berlin, Heidelberg (2008)
4. Pierrot, F.: Parallel mechanisms and redundancy. In: 1st International Colloquium, Collaborative Research Centre 562, pp. 261–277. Braunschweig, 29–30 May 2002
5. Lorenz, M., Corves, B., Riedel, M.: Kinetostatic performance analysis of a redundantly driven parallel kinematic manipulator. In *Proceedings of the ASME 2014 International Design Engineering Technical Conference & Computers and Information in Engineering Conference IDETC/CIE*. Buffalo, New York, 17–20 Aug 2014
6. Garg, V., Nokleby, S.B., Carretero, J.A.: Wrench capability analysis of redundantly actuated spatial parallel manipulators. *Mech. Mach. Theory* **44**, 1070–1081 (2009)
7. Corves, B., Brinker, J., Lorenz, M., Wahle, M.: Design methodology for translational parallel manipulators exhibiting actuation redundancy. *J. Mech. Eng. Sci.* **230**(3), 425–436 (2016)
8. Müller, A.: Redundant actuation of parallel manipulators. In: Huapeng, W. (ed.) *Parallel Manipulators, Towards New Applications*. I-Tech Education and Publishing, Wien (2008)
9. Xie, F., Liu, X.-J., Wang, J.: Performance evaluation of redundant parallel manipulators assimilating motion/force transmissibility. *Int. J. Adv. Robot. Syst.* **8**, 113–124 (2011)
10. Müller, A.: Internal preload control or redundantly actuated parallel manipulators—its application to backlash avoiding control. *IEEE Trans. Robot.* **21**(4), 668–677 (2005)
11. Kim, S.: Optimal redundant actuation of closed chain mechanisms for high operational stiffness. In: *Proceedings of the 2000 International Conference on Intelligent Robots and Systems (IROS)*, pp. 683–688. Takamatsu (2000)
12. Corbel, D., Gouttefarde, M., Company, O., Pierrot, F.: Actuation redundancy as a way to improve the acceleration capabilities of 3T and 3T1R pick-and-place parallel manipulators. *J. Mech. Robot.* **2**, 13 (2010)
13. Mitova, T., Vatkitchev, A.: Analysis of a Closed Space Mechanism with Three Degree of Mobility. XI COBEM, Rio de Janeiro (BR) (1991)

14. Brinker, J., Corves, B.: A survey on parallel robots with delta-like architecture. In: Proceedings of the 14th World Congress in Mechanism and Machine Science. Taipei, Taiwan, 25–30 Oct 2015
15. Brinker, J., Corves, B., Wahle, M.: A comparative study of inverse dynamics based on clavel's delta robot. In: Proceedings of the 14th World Congress in Mechanism and Machine Science. Taipei, Taiwan, 25–30 Oct 2015
16. Brinker, J., Corves, B.: Lagrangian based dynamic analyses of delta robots with serial-parallel Architecture. In: Proceedings of the ROMANSY 2016 21st CISM-IFTOMM Symposium on Robot Design, Dynamics, and Control, Udine (IT), 20–23 June 2016
17. Tsai, L.-W.: Robot Analysis: the Mechanics of Serial and Parallel Manipulators. Wiley, NY (1999)

6-PSS Based Parallel Manipulators

T.A. Dwarakanath, K.D. Lagoo and D.N. Badodkar

Abstract The 6-Prismatic-Spherical-Spherical (6-PSS) joint kinematic chain based parallel mechanism is discussed. The stationary active axes in 6-PSS mechanisms in reference to base serve many design concepts and the varied applications of this are detailed. The design concept of 6-axis stiff wrench sensor is presented; the prototype based on 6-PSS chain is demonstrated. The mechanical master-slave manipulator design is shown and a three dimensional model and simulation is presented. The cam and the follower for a joint space prismatic displacement are proposed and the design is presented. Single actuator, tunable, specific spatial path following manipulator design concept is presented. The design and implementation of a single actuator shaker to operate in a six dimensional space based on a PSS joint configuration is demonstrated. The kinematic design analysis for generating an infinite signature set is given. The specific path based single actuator concept is extended to an array of 6-PSS manipulator based on the cam and the leg follower connected to a common drive shaft.

Keywords 6 PSS parallel mechanisms • Design concepts for manipulator applications • Stationary active axes • Single actuator manipulator

1 Introduction

Universal-Prismatic-Spherical (UPS) jointed kinematic chain is a highly popular six DOF parallel mechanism [1, 2]. The mechanism originated with the prototype development for an application rather than theoretical designs translating into

T.A. Dwarakanath (✉) · K.D. Lagoo · D.N. Badodkar
DRHR, BARC, Mumbai, India
e-mail: tad@barc.gov.in

K.D. Lagoo
e-mail: klagoo@barc.gov.in

D.N. Badodkar
e-mail: badodkar@barc.gov.in

practice [3]. The potential application space of Prismatic-Spherical-Spherical (PSS) based mechanisms in comparison to 6-UPS has not been realized. The main reason is further shrinking of the work space for the given size of the mechanism. The best part of the PSS configuration is that the active axes (actuated axes) remain stationary unlike in a UPS configuration. The invariance of the axis of actuation has a large influence on basing PSS type parallel mechanisms for many applications. This single attribute can give rise to many useful design concepts to devise many applications. This is a critical requirement for high speed and remote actuation motion mechanisms. The elimination of the actuator mass inertia and the high mean time before fatigue failures are the main features of the PSS configuration. Fatigue failures in continuity at the cable-connector interfaces are also a serious concern.

In this paper we present the various kinematic arrangements based on 6-PSS kinematic chain and highlight the simplicity in the synthesis. The kinematic model of 6-PSS is presented in Sect. 2. In Sect. 3, design concept for the application of 6-axis stiff wrench sensor is presented; the prototype based on 6-PSS chain is demonstrated. In Sect. 4, the design concept is extended to 6-PSS based manipulator. A mechanical master-slave manipulator design is shown and a three dimensional model and simulation is demonstrated. The cam and the follower for a joint space prismatic displacement are proposed and the design is presented. In Sect. 5, the design and implementation of a single actuator shaker to operate in a six dimensional space based on a PSS joint configuration is demonstrated. Also in the section a single actuator, tunable, specific spatial path following manipulator design concept is presented. The specific path based single concept is extended to an array of 6-PSS manipulator based on the cam and the leg follower connected to a common drive shaft. A virtual simulator validates the design and motion signatures in six dimensions employing a single actuator. The paper is concluded in Sect. 6 highlighting the advantages of 6-PSS type of joint configuration.

2 6-PSS Kinematic Model

The kinetic arrangement of 6-PSS based parallel manipulator, design parameters and the variables are shown in Fig. 1a, b. Two coordinate frames, $F_B = [x_b, y_b, z_b]^T$ and $F_P = [x_p, y_p, z_p]^T$ are defined at the circum centre of the base and the platform disc respectively. The six legs connecting the platform and the intermediary base is of constant length, l . The leg connection points $B_i(B_{ix}, B_{iy}, B_{iz})$ and $P_i(P_{ix}, P_{iy}, P_{iz}), i = 1, \dots, 6$ both at the base and at the platform form the vertices of a semi-regular hexagon. The points are represented with respect to F_B . R_b and R_p are the circum radius of the connection points at the base and the platform respectively. They are in cyclic symmetry about z_b and z_p axis respectively. The origin of the frame F_P with respect to F_B is given as $O_p = [O_x, O_y, O_z]^T$ and the B_R is the rotation

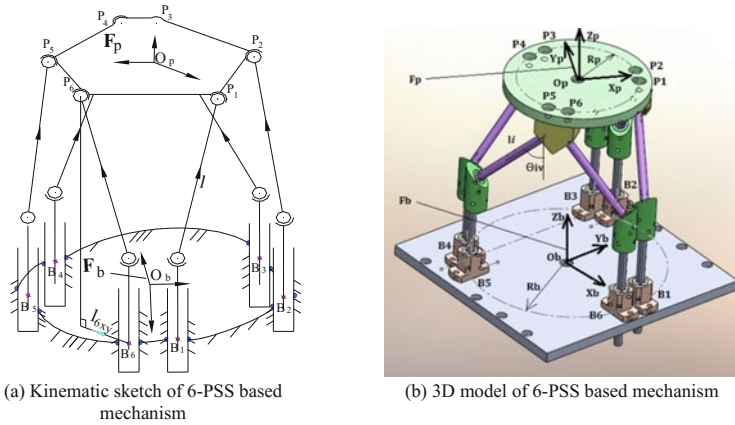


Fig. 1 **a** Kinematic sketch of 6-PSS based mechanism. **b** 3D model of 6-PSS based mechanism

of frame F_P with respect to F_B . The coordinates p_i of the leg connection points at the platform are expressed with respect to F_P , and can then with respect to F_B , given by:

$$P_i = O_P + {}^B_P R p_i \tag{1}$$

The projection of the leg i on the X_b - Y_b plane is given as

$$\begin{aligned} \bar{l}_{ixy} &= (P_{ix} - B_{ix})\hat{i} + (P_{iy} - B_{iy})\hat{j}; \quad l_{ixy} = \|\bar{l}_{ixy}\|; \\ \theta_{iv} &= \sin^{-1}\left(\frac{l}{l_{ixy}}\right); \quad \bar{l}_i = \bar{l}_{ixy} + (P_{iz} - S_i)\hat{k} \end{aligned} \tag{2}$$

Then the prismatic actuating distance, S_i along \hat{k} for the given position and the orientation of the platform is given as

$$S_i = P_{iz} - l \cos \theta_{iv} \tag{3}$$

The main feature of the 6-PSS arrangement is that the force sensing elements in case of force-torque sensors and actuators in case of manipulators are mounted at the base rather than on the legs and remain stationary. This feature is suitable for high sensitivity force-torque sensors, actuator isolation, high platform velocity and acceleration. Fatigue failures at the joints of the cable-connector interfaces are also a serious concern. Such concerns are minimized due to stationary sensing elements or actuators. The next sections deal with various applications and their design concepts based on 6-PSS arrangement.



3 6-PSS Joint Parallel Structure

Highly sensitive 6 axis force-torque sensor based on 6-PSS kinematic chain parallel structure developed in the laboratory is discussed in [4]. The prismatic joint, P in this case is the force sensing element (base beam transducer, shown in Fig. 2) fixed to the base. Unlike in Stewart platform based force-torque sensors, the axial leg forces are measured by the instrumented sensing element at the base. In the absence of a rigid body motion, the cantilever beams at the base can be designed to serve as extremely high sensitive force sensing element. The design of the each of the double beam bending elements is obtained by minimizing force to strain ratio or in other words, maximizing signal to noise ratio. The kinematic model is shown in Fig. 2. The successful implementation of the design and the prototype serving as the force table to capture the applied wrench trajectory (\bar{W}) is shown in Fig. 3.

In [5], the compliance of flexible legs is used for micro manipulation. The successful implementation of 6-PSS structure for sensing and manipulating applications is extended to a 6-PSS based manipulator in the paper.

Fig. 2 Kinematic sketch of 6-PSS, beam type hexapod structure

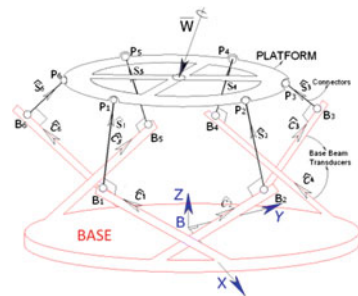


Fig. 3 A 6-PSS hexapod F-T sensor as a force table



4 6-PSS Joint Parallel Manipulator

Huge number serial articulated type master-slave manipulators are in operation. The advantage of serial mechanism is of larger workspace. High precision, high payload even with smaller workspace has found many applications in remote handling and assembly operations. 6-PSS based parallel architecture gives a straight forward solution for Master-Slave design. Figure 4 depicts a simple master-slave arrangement. The 6 DOF master-slave passive parallel manipulator can take the 6 dimensional twist as the input and generate reflected twist at the slave end. The twist applied at the master side mirrors the twist at the slave side. The other important feature of this arrangement is the wrench reflection. The wrench reflection capability is because of the nature of the parallel architecture.

Rest of the section is on 6-PSS based active manipulators. The cam and the follower displacement mechanisms for the joint space are proposed and the design is presented. The design, accuracy and practicability of the cams and the follower are given in [6]. The cam and the follower technology is one of the highly practiced motion transformation method with cyclic characteristics. This feature is utilized to synthesize the PSS based parallel mechanism devises which have cyclic characteristics. The design is described considering a winnowing application. Grain free fall and push sequence in winnowing has a cyclic multi axis motions with discontinuity in the displacement and rate of displacement. The simple way to achieve

Fig. 4 6-PSS based master-slave arrangement

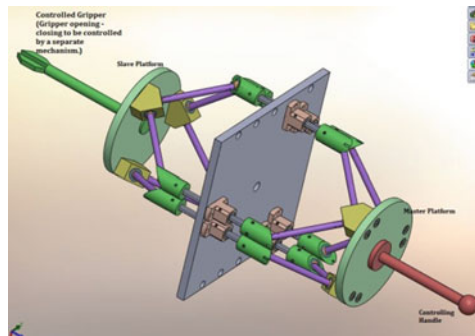
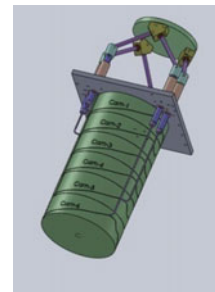


Fig. 5 6-PSS based common cam manipulator



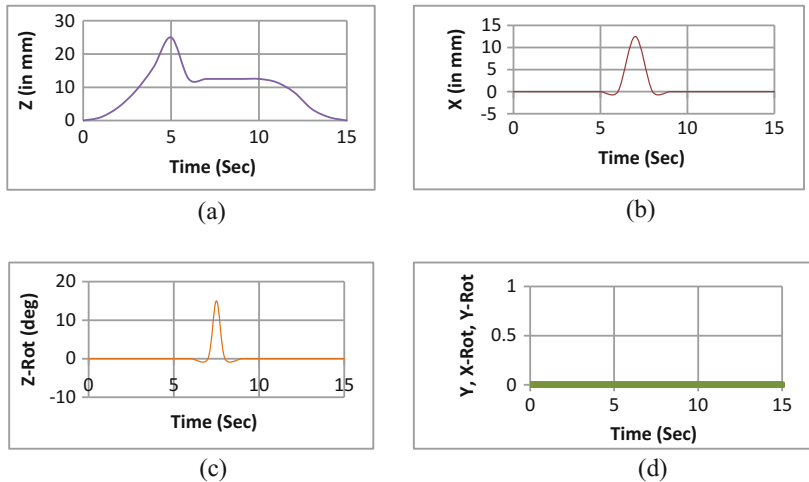


Fig. 6 Component S-T graphs of platform

this repeated multipart trajectory is through the combination of the six cam and the follower joint space displacement. The kinematic arrangement of the manipulator based on the cam and follower is shown in Fig. 5. To achieve the sequence of trajectories, The Distance-Time (S-T) graph of each component of the twist of the platform is made. Figure 6 shows the typical winnowing S-T graphs of six components.

Figure 6a–d are the 6 individual components of trajectories to be achieved in one time period (time for one cycle). The trajectory graphs show that during a time segment, the platform has to perform compound motions at varying rates. This is accomplished by using the cam and the prismatic leg follower transmissions for PSS based hexapod mechanism. From the task space S-T graphs of Fig. 6, the joint space trajectories are obtained using Eqs. 1–3. The one cycle trajectory of each of the legs is shown in Fig. 7.

The one cycle Time-Displacement graph is used to design the cam profile. It can be observed that the cycle time of all the six leg displacement profile is constant. Therefore all the cams are simultaneously rotated at constant angular velocity. Each of the cam connected to the prismatic leg follower is rotated at a constant speed of 4 rpm to provide the winnowing motion profile at the platform as described in Fig. 6. The point on position-time graphs in task space (Fig. 6) maps to a point on the joint space given as displacement-time graphs (Fig. 7). The reverse sequence serves as the forward kinematic solution look up graphs of a given 6-PSS winnowing system. The combinations of the cam and the leg displacement follower for PSS mechanism is described in the next section. The common cam, housing all the six leg profiles is shown in Fig. 5. The kinematic design of the 6-PSS common cam manipulator to generate the platform profile of Fig. 6 is given in Fig. 5.

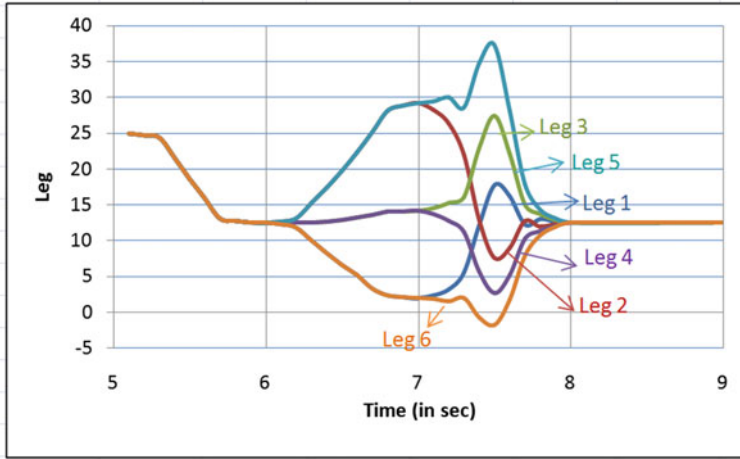


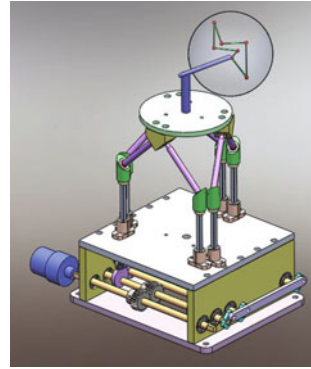
Fig. 7 Partial cycle Time-Displacement diagram of the legs

5 Single Actuator Spatial Manipulator

It is shown that the invariance active axes and the invariance of the cycle time of the legs are the features to produce a cyclic motion at the task space. These features can be utilized to build a single actuator based 6-PSS to generate the intended repeated trajectory at the platform. The task space Distance-Time graph for one time period is formulated (as in Fig. 6). The corresponding joint space for one time period is computed using Eqs. 1–3. The functional relationship between one cycle of actuator motion and each of the leg displacement is established through individual cam profile. There are six functions of Distance-Time profile, generating six cam profiles and transmitting it to corresponding leg followers from a single actuator is the task. The cam profiles shown in Fig. 5 are the common cam concept, housing all the 6 leg profiles on one surface. For a given time period, the path length of the profile can be very high; therefore the profile detailing can be achieved easily. The single cam concept can also make use of other geometrical surfaces like conical, spherical, stepped cylinder, combination of solids, etc. On the other hand multi cam surfaces, i.e. each leg is driven by independent cam surface is also possible and has distinct advantages. The individual cams are driven by a common gear transmission (as shown in Fig. 8). A central common spur gear or a bevel gear transmits the motion to the individual gear connected to the cam. Detailed discussion on individual cams is out of the scope of this paper.

Apart from above applications, large number of industrial manipulators are used to perform repeatable tasks. To extend the cam and the leg follower with single actuator to serve such manipulator actions, a simple toggle switch control is used.

Fig. 8 Single actuator, tunable, specific spatial path following manipulator

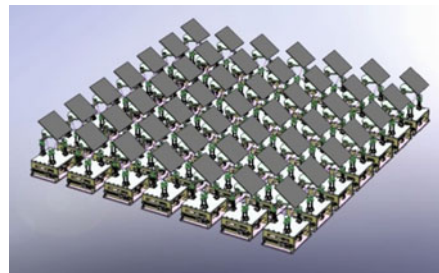


The design of the joint space to serve the pre-determined station points for a pre-determined dwell period in the workspace is feasible. The stationary platform at the station point signifies simultaneous dwell for all the legs. The long dwell time at station points is mapped to the actuation switch off time. The motion profiles between the station points are resolved as component motion as described in Sect. 4. The respective joint space S-T graph is obtained to design the individual cam profile for the manipulation task. Figures 8 and 9 depicts such an application. The feasibility of the widespread use of manipulators, which have to perform

Fig. 9 Prototype of single actuator, tunable, specific spatial path following manipulator



Fig. 10 An array of 6-PSS manipulator based on the cam and the leg follower connected to a common drive shaft



repetitive trajectory is simulated. An example of Heliostat trajectory is considered and the mechanism is synthesized with a single actuator to replicate the motion. An arrangement of array of mirror mounted 6-PSS based hexapod mechanism is illustrated in Fig. 10. Manipulators of each row in the array have a distinct platform profile influenced by its row position and the corresponding joint space displacement can be achieved easily by cam profiling. Also, it is important to note that all the manipulators in the array are actuated by one common drive shaft.

6 Conclusions

The various applications based on 6-PSS kinematic architecture are presented. Highly sensitive Force-Torque sensor is designed and the prototype is shown. A multi-component repeatable cyclic trajectory at the platform is generated using the simple cam and the leg follower. The design of a single actuator shaker to operate in six dimensional space based on PSS joint configuration is designed. An idea of using a single actuator driven manipulator to perform repeatable trajectories and serving stationary points is presented. The feasibility of array of manipulators driven through a common drive shaft is illustrated. The advantage of stationary active axes in 6-PSS mechanisms in serving various applications is demonstrated.

References

1. Gough, V.E.: Contribution to discussion to papers on research in automobile stability and control and in tyre performance. *Proc. Auto. Div. Inst. Mech. Eng.* 392–394 (1956–1957)
2. Stewart, D.: A platform with six degrees of freedom. *Proc. Ins. Mech. Eng.* **180**, 371–378 (1965)
3. Merlet, J.P.: *Parallel Robots*. Kluwer, Norwell (2006)
4. Dwarakanath, T.A., Bhutani, G.: Beam type hexapod structure based six component force-torque sensor. *Mechatronics* **21**(8), 1279–1287 (2011)
5. Du, Z., Shi, R., Dong, W.: Kinematics modeling of a 6-PSS parallel mechanism with wide-range flexure hinges. *J. Central S. Univ.* **19**(9), 2482–2487 (2012)
6. Rothbart, H.A.: *Cam Design Handbook: Dynamics and Accuracy*. McGraw-Hill Professional (2003)

Part X
Robotics—Sensors and Actuators
in Robotics

Compliant Rotary Actuator Driven by Shape Memory Alloy

H. Yuan, X. Balandraud, J.C. Fauroux and F. Chappelle

Abstract This paper presents a compliant rotary actuator composed of a monolithic plastic structure and a shape-memory-alloy (SMA) wire. The plastic structure features a helical shape. The SMA wire can be permanently deformed at ambient temperature. It is first pre-strained in tension, then wrapped on the helical structure and fixed at its two ends. The SMA wire is finally heated by Joule effect, leading to a continuous rotation between the two ends of the plastic structure. The rotation angle is driven by varying the intensity of the electric current. A preliminary prototype has been built and first results are presented.

Keywords Actuator · Rotation · Shape memory alloy

1 Introduction

This paper presents the design and the analysis of a rotary actuator driven by shape memory alloys (SMAs). Potential applications are for mechatronics or robotics, where actuators with low mass, high integration ability, and possibly hollow shaft are often needed (for instance as the central actuator of the OpenWHEEL i3R

H. Yuan · X. Balandraud (✉) · J.C. Fauroux (✉) · F. Chappelle (✉)
Sigma-Clermont, Institut Pascal, Université Clermont Auvergne,
BP 10448, 63000 Clermont-Ferrand, France
e-mail: xavier.balandraud@sigma-clermont.fr

J.C. Fauroux
e-mail: jean-christophe.fauroux@sigma-clermont.fr

F. Chappelle
e-mail: frederic.chappelle@sigma-clermont.fr

H. Yuan
e-mail: han.yuan@sigma-clermont.fr

H. Yuan · X. Balandraud · J.C. Fauroux · F. Chappelle
CNRS, UMR, 6602, IP, 63178 Aubière, France

mobile robot developed by the authors [1]). This actuator is composed of a compliant structure and a SMA wire. Numerous rotary actuators based on the use of SMA wires have been proposed [2–8]. In these technical solutions, SMA wires are coupled to a mechanism comprising several links and featuring a kinematic degree of freedom in rotation. It is worth noting that our rotary actuator is composed of a SMA wire and a monolithic helical structure without joints and whose flexibility allows movements between its two ends. This structure is obtained by 3D printing.

2 Recall About Shape-Memory Alloys

This section briefly recalls the main phenomena involved in SMAs (see [9, 10] for further information). The crystallographic state of the material depends on the stress and the temperature. The material can be either purely austenitic (A), purely martensitic (M) or a mixture of the two phases (A + M). Moreover, martensite can be obtained through different “variants” corresponding to the same crystal structure but with different orientations in space.

Upon cooling down at zero stress, the $A \rightarrow M$ transformation begins at temperature M_s (martensite start) and ends at temperature M_f (martensite finish). There is no change in the shape of the SMA component. Indeed, the different martensite variants are produced in equal proportions, resulting in no macroscopic strain. The martensite obtained in this case is said to be “self-accommodating”. From this martensite, so-called “oriented” martensite can be obtained by mechanical loading. The stretch is indeed accompanied by a change in the proportions of the martensite variants, leading to a macroscopic strain (in a range up to several % in tension). One can thus obtain different macroscopic shapes after unloading.

Starting now from oriented martensite, a return to austenite is obtained by a temperature rise. At zero stress, the $M \rightarrow A$ transformation starts at temperature A_s (austenite start) and ends at temperature A_f (austenite finish). The material recovers its original shape (shape recovery). If the strain is maintained constant during the $M \rightarrow A$ transformation, a mechanical stress (called recovery stress) is produced by the SMA to counterbalance the cancellation of the phase transformation strain upon return to austenitic state. If the SMA is fixed on a structure during the $M \rightarrow A$ transformation, the structure is deformed. The deformation of the structure depends on its structural stiffness (and on the strain to be recovered by the SMA).

3 Design of a Helical Rotary Actuator

For the considered application (OpenWheel), a minimal rotational range of 90° was required. We have considered a SMA wire with a contraction strain of 5 % which can be recovered from the martensitic state by thermal activation of the memory effect (return to austenite). So a rotational strain of 25 % was required (as 90°

represents 25 % of 360°). So five turns of wire are a priori sufficient for turning the end effector of 90° . However, coiling five turns of SMA wire around a rigid drum leads to a very small rotation angle because the tangential friction force of the tightened SMA wire cancels the sliding motion of the wire with respect to the drum beyond a certain winding angle. In order to avoid any sliding of the SMA wire with respect to its rigid support, contact should be avoided, lubricated or replaced by pulley sliding [11]. Another approach is used here by considering a compliant support for the SMA wire, so that the wire contraction will locally deform the support with minimal sliding. Main translational actuators use a beam compressed by one or several SMA wires parallel to the beam. For our rotary actuator, the wire is wrapped along a circular compliant beam so that the compression of the beam generates a rotation of the mobile terminal section with respect to the fixed initial section. This setting could be particularly useful for hollow-shaft rotary actuators. As five turns of wire are required, a compliant helical beam is designed to support the wire, inserted in a peripheral groove just larger than the wire (see groove G in Fig. 1a). The interval i between the spires should be long enough to avoid contact between consecutive turns of the deformed helix. The radial position of the wire into the beam has an influence on the beam bending. As h_1 is larger than h_2 , a

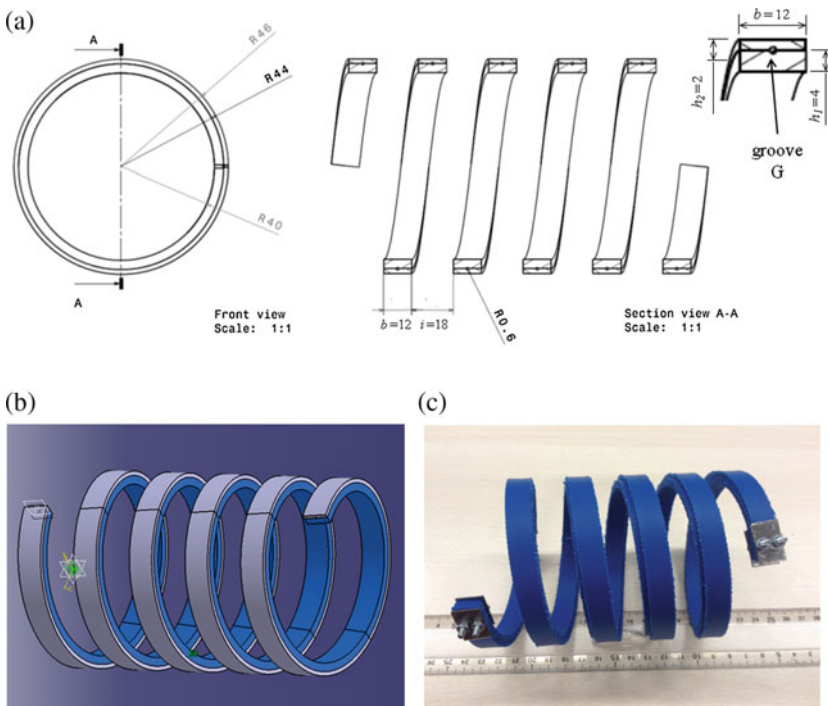


Fig. 1 Helical structure. **a** Dimensions. **b** CAD model. **c** Physical prototype

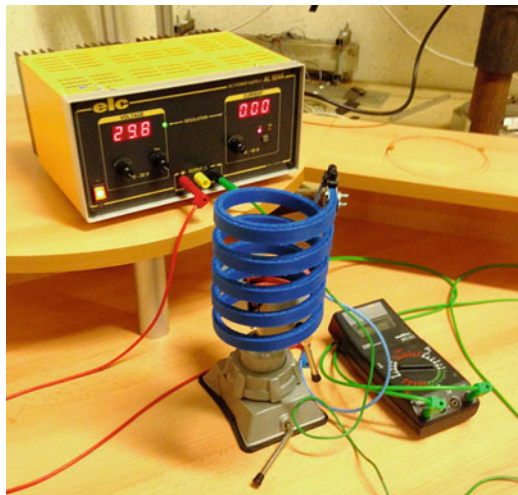
bending towards the outside of the spire should be superimposed to pure beam compression. The helix cross-section results from a compromise: too small and the actuator collapses; too large and it does not move. The last design feature is that the wire is caught between two helices so that it cannot escape the groove when the wire gets longer (rotating back).

Figure 1a gives the dimensions of the helical structure which has been designed and manufactured. Figure 1b shows a 3D view of the CAD model. Figure 1c is a photo of the structure. It is made of Acrylonitrile Butadiene Styrene (ABS). A nickel–titanium SMA wire, 1 mm in diameter, is used. It is provided by Nimesis Inc., France. The transformation temperatures are: $A_s = 57\text{ }^\circ\text{C}$, $A_f = 73\text{ }^\circ\text{C}$, $M_s = 48\text{ }^\circ\text{C}$ and $M_f = 24\text{ }^\circ\text{C}$. All tests are performed at an ambient temperature T_{amb} around $20\text{ }^\circ\text{C}$. The SMA is thus martensitic at ambient temperature. A self-accommodating martensitic state is first obtained by heating above A_f then returning to ambient temperature at zero stress. The wire is then pre-stretched to obtain an oriented martensite. Different values of residual strain have been considered for the tests. The wire is then wrapped in the groove G of the helical structure, and fixed at its ends. It is worth noting that the obtained helical structure is “monolithic” in the sense that it composed of a unique link. Similar idea (not devoted to rotary actuator) can be found in references [12, 13].

4 Experimental Setup and Processing

The experimental set up is composed of the system (helical support and SMA wire) described above, a power generator, a voltmeter and an ammeter (Fig. 2). The helical structure is placed vertically. One of its ends is fixed.

Fig. 2 Experimental set up



The objective is to analyze the rotational displacement of the other end with respect to the helix axis when the SMA wire is heated by Joule effect using the power generator. A camera is placed above the structure to capture images during the deformation and then extract the rotation angle at the free end of the helical structure by geometric measurements in the image space.

5 Results

Figure 3 shows the variation in time of the rotation angle, including a heating phase (with constant current intensity of 4 A) and a natural return to ambient temperature. A pre-strain of the SMA wire of 1.4 % was considered before placing the wire on the structure at ambient temperature. Following comments can be done from the figure:

- during the heating phase, the rotation angle continuously increases and stabilizes at a value of 250° . A stabilization of the SMA temperature is indeed expected due to equilibrium between the heat produced by Joule effect and the heat losses after a certain duration (here about 400 s). It can be noted that the maximum angle is greater than 90° . This is explained by the radial expansion of the helix accompanying the rotation, i.e. a modification in the helix diameter;

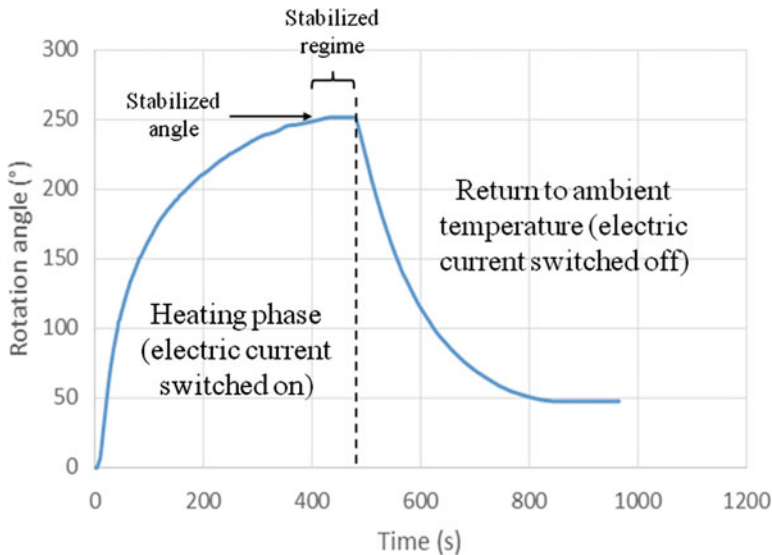


Fig. 3 Variation of the rotation angle as a function of time for a current intensity of 4 A

- during the natural return to ambient temperature, the rotation angle decreases continuously. A residual rotation is observed at the end of the procedure. This is probably due to too high stresses in the helical structure, leading to irreversible strain. Further studies concerning the optimization of the structure dimensions and its base material are in progress to prevent such irreversible response. It can be noted that the duration of the return to ambient temperature depends on the thermal boundary conditions of the wire with its environment. Indeed, temperature decrease was here merely done by stopping the electric current in the SMA wire.

Figure 4 shows the value of the *stabilized* rotation angle as a function of the current intensity. It can be seen that the higher the current intensity, the larger the stabilized rotation angle (with saturation from 4 A). Indeed, the higher the temperature, the more advanced the $M \rightarrow A$ transformation. Above 4 A, the rotation angle does not vary any more, meaning that the temperature in the SMA wire is such that the $M \rightarrow A$ transformation is completed.

Figure 5 shows the variation in time of the rotation angle for current intensities increasing from 0 A to 4 A then decreasing from 4 A to 0 A, by step of ± 0.5 A. The duration of each step is of 10 min because it was shown in Fig. 3 that 400 s were enough to achieve a maximum steady state deformation. It can be seen that the system is not fully reversible: residual rotation is observed at the end of the procedure, as explained above. The same residual rotation of 50° as in Fig. 3 is observed in Fig. 4. However, the present experimental curve shows that it will be possible to control the value of the rotation angle by modifying the current intensity. It is expected that the response time of our system is long because the temperature change is mainly governed by the heat diffusion inside the system and by the heat exchange with the outside.

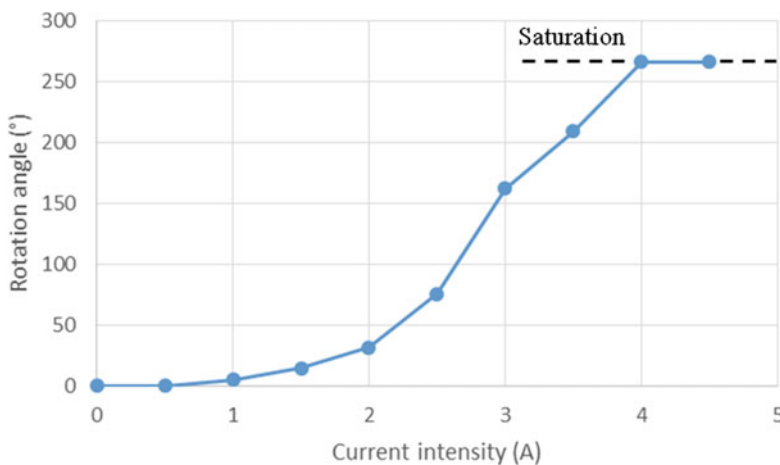


Fig. 4 Variation of the stabilized rotation angle as a function of the current intensity

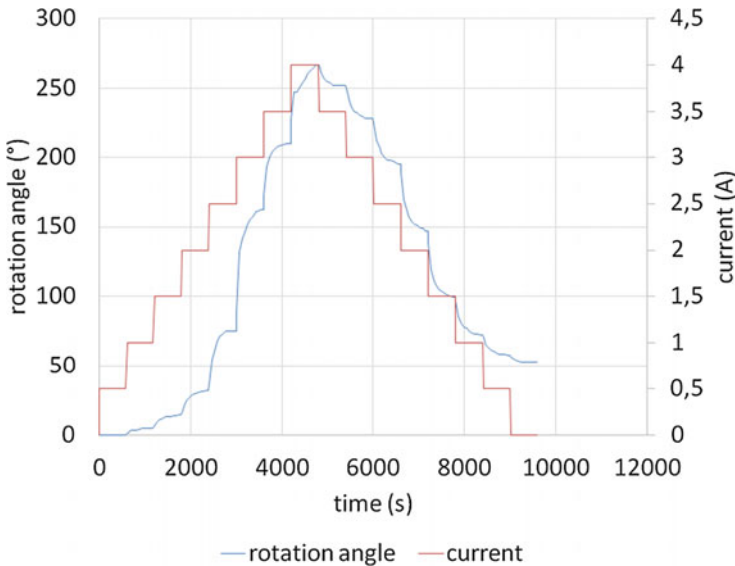


Fig. 5 Variation in time of the rotation angle for current intensities increasing from 0 A to 4 A then decreasing from 4 A to 0 A, by step of ± 0.5 A

6 Conclusions

This paper presents a concept of SMA compliant rotary actuator with potential applications to mechatronics and robotics. It is based on a shape-memory-alloy (SMA) component which is placed in a monolithic plastic structure. The deformation of the plastic structure when the memory effect is activated in the SMA wire leads to a global rotation movement. The experimental results show that the value of the rotation angle can be continuously modified by changing the intensity of the electric current applied to heat the SMA wire. Results also show that the structure must be optimized in order to prevent plasticity which limits the reversibility of the actuator response. This will therefore be addressed in further study.

Acknowledgments The authors want to acknowledge the Region Auvergne for supporting this research.

References

1. Fauroux, J.C., Chapelle, F., Bouzgarrou, B.C., Vaslin, P., Krid, M. Davis, M.: Mechatronic design of mobile robots for stable obstacle crossing at low and high speeds. Handbook on Research on Advancements in Robotics and Mechatronics, vol. II, Chapter 19, pp. 567–630 (2015). ISBN13: 9781466673878, DOI:10.4018/978-1-4666-7387-8. IGI Global, p. 953

2. Hwang, D., Higuchi, T.: A cycloidal wobble motor driven by shape memory alloy wires. *Smart Mater. Struct.* **23**(5), 055023 (2014)
3. Lan, C.C., Wang, J.H., Fan, C.H.: Optimal design of rotary manipulators using shape memory alloy wire actuated flexures. *Sens. Actuators A* **153**(2), 258–266 (2009)
4. Nespoli, A., Bassani, E., Besseghini, S., Villa, E.: Rotational mini-actuator activated by two antagonist shape memory alloy wires. *Phys. Procedia* **10**, 182–188 (2010)
5. Song, G.: Design and control of a Nitinol wire actuated rotary servo. *Smart Mater. Struct.* **16**(5), 1796–1801 (2007)
6. Takeda, K., Tobushi, H., Mitsui, K., Nishimura, Y., Miyamoto, K.: Torsional properties of TiNi shape memory alloy tape for rotary actuator. *J. Mater. Eng. Perform.* **21**(12), 2680–2683 (2012)
7. Tanaka, Y., Yamada, A.: A rotary actuator using shape memory alloy for a robot analysis of the response with load. In: *IEEE/RJS International Workshop on Intelligent Robots and Systems'91. Intelligence 39 for Mechanical Systems, Proceedings IROS'91, 1991, vol.2*, pp. 1163–1168 (1991)
8. Zhang, X.Y., Yan, X.J.: Continuous rotary motor actuated by multiple segments of shape memory alloy wires. *J. Mater. Eng. Perform.* **21**(12), 2643–2649 (2012)
9. LExcellent, C.: *Shape-Memory Alloys Handbook*. ISTE & Wiley, London (2013)
10. Otsuka, K., Wayman, C.M.: *Shape Memory Materials*, Cambridge University Press, pp. 27–36 (2002)
11. Mammano, G.S., Dragoni, E.: Modeling of wire-on-drum shape memory actuators for linear and rotary motion. *J. Intell. Mater. Syst. Struct.* **22**(11), 1129–1140 (2011)
12. Mekaouche, A., Chapelle, F., Balandraud, X.: Using shape memory alloys to obtain variable compliance maps of a flexible structure: concept and modeling. *Meccanica* **51**(6), 1287–1299 (2016)
13. Mekaouche, A., Chapelle, F., Balandraud, X.: FEM-based generation of stiffness maps. *IEEE Trans. Rob.* **31**(1), 217–222 (2015)

Modelling and Simulation of Linear Actuators in Mechatronic Systems

V. Dolga, L. Dolga and C. Moldovan

Abstract A large group of mechatronic systems currently consists of parallel robots, which are largely used in various applications due to their advantages over conventional serial mechanisms: high rigidity, high load capacity, high velocity and high precision. The synthesis of a mechatronic system, hereby represented by the parallel robots, envisages a balance between modelling and simulation and experiment. The structural modelling of the parallel mechanism within these robots is an essential stage of the synthesis and uses the concept of the kinematic connections. The paper outlines how a linear actuator materializes the KB(-1) and KC connections. The modelling, the simulation and the experimental analysis of a linear actuator are developed. The authors explain that using the theory of kinematic connections has the advantage of a fast and simple implementation.

Keywords Mechatronic system • Parallel robot • Kinematic connection • Linear actuator • Modelling • Simulation

1 Introduction

Mechatronics is a multidisciplinary field of engineering. A definition of essence outlines: “Mechatronics is a design philosophy, an integrating approach to engineering design” [1, 2]. Within the mechatronic philosophy, sensors and actuators are key-elements when developing optimal products and processes [3].

V. Dolga (✉) · L. Dolga · C. Moldovan
Politechnica University Timisoara, Timișoara, Romania
e-mail: valer.dolga@upt.ro

L. Dolga
e-mail: lia.dolga@upt.ro

C. Moldovan
e-mail: cristian.moldovan@upt.ro

A large variety of mechatronic systems are based on the integration of the linear actuators: high-precision component placement machines [4], various automated machinery [5], parallel robots, Stewart-Gough platform [6, 7]. Actuators play a primary role in mechatronic systems and their design and development within the integrative nature of a mechatronic approach is critical for the success of the entire design process. Decisions during the initial stages of this process launched with this aim of defining the actuators are essential.

The paper deals with the goal of identifying the best solutions for making a linear actuator to be an integrated part of a mechatronic system and with the design approach of this requirement.

The mechatronic philosophy, as a support in the design of parallel robot structures, makes the object of Sect. 2, as well as the structural analysis of the mechanisms related to the concept of kinematic connections. Section 3 presents the simulation and the experimental analysis of the linear actuator. Conclusions are outlined within Sect. 4.

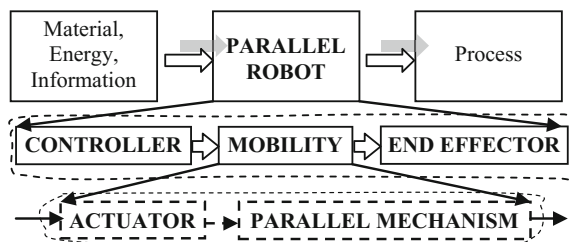
2 Mechatronic Philosophy and Parallel Robot Design

The V design model—V design cycle—is currently adopted in the field of mechatronic design [1, 2]. The main aspects referring to the mechatronic philosophy applied to the design process of the parallel robots were detailed in [8]. Starting from the initial design specifications—the check list—the importance of the optimization criteria was emphasized, followed by the selection and the evaluation of the solutions for a hardware and software integration process, accordingly to the V cycle.

Taking a decision in the design process can be greatly simplified by the system decomposition according to the system function. Patterns development is achieved by evolving from abstract to concrete, from simple to detail. Figure 1 shows a case of system decomposition for a parallel robot.

References [7, 9] broadly present the definitions and explanations on the notations and names in the field of parallel robots. Dedicated references define the parallel robot as a “... robot in which end effector is connected in parallel to reference link by $k \geq 2$ kinematic chains called limbs or legs”, while the fully

Fig. 1 Decomposition of the robot system, based on the function to be performed



parallel robot is "...a parallel robot in which the number of limbs is equal to the robot mobility and each limb integrates just one actuator" [3]. In this way, one can admit that a parallel mechanism is composed of a movable body and a fixed body connected by kinematic chains (Fig. 2). A fixed platform (FP) represents the support for the assembled mechatronic system, which is the parallel robot. The end effector (EF) is attached to a mobile platform (MP) of a particular geometrical shape. The characteristic point P is associated to the effector. A parallel mechanism assembles the mobile platform to the fixed one. Depending upon the particular employment requirements, various design solutions can be defined by modifying the spatial position of the platforms one relative to the other.

The configuration of the parallel mechanism integrating both platforms is obtained as a result of a structural synthesis, the complexity of the assumed application playing an essential role. The DOF of the mobile platform also depend upon the assumed application.

The structural synthesis for the parallel robots based on the kinematic connections theory [10] was approached by the authors [8, 11] by means of computation elements and illustrative examples.

The literature highlights the different types of actuators used in mechatronic systems: electrostatic [12], electric [4], electro-rheological [13], shape memory alloy, electrochemical or photostrictive [14, 15]. Electric linear actuators represent appropriate actuating solutions for mechatronic systems because of their parameters and facilities.

Figure 3 shows the kinematic connection $K_{B(-1)}$ for a linear actuator consisting of a rotary electric servomotor (E_S) and a helical kinematic joint (1, 2, 3 are elements of the mechanism and B, C are kinematic joints). The set out methodology established the connection type and the corresponding DOF [8].

A building block for physical integration within the mechatronic system can be attached to the linear actuator, thanks to its own construction. Spherical joints (S), revolute joint (R), universal joint (U) are several possible alternatives used in the construction of the parallel robots [6, 7, 9].

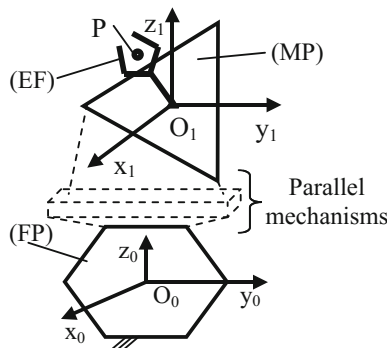


Fig. 2 Relative position of the two platforms within the structure of the parallel robot

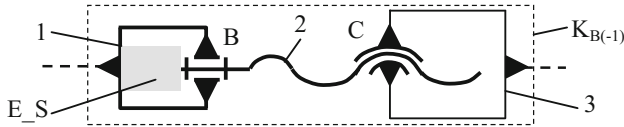


Fig. 3 The kinematic connection corresponding to the linear actuator

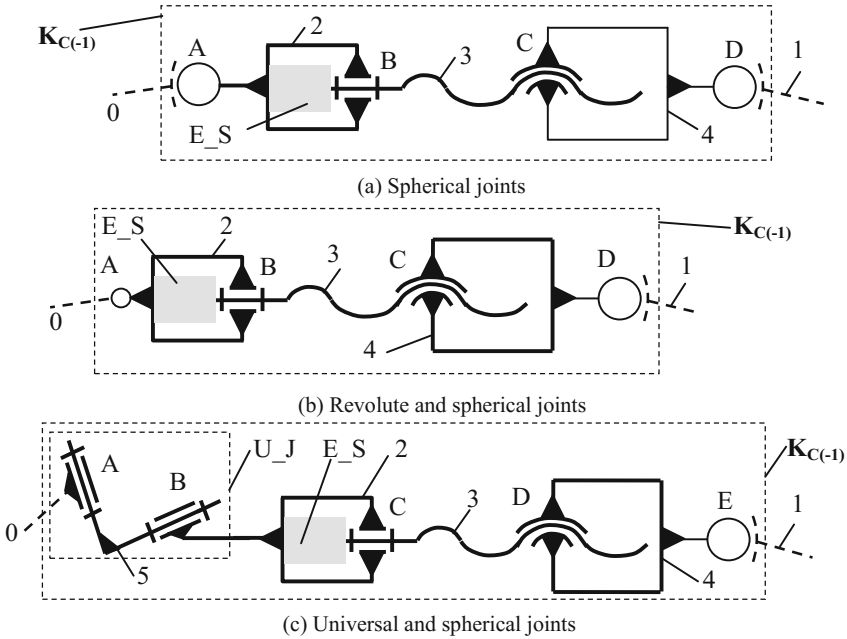


Fig. 4 Alternative structures of kinematic connections $K_{C(-1)}$ for a linear actuator

Figure 4 shows the structure of a kinematic connection $K_{C(-1)}$ that models a linear actuator using either spherical joints to connect the fix platform and the mobile platform of a parallel robot (Fig. 4a, joints A and D), or a spherical and a revolute joint (Fig. 4b, joints A and D) or a universal joint together with a spherical joint (Fig. 4c, joints U_J and E) (1, 2, 3, 4, 5 are mechanism elements and B, C are joints). These types of kinematic connections can be integrated in a symmetric manner (same connection) or an asymmetrical manner in view of composing parallel kinematic chains. The presented solutions are advantageous due to their compact structures with a reduced radial size.

3 Linear Actuator Simulation and Experimental Analysis

The linear actuator that was considered for the theoretical and the experimental study is presented in Fig. 5. The device includes: a d. c. tachogenerator (1) coupled to the shaft of the d. c. electric motor (2), a planetary gear (3), a resistive position transducer (4), a screw- nut transmission (5), the mobile element (6) rigidly attached to the nut and the housing (7). The housing allows assembling two spherical joints in view of integrating the actuator within the system.

A permanent magnet dc electric motor is used (Maxon A-max) (5 W, 10300 rpm). The servomotor electrical time constant can be established based on the catalogue data (R- the electric resistance [Ω], L- the inductivity [mH]).

$$\tau_e = \frac{L}{R} = \frac{0.64 \times 10^{-3}}{8.78} \cong 0.073 \times 10^{-3} s \tag{1}$$

The motor’s mechanical time constant is defined by the Eq. (2).

$$\tau_m = \frac{R \cdot J}{K^2} = \frac{8.78 \times 3.8 \times 10^{-7}}{(13.6 \times 10^{-3})^2} = 18 \times 10^{-3} s \tag{2}$$

where R [Ω] is the electric resistance, J [kgm²] is the rotor moment of inertia and K [V/rad/s] is the electrical constant of the motor.

When comparing the electrical and mechanical time constants, one can observe that $\tau_e \ll \tau_m$. This simplifies the mathematical model of the electric servomotor.

The integrated planetary gear (Maxon gear) has a transmission ratio $i_r = 19$ and the efficiency $\eta_r = 0.81$.

The dc tachogenerator is integrated within the actuator and has a sensitivity of 0.52 V/1000 rpm.

The resistive transducer was integrated within the actuator’s structure by means of a worm gear. The gear transmission ratio is:

$$i_{Trp} = \frac{\Omega_s}{\Omega_{Trp}} = 26 \tag{3}$$

where Ω_s [rad/s] is the screw angular speed and Ω_{Trp} [rad/s] is the angular speed for the input of the position transducer.

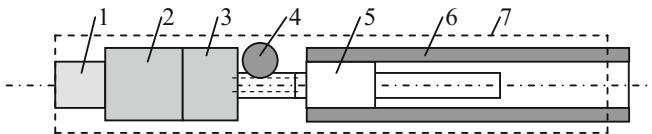


Fig. 5 The linear actuator

The reduced mass moment of inertia was estimated based on the actuator system parameters:

$$J_{red} = J_{rot} + J_{TG} + J_s \cdot \frac{1}{i_r^2} + m \cdot \left(\frac{p}{2\pi i_r} \right)^2 \tag{4}$$

where J_{rot} [kgm²] is the rotor’s moment of inertia, J_{TG} [kgm²] is the moment of inertia of the tachogenerator, J_s [kgm²] is the moment of inertia of the screw from the helical joint, m [kg] is the mass of the translation mobile element and p [m] is the pitch of the helical joint.

The values for the parameters required to develop the mathematical model of the actuator were revealed by using the classical models of the constructive elements and the experimental analysis of each component. Figure 6 shows the block diagram used for simulations within the Matlab/Simulink environment.

The experimental stand (Fig. 7) was developed around a power source (1), a linear actuator (2), an Arduino based development system (3), a Fluke oscilloscope (4) and a computing system (5).

Experiments targeted the behaviour of the mechatronic module “actuator” under a set of conditions proposed for study: the system response to a bang-bang command for a time interval Δt and a voltage supply of the servomotor U_0 ,

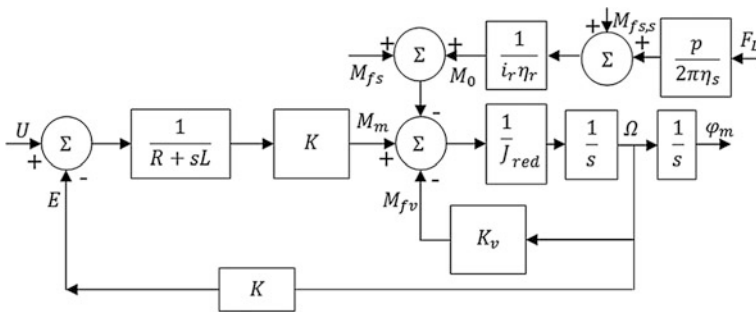


Fig. 6 The block diagram of the linear actuator

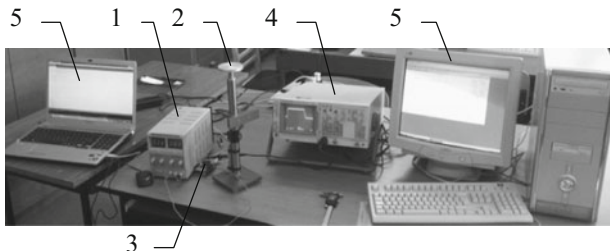


Fig. 7 The experimental stand used in the actuator analysis

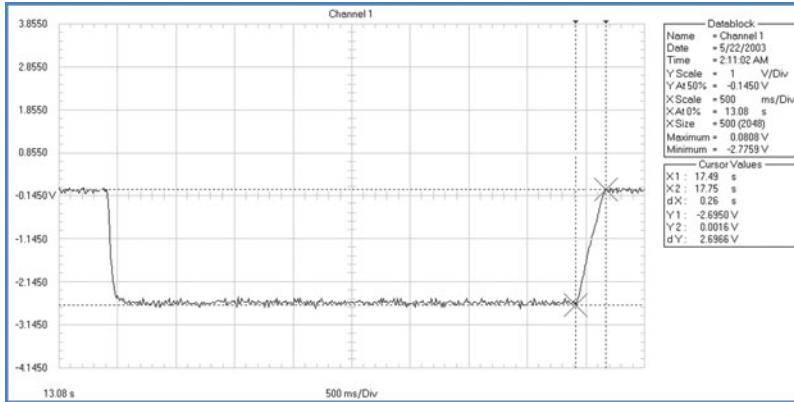


Fig. 8 The signal acquired from the tachogenerator

corresponding to an increase in actuator working quota (no load); the answer of the actuator under previous conditions for a shortening of the actuator working quota; the set out of the correlation between the movable stroke, the rotation angle of the motor and the best method to control the system; the system response to various axial loads applied to the movable element, both in terms of elongation and shortening of the actuator.

The acquisition of the tachogenerator voltage signal for an imposed movement of the actuator’s mobile element is shown in Fig. 8, aiming to determine the servomotor speed during the designed movement. As an exemplification of the previous statement, the authors show the modality of using the acquired signal in determining two new parameters: the speed and the angular acceleration of the motor during the system’s acceleration/braking phases:

$$\Omega_{mu} = \frac{U_{TG}}{K_{TG}} = \frac{2.658}{0.497 \times 10^{-2} \text{ V/rad} \cdot \text{s}^{-1}} = 534.8 \text{ rad/s} \tag{5}$$

$$\epsilon_{mf-\mu} = \frac{\Delta\Omega}{\Delta t} = -\frac{534.8 \text{ rad/s}}{0.26 \text{ s}} = -2056.92 \frac{\text{rad}}{\text{s}^2} \tag{6}$$

The experimentally determined values allow the comparison with similar values obtained from simulation and estimation of several complementary parameters. The experimental analysis on the behaviour of the mechatronic module allows asserting that, for the given case, the position control is recommended. The acquired signals allowed verifying the correlation of the experimental parameters and of the possibilities for a synergistic use of the information.

4 Conclusions

The paper continues a previous authors' activity in the field of structural analyses of mechanisms for parallel robots. The results obtained through the modelling of a linear actuator according to the theory of the kinematic connections allow rapidly defining structural variants and applying the criterial analysis on them. The results can be correlated with CAD facilities in view of developing the shape of the system.

The experimental analysis aimed the identification of certain functional parameters for the constructive elements as well as the verification of the hypotheses admitted in the mathematical modelling. It has been found that the precision and the dynamic performances were achieved. Both the experimental analysis and the system's mathematical modelling will allow synthesizing an efficient control system around the Arduino development systems.

References

1. Künzel, G.: The mechatronics design process. *Informačné a automatizačné technológie v riadení kvality produkcie Vernár* **12–14**(9), 67–73 (2005)
2. Amerongen, J.V.: Mechatronic design- a port-based approach. In: ISMA07, 26–29 Mar 2007
3. Bishop, R.H.: *Mechatronic Systems, Sensors and Actuators*. CRC Press (2007)
4. Braembussche, P.V., Swevers, J., Brussel H.V.: Design and experimental validation of robust controllers for machine tool drives with linear motor. *Mechatronics* **11**, 545 (2002)
5. Park, J.S.: Motion profile planning of repetitive point-to-point control for maximum energy conversion efficiency under acceleration conditions. *Mechatronics* **6**(6), 649–663 (1996)
6. Hetmanczyk, J., Stenzel, T., Grzesik, B.: Selected aspects of design and modelling of linear actuator based on PM BLDC motor. *Przegląd Elektrotechniczny* **91**(6), 100–107 (2015)
7. Zhang, D.: *Parallel Robotic Machine Tools*. Springer (2010)
8. Dolga, V., Dolga, L.: The structural synthesis of the parallel robots. *Mechanika* **17**(3), 288–295 (2011)
9. Gogu, G.: *Structural Synthesis of Parallel Robots, Part 1 Methodology*. Springer (2007)
10. Kovacs, F., Perju, D., Savii, G.: *New methods in Mechanisms Synthesis (in Romanian)*. Facla Publishing House, Timișoara (1976)
11. Dolga, V., Dolga, L.: *Elements of synthesis and experiment for parallel robots. MTM-Robotics* (2012)
12. Lee, S.-K., Esashi, M.: Design of the electrostatic linear microactuator based on the inchworm motion. *Mechatronics* **5**(8), 963–972 (1985)
13. Choi, S.-B., Park, D.-W., Cho, M.: Position control of a parallel link manipulator using electro-rheological valve actuators. *Mechatronics* **11**, 157–181 (2001)
14. Janocha, H.: New actuators from the point of view of mechatronics. *Mechatronics* **6**(5), 497–506 (1996)
15. Thielicke, E., Obermeier, E.: Microactuators and their technologies. *Mechatronics* **10**, 431–455 (2000)

Part XI
Robotics—Robotic Control Systems

Dynamic Control for a Class of Continuum Robotic Arms

M. Ivanescu, M. Nitulescu, V.D.H. Nguyen and M. Florescu

Abstract The paper deals with the control problem of a class of hyper-redundant robots constituted by a chain of continuum segments. The main parameter, the system state, is determined by the position and velocity generalised variables. The dynamic model is studied and the constraints of the state variables and nonlinear components are proved. The observability problems are solved by an approach derived from the Luenberger observer type extended for this class of non-linear distributed models. The inequality constraints on the gravitational components allow to introduce a decoupled control system. A PD boundary control algorithm is used in order to achieve a desired shape of the arm. The stability analysis and the resulting controllers are obtained using Liapunov techniques. The exponential stability of the (error-observer) system was proved. The constraints on the observer and controller gains are analysed. Experimental tests verify the effectiveness of the presented techniques.

Keywords Continuum arm · Distributed observer · Decoupled control · Distributed control

M. Ivanescu (✉) · M. Nitulescu · V.D.H. Nguyen · M. Florescu
Department of Mechatronics, University of Craiova, Craiova, Romania
e-mail: ivanescu@robotics.ucv.ro

M. Nitulescu
e-mail: nitulesu@robotics.ucv.ro

V.D.H. Nguyen
e-mail: donghai.spk@gmail.com

M. Florescu
e-mail: mihaelaflorescu@yahoo.com

1 Introduction

This paper is focused on the implementation of a control system for a class of hyper-redundant robots (HRR) with continuum components. Numerous examples of continuum robots can be found in [1]. The notion of continuum arms and the main properties of this class of systems were identified in [2–5]. The first kinematic models of HRR were discussed in [6] by using the “backbone curve” model and the kinematic algorithms for obstacle avoidance by using artificial potential field and differential geometric methods were implemented. The spatial curve method was used in [7] for the arm shape kinematic control and the shape-regulation laws were studied. In [8] were developed the grasping solutions for 3-D objects for continuum manipulators consisting of constant-curvature sections and the conditions for existence of control laws were investigated. A new kinematic model by using the differential geometry was derived in [9]. Jones and Walker [10] introduces new formulations for determining the maximum curvature, determines the range of arm trunk lengths and curvatures which can be physically achieved and proposes a real-time controller for continuum robots. Kapadia et al. [11] presents a new nonlinear model-based control strategy for continuum robots. The approach is applicable to continuum robots which can extend/contract as well as bend throughout their structure. Rucker et al. [12] describes a general coordinate-free energy formulation for modeling the shape of concentric tube continuum robots known as active cannulas. Cable-driven continuum robot control with variable stiffness was studied in [13]. A shape decoupled control is proposed in [14]. A control system by curvature gradient techniques is advanced in [15].

Our paper treats the control problem of a class of hyper-redundant robots constituted by a chain of continuum segments. The main parameter is determined by the position generalised variables. Standard feedback control design assumes full-state feedback with measurements of the entire state. However, the use of these sensors on all surface of continuum arms, is not practical due to mechanical constraints. In fact, measuring techniques allow the evaluation of motion parameters on the boundary of the arm components. In this case, the development of the state-feedback controllers needs to design state observers. The observability problems are solved by an approach derived from the Luenberger observer type extended for this class of non-linear distributed models. The inequality constraints on the gravitational components allow to introduce a decoupled control system. A PD boundary control algorithm is used in order to achieve a desired shape of the arm. The stability analysis and the resulting controllers are obtained using Liapunov techniques. The exponential stability of the system (error-observer) was proved. The constraints on the observer and controller gains are easy to be implemented. Numerical simulations and experimental tests verify the effectiveness of the presented techniques.

The primary benefit of the proposed method is that a non-linear distributed observer is used for the boundary state estimation and a robust decoupled PD algorithm is proposed for the shape control of the arm.

The paper is divided as follows: Sect. 2 presents the technological arm, Sect. 3 analyses the mathematical model, Sect. 4 discusses the control problem by distributed observer, Sect. 5 presents experimental results and Sect. 6 is dedicated to the conclusions.

2 Technological Model

The technological model basis is a 3D model, Fig. 1 consisted of a central, long and thin, highly flexible and incompressible backbone, with a distributed mass.

It is made from homogeneous materials, the bending represents the main motion and the deformations of axial tension/compression and shear are neglected. The arm is divided in several segments, each segment having its own driving system. The motion of the arm, the bending, is determined by antagonistic Bowden cables (tendons) attached to the terminal point of each segment and a DC motor driving system. These cables develop the driven torques. The driven system is a decoupled one, each torque controls the motion, bending, of its own segment. The placement of sensors at the boundary sub-regions of the arm segment requires to design the state observer. The position measuring of the segment is obtained by an angle sensor that is placed on the surface at the terminal sub-regions of each segment.

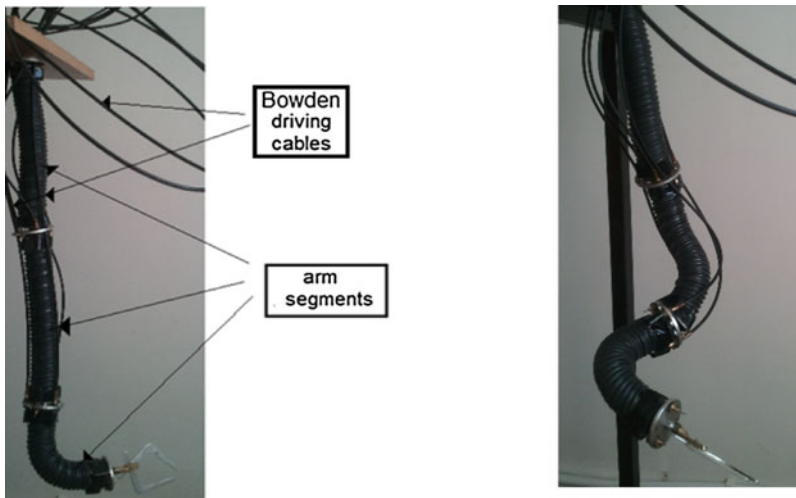


Fig. 1 Technological arm

3 Mathematical Model

The essence of the arm is the backbone curve Γ , Fig. 2 [2]. The independent parameter s is related to the arc-length from origin of the curve Γ , $s \in \Omega$, $\Omega = (0, L)$ with the boundary $\partial\Omega = \{0, L\}$, where L is the length of the inextensible arm. Further it is considered a robot arm constituted by a serial connection of a number of N continuum arm segments, with equal lengths $l_i, i = 1, 2, \dots, N, (l_i = l = \frac{L}{N})$. The orientation vector ω , $\omega \in ((L_2(\Omega) \times L_2(\Omega))$, is defined as $\omega(s) = \begin{bmatrix} \theta(s) \\ q(s) \end{bmatrix}, s \in \Omega$. The decoupled dynamics of a segment can be obtained by the same procedure as in [2], for the variables defined on the segment i . Following partial differential equations (PDE) are inferred

$$I_p \ddot{\omega}^i = EI \omega_{ss}^i - B \dot{\omega}^i - h^i(\omega) \tag{1}$$

where $\omega^i = \omega^i(t, s_i), \dot{\omega}^i = (\dot{\theta}^i, \dot{q}^i)^T, s_i \in [0, l_i], I_p$ is the (2×2) rotational inertial matrix, EI is a (2×2) bending stiffness matrix, B is the (2×2) equivalent damping matrix of the arm, The nonlinear component $h^i(\omega) = (h_1^i(\omega), h_2^i(\omega))^T$ is determined by the gravitational components evaluated with respect to the base of the arm. ($s = 0$) $(h_j^i \in L_2(\Omega), \frac{\partial h_j^i}{\partial \omega} \in L_2(\Omega), j = 1, 2)$. Gravitational components satisfy the inequality [15]

$$\|h^i(\omega)\| \leq \eta \|\omega\| = \rho g \sqrt{L} \|\omega\| \tag{2}$$

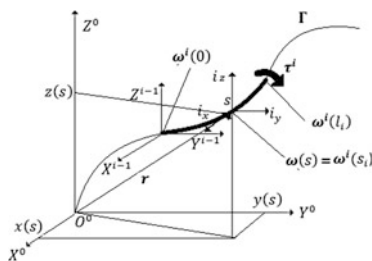
The initial and boundary conditions are

$$\omega^i(0, s_i) = \omega_0^i(s_i) \quad \omega^i(t, 0) = 0, \quad \omega_s^i(t, 0) = 0, \tag{3}$$

$$EI \omega_s^i(t, l) = \tau_i(t) = \begin{bmatrix} \tau_{\theta i} \\ \tau_{q i} \end{bmatrix} \tag{4}$$

where τ_i is the equivalent moment generated by the forces F_i at the end of the arm segment $i, \tau_i(t) = F_i \cdot r, r$ is the radix of the moment.

Fig. 2 Model parameters



4 Control Algorithm

A decoupled boundary torque control for a segment is presented in Fig. 3. The observer states are defined as

$$\hat{\omega}^i(t, s_i) = \begin{bmatrix} \hat{\theta}^i(t, s_i) \\ \hat{q}^i(t, s_i) \end{bmatrix} \tag{5}$$

and the observer dynamics will be,

$$I_\rho \ddot{\omega}^i = EI \hat{\omega}_{ss}^i - b \dot{\omega}^i - h^i(\hat{\omega}) + w_0(s)(\Delta \omega^i(t, l) - \omega^i(t, l)) + w_1(s)(\Delta \dot{\omega}^i(t, l) - \dot{\omega}^i(t, l)). \tag{6}$$

with the initial and boundary conditions

$$\begin{aligned} \hat{\omega}^i(0, s) &= \omega_0^i(s), \hat{\omega}_s^i(t, 0) = 0 \\ EI \hat{\omega}_s^i(t, l) &= \tau_i(t) - p_0(\omega^i(t, l) - \hat{\omega}^i(t, l)) - p_1(\dot{\omega}^i(t, l) - \dot{\hat{\omega}}^i(t, l)) \end{aligned} \tag{7}$$

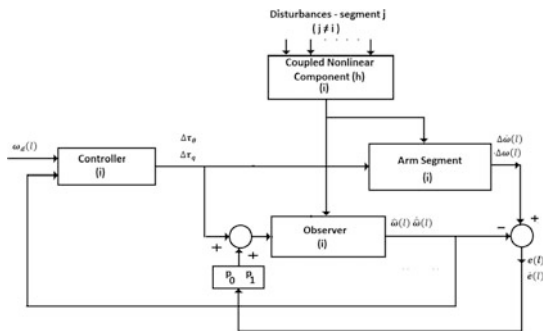
where $w_0(s), w_1(s), p_0, p_1$ are the observer gains, p_0, p_1 are constants, $p_0 > 0, p_1 > 0$. The gain functions $w_0(s), w_1(s)$ are defined as follows: we consider a (very small) finite interval Δ such that

$$w_i(s) = \begin{cases} 0, & s \in [0, l - \Delta) \\ W_i, & s \in [l - \Delta, l] \end{cases} \quad i = 0, 1 \tag{8}$$

Consider the following parameters that synthesise the observer gains: $\sigma_i = p_i + W_i \Delta, i = 0, 1$. The following error variables are introduced

$$\begin{aligned} e^i(t, s) &= \omega^i(t, s) - \hat{\omega}^i(t, s), \dot{e}^i(t, s) = \dot{\omega}^i(t, s) - \dot{\hat{\omega}}^i(t, s) \quad s \in \Omega \\ I_\rho \ddot{e}^i &= EI e_{ss}^i - b \dot{e}^i - \Delta h^i(e) - w_0(s)e^i(t, l) - w_1(s)\dot{e}^i(t, l) \end{aligned} \tag{9}$$

Fig. 3 Observer control system



$$EI \mathbf{e}_s^i(t, l) = p_0 \mathbf{e}^i(t, l) + p_1 \dot{\mathbf{e}}^i(t, l), \quad \mathbf{e}_s^i(t, 0) = 0 \quad (10)$$

Theorem 1 For the system described by (1) and (6), if the control law is given by

$$\Delta \boldsymbol{\tau}_i(t) = -\mathbf{K}_1 \boldsymbol{\omega}^i(t, l) - \mathbf{K}_2 \dot{\boldsymbol{\omega}}^i(t, l) \quad (11)$$

where $\mathbf{K}_j = \text{diag}(k_{0j}, k_{1j})$, $k_{0j} = k_{1j} = k_j, j = 1, 2$, are positive controller gains that satisfy the conditions

$$\mathbf{K}_1 > \frac{1}{\lambda} \left(\sigma_0 \lambda \delta^2 + \sqrt{2} \eta + \sqrt{2} \frac{\beta}{\mu} \eta \right) \mathbf{I} \quad (12)$$

$$\mathbf{K}_2 > \frac{1}{\lambda} \left(\sigma_1 \lambda \delta^2 - b + \frac{\mu}{\beta} I_\rho + \frac{\sqrt{2}}{4} \eta \right) \mathbf{I} \quad (13)$$

δ is a positive constant, \mathbf{I} is a (2×2) identity matrix, the observer parameters σ_0, σ_1 verify the relations

$$\sigma_0 > \frac{\sqrt{2}}{\lambda} \left(\eta + \frac{\beta}{\mu} \eta \right) \quad (14)$$

$$\sigma_1 > \frac{1}{\lambda} \left(\frac{\mu}{\beta} I_\rho + \frac{\sqrt{2}}{4} \eta - b \right) \quad (15)$$

the system is exponentially stable.

Proof See Appendix.

5 Experimental Results

In order to verify the suitability of the control algorithm, a platform with a 3D hyper-redundant robot arm has been employed for testing (Fig. 1). The manipulator consists of a cable-driven continuum arm. An elastic core is the robot's backbone ($EI \approx 2 \text{ Nm}^3, k_{el} = 0.8 \text{ Nm rad}^{-1}$). It is made from homogeneous materials, the bending represents the main motion. The compressive and shear loads are neglected due to the incompressibility of the modelled elastic core compared with its bending. The metallic disks separate the segments and are used as support points of the actuation cables. The mechanical parameters are: $\rho_b = 0.4 \text{ kg/m}, g = 10 \text{ m/s}^2, l_1 = 0.18 \text{ m}, l_2 = 0.14 \text{ m}, l_3 = 0.10 \text{ m}, L = 0.42 \text{ m}$. Three Bowden cables actuate each segment of the arm. The driving system of each segment is a decoupled one. A Quanser based platform and a PC system (Intel Core i5 (f = 3.2 GHz)) is used for control and signal acquisition. The driving system is determined by the DC

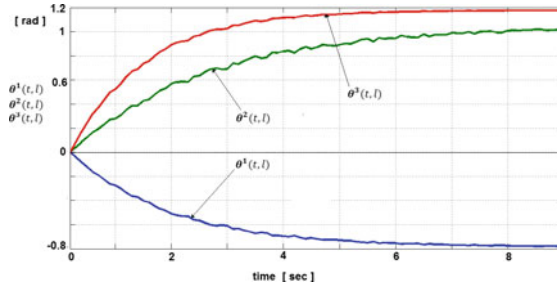


Fig. 4 Trajectories $\theta^i(t, l)$, $i = 1, 2, 3$ for $\theta_d^1 = -\pi/4$, $\theta_d^2 = \pi/3$, $\theta_d^3 = 3\pi/8$

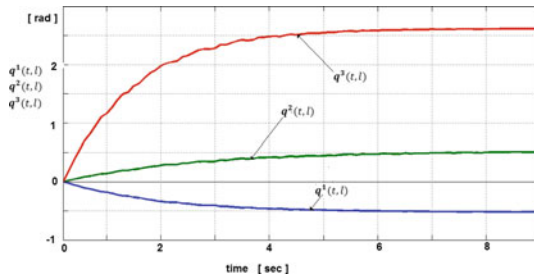


Fig. 5 Trajectories $q^i(t, l)$, $i = 1, 2, 3$ for $q_d^1 = -\pi/6$, $q_d^2 = \pi/6$, $q_d^3 = 5\pi/6$

motors of a Quanser QUBETM-servo system and a transmission system. An observer (6) and (7) is implemented with $p_0 = 20$, $p_1 = 5$, $W_0 = 600$, $W_1 = 200$ and $\Delta = 0.005$ m. The observer gains will be: $\sigma_0 = 23$, $\sigma_1 = 6$ and the relations (14) and (15) are verified for $\xi = 5$. A control law (13) is implemented and the controller gains are selected from (12) and (13) (for $\delta = 2 > 1$), $K_{1\theta} = K_{1q} = 100 > 86$, $K_{2\theta} = K_{2q} = 30 > 21.5$. A 3D motion of the arm is presented in Fig. 1 and the trajectories of the parameters θ, q at the segment boundaries are shown in Figs. 4 and 5, respectively. The good quality of motion and their convergence to the desired positions can be remarked.

6 Conclusions

The paper treats the control problem of a class of hyper-redundant robots constituted by a chain of continuum segments. The dynamic model is inferred. The constraints of the state variables on the boundary and inside of the arm segment are proved.

The gravitational forces are treated as uncertain components that satisfy the inequality constraints. A PD boundary control algorithm is used in order to achieve



a desired shape of the arm. The stability analysis and the resulting controllers are obtained using Liapunov techniques. Experimental tests verify the effectiveness of the presented methods.

Appendix

Consider the following Liapunov functional

$$V(t) = \frac{1}{2} \int_0^l \left(\alpha \tilde{\omega}^T \tilde{\omega} + \beta I_\rho \dot{\tilde{\omega}}^T \tilde{\omega} + \gamma \tilde{\omega}_s^T \tilde{\omega}_s + \mu I_\rho \tilde{\omega}^T \dot{\tilde{\omega}} \right) ds + \frac{1}{2} \tilde{\omega}^T(l) \mathbf{v} \tilde{\omega}(l) \quad (\text{A.1})$$

where, $\alpha, \beta, \gamma, \mu$ are positive constants that satisfy the following conditions (in order to simplify the notations, the index i was omitted):

$$\alpha - \frac{\mu}{4\delta^2} > 0, \quad \beta - \mu I_\rho \delta^2 > 0, \quad \alpha = \mu b, \quad \beta EI = \gamma$$

These conditions ensure that the functional (A.1) is positive definite $V > 0$. The time derivative of $V(t)$ is computed along the solutions of (11) and (12),

$$\dot{V}(t) = \int_0^l \left(\alpha \tilde{\omega}^T \dot{\tilde{\omega}} + \beta I_\rho \dot{\tilde{\omega}}^T \ddot{\tilde{\omega}} + \gamma \tilde{\omega}_s^T \dot{\tilde{\omega}} + \mu I_\rho \dot{\tilde{\omega}}^T \dot{\tilde{\omega}} + \mu I_\rho \tilde{\omega}^T \ddot{\tilde{\omega}} \right) ds + \tilde{\omega}^T(l) \mathbf{v} \dot{\tilde{\omega}}(l) \quad (\text{A.2})$$

Substituting (11) into (A.2), taking into account the boundary conditions (12), control law (13), after simple additional manipulations, it yields,

$$\dot{V}(t) \leq \int_0^l \left(-\mu \tilde{\omega}^T \mathbf{C} \tilde{\omega} - \dot{\tilde{\beta}} \tilde{\omega}^T \mathbf{B} \dot{\tilde{\omega}} - \mu EI \tilde{\omega}_s^T \tilde{\omega}_s \right) ds \quad (\text{A.3})$$

$$\mathbf{C} = \begin{bmatrix} \mathbf{C}_1 & \mathbf{0} \\ \mathbf{0} & \mathbf{C}_2 \end{bmatrix}, \mathbf{B} = \begin{bmatrix} \mathbf{B}_1 & \mathbf{0} \\ \mathbf{0} & \mathbf{B}_2 \end{bmatrix}, \mathbf{C}_1 = \left(\sigma_0 \lambda - \sqrt{2} \left(\eta + \frac{\beta}{\mu} \eta \right) \right) \mathbf{I} = c_1 \mathbf{I}$$

$$\mathbf{C}_2 = \lambda \mathbf{K}_1 - \left(\sigma_0 \lambda \delta^2 + \sqrt{2} \eta + \sqrt{2} \frac{\beta}{\mu} \eta \right) \mathbf{I} = c_2 \mathbf{I},$$

$$\mathbf{B}_1 = \left(\lambda \sigma_1 - \left(\frac{\mu}{\beta} I_\rho + \frac{\sqrt{2}}{4} \eta - b \right) \right) \mathbf{I} = b_1 \mathbf{I},$$

$$\mathbf{B}_2 = \left(\lambda \mathbf{K}_2 - \left(\sigma_1 \lambda \delta^2 - b + \frac{\mu}{\beta} I_\rho + \frac{\sqrt{2}}{4} \eta \right) \right) \mathbf{I} = b_2 \mathbf{I}$$

Then by the conditions (12)–(15) it follows that the Liapunov functional (A.3) is negative definite, $\dot{V}(t) < 0$.

References

1. Robinson, G., Davies, G.B.C.: Continuum robots—a state of the art. In: Proceedings of IEEE International Conference on Robotics and Automation, Detroit, May 1999, pp. 2849–2854 (1999)
2. Gravagne, I.A., Walker, I.D.: On the kinematics of remotely—actuated continuum robots. In: Proceedings of 2000 IEEE International Conference on Robotics and Automation, San Francisco, April 2000, pp. 2544–2550 (2000)
3. Gravagne, I.A., Walker, I.D.: Kinematic transformations for remotely-actuated planar continuum robots. In: Proceedings of 2000 IEEE International Conference on Robotics and Automation, San Francisco, April 2000, pp. 19–26
4. Gravagne, I.A., Walker, I.D.: Uniform regulation of a multi-section continuum manipulators. In: Proceedings of 2002 IEEE International Conference on Robotics and Automation, Washington DC, May 2002, pp. 1519–1525
5. Gravagne, I.A., Walker, I.D.: Manipulability and force ellipsoids for continuum robot manipulators. In: 2001 IEEE/RSJ International Conference on Intelligent Robots and Systems, Maui, Hawaii, Oct 29–31, pp 304–310
6. Chirikjian, G.S., Burdick, J.W.: An obstacle avoidance algorithm for hyper-redundant manipulators. In: Proceedings of IEEE International Conference on Robotics and Automation, Cincinnati, Ohio, May 1990, pp. 625–631 (1990)
7. Mochiyama, H., Kobayashi, H.: The shape Jacobian of a manipulator with hyper degrees of freedom. In: Proceedings of 1999 IEEE International Conference on Robotics and Automation, Detroit, May 1999, pp. 2837–2842 (1999)
8. Li, J., Xiao, J.: Determining grasping configurations for a spatial continuum manipulator. In: 2011 IEEE/RSJ International Conference on Intelligent Robots and Systems, Sept 25–30, 2011, San Francisco, pp 4207–4213
9. Walker, I.D., Hannan, M.W.: A novel elephant’s trunk robot. In: AIM ’99, pp. 410–415 (1999)
10. Jones, B., Walker, I.D.: Practical kinematics for real-time implementation of continuum robots. *IEEE Trans. Robot.* **22**(6), 1087–1099 (2006)
11. Kapadia, A.D., Walker, I.D., Dawson, D.M.: A model—based sliding mode controller for extensible continuum robots. In: Recent Advances in Signal Processing, Robotics and Automation, ISRA Conference, 2009, pp. 103–120 (2009)
12. Rucker, D.C., Webster, R.J.I.I.I., Chirikjian, G.S., Cowan, N.J.: Equilibrium conformations of concentric-tube continuum robots. *Int. J. Robot. Res.* **29**(10), 1263–1280 (2010)
13. Popescu, N., Popescu, D., Ivanescu, M.: A spatial weight error control for a class of hyper-redundant robots. *IEEE Trans. Robot.* **29**(4), 1043–1050 (2013)
14. Ivanescu, M., Popescu, N., Popescu, D.: The shape control of a tentacle arm. *Robot. Cambridge J.* **33**(03), 684–703 (2015)
15. Ivanescu, M., Popescu, N., Popescu, D.: A decoupled sliding mode control for a continuum arm. *Adv. Robot. Special Issue: Continuum Robots Manipulation* **29**(13), 831–845 2015

Actuator Design for Stabilizing Single Tendon Platforms

D. Haarhoff, M. Kolditz, D. Abel and S. Brell-Cokcan

Abstract In this paper we illustrate the feasibility of using control moment gyroscopes (CMGs) for the stabilization of free swinging robots hanging from single tendons. Such systems may provide robotic workspaces of unprecedented size, especially in the vertical. Taking typical base reaction forces of industrial robots we show that control moment gyroscopes may provide means for compensation. From the basic principles of CMGs we derive design criteria for a free swinging robot platform. These criteria are illustrated in the design of a scissored pair CMG for a single DoF demonstrator.

Keywords Platform stabilization · Tendon robotics · Control moment gyroscopes

1 Introduction

Conventional serial robot kinematics are limited in their workspace by the simple fact that the first actuator must carry the weight of all subsequent actuators. Parallel kinematics solve this weight issue to a certain degree but at the cost of large system envelopes compared to their workspaces. Established solutions employ linear axes to extend the workspace of serial kinematics. To move beyond the size limits of these axes several approaches have been suggested: mobile robot platforms, gantries and parallel tendon kinematics. Both mobile robot platforms and gantries are severely restricted in their vertical workspace. This leaves parallel tendon kinematics, which have already seen commercial use for example as camera platforms in stadiums. Making such platform suitable for carrying industrial robots involves hard control

D. Haarhoff (✉) · S. Brell-Cokcan
Chair for Individualized Building Production, RWTH Aachen University,
Aachen, Germany
e-mail: haarhoff@ip.rwth-aachen.de

M. Kolditz · D. Abel
Institute of Automatic Control, RWTH Aachen University, Aachen, Germany

© Springer International Publishing AG 2017
B. Corves et al. (eds.), *New Advances in Mechanisms,
Mechanical Transmissions and Robotics*, Mechanisms and Machine Science 46,
DOI 10.1007/978-3-319-45450-4_37

371

engineering due to the non-linear flex of varying length tendons [1, 12]. Yet maybe the most critical barrier is the way that the tendons intrude into the workspace.

To solve these issues we propose a robotic platform hanging from a single tendon. Such a platform would provide cheap and flexible positioning of industrial robots due to the ubiquity of cranes, gantries and ceilings suited for mounting. Large vertical and horizontal workspaces could be covered while requiring minimal space for the actuators.

With only one degree of freedom controlled by the tendon novel approaches are needed to control the platform in the remaining degrees. In this contribution we show that, given the forces involved, control moment gyroscopes (CMG) are ideally suited for this task.

Control moment gyroscopes have a proven track record in space as attitude control systems [7]. They have seen little use in terrestrial applications [3, 4, 6, 11, 14], and therefore most literature is heavily influenced by the requirements of spacecraft. Terrestrial application benefits CMGs in several ways. Greater masses and stronger motors may be used due to more lenient weight restrictions but also higher performance control algorithms due to space compatible computers lagging terrestrial ones by about ten years.

From the working principles of CMGs and typical process forces we show that CMGs are well suited for stabilizing such a platform. Principles for their sizing and a prototypical design are illustrated.

2 Control Moment Gyroscopes

The operating principle of CMGs is non-intuitive, as are most effects involving gyroscopes [5]. The following is a brief overview of CMG principles, for a more complete understanding see [7]. Fundamental to understanding gyroscopes is that torque is change in angular momentum ($\tau = \dot{h}$). When the applied torque is aligned with the angular momentum the momentum simply increases. When the applied torque is orthogonal to the angular momentum the momentum maintains its magnitude, but changes in direction. This effect is known as gyroscopic precession. CMGs invert the principle by rotating the angular momentum, causing a reaction torque (this is illustrated in Figs. 1 and 2).

The general case for the torque is:

$$\underline{\tau} = -\underline{\omega} \times \underline{h} \quad (1)$$

For the case where $\omega \perp h$ this may be simplified to scalar form:

$$\tau = \omega \cdot h \quad (2)$$

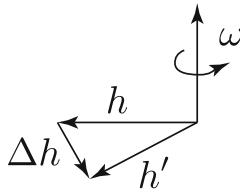


Fig. 1 The above figure helps illustrate the non-intuitive nature of gyroscopic reaction torques. The angular momentum h is rotated with an angular velocity ω about an axis perpendicular to itself. This leads to the magnitude of the angular momentum remaining constant while its direction changes. This change in angular momentum Δh is then the resulting torque. This mechanism leads to the efficient torque generation with CMGs compared to reaction wheels, since the resulting torque is not directly dependant upon the torque needed to rotate the angular momentum

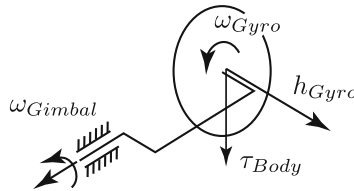


Fig. 2 Principle of single gimbal CMGs. The gimbal motor rotates the angular momentum generated by the gyroscope. The gimbal motor only has to overcome the inertia of the gyroscope. The gyroscopic reaction torque is applied to the system via the gimbal bearings. The resulting torque depends on the gyroscopes angular momentum and the angular velocity of the gimbal. This lets single gimbal CMGs generate torques much larger than their gimbal motor torques

The torque required to change the direction of the angular momentum i.e. induce ω only has to overcome the rotational inertia of the gyroscope. This means that torques applied to rotate the gimbal may lead to much higher reaction torques simply by producing a large the angular momentum. The produced reaction torque is then transferred to the body via the gimbal’s bearing, which governs their sizing.

Sadly the sizing of the gimbal motor is not only dependant upon the torque needed to gimbal the gyroscope. The body to which the CMG is attached may be rotated by external forces or torques generated by the CMG. This rotation of the gyroscopes angular momentum of course also leads to a reaction torque. In the worst case the rotations are orthogonal to gimbal and gyroscope axis, meaning that the reaction torque has to be sustained solely by the gimbal motor. This leads to the following relationship relevant to sizing the gimbal motor [7]:

$$\frac{\tau_{Body}}{\tau_{Gimbal}} = \frac{\omega_{Gimbal}}{\omega_{Body}} \tag{3}$$

Stabilizing the platform should ideally lead to the bodies angular velocity ω_{Body} being zero. So a large torque amplification between the torque of the gimbal motor τ_{Gimbal} and torque produced on the body τ_{Body} is achievable in theory. Angular rates



from pendular motion of the platform are dependent on the current tendon length and the excitation height caused by the external forces. As such they are dependent upon process requirements imposed upon the platform and require further study.

To generate torque along multiple axis several CMGs need to be combined. Multiple configurations are covered in literature [7]. The most straightforward array is a scissored-pair in which two CMGs are mirrored so that the resulting torque is constant along a single axis (see Fig. 5). The straightforward steering law led to arrays of three scissored pairs being used in early space flight applications [13]. The need for six CMGs to cover only three degrees of freedom makes this array unattractive. Therefore pyramid or box arrays of four CMGs are used. The redundancy of one CMG is attractive for space applications, yet our application can also profit from this due the null-space maneuvers this redundancy makes possible.

3 Forces to Compensate

A single tendon constrains translation to a sphere surrounding its base. This means two translational and three rotational degrees of freedom need to be controlled using the CMGs. The forces acting upon the platform are illustrated in Fig. 3. The main concern is the base reaction caused by the industrial robot. This reaction consists of two parts: forces caused by robot movement and reaction forces from the end effector acting upon external objects.

Failure to compensate base reactions will, in addition to external disturbances, would lead to pendulum motion of the platform. Prior to dampening results of any external forces it is therefore necessary to ascertain whether CMGs may compensate common base reactions of industrial robots.

Table 1 lists the weight, lift capacity and normal base reactions when the robot is mounted to a ceiling. Even from this small sample we can see that neither tipping nor rotational torques consistently dominate. Also the payload alone does not govern the magnitude of the base reactions, the inertia and attainable accelerations play an important role. This means that by adjusting the robots paths and accelerations

Fig. 3 Forces relevant to CMG platform: **a** external disturbances, **b** base reactions due to robot movement, **c** process forces to be exerted

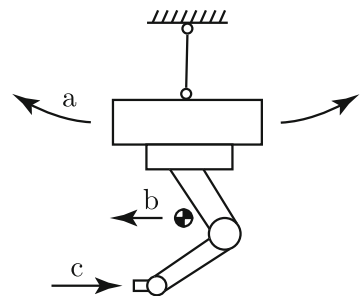


Table 1 Payloads and base reactions for two small industrial robots intended for use with the demonstrator

Robot	Payload (kg)	Base torque		Base forces	
		Rotational (Nm)	Tipping (Nm)	Vertical (N)	Horizontal (N)
Kuka Agilus sixx	6	367	788	967	1223
Kuka iiwa 14	14	282	172	541	228

one can overcome insufficient torque generation by the CMGs, be that due to sizing constraints or the approach of singularities in the CMG array.

Assuming effective control of the CMGs, the platform is a joint capable of resisting torque, but not linear forces. The tendon can easily be sized to overcome the vertical forces, an 8 mm steel cable already has a safe load capacity of 7.5 kN. What remains is the horizontal force, which then acts in addition to external forces in creating a pendulum motion. The interplay of the platforms weight, horizontal forces, non-rigid tendon and resulting pendulum motion is still under research.

The limited payloads in space robotics have led to research into reducing the base reactions caused by robot maneuvers [2, 8–10, 15, 16]. By optimizing trajectory planning and prohibiting paths with high base reactions the required CMGs are reduced in size and prevented from saturating (i.e. reaching singularities). This in turn reduces the fuel required during robotic maneuvers. Such path optimization will also be suited for the platform proposed here. The significant difference in space is that the robotic paths are executed at timescales orders of magnitude larger than common on earth [15].

Adaptation of such optimization techniques for the control of CMGs to a terrestrial platform bears great potential. Control and optimization algorithms for space applications have to deal with the limited processing power available in space faring platforms. Yet the high turning speeds of most terrestrial platforms in need of stabilization have meant that so far only few modern terrestrial CMG applications exist [7]. Single tendon platforms therefore provide an opportunity to combine decades of theoretical work with high-performance hardware to create a flexible robotics platform for large workspaces.

4 Proposed Setup

To validate the potential of single tendon robotic platforms we outline the design of a single degree of freedom platform suited for stabilizing a small industrial robot. Given the forces in Table 1 and assuming that we won't use the robot at full speed or load the platform should produce 300 Nm along one axes. One constructive constraint regarding the platform is a gyroscope diameter of no more than 15 cm.

From the moment of inertia of a thick walled cylinder and the equation of gyroscopic torque one can obtain:

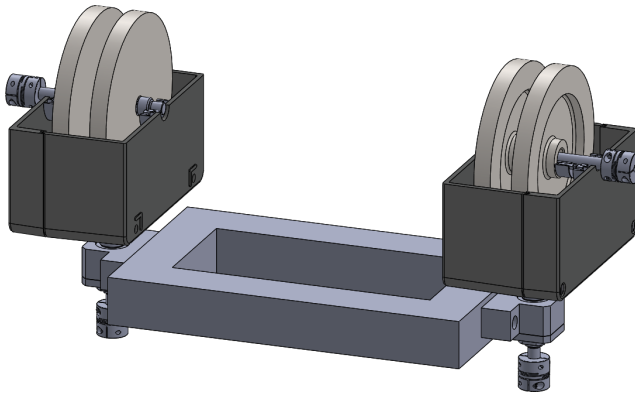


Fig. 4 Design for initial demonstrator. A scissored pair assembly is used to create torque along a single axis yet may be expanded to a box, pyramid or other array. By adding flywheels to the axis the output torque may be increased

$$\tau_{Body} = \frac{\pi \rho h}{2} (r_2^4 - r_1^4) \cdot \omega_{Gyro} \cdot \omega_{Gimbal} \tag{4}$$

Commonly available DC-motors can easily sustain 10.000 rpm so a 3 cm thick steel flywheel with a diameter of 14 cm with a 3 cm thick rim gimballed at 400 rpm will produce 364 Nm. By attaching additional flywheels to the gyro axis the available torque may be doubled at the cost of also doubling the time until the gyroscope reaches its operating speed. This design is illustrated in Fig. 4.

For evaluation a scissored pair array (Fig. 5) is used but the CMGs can also be arranged in a box or pyramid fashion. Since the reaction forces of the robots movement can be calculated straightforwardly the generated forces can be used as input for feed-forward control systems. The remaining disturbance is controlled using feedback control.

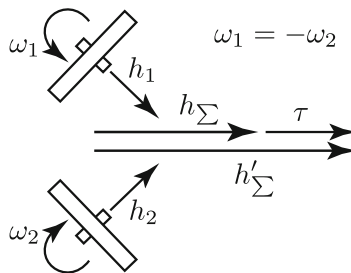


Fig. 5 In a scissored pair array two CMGs have their gimbal axes aligned in parallel. Gimbal rotation is mirrored leading to a combined angular momentum that remains constant in orientation. This makes control of the array straightforward and provides torque around a single axes i.e. 1° of freedom

5 Summary and Outlook

Novel approaches are required to increase the use of robots in manufacturing and other tasks outside of line production. Current systems are severely limited in their workspace, both vertically and horizontally. Approaches using linear axes or mobile platforms still remain limited vertically. Parallel tendon kinematics impose restrictions on the workspace by spanning their tendons through the workspace.

A single tendon platform may provide a solution to this dilemma. Such a platform may be positioned freely and cheaply horizontally but especially vertically.

We have shown that CMG technologies proven in space applications may be used to compensate the base reactions generated by common industrial robots. Relevant forces for compensation have been identified and guiding principles for the design of CMGs for this application derived.

Previous research into platform actuation using CMGs in space applications provides useful input. Yet the stark differences in requirements necessitate further work in adapting CMG research for terrestrial application. This is particularly true for control algorithms and patch optimizations since terrestrial applications have access to much higher computational performance but also require more dynamic actuation.

Overall we have shown that CMGs may provide the means for single tendon robotics platforms. These may in turn provide novel means for robotic applications in large workspaces.

References

1. Bruckmann, T.: Auslegung und Betrieb redundanter paralleler Seilroboter. Ph.D. thesis, Universität Duisburg-Essen, Fakultät für Ingenieurwissenschaften Maschinenbau und Verfahrenstechnik Institut für Mechatronik und Systemdynamik (2010)
2. Carpenter, M.D., Peck, M.: Others: reducing base reactions with gyroscopic actuation of space-robotic systems. *IEEE Trans. Rob.* **25**(6), 1262–1270 (2009)
3. Chiu, J., Goswami, A.: Design of a wearable scissored-pair control moment gyroscope (SP-CMG) for human balance assist. In: 38th Mechanisms and Robotics Conference, vol. 5A, p. V05AT08A023. ASME (2014). doi:[10.1115/DETC2014-35539](https://doi.org/10.1115/DETC2014-35539)
4. Gagne, J., Laroche, E., Piccin, O., Gangloff, J.: Active heart stabilization using adaptive noise cancelling techniques with gyroscopic actuation. In: 2010 3rd IEEE RAS and EMBS International Conference on Biomedical Robotics and Biomechatronics (BioRob), pp. 802–807. IEEE (2010)
5. Grossman, L.: 7 Questions with Randall Munroe (2015). <http://time.com/4116921/randall-munroe-draws-his-own-conclusions/>
6. Kim, D.K.Y., Bretney, K., Shao, A., Tsang, A.L.: Electronic control system for gyroscopic stabilized vehicle (2013). U.S. Classification 701/124, 446/468, 446/440, 180/252; International Classification G06F17/10, A63H17/36, B60K17/30, G06G7/48, A63H17/00; Cooperative Classification B62K11/00, B62D37/06, B62D61/02, B62K2204/00, B62J17/08, B62J27/00, B62M7/12, B62K3/007
7. Leve, F.A., Hamilton, B.J., Peck, M.A.: *Spacecraft Momentum Control Systems*, vol. 1010. Springer (2015)

8. Li, Z., Liu, H., Wang, B.: Motion planning and coordination control of space robot using methods of calculated momentum. In: 2013 IEEE International Conference on Robotics and Biomimetics (ROBIO), pp. 1151–1156. IEEE (2013)
9. Mitsushige, O.: Motion control of the satellite mounted robot arm which assures satellite attitude stability. *Acta Astronaut.* **41**(11), 739–750 (1997)
10. Quinn, R.D., Chen, J.L., Lawrence, C.: Base reaction control for space-based robots operating in microgravity environment. *J. Guidance Control Dyn.* **17**(2), 263–270 (1994)
11. Thornton, B., Ura, T., Nose, Y., Turnock, S.: Internal actuation of underwater robots using control moment gyros. In: *Oceans 2005-Europe*, vol. 1, pp. 591–598. IEEE (2005)
12. Verhoeven, R.: Analysis of the workspace of tendon-based Stewart platforms. Ph.D. thesis, Universität Duisburg-Essen, Fakultät für Ingenieurwissenschaften Maschinenbau und Verfahrenstechnik (2004)
13. Whitsett Jr., C., Cramer, P.: An experimental investigation of attitude control systems for astronaut maneuvering units. AIAA Paper, pp. 73–250 (1973)
14. Yime, E., Quintero, J., Saltaren, R., Aracil, R.: A new approach to avoid internal singularities in CMG with pyramidal shape using sliding control. In: 2009 European Control Conference (ECC), pp. 3899–3903. IEEE (2009)
15. Yoshida, K., Hashizume, K., Abiko, S.: Zero reaction maneuver: flight validation with ETS-VII space robot and extension to kinematically redundant arm. In: IEEE International Conference on Robotics and Automation, 2001, Proceedings 2001 ICRA, vol. 1, pp. 441–446. IEEE (2001)
16. Yoshida, K., Kurazume, R., Umetani, Y.: Dual arm coordination in space free-flying robot. In: IEEE International Conference on Robotics and Automation, 1991. 1991, Proceedings, pp. 2516–2521. IEEE (1991)

Model-Based Stability Prediction of a Machining Robot

S. Mousavi, V. Gagnol, B.C. Bouzgarrou and P. Ray

Abstract Machining with anthropomorphic robotic manipulators is used to increase the flexibility and reduce the costs of production. The productivity in robotic machining process is limited by low rigidity of robot structure and vibration instability in machining (chatter). Chatter analysis in robotic machining process is a challenging issue due to the variability of the dynamic behavior of the serial robot in its workspace. Hence, a dynamic model which correctly takes into account these variations is important to define adequate cutting parameters and adequate robot configurations to be adapted along the machining path. In this paper, a multi-body dynamic model of a machining robot is elaborated using beam elements which can be easily simulated for machining trajectory planning. The beam elements geometry, elasticity and damping parameters are adjusted by experimental identifications. A stability diagram based on regenerative chatter in milling operations is established. Due to variations in the robot's dynamic behavior along a machining trajectory each posture of the robot has its own stable cutting conditions. Therefore, this paper proposes a three-dimensional representation of a stability lobes diagram for the prediction of chatter vibrations in robotic machining. Stability prediction established through the proposed numeric model is validated by experimental machining tests with the ABB IRB 6660 industrial robot.

Keywords Multi body model · Dynamic prediction · Flexible body · Machining · Stability

S. Mousavi (✉) · V. Gagnol · B.C. Bouzgarrou
Clermont Université Sigma, Institut Pascal UMR 6602 UBP/CNRS/IFMA,
Clermont-Ferrand, France
e-mail: said.mousavi@ifma.fr

V. Gagnol
e-mail: vincent.gagnol@sigma-clermont.fr

B.C. Bouzgarrou
e-mail: belhassen-chedli.bouzgarrou@sigma-clermont.fr

P. Ray
Mines Saint-Etienne, Saint-Etienne, France
e-mail: pascal.ray@mines-stetienne.fr

1 Introduction

Robotic machining productivity can be limited by the appearance of instability phenomena due to chatter vibrations. Hence, the exploitation of industrial robots in a machining context requires machining stability to be mastered. Most robotic machining research in the literature focuses on robot precision in terms of pose exactitude (end-effector position and orientation) and repeatability [1, 2]. Studies on chatter vibrations during robotic machining operations are much rarer.

The dynamic behavior of the robot within the workspace depends on its configuration. Several researchers have reported their studies on the dynamic modeling and identification of robot [1, 3–5]. Two approaches are generally used for numerical modeling of the robot's dynamic behavior: (a) flexible joints and rigid bodies approach and (b) both flexible joints and bodies approach [4].

The flexible joints and rigid bodies approach is an effective tool to model machine-tools dynamics. The advantages in term of computing time justify the application of this method in many researches, where dynamic behavior is mainly influenced by low frequency dominant modes and the rigidity of the joints are weak compared to the rigidity of the links [1, 6].

Mejri et al. [3], Tunc et al. [5] and Bisu [7] experimentally investigated effect of end-effector position on the machining robot dynamic behavior. The experimental identification permits to determine the actual dynamic parameters of the structure, but they are valid for a given position and configuration where the tests are realized. Moreover, experimental identifications are very expensive and time consuming. However, these tests are usually required as effective tools to calibrate numerical models [8].

Mousavi et al. [4] have studied two modeling approaches and compared them according to their respective capabilities to predict machining stability. This comparison demonstrates the necessity of considering link flexibilities for stability analysis in robotic machining. In order to consider the flexibility of the robot links, three methods can be used: finite element method (FEM) [9], Matrix structural analysis method (MSA) [10], Virtual joint method (VJM) [11].

Based on the VJM only low frequencies for the robot can be obtained, and these are far from machining frequencies, especially in high-speed machining. FEM due to the high model complexity and calculation cost is impracticable [8]. Matrix structural analysis method (MSA) as a simplified FEM uses equivalent beam elements for the modeling of mechanical structure. It is used for model reduction. This method has been applied to predict dynamic behavior of machine parts such as spindle rotor [10] as well as complete machine-tools [8].

In Sect. 2, the MSA method is used to elaborate a reduced, but enough accurate dynamic model of the ABB IRB 6660 industrial machining robot. This model is used in Sect. 3 to predict stability conditions, according to the configurations of the robot. Finally, conclusions are presented in Sect. 5.

2 Dynamic Modeling of the ABB IRB Robot

The ABB IRB 6660 industrial machining robot with six active joints ($q_1, q_2 \dots q_6$) and three passive joints (q_{p1}, q_{p2}, q_{p3}) has 6 robot’s degrees of freedom as shown in Fig. 1a. It is a hybrid robot with a serial part (with three active joints q_4, q_5 and q_6) and a parallel part (two active joints q_2 and q_3). The joints stiffness are identified experimentally by Subrin et al. [2] (Table 1).

The dynamic modeling of the robot, for a given configuration x_0 in Cartesian space, can be expressed by the following differential equation:

$$M_x(x_0)\delta_x(t) + C_x(x_0)\delta_x(t) + K_x(x_0)\delta_x(t) = F(t) \tag{1}$$

where $\delta_x(t) = x(t) - x_0$ is an infinitesimal displacement of the end-effector relative to a reference configuration x_0 . M_x , C_x and K_x are respectively robot system mass, damping and stiffness matrices in Cartesian space (Global frame). $F(t)$ is the exiting cutting force vector in milling operations. The proportional damping model is used which makes damping matrix (C_x) as a linear combination of the mass (M_x) and rigidity (K_x) matrices (*Rayleigh hypothesis*).

$$C_x = \alpha K_x + \beta M_x \tag{2}$$

α and β values are determined through a calibration procedure on the basis of experimental results.

Mousavi et al. [4] proposed the flexible joint and body approach for analyzing dynamics properties and then machining stability of the ABB IRB 6660 robot. In this paper, the body flexibility is taken into account by the MSA modeling method.

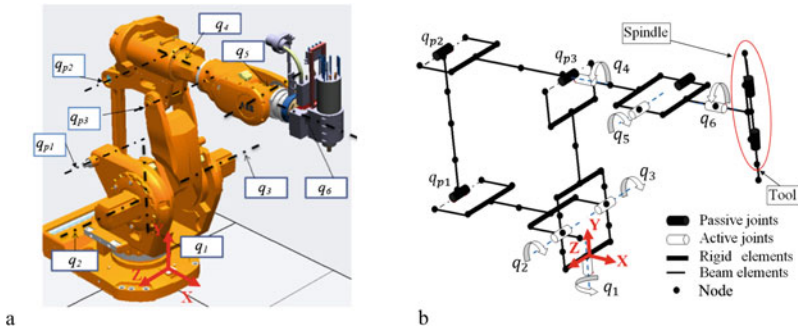


Fig. 1 a ABB IRB 6660 serial robot CAD model, b robot modeling by 3D beam elements

Table 1 Joint stiffness values [2]

Axis 1	Axis 2	Axis 3	Axis 4	Axis 5	Axis 6
10^6	2×10^6	2×10^6	4×10^5	4×10^5	4×10^5 N.m/Rad

In this method, each robot body is modeled by a 3D (three dimensions) beam elements combination. The ABB IRB 6660 robot model is composed of an assembly of 3D beam elements as presented in Fig. 1b.

The simplified beam element model of the ABB IRB 6660 robot (Fig. 1b) requires to be readjusted to simulate accurately the dynamic behavior. The equivalent beam elements geometries and damping rates of the structure represent the numeric model parameters to readjust.

2.1 Model Calibration

The robot structure is modeled by beam elements (Fig. 1b) which are a geometric and material approximation of real parameters. The numeric model calibration aims at adjusting these parameters in a two steps procedure:

- **Step 1:** Readjustment of the geometric and materials parameters of robot elements compared to refine FEM model.
- **Step 2:** Readjustment of the spindle-tool model parameters and the robot structure damping rates on the basis of experimental modal analysis results.

In the first step, the beams elements dimensions developed in MATLAB® (MSA method as shown in Fig. 1b) are established as near as possible to the robot body CAD models (provided by ABB company). Figure 2 presents the first step numeric model calibration for a robot component (excepted the spindle, tool-holer and tool). The comparison criteria between the two numerical models developed respectively with MATLAB® and ANSYS® with the same boundary conditions are the weights, mode shapes and natural frequencies.

In the second step, the comparison between the FRF (Frequency Response Function) from the numerical model and from experimental modal analysis enables us to identify the unknown parameters. The numerical model FRF for n mode shapes is determined by the Eq. 3 where ω_{0k} , P_i , η_k and ω are respectively natural

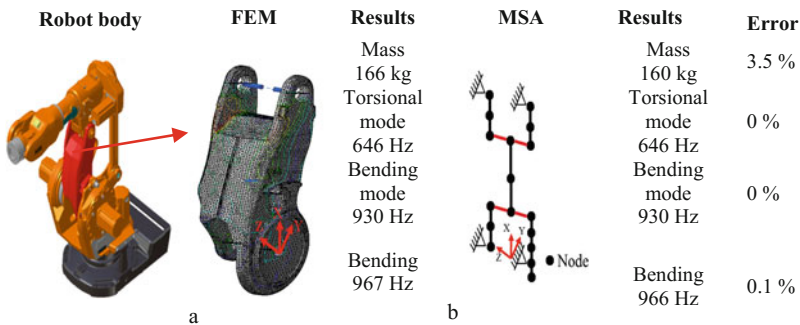


Fig. 2 First calibration step: a FEM on ANSYS, b simplified beam elements on MATLAB

frequencies, mode shape vectors and damping ratios (approximate) of the numerical model.

$$H_{ij}(\omega) = \frac{X_i(\omega)}{F_j(\omega)} = \sum_{k=1}^n \frac{P_{ik}P_{jk}}{-\omega^2 + \omega_{0k}^2 + 2j\eta_k\omega_{0k}\omega} \tag{3}$$

The second calibration step is composed of two levels, respectively the frequency and damping calibrations as shown in Fig. 3 (H_{yy} is the FRF measured and fierce excited in y direction (Global frame as shown in Fig. 4). Figure 3a presents experimental and numeric tool tip FRF before calibration. Figure 3b presents the frequency calibration of the overall structure numeric model (robot-tool holder-tool) compared to experimental modal results as the reference. The spindle and tool holder geometries and materials are defined as optimization variables for model calibration. In the second calibration level (Fig. 3c), the damping parameters (α and β Eq. 2) are readjusted by minimizing the gap between the measured and the modeled tool tip node FRF, using a Matlab[®] optimization routine and a least squares type objective function.

Due to the continuous variation in robot posture along a machining trajectory, the dynamic behavior of the robot varies in consequence. A straight trajectory discretized in 4 points (X1...X4) is selected as shown in Fig. 4a to investigate the modal property evolution. Figure 4b presents the tool-tip FRFs evolution corresponding to the ratio of the tool-tip point frequency response to an impact at the same point.

In Fig. 4b, the appearance and disappearance of the frequency peaks corresponding to the modes shapes during the robot displacement from X1 to X4 can be observed. It can be deduced that the robot displacement changes the stucture modal properties (frequency and mode shapes), and then the robot vibrations behavior.

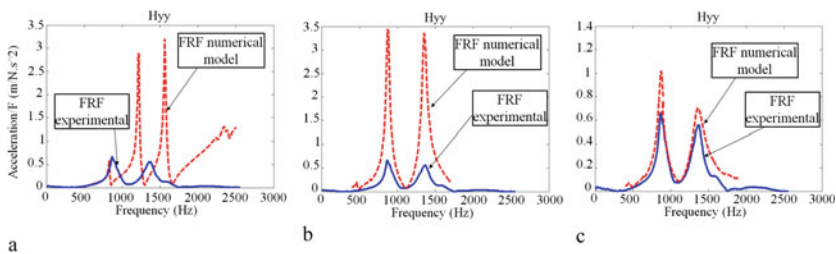


Fig. 3 Second calibration step: comparison between model-based and experimental tool-tip FRF. **a** Initial FRF, **b** frequency calibration, **c** damping calibration



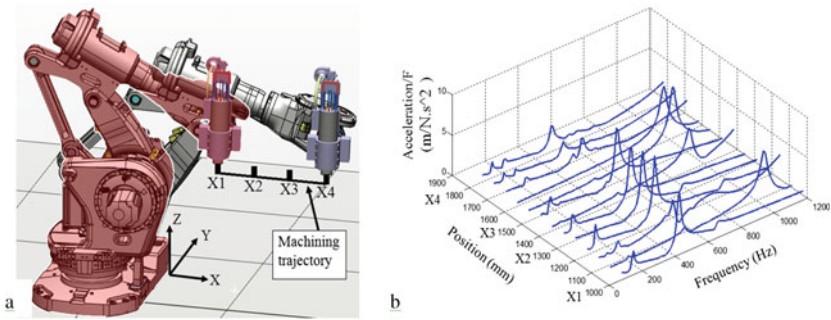


Fig. 4 a Selected machining trajectory. b FRF's variations along the straight trajectory

Therefore, this dynamic behavior variations must necessarily be taken into account for stability analysis in order to identify stable and unstable zones along a machining trajectory.

3 Stability Lobes Diagram of a Robot Machining Operation

In this section, a new representation is proposed to establish machining stability limits with respect to the cutting parameters as well as to robot configurations along the machining trajectory.

The stability lobes based on milling theory proposed by Budak and Altintas [12] are plotted for every point of the trajectory (Fig. 5a). Hence, a three-dimensional stability diagram is established according to the spindle speed, the depth of cut (a_p) and an additional parameter which is the cutting tool position along the machining trajectory (Fig. 5b). The cutting parameters are presented in Table 2:

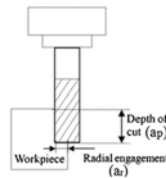


Table 2 Machining parameters

Spindle speed (rpm)	Feed mm/min (mm/rev/tooth)	Cutting speed (m/min)	a_r (mm)
6000	600 (0.05)	226	6



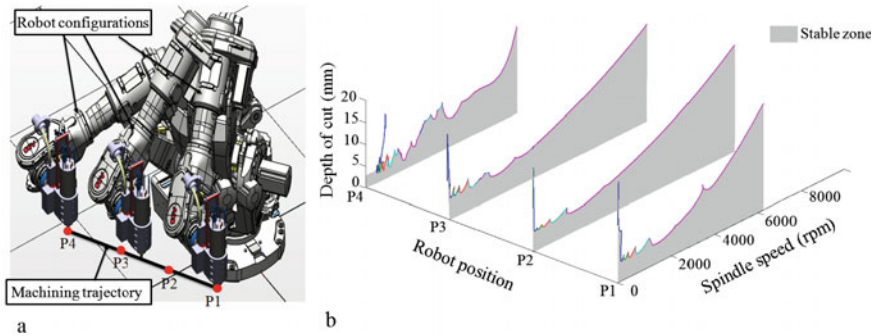


Fig. 5 a Machining trajectory, b three dimensional stability elaboration

Once the 3D stability lobes diagram is obtained, it can be used for the definition of machining strategies according to different criteria as machining with a constant depth of cut, with a constant spindle speed or with a desired configuration. Figure 6 presents a 3D stability lobes diagram according to a straight machining trajectory. If the objective of machining strategy is to machining with a constant depth of cut (a_p) of 8 mm (Fig. 6b) or 5 mm (Fig. 6c); a cross-section of the 3D stability surface through a constant depth-of-cut plane (Fig. 6a) gives the instability zones as a

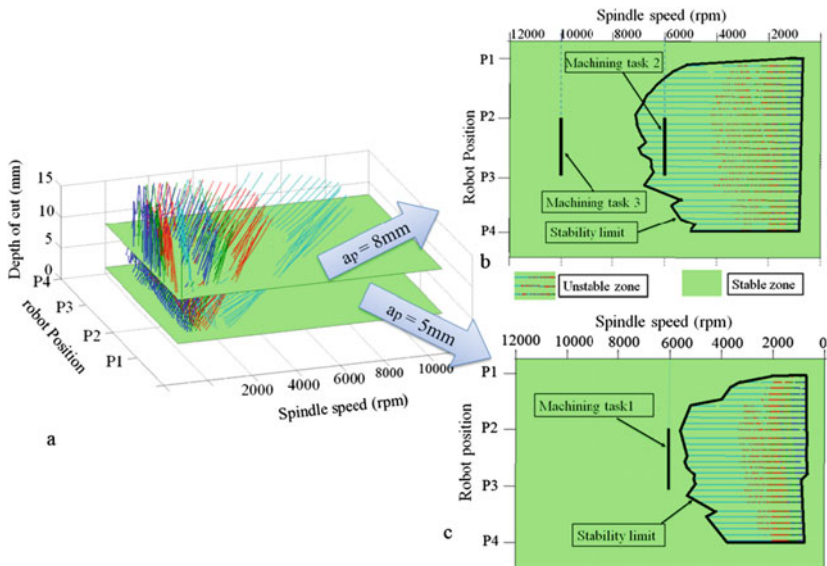


Fig. 6 a 3D stability lobes cross-section for machining with constant a_p , b 8 mm, c 5 mm

Table 3 Experimental Machining task

Task	Spindle speed (rpm)	Feed (Vf) mm/min (mm/rev/tooth)	Cutting speed (m/min)	a_p	a_r	Cutting condition
1	6000	600 (0.05)	226	5	6	Stable
2	6000	600 (0.05)	226	8	6	Instable
3	10000	1000 (0.05)	346.8	8	6	Stable

function of spindle speed and robot end-effector position along the considered machining trajectory (Fig. 6b, c).

The validations of these numerical results are carried out by experimental machining tests with the ABB IRB 6660 industrial robot. Three machining tasks are presented in Table 3.

The experimental machining results indicate a good agreement with the numeric model prediction as shown in Fig. 6b, c.

4 Conclusions

The principal objective of this work was to develop an adaptive dynamic model of a machining robot to posture changes during machining operation. This model enables to determine stability limits along machining trajectories. A numeric model of the industrial machining robot ABB IRB 6660 is developed applying the flexible joints and body approach (MSA method). This numeric model is readjusted by a calibration procedure on the basis of experimental results. The model simulation results show a strong dependence of the robot dynamic behavior according to the posture change along a machining trajectory.

A three-dimensional stability lobes diagram is established in this paper to enable the separation of stable and unstable zones as a function of cutting parameters, taking into account the dynamic variations of the robot along a considered machining trajectory.

Acknowledgments This work was sponsored by the French government research program Investissements d'avenir through the RobotEx Equipment of Excellence (ANR-10-EQPX-44), by the European Union through the program Regional competitiveness and employment 2007–2013 (Auvergne region), by the French Institute for Advanced Mechanics (IFMA) and by the Auvergne regional council.

References

1. Dumas, C., Caro, S., Garnier, S., Furet, B.: Joint stiffness identification of six-revolute industrial serial. In: Conference Papers of Flexible Automation and Intelligent Manufacturing-Intelligent manufacturing and services, vol. 27, pp. 881–888 (2011)

2. Subrin, K., Sabourin, L., Gogu, G., Mezouar, Y.: Performance criteria to evaluate a kinematically redundant robotic cell for machining tasks. *Appl. Mech. Mater.* **162**, 413–422 (2012)
3. Mejri, S., Gagnol, V., Le, T.P., Sabourin, L., Ray, P., Paultre, P.: Dynamic characterization of machining robot and stability analysis. *Int. J. Adv. Manuf. Technol.* (2015)
4. Mousavi, S., Gagnol, V., Bouzgarrou, B.C., Ray, P.: Dynamic behavior model of a machining robot and stability prediction. *ECCOMAS, Zagreb* (2013)
5. Tunc, L.T., Barnfather, J.: Investigation of hexapod robot dynamics and effects in milling. *HSM 2014, Prague, Czech Republic*
6. Pan, Z., Zhang, H., Zhu, Z., Wang, J.: Chatter analysis of robot machining process. *J. Mater. Process. Technol.* **173**, 301–309 (2006)
7. Bisu, C., Cherif, M., Gérard, A., K'nevez, J.Y.: Dynamic behavior analysis for a six axis industrial machining robot. In: *Advanced Materials Research*, vol. 423, pp. 65–76. *Trans Tech Publications* (2011)
8. Kessentini, A., Chevalier, G., Louati, J., Rivière, A., Haddar, M.: F.E.M. of the Drilling machine-tool including the gyroscopic effect. *Adv. Produc. Eng. Manag.* **2**, 63–78 (2007)
9. Bouzgarrou, B.C., Ray, P., Gogu, G.: New approach for dynamic modeling of flexible manipulators. In: *Proceedings of the Institution of Mechanical Engineers, Part K, Journal of Multi-body Dynamics*, vol. 219, pp. 285–298 (2005)
10. Gagnol, V., Bouzgarrou, B.C., Ray, P., Barra, C.: Model-based chatter stability prediction for high-speed spindles. *Int. J. Mach. Tools Manuf* **47**, 1176–1186 (2007)
11. Klimchik, A., Bondarenko, D., Pashkevich, A., Briot, S., Furet, B.: Compliance error compensation in robotic-based milling. In: *Informatics in Control, Automation and Robotics*, pp. 197–216. *Springer International Publishing* (2014)
12. Altintas, Y.: Analytical prediction of three dimensional chatter stability in milling. *JSME Int. J.* **44**(3), 717–723 (2001)

Part XII
Robotics—Biomedical Engineering

Augmented PID Control of a 2PPR-2PRP Planar Parallel Manipulator for Lower Limb Rehabilitation Applications

J.K. Mohanta, M. Santhakumar, S. Kurtenbach,
B. Corves and M. Hüsing

Abstract This paper addresses the dynamic control of a 2PRP-2PPR vertical planar parallel manipulator. This proposed manipulator can be used for the purpose of lower limb rehabilitation applications (in specific sitting/lying type of lower limb rehabilitation applications). The kinematic and dynamic model of the proposed manipulator are derived and discussed. An augmented PID control along with an uncertainty estimator is proposed for the motion control of the manipulator. The proposed system performance along with the motion controller is demonstrated numerically for the application of lower limb rehabilitation therapies using a clinically recorded gait data. The robustness of the controller and its parameter sensitivity are analysed through different operating conditions and their results are presented. Note: P—stands for Prismatic/translation joint and R—stands for Rotary/revolute joint.

Keywords 2PRP-2PPR · Parallel planar manipulator · Dynamic control · Augmented PID · Lower limb rehabilitation

J.K. Mohanta · M. Santhakumar (✉)
Indian Institute of Technology Indore, Indore, India
e-mail: santhakumar@iiti.ac.in

J.K. Mohanta
e-mail: jkmjayant@gmail.com

S. Kurtenbach · B. Corves · M. Hüsing
RWTH Aachen University, Aachen, Germany
e-mail: kurtenbach@igm.rwth-aachen.de

B. Corves
e-mail: corves@igm.rwth-aachen.de

M. Hüsing
e-mail: huesing@igm.rwth-aachen.de

1 Introduction

Recovery after a severe damage to the nervous system is the main concern of physiotherapy. The systematic recovery treatment is called motor rehabilitation therapy. These are done by continuous movement of the affected limb [1]. For lower limb rehabilitation many mechanisms has been available and proposed. The clinically used systems are either body weight supported or sitting/lying type. Among the sitting/lying type systems, commercially available Motion Maker [2] has RRR serial configuration which is simple but the entire load comes to the actuator as actuators are on the orthoses. Another mechanism namely Physiotherabot [3] is used a counter weight and strategic belt drive system so that all the motors remains at the base and orthoses is actuators free, this mechanism doesn't provide any movement for the ankle joint. A proposed mechanism [4] to improve the dynamic stability used eccentric lead screw based joint, this makes the mechanism highly safe and stable but orthosis consists of actuators which makes it bulky. Another partially parallel manipulator for the purpose of physical fitness is 'The Lambda' [5]. This has 2PRR configuration manipulator for each leg, which resembles Greek letter ' λ '. This uses passive method to move the limbs of the user, in the absence of any orthoses it can't treat patients in bedridden condition. To make this mechanism suitable for lower limb rehabilitation an improved lambda mechanism [6] was proposed. This has as actuator free orthoses connected with the mechanism. Another gait rehabilitation device which treats the person in sitting/lying position is 'Supine' [7]. This device has three linear actuators which take care of the leg movements. Two actuators are on base to control hip and knee joint while the third linear actuator controls the ankle movement. This mechanism is also partially parallel and orthosis contains actuators. NEUROBike [8] another partially parallel manipulator which controls the leg movement passively by the help of the footplate, no orthoses is provided in this mechanism.

To overcome above limitations and improve the existing lower limb rehabilitation mechanisms, this paper proposes a 2PRP-2PPR manipulator for sitting/lying type lower limb rehabilitation tasks. The proposed 2PRP-2PPR is very similar to 2PRP-1PPR [9], but an additional PPR leg has been provided for better compliance and rigidity. The proposed manipulator is completely parallel, so it has advantage over partially parallel and serial mechanisms in terms of error accumulation as serial manipulator faces more error accumulation than parallel manipulators [10]. This manipulator is vertical, planar and parallel, whose end effector serves as a footplate for the leg orthosis to follow desired gait motion trajectories in the vertical plane. The proposed manipulator provides the hip, knee and ankle joint motions of the orthosis (lower limb) through the help of three active prismatic/translation joints. The proposed manipulator is fully decoupled parallel manipulator with lower occupancy on clinical space; this is as less as serial orthosis based LLRR.

The organization of the remaining paper as follows as: Sect. 2 discusses the kinematic model of the proposed manipulator and the dynamic model of the proposed

system is described in Sect. 3. The proposed control scheme is presented in Sect. 4 and followed by the performance analysis in Sect. 5. Finally, Sect. 6 discusses the concluding remarks of this work.

2 Kinematic Model of the Proposed System

The proposed system comprises of a parallel manipulator and a leg orthosis as shown in Figs. 1 and 2, respectively. The proposed parallel manipulator consists of four active prismatic joints as named in Fig. 1 as joints r_1, r_2, r_3 and r_4 .

Among which prismatic joints r_2 and r_4 moves together, as previously mentioned that this arrangement is made for better compliance and rigidity. The prismatic joints r_1 and r_3 are independent of each other, in this way there is only 3 DOF as previously mentioned. The end effector is placed at intersection of linear guides connecting prismatic joints r_1 with r_3 and r_2 with r_4 , which rotates with the linear guide connecting prismatic joints r_1 with r_3 . The leg orthosis consist of three links namely, L_{thigh}, L_{crus} and L_{ankle} in RRR configuration. Generally the clinical gait pattern data is recorded in terms of the limb's hip, knee and ankle joint movements which are

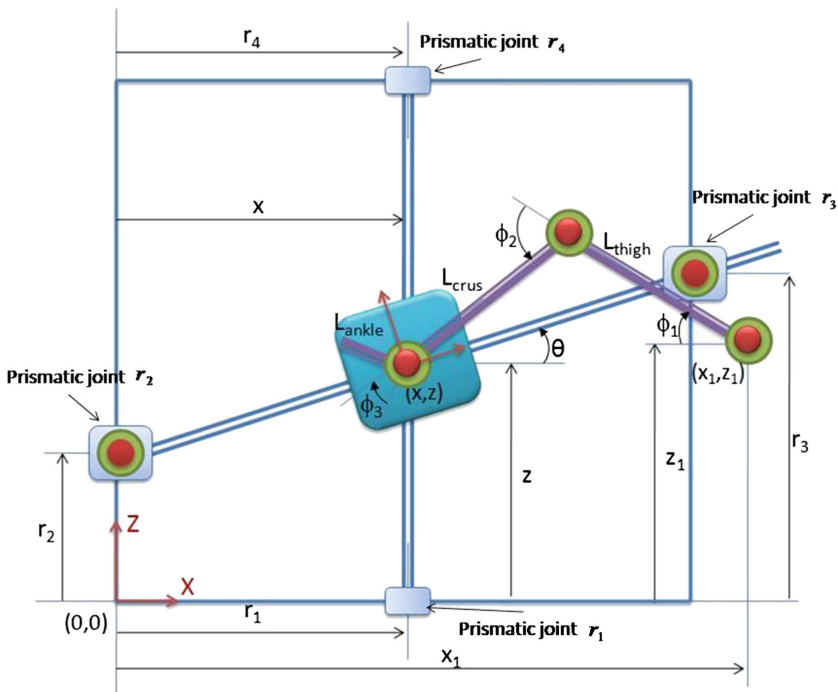


Fig. 1 Conceptual and virtual diagram of 2PPR-2PRP vertical parallel manipulator



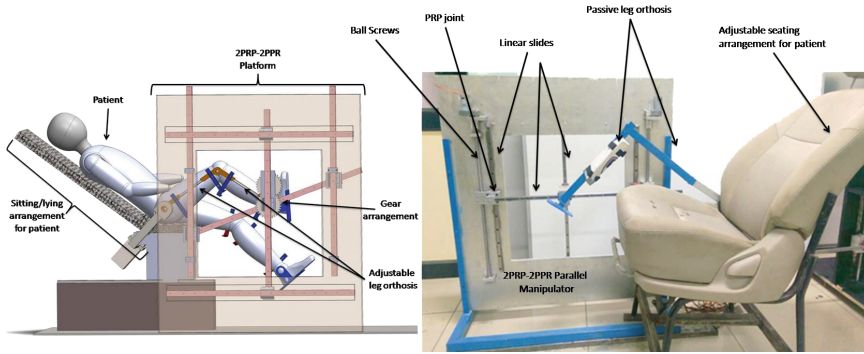


Fig. 2 Solid model and preliminary prototype

here represented by ϕ_1 , ϕ_2 and ϕ_3 respectively. The forward kinematics of the leg orthosis is given by

$$\begin{aligned}
 x &= x_1 - L_{thigh} \cos \phi_1 - L_{crus} \cos(\phi_1 + \phi_2) \\
 z &= z_1 + L_{thigh} \sin \phi_1 + L_{crus} \sin(\phi_1 + \phi_2) \\
 \theta &= \phi_1 + \phi_2 + \phi_3
 \end{aligned}
 \tag{1}$$

where, x and z are the positions of the ankle joint of the orthosis and θ represents angle of the link L_{ankle} with respect to the horizontal axis in the x - z plane, whereas x_1 and z_1 are the coordinates of the hip joint. The expressions in (1) convert the gait pattern data to end effector data for the platform. Using inverse kinematics of the 2PRP-2PPR manipulator the actuators can be controlled to obtain the required task trajectories.

Inverse kinematics of the parallel manipulator is given as follows:

$$\begin{aligned}
 r_1 &= r_4 = x \\
 r_2 &= z - x \tan \theta \\
 r_3 &= z + (s - x) \tan \theta
 \end{aligned}
 \tag{2}$$

Here, s is the horizontal distance between the actuator r_2 and r_3 or the span of the manipulator. Using Eqs. (1) and (2) all the physiotherapeutic motion can be obtained by actuating the proposed mechanism.

3 Dynamics of the Proposed Manipulator

Understanding the dynamic relationship between the joint forces and their effect on the joint parameters is crucial in designing the system as it communicates the effect of the driving forces on the end effector. The method adopted for the formulation of the

dynamic model is Euler-Lagrange formulation which is based on the total energy of the system. This method has been adopted because of its simplicity and its accuracy in prediction of the relationships aforementioned. The generalized equations of motion of the manipulator can be written as follows:

$$\mathbf{M}(q)\ddot{\mathbf{q}} + \mathbf{C}(q, \dot{q})\dot{\mathbf{q}} + \mathbf{g}(q) = \boldsymbol{\tau} + \mathbf{f}_{dis} \quad (3)$$

where, \mathbf{q} is the vector of joint variables and, $\mathbf{q} = [r_1, r_2, r_3]^T$, r_1 , r_2 and r_3 are the joint translational displacements of the corresponding manipulator joints. $\mathbf{M}(q)\ddot{\mathbf{q}}$ is the vector of inertial forces and moments of the manipulator, $\mathbf{C}(q, \dot{q})\dot{\mathbf{q}}$ is the vector of Coriolis and centripetal effects of the manipulator, $\mathbf{g}(q)$ is the gravity vector of the manipulator, \mathbf{f}_{dis} is the vector of total disturbance (unknown) which includes both system uncertainties and external disturbances. The actual disturbance vector (\mathbf{f}_{dis}) can be expressed as follows:

$$\mathbf{f}_{dis} = \mathbf{f}_{idis} + \mathbf{f}_{edis} \quad (4)$$

where, \mathbf{f}_{edis} is the vector of external disturbances such as disturbances due to underwater current, waves, etc. \mathbf{f}_{idis} is the vector of internal disturbances such as disturbances due to system uncertainties, sensor noises, etc., it can be expressed as:

$$\mathbf{f}_{idis} = \Delta\mathbf{M}(q)\ddot{\mathbf{q}} + \Delta\mathbf{C}(q, \dot{q})\dot{\mathbf{q}} + \Delta\mathbf{g}(q) + \mathbf{F}(q, \dot{q})\dot{\mathbf{q}} + \nu \quad (5)$$

where, $\Delta\mathbf{M}(q)\ddot{\mathbf{q}}$, $\Delta\mathbf{C}(q, \dot{q})\dot{\mathbf{q}}$ and $\Delta\mathbf{g}(q)$ are the components which represent the variation of the actual system model from the nominal model (variations due to parameter uncertainties). Is the manipulator joint frictional effects which includes static, Columb and viscous frictional components. Is the vector of internal disturbances due to the system process noises and the measurement noises.

4 Augmented PID Position Tracking Control Scheme

In this paper, an improved augmented robust nonlinear PID controller along with uncertainty estimator is proposed which is an improved version of the controller proposed by Meysar [11] to track a desired reference position trajectory of the parallel manipulator. The proposed control vector along with estimated uncertainty/disturbance vector is given as follows:

$$\boldsymbol{\tau} = \hat{\mathbf{M}}(q) \left(\ddot{\mathbf{q}}_r + \mathbf{K}_C \text{sign}[\chi_{PID}]^\gamma + \mathbf{K}_O \int \chi_{PID} dt \right) + \hat{\mathbf{C}}(q, \dot{q})\dot{\mathbf{q}} + \hat{\mathbf{g}}(q) \quad (6)$$

where,

$$\begin{aligned} \ddot{\mathbf{q}}_r &= \ddot{\mathbf{q}}_d + 2\Gamma\dot{\tilde{\mathbf{q}}} + \Gamma^2\tilde{\mathbf{q}} \\ \chi_{PID} &= \dot{\tilde{\mathbf{q}}} + 2\Gamma\tilde{\mathbf{q}} + \Gamma^2 \int \tilde{\mathbf{q}} dt \end{aligned} \quad (7)$$

\mathbf{K}_C and \mathbf{K}_O are the controller and estimator gain matrices of the proposed controller, respectively and chosen as symmetric positive definite matrices. $\ddot{\mathbf{q}}_r$ is the virtual reference (desired) acceleration vector. $\ddot{\mathbf{q}}_d$, $\dot{\mathbf{q}}_d$ and \mathbf{q}_d are the given desired joint position, velocity and acceleration vectors, respectively. Γ is a positive diagonal matrix. χ_{PID} is the centralized PID control input vector. $\hat{\mathbf{M}}(q)$, $\hat{\mathbf{C}}(q, \dot{q})$ and $\hat{\mathbf{g}}(q)$ are the known values (approximated model parameter values) of inertia matrix, Coriolis and centripetal matrix and restoring effects of the manipulator, respectively.

5 Controller Performance Analyses Through Simulations

The effectiveness of the controller in following a given desired trajectory in the presence of internal and external disturbances namely friction, system uncertainties, payload variations, unmodelled dynamics and unknown disturbance are validated by performing the task of a complex trajectory tracking task based on a clinical data. Further, the proposed controller performance compared with the weighted PID control with gravity compensation and comparative results are presented in Fig. 3. The weighted PID control scheme with gravity compensation is given as [12]:

$$\tau = \hat{\mathbf{M}}(q) \left(\mathbf{K}_p \tilde{\mathbf{q}} + \mathbf{K}_I \int \tilde{\mathbf{q}} dt + \mathbf{K}_D \dot{\tilde{\mathbf{q}}} \right) + \hat{\mathbf{g}}(q) \tag{8}$$

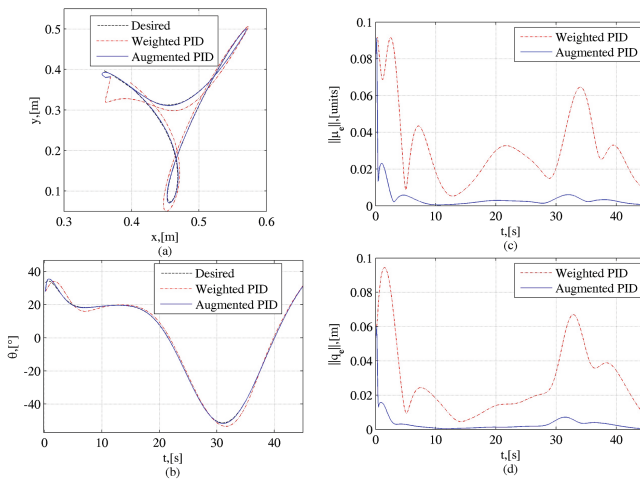


Fig. 3 Controller performance for the clinical gait pattern; **a** task space position trajectories, **b** task space end effector orientation trajectories, **c** time trajectories of norm of task space tracking errors, and **d** time trajectories of norm of joint space tracking errors



where, \mathbf{K}_p , \mathbf{K}_I and \mathbf{K}_D are the proportional, integral and derivative gains of the controller, respectively. Both controllers are considered when both controllers are presented almost same results at an ideal working condition.

The simulation parameters are as follows: $\mathbf{K}_C = 10\mathbf{I}_{3 \times 3}$, $\mathbf{K}_O = 4\mathbf{I}_{3 \times 3}$, $\gamma = 0.9$, $\Gamma = 3\mathbf{I}_{3 \times 3}$, $\mathbf{K}_p = 10\mathbf{I}_{3 \times 3}$, $\mathbf{K}_I = 10\mathbf{I}_{3 \times 3}$, $\mathbf{K}_D = 10\mathbf{I}_{3 \times 3}$. The computer simulations are conducted through the help of MATLAB with a step size of 0.1 s, and the Runge-Kutta fourth order numerical integration solver is used for the simulations. The mass of the end effector (ankle/foot mass) is taken as 1.5 kg and the mass of the patients limbs are assumed as 7 and 9 kg for thigh and crus, respectively. The manipulator parameters are as follows:

$m_1 = 0.8 \text{ kg}$; $m_2 = 0.8 \text{ kg}$; $m_3 = 0.8 \text{ kg}$; $m_4 = 0.8 \text{ kg}$; $m_5 = 2.08 \text{ kg}$; $m_6 = 2.08 \text{ kg}$; $m_7 = 2.02 \text{ kg}$; $g = 9.81 \text{ m/s}^2$; $L_{thigh} = 0.45 \text{ m}$; $L_{crus} = 0.42 \text{ m}$; uncertainty is 10 %.

From Fig. 3, it is observed that the performance of the proposed controller is better than the conventional controller in terms of norm of tracking errors.

The robust and sensitivity analyses results are presented in Fig. 4. From the results, the following observations can be found as: variation of \mathbf{K}_C provide faster convergence with increase in value, variation of \mathbf{K}_O is not affecting much to the overall performance. However, variation of γ is sensitive, in specific for lower values, the errors are reaching high (response had oscillations) and while increasing this value contributes reduction in tracking errors. Similarly, the proposed controller is robust in

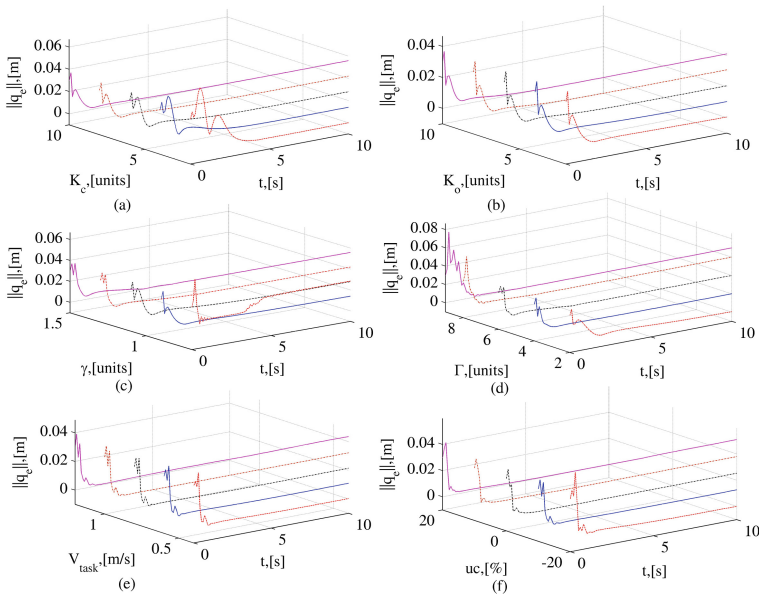


Fig. 4 Robustness and sensitivity analyses results, The change in the norm of the joint-space errors during variation of: **a** K_C gain, **b** K_O gain, **c** Γ gain, **d** γ constant, **e** uncertainty and **f** end effector velocity



terms of variation in system uncertainties and working conditions which can be found in Fig. 4e, f. This is due to the adaptive and robust control ability of the proposed control scheme.

6 Concluding Remarks

In this paper, a light weight 3DOF planar parallel manipulator 2PRP-2PPR is proposed. An augmented robust PID control scheme along with an uncertainty estimator is designed and applied for a predefined trajectory tracking for lower limb rehabilitation tasks.

As proposed augmented PID controller uses weighted matrix and for simplicity in this paper it is considered as the inertia matrix of the manipular. This weighted matrix along with controller gain matrices which will scale the gain values and eliminates the tuning of controller gains. Poor knowledge of the system parameters is sufficient to design the proposed controller. Proposed controller has simple control structure and design. Hence, it can be used for real time implementation with low cost microprocessor. This guarantees the performance of the pro-posed system along with control scheme for usage in lower limb rehabilitation applications which is the sole motive behind developing this proposed manipulator system.

Acknowledgments This research was supported in part by the Humboldt Fellowship funded by the Alexander von Humboldt (AvH) Foundation, Germany and in part by the Extramural Research scheme funded by the Council of Scientific and Industrial Research (CSIR), India (22 (0698)/15/EMR-II/5767).

References

1. Johnson, M.J., Schmidt, H.: Robot assisted neurological rehabilitation at home: motivational aspects and concepts for tele-rehabilitation. In: Public Health Forum, vol. 17, no. 4, pp. 8e1–8e4 (2009)
2. Schmitt, C., Metrailler, P., Al-Khodairy, A.: The motion maker: a rehabilitation system combining an orthosis with closed-loop electrical muscle stimulation. In: Proceedings of the 8th Vienna International Workshop on Functional Electrical Stimulation (2004)
3. Akdogan, E., Adli, M.A.: The design and control of a therapeutic exer-cise robot for lower limb rehabilitation: physiotherabot. *Mechatronics* **21**, 509522 (2011)
4. Wang, W., Hou, Z., Tong, L., Zhang, F., Chen, Y., Tan, M.: A novel orthosis for lower limb rehabilitation robots of the sitting/lying type. *Mech. Mach. Theor.* **74**, 337–353 (2014)
5. Bouri, M., Le Gall, B., Clavel, R.: A new concept of parallel robot for rehabilitation and fitness: the Lambda. In: Proceedings of the IEEE International Conference on Robotics and Biomimetics, (ROBIO 09) (2009)
6. Mohanta, J.K., Saxena, C., Gupta, G., Santhakumar, M.: Kinematic analysis of a passive sitting/lying type lower limb rehabilitation robot. In: Proceedings of the 2nd international and 17th National Conference on Machines and Mechanisms (iNaCoMM15) (2015)
7. Lim, F.M., Foong, R., Yu, H.: A Supine gait training device for stroke rehabilitation. *J. Med. Devices* (2014)

8. Monaco, V., Galardi, G., Coscia, M., Martelli, D., Micera, S.: Design and evaluation of NEUROBike: a neurorehabilitative platform for bedridden post-stroke patients. *IEEE Trans. Neural Syst. Rehabil. Eng.* **20**, 845–852 (2012)
9. Singh, Y., Santhakumar, M.: Inverse dynamics and robust sliding mode control of a planar parallel (2-PRP and 1-PPR) robot augmented with a nonlinear disturbance observer. *Mech. Mach. Theor.* **92**, 29–50 (2015)
10. Merlet, J.P.: *Solid Mechanics and Its Applications*. Springer (2006)
11. Zeinali, M., Notash, L.: Adaptive sliding mode control with uncertainty estimator for robot manipulators. *Mech. Mach. Theor.* **45**, 80–90 (2010)
12. Kelly, R., Santibanez, V., Loria, A.: *Control of Robot Manipulators in Joint Space*. Springer, London, UK (2005)

Human Motion Characterization Using Wireless Inertial Sensors

M. Olinski, A. Gronowicz, M. Ceccarelli and D. Cafolla

Abstract In this paper the developed wireless IMU (inertial measurement unit) system for human motion characterisation has been described. The experimental layout, test modes and protocols were defined. The experiments for the knee joint characterisation during walking on an inclined treadmill were presented. The human knee joint's characterisation with the usage of IMU sensors communicating with an Arduino board connected to a computer, was presented by plots and numerical data from experiments.

Keywords Experimental biomechanics · IMU motion tracking · Gait · Inclined treadmill

1 Introduction

The possibility of a comprehensive diagnosis of the limb's state both in terms of mobility and strength is an important step in proper treatment and rehabilitation process. For instance, slight differences in gait pattern of individual people can be recognized, but those variations extent is sufficiently narrow to allow an analysis of

M. Olinski (✉) · A. Gronowicz

Department of Biomedical Engineering, Mechatronics and Theory of Mechanisms, Wrocław University of Science and Technology, Wrocław, Poland
e-mail: michal.olinski@pwr.edu.pl

A. Gronowicz

e-mail: antoni.gronowicz@pwr.edu.pl

M. Ceccarelli (✉) · D. Cafolla

Laboratory of Robotics and Mechatronics, University of Cassino and South Latium, Cassino, Italy
e-mail: ceccarelli@unicas.it

D. Cafolla

e-mail: cafolla@unicas.it

© Springer International Publishing AG 2017

B. Corves et al. (eds.), *New Advances in Mechanisms,*

Mechanical Transmissions and Robotics, Mechanisms and Machine Science 46,

DOI 10.1007/978-3-319-45450-4_40

a standard gait model. Differences in the leg joints motion can be detected and thus the gait pathologies may be identified [12]. The position of characteristic points of gait in comparison with correct patterns of movement characteristics can be useful not only in problems detection and identification, but also for sport and training to control performing desired movements. The knee joint's motion, often simplified to a one degree of freedom joint with the main movement of flexion/extension in sagittal plane, is particularly important for this assessment [9].

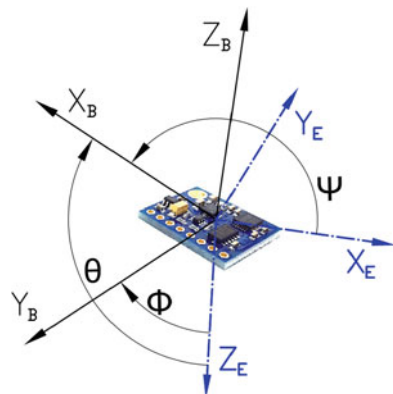
These kind of measurements are typically available by applying stationary systems utilizing a group of cameras like Contemplas motion analysis equipment with two high speed video cameras [6] or the motion capture systems for instance Optotrak Certus with infrared cameras [13]. Other systems include among others Kinect measurement system or based on cables CaTraSys [11]. However, the space and scope of application are limited for these and similar systems, since the detection is correct only in a quite small working space. For these reasons, the above methods cannot be utilized widely and out from the laboratory.

Alternatively to the previously mentioned systems the proposed system including software and inertial measurement units (IMUs) can be used for wireless, outdoor biomechanical measurements and characterization of movement [7, 9, 10]. This paper is focused on a knee joint performance characterization for human gait on an inclined treadmill through evaluation by means of the developed system.

2 Measurement—Method and Technology

The measurement IMU sensor GY-85 Arduino board can measure nine variables: linear acceleration (accelerometer), angular velocity rate (gyroscope), vector of magnetic field (magnetometer)—all in its local three-dimensional coordinate system [11]. Basing on these data, calculation of the sensors orientation in the form of Euler angles (combined data), Fig. 1, is possible by applying one of the sensor fusion methods [7].

Fig. 1 IMU sensor with a scheme of the measured Euler angles



The measured Euler angles— Ψ , θ , Φ —yaw, pitch, roll are presented in Fig. 1, together with the local coordinate system {B} for an IMU sensor (X_B , Y_B in the board’s plane) and the global coordinate system {E}—fixed with the earth axes of northern magnetic pole X_E , gravity Z_E and third perpendicular axis Y_E . Since the earth coordinate system’s Y_E and Z_E axes were considered coincident with the human body’s sagittal plane, the yaw, pitch and roll angles constituted respectively the leg parts’ internal/external rotation, abduction/adduction and flexion/extension angles.

In order to perform the knee joint measurements the sensors were fixed to the human thigh and shin, Fig. 2. The methodology of calculating the knee joint’s flexion/extension angle (Φ_{knee}), as the appropriate difference between the roll angles (Φ_1 , Φ_2) measured by two IMU sensors, by means of

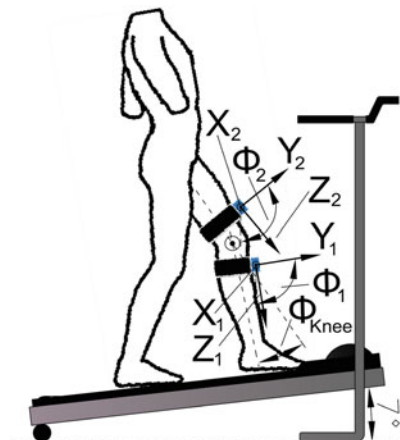
$$\Phi_{knee} = (\Phi_2 - \Phi_{2_calib}) - (\Phi_1 - \Phi_{1_calib}) \tag{1}$$

Furthermore, “online calibration angles” (Φ_{1_calib} , Φ_{2_calib}) were obtained, in order to correct the zero error of sensors axes initial orientation, from averaged IMU measurements of angles in 10 s of experimental subject’s standing straight and still. The measurement system was prepared in the form of two wireless IMU sensors named LARM Sensing IMU System, Fig. 3. Each of the sensors’ assemblies was made by arranging IMU sensor, Arduino nano, Bluetooth module and battery. Building of proper circuit connecting these elements was worked out and tests of the device and its communication with the computer were conducted.

While preparing IMU sensors, for performing the final measurements during experiments, programming and calibration process has been carried out. The appropriate Arduino code enabling communication with the device and data collection was implemented basing on a program for Euler angles calculation using the theory of Direct Cosine Matrix [8]. In order to gather and save raw and combined data, as well as the online calibration angles (15 totally), another program in Processing environment was elaborated.

Using the developed programs and IMU sensors experiments were worked out in order to gather data for knee motion characterization. First, the experimental layout

Fig. 2 Figure of reference for treadmill gait experiments



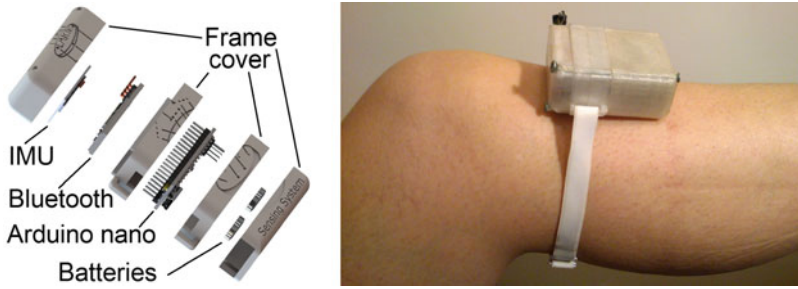
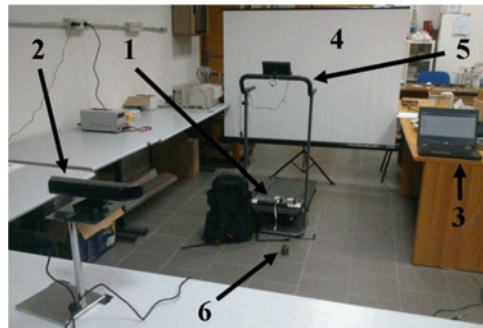


Fig. 3 The LARM sensing IMU system: a a design scheme, b sensor attached to the shin

Fig. 4 Photo of the experimental layout at LARM: a 1—IMU sensors, 2—Kinect, 3—computer, 4—white screen, 5—treadmill/chair, 6—additional weight for the leg



was precisely planned and the positions of elements during experiments were marked in the laboratory, Fig. 4.

Number of tests and measurements were carried out with IMU sensors for knee joint characterization according to the prepared experimental protocol. This paper is focused on the biomechanical data for the knee joint characterization that was



Fig. 5 Photo of the experiment for walking on a treadmill: a normal shoes, b sport shoes

measured while walking on the treadmill with normal shoes and sport shoes, Fig. 5. Kinds of shoes were distinguished similarly as in [11]. The experiments were carried out with normal speed, which in this case means a self-selected velocity according to the comfort of the testing subject.

3 Results of Experiments

Planned experiments were executed with both IMU sensors and Kinect measuring system likewise for preliminary evaluation trials. For each subject experimental modes with 3 trials were performed, with at least nine repetitions of the experimental gesture. The results of relative rotation between the IMU sensors for the right knee joint, were elaborated in the form of plots Figs. 6, 7 and 8.

In the treadmill walking the characteristic points of gait were approximately identified in the plots and the phases of gait were precisely distinguished according to [2, 10], Fig. 6. Repetitions of the analyzed steps can be recognized in plot data.

The experiments' results for an inclined treadmill walking were compared with the ground gait data obtained with various equipment [3–5]. Since the treadmill was unpowered and inclined by about 7° , walking needed some effort and was not fully comparable with the ground gait. Nevertheless, the overall character of ground movement could be used and a more thorough comparison was also useful to show the existing differences between the ground gait and walking on an inclined treadmill. Couple of general determinants of correct ground gait were also used. These claim that the knee angle close to 20° and 65° should be achieved respectively at midstance point and approximately the midswing point [12].

Not only the numerical values for the characteristic points were obtained, but also ranges and averages were calculated (Table 1), where: Range_A—range of the

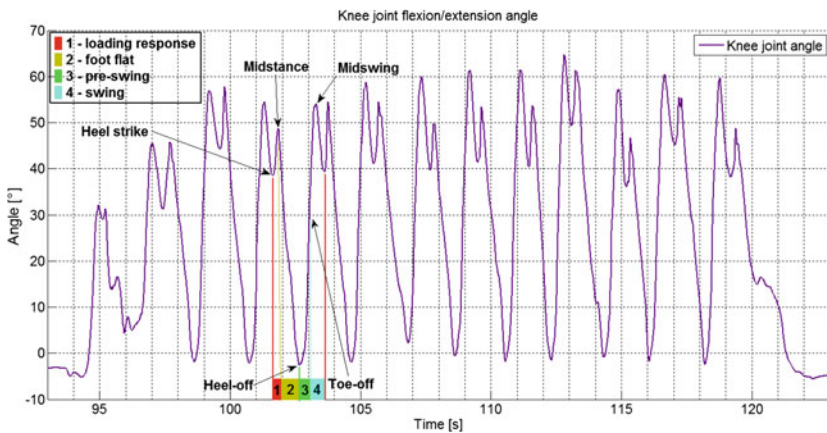


Fig. 6 Angle Φ_{knee} for knee flexion/extension—normal shoes, subject 2

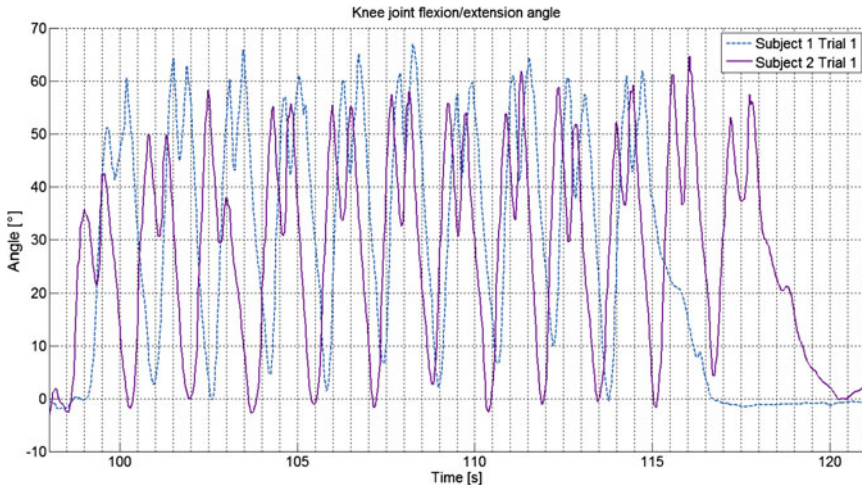


Fig. 7 Angle Φ_{knee} for knee flexion/extension—sport shoes, subject 1 and 2

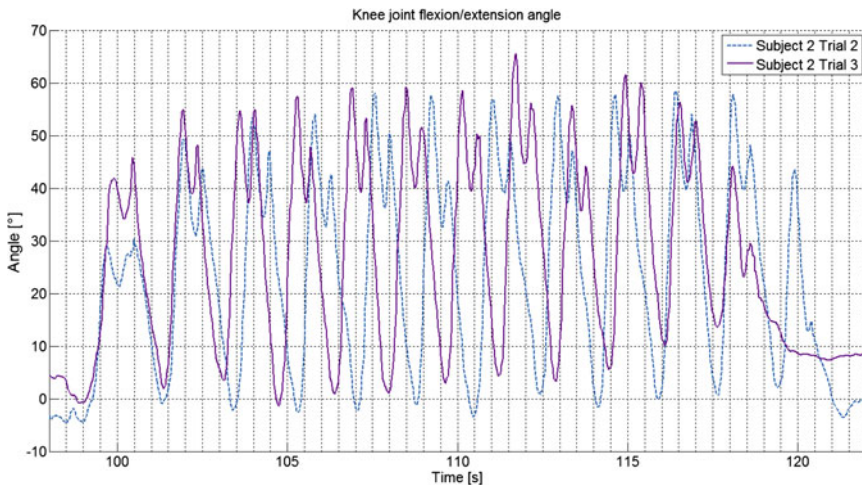


Fig. 8 Angle Φ_{knee} for knee flexion/extension—normal shoes, subject 2

knee’s flexion in the loading response phase for absorption of impact (called the range of absorption); Range_S—range of angle change obtained in the pre-swing and swing phases, so difference between the heel off and midswing points that is in most cases equal to the maximum ROM in the step (the range of swing).

The comparison of trials for normal and sport shoes revealed, that both checked ROMs showed only small differences. Range of absorption (Range_A) was higher



Table 1 The average values of knee joint's flexion/extension angular characteristics calculated from all trials for each experimental subject (in deg)

Subject and mode	Heel strike	Midstance	Range_A	Heel off	Mid-swing	Range_S
Sub 1—normal shoes	41.40	58.18	16.77	6.89	61.96	55.07
Sub 2—normal shoes	38.33	50.12	11.79	-0.07	58.27	58.33
Sub 1—sport shoes	41.69	62.09	20.40	6.52	58.92	52.40
Sub 2—sport shoes	39.58	57.95	18.37	2.87	59.89	57.02

for sport shoes by about 4° and 7° respectively for the first and second subject. The range of swing (Range_S) was only a little smaller in case of sport shoes, approximately by 3° and 1° respectively for the subjects. As for the characteristic points, the only significant difference was observed for the midstance point, for which the angle was larger in case of sport shoes by about 4° and 7° .

Generally, according to the obtained results for walking on an inclined treadmill, the point of heel strike takes place at a larger angle—about 40° instead of 0° for level gait to shorten the leg and compensate for the height of the treadmill over flat ground in the point of initial contact. The angle reaches at midstance about 50° to 62° , instead of 20° , so the obtained range of angle absorption equals 11° to 20° . Despite, the fact that both points—heel strike and midstance show significantly larger values than for level walking, the compatibility of the obtained Range_A with the one in typical gait—about 15° to 20° is worth to be noted. Furthermore, the point heel-off takes values of approximately 0° to 6° , while the midswing is around 60° and the Range_S reaches about 52° to 58° . It is nearly the typical gait value, since angles at both points are very close to the expected 0° and 65° . This may be explained by the fact, that the inclined position of treadmill does not affect the swing phase (leg above ground).

The data obtained for the treadmill could have been further evaluated by comparing it for example with results in [1], where walking on a treadmill at four different grades (inclination angles) was presented. The case with 10° inclination was analyzed. The heel strike took place at a raised knee flexion— 40° . This increased flexion continued in further parts of the gait resulting in 50° for midstance, 10° for heel-off and nearly 70° for midswing. These values were very close to the ones obtained in experiments, thus also similar conclusions concerning the differences in comparison to the level walking could be derived from [1], as from the results of performed experiments.

Obtained plots and numerical values prove that the measurement system works properly in an acceptable manner. Data from IMU and Kinect were of comparable range (relative difference less than 1.5 %) suggesting that both systems can be used for joint characterization, but the IMU sensors are easier to apply and offer more kinds of biomechanical data.

4 Conclusions

The experimental characterization of human motion has been worked out with specific reference to walking gait for knee operation by using IMU sensors. A specific procedure has been designed for the usage of IMU sensors that have been designed and built on purpose. The results report numerical characterization of human walking with the wireless IMU sensors that can be used efficiently outdoor, home and with a fairly simple operation that permits tele-monitoring and data evaluation. Further experiments and comparison with other measurement systems will be performed to thoroughly evaluate the developed system's accuracy.

Acknowledgments Part of this work has been developed during an internship of the first author at LARM, Cassino, Italy in 2015, with a scholarship from the project NJK at the Faculty of Mech. Eng. of Wrocław UT supported by EU. The first author wishes to thank staff and students at LARM for the continuous support.

References

1. Alain, L., Fung, J., Barbeau, H.: Adaptation of the walking pattern to uphill walking in normal and spinal-cord injured subjects. *Exp. Brain Res.* **126**, 359–368 (1999)
2. Al-Shuka, H.-F.-N., Allmendinger, F., Corves, B., Zhu, W.-H.: Modeling, stability and walking pattern generators of biped robots: a review. *Robotica* **32**, 907–934 (2014)
3. Cappozzo, A., Croce, U., Leardini, A., Chiari, L.: Human movement analysis using stereophotogrammetry, Part 1: theoretical background. *Gait Posture* **21**, 186–196 (2005)
4. Dathe, H., Gezzi, R., Kubein-Messenburg, D., Nägerl, H.: Characteristic points and cycles in planar kinematics with application to the human gait. *Acta Bioeng. Biomech.* **17**(1), 75–86 (2015)
5. Dziuba, A., Żurek, G., Garrard, I., Wierzbicka-Damska, I.: Biomechanical parameters in lower limbs natural walking and Nordic walking at different speeds. *Acta Bioeng. Biomech.* **17**(1), 95–101 (2015)
6. Geonea, I., Ceccarelli, M., Carbone, G.: Design and analysis of an exoskeleton for people with motor disabilities. In: *The 14th IFToMM World Congress*, Taipei, Taiwan (2015)
7. Moreno, J.-C., et al.: Wearable robot technologies. In: *Wearable Robots: Biomechatronic Exoskeletons*. Wiley, Chichester, UK (2008)
8. Premerlani, W., Bizard, P.: Direction cosine matrix IMU: theory (2009). <https://github.com/ptrbrtz/razor-9dof-ahrs/wiki/Tutorial>
9. Qiu, S., et al.: Ambulatory estimation of 3D walking trajectory and knee joint angle using MARG sensors (2014). *IEEE 978-1-4799-4233-6/14*
10. Seel, T., Raisch, J., Schauer, T.: IMU-based joint angle measurement for gait analysis. *Sensors* **14**, 6891–6909 (2014)
11. Varela, M., Ceccarelli, M., Flores, P.: A kinematic characterization of human walking by using CaTraSys. *Mech. Mach. Theor.* **86**, 125–139 (2015)
12. Zembya, A.: *Kinezyterapia*, vol. II. Kasper Publishing House (2002)
13. Żuk, M., Pezowicz, C.: Kinematic analysis of a six-degrees-of-freedom model based on ISB recommendation: a repeatability analysis and comparison with conventional gait model. *Appl. Bionics Biomech.* (2015)

Trajectory Analysis for Modified Jansen Leg Mechanism Configuration

F. Pop, E.-C. Lovasz, C. Pop, V. Dolga and S.M. Grigorescu

Abstract Starting from a previous research regarding Jansen type leg mechanism that was implemented in the structure of a walking robot, few problems were identified. One of these problems was related to the reduced number of DOFs that it possesses and the step height described by the end point of the leg during walking. After conducting a series of simulations regarding the path curves described by the end point of Jansen's leg configuration, a limited number of paths are analysed. In spite of the numerous possibilities for varying the link lengths, it has been observed that for a slight variation of the distance between the fixed joints along horizontal axis, the step height can be increased. The shapes of the path curves described by these modified configurations are analysed and compared with the original one based on the length and the height of the step values. Based on the observations made upon the new path curves obtained a practical solution is proposed. This consists in adding a second DOF to the leg mechanism that will allow adjusting the distance between the fixed joints.

Keywords Leg mechanism · Walking robot · Kinematic analysis · Path curve

F. Pop (✉) · E.-C. Lovasz · C. Pop · V. Dolga · S.M. Grigorescu
Politechnica University of Timisoara, Timisoara, Romania
e-mail: florina.pop@upt.ro

E.-C. Lovasz
e-mail: erwin.lovasz@upt.ro

C. Pop
e-mail: cristian.pop@upt.ro

V. Dolga
e-mail: valer.dolga@upt.ro

S.M. Grigorescu
e-mail: sanda.grigorescu@upt.ro

1 Introduction

Leg mechanisms are widely used in the construction of walking robots. The advantages brought by these mechanisms determined many researchers to develop a series of walking machines for different purposes [1, 2]. Finding the best leg configuration for each design concept implies passing through a series of analysis and simulation processes.

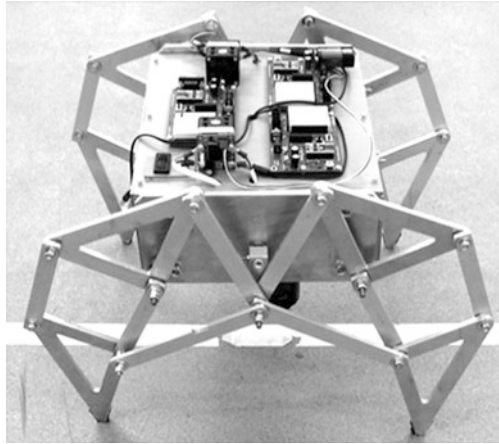
Trajectory described by the end point of the leg is also one of the key aspect that should be analyzed for a leg mechanism in order to implement it in a walking machine structure [3, 4].

In the literature, various types of configurations based on spatial and planar linkages are analyzed [5]. A variety of these linkages were effectively been used in practical applications. For example, pantograph mechanism combined with Chebyshev mechanism was implemented in the structure of a biped robot which described a path similar to a human [6]. Klann linkage is another example of mechanism that has been utilized for an autonomous underwater walking robot due to its particular path curve similar to a lobster [7]. Jansen type of linkage gained popularity and has been implemented in a series of walking vehicles and walking robots during the last years [8–11]. The reduced number of degrees of freedom (DOF's) possessed by this linkage (1 DOF) combined with the specified proportions of the eight bar leg configuration and the particular shape of the path curve described during walking, contributed to the rising scientific interest on its practical applicability.

One low-cost application of this linkage consisted in the design and construction of a quadruped robot (Fig. 1) that is supported by two pairs of linkages connected through two cranks and disposed at each side of the robot chassis [12]. Based on the studies and analysis conducted on the mechanism itself and on the robot, certain conclusions were stated regarding the behavior of the mechanism. In this particular application, the reduced number of DOFs (one actuator for each pair of legs) and the characteristics of its path curve (step length and height) conducted to the necessity to find new improved solutions of Jansen mechanism configuration. The constructed robot structure did not meet all the requirements related to passing over certain types of obstacles. For improving the performance of this mechanism during walking, a method was presented in [13].

For Jansen linkage, the shape and size of the path curve is depending on the links lengths. In order to find a solution regarding the possibility to increase the height of the step for crossing over obstacles, a series of simulations are conducted. From these simulations a solution is proposed by modifying the length of the fixed element. It is observed that a second DOF can be added to the mechanism in order to adapt the step height related to the type of obstacle encountered by the robot. The aim of the article consists in finding a practical solution to be implemented on the leg mechanism in order for the robot to overcome obstacles.

Fig. 1 The variant of quadruped robot built based on Jansen mechanism



2 Kinematic Position Analysis of Leg Mechanism

One important aspect in the study of walking mechanisms is referred to kinematic analysis. The kinematic analysis of Jansen’s type of leg mechanism using closed loop contours based on complex number method as in Eq. (1) was presented in [13]. From this analysis was determined the position of the end point M as in Eq. (2). Details of the notations and angle symbols used in equations for Jansen mechanism can be viewed in Fig. 2.

Fig. 2 Jansen leg mechanism

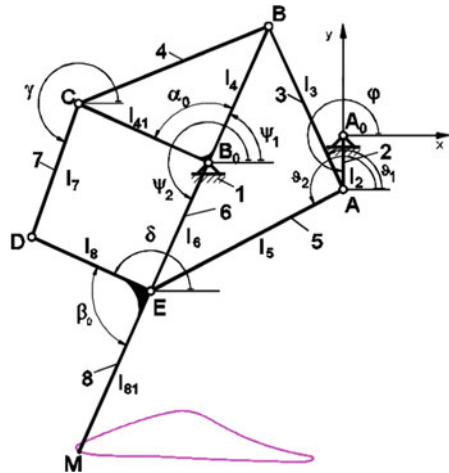
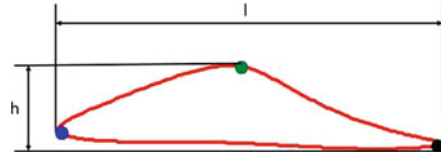


Fig. 3 Path curve and step characteristics of Jansen leg mechanism



$$\begin{aligned} l_2 \cdot e^{i \cdot \varphi} + l_3 \cdot e^{i \cdot \theta_1} &= (x_{B_0} + i \cdot y_{B_0}) + l_4 \cdot e^{i \cdot \psi_1}, \\ l_2 \cdot e^{i \cdot \varphi} + l_5 \cdot e^{i \cdot \theta_2} &= (x_{B_0} + i \cdot y_{B_0}) + l_6 \cdot e^{i \cdot \psi_2}, \\ l_{41} \cdot e^{i \cdot (\alpha_0 + \psi_1)} + l_7 \cdot e^{i \cdot \gamma} &= l_6 \cdot e^{i \cdot \psi_2} + l_8 \cdot e^{i \cdot \delta}. \end{aligned} \quad (1)$$

The end point position analysis offers details about the shape of the trajectory it describes during a complete walking cycle and about characteristics of the step.

The parametric coordinates of the point M are described through the following relations:

$$x_M + i \cdot y_M = x_{B_0} + i \cdot y_{B_0} + l_6 \cdot e^{i \cdot \psi_2(\varphi)} + l_{81} \cdot e^{i \cdot (\delta(\varphi) + \beta_0)}, \quad (2)$$

$$\begin{cases} x_M(\varphi) = x_{B_0} + l_6 \cdot \cos \psi_2(\varphi) + l_{81} \cdot \cos(\delta(\varphi) + \beta_0) \\ y_M(\varphi) = y_{B_0} + l_6 \cdot \sin \psi_2(\varphi) + l_{81} \cdot \sin(\delta(\varphi) + \beta_0) \end{cases} \quad (3)$$

Based on Eq. (3) the path curve shape was obtained in MathCAD program as presented in Fig. 3. This path is approximately similar to an ovoid non-uniform shape trajectory that depends on the positional parameters of both the driving and the driven element, of the link lengths and of the coordinates of the fixed joints.

The crank is considered as input element and realizes a full rotation during a walking cycle. All the other position angles are expressed depending on crank angle φ .

Table 1 Initial link lengths based on Jansen

Elements	Lengths (mm)	Description
x_{B_0}	-38	x coordinate of joint B_0
y_{B_0}	-7.5	y coordinate of joint B_0
l_2	15	Crank A_0A
l_3	50	Connecting rod AB
l_4	41.5	Rocker B_0B
l_{41}	40.1	Element B_0C
l_5	61.9	Connecting rod AE
l_6	39.3	Rocker B_0E
l_7	41.5	Element CD
l_8	36.7	Element DE
l_{81}	49	Trajectory generation element EM
$\alpha_0 = \beta_0$	90°	Angles of ternary elements

The original dimensions of the Jansen mechanism that were used for determining the trajectory are presented in Table 1.

Knowing the link lengths of each element proposed by Jansen [11] presented in Table 1, the position angles are calculated. The coordinated system was set in A_0 fixed joint. The length “l” and height “h” of the step realized by Jansen mechanism is calculated between the point’s positions from horizontal and vertical direction of the path curve. These positions marked with colored dots in Fig. 3 correspond to certain φ [°] crank angles.

3 Analysis of Modified Jansen Leg Mechanism Path Curves

From simulations of Jansen leg configuration, it was considered that by varying the distances between the fixed joints A_0 and B_0 along x-axis, the step height could be increased or decreased while maintaining a straight line at the contact with the ground. The range of modified distances is around $[-36.8; -40]$ mm. These possibilities are distinctly presented in Fig. 4 and the step characteristics of all analyzed variants are presented in Table 2.

Underneath or above this range, the path curves obtained cannot be taken into consideration because do not satisfy the conditions related to walking.

The path curves represented in Fig. 4 were obtained in MathCad program after computing Eq. (3). The graphs emphasize dependency between coordinates of point M on y and x-axis. Three distinct φ crank angles were considered ($265, 108$ and 190°) to determine the extreme positions of point M for calculating step characteristics.

Jansen leg mechanism has the x coordinate of B_0 joint position set at -38 mm. After modifying the x coordinate position of the fixed joint at -36.8 and -37 mm, the step height has increased in comparison with Jansen initial distance. In case of the other two analyzed possibilities, -39 and -40 mm distances, the step height and length decreased in comparison with Jansen’s.

These observations conducted to the proposal of introducing a 2nd DOF based on a translational kinematical pair that will offer the ability to adjust the distances between the fixed joints in the range $[-36.8; -40]$ mm in order for the leg to cross over higher obstacles. The solution of modified leg mechanism configuration is presented in Fig. 5. A special screw-type coupling nut fitted with spring is considered to be introduced in B_0 articulation. No other initial link lengths are modified.

Jansen mechanism configuration allows modification to the values of each element. These modifications can be done by trial and error method or by other analytical or experimental methods and finally conduct to different path curves. From these paths, only certain types of curves can be considered suitable for walking and for implementation into a walking robot structure that fulfills certain

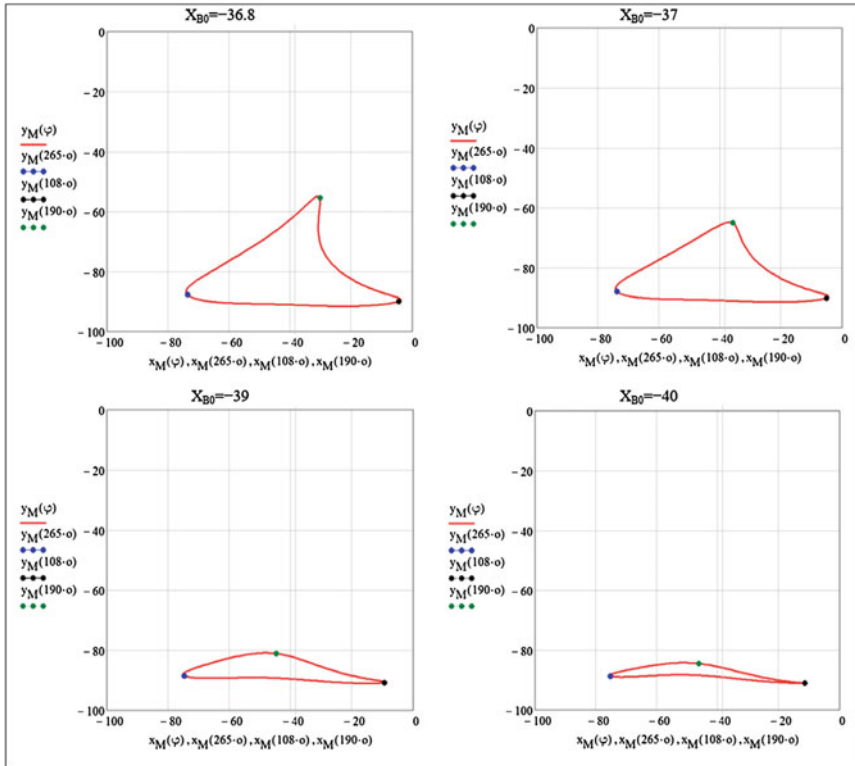


Fig. 4 Path curves obtained after modifying the distance between the fixed joints. All the units are in millimeters

Table 2 Characteristics of the step for all analyzed leg configurations

X_{B0} position (mm)	-36.8	-37	-38	-39	-40
Step height h	30	26	15	10	5
Step length l	69	69	69	67	65

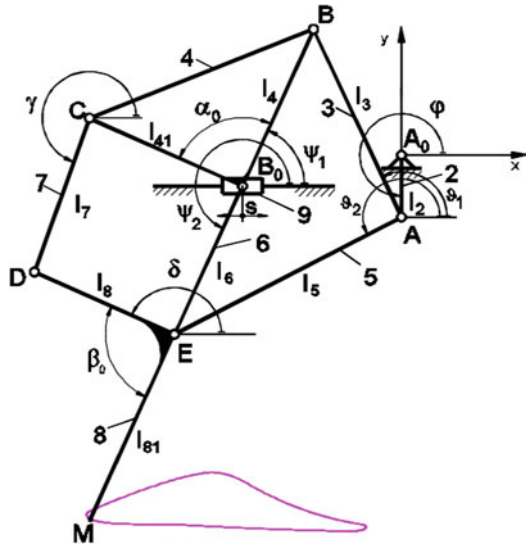
conditions. These conditions are set for assuring a stable walking and often refer to the existence of a flat portion in the coupler trajectory [14]. This portion is necessary for maintaining a good balance for the walking robot platform by keeping it, as much as possible, in a parallel position to the ground.

From the investigation of the path curves described by Jansen’s mechanism, only few assure an approximate straight line at the contact with the ground. These correspond to a reduced range of X_{B0} position coordinates $[-36.8; -38]$.

Also, if is considered an environment with obstacles for the robot to deal with, then the leg mechanism should be able to adapt in order to cross over obstacles. In this particular situation, is necessary to increase the height of the step. This increase



Fig. 5 Modified leg mechanism with 2 DOFs



is related to the addition of a second DOF to the leg mechanism that should not influence the balance of the platform.

The solution proposed in Fig. 5 was thought in order to ensure a stable walking and a better adaptability of the robotic leg to road inequalities. For this reason, the insertion of an actuated screw-type coupling nut fitted with a spring instead the fixed joint B_0 is intended to produce a change only in vertical plane of the robot. The mobile platform of the robot is intending to be kept parallel to the ground.

4 Conclusions

A practical solution for an adaptable Jansen leg configuration suitable for overcoming larger obstacles was presented. This consisted in the addition of a 2nd DOF to the leg mechanism by introducing a translational kinematic pair. In practice, this kinematic pair will consist of screw-type coupling nut fitted with a spring that will be actuated and controlled by the robot controller. This allows varying, in a restricted range of values, the distances between the fixed joints of the leg along horizontal direction. It also offers the possibility to modify the step characteristics, length and especially the height during movement of the leg mechanism. The other elements of the leg mechanism were kept at the same length values. Few disadvantages of this solution consists in the increase of power consumption due to the second actuator and the increase of the robot weight.

Simulations and further analysis will be performed in order to evaluate the improvements in the movement of the investigated walking robot structure after implementing the proposed solution.

A sensor could help the robot determine the presence of obstacles and send information to the controller in order to actuate the 2nd actuator which will consist in a step by step motor and a screw-nut transmission.

References

1. Bekey, G.: *Autonomous Robots. From Biological Inspiration to Implementation and Control*, MIT (2005)
2. Maniu, I., Rădulescu, C., Bogdanov, I., Varga, S., Dolga, V., Ciupe, V.: *Robotică. Aplicații robotizate*, Politehnica, Timișoara (2009)
3. Liang, C., Ceccarelli, M.; Carbone, G.: A novel biologically inspired tripod walking robot. In: *Proceedings of the 13th WSEAS International Conference on Systems, USA*, pp. 83–9 (2009)
4. Mehdigholi, H., Akbarnejad, S.: Optimization of watt's six-bar linkage to generate straight and parallel leg motion. *Int J. Adv. Robot. Syst.* **9**(22) (2012)
5. Angeles, J., Evtim, Z.: *Computational Methods in Mechanical Systems: Mechanism Analysis, Synthesis and Optimization*, Computer and System Science, F series, p. 161. Springer (1997)
6. Ceccarelli, M.: LARM PKM solutions for torso design in humanoid robots. *Front. Mech. Eng.* **9**(4), 308–316 (2014)
7. Kim, H., et al.: Comparative study of leg mechanisms for fast and stable water-running. *Int. J. Precis. Eng. Manuf.* **17**(3), 379–385 (2016)
8. Ingram, A.J.: *A new type of walking machine*. Ph.D. Thesis, University of Johannesburg (2006)
9. Kim, S.W., Han, S.H., Kim, D.H.: Analysis of a crab robot based on Jansen mechanism. In: *2011 11th International Conference on Control, Automation and Systems (ICCAS)* (2011)
10. Shunsuke, N., et al.: Dynamic modeling and nonlinear position control of a quadruped robot with theo jansen linkage mechanisms and a single actuator. *J. Robot.* (2015)
11. Jansen T.: *The Great Pretender*. 010 Publishers, Rotterdam, (2007)
12. Moldovan (Pop), F.: *Research regarding analysis and synthesis of a bar mechanism for constructing a walking robot (in Romanian)*. PhD Thesis, Timisoara (2013)
13. Lovasz, E.C., Pop, C., Pop, F., Dolga, V.: Novel solution for leg motion with 5-link belt mechanism. *Int. J. Appl. Mech. Eng.* **19**(4), 699–708 (2014)
14. Giesbrecht, D., Qiong Wu, C., Sepehri, N.: Design and optimization of an eight-bar legged walking mechanism imitating a kinetic sculpture, Wind Beast. *Trans. Can. Soc. Mech. Eng.* **36** (4), 343–355 (2012)

Development of an Assisting Instrument of Standing-Up Motion Using Driving Springs for Elderly Persons

H. Terada, K. Makino, K. Ishida and M. Ichikawa

Abstract To assist standing-up motion from the deep flexion state, an assisting instrument using driving springs on the hip and knee joints has been developed. This instrument consists of an assisting mechanism for the hip joint which has an oscillating follower type cam with a spring drive, and an assisting mechanism for the knee joint which has a non-circular gear, two grooved cams and a loading flat spiral spring. Especially, to apply it to the deep flexion and extension motions of the hip and knee joints, a motion of standing-up from a flat floor is analysed. As a result, it is clear that the assisting force on the hip joint are needed in case of an extension from the deep flexion state, and that force on the knee joint are needed during all extension motion state. Furthermore, the prototype instrument has been tested, and it is confirmed that the instrument is useful for the standing-up motion.

Keywords Assisting instrument · Elderly person · Standing-up · Deep flexion and extension · Spring drive

1 Introduction

In Japan and Asia area, many people lives on the floor or “Tatami”. Therefore, deep flexion motions of the hip and knee joints are an ordinary motion. At these motions, the hip joint is flexed over 90° , and the knee joint is flexed over 130° [1, 2].

H. Terada (✉) · K. Makino · K. Ishida · M. Ichikawa
University of Yamanashi, Yamanashi, Japan
e-mail: terada@yamanashi.ac.jp

K. Makino
e-mail: kohjim@yamanashi.ac.jp

K. Ishida
e-mail: isawa@yamanashi.ac.jp

M. Ichikawa
e-mail: g15mm005@yamanashi.ac.jp

Especially, the Japanese elderly person likes that traditional life-style, and deep flexion motions are often used. In general, the knee joint is flexed to 60° at the walking on a flat floor and flexed to 100° at the standing-up from a chair. However, the motion range of standing-up motion from the floor or “Tatami” exceeds the normal motion range. Furthermore, a muscular strength of leg of elderly persons often declines [3], and the assisting for the standing-up motion is required.

On the other hand, to improve the walk state, a knee assisting instrument for the rehabilitation has been developed [4]. That instrument assists the flexion or extension of a knee joint and cures an abnormal walk habit caused by the knee-osteoarthritis. However, that instrument does not consider the deep flexion and ex-tension motions of the hip and knee joints for the standing-up motion from the floor or “Tatami”. Furthermore, various walk assisting devices support only the walk on a flat floor [5]. In this paper, to realize the assisting motion at the deep flexion and extension motions of the hip and knee joints, a motion of standing-up with the deep knee flexion motion from the floor and a motion of keeping the posture in a half sitting are analyzed, at first. Then, considering the usage by elderly persons in daily life, a light weight structure of a gait assisting instrument is designed. In addition, to verify the usefulness, the prototype instrument is tested using the reduction of the required muscle activities on the hip and knee joints.

2 Motion Analysis of a Standing-Up Motion

At the Japanese traditional sitting “Seiza”, a standing-up motion from the sitting state needs various pose changes as shown in Fig. 1. At first, both ankles bend from the flat state to about 90° , and the deep kneeling state in double leg motions with a swing of a hip joint is taken as “Phase-1”. Then, at the normal standing-up motion, both knees are raised and a squatting down state is kept in double leg motions as “Phase-2”. Furthermore, the somatic center of gravity is raised to the upper direction to take a standing-up state with an extension of the hip and knee joints as “Phase-3”. In these state, the muscular strength of leg joint is needed to lift up the body and to adjust the somatic balance.

However, the muscular strength of elderly persons often decreases at the standing-up motion, and they use other procedures. In this case, they raise up one knee and kneel down the opposite side knee to keep a posture, after “Phase-1”. Then, they stand up with one step which is shifted to forward direction, and then, they arrange the steps to make a straight pose. Especially, at the procedure using kneeling down on one knee, the knee extension muscular strength decreases 14 % for the normal standing-up motion [6]. Then, because the somatic center of gravity becomes unstable, these procedures have a risk of the tripping over. Therefore, we have to investigate the assisting method of a standing-up motion. Considering these points, the standing-up motion from the Japanese traditional sitting “Seiza” state to standing-up state is analyzed by the image processing and the muscle activity evaluated by the integrated myogenic potential [7]. This signal is the micro-voltage

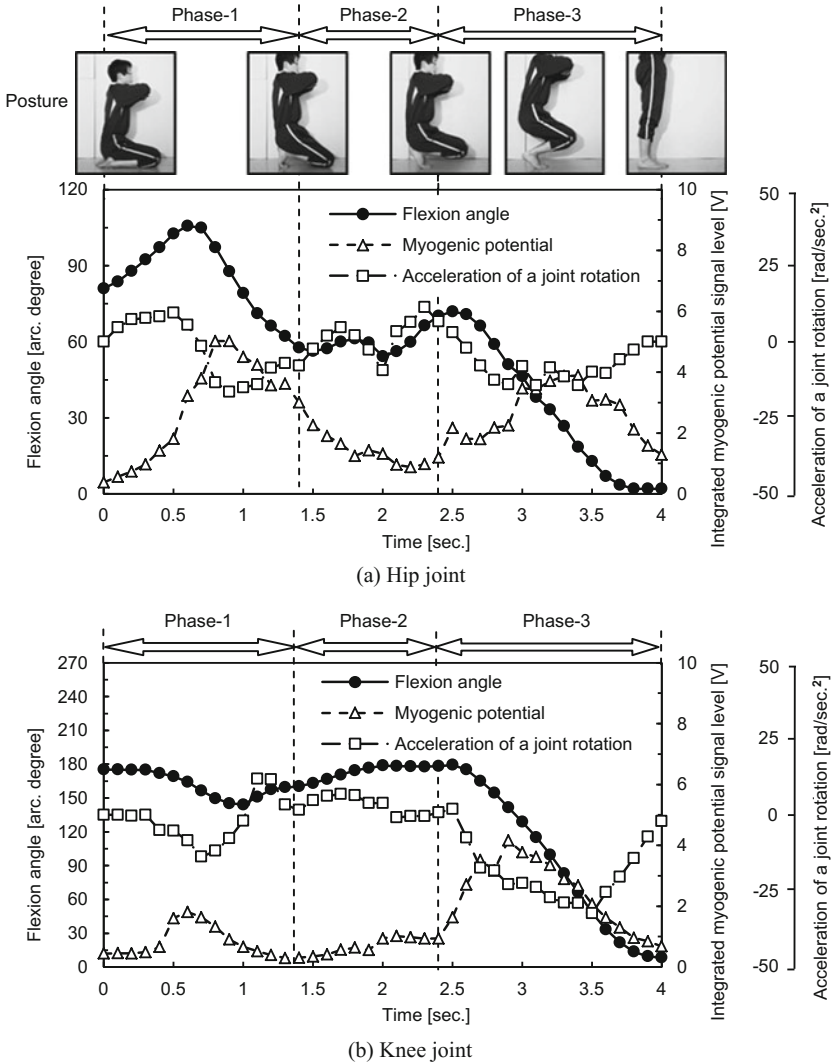


Fig. 1 Relations between the posture of standing-up motion and the flexion angle, the integrated myogenic potential signal level and the accelerations

generated in proportion to muscle activity, and it is popular to use the change rate of this voltage which is measured by an electromyograph [8]. At these hip and knee joints, relations between the posture of standing-up motion and the flexion angle, the integrated myogenic potential signal level and the accelerations are shown in Fig. 1. When the somatic center of gravity is raised up with a constant acceleration

in “Phase-3”, the muscle activities of the hip and knee joints take large values. Then, at the start timing in “Phase-1”, a muscle activity of a hip joint takes a large value. Considering these characteristics, the assisting mechanism of the hip and knee joints will be designed. Furthermore, a behavior of a standing-up motion at “Phase-3” is similar to the lifting motion of the heavy weight box on a flat floor, and the assisting instrument for lifting motion can be designed.

3 Structure of an Assisting Instrument

In Japan, various wearable assisting robot systems have been developed. However, almost systems have heavy weight, and it is difficult to use these systems for elderly persons. In addition, these systems have to be used only under the restrictive environments, because the running time is not long. Then, an assisting motion is required during the deep flexion which the hip joint flexes from 30 to 90°, and at the motion of a knee, the extension force is needed to oppose the influence of body weight. Nevertheless, the gait motion should not assist too much, because the muscular strength of the elderly persons decreases. In other words, the assisting motion has to be restrictive.

Considering these points, the structure of an assisting instrument in which a flat spiral spring and a cantilever beam type plate spring are used as the power unit is developed without the electric devices, as shown in Fig. 2 [9]. These braces are attached on these positions to avoid a big blood vessel near the skin surface. An assisting mechanism of the hip joint uses an oscillating follower type cam to restrict the assisting ranges, and an assisting mechanism of the knee joint uses a non-circular gear to adapt a roll back motion. Then, total weight is less than 4.5 kg, and the elderly persons can walk wearing this instrument.

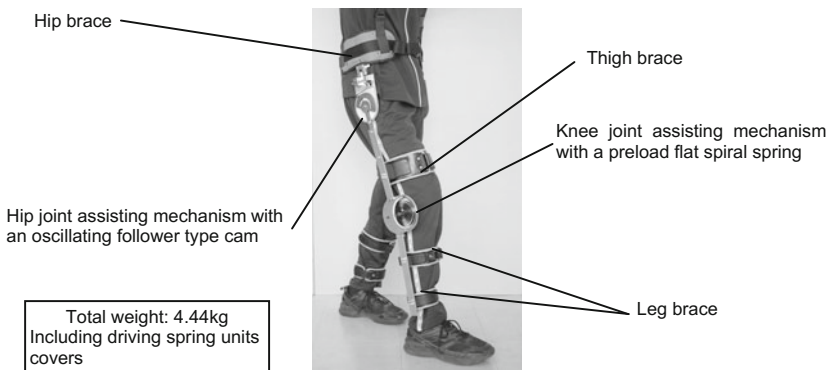


Fig. 2 An assisting instrument of the standing-up motion using driving springs

4 Design of a Hip Joint Assisting Mechanism

To assist the standing-up motion, the assisting mechanism of a hip joint is made by an oscillating follower type cam, and when that follower itself has the spring characteristics, that structure can be simplified. Therefore, this oscillating follower has a cantilever beam type plate spring to generate the assisting torque of a hip joint rotation, as shown in Fig. 3. This assisting torque is adjusted by a preload screw. Then, this mechanism is attached to a leg strictly using a hip brace and a thigh brace, and to eliminate the influence of abduction or adduction, a free rotational joint is installed on this mechanism. Nevertheless, an influence of medial rotation or lateral rotation is not large, so this influence is eliminated by the elasticity of thigh brace.

Considering the relations between the standing-up motion and the muscle activity, the plate cam shape is generated. Especially, to avoid the difficulty of a hip joint flexion at the walking on a flat floor, an assisting angle “ θ ”, is restricted from 30 to 90°, and a compression force “ F_c ” is proportional to the displacement of a cam follower. Then, to rotate smoothly, the acceleration curve of a modified sine motion curve is used to this cam [10], and that force is defined using the non-dimensional displacement “ S ”, the non-dimensional time “ T ”, the start angle of that cam motion “ θ_s ”, the end angle of that cam motion “ θ_e ”, and the equivalent spring constant “ k_{mx} ”, as shown in Eqs. (1)–(5)

$$F_c = k_{mx} \cdot S \tag{1}$$

$$T = \frac{\theta - \theta_s}{\theta_e - \theta_s} \tag{2}$$

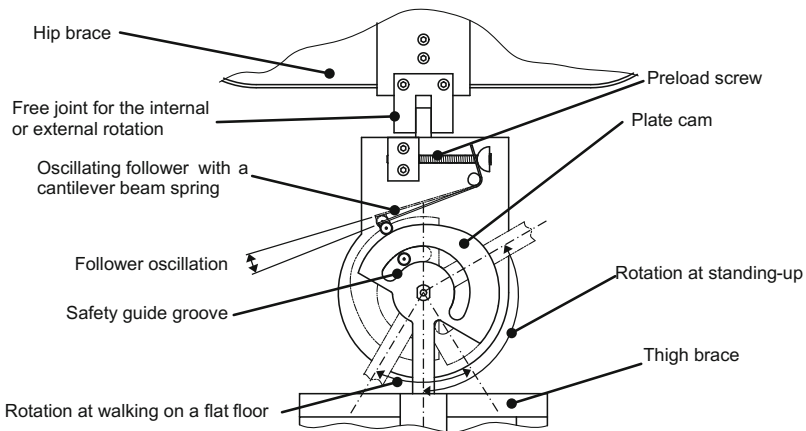


Fig. 3 An assisting mechanism of a hip joint



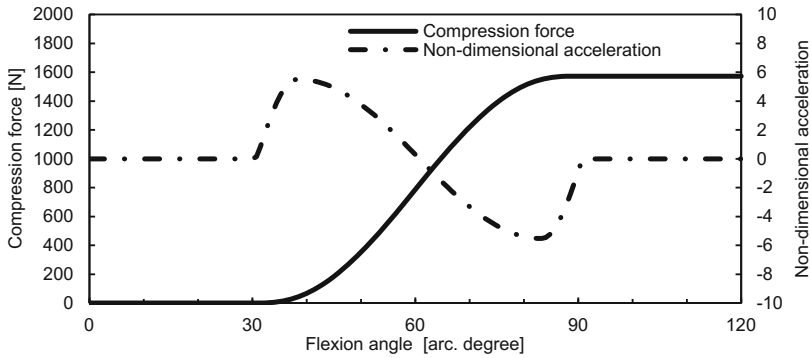


Fig. 4 Characteristics of a cam shape

$$S = \frac{\pi}{\pi + 4} \left(T - \frac{1}{4\pi} \sin 4\pi T \right), \quad (0 \leq T \leq 1/8) \quad (3)$$

$$S = \frac{9}{4(\pi + 4)} \left\{ 1 - \cos \frac{(8T - 1)\pi}{6} \right\} + \frac{\pi}{\pi + 4} \left(T - \frac{1}{8} \right) + \frac{1}{\pi + 4} \left(\frac{1}{8} - \frac{1}{4\pi} \right), \quad (1/8 \leq T \leq 7/8) \quad (4)$$

$$S = \frac{1}{4(\pi + 4)} \left\{ \cos \frac{(8T - 7)\pi}{2} - 1 \right\} + \frac{\pi}{\pi + 4} \left(T - \frac{7}{8} \right) + \frac{1}{\pi + 4} \left(\pi + \frac{31}{32} + \frac{1}{4\pi} \right), \quad (7/8 \leq T \leq 1) \quad (5)$$

The theoretical relations between the rotation angle of a hip joint and the acceleration and the compression force of a plate cam are shown in Fig. 4. In case of over 90°, the compression force keeps the constant value.

5 Design of a Knee Joint Assisting Mechanism

To assist a knee joint rotation including the roll-back motion which is the rotation with gliding-motion to the back direction, the knee joint assisting mechanism consists of a non-circular gear and two grooved cams. The fundamental structure is similar to the wearable knee assisting instrument [11]. At this mechanism, the rotation range is extended from 125 to 180°. When the knee joint is flexed from the full extension state, the rotating force is accumulated on the spring. Then, it is released that force at the extension state. In addition, a rotation of a knee joint can be assisted in the gait by gravity and the inertia, and in case of the standing-up

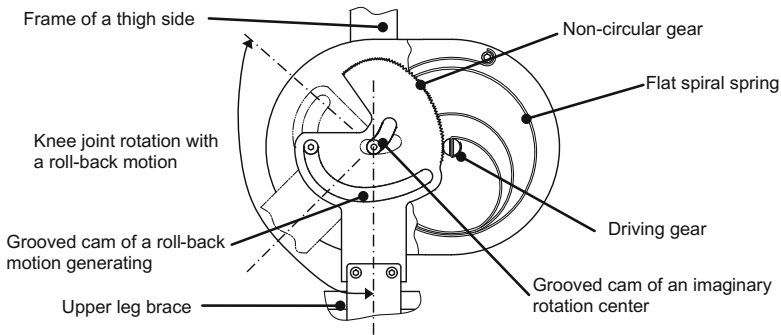


Fig. 5 A knee joint assisting mechanism

motion, an assisting motion should be considered. Therefore, this mechanism uses a flat spiral spring without electric devices as shown in Fig. 5.

Considering the knee motion data of Japanese people [12], these profiles and the center locus of a non-circular gear are generated using the asymmetrical modified trapezoid motion curve. In case that the mean standing height is 1.7 m, the theoretical relations between the rotating angle of the knee joint and the roll-back motion displacement and the generating torque of a flat spiral spring are shown in Fig. 6. Then the roll-back motion is saturated with 120°. Furthermore, the assisting torque is less than the maximum torque which is 25 Nm around the knee joint generated by the weight of lower leg and foot.

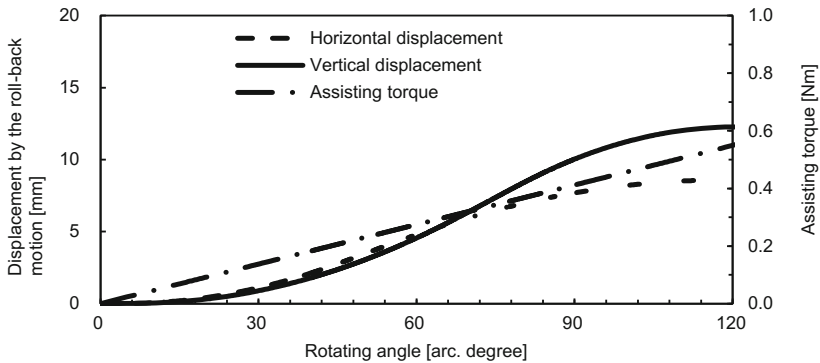


Fig. 6 Relations between the rotating angle and roll-back motions and assisting torque of a flat spiral spring

Table 1 Muscle activities and the reduction rate of each joint

Items	Hip joint	Knee joint
Max. integrated myogenic potential without assisting (V)	3.91	2.86
Max. integrated myogenic potential with assisting (V)	3.05	2.33
Reduction rate of the muscle activity (%)	22.0	18.6

6 Verifications of a Prototype Instrument

Based on a proposed design, the usefulness for the standing-up motion has been verified using the prototype of an assisting instrument. At this verification, to avoid the risk of tripping over, this instrument is attached to the healthy person. Then, the standing-up motion from a squatting down state which is needed the largest assisting torque is evaluated using the integrated myogenic potential as the muscle activities. As a result, this prototype instrument can assist in the standing-up motion. Especially, the required muscle activity of each joint is reduced about 20 % as shown in Table 1, even if the healthy persons use this prototype. When this instrument is applied to the elderly persons that the muscular strength is decreased, it will be more effective.

7 Conclusions

To assist the standing-up motion for the elderly persons, an assisting instrument using driving springs has been developed. Especially, considering the motion analysis of a standing-up motion, it is clear that the assisting forces on the hip joint are needed on the full flexion and the full extension. In addition, it is confirmed that this instrument can reduce the required muscle activities of hip and knee joints by about 20 %. In other words, this instrument assists the muscular strength of the hip and knee joints, and this assisting rate conforms to the reduction rate of muscle activity for elderly person. Therefore, they will be able to stand up easily. In future work, to apply it to assist the package lifting which has the similar characteristics of muscle activities, we have to investigate the adjusting mechanism of an assisting timing, a start angle and an end angle.

References

1. Fukunaga, M., Koguchi, K., Hirokawa, S.: Effect of the thigh-calf contact forces to the knee joint force during deep knee flexion. *Trans. Jpn Soc. Mech. Eng. Part C* **79**(806), 459–466 (2013)
2. Zelle, J., et al.: Thigh-calf contact force measurements in deep knee flexion. *Clin. Biomech.* **22**, 821–826 (2007)

3. Fujimoto, M., Nakade, Y., Okubo, K., Fujii, T.: Study on a device to assist stand-up motion of the aged: estimating dynamical factor for optimum assistance. *Jpn Soc. Mech. Eng. Symp. Welfare Eng.* **2004**, 181–184 (2004)
4. Terada, H. et al.: Development of a wearable assist robot for walk rehabilitation after knee arthroplasty surgery, *Applications Advances in Mechanisms Design, Proceedings of TMM 2012*, Springer, pp. 65–71 (2012)
5. Sano, A., Suzuki, M.: Novel walking assist by non-powered passive walking. *Japan Soc. Mech. Eng. Symp. Welfare Eng. OS1-1-7* (2012)
6. Hara, S., et al.: The relationship between motor function and getting up from the floor. *Rigakuryoho Kagaku* **29**(3), 367–370 (2014)
7. Nagura, T., Dyrby, C.O., Alexander, E.J., Andriacchi, T.P.: Mechanical loads at the knee joint during deep flexion. *J. Orthop. Res.* **20**, 881–886 (2002)
8. Hara, Y., Yoshida, M., Matsumura, M., Ichihashi, N.: The quantitative evaluation of the muscle activity by integrated electromyogram. *Trans. Inst. Electr. Eng. Jpn Part C* **124**(2), 431–435 (2004)
9. Terada, H., et al.: Assistive apparatus for lower limb motion. Japanese patent, Tokugan 2014-192722, (2014)
10. Makino, H.: Automatic assembly machine kinematics. *Nikkan-Kogyo-Shimbun*, pp. 29 (1976)
11. Terada, H., et al.: Assistive apparatus for knee joint motion. Japanese patent No. 5713388 (2015)
12. Terada, H., et al.: Developments of a Knee Motion Assist Mechanism for Wearable Robot With a Non-Circular Gear and Grooved Cams, pp. 69–76. *Mechanisms Transmissions and Applications*, Springer (2012)

An Evolutionary Computational Algorithm for Trajectory Planning of an Innovative Parallel Robot for Brachytherapy

F. Gîrbacia, D. Pîslă, S. Butnariu, B. Gherman, T. Gîrbacia and N. Plitea

Abstract Brachytherapy (BT) is a procedure used to treat cancer by inserting needles directly into the patient's tumour tissue in order to deliver radioactive seeds. The efficiency of this procedure is obtained by minimizing the number of inserted needles and generating safe trajectories that avoid critical areas. To increase the accuracy of needle insertion, the physician is replaced by a robot. The paper presents an evolutionary algorithm used to generate trajectories for needles inserted by an innovative BT parallel robot. Given the locations of the points representing the seeds and the 3D virtual model of the treatment area, the proposed solver allows the minimization of the number of inserted needles and the planning of needles trajectories that avoid high risk areas. The solver was validated for a complex BT liver treatment scenario.

Keywords Robot-assisted brachytherapy · Trajectory optimization · Evolutionary algorithm

F. Gîrbacia (✉) · S. Butnariu · T. Gîrbacia
Transilvania University of Braşov, Braşov, Romania
e-mail: garbacia@unitbv.ro

S. Butnariu
e-mail: butnariu@unitbv.ro

T. Gîrbacia
e-mail: teodora.girbacia@unitbv.ro

D. Pîslă · B. Gherman · N. Plitea
Technical University of Cluj-Napoca, Cluj-Napoca, Romania
e-mail: dpisla@mail.utcluj.ro

B. Gherman
e-mail: bgherman@mail.utcluj.ro

N. Plitea
e-mail: nplitea@mep.utcluj.ro

1 Introduction

Recently, for the treatment of certain types of cancers, especially those strictly located, the brachytherapy technique has been frequently used [1, 2]. This treatment involves the use of low-dose local radiation by means of radioactive seeds (Low Dose Rate—LDR), applied directly in the tumour using special needles [3]. The classical technology involves the use of matrix template (grid) to guide needles, which helps the surgeon to position seeds correctly, according to the predefined positions. Nowadays, the physician manually inserts needles in the tumour, based on planning and verifies the process using imaging systems [3, 4]. In literature, there are many researches that handle the BT operation planning, regarding the calculation of the radioactive seeds position inside the tumour. The advantages of using robots in surgery are detailed in [5]. This method of inserting the needles into the tumour has a special feature—it does not imply the usage of a template for guiding the needles. To access the tumour the robot can start from anywhere in its workspace, taking into account the imposed conditions related to technical characteristics of the equipment and the patient. This paper proposes the use of a parallel robot (Fig. 1), specially designed for BT operation, which will provide more accuracy than a surgeon [6–8]. An important research direction is the study of human body BT needles insertion and tracking their trajectories [9–12]. Various methods of needles insertions were highlighted, by performing calculations and experiments, suggesting optimal solutions. In [9] is presented a trajectory planning of the BT needles using the Markov method, but in 2D which not allows specification completely of trajectories. In [3] is presented a detailed mathematical model of the distribution of seeds and the achieving of the insertion position of the needles on the matrix template using genetic algorithms. The proposed algorithm is designed for manual BT procedure and uses the grid template for guiding the needles. From literature review, it was found that the problem of trajectory optimization for BT robotic procedure has not been investigated. On the other hand, there is an approach of the same research team in determining an optimized trajectory of a parallel robot in case of prostate biopsy interventions [13].



Fig. 1 PARA-BRACHYROB robot (Experimental model)

2 PARA-BRACHYROB System Description

Considering all the issues presented in the literature review, the Research Center CESTER of Technical University of Cluj Napoca has developed an innovative parallel robot to be used in brachytherapy procedures (Fig. 1). The figure presents the mechanical structure of PARA-BRACHYROB: the first five motors are placed on top of the aluminium frame, which hold the two 3-DOF modules [6, 7]. The kinematic diagram of PARA-BRACHYROB is presented in Fig. 2. The two modules are connected by means of two Cardan joints which withhold the needle insertion module. On the left of the mechanical structure, we have the control unit of the robot and on the right, the power supply unit. From the constructive point of view, the robotic structure sits on an aluminium plate frame supported by a base plate which can be fixed to the CT table, with the main five active joints (motors) fixed to the top of the frame. The needle insertion modules motion will be obtained by rotating the ball screws or grooved shaft held by bearings connected to the fixed frame. The needle insertion module was designed to enable the easy insertion and retraction of the needle for any given trajectory. Since the different types of tissue (layers of skin, fat, muscles, internal organs parenchyma) have different resistances and if the force exceeds certain limits the needle will deflect from the trajectory risking an unwanted damage of proximal structures, a force sensor will be integrated to monitor the force variation during the needle insertion though the body. The mechanism itself consists of a linear module that moves along a screw with a fine pitch (0.8 mm) and it is actuated through a timing belt which enables the positioning of the actuator itself in parallel with the module, making it very compact [13].

The robot should introduce, based on radiologic data, needles following a linear trajectory. This task will be achieved through a motion decomposed in two different parts: (i) the approach stage, when the first five actuators are used, to reach the point of entry inside the patient, with the defined orientation; (ii) the needle insertion stage, when the sixth actuator is used to push the needle, on a straight line, to reach the target point. The system should also allow the control of the insertion force into the patient’s tissue. Figure 3 present two robotic brachytherapy needle trajectories.

Fig. 2 The kinematic diagram of PARA-BRACHYROB robot

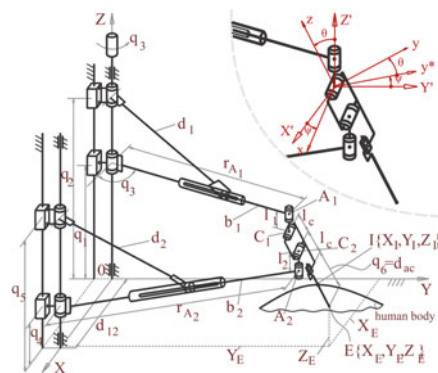
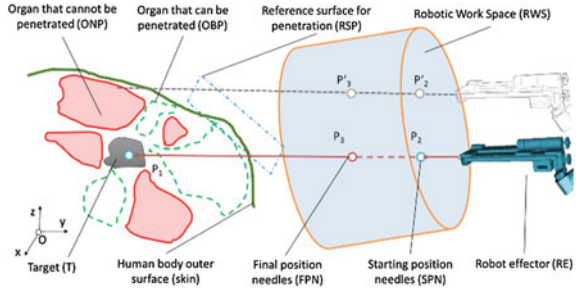


Fig. 3 BT needle trajectories in the robot workspace



The brachytherapy robot has an effector element with translational coupling which will insert the needle, passing through the patient's skin, following a previously set path. The main problem for programming the robot is to find a linear segment, which starts from a point in the Robot Workspace (RWS) and ends in the target point. All these trajectories will take into account that the needle does not intersect vital organs.

3 The Algorithm for Planning BT Needles Trajectories

In this study, the selection of needle trajectories used to formulate optimal solutions requires the following optimization objectives: (i) optimize needle trajectories to avoid vital organs intersection; (ii) minimize the number of needles insertions to reach all the target points. The following input parameters are provided to a Genetic Algorithm (GA): 3D model of the patient including geometry model of the internal organs, OBP and ONP (Fig. 3); position of the patient in the treatment area; initial position of the robot; workspace of the robot; position (X, Y, Z) of the target points (radioactive seeds). In the genotypic space each candidate solution is represented as a chromosome of n genes (needle trajectories) identified by an ID and position of the insertion point in the RWS (Fig. 3). Initial population necessary to begin the genetic search can be generated using the following algorithm:

(i) process the 3D model of the patient reconstructed from CT images; (ii) load the 3D model of the patient into the application; (iii) define the target area for treatment (tumour position); (iv) define the position of each seed point; (v) select a random inserting point that is located inside the robot workspace; (vi) simulate the needle insertion process and check whether there is an intersection with vital organs or the treatment area; (vii) repeat steps 5 and 6 until there are generated a specified number of needles trajectories.

Using the conceived algorithm developed for automatic generation of linear robot trajectories is obtained a set of trajectories $T = \{t_1, t_2, \dots, t_i, \dots, t_n\}$, where t_i

represents the linear trajectories of a set with: $t_i = \{tg_1, \dots, tg_i\}$, where i represent the gene number. These trajectories can be classified into three types: tg_a, tg_b, tg_c and $t_i = tg_a \cup tg_b \cup tg_c$. The tg_a type contains the trajectories that do not intersect the vital organs, but intersect the tumour area at a point corresponding to a radioactive seed set by the physician. The tg_b type contains the trajectories that do not intersect the vital organs but the distance between the needle tip and a target point corresponding to a radioactive seed set by the physician is less than a specified threshold. The tg_c type contains the trajectories that intersect the vital organs.

To estimate the way in which each chromosome contributes to achieving the objectives, evaluation functions are created for each goal. The sum of the evaluation functions determines the degree of optimization for the obtained solution. The fitness function for evaluating objectives is calculated using the following steps:

- Each gene from the chromosome can have from zero to five points.
- Check whether a tg_i gene intersects a vital organ. If such an intersection does not exist, then increase its score. Otherwise the trajectory $tg_i \in tg_c$ and its score is not incremented.
- If there is no intersection with a vital organ, check whether the tg_i gene intersects the tumour. If such an intersection exists, then $tg_i \in tg_a$, and its score is increased.
- If there is no intersection with a vital organ, check whether the tg_i gene intersects the tumour at a target point corresponding to a radioactive seed set by the physician. If such an intersection exists, then $tg_i \in tg_a$ and its score is increased.
- If there is no intersection with a vital organ or a target point corresponding to a radioactive seed set by the physician but the distance between the needle tip and a target point corresponding to a radioactive seed set by the physician is less than a specified threshold, then $tg_i \in tg_b$, and its score is increased.
- If tg_i intersects the tumour in more than one target points, its score is increased.
- The total score of a chromosome is the sum of points of all genes.
- The fitness value is calculated as the chromosome total score divided by the maximum score, and the maximum score represents the number of needle trajectories multiplied by five.

The parents from which begins the process of evolution are established after applying the Rank Selection method. Each chromosome in the population is ranked in increasing order of their fitness values from one to N , where N is the population size, assuming that R_i is the ranking for the each chromosome. The ranking is the used to select the parents for the reproduction process. Starting from both chromosomes parents, the descendants are obtained by applying a multi-point crossover operator. For the mutation operation, first the chromosomes with the lowest rank are selected, than they are replaced with the new ones to complete the forming of a new generation. The algorithm runs until the best chromosome reaches a fitness value equal to one or the number of evolutions is higher than a specified value. The optimization process was designed and coded according to the following:

```

BEGIN
  GENERATE initial random needles population
  INITIALISE the algorithm with the following parameters
    POPULATION SIZE (N)
    NUMBER OF EVOLUTIONS (STOPPING CRITERION)
  EVALUATE each candidate based on its fitness value;
  DO WHILE (STOPPING CRITERION is not met)
    • Randomly selects N pairs of parents from the current population
      based on the Rank Selection method.
    • Produce N new chromosomes by performing a crossover operation on
      the pair of parents.
    • Evaluate all the new chromosomes.
    • Select the chromosome with the lowest fitness value from the cur-
      rent population and replaces it with the best solution found on
      the new ones.
    • Complete the forming of a new generation;
  LOOP
END

```

4 Implementation Details and Results

In the conducted experiment, a virtual environment has been modelled containing a 3D reconstructed abdominal model of a patient (Fig. 4). To build the 3D model of the patient was used 3D Slicer software (<http://www.slicer.org/>) and a set of CT files (DICOM format). Our test started by choosing the liver as target treatment area. The BT procedure for liver treatment represents a complex process because of the increased number and density of anatomical elements that need to be avoided by the BT needles. The experiment consisted in using the developed GA algorithm for planning the trajectories of needles for the BT robot considering eight preconfigured target seed points presented in Fig. 5. The seeds point's positions are configured by a physician using dedicated software for brachytherapy. This stage is not the purpose of the presented study. In this experiment failure is defined by the collision with a high risk area or exiting the feasible workspace of the BT robot. For the representation of the 3D model geometry of the liver target area (Fig. 3) was used the ISO standard VRML2.0 (Virtual Reality Modelling Language). In order to determine the intersection between the linear trajectories and the high risk areas a ray hit collision detection algorithm was used. There are defined control points on the linear segment, used for collision detection. The algorithm returns the

Fig. 4 The 3D model of the liver area obtained from CT images

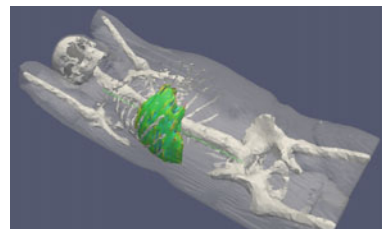
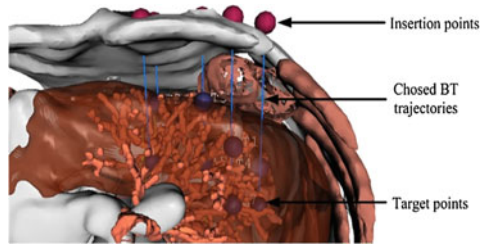


Fig. 5 Generated BT needles trajectories



intersection point between these points and a line corresponding to the brachytherapy needle mounted on the robot effector. The rendering of the 3D virtual environment was realized through the program BS Contact VRML player. For the implementation of the GA algorithm was used the C++ language. The implemented software contains a display area of the virtual environment and a Graphical User Interface area that contains a menu that allows sending events to VE.

Figure 5 presents the result obtained using the developed GA algorithm. Only five needles were needed to reach the eight target points because there are three needles that allow the insertion of two seeds at the same time. Also the needles trajectories do not intersect anatomical areas around the treatment area: inferior vena cava, caudate veins, portal vein and branches, hepatic vein and branches. The simulation shows that the proposed algorithm works well and allows minimization of number of needles insertions. Also, it was determined the time for paths analysis and processing in a treatment zone, using a reference surface for penetration (RSP) with the dimensions of 120×60 mm (see Fig. 5). The resolution step used to increment the starting point of the calculated trajectory was set at the following values 0.1; 0.5; 1; 1.5 and 2 mm. Using this procedure was determined the total number of analysed trajectories which is used as an input parameter for the GA algorithm (Table 1). It can be observed that at very high resolution step, the

Table 1 Number of BT trajectories

Resolution step (mm)	0.1	0.5	1	1.5	2
Number of trajectories	84,339	39,160	7380	3320	1890
Computation time (s)	3152	1675	246	126	72

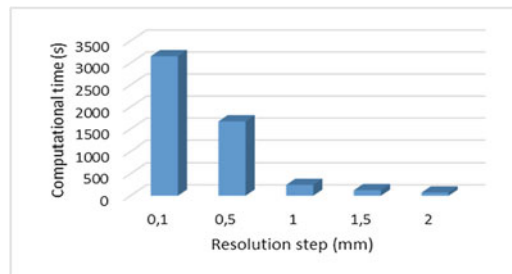


Fig. 6 Processing time of the GA algorithm

computational time increases (Fig. 6). We conclude that using a high resolution step determines a slow simulation and the accuracy is not visible improved due to the low precision of the reconstructed patient mesh.

5 Conclusions

An approach for needle trajectory planning for a BT parallel robot based on an evolutionary algorithm was presented in this paper. We developed a software application framework that allows the optimization of the number of needles to be inserted and to define needles trajectories that avoid high risk areas. We validated our approach for a complex BT liver treatment scenario. The performed test showed that the developed genetic algorithm makes possible to minimize the number of needles required for the seeds configurations and to find the needle trajectories that do not intersect high risk areas. Future work should examine the different types of crossovers and mutation operators that will allow reducing the search effort of the optimal solution.

Acknowledgments The publishing of this paper was supported by the project no. 173/2012, code PN-II-PT-PCCA-2011-3.2-0414, entitled “Robotic assisted brachytherapy, an innovative approach of inoperable cancers—CHANCE” financed by UEFISCDI Romania.

References

1. Prostate brachytherapy. http://en.wikipedia.org/wiki/Prostate_brachytherapy. Accessed 10 Mar 2016
2. Prostate cancer—Treatment options by stage. <http://www.webmd.com/prostate-cancer/guide/treatments-by-stage>. Accessed 10 Mar 2016
3. Ferrari, G., Kazareski, Y., Laca, F., Testuri, C.E.: A model for prostate brachytherapy planning with sources and needles position optimization. *Oper. Res. Health Care* **2014**(3), 31–39 (2013). doi:10.1016/j.orhc.2013.12.00200172. RO 129698 A2, Int. CI. A61B 19-00, Febr. 22th
4. Polo, A., Salembier, C., Venselaar, J., Hoskin, P.: Review of intraoperative imaging and planning techniques in permanent seed prostate brachytherapy. *Radiother. Oncol. J. Eur. Soc. Ther. Radiol. Oncol.* **94**(1), 12–23 (2010). doi:10.1016/j.radonc.2009.12.012
5. Davies, Brian: Robotic surgery—a personal view of the past, present and future. *Int. J. Adv. Robot. Syst.* **12**, 54 (2015). doi:10.5772/60118
6. Gîrbacia, F., Gherman, B., Butnariu, S., Plitea, N., Talabă, D., Pîslă, D.: Virtual planning of needle trajectories using a haptic interface for a brachytherapy parallel robot: an evaluation study, *Appl Mech Mater* **762**, 155–160 (2015). doi:10.4028/www.scientific.net/AMM.762.155
7. Pîslă, D., Cocorean, D., Vaida, C., Gherman, B., Pîslă, A., Plitea, N.: Application oriented design and simulation of an innovative parallel robot for brachytherapy, Proceedings of the ASME 2014 IDETC/CIE 2014: 38th Mechanisms and Robotics Conference, 17–20 Aug 2014, Buffalo, New York, USA, vol 5B. doi:10.1115/DETC2014-35047

8. Plitea, N., Pîslă, D., Vaida, C., Gherman, B.: Robot parallel pentru brahiterapie cu două lanțuri cinematice de ghidare a platformei de tip CYL-U, Patent pending no. a 2013 00172, RO 129698 A2, Int. CI. A61B 19-00, Febr. 22th 2013
9. Asadian, A., Kermani, M.R., Patel, R.V.: Robot-assisted needle steering using a control theoretic approach. *J. Intell. Rob. Syst.* **62**(3–4), 397–418 (2010). doi:[10.1007/s10846-010-9455-2](https://doi.org/10.1007/s10846-010-9455-2)
10. Elgezua, I., Kobayashi, Y., Fujie, M.G.: Survey on current state-of-the-art in needle insertion robots: open challenges for application in real surgery. *Procedia CIRP* **5**, 94–99 (2013). doi:[10.1016/j.procir.2013.01.019](https://doi.org/10.1016/j.procir.2013.01.019)
11. Gao, D., Lei, Y., Zheng, H.: Needle steering for robot-assisted insertion into soft tissue: a survey. *Chin. J. Mech. Eng.* **25**(4), 629–638 (2012). doi:[10.3901/CJME.2012.04.629](https://doi.org/10.3901/CJME.2012.04.629)
12. Strassmann, G., Olbert, P., Hegele, A., Richter, D., Fokas, E., Timmesfeld, N., Hofmann, R., Engenhart-Cabillic, R.: Advantage of robotic needle placement on a prostate model in HDR brachytherapy. *Strahlentherapie und Onkologie: Organ der Deutschen Röntgengesellschaft [et al]* **187**(6), 367–372 (2011). doi:[10.1007/s00066-011-2185-y](https://doi.org/10.1007/s00066-011-2185-y)
13. Pîslă, D., Gherman, B., Gîrbacia, F., Vaida, C., Butnariu, S., Gîrbacia, T., A., Plitea, N.: Optimal planning of needle insertion for robotic-assisted prostate biopsy. In: *Advances in Robot Design and Intelligent Control*, SpringerLink. *Advances in Intelligent Systems and Computing*, vol. 371, pp. 339–346, 08 Aug 2015. doi:[10.1007/978-3-319-21290-6_34](https://doi.org/10.1007/978-3-319-21290-6_34)

Inverse Kinematics and Dynamics of an Overconstrained Manipulator for Upper Extremity Rehabilitation

Ö. Selvi and K. Yilmaz

Abstract In this paper, an overconstrained manipulator is selected for the purpose of rehabilitation of the upper extremity. The geometry of the selected manipulator fits the exact motion of the upper extremity and acts as an exoskeleton. Inverse kinematics calculations are shown for describing the motion of actuators for a desired arm motion. Lagrange Formulation is used for the inverse dynamic model of the system. Due to the geometry of the manipulator, kinematic and dynamic calculations are applied to the two spherical subspaces of the manipulator using imaginary joints.

Keywords Rehabilitation robotics · Overconstrained manipulators · Lagrange dynamic analysis · Exoskeleton

1 Introduction

The increase in lifespan increased the likelihood of confronting physical health problems as well [8]. Rehabilitation Robotics is a challenging field with a high potential to support people with severe disabilities. The objective is to support people to perform their tasks in daily life, at work and home [2]. The arm plays an important role to perform daily tasks thus many research has been done on arm rehabilitation. The robots used in this area can be classified according to their kinematic structures, such as serial robots, parallel robots and hybrid robots [6]. Serial manipulators (open-loop manipulators) have good operating characteristics (large workspace, high flexibility and maneuverability) but have disadvantages such as low precision, low stiffness and low power. Parallel manipulators provide advantages like lower moving masses, higher rigidity, better accuracy and

Ö. Selvi (✉) · K. Yilmaz
Çankaya University, Etimesgut, Turkey
e-mail: ozgunselvi@cankaya.edu.tr

K. Yilmaz
e-mail: knty.yilmaz@gmail.com

payload-to-weight ratio but these manipulators usually have limited workspace and non-isotropic input/output relations [1]. Manna and Bhaumik [4] introduced a 10 DoF (degree of freedom) serial rehabilitation robot to operate in the range of shoulder girdle to the wrist. Serial manipulators are not good in terms of weight distribution due to motor positioning, which causes the need for stronger motors. Mao and Agrawal [5] proposed a 5 DoF cable driven and force controlled parallel manipulator for the upper arm. Usage of cables decreases the sturdiness specification of parallel manipulators. In this paper, kinematics and dynamics of an overconstrained parallel manipulator, acting as an exoskeleton, is presented for the purpose of upper arm rehabilitation.

2 Manipulator and the Rehabilitation Task

Shoulder and wrist injuries are widely encountered in the upper extremity rehabilitation cases. The injuries require orthopedic and/or neurological treatment. The need for controlled repetitive motion has encouraged the usage of robots for rehabilitation. The overconstrained manipulator proposed to be used in arm rehabilitation can be found in the works of Kong and Gosselin [3]. This mechanism can be designed to be used in the region of shoulder-elbow and a RoM suited to perform the rehabilitation tasks is intended to be achieved. The movements in the specified region can be expressed in a special five DoF subspace and an exact kinematical solution can be found with two spherical manipulators positioned at the elbow and shoulder joint. The rotations occurring in this region is shown in Fig. 1a and the separation of these rotations into two different manipulators are enabled by the rotation matrices and their vector representations as given in Fig. 1b.

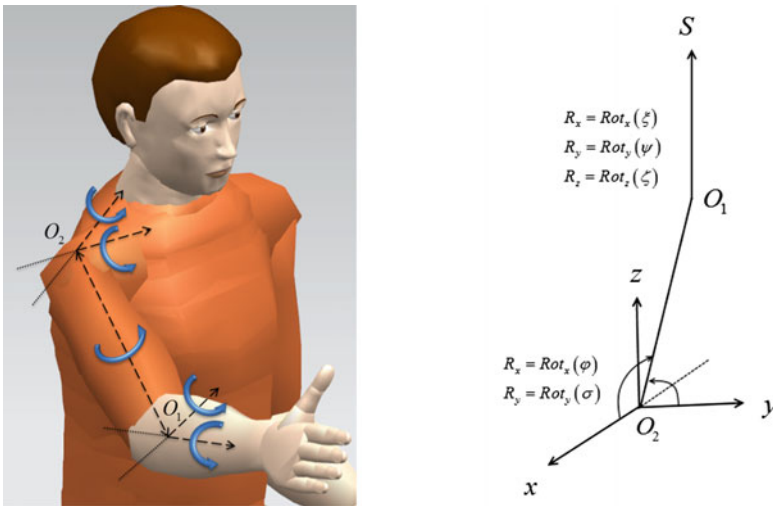


Fig. 1 a Human arm motion, b Manipulator position

2.1 Kinematic Analysis

The system consists of a five DoF double spherical manipulator with a configuration of (RRR)-(RR) and 3 limbs, the schematic drawing of the manipulator is given in Fig. 2a. The kinematic solving of such structure can be simplified by adding an imaginary joint and separating the system into two separate manipulators as upper and bottom manipulator. The schematic drawing of the double spherical manipulator with an added imaginary joint is given in Fig. 2b.

After the separation, 3RRRR and 3RRR manipulators are produced and both of these systems can be solved using the inverse kinematic approach (Fig. 3).

Orientation of these systems are found by rotation matrices and these are constructed by **u** and **t** vectors for the upper and bottom manipulators respectively.

$$\mathbf{u} = [0 \ 0 \ -1]^T \quad \mathbf{t} = [0 \ 0 \ 1]^T \tag{1}$$

Upper manipulator has three DOF motion and the bottom manipulator has two DOF motion. Upper manipulator end effector vector **O_r**, and bottom manipulator end effector vector **O_{b_r}**, are found by the inverse kinematic approach as shown in Eq. (2).

$$\begin{aligned} R_{upper} &= Rot_z(\zeta) \cdot Rot_y(\psi) \cdot Rot_z(\xi) \quad \mathbf{O}_r = R_{upper} \cdot \mathbf{u} \\ R_{bottom} &= Rot_x(\varphi) \cdot Rot_y(\sigma) \quad \mathbf{O}_{b_r} = R_{bottom} \cdot \mathbf{t} \end{aligned} \tag{2}$$

The vectors **w_i** and **r_i**, end effector joint positions for the upper and bottom manipulator, can be found from the above equations. For simplicity of use they are defined as in Eq. (3). The subscript i has values from 1 to 3 and is used to denote the relevant leg.

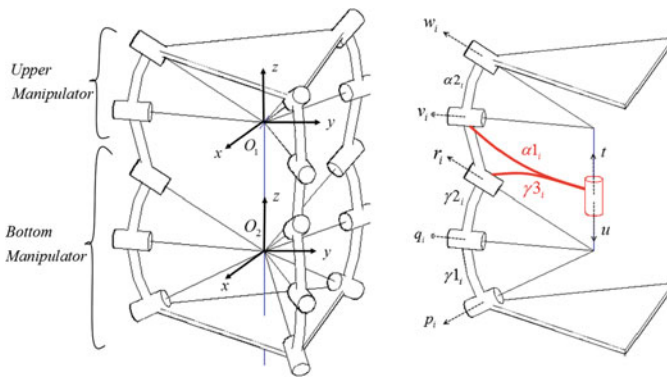


Fig. 2 a Schematic view of the manipulator, b The double spherical manipulator with imaginary joints added

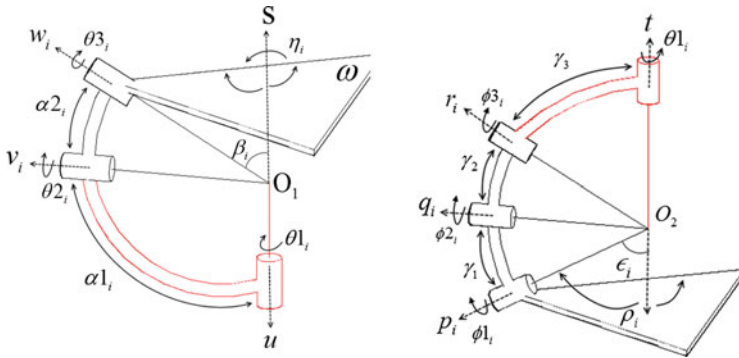


Fig. 3 **a** The *upper* manipulator (3RRR) with vector assignments, **b** The *bottom* manipulator (3RRRR) with vector assignments

$$\mathbf{w}_i = [wx_i \ wy_i \ wz_i]^T \quad \mathbf{r}_i = [rx_i \ ry_i \ rz_i]^T \tag{3}$$

The use of rotation matrices from a forward kinematics approach reveal the position of the vectors \mathbf{w}_i and \mathbf{r}_i with respect to \mathbf{u} and \mathbf{t} vectors for upper and bottom manipulator respectively.

$$\begin{aligned} \mathbf{w}_i &= Rot_z(\theta_{1_i}) \cdot Rot_x(\alpha_1) \cdot Rot_z(\theta_{2_i}) \cdot Rot_x(\alpha_2) \cdot \mathbf{u} \\ \mathbf{r}_i &= Rot_z(\rho_i) \cdot Rot_x(\epsilon_i) \cdot Rot_z(\phi_{1_i}) \cdot Rot_x(\phi_1) \\ &\quad \times Rot_z(\phi_{2_i}) \cdot Rot_x(\gamma_2) \cdot \mathbf{t} \end{aligned} \tag{4}$$

The closure formed by the usage of Eqs. (2) and (4) gives three separate closure equations for both the upper and bottom manipulator. The first two equations are used to find θ_{2_i} and ϕ_{2_i} for the upper and bottom manipulator respectively by using the four-quadrant inverse tangent atan2 [7]. The values found are used as inputs for the third equation and with the use of half-angle formulas shown in Eq. (5), θ_{1_i} and ϕ_{1_i} values for the upper and bottom manipulator are found.

$$\begin{aligned} \sin \theta_{1_i} &= \frac{2 \tan \theta_{1_i}/2}{1 + \tan^2 \theta_{1_i}/2} \quad , \quad \cos \theta_{1_i} = \frac{1 - \tan^2 \theta_{1_i}/2}{1 + \tan^2 \theta_{1_i}/2} \\ \sin \phi_{1_i} &= \frac{2 \tan \phi_{1_i}/2}{1 + \tan^2 \phi_{1_i}/2} \quad , \quad \cos \phi_{1_i} = \frac{1 - \tan^2 \phi_{1_i}/2}{1 + \tan^2 \phi_{1_i}/2} \end{aligned} \tag{5}$$

2.2 Dynamic Analysis

Dynamic analysis plays an important role to this manipulator because of its need for precise control. After achieving the kinematic analysis and obtaining the joint rates as functions, the obtained values can be used to determine the external forces and moments of the system through dynamic analysis. The method used will be the

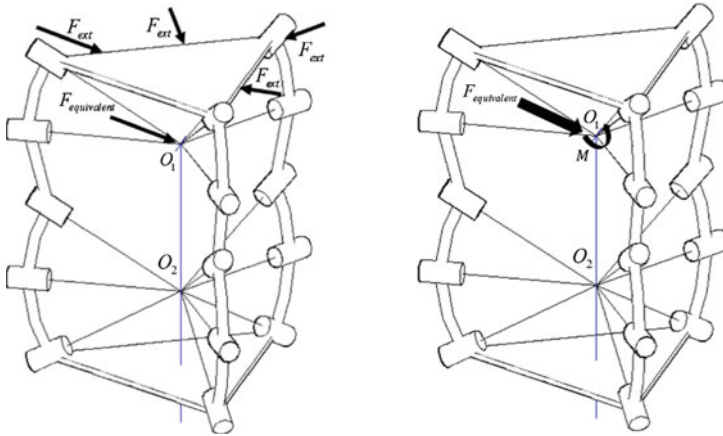


Fig. 4 **a** Manipulator while external forces are acting, **b** External forces composed as force-moment couple

Lagrange Formulation, by taking the external forces and moments of the system as a couple acting on joint O_1 and moving the couple on the same axis and directing it to O_2 both systems can be solved independently. The system in the presence of external forces is shown in Fig. 4.

The Lagrange formulation used is given in Eq. (6) [7].

$$\frac{d}{dt} \left(\frac{\delta L}{\delta \dot{q}_j} \right) - \frac{\delta L}{\delta q_j} = Q_j + \sum_{i=1}^k \lambda_i \left(\frac{\delta \Gamma_i}{\delta q_j} \right) \quad \text{for } j=1 \text{ to } n \tag{6}$$

where L denotes the Lagrangian function, q_j the j th generalized coordinate, Q_j as j th generalized force, Γ_i as i th constraint function, k as number of DOF, n as number of coordinates and λ_i as the Lagrangian Multiplier.

The angular velocity of the end effectors are found from Eq. (7) [7].

$$\omega_n = \sum_{i=1}^n \dot{\theta}_i z_{i-1} \tag{7}$$

where ω_n denotes the angular velocity of the end effector, $\dot{\theta}_i$ being the angular velocity of the i th link and z_{i-1} being the respective axis. This equation implies that the angular velocity of the links are additive, thus the resulting end effector velocity equations for the upper and bottom manipulators, ω_u and ω_b respectively, are given in Eq. (8).

$$\begin{aligned} \omega_u &= \mathbf{u} \cdot \dot{\theta}_1 \mathbf{i}_1 + \mathbf{v}_1 \cdot \dot{\theta}_2 \mathbf{i}_2 + \mathbf{w}_1 \cdot \dot{\theta}_3 \mathbf{i}_3 \\ \omega_b &= \mathbf{p}_1 \cdot \dot{\phi}_1 \mathbf{i}_1 + \mathbf{q}_1 \cdot \dot{\phi}_2 \mathbf{i}_2 + \mathbf{r}_1 \cdot \dot{\phi}_3 \mathbf{i}_3 \end{aligned} \tag{8}$$



The velocity of the end effectors are found as shown in Eq. (9).

$$\begin{aligned}\omega_u &= \frac{\delta R_u}{\delta \varphi} \cdot R_u^T \cdot \dot{\varphi} + \frac{\delta R_u}{\delta \sigma} \cdot R_u^T \cdot \dot{\sigma} + \frac{\delta R_u}{\delta \xi} \cdot R_u^T \cdot \xi \\ &\quad + \frac{\delta R_u}{\delta \psi} \cdot R_u^T \cdot \dot{\psi} + \frac{\delta R_u}{\delta \zeta} \cdot R_u^T \cdot \zeta \\ \omega_b &= \frac{\delta R_b}{\delta \varphi} \cdot R_b^T \cdot \dot{\varphi} + \frac{\delta R_b}{\delta \sigma} \cdot R_b^T \cdot \dot{\sigma} + \frac{\delta R_b}{\delta \theta 1_i} \cdot R_b^T \cdot \theta 1_i\end{aligned}\quad (9)$$

The Jacobian matrix is an important calculation which can reveal the dexterity and singularity characteristics of a mechanism. Jacobian matrix of parallel manipulators usually are in the form as given in Eq. (10).

$$J_q \cdot \dot{\mathbf{q}} = J_x \cdot \dot{\mathbf{x}} \quad (10)$$

The closure equations shown in Eq. (8) can be used for the Jacobian matrix by the use of elimination. Upper manipulator first joints of each leg are the actuator joints, thus passive joints $\theta 2_i$ and $\theta 3_i$ can be eliminated by multiplying the closure equations with $(\mathbf{v}_i \times \mathbf{w}_i)$.

$$\mathbf{u} \cdot (\mathbf{v}_i \times \mathbf{w}_i) \cdot \dot{\theta} 1_i = \omega_u \cdot (\mathbf{v}_i \times \mathbf{w}_i), \quad \text{for } i = 1, 2, 3 \quad (11)$$

Bottom manipulator active joints are the first joint in first leg and the first two joints in the second and the third leg. This brings a different approach to elimination compared to the upper manipulator and the resultant equations, which are shown below in Eq. (12).

$$\begin{aligned}\omega_{b,1} &= (\mathbf{p}_1 \cdot \dot{\phi} 1_1 + \mathbf{q}_1 \cdot \dot{\phi} 2_1 + \mathbf{r}_1 \cdot \dot{\phi} 3_1) \cdot (\mathbf{q}_1 \times \mathbf{r}_1) \\ &\quad \dot{\phi} 1_1 p_1 \cdot (q_1 \times r_1) - \omega_{b,1} \cdot (q_1 \times r_1) = 0 \\ \omega_{b,2} &= (\mathbf{p}_2 \cdot \dot{\phi} 1_2 + \mathbf{q}_2 \cdot \dot{\phi} 2_2 + \mathbf{r}_2 \cdot \dot{\phi} 3_2) \cdot (\mathbf{r}_2) \\ &\quad \dot{\phi} 1_2 \cdot (p_2 \times r_2) + \dot{\phi} 2_2 \cdot (q_2 \times r_2) - \omega_{b,2} \times r_2 = 0 \\ \omega_{b,3} &= (\mathbf{p}_3 \cdot \dot{\phi} 1_3 + \mathbf{q}_3 \cdot \dot{\phi} 2_3 + \mathbf{r}_3 \cdot \dot{\phi} 3_3) \cdot (\mathbf{r}_3) \\ &\quad \dot{\phi} 1_3 \cdot (p_3 \times r_3) + \dot{\phi} 2_3 \cdot (q_3 \times r_3) - \omega_{b,3} \times r_3 = 0\end{aligned}\quad (12)$$

The Jacobian Matrices for both of these manipulators are formed by separating the inputs and outputs as shown in Eq. (10). Using the J_x matrix shown in Eq. (10) instead of Γ in Eq. (6), replacing the generalized coordinate q_j with the output values vector and using known moments, a list of λ_i are obtained. Torque values are found by using the derived λ_i values, replacing the Γ term with J_q and the generalized coordinate with the input values vector. Three torque values for the upper manipulator and five torque values for the bottom manipulator are found with these equations.

3 Conclusions and Future Work

The inverse kinematic and dynamic calculations were made for a 5 DOF overconstrained manipulator defined for the shoulder-elbow motion of the human arm. The mechanism was separated into two parts by the use of an imaginary joint and the calculations were made accordingly. The usage of imaginary joints and solving the system separately proves to be a viable method for kinematic and dynamic solving of overconstrained manipulators.

For future work the control for active and passive rehabilitation tasks is planned. Scapula motion can be added to the mechanism for better and more diverse ways of conducting rehabilitation.

References

1. Angeles, J.: *Fundamentals of Robotic Mechanical System*. Springer (2002)
2. Bühler, C.: Robotics for rehabilitation—a European (?) perspective. *Robotica* **16**(5) (1998)
3. Kong, X., Gosselin, C.M.: *Type Synthesis of Parallel Mechanisms*. Springer Tracts in Advanced Robotics, vol. 33 (2007)
4. Manna, S.K., Bhaumik, S.: A Bioinspired 10 DOF wearable powered arm exoskeleton for rehabilitation. *J. Robot.* **2013**, Article ID: 741359 (2013)
5. Mao, Y., Agrawal, S.K.: A cable driven upper arm exoskeleton for upper extremity rehabilitation. In: *IEEE International Conference on Robotics and Automation*. Shanghai, China (2011)
6. Pan, M.: *Improved Design of a Three-Degree of Freedom Hip Exoskeleton Based on Biomimetic Parallel Structure* (2011)
7. Tsai, L.W.: *Robot Analysis: The Mechanics of Serial and Parallel Manipulators*. Wiley, Canada (1999)
8. Wrosch, C., et al.: Physical health problems, depressive mood, and cortisol secretion in old age: buffer effects of health engagement control strategies. *Health Psychol.* **26**(3) (2007)

Part XIII
Robotics—Teleoperation, Haptics,
Virtual Reality

Image Processing Based Stiffness Mapping of a Haptic Device

B. Taner and M.İ.C. Dede

Abstract The widely accepted performance criteria of haptic devices, which are transparency and z-width, are affected by the stiffness characteristics of the haptic device's mechanism. In addition indirect measurement of the handle pose of a haptic device is also affected by the stiffness characteristic. In this study, image processing techniques are used in the experimental setup to develop a stiffness map of a haptic device. The experimentally developed stiffness map is presented and the results are discussed by addressing future works.

Keywords Stiffness mapping · Image processing · Haptic device

1 Introduction

Haptic feedback in teleoperation systems provide users increased information about the distant site and enhances the feeling of being present in the remote site, which is generally termed as telepresence. During the haptic interaction, the interaction force and/or position information about the remote environment is provided to the user and also the haptic device allows the user to manipulate (by means of a telerobotic manipulation) the remote environment, which is called the slave environment in a teleoperation setting or virtual environment in virtual reality (VR) applications. In order to manipulate the slave, the pose of the haptic device's handle should be acquired. For precise operations, the motion tracking of the handle should be improved [8]. These systems are human-in-the-loop-systems and the performance of the haptic system highly relies on the physical coupling and visuo-haptic co-location of the user's hand and the slave device in remote environment through a haptic interface [2].

B. Taner · M.İ.C. Dede (✉)
Izmir Institute of Technology, Urla, Turkey
e-mail: candede@iyte.edu.tr

B. Taner
e-mail: baristaner@iyte.edu.tr

Level of coupling of human and remote environment are dependent on properties of haptic devices in terms of transparency [9] and impedance width or z-width [7, 10]. These properties, which are also called the performance criteria of haptic devices, are affected by several non-geometric inaccuracy factors; in particular, by the compliance of the haptic device mechanism. The effect of this inaccuracy factor on the performance of the haptic device can be reduced in preliminary design or in operation, using compensation techniques. Therefore, the compliance of the haptic devices must be calculated and/or obtained by using modeling by Finite Element Analysis (FEA), Structural Matrix Analysis (SMA), Virtual Joint Method (VJM) or by experimental methods that rely on absolute measurement of the compliant displacements of the haptic mechanism.

This paper describes procedure and results of obtaining the compliance mapping of a haptic device called HIPHAD v1.0, which is previously developed in IzTech Robotics Laboratory [3], experimentally. A stereo camera system is used to reveal the compliant properties of this haptic device, which has an R-CUBE type translational mechanism. The novelty of the presented method is that cameras are used instead of interfering the mechanical systems impedance by additional hardware for measuring compliance matrix. Also, the stiffness properties of the haptic device HIPHAD are measured for the first time. This paper is organized so that the next section covers a brief description of the previously employed methods for calculating the stiffness properties of mechanisms. Later, the experimental test setup and camera calibration is explained. In the fourth section, the results of experimental compliant displacement measurements are given. Finally, the results are discussed and future works are addressed.

2 Background Information

In the previous works, modeling methods are formulated to obtain the stiffness matrix of mechanisms. Among these some provide relatively accurate results like the FEA methods and some provide computationally effective solution so that they can be used in on-line calculations. Although, the difference between the modeling-based results and experimental result are narrowing down with the improvements in the models, there is still a noteworthy error between these methods for high precision applications [4]. To identify the reason of deviation between the modeling and experimental methods, experimental methods can be studied. The previously conducted experiments share the same methodology of measuring the compliant displacement of the robot mechanism's end-effector under external forcing. In the literature, researchers have measured the end-effector displacements by various absolute measurement devices; for example, [6] used dual indicators in measurement and followed the test procedure outlined in ASME Standard B5.54 (1993).

In another study, [1] made use of laser tracker for measuring the compliant displacement of a serial robot at heuristically determined points in its workspace. In

this study, force is applied through a wire on the end-effector and resultant forces in three axes are measured via a force sensor.

In the work of [11], a 5 step cycle procedure is defined for compliance measurements which is executed using inclinometer and a dial indicator; (1) dividing the workspace to nodes, (2) positioning the end-effector for each node, (3) preloading the end-effector, (4) measuring the initial position of the end-effector along each axis, (5) measuring the full loaded position of the end-effector along each axis.

Another method for measuring the compliant displacements is defined by [12], which they named it as Milli-CATRASYs. In this method, the compliant displacements measurement procedure initiates by acquiring the displacement information through the LVDT (Linear Variable Differential Transformers) sensors placed on the cables that are attached to the end-effector. Then, these displacements are used in calculating the end-effector's compliant displacements using the trilateration technique [5]. A possible problem with this measurement method is that the flexibility of the cables also play a part in the measurements. Therefore, observing the previous methods, our aim is to develop an experimental setup that can acquire the end-effector's compliant displacement without physically interacting with the mechanism. Vision-based absolute measuring system is an obvious solution, which is described next.

3 Experimental Setup

HIPHAD v1.0 was designed as a 6 degrees-of-freedom (DoF) kinesthetic haptic device that has a hybrid structure, which is composed of a 3 DoF active parallel translational mechanism, R-CUBE type, and a 3-DoF passive serial-spherical wrist mechanism. HIPHAD has a cubic workspace although R-CUBE mechanism has all active and passive revolute joints. More information on the mechanical design of the device can be found in [3]. Experimentation is executed by processing images taken by two cameras. Image processing algorithms used in this experimentation are run in Matlab.

Test rig is placed inside an enclosed dark room that is covering the surrounding of the test rig and LED light sources are used to provide uniform measurements with the vision system. The complete experimentation setup is presented in Fig. 1a with the numbers: (1) HIPHAD mechanism, (2) QUANSER Q8 data acquisition card (DAQ) for acquiring encoder measurements, (3) PC using the DAQ signals for calculating end-effector position indirectly by forward kinematics, (4) PC for processing images for stereo camera images to calculate the absolute position of the end-effector, (5) dark room, (6) LED strays, (7) one of the two cameras.

Stereo cameras are used for direct (absolute) measurement of the mobile platform/end-effector position. Therefore, the accuracy of the experimentation depends on the appropriate selection of these cameras. The lenses used in the cameras are FUJINON HF16HA-1B that have 16 mm focal length. Using this

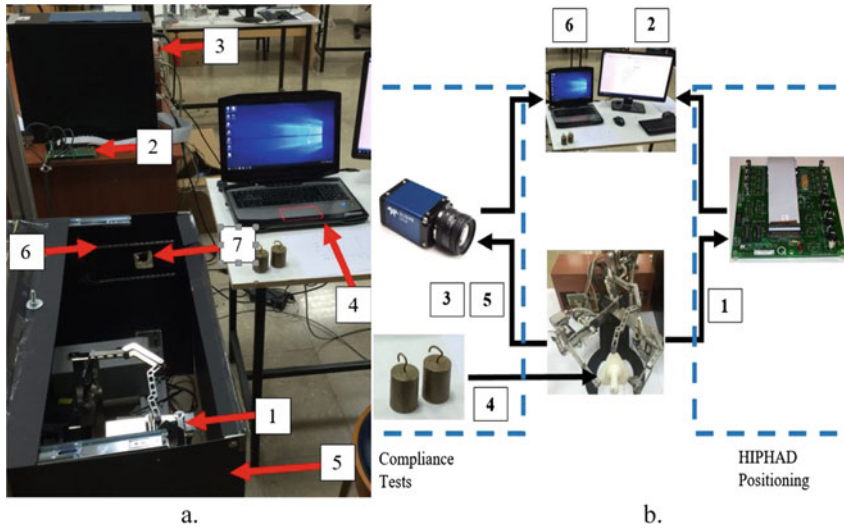


Fig. 1 Experimental test setup and procedure

camera-lens composition, smallest feature that can be detected by cameras is calculated to be at 0.165 mm for the camera axis that has 1600 pixels. A sub-pixel interpolation is implemented in vision algorithm to enhance the smallest feature that can be detected. To accommodate recalculation, radii of 4 circles that have different radii are measured using the measurement pattern. The selected diameters of the circles are 3.03, 3.08, 3.5, 4 mm. The diameter of the circle with 3.03 mm diameter is measured 20 times with the cameras and average of this measurement came out to be 68.2289 pixels with a standard deviation of $\sigma = 0.0277$. For the circle having 3.08 mm diameter, image processing algorithm resulted in 70.2525 pixels for average diameter measurement with a standard deviation of $\sigma = 0.0798251$. As a result, cameras along with the developed image processing algorithm found to be capable of measuring 0.025 mm with 1 pixel.

4 Experimentation Methodology

The experiments are carried out by first determining the nodes to be used for measuring compliant displacements under external loads. The cubic workspace of the mechanism defined for the motion of the wrist point (in this case the end-effector) on the mobile platform is divided into three equal parts on each side of the cube resulting in 27 measurement nodes. To settle the wrist point of the HIPHAD on these specified nodes, the forward kinematics solution of HIPHAD is employed by using the acquired angular position values from encoders. It should be noted that the joint actuators are replaced with stoppers in order to restrain the

motion of the first link rigidly. Whenever the HIPHAD mechanism is positioned on a specified node, the image acquisition process is initiated.

At this stage, 2 images are acquired which are taken before and after the force along the direction of measurement is applied on the mobile platform of HIPHAD. These images are processed by high pass filter and converted to a binary image. Following that, a blob analysis is applied on this binary image that is extracted from the raw image and coordinates of the tracking pattern in each position, which is the position of one of the calibration circles in initial and final positions. Then the positional difference is calculated and converted to world coordinate units in mm. This testing procedure is schematically explained in Fig. 1b, in which the numbers denote the sequence of the stages. The sequence from 1 to 6 in Fig. 1b is explained as follows: (1) measurement of the mobile platform's indirect position using encoders and acquiring the sensory data via Quanser Q8 DAQ, (2) position calculation of mobile platform by using forward kinematics to guarantee the settling of the mobile platform on the designated node, (3) image acquisition of the mobile platform when no external forces are applied, (4) application of external forces on the mobile platform by using calibrated weights, (5) image acquisition of the mobile platform under external forces, (6) image processing and compliant displacement calculation.

5 Experimental Test Results

Compliant displacement measurements are carried out when forces are applied along the Cartesian frame axes. The force along each axis is provided by pulling the mobile platform by a 700 g of calibrated mass that is passing through a plate with holes (to resemble the action of a pulley system), which is used to change the direction of the force. The calibrated mass provides forces in positive directions with respect to the world frame along x- and y-axes. However, along z-axis, the force created by the calibrated mass is in the negative direction. It should be noted that the compliant displacement measurements obtained at 9 nodes, which are on the same plane, are used in a cubic interpolation algorithm to estimate the compliant displacement values in between the nodes.

The workspace of the mechanism is placed in between 160 and 280 mm along each Cartesian axis. Test results for compliant displacement when the forces are applied along the x-direction measured for the nodes on plane 1, which intersects y-axis at 160 mm, yield the results provided in Fig. 2. In Figs. 2, 3 and 4, dark gray regions denote the workspace locations in which the mechanism has the highest stiffness on the respective plane and the light gray regions denote the workspace locations in which the mechanism has the highest compliance on the respective plane. In Fig. 2, the compliant displacement values range between 0.7 and 1.75 mm. The maximum compliant displacement on this plane is found on node defined at N(160, 280) by 1.72 mm and minimum compliant displacement is measured at node N(160, 160) by 0.84 mm along the direction of the applied force,

Fig. 2 Compliant displacement measurements of HIPHAD in x-axis on Plane 1

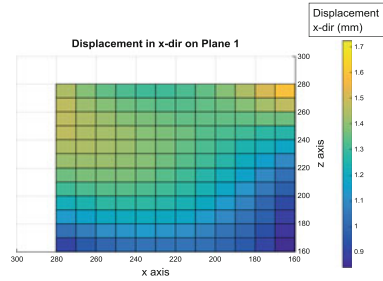
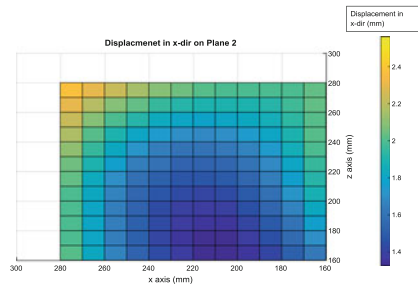


Fig. 3 Compliant displacement measurements of HIPHAD in x-axis on Plane 2

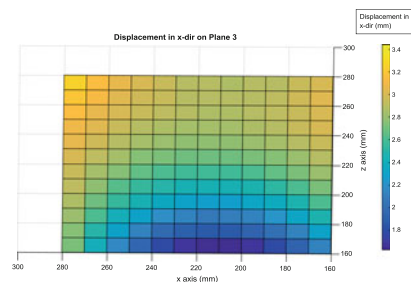


(+) x-direction. The stiffness variations indicate that for plane 1, HIPHAD has a greater stiffness at the bottom corners and less stiffness at the top corners.

On Plane 2, which intersects y-axis at 220 mm, the compliant displacement values that are measured at the 9 nodes are presented in Fig. 3 in which the areas in between the nodes are calculated by cubic interpolation. Maximum and minimum displacement values on this plane are found on the nodes defined at N(280, 280) and N(210, 160), which are 2.56 and 1.33 mm, respectively.

Figure 4 is plotted according to the compliant measurement data acquired on Plane 3, which intersects y-axis at 280 mm. For this measurement set, maximum and minimum values of compliant displacements are measured on nodes N(280, 280) and N(210, 160), which came out to be 3.442 and 1.630 mm, respectively. Similarity between the measurements on all planes is that the compliant

Fig. 4 Compliant displacement measurements of HIPHAD in x-axis on Plane 3



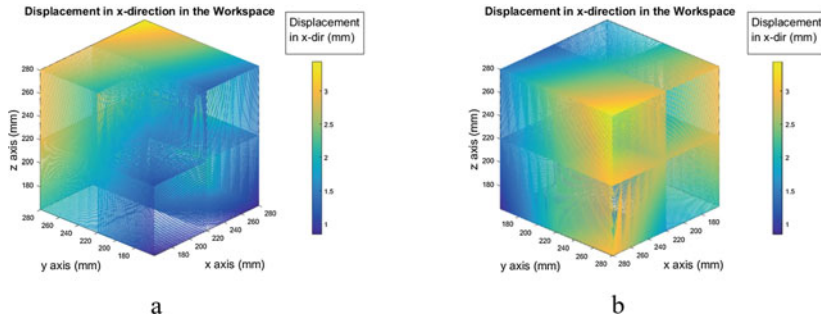


Fig. 5 Compliant displacement map under 700 g force along (+) x-axis throughout its workspace

displacements are increased towards the outer boundary of the workspace along z-axis, which was expected.

To provide better visualization of HIPHAD compliance map, in between the nodes that measurements are received, interpolation is carried out for the whole workspace. It can be observed from Fig. 5 that HIPHAD displays an increasing compliance (or in other terms decreasing stiffness) values when the mobile platform is moved from the fully folded position at 160, 160 and 160 mm to the fully extended position at 280, 280 and 280 mm along x, y and z directions, respectively. Figure 5a, b show the same experiment results received for the external forces acting along (+) x-axis in different views.

6 Discussions and Conclusions

In this study, stiffness characteristic of the HIPHAD haptic device is evaluated and mapped by using vision-based absolute position measurement method. The measurements are accommodated by using stereo cameras to capture absolute positions of the mobile platform and finding the difference between two cases; when no external load is applied and when external load is applied. It can be concluded from the results of this study that HIPHAD becomes more compliant on the most extended positions. However, it can be discussed that the measured displacement of the mobile platform under external forces is not only a result of the compliant behavior of the mechanism but joint wear and joint clearance also play a part.

Based on the obtained stiffness characteristics of HIPHAD, future work on the design changes for the HIPHAD mechanism can include an improved joint structure design that has smaller joint clearances and use of materials with high strength-to-weight ratio, such as carbon-fiber pipes, for constructing the links.

Another future work is to obtain a computationally effective and relatively accurate stiffness model of HIPHAD to be used in increasing the precision in the handle's motion acquisition under the influence of the forces applied by the human.

Acknowledgments This work is supported in part by The Scientific and Technological Research Council of Turkey via grant number 115E726.

References

1. Alici, G., Shirinzadeh, B.: Enhanced stiffness modeling, identification and characterization for robot manipulators. *IEEE Trans. Robotics* **21**(4), 554–564 (2005)
2. Barbieri, L., Bruno, F., Cosco, F., Muzzupappa, M.: Effects of device obtrusion and tool-hand misalignment on user performance and stiffness perception in visuo-haptic mixed reality. *Int. J. Hum Comput Stud.* **72**(12), 846–859 (2014)
3. Bilginçan, T., Gezgin, E., Dede, M.I.C.: Integration of the hybrid-structure haptic interface HIPHAD v1.0. In: *Proceedings of the International Symposium of Mechanism and Machine Theory*, Izmir, Turkey, pp. 267–284, 5–8 Oct 2010
4. Carbone, G.: Stiffness analysis and experimental validation of robotic systems. *Frontiers Mech. Eng.* **6**(2), 182–196 (2011)
5. Carbone, G.: Stiffness evaluation of multibody robotic systems PhD Dissertation, LARM, University of Cassino, Cassino (2003).
6. Clinton, C.M., Zhang, G., Wavering, A.J.: Stiffness Modeling of a Stewart Platform Based Milling Machine (1997)
7. Colgate, J.E., Brown, J.M.: Factors affecting the z-width of a haptic display. In: *1994 IEEE International Conference on Robotics and Automation. Proceedings*, (pp. 3205–3210). IEEE (1994)
8. Hirche, S., Buss, M.: Human-oriented control for haptic teleoperation. *Proc. IEEE* **100**(3), 623–647 (2012)
9. Hokayem, P.F., Spong, M.W.: Bilateral teleoperation: An historical survey. *Automatica* **42**(12), 2035–2057 (2006)
10. Lawrence, D.A.: Stability and transparency in bilateral teleoperation. *IEEE Trans. Robot. Autom.* **9**(5), 624–637 (1993). doi:[10.1109/70.258054](https://doi.org/10.1109/70.258054)
11. Pinto, C., Corral, J., Altuzarra, O., Hernández, A.: A methodology for static stiffness mapping in lower mobility parallel manipulators with decoupled motions. *Robotica* **28**(05), 719–735 (2010)
12. Ceccarelli, M., & Carbone, G. (2005). Numerical and experimental analysis of the stiffness performances of parallel manipulators. In *2nd international colloquium collaborative research centre* **562**, 21–35 (2005)

Part XIV
Robotics—Compliant Structures

Kinematic Analysis of a Flexible Tensegrity Robot

O. Altuzarra, M. Diez, J. Corral and F.J. Campa

Abstract In the field of parallel kinematics few designs use highly deformable elements to obtain the end effector movement. Most compliant mechanisms rely on notches or shape changes to simulate a standard kinematic joint. In this work a kinematic model of a simple parallel continuum mechanism that combines a deformable element and cable is presented. The kinematic model is used to study the workspace of the manipulator and is validated by experimental measurements of a prototype.

Keywords Parallel continuum robot · Compliant mechanism · Kinematic analysis · Experimental mechanics

1 Introduction

A new trend in parallel kinematic manipulators design is the use of ultradeformable elements in order to obtain the end effector movement [1, 2]. One critical problem in the design process of this type of robots is the lack of available information, which usually is reduced to classical texts about nonlinear deformations [3]. Some MEMS (Micro Electro Mechanisms) [4, 5] do share the parallel morphology but lack the non-linear deformations that their macroscopic counterparts do suffer.

In this paper a two-degree of freedom parallel continuum robot is studied. The mechanism combines a highly deformable element with a cable, being possible to change either the cable or the beam lengths, thus, obtaining a larger workspace. In

O. Altuzarra · M. Diez (✉) · J. Corral · F.J. Campa
University of the Basque Country UPV/EHU, Leioa, Spain
e-mail: mikel.diez@ehu.eus

O. Altuzarra
e-mail: oscar.altuzarra@ehu.eus

J. Corral
e-mail: j.corral@ehu.eus

F.J. Campa
e-mail: fran.campa@ehu.eus

order to solve the kinematics of the robot, the fundamentals of non-linear analysis of flexible bars are briefly explained. The kinematic problem of the parallel continuum robot is then solved using an analytical procedure. To validate the results a prototype has been built in which the beam deformation and the tension suffered by the cable have been measured.

2 Fundamentals of Nonlinear Analysis of Flexible Bars

In the following we will state some fundamentals about the analytical solution of the non-linear deflection of a slender element under bending in a plane. To start with, it acquires the form of a planar curve as in Fig. 1, Navier-Stokes hypothesis assumes that its cross sections remain planar and perpendicular to the bent curve, and Bernoulli-Euler law establishes that the bending moment M at a point is proportional to the curvature κ :

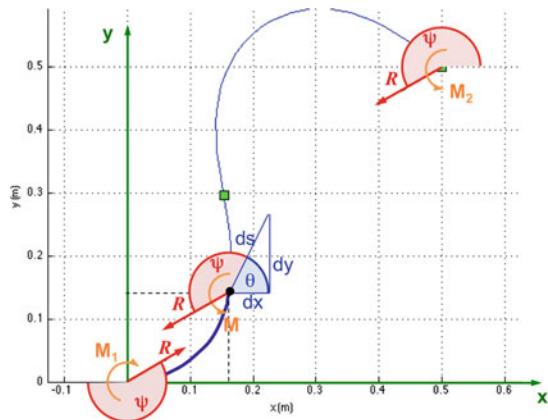
$$\kappa = \frac{d\theta}{ds} = \frac{M}{EI} \tag{1}$$

where E is the elastic modulus and I is the moment of the cross section about the neutral axis.

We define for a section in equilibrium (see Fig. 1): R and ψ as the reaction force's magnitude and direction at the extreme, M_1 and M_2 as the bending moments at a extremes, and M as the bending moment at a cross-section. The static equilibrium of moments for a portion of the bar can be expressed to get M and substitute into Eq. 1:

$$\kappa = \frac{d\theta}{ds} = \frac{M}{EI} = \frac{M_1}{EI} + \frac{R}{EI} \cos \psi \ y - \frac{R}{EI} \sin \psi \ x \tag{2}$$

Fig. 1 A section of the bar at equilibrium



Its derivative with respect to the arc length s , expressed in terms of θ , yields:

$$\begin{aligned} \frac{d\kappa}{ds} &= \frac{d^2\theta}{ds^2} = \frac{R}{EI} \cos \psi \frac{dy}{ds} - \frac{R}{EI} \sin \psi \frac{dx}{ds} = \\ &= \frac{R}{EI} \cos \psi \sin \theta - \frac{R}{EI} \sin \psi \cos \theta = \frac{R}{EI} \sin(\theta - \psi) \end{aligned} \quad (3)$$

Its integration requires a complex mathematical manipulation. Several approaches exist in the literature, here we will follow [4], where we get an integral from one extreme of the bar of length L to the other as:

$$\sqrt{\frac{RL^2}{EI}} = \int_{\phi_1}^{\phi_2} \frac{1}{\sqrt{1 - k^2 \sin^2 \phi}} d\phi = F(k, \phi_2) - F(k, \phi_1) \quad (4)$$

being $F(k, \phi)$ the incomplete elliptic integral of the first kind, and k and ϕ are some auxiliary variables for integration. And the curvature at each point is given by:

$$\kappa = \frac{d\theta}{ds} = 2k \sqrt{\frac{R}{EI}} \cos \phi \quad (5)$$

If we are interested in the case of a bar with a clamped end and the other pinned, boundary condition on the slope of the bar at the first extreme, θ_1 , is given (and always can be taken null), while the other end has a null curvature. For a given force at extremes R and ψ , we can state the limits for integration, ϕ_1 and ϕ_2 :

$$\phi_1 = \arcsin\left(\frac{1}{k} \cos\left(\frac{\psi}{2}\right)\right) \quad \phi_2 = q\pi/2 \quad (6)$$

where $\phi_1 = [-\pi/2, \pi/2]$, and q has even values that determine the Mode of buckling (see Fig. 2). The angle ϕ will vary continuously from ϕ_1 to ϕ_2 . Then, modulus $k = [-1, 1]$ can be obtained iteratively on Eq. (4) for a certain value of q . Inflection points of the bar correspond to values $\phi = n\pi/2$ with even values of n below q if they exist.

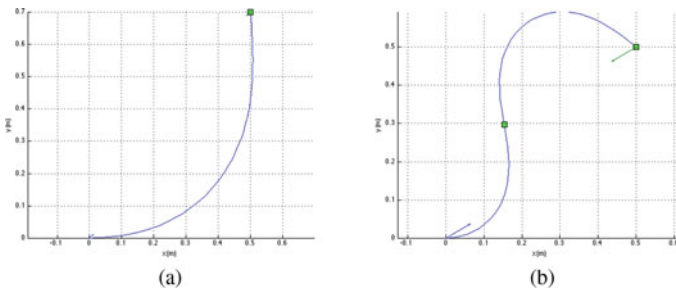


Fig. 2 Modes 1 and 2 of the buckling of a clamped-pinned bar

In order to get the x coordinate of a point in the curve we can manipulate Eq. (5) to get the integral:

$$\begin{aligned}
 x = & -\sqrt{\frac{EI}{R}} \cos \psi [2E(k, \phi_i) - 2E(k, \phi_1) - F(k, \phi_i) + F(k, \phi_1)] + \\
 & + \sqrt{\frac{EI}{R}} 2k \sin \psi [\cos \phi_i - \cos \phi_1]
 \end{aligned}
 \tag{7}$$

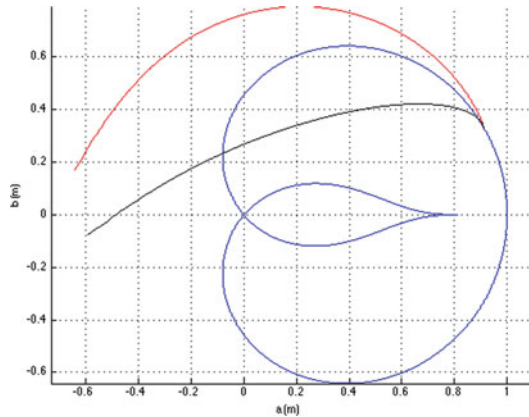
where $E(k, \phi)$ is the incomplete elliptic integral of the second kind. In order to get the y coordinate an analogous deduction to the one followed for x can be done.

For a given value of the coordinates of the extreme of the deflected bar, i.e. a, b , and the boundary conditions, we must iterate on ψ and k in Eq. (4), obtaining a and b from Eq. (7) and analogous, and verifying that the error obtained is below a given threshold.

From the above results we can infer that solutions can be found between some limiting values for k in an unknown range of ψ and for each mode separately. A minimum value for k , upon analysis of Eq. (6), corresponds to $k_{min} = \|\cos(\frac{\psi}{2})\|$, positive for the range $k = [k_{min}, 1]$ and negative for the range $k = [-k_{min}, -1]$.

If we restrict ourselves to positive values of k , and plot the end positions of the bar for a given value of ψ in the range from k_{min} to $k = 1$ we get the plot in Fig. 3. As it can be seen, solutions for both modes start from the limiting curve of k_{min} and go up to a k value of 1.

Fig. 3 Solutions for Modes 1 (red curve) and 2 (black curve) for $\psi = 200$ from k_{min} to $k=1$ (color figure online)



3 Kinematic Analysis of the 2 DoF Parallel Continuum Robot

The mechanism proposed is a closed loop device, see Fig. 4. A slender bar is actuated through a fixed support that keeps a constant orientation at that section, so the length l of the deformed bar is variable. Also, a cable is attached to the extremity of the bar in P and its length λ can also be controlled varying δ . Hence, the system has 2 degrees of freedom that control the position on the plane of the end-point P .

In order to solve the inverse position problem, given the desired coordinates for P , i.e. x_P and y_P , we can find the required length for the cable straightforward. The orientation of the end-force R , i.e. the angle ψ of the force applied at the end-point is found. Then, we can iterate in the k parameter for equations Eqs. 6 and 7 until we find a value that produces an end-point position closer to the objective than a given threshold. The analytical solution is quite simple and the iterative process reaches a solution quickly.

The described methodology has been used to obtain information regarding the workspace of the manipulator. The tension of the cable, the Von Mises stress in the exit point of the beam have been calculated. As the analytical procedure solves the inverse kinematic problem, the error between the objective position and the obtained position has also been calculated. All these values can be seen in Fig. 5.

Cable tension and Von Mises stress behave as expected, increasing as deformation in the beam increases. The same happens with the error, as it becomes higher with as the location of the end effector requires a bigger deformation of the beam.

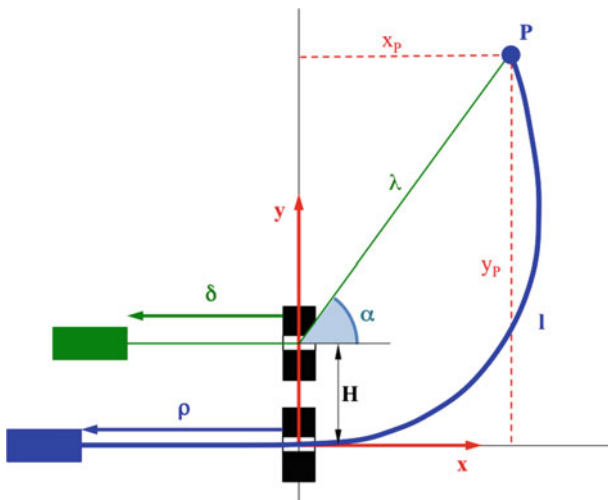


Fig. 4 Continuum Parallel Robot

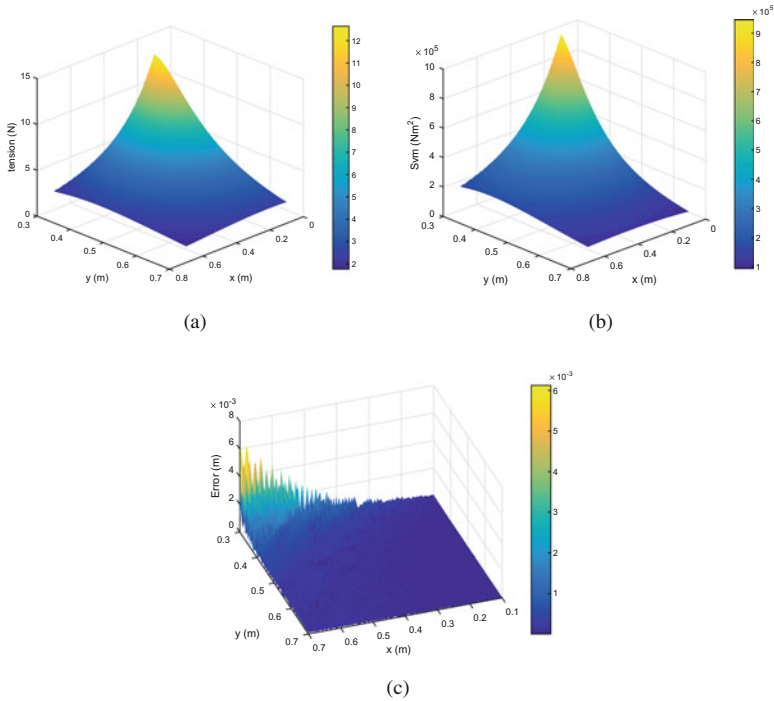


Fig. 5 Study of the workspace of the manipulator. **a** Force in the cable. **b** Von Mises stress in the beam. **c** Analytical procedure error

4 Numerical and Experimental Validation

In order to verify the analytical model of the parallel robot a prototype has been built. In the prototype it is possible to measure the deformation of the beam and the tension in the cable. Measurements have been made using a MC 850 ZEISS three-dimensional measuring machine (precision is ± 0.005 mm). The experimental setup can be seen in Fig. 6. Two different positions have been measured, corresponding to $x = 556.7$ mm $y = 335.3$ mm and $x = 650.4$ mm $y = 199.8$ mm.

The numerical approach based on FEM has only been used to derive the direct kinematic problem. The model consists of two elements where the thinner represents the cable under tension and, the bigger one, the element of the model which is subject to bending. Both the elements have been considered as two beams, the cable is a bi articulated beam so it behaves as the cable and the other is a cantilever beam with the free end attached to the cable. The software used in the simulation has been ANSYS®.

Regarding the deformed shape of the robot, analytical, numerical and experimental model results are compared in Fig. 7. The shape of the deformed models match perfectly the experimental data. Calculated cable length also matches the experimen-

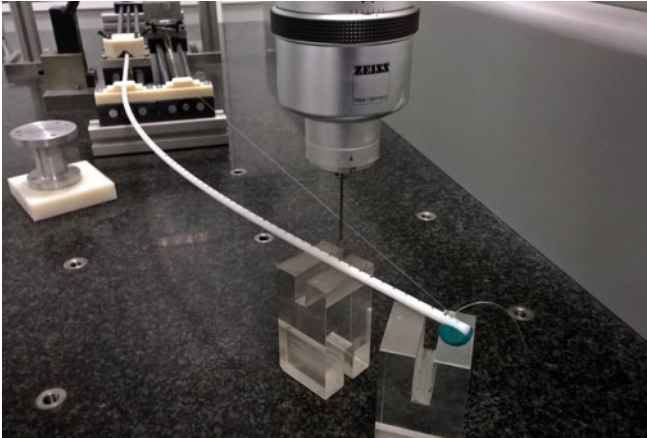
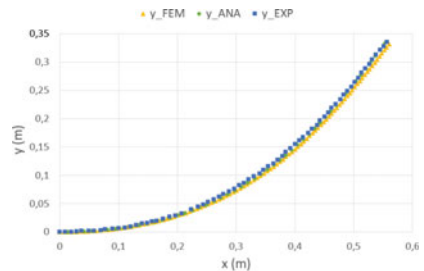
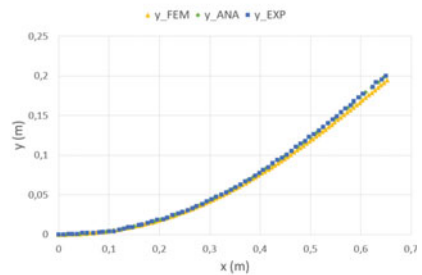


Fig. 6 Experimental setup for experimental measurements

Fig. 7 Deformed shape comparison for **a** cable force 3.6 N and **b** cable force 2.55 N



(a)



(b)

tal model measures. Discrepancies appear on the applied force. In Fig. 7b, a cable force of 2.94 N is applied whereas the analytical model predicts a 2.55 N force. The same happens in Fig. 7a where 4.9 N where applied when the analytical model yielded 3.65 N. For this latter case, the value of the force in the cable obtained from the numerical model yields 3.603 N. This deviation may happen because of the experimental error derived from the accuracy of the measuring devices and the

friction suffered by the cable and the guide. The force in the cable has been measured by means of a load cell with a precision of 10 g.

5 Conclusions

Combination of deformable elements and cables may produce a feasible parallel continuum robot, that still benefit from the compliant mechanism properties. In this paper a methodology to solve the kinematic problem of such mechanism is proposed. The analytical procedure solves the inverse kinematic problem whereas the direct kinematic problem is solved using FEM. The numerical results are validated with an experimental model, showing good correlation between the numerical and experimental data.

Acknowledgments The authors wish to acknowledge the financial support received from the Spanish Government through the Ministerio de Economía y Competitividad (Project DPI2015-64450-R) and the Regional Government of the Basque Country through the Departamento de Educación, Universidades e Investigación (Project IT445-10) and UPV/EHU under program UFI 11/29.

References

1. Bionic Tripod 3.0. Festo Innovation and Technology. <http://www.festo.com>
2. Bryson, C.E., Rucker D.C.: Toward parallel continuum manipulators. In: IEEE International Conference on Robotics and Automation, pp. 778–785 (2014)
3. Antman, S.S.: Nonlinear Problems of Elasticity. Springer (2005)
4. Holst, G.L. et al.: Modeling and experiments of buckling modes and deflection of fixed-guided beams in compliant mechanisms. *J. Mech. Des.* **133**, 051002-1-10 (2011)
5. Zhang, A., Chen, G.: A comprehensive elliptic integral solution to the large deflection problems of thin beams in compliant mechanisms. *J. Mech. Robot.* **5**, 021006–1 (2013)

Adaptive Compliant Gripper Finger with Embedded Contracting and Extending Actuators

A. Milojević, N.D. Pavlović and H. Handroos

Abstract Developing a gripper that can realize different shapes of its grasping surface and thus grasp different shaped objects, represents a challenging task. Compliant monolithic structures known as compliant mechanisms represent one way to obtain the gripper that can adapt its grasping surface to different shaped objects. This paper introduces a new concept of an adaptive compliant gripper finger with embedded actuators. By using embedded actuators gripper finger can change the shape of its grasping surface and achieve multiple grasping patterns. Synthesis approach for the gripper finger is also presented. It will be shown that gripper finger can realize complex grasping patterns via embedded actuators (in this paper via combination of contracting and extending actuators).

Keywords Adaptive gripper finger • Compliant mechanism • Embedded contracting and extending actuators • Shape morphing surface • Synthesis

1 Introduction

Developing a gripper that can realize grasping of different shaped objects represents a challenging task. Grasping such objects essentially requires adaptability for safe and reliable object manipulation. Many researchers developed different universal flexible grippers that can in some sense achieve adaptability [1–3, 6]. But most of

A. Milojević (✉) • N.D. Pavlović
Faculty of Mechanical Engineering, University of Niš, Niš, Serbia
e-mail: andrija.milojevic@masfak.ni.ac.rs; Andrija.Milojevic@lut.fi

N.D. Pavlović
e-mail: pavlovic@masfak.ni.ac.rs

H. Handroos
Lappeenranta University of Technology, Lappeenranta, Finland
e-mail: heikki.handroos@lut.fi

these grippers require external drive (compressed air or electrical motor) [1–3] and assembling. Moreover, there is no unique synthesis methodology for the adaptive grippers.

A different approach to achieve adaptability is to use compliant mechanisms [4]. A compliant mechanism can be defined as a monolithic flexible structure which uses elastic deformation to achieve force and motion transmission [4]. Compliant mechanisms deform smoothly as a whole. This represents unique feature of compliant mechanisms that could be used to realize shape-adaptable structures and provides a novel means to morph structural shape. Compliant mechanisms that change their shapes through structural deformations offer many benefits: reduced complexity, no wear, ease of manufacture, no assembly, better scalability, better accuracy, etc.

Synthesis of compliant mechanisms has been well studied in the past [5, 13], but little attention has been directed to problems related to synthesis of compliant mechanisms for shape morphing applications [7, 15]. Synthesis methods presented in [7, 15] are focused on developing a compliant mechanisms that can achieve only one target shape. These methods cannot be applied when developing a gripper that can adapt to different shaped objects as multiple shape patterns need to be created. In this paper shape-changing problem is set as the challenge of how to design an adaptive compliant gripper that is controllable and capable of achieving multiple shapes. One such adaptive gripper could be formed as compliant mechanism with inherent actuators and sensors. By embedding actuators and sensors within the compliant mechanism structure, gripper would be able to realize both sensing (via sensors) and appropriate response (via actuators and internal structure) to the unknown external environment, thus making the gripper adaptive.

More attention is paid to the problem of embedding actuators since the primary goal of the paper is to develop gripper that have structural adaptability. By embedding actuators within a compliant gripper structure, gripper may be capable of producing many complex grasping patterns.

The synthesis methodology for distributed actuation and sensing within a compliant active structure has been first introduced in [14], but the proposed method often produces compliant mechanism with lot of intersections between elements as well as elements and actuators, which are very difficult to manufacture. Beside this, intersection between elements often increases complexity and stiffness of the structure which can significantly lower the system functionality [10].

This paper presents the solution of adaptive compliant gripper (in this paper only one gripper finger) with embedded actuators. An improved design methodology for the simultaneous synthesis of compliant mechanism and actuator placement is presented in our previous paper [10]. The design methodology is improved so that compliant mechanisms with embedded actuators and without intersecting elements are obtained [10]. We will demonstrate that obtained adaptive compliant gripper finger with embedded actuators may be capable of achieving many different grasping patterns and thus having many advantages over existing grippers. The

results of behavior of the gripper finger with only contracting and only extending actuators is presented in [11]. Here we present results when combination of contracting and extending actuators are used.

2 Synthesis Methodology

To develop adaptive compliant gripper we use compliant mechanisms with distributed compliance [5], since the distributed compliance throughout the compliant mechanism provides a smooth deformation field, which reduces the stress concentration. The topology optimization approach is usually used for the design of mechanisms with distributed compliance [5, 8, 13].

Adaptive compliant gripper could be seen as compliant mechanism with embedded actuators. To develop an adaptive gripper, the structural topology of a compliant mechanism and actuator placement must be simultaneously synthesized.

The outline of the methodology that we use for developing adaptive compliant gripper with embedded actuators is shown in a pictorial example (Fig. 1). More detailed explanation regarding the synthesis methodology is given in [10], here we only present the overview. First the problem specifications are defined only for one gripper finger (Fig. 1a and Table 1). These includes: size of the design domain (allowable space for the design), grasping surface (left boundary of the design domain) and number of output points (three output points are chosen to represent the output region where horizontal direction is set to be the desired direction of the output deflection) [10], supports (the bottom boundary of the design domain - one part only), property of the material (Young modulus) from which the mechanism should be built and other constraints such as minimum value of the output

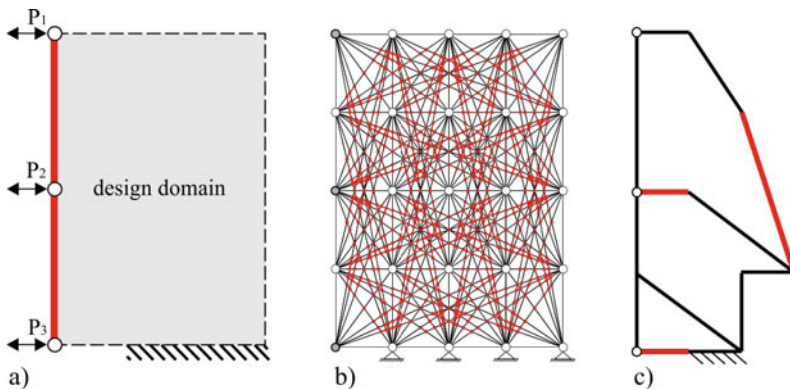


Fig. 1 The steps in the synthesis methodology: **a** problem specifications; **b** parameterization (intersections between elements are indicated by *red dots*); **c** optimized topology of adaptive compliant gripper finger with embedded actuators (actuators are indicated by *red lines*) [10, 11] (color figure online)

Table 1 Design specification for developing adaptive compliant gripper with embedded actuators

Design parameters	
Design domain	120 mm × 80 mm
Grid size	5 × 5
Degree of nodal connectivity	4
Number of beam elements	168
Element modulus	$E_{el} = 2.48 \text{ GPa}$
Actuator modulus	$E_{akt} = 500 \text{ MPa}$
Actuator block force	90 N
External load	0.1 N
Element out-of-plane thickness	1.5 mm
Element thickness choice	0.5, 1, 1.5 mm
Thickness of shape morphing surface	0.5 mm

deflection $d_{\min, \text{target}}^{\text{act}}$ and total element length L_t which is equivalent to the volume constraint [10]. All the design parameters are given in Table 1.

Next the design domain is parameterized (Fig. 1b). The physical design space must be broken down so as to be represented by a set of variables that an optimizer can act on. The Grounded Structure Approach (GSA) [5, 8, 13] is used for the parameterization. Therefore, the prescribed design domain is divided into a number of nodes, and a network of beam elements connecting these nodes serves as an initial guess. The design variables are the thickness of each element and variable that marks the element selected to be actuator; this variable has a value between 1 and the total number of elements (Table 1). The linear actuator model is used where at the ends of the beam axial force, equal to the block force [10], is applied. A thickness value of zero deactivates the element, removing it from the structure; other values represent thickness values (Table 1) [10].

It is important to mention that partially connected ground structure is used to parameterize the design domain. When using such ground structure the solutions with intersecting elements are usually obtained [5, 8] where elements and actuators would intersect also [14]. Producing a structure with intersecting elements as well as actuators is very difficult. Moreover intersections between elements often increase complexity and stiffness of the structure which can significantly lower the system functionality. This deficiency has motivated us to improve the existing topology optimization technique [14] so that the intersections between elements as well as actuators would be eliminated in the process of optimization. We apply the same idea as in [9], but now for the problem of synthesis of adaptive compliant gripper with embedded actuators. All the parameters regarding the parameterization are given in Table 1 [10].

After the parameterization is done, search method is applied to find the optimal compliant mechanism with embedded actuators. Because of the broad design space and number of elements, topology synthesis problems are solved with optimization methods. The goal of the optimization in the synthesis of compliant mechanisms with embedded actuators is to minimize the actuator number and maximize

structural adaptability of a compliant system (maximize controllability [10, 14]) while meeting given constraints. By maximizing controllability gripper will be able to achieve multiple grasping patterns of its shape morphing surface. Three actuators are required minimally to fully control the three output points (Fig. 1a) [10]. The objective function that we used for the synthesis of the adaptive compliant gripper with embedded actuators is presented in [10].

All objective function terms and constraints are calculated from the results of the linear finite element analysis (FEA), implemented in the computer-coded algorithm [10].

When the parameterization is discrete i.e. elements are either on or off, the discrete optimizations methods are used, of which Genetic Algorithms (GA) [12] are applied here. The genetic algorithm parameters used in the synthesis of the adaptive compliant gripper are: initial population of 200 designs, total number of 1000 generations, roulette selection function, crossover probability of 95 %, elite count of 2 members, and mutation probability of 9 %.

To obtain the adaptive compliant gripper with embedded actuators more than twenty GA's are run. The optimization process starts with 168 beam variables and total number of 1664 intersections in the initial ground structure (Fig. 1b). Figure 1c shows the result. This obtained solution contains the compliant structure in which some of the elements are eliminated and some chosen as actuators in the process of optimization. The remaining elements together with elements selected to be actuators define the optimal topology of the adaptive compliant gripper finger. High controllability ($\eta_C = 97.57\%$) of a compliant system is achieved. Unlike solutions in [14] here the compliant system without intersections is obtained (Fig. 1c).

3 FEM Analysis of the Adaptive Compliant Gripper Finger with Embedded Contracting and Extending Actuators

Based on the obtained solution (Fig. 1c) 3D solid model of the adaptive compliant gripper finger with embedded actuators was designed (Fig. 2a). Instead of using real actuators, here the actuators were modeled as thin elastic elements (in a form of a spring) that allow the actuation (Fig. 2a). Only one finger of the gripper is modeled as the fingers in two-fingered or multi-fingered gripper would have the same behavior.

To investigate adaptability of the compliant gripper finger to different shapes of the gripping objects, FEM simulations were performed (ABAQUS software was used). To simulate the contraction and extension of the actuators, a displacement of ± 5 mm as input (stroke of actuator) in the direction of the actuators axis was introduced at the both ends of the all actuators (Fig. 2a). The results of simulation of the gripper finger behavior with only contracting and only extending actuators

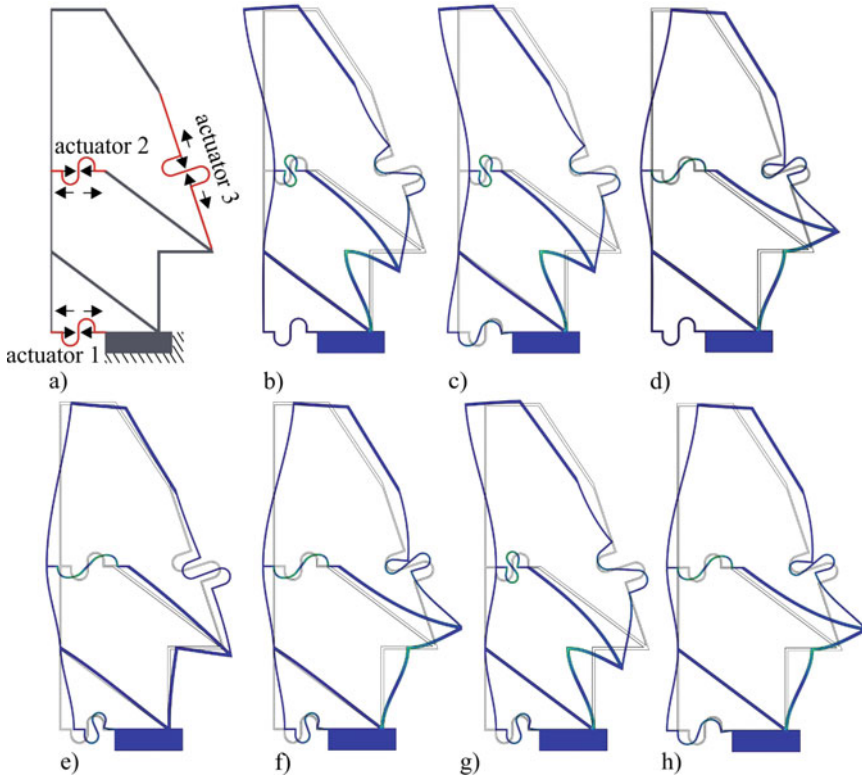


Fig. 2 Design of adaptive compliant gripper finger with embedded actuators (a) and FEM simulations when actuator 2 (contracting) and 3 (extending) are active (b), 1 (extending), 2 (contracting) and 3 (extending) are active (c), 2 (extending) and 3 (contracting) are active (d), 1 (contracting) and 2 (extending) are active (e), 1 (contracting), 2 (extending) and 3 (contracting) are active (f), 1 (contracting), 2 (contracting) and 3 (extending) are active (g), 1 (extending), 2 (extending) and 3 (contracting) are active (h)

were presented in [11]. In this paper we simulate the case when combination of contracting and extending actuators are used (some combination of contracting and extending actuators were presented in [11]). To show the capability of the gripper finger to produce multiple shapes of its shape morphing surface the FEM simulations were performed without any grasping object (Fig. 2).

The FEM results show that two main grasping patterns could be created: 'convex' (Fig. 2b, c) and 'concave' patterns (Fig. 2d–f); when actuators 2 (contracting) and 3 (extending) are active an object of convex shape could be grasped (Fig. 2b), and when actuators 2 (extending) and 3 (contracting) are active an object of concave shape could be grasped (Fig. 2d). Also convex-concave grasping patterns could be achieved when actuators 1 (contracting), 2 (contracting) and 3 (extending) are active (Fig. 2g). The results (Fig. 2) show that gripper finger has capability to grasp objects of different shapes and sizes.

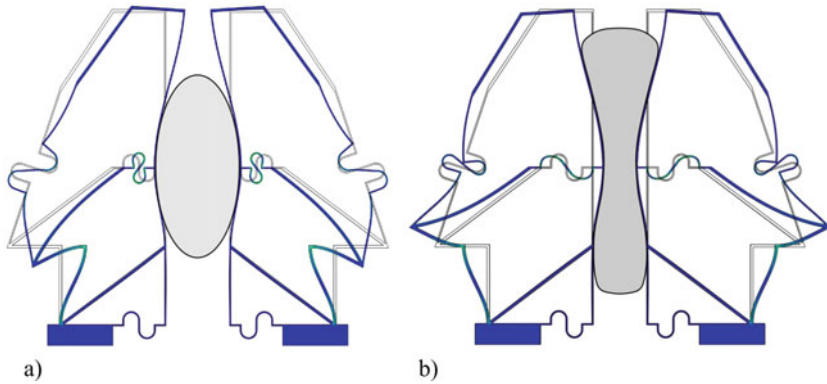


Fig. 3 The concept of two finger gripper with embedded contracting and extending actuators: **a** grasping of convex shaped object; **b** grasping of concave shaped object

Figure 3 shows the concept of two finger gripper grasping convex (Fig. 3a) and concave (Fig. 3b) shaped object.

With different stroke of the actuators grasping patterns of a different radii could be created. For example, for a different stroke of contracting actuator 2 (1 mm, 2 mm ...) and extending actuator 3 (1 mm, 2 mm ...) convex grasping patterns of a different radii could be achieved, which means that the gripper could grasp convex objects of a different size. The same case is if embedded contracting and extending actuators realize different values of strokes; for example if contracting actuator 2 realize stroke of 2 mm and extending actuators realize stroke of 5 mm.

4 Conclusions

This paper presents the original adaptive compliant gripper finger with embedded contracting and extending actuators. The presented gripper has capability to adapt to different shaped objects. The design methodology for the adaptive gripper finger was also presented; the synthesis methodology represents one novel approach to synthesis of adaptive compliant systems. This methodology could be used to develop different adaptive grippers according to designer needs. The FEM simulations were performed and the results demonstrate that by embedding contracting and extending actuators within the gripper finger structure the developed adaptive compliant finger has ability to produce many complex grasping patterns, thus having many advantages over existing grippers.

References

1. Amend Jr., J.R., Brown, E., Rodenberg, N., Jaeger, H., Lipson, H.: A positive pressure universal gripper based on the jamming of granular material. *IEEE Trans. Rob.* **28**, 341–350 (2012)
2. Choi, H., Koc, M.: Design and feasibility tests of a flexible gripper based on inflatable rubber pockets. *Int. J. Mach. Tools Manuf* **46**, 1350–1361 (2006)
3. Giannaccini, M.E., Georgilas, I., Horsfield, I., Peiris, B.H.P.M., Lenz, A., Pipe, A.G., Dogramadzi, S.: A variable compliance, soft gripper. *Auton. Robots* **36**, 93–107 (2014)
4. Howell, L.L., Magleby, S.P., Olsen, B.M.: *Handbook of Compliant Mechanisms*. Wiley, Somerset, NJ, USA (2013)
5. Joo, J., Kota, S., Kikuchi, N.: Topological synthesis of compliant mechanisms using linear beam elements. *Mech. Struct. Mach.* **28**, 245–280 (2000)
6. Jung, G.-P., Koh, J.-S., Cho, K.-J.: Underactuated adaptive gripper using flexural buckling. *IEEE Trans. Rob.* **29**, 1396–1407 (2013)
7. Lu, K.-J., Kota, S.: Design of compliant mechanisms for morphing structural shapes. *J. Intell. Mater. Syst. Struct.* **14**, 379–391 (2003)
8. Milojević, A., Pavlović, N.D., Milošević, M., Tomić, M.: New software for synthesis of compliant mechanisms. In: *Proceedings of The 2nd International Conference Mechanical Engineering in XXI Century*, Niš, Serbia, pp. 273–278 (2013)
9. Milojević, A., Pavlović, N.D.: Software for synthesis of compliant mechanisms without intersecting elements. *FACTA Universitatis, Series: Mech. Eng.* **11**, 153–168 (2013)
10. Milojević, A., Pavlović, N.D.: Development of a new adaptive shape morphing compliant structure with embedded actuators. *J. Intell. Mater. Syst. Struct.* (Accepted) doi:[10.1177/1045389X15590270](https://doi.org/10.1177/1045389X15590270), first publish on June 16 (2015)
11. Milojević, A., Pavlović, N.D.: Development of Adaptive Compliant Gripper Finger with Embedded Actuators. *Microactuators Micromechanisms Mech. Mach. Sci.* **30**, 33–49 (2014) (Springer)
12. Reeves, C.R., Rowe, J.E.: *Genetic Algorithms-Principles and Perspectives: A Guide to GA Theory*. Kluwer Academic Publishers, Dordrecht (2002)
13. Saxena, A., Ananthasuresh, G.K.: On an optimal property of compliant topologies. *Struct. Multi. Optim.* **19**, 36–49 (2000)
14. Trease, B., Kota, S.: Design of adaptive and controllable compliant systems with embedded actuators and sensors. *J. Mech. Design* **131**, 111001 (12 pp) (2009)
15. Zhao, K., Schmiedeler, J.P.: Using rigid-body mechanism topologies to design shape changing compliant mechanisms. In: *Proceedings of 2013 ASME Design Engineering Technical Conference, DETC2013–12576* (11 pp) (2013)

Kinematic and Dynamic Analysis of a 4DOF Parallel Robot with Flexible Links

N. Cretescu, M. Neagoe and R. Saulescu

Abstract The paper deals with the dynamic behaviour of a 4DOF parallel robot with decoupled motions, three orthogonal translations and one rotation, in a comparative approach of flexible versus rigid links, and also the influence of friction in the four active prismatic joints. The ADAMS software and its AUTOFLEX module were used to model the parallel robot and further to identify the end-effector motion errors on a representative trajectory, due to the natural flexibility of the robot links, and the variation of the actuating forces needed in the input joints with both links flexibility and active joints friction. The obtained numerical results show significant resultant errors of the end-effector from the planned trajectory, generated by link elastic deformations, and important errors of actuating forces (up to 300 %) in the assumption of both link flexibility and active joint friction. The results are useful for robot designers to optimally select the actuators and appropriate design the control system to ensure trajectory high accuracy on the robot workspace.

Keywords Parallel robot · ADAMS modelling · AUTOFLEX module · Flexible link · Friction · Analysis

1 Introduction

The parallel robots are closed kinematic chain type mechanisms, composed by a mobile platform (the end-effector) connected to the fixed base by two or more kinematic chains called limbs or legs [4]. Comparing with serial manipulators, parallel robots have the advantages of higher speeds and precision, higher loads and

N. Cretescu (✉) · M. Neagoe (✉) · R. Saulescu
RESREC Research Centre, Transilvania University of Brasov, Brasov, Romania
e-mail: ncretescu@unitbv.ro

M. Neagoe
e-mail: mneagoe@unitbv.ro

R. Saulescu
e-mail: rsaulescu@unitbv.ro

thinness of links. As consequence, the link flexibility under heavy operational conditions can be an important factor influencing significantly the end-effector trajectory accuracy and the driving forces/torques in active joints. Furthermore, friction forces in robot joints influence directly the driving generalised forces and implicitly the design of the actuating system by appropriate choice of actuators.

The link flexibility was approached in many works [1, 2, 5–10], using different modelling methods aiming especially to develop dynamic models and to study the robot mechanism behaviour in the assumption of elastic deformations of robot links. A dynamic finite element analysis of a planar fully parallel robot with flexible links is developed in [9]. By formulating and solving a set of linear ordinary differential equations of motion, the influence of mechanism configurations at high speed motions on the elastic vibrations was highlighted. A numerical kinematical and dynamical modelling in rigid and flexible links hypothesis was presented in [1, 2], using a simplified CAD model developed in ADAMS software and analysed as flexible link system in ADAMS AutoFlex module.

The dynamic behaviour a flexible space robot with joint friction was analysed in [6] by developing the dynamic equations using Jourdain's velocity variation principle and the single direction recursive construction method, concluding that the Coulomb friction model is limited in describing the nonlinear features of friction. Furthermore, an active controller of a flexible space robot considering joint friction was designed, studied and validated using ADAMS software [5]. A review of the main principal methods used in literature for kinematical and dynamical analysis of flexible mechanical systems is presented in [10].

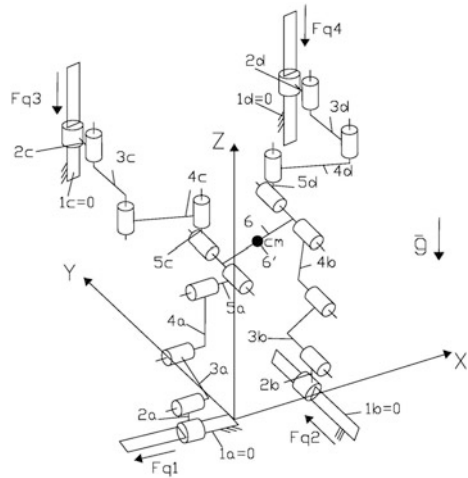
The paper aims at presenting representative results on the influence of the link flexibility and active joint friction on the dynamic behaviour of parallel robots, based on a case study of the 4DOF Isoglide4 manipulator [3] by approaching the robot modelling in ADAMS software and ADAMS Autoflex module to highlight their effect on the end-effector motion accuracy and the driving forces.

2 Problem Formulation

The paper deals with the modelling and simulation of the Isoglide4 parallel robot with decoupled motions [3], Fig. 1, in the assumption of flexible links 3a, b, c, d and 4a, b, c, d and considering friction in the four prismatic active joints $q_1 \dots q_4$.

This parallel robot (Fig. 1) is composed by four arms (a, b, c and d), containing each 3 revolute joints with parallel axes, and connected to the end-effector 6 through revolute joints. And additional load 6' is added in the centre of mass (cm) of the mobile platform 6. The end-effector has three decoupled translational motions (along X, Y and Z axis) and one coupled rotational motion (on Y axis) obtained through differential motion of the two vertical linear drivers. This robot is included in a parallel mechanism family proposed in literature [4] as parallel tool machine, raising multiple issues on the link flexibilities and joint frictions.

Fig. 1 Kinematical scheme of the Isoglide4 parallel robot



This study is based on the CAD model developed in the ADAMS software considering the following assumptions:

- the robot links are modelled using simple shape steel bodies: cylinders and parallelepipeds, with physical properties systematized in Table 1. The masses of links 5a, c, d are not significant and thus neglected;
- the gravity acts in the negative sense of the Z axis;
- a supplementary mass 6' of 10 kg is used as robot load;
- using ADAMS AutoFlex module, the links 3 and 4 of each arm are transformed into flexible links; their natural frequencies up to 1000 Hz are considered in simulations;
- the open loop control is applied in the parallel robot simulations;

Table 1 Geometric and mass parameters (according to Fig. 1)

Lengths		Masses	
$l_{2a} = l_{2b} = l_{2c} = l_{2d}$	130 mm	$m_{2a} = m_{2b} = m_{2c} = m_{2d}$	17.10 kg
l_{3a}	677 mm	m_{3a}	26.90 kg
l_{3b}	711 mm	m_{3b}	28.65 kg
l_{3c}	752 mm	m_{3c}	22.81 kg
l_{3d}	638 mm	m_{3d}	23.58 kg
l_{4a}	792 mm	m_{4a}	31.98 kg
l_{4b}	698 mm	m_{4b}	27.99 kg
l_{4c}	630 mm	m_{4c}	28.99 kg
l_{4d}	702 mm	m_{4d}	28.97 kg
l_6	300 mm	m_6	17.00 kg
l_5	120 mm	m_5	0 kg

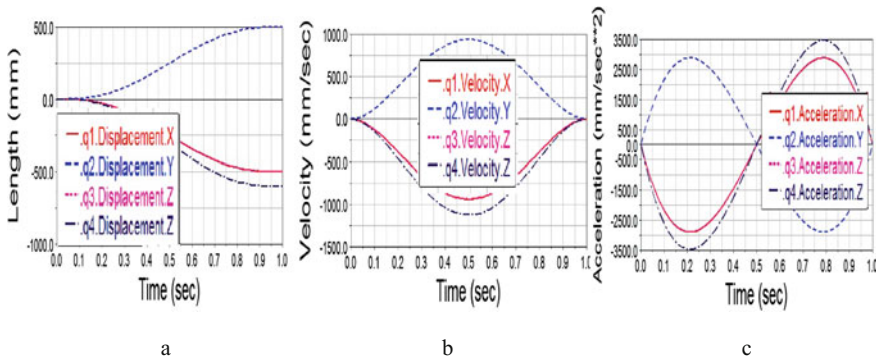


Fig. 2 Motion generated in the active joints q1, q2, q3 and q4: **a** displacement, **b** velocity, **c** acceleration

- the numerical simulations are carried out considering a representative linear trajectory in the Cartesian space between two points, using a fifth degree polynomial movement law in each active joint (Fig. 2, q1 and q3 have identical motion laws), which allow the end-effector maximum acceleration reaching 5.5 m/s^2 , while the linear actuators develop a maximum acceleration of 3.5 m/s^2 and a maximum velocity of $\sim 1 \text{ m/s}$; the strokes of the driving motions along the X (q1), Y (q2) and respectively Z (q3) axis are each of 500 mm and the coupled rotational motion along Y axis is done by the difference between the motions q3 and q4 (the q4 stroke equals 600 mm);
- the coefficient of friction in active joints are 0.016 (static) and 0.01 (dynamic).

Starting from these data, a comparative analysis on the kinematic and dynamic behaviour of the Isoglide4 parallel robot with flexible vs. rigid links, in both assumptions of considering and neglecting the friction in the active joints, is performed in the next chapters. The motion errors on a planned trajectory, due to the link flexibility, are investigated; the influence of friction and link flexibility on the driving forces is also approached in the paper.

3 Effects of Links Flexibility on Robot Behaviour

Based on the CAD simplified rigid link model developed in the ADAMS software (Fig. 3a), the flexible link robot model (Fig. 3b) is obtained using ADAMS AutoFlex module.

The links elasticity influence on the robot kinematic behaviour is highlighted in Fig. 4 by drawing the time variation of the resultant motion (displacement—Fig. 4a, velocity—Fig. 4b and acceleration—Fig. 4c) of the mobile platform mass centre (cm, Fig. 1) in relation to the ideal trajectory achieved by the robot with rigid links. The results show that the elasticity has a significant impact on the end-effector

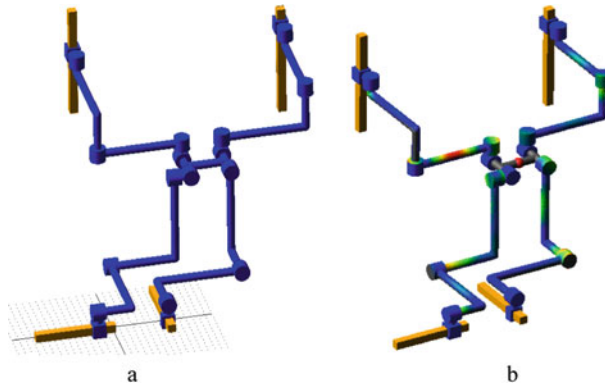


Fig. 3 ADAMS model of parallel robot in the initial position on the selected trajectory: **a** rigid links model and **b** flexible links model

motion, causing an oscillating evolution of the kinematic parameters relative to the planned trajectory and hence significant displacement, velocity and acceleration errors. Thus, for the considered trajectory (Fig. 2) the maximum resultant displacement error reaching worth ~ 45 mm is recorded at the trajectory ends (Fig. 4a) due to inertial effect. The maximum resultant errors of the velocity on the trajectory reach values up to 15 mm/s (Fig. 4b), and the resultant acceleration records errors up to 7500 mm/s^2 (Fig. 4c), i.e. acceleration maximum relative errors of $\sim 125\%$. Larger errors are registered for the angular motion of the mobile platform, e.g. velocity relative errors up to 175% (Fig. 4d).

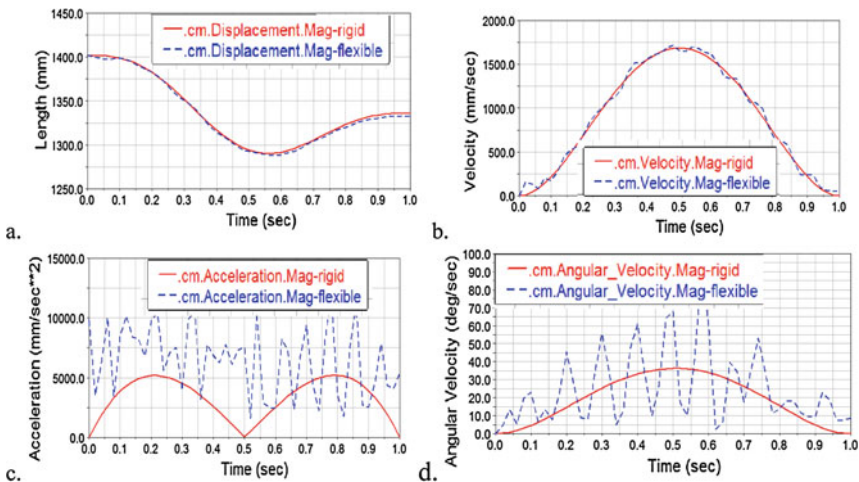


Fig. 4 End-effector motion magnitude (the length of the resultant vector) on the planned trajectory, in rigid (*red—continuous line*) and flexible link hypothesis (*blue—dashed line*): **a** the resulting displacements, **b** the resulting linear velocities, **c** the resulting linear accelerations, **d** the angular velocities

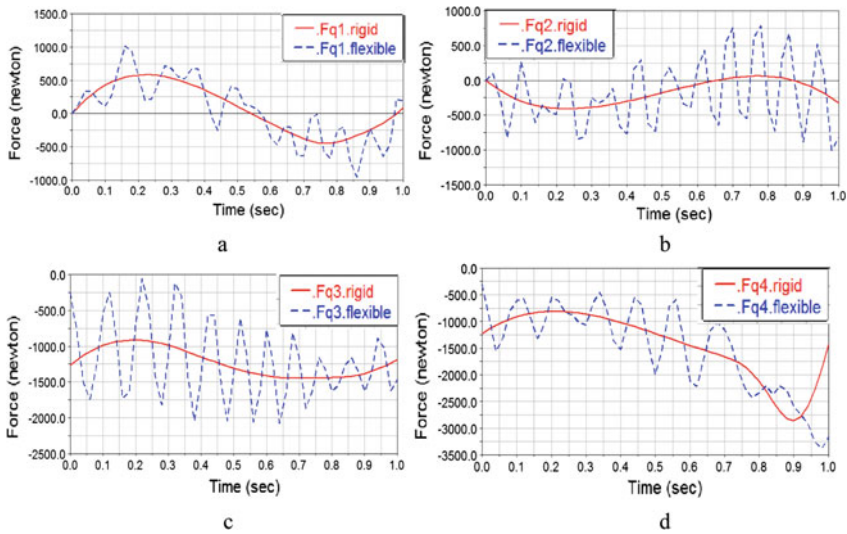


Fig. 5 Driving forces needed in the active joints: **a** q1, **b** q2, **c** q3 and **d** q4, in rigid links hypothesis (red—continuous line) and flexible links hypothesis (blue—dashed line) (color figure online)

The links elasticity influence on the robot dynamic behaviour is determined by analyzing the evolution of the axial forces in the active joints ($q1\dots q4$) and their errors in relation to the ideal case of rigid links. The obtained results (Fig. 5) show a relatively high frequency oscillatory regime of active forces, with negative impact on the robot operation due to the additional rapid varying loads on the linear actuators. It can be remarked that all four actuators are affected by the links elasticity effects to a similar extent, the driving force relative errors registering maximum values of approximately 100 % (Fig. 5).

4 Influence of Friction on Driving Forces

The joint friction influences the robot dynamic behaviour in both assumptions of rigid and flexible links, having a major impact on the driving forces in the active joint, as Fig. 6 shows. The normal forces in the active prismatic joints, transmitted to the base link, generate additional resistant friction forces for the linear actuators and thus changing the magnitude of the driving forces. In the case of rigid links robot, the driving forces with friction are registering significant absolute errors in relation with the ideal joints assumption for the active joints q1 (up to 475 N, Fig. 6a, b) and q2 (up to 700 N, Fig. 6c, d), and friction has less influence on the other two vertical actuators (Fig. 6e–h).

The links flexibility increases in some extent the impact of friction forces on the driving forces, but keep the same frequency profile of active forces variation

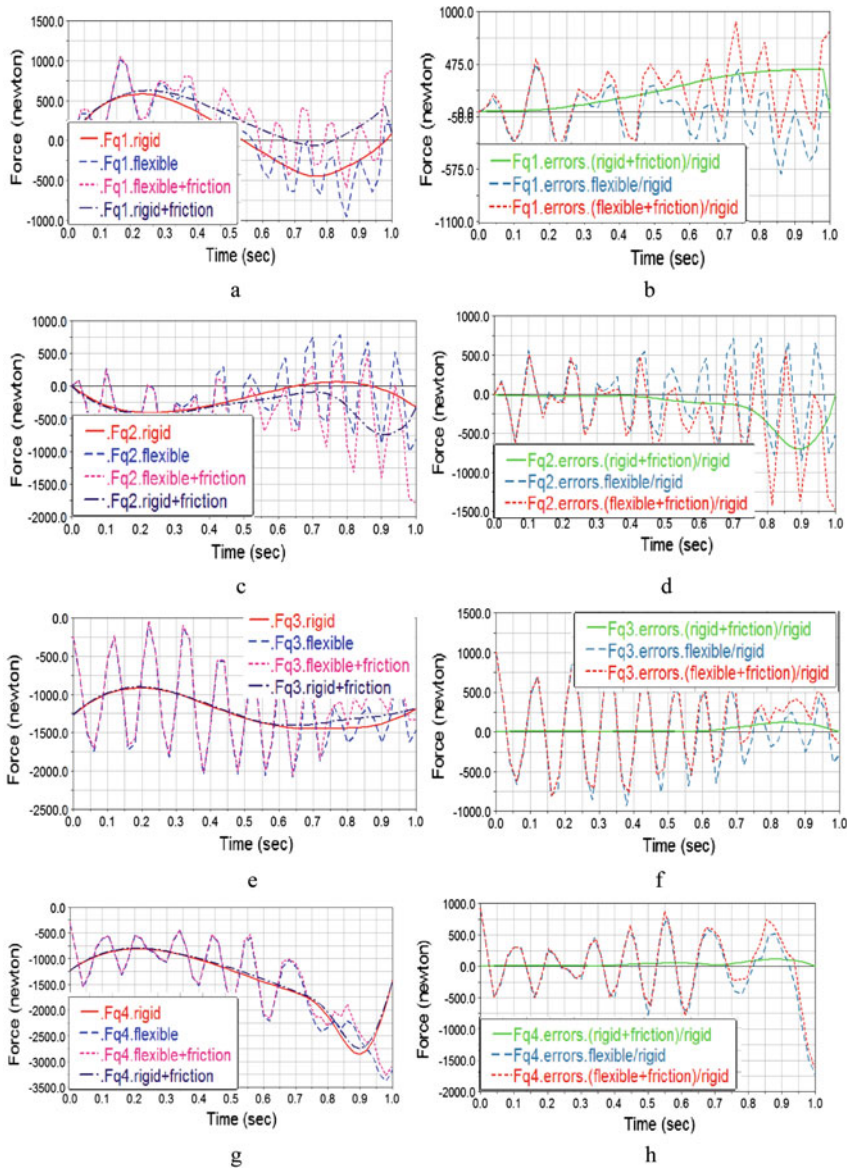


Fig. 6 a, c, e, g Driving forces: *red*—rigid link hypothesis, *blue*—flexible link hypothesis, *dark blue*—rigid link hypothesis with friction in active prismatic joints, *pink*—flexible link hypothesis with friction in active prismatic joints; b, d, f, h absolute errors of active forces, relative to the rigid links case: *green*—rigid links and joint friction, *blue*—flexible links, *red*—flexible links and joint friction (color figure online)

comparing with the no friction assumption. Comparing with the rigid link robot without friction, it can be highlighted that the driving forces are doubled when only the elasticity is considered and are tripled if the joint friction occurs, mainly for the active joints q_1 (Fig. 6a) and q_2 (Fig. 6c).

5 Conclusions

This comparative study of the Isoglide4 parallel robot with flexible links and friction in the four active prismatic joints in relation with its ideal variant (rigid link and no friction assumption), allows us to draw the following conclusions:

- the link flexibility has a significant influence on the robot trajectory accuracy, large variations of the end-effector displacements, velocities and especially accelerations can occur from the planned motion trajectory;
- the link flexibility has an important influence on the time variation of driving forces, increasing both the forces magnitude and frequency;
- the joint friction generates relevant additional resistance forces and thus increases the driving forces.

According to the presented results and conclusions, the designers of parallel robots should develop deep knowledge on the kinematic and dynamic behaviour of the robot with flexible links and joint friction in order to identify the best solutions for a high accuracy operation and appropriate selection of the actuators according to the real power and force requirements. Also, a future work will aim at comparing the simulation results with real robot measurements.

References

1. Cretescu, N.R.: Kinematic and Dynamic Simulation of a 3DOF Parallel Robot. Bulletin of the Transilvania University of Brasov, vol. 8 (57) No. 1, Series I—Engineering Sciences, ISSN 2065-2119 (Print), ISSN 2065-2127 (CD-ROM), pp. 73–78 (2015)
2. Cretescu, N., Neagoe, M.: Rigid versus flexible link dynamic analysis of a 3DOF Delta type parallel manipulator. Appl. Mech. Mater. **762**, 101–106 (2015). Trans Tech Publications, Switzerland, ISBN: 978-3-03835-444-4. <http://www.scientific.net>
3. Gogu, G.: Mobility criterion and overconstraints of parallel manipulator. In: Proceeding of CK005 (2005)
4. Gogu G.: Structural synthesis of parallel robots. Part 1: Methodology. Springer (2008)
5. Liu, X.-F., Li, H.-Q., Chen, Y.-J., Cai, G.-P.: Dynamics and control of space robot considering joint friction. Acta Astronaut. **111**, 1–18 (2015)
6. Liu, X.-F., Li, H., Wang, J., Cai, G.: Dynamics analysis of flexible space robot with joint friction. Aerosp. Sci. Technol. 164–176 (2015)
7. Lovasz, E.-C., Perju, D., Modler, K.-H., Modler, M., Gruescu, C.M., Maniu, I., Comşa, A.: On the structural analysis of the mechanisms with elastic connections. In: The 11th IFToMM International Symposium on Science of Mechanisms and Machines, Springer Series Mechanisms and Machine Science, vol. 18, pp. 59–67 (2014)

8. Modler, N., Modler, K.-H., Hufenbach, W., Lovasz, E.-C., Perju, D., Margineanu, D.: A design of compliant mechanism with integrated actuators. In: 10th International Symposium on Science of Mechanisms and Machines SYROM, Brasov, pp. 655–664 (2010)
9. Piras, G., Cleghorn, W.L., Mills, J.K.: Dynamic finite-element analysis of a planar high-speed, high-precision parallel manipulator with flexible links. *Mech. Mach. Theory* **40**(7), 849–862 (2005)
10. Shabana, A.: Flexible multibody dynamics review of past and recent development. *Multibody Sys. Dyn.* **1**, 189–222 (1997)

Part XV
Robotics—Robotic Applications

Automated Handling and Draping of Reinforcing Textiles—Challenges and Developments

J. Brinker, I. Prause, P. Kosse, H.-C. Früh, S. Printz, C. Henke, M. Hüsing, B. Corves, R. Schmitt, T. Gries and S. Jeschke

Abstract The handling of dry, pre-impregnated semi-finished textiles in the production of fibre-reinforced structures with complex geometries is still performed mainly manually resulting in long processing times, low reproducibility and high manufacturing costs. In this context, the scope of the project AutoHD is to fully automate the draping and handling process of complex, three-dimensional fibre composite structures with high degrees of deformation and multiaxial curvature. Based on the involved subsystems, this contribution presents challenges and progresses of ongoing research and future investigations.

Keywords Automated handling · Draping · Preforming · Mechanism design · Composite materials

J. Brinker (✉) · I. Prause · M. Hüsing · B. Corves
Department of Mechanism Theory and Dynamics of Machines (IGM), RWTH Aachen University, Aachen, Germany
e-mail: brinker@igm.rwth-aachen.de

P. Kosse · R. Schmitt
Laboratory for Machine Tools and Production Engineering (WZL) of RWTH, Aachen University, Aachen, Germany
e-mail: p.kosse@wzl.rwth-aachen.de

H.-C. Früh · T. Gries
Institute of Textile Technology (ITA) at RWTH Aachen University, Aachen, Germany
e-mail: hans-christian.frueh@ita.rwth-aachen.de

S. Printz · C. Henke · S. Jeschke
Institute for Management Cybernetics e.V. (IfU), RWTH Aachen University, Aachen, Germany
e-mail: stephan.printz@ifu.rwth-aachen.de

1 Introduction

The objective of the German industry sponsored AiF research project AutoHD is to develop innovative solution strategies in order to fully automate the draping and handling process of complex, three-dimensional fibre-reinforced plastics (FRP) structures with high degrees of 3D-contours and multiaxial curvature [1]. In this context, draping defects (e.g. wrinkles, gaps, and loops) need to be detected early during the draping process in order to meet the strict quality requirements under industrial conditions (e.g. short cycle times, robustness, and reliability). Therefore, inline optical measurement systems are integrated directly into the process. However, such integration does not allow the use of moulding press tools but requires the use of handling systems. The connection of the sensor system to the control loop of the draping process allows for a direct intervention of the handling system on these defects.

In summary, the innovative aspects of the research undertaken in this project are the automation of the handling and draping process. In particular, preforming of objects with varying multiaxial geometries, online detection of defects, and online data reconciliation comparing the 3D fibre orientation between the real and the simulated draped preforms are considered as challenges.

Figure 1 illustrates the subsystems involved in the handling and draping process. The planar textile is grasped by means of suitable grippers (Sect. 3.1). The motion of these grippers (i.e. the drape motion) is performed by individually controlled mechanisms. The mechanisms are attached to a platform constituting the end-effector (Sect. 3.2) which in turn is attached to an industrial robot (i.e. the regional structure). The process is monitored by three on-board sensor systems attached to the end-effector and one external system (Sect. 3.3).

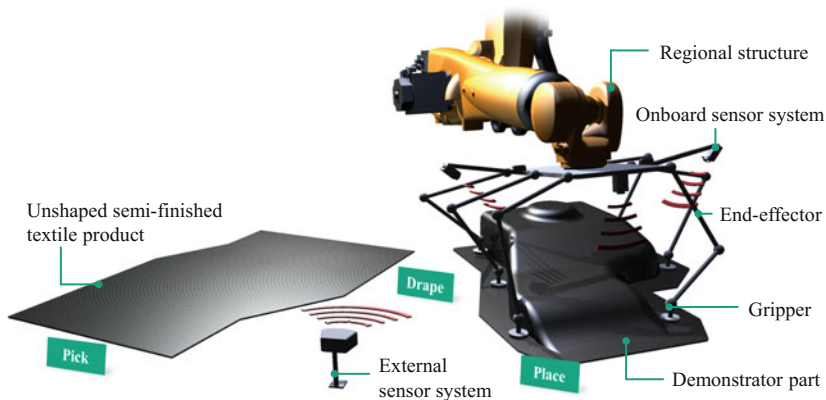


Fig. 1 Illustration of the automated handling and draping process during preforming of FRP

2 Task Definition

2.1 Demonstrator Part

The characteristics of a representative demonstrator part (cf. Fig. 2) are defined within workshops and in partnership with the project supporting committee. This part exhibits a multi-axial complex shape including varying edges and curves of different radii. It thus combines several draping challenges in one part. Accordingly, a single-layer, biaxial carbon FRP part with a size of about $760 \times 880 \text{ mm}^2$ is considered. In addition to the inherent limpness of the FRP part, challenges from the material point of view include the air permeability and the high anisotropy. The geometry was specifically chosen for its unsymmetrical characteristics that induce regions where drape defects (e.g. wrinkles, gaps, and loops) potentially occur. Alongside this, small convex and concave radii (24–56 mm) were added.

In addition, a cylindrical elevation was added to the top of the demonstrator part. The region around this elevation tends to encourage wrinkles to form if no homogenous circular force is applied to drape the textile. Furthermore, the behaviour of the preform regarding different fibre directions relative to the rounded shear edge can be investigated.

2.2 Drape Paths

Forming or draping of textile structures is an essential part of the manufacturing process of textile preforms. The deformation behaviour of flexible semi-finished textile products is very complex. Therefore, the material selection of the semi-finished textile is typically performed for a given component geometry using a trial-and-error process. Draping is performed manually by experienced professionals correcting the resulting draping defects. This procedure is technically and economically deficient with respect to a large-scale production of FRP components. The time and cost-intensive process of material selection by trial-and-error and manual production can be improved by proper material modelling and process

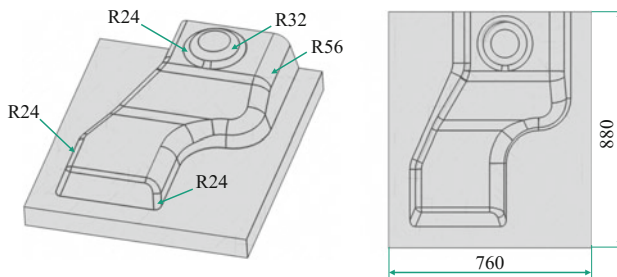
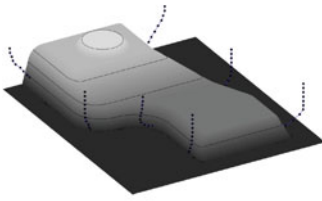


Fig. 2 The mould for the demonstrator part and its characteristics

a) Simulated paths



b) Planar paths

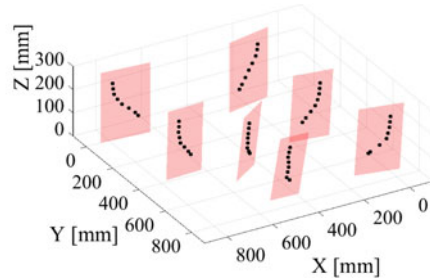


Fig. 3 Derivation of trajectories from drape simulations

simulation. The objective of such simulation is to predict the deformation behaviour of a fabric with a given force applied during preforming.

There are several computer-based methods for the so-called drape simulation. The available methods differ in their computational complexity and level of detail. Purely kinematic or finite element method (FEM) based models can be applied [2]. As input for the simulation, the mechanical material properties of the semi-finished textile (e.g. Young's modulus of elasticity, bending stiffness, friction coefficients between the reinforcing fibres as well as between the reinforcing fibres and the tool) are determined using different testing methods such as picture frame and cantilever trials.

Material tests are carried out to determine the minimum number of grasping points and the minimum distance between them (depending on the bending stiffness). To define the corresponding drape motions, here, kinematic drape simulations are performed. According to the test and simulation results, seven gripper arms are required to grasp the textile and to perform the draping. During stepwise simulation, each grasping point is tracked and finally defines a set of coupler points (cf. Fig. 3a).

It can be seen that these points for each individual gripper approximately lie on planes. For reasons of simplification and concerning the end-effector design (Sect. 3.2), each set of points is approximated by means of principal component analysis identifying least square best-fit planes (Fig. 3b). In these planes, the desired movement space ranges between 154–171 mm in height and 22–108 mm in width. The minimum and maximum absolute deviations of the regression are theoretically 0.0025 or 3.9836 mm, respectively. The average standard deviation is found to be 1.4342 mm.

3 Development of Subsystems

3.1 Grippers

Many research projects have focused on handling systems and the related handling principles (e.g. needle, vacuum), respectively (cf. e.g. [3–5]). When selecting a

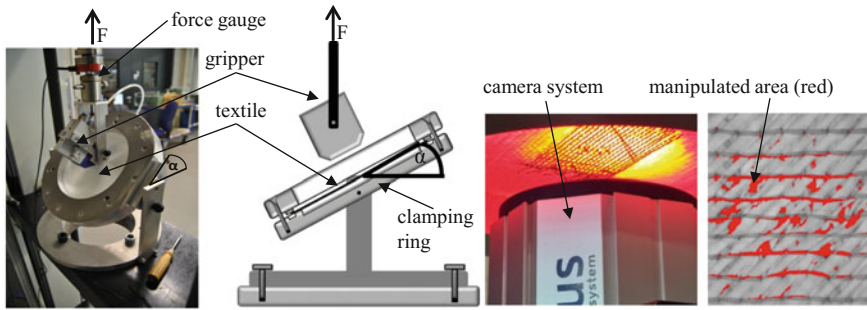


Fig. 4 Test stand (*left*) and optical analysis of manipulated area (*right*)

suitable gripper for textile semi-finished products, different criteria must be considered, e.g. the geometry of the gripping and placing position, the dimensions of the workpiece as well as its material properties [4]. An important criterion is the reliability of the gripping process. According to [6], the reliability depends on a variety of factors, such as material flexibility, operating speed, gripping technology, and environment. However, a methodology to select gripper technologies for an optimized textile handling process with minimized damages to the textile and reduced energy consumption is still missing.

Based on these challenges a methodology is developed to select the right gripper technology for the automated handling of reinforcement textiles. The methodology includes pull-out-experimentations and optical analysis (cf. Fig. 4) with which a so-called handling-value can be evaluated. This characteristic figure considers textile damages as well as the achievable gripping force. With this method a comparison between different gripping technologies and the selection of a suitable gripping concept are possible.

The methodology is applied and validated on non-crimp-fibre textiles using vacuum- and needle-technology. The maximum gripping forces of vacuum based grippers are relatively low compared to needle grippers though no measurable damage occurs on the reinforcement textiles. The positive locking of the needles with the rovings of the textile causes imperfections of the gripped textile. In contrast to vacuum based grippers, there is no maximum gripping force measurable but instead the tests are stopped at discrete gripping forces where the imperfection area reaches a discrete size.

Under certain circumstances (e.g. combination of gripping force, force vector angle, and textile type) the needle grippers show better handling-values over vacuum based grippers. This is partly due to spring back effects of the textiles when pulling out the needles. However, vacuum based grippers are selected since sliding of the textile on the gripper surface is allowed and sometimes even welcome.

3.2 End-Effector

Due to reasons of cost, it is intended to design a mechanism with planar output motion for each of the seven drape paths (Sect. 2.2). Also, a single mechanism whose motion space covers the coupler points of all seven drape paths is desired. The desired motion space is $250 \times 200 \text{ mm}^2$. The orientation of the grippers needs to remain constant with its contact area parallel to the X-Y-plane (cf. Fig. 3). Thus, a translational 2-degrees-of-freedom output motion is desired. Loads (i.e. components weights, inertial forces, and drape forces) are less than 15 N (including buffer for task adaptations) and predominantly imposed parallel to the movement space. Process speeds are considered not crucial for the preliminary design. Further requirements are the minimum installation space in order to avoid interference with the sensor system and high adaptability and scalability for potential future task adaptations.

Based on known type synthesis approaches, 242 possible structures with planar translational output motions can be identified [7]. Appropriate selection criteria (e.g. restricting the maximum number of kinematic chains and joints or excluding certain drive positions to reduce the inertia effects) are formulated and applied. In doing so, the number of potential structures is reduced to nine [8, 9].

Subsequent weighted evaluation by different criteria, such as the degree of complexity, the practicability, and the kinetostatic performance, revealed two predestined structures whose kinematic chains, due to the demand for a translational output motion, contain parallelograms (cf. Fig. 5). These structures are analysed in the course of a preliminary dimensional synthesis. In this context, their installation space and kinetostatic performance have been assessed quantitatively [9].

On the one hand, due to the parallel architecture the transmission capabilities of III-RRR are superior. More importantly, on the other hand, reasonable results can also be achieved with the IIII-manipulator. Taking into account the installation space as additional performance index, the IIII-manipulator requires only 33 % of the installation space required by the translational parallel manipulator. Hence, future investigations will focus on the detailed design of IIII-manipulators and their integration into the end-effector. Against this background, a major challenge will be to mount the mechanisms individually to the platform in accordance with the spatial arrangement and inclinations of the motion planes.

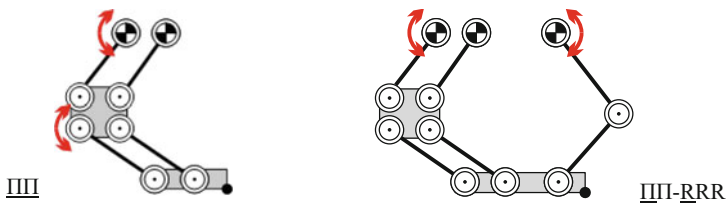


Fig. 5 Translational serial manipulator (left) and translational parallel manipulator (right)

3.3 Sensor Systems

Two separate machine vision systems are developed to control the handling and draping process. The first one is positioned externally next to the pick-up place of the cut textile. The second system will be integrated into the end-effector to detect potential drape defects.

The external machine vision system is deployed to measure the exact position and orientation of the textile. Furthermore, the locations of attached markers relative to the textile are refined and registered into the fixed world coordinate system of the robot, thus providing the required information for the robot control loop. A very important quality characteristic for the final part stability is the fibre orientation. The measurement of these black fibres requires a special illumination. In [10] a diffuse dome illumination is used. Alternatively, a flat diffuse illumination is possible [11]. However, both variants require the coverage of the whole measurement area which is typically below $100 \times 100 \text{ mm}^2$. An adaption for this handling and draping process is not possible. The space above the textiles needs to be accessible by the handling system and the dimensions of the textile (Sect. 2.1) exceed the conventional measurement by factors.

In the scope of this project, the influence of an external spot-like illumination source in combination with varying camera positions have been analysed (cf. Fig. 6). It turns out, that the vertical angle β between the textile plane and the direction from the illumination to the textile centre point is insignificant compared to angle α between the fibre orientation and light source direction (cf. Fig. 6). Interfering reflections leading to overexposure only become visible at angles $\alpha > \pm 50^\circ$. Despite the non-optimal illumination, an estimation of the global fibre orientation seems possible and is subject of ongoing research.

The second machine vision system will be integrated into the end-effector. In the past, laser triangulation sensors have been used to measure the geometry [11]. Typically, these sensors are guided by a handling system. Since this concept cannot be integrated into the end-effector itself, a photogrammetric approach is chosen. Three industrial cameras are directed to the same measurement area from three complementary directions. The current research focus lies on the analysis of the

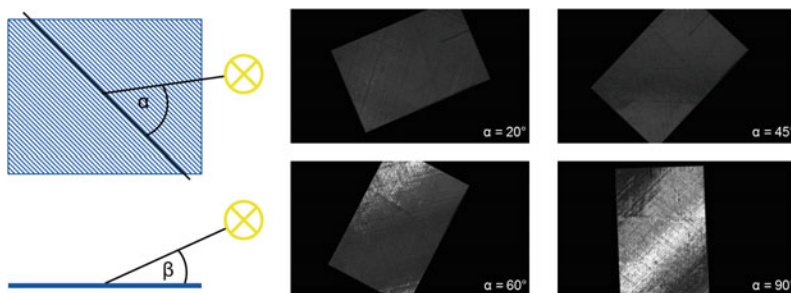


Fig. 6 Analysis of illumination strategies regarding the visible fibre orientation

achievable measurement uncertainty especially in respect of simple calibration procedures and nominal geometry.

4 Conclusions

This contribution presented the key aspects of the research project AutoHD. A demonstrator part and its characteristics were introduced providing the basis for the derivation of the drape paths to be performed by the handling system. Against this background, current challenges and developments of the subsystems grippers, end-effector and sensor systems were presented.

Acknowledgments The authors thank the German Federation of Industrial Research Associations “Otto von Guericke” eV (AiF) for the financial support of the research project “Automated handling and draping of reinforcing textiles for multiaxially curved composite structures—AutoHD” Project No 18264 N/4 (cf. www.auto-hd.de).

References

1. Corves, B., Brinker, J., Prause, I., Hüsing, M., Abbas, B., Krieger, H., Kosse, P.: AutoHD—Automated Handling and Draping of Reinforcing Textiles; Aufl. 2015. Mechanisms, Transmissions and Applications: Proceedings of the Third MeTrApp Conference 2015/Corves, Burkhard J. [Hrsg.] Third MeTrApp Conference 2015, Mechanisms and Machine Science, vol. 31, pp. 301–309 (2015)
2. Biermann, D., Hufenbach, W., Seliger, G.: Serientaugliche Bearbeitung und Handhabung faserverstärkter Hochleistungswerkstoffe. In: Untersuchungsbericht zum Forschungs- und Handlungsbedarf, TU Dresden (2008)
3. Gries, T. et al.: Technologies for Series Production of near-net-shape Textile Preforms. In: Hui, D., Loboda, P., Chen, X., Wang, Y. (eds.), Use of Textile Composites Technology for Safer Vehicles; Nato Advanced Research Workshop, Kiev, Ukraine 18–21 May, Kiev: National Technical University of Ukraine, Kiev Polytechnic Institute (2009)
4. Straßer, G.: Greiftechnologie für die automatisierte Handhabung von technischen Textilien in der Faserverbundfertigung. Technical University Munich, Dissertation (2012)
5. Kordi, M.T., Hüsing, M., Corves, B.: Development of a multifunctional robot endeffector system for automated manufacture of textile preforms. In: IEEE/ASME International Conference on Advanced Intelligent Mechatronics (2008)
6. Stephan, J.: Beitrag zum Greifen von Textilien. Technical University Berlin, Fraunhofer IPK, Dissertation (2001)
7. Nurahmi, L.: Conceptual Design and Analysis of 2 Degrees of Freedom Translational Manipulators. Master Thesis, Institut de Recherche en Communications et Cybernétique de Nantes (IRCCyN), Nantes (2012)
8. Brinker, J., Paris, J., Müller, M., Hüsing, M., Corves, B.: Mechanism type synthesis approach for automated handling and multiaxial draping of reinforcing textiles. In: EUCOMES: 6th European Conference on Mechanism Science, Nantes, France, 20–23 Sept 2016 (under review)
9. Brinker, J., Müller, M., Paris, J., Hüsing, M., Corves, B.: Mechanism design for automated handling and multiaxial draping of reinforcing textiles. In: ASME 2016 International Design Engineering Technical Conferences and Computers and Information in Engineering Conference, Charlotte, North Carolina, 21–24 August 2016 (under review)

10. Schmitt, R., Fürtjes, T., Abbas, B., Abel, P., Kimmelmann, W., Kosse, P., Buratti, A.: Real-time machine-vision-system for an automated quality monitoring in mass production of multiaxial non-crimp fabrics. In: 15th IFAC Symposium on Information Control Problems in Manufacturing (INCOM), Ottawa, Canada (2015)
11. Kosse, P., Soemer, E., Schmitt, R., Engel, B., Deitmerg, J.: Optische Erfassung und Analyse der Faserwelligkeit gebogener Faser-Thermoplast-Verbunde. In: *tm – Technisches Messen* **83** (1), 43–52 (2016)

Author Index

A

Abel, Dirk, 371
Altuzarra, Oscar, 457
Amezua, Enrique, 311
Arjana, Davidescu, 37, 69

B

Badodkar, D.N., 331
Balandraud, Xavier, 343
Balbayev, Gani, 125
Barreto, Juan Pablo, 89
Bouton, Nicolas, 279
Bouzzgarrou, Belhassen-Chedli, 133, 379
Brell-Cokcan, Sigrid, 371
Brinker, Jan, 321, 485
Butnariu, Silviu, 427

C

Cafolla, Daniele, 401
Campa, Francisco J., 457
Carmen, Sticlaru, 69
Ceccarelli, Marco, 401
Chapelle, Frédéric, 343
Chebab, Zine Elabidine, 279
Chen, Hu, 177
Chen, Y., 155
Ciupe, Valentin, 197
Ciupitu, Liviu, 59
Corral, Javier, 457
Corves, Burkhard, 89, 177, 241, 299, 321, 391, 485
Craciun, Dan, 269
Cretescu, Nadia, 143, 473

D

Dan, Perju, 47
Dede, Mehmet Ismet Can, 447

Detert, Tim, 241, 299
Diez, Mikel, 457
Ding, Wan, 241
Dolga, Lia, 351
Dolga, Valer, 351, 409
Drewniak, Józef, 15
Dwarakanath, T.A., 331

E

Éné, Marin, 167

F

Fauroux, Jean-Christophe, 133, 279, 343
Florescu, Mihaela, 361
Früh, Hans-Christian, 485

G

Gagnol, Vincent, 133, 379
Garlicka, Paulina, 15
Gherman, Bogdan, 427
Girbacia, Florin, 427
Girbacia, Teodora, 427
Gogu, Grigore, 133, 279
Goldfarb, Veniamin, 209
Gosselin, Clement, xv
Gries, Thomas, 485
Grigorescu, Sanda Margareta, 37, 77, 409
Gronowicz, Antoni, 251, 401
Gruescu, Corina, 3, 229

H

Haarhoff, Daniel, 371
Handroos, Heikki, 465
Harmeling, Frank, xvii
Haschke, Tobias, 321
Hatton, Benjamin, 133
Henke, Christoph, 485

Hernández Frías, Alfonso, 311

He, S.-H., 155

Hüsing, Mathias, 177, 321, 391, 485

I

Ichikawa, Masahiro, 417

Ishida, Kazuyoshi, 417

Iskakov, Zharilkassin, 107

Iurkova, Galina, 217

Ivanescu, Mircea, 259, 361

Ivanov, Konstantin, 125

J

Jaliu, Codruta, 143

Jerzy, Kopec, 15

Jeschke, Sabine, 485

K

Kane, Mark, 209

Kolditz, Melanie, 371

Kopec, Jerzy, 15

Kosse, Philipp, 485

Kuantama, Endrowednes, 269

Kurtenbach, Stefan, 177, 391

L

Lagoo, Ketan, 331

Liu, Z.-H., 155

Lorenz, Michael, 321

Lovasz, Erwin-Christian, 3, 37, 47, 77, 197, 229, 409

M

Macho, Erik, 311

Mailloux, Maxime, 167

Makino, Koji, 417

Maniu, Inocentiu, 47, 229

Mănoiu-Olaru, Sorin, 259

Mărgineanu, Dan Teodor, 69, 77, 197

Mărgineanu, Eugenia, 69

Matsuo, Hiroshi, 187

Matsuura, Daisuke, 187

Mesaros-Anghel, Voicu, 3

Mezouar, Youcef, 279

Milojević, Andrija, 465

Müller, Mario, 177

Modler, Karl-Heinz, 47

Mohan, Santhakumar, 391

Mohanta, Jayant Kumar, 391

Moldovan, Cristian, 3, 47, 351

Moldovan, Macedon, 99

Mousavi, Said, 379

N

Neagoe, Mircea, 99, 143, 473

Nefzi, Marwène, xvi

Nguyen, T.T.N., 177

Nitulescu, Mircea, 259, 361

O

Olinski, Michał, 401

P

Pan, C., 177

Patic, Paul, 287

Paulina, Garlicka, 15

Pavlović, Nenad, 465

Perju, Dan, 47

Petuya, Victor, 311

Pîslă, Doina, 427

Plitea, Nicolae, 427

Pop, Cristian, 37, 77, 409

Pop, Florina, 37, 77, 409

Prause, Isabel, 485

Printz, Stephan, 485

R

Ray, Pascal, 379

S

Sabourin, Laurent, 279

Santhakumar, Mohan, 391

Saulescu, Radu, 143, 473

Schmitt, Robert, 485

Schöler, Frederic, 89

Selvi, özgün, 437

Shalobaev, Evgenii, 209, 217

Shen, Huiping, 25

Shil'ko, Serge, 217

Simionescu, Ion, 59, 167

Sperzyński, Przemyslaw, 251

Starzhinsky, Victor, 209, 217

Sticlaru, Carmen, 69

Stoian, Ana Maria, 229

Sugahara, Yusuke, 187

Sun, Chi-Yu, 25

Surikov, Dmitry, 217

T

Tabara, Iulian Alexandru, 167

Takeda, Yukio, 187

Taner, Baris, 447

Tarca, Ioan Constantin, 269

Tarca, Radu, 269

Terada, Hidetsugu, 417

Tolocka, Rymantas Tadas, [217](#)

Tultayev, B., [125](#)

V

Van Dong Hai, Nguyen, [259](#), [361](#)

Visa, Ion, [99](#)

X

Xie, Jin, [155](#)

Y

Yang, Tingli, [25](#)

Yao, Yan-An, [241](#)

Yilmaz, Kuntay, [437](#)

Yuan, Han, [343](#)

Z

Zawiślak, Stan, [15](#)

Zemouri, Ryad, [287](#)

Zhang, Dan, [25](#)

Zhang, zhang, [311](#)

Zhao, Yaping, [117](#)